



EUROPEAN
COMMISSION

Community research

RECOSY

(Contract Number: **FP7-212287**)

DELIVERABLE (D-N°: **7.6**) Proceedings of the fourth Annual Workshop

Author(s): **AMPHOS**

Reporting period: e.g. **01/04/2011 – 30/03/2012**

Date of issue of this report : **01/06/2012**

Start date of project : **01/04/2008**

Duration : **48** Months

Project co-funded by the European Commission under the Seventh Euratom Framework Programme for Nuclear Research & Training Activities (2007-2011)		
Dissemination Level		
PU	Public	X
RE	Restricted to a group specified by the partners of the RECOSY project	
CO	Confidential, only for partners of the RECOSY project	





KIT SCIENTIFIC REPORTS 7626

4th Annual Workshop Proceedings of the Collaborative Project “Redox Phenomena Controlling Systems” (7th EC FP CP RECOSY)

Marcus Altmaier, Bernhard Kienzler, Lara Duro,
Mireia Grivé, Vanessa Montoya (eds.)

Marcus Altmaier, Bernhard Kienzler, Lara Duro,
Mireia Grivé, Vanessa Montoya (eds.)

**4th Annual Workshop Proceedings of the Collaborative Project
“Redox Phenomena Controlling Systems” (7th EC FP CP RECOSY)**

4th Annual Workshop Proceedings of the Collaborative Project “Redox Phenomena Controlling Systems” (7th EC FP CP RECOSY)

Marcus Altmaier
Bernhard Kienzler
Lara Duro
Mireia Grivé
Vanessa Montoya
(eds.)

Report-Nr. KIT-SR 7626

The report is printed without colours. The report with the original colours in different photos, tables, figures and logos, can be downloaded from the KIT Scientific Publishing homepage.

Karlsruher Institut für Technologie (KIT)
Institut für Nukleare Entsorgung

Amphos XXI Consulting S.L.
Passeig de Garcia i Faria, 49-51, 1^o-1^a
E08019 Barcelona
SPAIN

Impressum

Karlsruher Institut für Technologie (KIT)
KIT Scientific Publishing
Straße am Forum 2
D-76131 Karlsruhe
www.ksp.kit.edu

KIT – Universität des Landes Baden-Württemberg und
nationales Forschungszentrum in der Helmholtz-Gemeinschaft



Diese Veröffentlichung ist im Internet unter folgender Creative Commons-Lizenz
publiziert: <http://creativecommons.org/licenses/by-nc-nd/3.0/de/>

KIT Scientific Publishing 2012
Print on Demand

ISSN 1869-9669
ISBN 978-3-86644-921-3

FOREWORD

The present document is the proceedings of the 4th Annual Workshop of the EURATOM FP7 Collaborative Project ReCosy (Redox Phenomena Controlling System). The electronic version of these proceedings is also available in the webpage of the project (www.recosy.eu). The Workshop was hosted by KIT and held in Karlsruhe (Germany) 23rd – 26th January 2012. The project started April 2008 and has four years duration. It has 32 Contractors and 6 Associated Groups. Annual workshops bring together, Beneficiaries/Contractors, Associated Groups and external interested groups.

The proceedings serve several purposes. The key purpose is to document and make available to a broad scientific community the outcome of the RECOSY project. For this purpose, a considerable part of the project activity reporting is done through the proceedings, together with the outcome of a large number of scientific-technical contributions and Topical Sessions on different topics, which could be important for the development of the project. In the 4th Annual Workshop this topic focused on integration of redox processes in the Safety Case. Additional purposes of the proceedings are to ensure ongoing documentation of the project outcome, promote systematic scientific-technical development throughout the project, and to allow thorough review of the project progress.

All Scientific and Technical papers submitted for the proceedings have been reviewed by the EUCG (End-User-Consultancy-Group). The EUCG is a group specifically set up within the project in order to represent the interests of the end users to the project and its desired outcome. To this aim, the composition of the EUCG includes organizations representing national waste management or national regulatory interests and competence.

The proceedings give only very brief information about the project structure and the different activities around the project, such as training measures and dissemination of knowledge. Such information about the project can be found in detail under www.recosy.eu.

Finally, we want to thank all those who submitted Scientific and Technical contributions for review and, especially, the Workpackage leaders who provided the summary of the different workpackages for publication in these proceedings. We also want to give a special thanks to the reviewers, whose effort and hard work reflect their commitment and dedication to the project.

TABLE OF CONTENTS

THE PROJECT	1
THE FOURTH ANNUAL WORKSHOP	1
<i>Objectives</i>	2
<i>RTD sessions</i>	2
<i>Poster presentations</i>	5
<i>Topical session</i>	6
<i>Additional presentation</i>	7
<i>Structure of the proceedings</i>	7
SUMMARY OF WP ACTIVITIES	9
Introduction.....	11
Work performed by partners.....	11
References.....	20
WORK PACKAGE 3:.....	21
Introduction.....	21
Work performed by partners.....	21
WORK PACKAGE 4:.....	27
Introduction.....	27
WP 4.1.	28
WP 4.2.	44
WORK PACKAGE 5:.....	49
Introduction.....	49
Work performed by partners.....	49
References.....	51
WORKPACKAGE 6:.....	53
Introduction.....	53
Work performed by partners.....	54
References.....	64
S + T CONTRIBUTIONS	69
List of contributions	71

THE PROJECT

The EURATOM 7th EC Framework Program Collaborative Project REdox phenomena Controlling SYstems (RECOSY) started in April 2008 and extends over 4 years. Although redox is not a new geochemical issue, different questions are still not resolved. For this reason, main objectives of RECOSY project are a) the sound understanding of redox phenomena controlling the long-term release/retention of radionuclides in nuclear waste disposal, b) providing tools to apply the result to Performance Assessment/Safety Case, c) training of next generation and d) documentation and communication of the results. To this aim, the project set up a consortium of 32 Beneficiaries/Contractors and 6 Associated Groups. The consortium includes key European Research Institutes, Universities, National Waste Management Agencies and SMEs, from 13 EURATOM signatory states, Russia, Japan, Korea, USA and one European Joint Research Centre. The ReCosy concept is innovative in the scientific approach to the redox phenomena. It includes i) advanced analytical tools, ii) investigations of processes responsible for redox control (thermodynamically and kinetically controlled processes, surface reactions and microbial processes,...), iii) provision of required data on redox controlling processes, and iv) response to disturbances in disposal systems. The work program is structured along six RTD workpackages (WP1-6). They cover near-field and far field aspects as well as all relevant host-rocks considered in Europe. In WP1, the scientific state-of-the-art and its application to Performance Assessment/Safety Case is documented and regularly updated. WP2 focuses on development of redox determination methods. WP3 focuses on redox response of defined and near-natural systems. WP4 studies the redox reactions of radionuclides. WP5 focuses on Redox processes in radionuclide transport and WP6 deals with redox reactions affecting the spent fuel source-term. Specific workpackages on knowledge management, education and training (WP7) and administrative management issues (WP8) are also included in the project

The present proceedings document the outcome of the 4th Annual Project Workshop and give an overview of the outcome of the 4th project year.

THE FOURTH ANNUAL WORKSHOP

The 4th Annual Project Workshop was held in Karlsruhe (Germany) 23rd – 26th January 2012. The Workshop was hosted by KIT. There were 60 attendees at the workshop, representing Beneficiaries/Contractors, Associated Groups, the End-User Consultancy Group, and project external organizations. The workshop was organized in four days of oral presentations on results obtained within the project, two poster sessions, and a topical session on integration of redox processes in the Safety Case.

Objectives

The Workshop combines different activities and meetings with the following objectives:

- Informing about the scientific progress. For this purpose, plenary sessions are used for communicating results from the different technical workpackages and poster sessions.
- Informing about the administrative status.
- Informing/agreeing upon forthcoming reporting.
- Discussing various topics of interest for the consortium.
- Agreeing upon the forthcoming work program.

Emphasis was on scientific-technical topics with administrative issues kept to the minimum necessary.

RTD sessions

The workshop included plenary sessions where the results from the different workpackages were presented. Next to an overview of the achievements within the respective WP, scientific highlights were presented. The following presentations were given within the project.

WP2 session:

- M. Perdicakis, A. Chebil, M. Etienne. Can we use ultramicroelectrodes to perform electrochemistry in brines?
- S. Hagemann, B. P. Bischofer, , T. Scharge. Spectrophotometric and potentiometric investigation of iron (III) hydrolysis in chloride media
- M. Altmaier, D. Fellhauer X. Gaona, T. Kobayashi, V. Petrov. Np and Tc redox processes and solubility in aqueous media
- D. Steinbrück, F. Geißler, M. U. Kumke. Recent advances in multiplexed fiber-optical sensing for environmental applications

WP3 session:

- Ignatiadis, S. Betelu, C. Lerouge, G. Berger. Mechanistic and kinetic study (using electrochemical techniques) of pyrite (FeS₂) reduction by hydrogen (H₂) produced in situ by water electrolysis) in NaCl 0.1 M at 25°C
- L. Charlet. Se redox chemistry in presence of carbonates and Fe(II)-rich sulfides.
- M. J. Gimeno, L. F. Auqué, P. Acero, J. Gomez, M. P. Asta, M. Laaksoharju. Partial equilibrium-based redox estimations in groundwaters from crystalline systems
- K. Lázár, Z. Máthé. Redox changes in Boda Claystone samples as traced by monitoring the Fe²⁺/Fe³⁺ ratios in minerals
- F. Huber, D. Schild, T. Vitova, J. Rothe, T. Schäfer. U(VI) removal kinetics in the presence of magnetite and maghemite nanoparticles
- F. Bardelli, L. Charlet, M. Kang, A. Gehin, F. Chen. Nano-sized pyrite/greigite reactivity towards selenite and selenate
- K. Pedersen. Microbial redox controlling processes

WP4 session

- R. Hallam, N. Evans. Effect of Gluconate, EDTA, ISA and Picolinate on the Redox Chemistry of Technetium.
- M. Perdicakis, C. Malhomme, C. Bouchereau. Reactivity of pyrite towards soluble species of iodine and selenium
- S. Holgersson. Agreement between measured Eh and quantification of actinide oxidation states
- Ch. Marquardt, N. L. Banik, J. Luetzenkirchen, J. Rothe, T. Schäfer, D. Schild. Redox behaviour of neptunium, plutonium and technetium in Opalium Clay / Callovo-Oxfordian argillite – pore water systems.
- A. Romanchuk, A. Egorov, Y. Zubavichus, A. Shiryaev, S. Kalmykov. Redox speciation of plutonium upon sorption to hematite at ambient atmospheric conditions
- O. Riba, V. Montoya, M. Grivé, L. Duro. Study of uranium solubility under alkaline conditions with different reducing agents
- J. Tits, X. Gaona, A. Laube, E. Wieland. Actinide uptake by cementitious materials under hyperalkaline Conditions: Effects of the Redox State

- B. Lukšienė, R. Druteikienė, D. Baltrūnas, A. Gudelis, K. Mažeika, G. Lujanienė, D. Pečiulytė, V. Remeikis. Biogenic redox-active radionuclide/metal transformation. Peculiarities of radionuclide sorption onto iron-bearing phases.
- E. Krawczyk-Bärsch, K. Pedersen, A. Lehtinen, Speciation of uranium in biofilms and groundwater seeps from the granitic rock walls in the ONKALO tunnel (Finland)

WP5 session

- S. Savoye, B. Grenut, B. Frasca,, M. Schlegel, Th. Vercouter, How mobile are redox-sensitive elements (I, Se, U) in the Callovo-Oxfordian claystones under experimental conditions close to the in-situ ones?
- K. Lázár, J. Megyeri, Zs. Mácsik, É. Széles, Z. Máthé, J. Suksi. Retarded migration of uranyl ions with absence of coupled $\text{Fe}^{2+} \rightarrow \text{Fe}^{3+}$ redox process in Boda Claystone
- F. Papanicolaou, S. Antoniou, I. Paschalidis. Uranium chemistry in Phosphogypsum under oxic and anoxic Conditions
- S. Kalmykov. Redox behavior of actinides in organic-rich industrial pond (PA MAYAK)
- J. Suksi, S. Salminen-Paatero. U mobilisation/immobilisation in fractures - an evidence of redox-impact
- F. Huber, E. Stage, S. Heck, M. Bouby, B. Kienzler, D. Schild, W. Hauser, T. Schäfer, The influence of glacial melt water intrusion on the mobility of redox sensitive radionuclides in crystalline rock

WP6 session

- A. Loida, N. Müller, V. Metz, E. Bohnert, B. Kienzler, D. Schild, E. Soballa. Trapping of radionuclides/actinides onto canister (Fe) corrosion products.
- P. Carbol, P. Fors, S. Van Winckel, K. Spahiu. Corrosion of spent fuel in presence of H_2
- H. Wegen, T. Gouder, a. Seibert. Studies on thin film model systems and on UO_2 in presence of Corroding Fe
- Dobrev, R. Červinka, A. Vokál. The effect of carbon steel corrosion on the evolution of conditions in a deep geological repository.

- D.Cui, V. Rondinella, P. Carbol, C. Kütahyali, M. Amme, T. Wiss, M. Granfors, C. Borca, D. Grolimind, K. Spahiu. Np-Pu immobilization on iron surface at simulated HLW repository conditions

Poster presentations

The following posters were presented during the 4th Annual Workshop:

- M. Altmaier, X. Gaona, D. Fellhauer, G. Buckau. RECOSEY intercomparison exercise on redox determination methods- Final report on main conclusions and recommendations
- X. Gaona, D. Fellhauer, J. Rothe, M. Altmaier. Solubility of Np(VI) in dilute to concentrated alkaline NaCl solutions
- Andreas Loida, Volker Metz, Elke Bohnert, Bernhard Kienzler, Nikolaus Müller, Dieter Schild, Eva Soballa. Trapping of Radionuclides / Actinides onto Canister Corrosion Products
- Th. Schaefer. The influence of glacial melt water intrusion on the mobility of redox sensitive radionuclides in crystalline rock
- N. L. Banik, C.M. Marquardt, D. Schild, J. Rothe, T. Schäfer. Redox behavior of neptunium, plutonium and technetium in Opalinus Clay / Callovo-Oxfordian argillite – pore water system
- Catherine Landesman, Céline Bailly, Véronique Baty, Johan Vandenborre, Bernd Grambow. Speciation of reduced selenium species in hyperalkaline solutions: development of an analytical protocol.
- I. Ignatiadis and S. Betelu. Abiotic pyrite reactivity versus nitrate in NaCl 0.1 M at 25°C using chemical and electrochemical methods
- Duro, L., Grivé, M., Domènech, C., Arcos, D., Rojo, I., Clarens, F., de Pablo, J. Use of pyrite oxidation kinetic data to quantify O₂ consumption by pyrrhotite or other Fe-bearing sulphides
- M. Grivé, V. Montoya, O. Riba, L. Duro. Uranium solubility and redox determination at alkaline conditions.
- Pidchenko, S. Salminen-Paatero and J. Suksi. Wet chemistry or XANES: A case study for low U geomaterial
- J. Tits, X. Gaona, A. Laube, E. Wieland. Neptunium uptake by calcium silicate hydrates: effect of the redox state.

- Michel Perdicakis, Carine Streiff and Cindy Malhomme. Potentiometry Revisited: some Practical Considerations
- Michel Perdicakis, Yuliang Xu, Lise Rouillard, Cindy Malhomme and Margaux Beretta. Voltammetry of Microparticles, Voltammetry of Microparticles in Thin Layer, and Clay Matrix Voltammetry three powerful electrochemical techniques for characterizing clays.
- K. Lázár, Z. Máthé, J. Megyeri, É. Széles, Zs. Mácsik, J. Suksi. Interaction of iron bearing minerals with dithionite in Boda Claystone samples.
- V.G. Alexandratos, T. Behrends and P. Van Cappellen. Reduction of iron oxides by S(-II) and its effect on adsorbed U(VI).
- Vladimir G. Petrov, Xavi Gaona, David Fellhauer, Kathy Dardenne, Stepan N. Kalmykov, Marcus Altmaier. Pentavalent neptunium solubility and solid phase transformation in solutions of different ionic strengths
- Romanchuk, A. Egorov, Y. Zubavichus, A. Shiryaev, S. Kalmykov. Redox speciation of plutonium upon sorption to hematite at ambient atmospheric conditions
- Rajiv Kay, Nick Bryan, Nick Evans, Peter Warwick. The environmental biogeochemistry of neptunium – an XAS study
- Gareth TW Law, Andrea Geissler, Jonathan R Lloyd, Francis R Livens, Christopher Boothman, Melissa A Denecke, Jörg Rothe, Kathy Dardenne, and Katherine Morris. Plutonium behaviour in humic acid-quartz sand ternary systems: the effect of oxidation state.
- Donald T. Reed, Marian Borkowski, Michael Richmann, Juliet Swanson, Jean-Francois Lucchini and David Ams. Plutonium Solubility and Redox Distribution in WIPP Brine

Topical session

The Topical Sessions aim at covering the key areas of redox determination methods along with the project. The Topical Session focuses on integration of redox processes in the Safety Case

Presentations within this topic were:

- Scott Altman, How redox is considered in the ANDRA SA
- David Shoesmith, A Model for the Influence of Steel Corrosion Products on Nuclear Fuel Corrosion under Permanent Disposal Conditions

- Ignasi Puigdomenech and Kastriot Spahiu, Redox processes considered in the SR-Site PA exercise
- Budhi Sagar, SWRI. Redox Processes in the Safety Case for the Proposed U.S. Repository

Additional presentation

Additional presentation was given on a topic of general interest, especially the context of the present project within the Euratom FP7 program on geologic disposal.

One additional presentation was given:

- T. Sasaki. Geochemical implications of the Fukushima accident

Structure of the proceedings

The proceedings are divided into the following sections:

- WP activity overviews, with summaries of the Research, Technology and Development Components
- Individual Scientific and Technical Contributions, containing reviewed scientific and technical manuscripts

All the Scientific-technical contributions submitted were reviewed by the EUCG members (End-User Consultancy Group).

SUMMARY OF WP ACTIVITIES

WORKPACKAGE2: DEVELOPMENT OF REDOX DETERMINATION METHODS

M.U. Kumke

Institute of Chemistry, University of Potsdam, Karl-Liebknechtstr. 24-25, 14476
Potsdam, Germany

Introduction

The objective of WP2 was the development and testing of redox determination methods using different type of electrodes as well as optical sensors in order to provide the scientific-technical basis for the application in natural systems relevant for a disposal of nuclear waste. The major topics addressed are (i) redox determination methods specifically designed for environmental applications, and (ii) a broader information base for interpretation of system conditions. The first point reflects the limitations of existing determination methods due to poisoning of electrode material, diffusion potentials in electrode bridges, drift through catalytic reactions on electrode material, drift through changes in electrolytes via diffusion, analytical difficulties in determining concentrations of redox sensitive system components or state of involved solids/minerals, and insufficient/inadequate thermodynamic data for calculation of the redox state. The second point is considered by including information from additional analytical techniques. In combination with chemical analysis and associated thermodynamic modeling the redox state of systems (relevant for nuclear waste repositories) is assessed.

In the following paragraphs a summary of work performed during the fourth project year is given by partners. Note, that the duration of WP2 was extended to PM 42 in order to give some of the partners the opportunity to continue and/or finish experimental work – this was not used by all partners. Consequently, only work of those partners active in this period is summarized here.

Work performed by partners

At **KIT-INE** solubility experiments with Np(VI) were conducted in dilute to concentrated NaCl solutions ($0.1 \text{ M} \leq I \leq 5.0 \text{ M}$) to assess the thermodynamic properties of the aqueous species and solid compounds forming under alkaline conditions. The solubility controlling solid phases were characterized by XRD, chemical analysis and SEM-EDS, which indicated the prevalence of a solid phase with a Na:Np ratio 1:1, likely $\text{NaNpO}_2\text{O}(\text{OH})(\text{cr})$ (or $\text{Na}_2\text{Np}_2\text{O}_7 \cdot \text{H}_2\text{O}$). EXAFS further indicated the predominance of a neptunate-like structure with significantly short Np–O_{ax} and Np–O_{eq} distances ($1.76 \pm 0.02 \text{ \AA}$ and $2.12 \pm 0.03 \text{ \AA}$, respectively).

In all the systems studied ($0.1 \text{ M} \leq I \leq 5.0 \text{ M}$), the solubility curve can be divided into three different regions: a: $\sim 7 \leq -\log[\text{H}^+] \leq \sim 9.5$, showing a steep decrease in the Np solubility with a slope between -2 and -3 ; b: $\sim 9.5 \leq -\log[\text{H}^+] \leq \sim 11$, with a nearly pH-independent $[\text{Np}]$ and c: $\sim 11 \leq -\log[\text{H}^+] \leq \sim 13.5$, showing an increase in the solubility with a well-defined slope of $+1$ (see Figure 1). The slope analyses of these solubility data, together with the stoichiometries determined for the solid phases as well as direct analogies with U(VI), led to the definition of the equilibrium reactions $\text{NaNpO}_2\text{O}(\text{OH})(\text{cr}) + \text{H}_2\text{O} \rightleftharpoons \text{Na}^+ + \text{NpO}_2(\text{OH})_3^-$ and $\text{NaNpO}_2\text{O}(\text{OH})(\text{cr}) + 2\text{H}_2\text{O} \rightleftharpoons \text{Na}^+ + \text{NpO}_2(\text{OH})_4^{2-} + \text{H}^+$ to prevail in the regions “b” and “c” of the solubility curves.

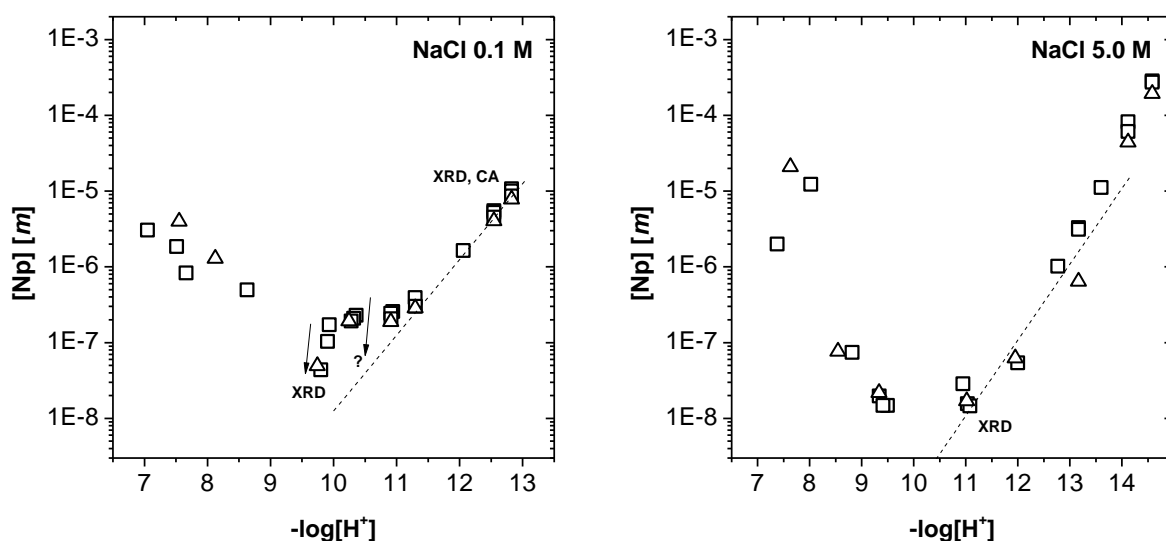


Figure 1: Np(VI) solubility data determined for 0.1 M and 5.0 M NaCl. Samples equilibrated for 74 – 305 days. Samples for which solid phase analysis was performed are marked in the figures. Triangles indicate the results from the last sampling. Solubility data for 0.5 M, 1.0 M and 2.5 M NaCl not shown.

Two characteristic features were observed for those samples in region “a”: first, the Np concentration is unexpectedly high (with regard to previous U(VI) study under similar conditions); second: a continuous decrease of the E_h with time was found (from $+800$ – 1000 mV to $+500$ – 700 mV). This is probably related to the degradation of NaClO and might be linked with a partial reduction of Np(VI) to Np(V). The solubility of $\text{Np}^{\text{V}}\text{O}_2\text{OH}(\text{am})$ under these $-\log[\text{H}^+]$ and I conditions is significantly higher (Neck et al., 1992; Petrov et al., 2011); we hypothesize that the equilibrium reaction $\text{NaNpO}_2\text{O}(\text{OH})(\text{cr}) + 3\text{H}^+ + \text{e}^- \rightleftharpoons \text{Na}^+ + \text{NpO}_2^+ + 2\text{H}_2\text{O}$ is controlling both E_h and $[\text{Np}]$ in the system (slope of -3 to be expected), although other interpretations may also apply (*i.e.* partial formation of $\text{Np}^{\text{VI}}\text{O}_3(\text{s})$ or $\text{NaNp}^{\text{V}}\text{O}_2(\text{OH})_2(\text{s})$). This hypothesis is to be experimentally assessed by solid phase characterization and VIS–NIR spectroscopy of the aqueous phase.

The specific ion interaction theory (SIT) was considered to derive $\log^\circ K_{s,1,4}^*$ and $\Delta\epsilon$ for the equilibrium reaction $\text{NaNpO}_2\text{O}(\text{OH})(\text{cr}) + 2\text{H}_2\text{O} \rightleftharpoons \text{Na}^+ + \text{NpO}_2(\text{OH})_4^{2-} + \text{H}^+$ (region c). Region b was disregarded in this step because thermodynamic equilibrium

had not been reached (even after 305 days). The combination of experimental $\Delta\epsilon$ with $\epsilon(\text{H}^+, \text{Cl}^-) = 0.12 \text{ kg}\cdot\text{mol}^{-1}$ and $\epsilon(\text{Na}^+, \text{Cl}^-) = 0.03 \text{ kg}\cdot\text{mol}^{-1}$ reported in Guillaumont et al. (2003) allowed the calculation of $\epsilon(\text{Na}^+, \text{NpO}_2(\text{OH})_4^{2-}) = -0.16$, whereas $\log^* K_{s,1,4}^\circ = -19.4$. Note that these values might be subject of further modifications as a result of the planned thermogravimetry experiments.

These results further indicate the potential relevance of Na–Np(VI) solid phases in controlling Np(VI) solubility in cementitious and NaCl-dominated saline environments.

Laboratory experiments show that selenium speciation cannot be deduced directly from E_h measurements with Pt electrodes and geochemical equilibrium calculations. The aim of the experimental work at **ARMINES (Subatech)** is then to determine low level concentrations of Se(-II) species in order to use the speciation of Se(-II) as a probe for a direct redox state determination in hyperalkaline solution representative of cement matrices which could be used for conditioning or stabilizing radwastes. Se speciation in hyperalkaline solution is further complicated by the formation of polyselenide species such as Se_2^{2-} , Se_3^{2-} and Se_4^{2-} which formal oxidation states range between -II and 0. All these reduced Se species are very reactive towards oxidation.

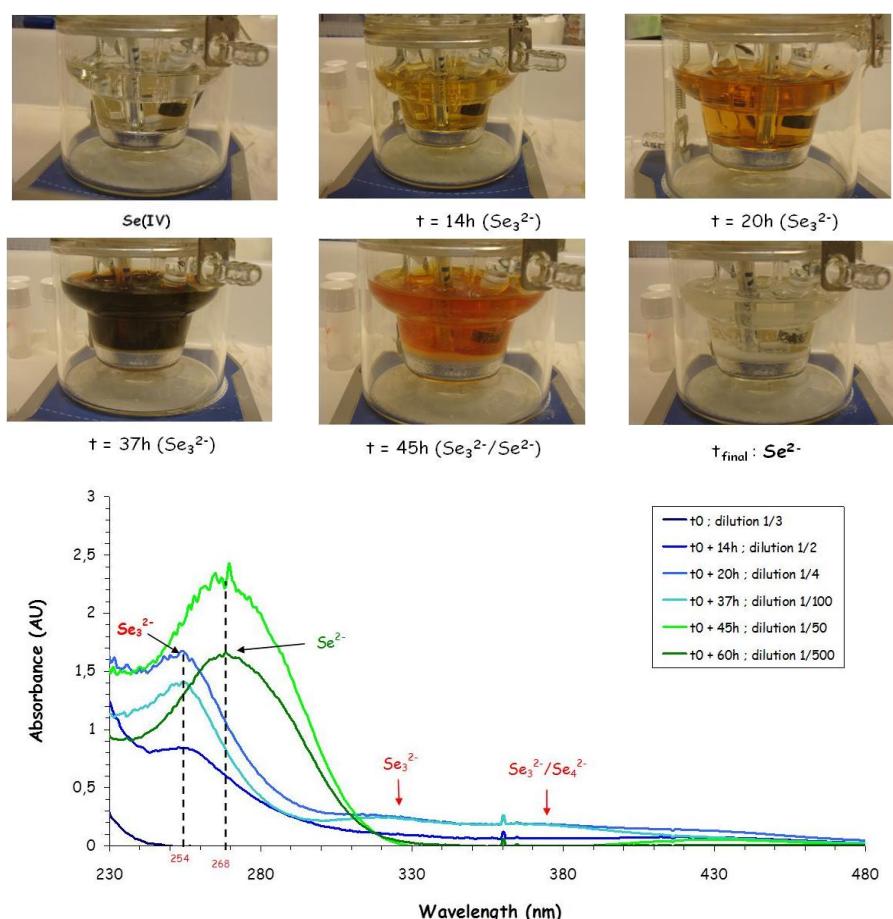


Figure 2: Evolution of Se species during the electrochemical reduction

UV-visible spectrophotometry is the efficient technique for the characterization of Se(-II) species but its sensitivity is too low for determining concentrations lower than 10^{-5}

⁴M. The *in fine* analytical approach is then to use a speciation technique (high performance anion exchange chromatography, HPAEC) *off line* coupled with a high sensitivity analytical technique (ICP-MS).

For that purpose, sodium selenide is electrochemically synthesized (adapted from Licht *et al.*), characterized as $\text{Na}_2\text{Se} \cdot 9\text{H}_2\text{O}$ and used as a source solution for the analysis of both monomer and polymer reduced selenium species.

The electroreduction is performed in a glove box flushed with N_2 ($\text{O}_2 < 100$ ppbv) from a selenium(IV) solution (0.4 mol/L in 4 mol/L NaOH). The experimental set-up is based on a standard three electrodes cell. A very negative potential (-1.285 V/SHE) is imposed between a mercury pool (working electrode) and a Pt wire (counter electrode). Coulometric recordings show that the reduction from Se(IV) to Se(-II) is quantitative. UV spectra are also recorded inside the glovebox (with a fibre-optic line) during the synthesis (Figure 2).

In these experimental conditions, Se(IV) is first reduced to the polymeric species Se_3^{2-} ($\lambda = 258, 328$ and 379 nm) then Se_2^{2-} ($\lambda = 251, 431$ nm). During the reduction, the solution becomes yellowish which is consistent with the presence of polymer species. A white frothy solid (sodium selenide) appears then (after 37h) as the solution turns more reddish. Finally a colorless solution is obtained and the aqueous species identified as Se^{2-} ($\lambda_{\text{max}} = 274$ nm).

Analysis of monomer species

Speciation experiments are firstly performed on HSe^- solution. The HPAEC system is an IC 2500 Dionex® chromatograph. The separation of the monomer and polymer Se(-II) species are performed with a specific column design for the separation of ionizable anion (Dionex® Ionpac AS16). The separation protocol is optimized for an on line detection of all Se species (HSe^- , Se(IV) and Se(VI)) related to the different redox states of selenium in order to get information on a potential re-oxidation of reduced species. This is done by connecting in series an UV-visible single wavelength detector and a conductimetry cell detector. HSe^- can only be detected by UV-visible spectrometry at 245 nm. For the other species (Se(IV) and Se(VI)), conductimetry detection is efficient. Figure 3 shows the two chromatograms obtained for the analysis of a HSe^- solution ($6.33 \cdot 10^{-4}$ mol/L in 0.5 mol/L NaOH).

HSe^- is very well detected at 12.6 min. A partial re-oxidation of HSe^- into Se(IV) and Se(VI) is observed during the analysis (5% and 0.2% respectively). This result shows that HPAEC is sensitive enough for identifying and quantifying HSe^- at millimolar level. The quantification limit is around $0.05 \cdot 10^{-3}$ mol/L. Coupling subsequent off line ICP-MS analysis (after fraction collection) decreases drastically the quantification limit to 10^{-9} mol/L.

Attempts for separating a mixture of HSe^- and Se_2^{2-} species with a adapted protocol (gradient elution mode from 0.05 to 0.5 mol/L KOH at 0.4 ml/L ; $T = 45^\circ\text{C}$) were unsuccessful. The two peaks remained partially resolved (retention time are separated by only 40 s). Retention time for Se_2^{2-} species (slightly greater than this of HSe^-) is consistent with the retention of a higher charged species (stronger interaction with the functional groups of the anion resin). Nevertheless, Gaussian deconvolution of the peaks allow to quantify the two species at a submillimolar level (ie : $3 \cdot 10^{-3}$ mol/L).

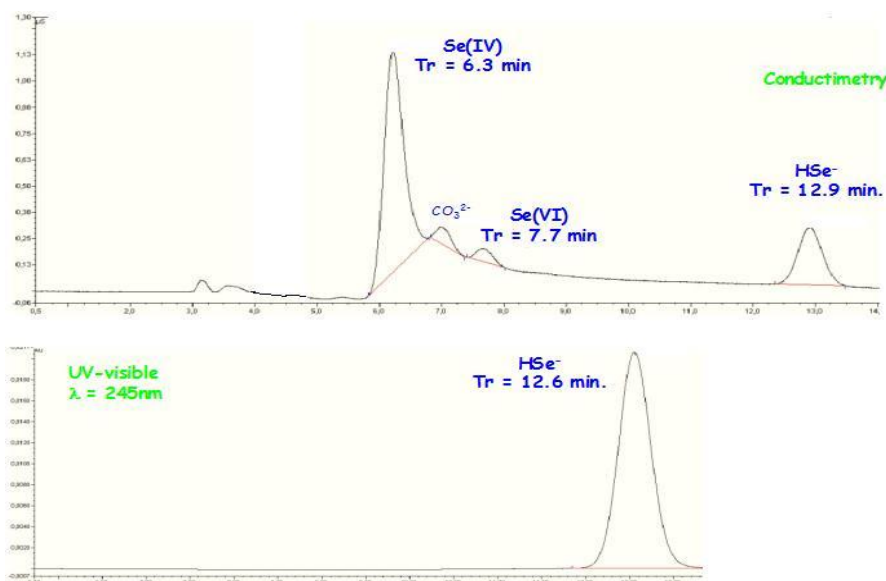


Figure 3: Chromatograms of a HSe^- solution (isocratic elution with 0.02 mol/L KOH at 1 mL/min ; $T = 30^\circ\text{C}$)

Analysis of polymer species

A mixture of polymer species was synthesized by adding a known mass of Se(0) to a Se(-II) solution with a 1:1 molar Se(-II)/Se(0) ratio, in 4 mol/L KOH. The analysis was based on the previous described protocol. Improvements were obtained with an isocratic elution with 0.5 mol/L KOH. Figure 4 shows the chromatogram of this mixture and is representative of all results obtained with polymer species.

Two peaks can be distinguished at 10.72 and 11.31 minutes which means that the analyzed species have a real chemical interaction with the functional groups of the resin, but that the resolution is still too low for achieving a full separation.

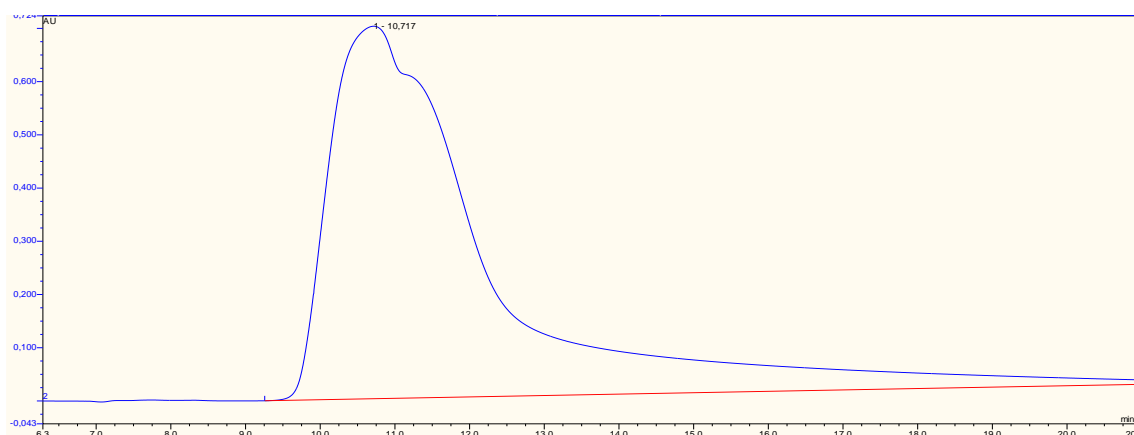


Figure 4: Chromatogram of a 1:1 Se(-II)/Se(0) molar ratio mixture of polymer species
Flow rate = 0.4 mL/min ; $T = 45^\circ\text{C}$; UV detection at $\lambda = 360\text{ nm}$

Conclusion

The main result is that we achieve to develop for the first time a specific analytical protocol aiming at quantifying the monomer species HSe^- by UV spectrometry at a sub millimolar level (conductimetry cell detector) and at a sub micromolar level (*ie* : $0.1 \cdot 10^{-6}$ mol/L) by coupling a speciation technique (HPAEC) with a high sensitive elemental technique (ICP-MS). Unfortunately, this protocol is not efficient enough for a direct quantitative analysis of the other reduced selenium species (monomer Se^{2-} and polymer species). Despite many analytical efforts, only partial separations were obtained because of the too close interaction properties developed by those species towards the anion exchange columns which are commercially available. Based on these results, a new route making use of aminoacids as cationic complexants, will be tested in the near future to improve the separation of Se reduced species.

The main activities of **CNRS/LCPME** during the last project year consisted in: (i) complementary tests performed in the laboratory with a series of commercial instruments usually employed for the measurement of E_h , (ii) researches for fabricating ultramicroelectrodes compatible with concentrated brines and (iii) the presentation of certain results in meetings and workshops.

i) Tests performed with a series of commercial instruments

In order to check if the nature of the apparatus used for the potentiometric determinations could have an influence on the measurements performed, we tested a dozen of commercial instruments by measuring the current that flows through the instruments when they operate.

Two kinds of experiments were carried out: First, the flowing current was measured by connecting directly a femtoamperemeter to the instrument under test. Then, an electrochemical cell was inserted in series in the preceding electrical circuit.

During the first kind of measurements we confirmed measurements performed during the third year of the project where we detected the presence of oscillations of about 10 nA for the worst instrument and less than 5 pA for the best one (factor of 1000!). The relatively high currents that flow when certain devices are used, which can polarize the electrodes, must be taken into account during the interpretation of potentiometric measurements.

During the second kind of measurements we found that currents in the $0.1 \mu\text{A}$ range flow through the electrodes whatever the measuring instrument and whatever the composition of the under test solution! If the exchange currents relative to the species that fix the redox potential are too small, current pulses in the 10^{-7} A range, with durations of about 1 ms, will irremediably polarize the potentiometric electrodes. Experiments are in progress in order to understand the reasons for a so high increase of the current when the solution is present.

ii) Researches for fabricating ultramicroelectrodes compatible with concentrated brines

When we tried to make use of the higher sensitivity of UMEs to measure very low concentrations of redox species in concentrated NaCl solutions the attempts completely failed.

Actually, the voltammetric response of UMEs –that perfectly work in diluted media or pure water– becomes completely meaningless once immersed in NaCl brines.

We tested nine platinum UMEs having diameters ranging between 10 and 50 μm in NaCl solutions whose concentration varied from 5.84 to 29.22% w:w. The UMEs used were either commercial or homemade, and their insulating body was formed of various glasses (Pyrex, soft glass, quartz, quartz suprasil...) or polymeric resins (epoxy, polyester, PTFE). For convenience, dissolved oxygen was used as the main electroactive species but several experiments were also carried out with the model species ferrocene dimethanol. The results achieved with the different UMEs were compared with those obtained using a routine 2mm diameter platinum rotating disc electrode.

The voltammetric response of the platinum UMEs that we tested strongly depends on the nature of the insulating material used to make the body of the electrodes. And the more concentrated the solution is, the more the resulting voltammetric signal is distorted. This distortion is particularly noticeable during the reverse scans.

The UMEs that the insulating part is made of "quartz-suprasil" are the less affected by the brines. However, the fabrication of such an electrode is quite difficult because the melting point of platinum (1772°C) and the softening point of quartz-suprasil (~1600°C) are relatively close. The use of platinum wires insulated with PTFE is an interesting alternative but there are problems with their mechanical behaviour and then with polishing. We classified the UMEs as a function of the insulating materials in the following order, from least to most resistant: quartz fiber < epoxy, softglass < polyester, Pyrex < quartz-suprasil, PTFE.

The distortions of voltammograms that are observed when the UMEs are immersed in brines are linked with phenomena occurring at the metal/insulating material interface. The same phenomena must occur when millimetric electrodes are used, but they are not detected because of the much higher distance between this interface and the main surface area of the platinum disc.

When we tried to make use of the higher sensitivity of UMEs to measure very low concentrations of redox species in concentrated NaCl solutions the attempts completely failed.

In the fourth project year **GRS** continued developing a thermodynamic model for iron, explicitly considering Fe(III) complex species. Therefore, pH titrations with saline solutions (NaCl, MgCl_2 , and CaCl_2) including Fe(II) and Fe(III) were carried out at 25°C. The redox potential and UV spectra were recorded at any titration step.

A decline of the redox potential with increasing pH was observed during all measurements. There was no change in media composition apart from the varying H^+ concentration, i.e. the background ion concentration remained constant. Also the

concentration of Fe^{2+} is likely to be constant as Fe(II) hydroxo complex formation is negligible in acidic and neutral solutions.

In that case, the decrease of the redox potential E_{Rx} must be caused by a decrease of the Fe(III) activity according to:

$$E_{\text{Rx}} = E_{\text{Rx}}^0 + 0.05916 \log \frac{a_{\text{Fe}^{3+}}}{a_{\text{Fe}^{2+}}}$$

This in turn is due to the formation of Fe(III) hydroxo complexes. Without knowing the exact composition of hydroxo (“FeOH”) and chloro complexes (“FeCl_n”) the relative concentration of hydroxo complexes can be calculated according to the following equation:

$$\frac{C_{\text{FeOH}}}{C_{\text{FeCl}_n}} = 1 - 10^{\frac{\Delta E_{\text{Rx}}}{0.05916}}$$

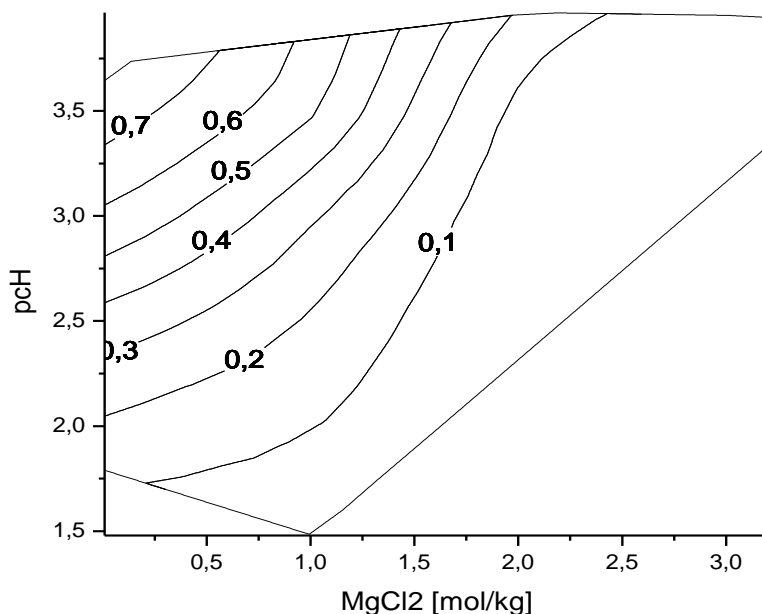


Figure 5: Calculated fraction of hydroxo complexes in relation of total Fe(III) in MgCl_2 solutions

Figure 5 summarizes the results of the model calculation for the fraction of hydroxo complexes in relation of total Fe(III) in MgCl_2 solutions as a smoothed contour diagram. Using the information about relative concentration of hydroxo complexes the UV-spectra were evaluated. With this, a single species spectrum of FeOH^{2+} could be calculated. It shows a maximum at 294 ± 3 nm, which is consistent with earlier literature data.

With these measurements we could show that FeOH^{2+} is the only hydroxo complex in chloride concentrations between 1 and 4 mol/kg and $-\log c(\text{H}^+)$ values up to 4. No

evidence was found for mixed chloro hydroxo complexes. Only at very low chloride concentrations, around 0.02 mol/kg, the formation of a different hydroxo complex, probably $\text{Fe}(\text{OH})_2^+$ could be observed.

Within the last year **UPPC** continued to work on the development and improvement of multiparameter fiber-optical chemical sensing (FOCS, see Figure 6). Especially the integration of optodes for the determination of oxygen concentration and of pH was pushed forward. The research was focused on the evaluation and integration of decay-time based optical sensing scheme, because it offers intrinsic advantages over intensity-based approaches for applications under real-world conditions.

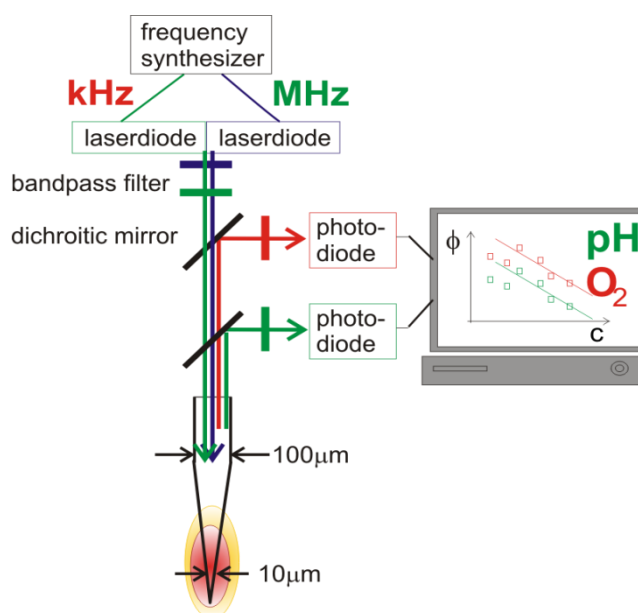


Figure 6: Scheme of multiparameter fiber-optical chemical sensing

The limit of detection (LOD) for oxygen was distinctly improved by the integration of Pt-based luminescence probes down to the ppb-range [Steinbrück et al. (2010)]. Measurements can be made also using a “wire-less” set-up, in which micro- and nano-beads are applied as sensors. These beads can be as small as a few nanometers and underline the outstanding miniaturization potential of the optical detection approach.

Moreover, a novel optode based on a time-resolved luminescence detection scheme for the determination of pH was developed and tested for different cross sensitivities (see Figure 7). The optode consists of a tailored proton permeable polymer (P1), in which a pH sensitive dye is embedded.

This dye changes its photo physical properties (here especially its fluorescence decay time) in dependence on the proton activity. Different dyes were tested and Carboxyfluorescein (CF) best matched the requirements for a decay-time based determination of pH [Steinbrück and Kumke (2009)]. Both optodes are currently integrated into a multiparameter FOCS scheme for the simultaneous measurement of pH and oxygen content (see Figure 5).

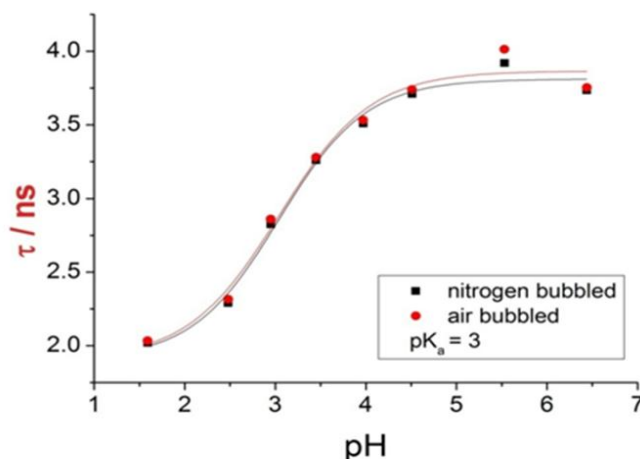


Figure 7: Decay-time based fiber-optical pH determination

Acknowledgements

The research leading to these results has received funding from the European Union's European Atomic Energy Community's (Euratom) Seventh Framework Programme FP7/2007-2011 under grant agreement n° 212287 (RECOSY project).

References

- Guillaumont, R., Fanghänel, J., Neck, V., Fuger, J., Palmer, D.A., Grenthe, I., Rand, M.H. (2003) Chemical Thermodynamics Vol. 5. Update on the Chemical Thermodynamics of Uranium, Neptunium, Plutonium, Americium and Technetium. (OECD, NEA-TDB) Elsevier, North Holland, Amsterdam
- Licht, S., Forouzan, F. (1995). Speciation analysis of aqueous polyselenide solutions. Journal of the Electrochemical Society, 142, 1546-1551
- Neck, V., Kim, J.I., Kanellakopulos, B. (1992). Solubility and hydrolysis behaviour of Neptunium(V). Radiochimica Acta, 56, 25-30
- Petrov, V., Gaona, X., Fellhauer, D., Dardenne, K., Kalmykov, S., Altmaier, M. (2011). Np(V) solubility and solid phase transformation in dilute to concentrated NaCl solutions. Proceedings of the Migration 2011 Conference, Beijing (China).
- Steinbrück D., Kumke M. U. (2009) Development of multiparametric optical sensing for environmental applications, Wissenschaftliche Berichte - Forschungszentrum Karlsruhe (FZKA 7466) 103-110
- Steinbrück D., Schmäzlin E., Kumke, M.U. (2010) Development of a fiber optical chemical sensor (FOCS) for the determination of low oxygen concentrations, wissenschaftliche Berichte - Karlsruhe Institut für Technologie, (KIT-SR 7557) 103-11

WORK PACKAGE 3: REDOX RESPONSE OF DEFINED AND NEAR NATURAL SYSTEMS

Laurent Charlet

(CNRS)-Laboratoire de Géophysique Interne et tectonophysique LGIT- (UMR 5559)
Rue de la Piscine, 1381
38041/19 Grenoble
France

Introduction

The “Redox processes of defined and near-natural system” WP3 group has in Year 4 performed work on (i) Field data, (ii) Field samples, (iii) Microbiology, (iv) Sorption experiments, (v) Redox experiments and (vi) Conceptual Model. This work is summarized below.

Work performed by partners

CNRS main outcomes were the following.

Selenium reduction by synthetic nano-sized pyrite/greigite mixture

Nano-pyrite was synthesized upon reaction of FeCl_3 and NaHS in the ratio of 1:2. Following this protocol, 28% of greigite ($\text{Fe}^{2+}\text{Fe}^{3+}_2\text{S}_4$) was found in the solid phase. Greigite is an important precursor for pyrite formation, and its occurrence in the present study may originate from HS^- loss during the synthesis. Batch reactor experiments were performed upon adding selenite or selenate to the nano-sized pyrite-greigite suspension at different pH values and with or without the addition of extra Fe^{2+} . Both XANES and EXAFS spectroscopy revealed, for the first time, the formation of ferroselite (FeSe_2), the thermodynamically most stable species, as the predominant reaction product along with elemental Se. The nucleation and growth of FeSe_2 is believed to occur at the nano-pyrite/greigite surface via several steps and reaction kinetics and aging time may play a significant role. The present study demonstrates that, in Fe^{2+} /sulfide-bearing environment, Se can be immobilized in its most insoluble form, which leads to its reduced mobility in the environment. Thermodynamic modeling was performed with PHREEQC software package. The results of the calculations for pyrite suggest that under acidic to neutral condition $\text{Se}(0)$ is the unique/predominant reaction product, while, in the neutral to slightly alkaline range, FeSe_2 becomes the thermodynamically favored species with approximately the same molar fraction of $\text{Se}(0)$. In strongly alkaline conditions, part of the $\text{Se}(0)$ can further be reduced to HSe^- , leading to FeSe_2 as the predominant solid species. For greigite, PHREEQC calculations indicated that FeSe_2 is the main equilibrium product, except at acidic ($\text{pH} < 4$) and strong alkaline ($\text{pH} > 12$)

conditions, where elemental Se and FeSe become the predominant species, respectively. Therefore, the observation of FeSe₂ formed on the pyrite-greigite nanocomposite in the pH range of ~ 5.9 to ~ 10.3 considered in this study is thermodynamically allowed. Both thermodynamic calculations and experimental observations (spectroscopic and aqueous analysis) indicate that pyrite can significantly attenuate the mobility of Se by reductive precipitation. This study reports the abiotic formation of FeSe₂ in laboratory experiments for the first time, suggesting that stabilization of selenium in its most insoluble form is possible in Fe²⁺/sulfide-bearing environment.

Interactions of fulvic acids-like compounds with iodide ion in alkaline media

Fulvic acid-like compounds containing only two functional groups, alcohol and ether, have been synthesized at pH 13 starting from catechol and acetic acid. An experimental study of interactions involved in the “KI–synthetic fulvic acid-like compounds–H₂O” ternary system as a function of iodide ion concentration and pH has been carried out using optical spectrometric techniques. Results obtained from UV-visible and fluorescence measurements have indicated that iodide anion weakly interacts with synthetic fulvic acid-like compounds in the 4-12 pH range. The work aimed to answer two questions: (i) Is it possible to synthesize fulvic acid-like compounds (FALCs) containing only two functional groups: alcohol and ether, in basic solution? (ii) Is the optical spectrometry can be an effective measurement technique to detect iodide complexes with fulvate ligands? The approach taken is to use: (i) an initial mixture of catechol and acetic acid to synthesize humic and fulvic acids in NaOH solution (pH 13) under argon atmospheric condition. Synthesized FALCs were characterized using ATR-FTIR technique. (ii) a set of two UV-visible and fluorescence spectroscopies to detect the eventual complex formation of iodide ions with FALCs at different pH values. Synthesized FALCs are composed of many molecules containing two functional groups: alcohol and ether. Due to the impossibility of a polyaromatic ion to interact with an acetate ion under argon atmosphere, of carboxylate-bearing FALCs could not be formed in the present work. From a practical point of view, the synthesis procedure has to be improved by passing the FALCs aqueous solution through ion exchange resins prior to the lyophilisation process in order to remove sodium chloride that is formed during the process. To our knowledge, for the first time, the treatment of UV-visible and fluorescence spectra of aqueous solutions containing iodide ions and FALCs have showed that slight but significant differences are observed between the spectrum of the “FALCs + KI” mixture and the sum of the spectra of initial potassium iodide and FALCs. However, the relative concentrations of FALCs and KI in the mixture are worth to be optimized in order to increase the amount of the FALCs–I⁻ complex formed. Based on this work, different lines of research can be suggested including: (i) determination stability constants values of iodide–FALCs complexes, (ii) synthesis of humic and fulvic acids containing more functional groups (carboxylate, amine, thiol) and their interactions with iodide anion as a function of pH, and (iii) use of high-precision potentiometry as a complementary tool for the study of the formation of the above cited complexes.

The mechanisms of of pyrite reduction by hydrogen in NaCl 0.1 M at 90 °C and 25°C using electrochemical techniques have been investigated by **BRGM**.

Nuclear waste repositories are being installed in deep excavated rock formations in some places in Europe to isolate and store radioactive waste. In France, the Callovo-Oxfordian formation (COx) is a potential candidate for a nuclear waste repository. The COx formation contains pyrite (FeS₂), which would, a priori, react to Hydrogen gas (H₂).

After the closure of the underground nuclear waste repository, aqueous corrosion of the steel canister and, to a lesser extent, radiolysis of water should produce significant amounts of H₂. This H₂ can interact with materials from the repository and with the surrounding clay host formation. This work aims at understanding these interactions. Given the mineralogical complexity of clay formation, this work focused on the study of the interaction of FeS₂ alone with H₂, using electrochemical techniques and the analysis of solutions and interfaces. After pyrite electrodes had been assembled, various electrochemical disturbances were applied to this material (and to platinum for comparison) while it was submerged in a partially reconstituted solution of COx pore water, enclosed in a High Pressure Thermo-Reactor (HPTR) at 90 °C, or in a Low Pressure Thermo-Reactor at 25°C in the absence and in the presence of pyrite grains (particle size between 40 and 63 µm) and H₂ (0 partial pressure or 1 bar). In addition to the electrochemical behavior of the platinum and the pyrite, the pH, temperature and pressure of the liquid medium were monitored.

The principal result of this work is the elucidation of the mechanism governing the reduction of the sulphur S° of the FeS₂. Indeed, at 90°C, the S° is reduced to sulphide (HS⁻/S²⁻), which is freed in solution, whereas the pyrite turns superficially into pyrrhotite (FeS_{1+x} with 0<x<0.125), forming a layer that slows down the reduction process (Betelu et al., 2012). At 25°C the S° is metastable and simultaneously reduced to sulphide and oxidized to thiosulphate, both are freed in solution, whereas the pyrite turns superficially into pyrrhotite (Ignatiadis et al. 2012). All of the measurements agree, and the qualitative exploitation of these data (open circuit electrode potential, Tafel curves, and electrochemical impedance measurements on platinum and pyrite electrodes) and surface analyses, made it possible to provide evidence of the reduction of pyrite into pyrrhotite and to create a large electrochemical database. The future exploitation of this electrochemical database will make it possible to determine the kinetics of the reaction of reduction of pyrite by H₂ in a HPTR and in a LPTR and, by extrapolation, to storage conditions.

An important work was devoted by **BRGM** to modeling the di-octahedral smectites CEC variation versus structural iron level, in the framework of the PhD position of J. Hadi (Hadi et al., 2010a; 2010b; 2011; 2012).

Iron is one of the most common redox species in soils and sedimentary rocks. Amongst iron-bearing phases, phyllosilicates might play key roles in various bio-geochemical processes involving redox reactions, where structural Fe (Fe_{str}) acts as a renewable source/trap of electron. A large set of data from kinetics, spectroscopic or electrochemical studies on dioctahedral smectites demonstrate that reduction of Fe_{str} impacts many clay properties such as color, layer charge, swelling pressure, and colloidal properties that are linked to layer structural changes. Experiments also suggest that this mechanism is partly reversible, depending on type and properties of the primary oxidized clay and on extent of iron reduction level. The complexity of the involved mechanisms makes the prediction of Fe_{str} redox properties challenging. For instance, only empirical models are currently available to quantify structural changes as

a function of reduction level. However, a predictive and mechanistic model of these changes is a prerequisite to develop a thermodynamic model for Festr redox properties. In this contribution (Hadi et al. 2012), we propose a mechanistic statistical model to explain 2:1 layer excess negative charge changes induced by chemical (dithionite) or electrochemical reduction of structural Fe(III) to Fe(II). This model was calibrated on data from our own and from the literature and conclusively agrees and completes this published by Drits and Manceau (2000).

An important work was devoted by BRGM to investigate the structural iron electrochemical properties in layered silicates using massive mica electrodes, in the framework of the PhD position of J. Hadi (Hadi et al., 2010a; 2010b; 2011; 2012) and the “training-on-the-job mobility measure” accepted by RECOSY project. The applicant, M. Jebril HADI, currently preparing his PhD in BRGM, realized the work during a two months stay in Australia.

Nuclear waste repositories are being installed in deep excavated rock formations in some places in Europe to isolate and store radioactive waste. In France, the Callovo-Oxfordian formation (COx) is a potential candidate for a nuclear waste repository. The redox reactivity (kinetics and thermodynamic redox potential) of COx clay rock samples are already under study using microscopic, spectrometric and wet analysis techniques. In order to cross and overcome certain limits by improvement in the knowledge, specific electrodes should be constructed and devoted to the deepening of the electrochemical behaviour of the COx system in different situations.

Iron is one of the most common redox species in soils and sedimentary rocks. Iron-bearing phyllosilicates play key roles in various biogeochemical processes. The complexity of the physical and chemical (along with structural) changes involving their structural iron makes the studies of its redox properties challenging. Most of the recent reported efforts were focused on probing Fe redox on finely powdered clay (and often micas) particles, and have been hampered by inadequate interactions between particles and electrodes. Moreover, such experiments usually involve redox probe ions, thus adding supplementary difficulties in the determination of structural iron redox parameters such as redox potential (Eh) and kinetics.

The present study aims at qualitatively investigating the above mentioned phenomena on minerals like iron-bearing micas. In the current work, we present initial insights regarding efforts to build a direct electrical interface between solid electrodes and conveniently shaped macroscopic mica crystals in order to investigate the redox properties of structural iron in dry and aqueous environments, in the presence of representative perturbations. Results of these experiments show that several aspects of the designs of such electrodes have to be improved for further experiments. First, lowering of the water content in the mineral must be realised, using smaller crystals, longer drying and vacuuming time, and using more penetrating and impregnating resins. Platinum plates and evaporated platinum or carbon are envisioned for the inert support electrode. Using thinned slices should reduce electrical resistivity of the whole bulk structure, allowing more convenient observations of the coupled electrons transfers that might occur between separated crystal surfaces. Hence, more suitable cutting techniques, such as wire sawing, should be planned to obtain thinner slices. More mica samples must also be selected, with higher and lower iron contents than the one used in the present experiments. This first set of experiments in interfacing solid electrodes and

conveniently shaped mica crystals offers hope that this will be a valuable technique for probing structural iron.

CTM has performed two series of experiments adding U(VI) once the pyrrhotite was equilibrated with 0.01 M NaClO₄ under N₂ atmosphere. In one series equilibrium pH (around 5.3) was kept while in the second series pH was adjusted with NaOH at around 7.8. Spikes of U(VI) at three different initial concentrations were performed: $2 \cdot 10^{-7}$, $6 \cdot 10^{-7}$ and $2 \cdot 10^{-6}$ M. pH and redox potential were monitored with combined pH, Au and Pt electrodes. Changes in chemical aqueous composition was determined through analysis of Fe(II), Fe_{total}, U_{total}, U(VI), SO₄²⁻ and S₂O₃²⁻ with time, by means of UV-Vis, ICP-MS, IC and TRLFS. Solid observations by SEM-EDX were performed.

Experiments on the dissolution kinetics of natural pyrrhotite (Fe_{1-x}S) and pyrite (FeS₂) under imposed redox conditions have been carried out at 25°C and 1 bar by **AMPHOS** to evaluate the oxygen uptake capacity of both minerals. Measured data indicate that in both cases, Fe(II) released from kinetic dissolution of Fe-bearing sulphides is kinetically oxidized to Fe(III), precipitating as Fe(III)-oxyhydroxides. While the pH of the system is controlled by the extent of sulphide minerals oxidation, the Eh is controlled by the redox pair Fe²⁺/Fe(III)-oxyhydroxides. Pyrrhotite dissolution is faster than that of pyrite but generates less acidity. Consequently, the achieved redox value is more reducing. Experimental data show that oxidation rates of both minerals (in) are within ± 1 order of magnitude expressed in mol_{O₂}·g⁻¹·s⁻¹. This equivalence can be used to model pyrrhotite behavior for which an oxidation kinetic law is not still well defined.

An integrated methodology for the redox characterisation of crystalline systems has been developed and applied to the study of the Laxemar-Simpevarp area (SE Sweden) by **UNIZAR**, which has been extensively studied as a part of the Swedish program for the characterisation of the candidate sites for the deep geological disposal of spent nuclear fuel

Thermodynamic calculations based on partial equilibrium assumptions have been performed in order to clarify the main process and the role of the microbial activity in the redox features and evolution of the groundwaters in the Swedish candidate sites for the geological storage of spent nuclear fuel

Evaluation of the uncertainties associated with redox data and calculations in the Swedish candidate sites

The results of Mössbauer measurements to monitor the changes in Fe²⁺/Fe³⁺ ratios in clay minerals having exposed to natural or artificial changes in redox conditions are compared by **II-HAS**. The effects of changes in the natural conditions are clearly reflected, whereas effects originating from changes by artificial treatments cannot be detected (exception: treatment with sodium dithionite).

The interaction of hexavalent U with a fresh synthetic nanoparticulate magnetite (Fe^{II}Fe^{III}O₄), a partly oxidized synthetic nanoparticulate magnetite and maghemite nanoparticles under anoxic conditions and exclusion of CO₂ as function of pH, contact time and total U concentration has been examined by **KIT-INE**. Short term kinetic

batch experiments (contact time of 90 d) for four different pH values have been conducted. Moreover, classical batch pH sorption edges have been prepared for two different uranium concentrations for a contact time of 550 d. Spectroscopic techniques (XPS, XAS) were applied to probe for the presence and amount of reduced U on the magnetite surface. Batch kinetic studies revealed a fast initial U removal from aqueous solution with > 90% magnetite associated U after 24 hours within the pH range 5-11. Long term contact time batch experiments (550 d) showed neither a U removal below pH < 3 nor a decrease in the magnetite associated U at pH \geq 9. Redox speciation by XPS verifies the presence of tetravalent U on the magnetite surface up to a contact time of 550 d. A clear correlation of the amount of available Fe(II) on the magnetite surface and the amount of tetravalent U is observed. XANES investigations confirm the presence of tetravalent U, but cannot resolve the occurrence of pentavalent U doubtlessly. EXAFS results indicate the formation of a U(IV)-oxide-species coordinated to Fe. Thermodynamic calculations based on the experimentally determined redox potentials corroborate the spectroscopic findings. Overall, the results reflect the importance of structural bound Fe(II) in magnetite as redox agent for U. Furthermore, the assumption of full accessibility of surface associated Fe(II) (redox capacity) available for U(VI) reduction could not be experimentally verified.

New series of experiments with three circulation systems was started in March 2011 by **MICANS** with different hydrogen and methane concentrations and with oxygen with microbial populations from 360 m depth in ONKALO, Finland. The influence of microbial metabolism of hydrogen, methane and oxygen on redox in the circulation systems discussed above was analysed. Oxygen was used to inactivate the microbial populations. This experiment aimed at understanding redox buffering capacity of microbial ecosystems with high concentrations of methane and hydrogen

WORK PACKAGE 4: REDOX REACTIONS OF RADIONUCLIDES

¹Perdicakis, M., ¹Malhomme, C., ¹Bouchereau C., ²Allard, S., ²Holgersson, S., ³Bryan, N., ³Kay, R.R., ³Li, N., ³Stockdale, A., ⁴Remeikis, V., ⁴Baltrunas, D., ⁴Lukšienė, B., ⁴Druteikienė R., ⁴Lujanienė, G., ⁵Schäfer, Th., ⁵Marquardt, Ch., ⁶Evans, N., ⁶Hallam, R., ⁶Warwick, P., ⁷Grivé, M., ⁷Riba, O., ⁷Montoya, V., ⁷Duro, L., ⁸Gaona, X., ⁸Tits, J., ⁸Wieland, E., ⁹Krawczyk-Bärsch, E.

¹Laboratoire de Chimie Physique et Microbiologie pour l'Environnement (CNRS/LCPME), Nancy-Université, CNRS -54600 VILLERS-LES-NANCY (FR)

²Chalmers University of Technology (CTH), SE-412 96 Gothenburg, (SE)

³University of Manchester, Centre for Radiochemistry Research, School of Chemistry, , Manchester, M13 9PL, (UK)

⁴Institute of Physics of Lithuania (FTMC), LT-02300 Vilnius, (LT)

⁵Karlsruhe Institute of Technology (KIT), Institute for Nuclear Waste Disposal, Karlsruhe (DE)

⁶Loughborough University, Department of Chemistry, Loughborough, Leics, LE11 3TU, (UK)

⁷AMPHOS 21 Consulting, S.L., E08019 Barcelona, (ES)

⁸Paul Scherrer Institut (PSI), Laboratory for Waste Management, CH-5232 Villigen-PSI (CH)

⁹Helmholtz-Zentrum Dresden-Rossendorf (HZDR), Institute of Radiochemistry Dresden (DE)

Introduction

The goal of the activities within work package 4 is to provide fundamental process understanding of the redox behaviour of radionuclides in solution and in solid matrices, including the question of equilibrium / disequilibrium with the system redox conditions. The objectives of this work package result from gaps in the knowledge identified from previous projects dealing with redox processes involving radionuclides.

The work package is divided in 2 parts:

- 4.1. Chemical and redox behaviour of the investigated radionuclides in the different systems.
 - 4.1.1. Interactions of radionuclides with pyrite
 - 4.1.2. Interactions of radionuclides with far-field solids
 - 4.1.3. Redox processes under hyperalkaline conditions

4.2.: Chemical and redox behaviour of the investigated radionuclides in the different systems through microbial mediated processes.

WP 4.1.

CHEMICAL AND REDOX BEHAVIOUR OF THE INVESTIGATED RADIONUCLIDES IN THE DIFFERENT SYSTEMS

Work performed by partners

Interactions of pyrite with elemental iodine and iodide, iodate, selenite and selenate ions

During the fourth year of the project, the CNRS/LCPME activities consisted mainly in investigations performed in neutral and alkaline media. In this way, voltammetric measurements were performed using massive rotating pyrite electrodes and pyrite microparticles conditioned with soluble iodine and selenium species. After conditioning, the pyrite microparticles were characterized electrochemically and using XPS, Raman spectrometry. Moreover, the oxidation of pyrite by oxygen was monitored dielectrically.

Voltammetric measurements at massive rotating pyrite electrodes in the presence of elemental iodine as well as iodide, iodate, selenite and selenite ions

Measurements performed previously in acidic media were confirmed, and new voltammograms were recorded at pH 7 and 12 using pyrite electrodes immersed in 1 mM solutions of iodate, selenite and selenate ions as well as in a saturated solution of elemental iodine at pH 7. The measurement of corrosion currents brought information on the kinetics of oxidation of FeS₂ by the different oxidizers.

The experiments performed with I₂ neutral media (I₂ is not stable in alkaline media) showed the existence of important corrosion currents close to those recorded previously in acidic media. Because the iodate ions oxidizing properties decrease with the pH increasing, there are no corrosion currents at pH 7. On the other hand, the voltammograms indicate the presence of a corrosion process at pH 12 (probably because of the very high oxidizability of pyrite in alkaline media). No corrosion currents were observed with selenite ions. In neutral medium, the i-E curves are highly disturbed by the presence of a cathodic peak that is located very close to the rest potential (Fe₂(SeO₃)₃ precipitate?). The voltammograms recorded in alkaline medium are not exploitable. No corrosion currents were observed with selenate ions whatever the pH.

Chemical conditioning of pyrite microparticles with soluble iodine and selenium species at pH 7 and 12.

Sorption experiments were performed under argon atmosphere at room temperature by stirring the conditioning containers in the dark. The solution pH was adjusted to either

7.0 or 12 at the beginning of the experiment. The conditioning of pyrite suspensions has been performed using a 0.5% (w:w) solid/liquid ratio with $[I^-] = [IO_3^-] = [SeO_3^{2-}] = [SeO_4^{2-}] = 1$ mM. A saturated solution elemental iodide was used at pH 7 (solid I_2 was always present).

A good number of the solutions analysis data are still under processing. The most important and relevant results deriving from the analyses are the following: (i) when pyrite is treated with water adjusted at pH 12 it releases continuously sulphide ions (S^{2-}) in the solution. (ii) iodide ion is sorbed at the "pyrite" surface at pH 12; however, the amount adsorbed is extremely weak, and it is probably related to the presence of iron oxides on the FeS_2 surface. (iii) the reaction of iodate ions is slow at pH 12, (iv) as in acidic media, iodine quantitatively reacts with pyrite at pH 7.

Characterization of pyrite microparticles sampled after interaction with soluble iodine and selenium species by XPS, Raman and voltammetric measurements

The results of characterization of the pyrite microparticles, separated from the reaction media, rinsed and dried, by XPS and Raman microscopy, are rather disappointing. Some oxidized iron species but no selenium or iodine were detected with XPS. The samples appeared as well etched pyrite containing some silicate. Similar information was obtained from the Raman microscopy analyses and the electrochemical measurements using scan rates of 5 mV/s.

The results from the dielectric and electrochemical (under particular conditions) characterizations of pyrite microparticles sampled after reaction with iodine and selenium species were compared with the observations of Demoisson et al (2008). These authors investigated the oxidation processes of pyrite by dissolved oxygen and chromate using Raman spectroscopy. In particular, they have observed a drift of the vibration modes E_g and A_g of -3 and -6 cm^{-1} respectively. The present Raman measurements clearly demonstrate that the drift observed by Demoisson et al. was an artefact due to the heating of the samples by the laser beam.

Dielectric measurements further showed that (i) the resistance of the pyrite particles conditioned with deionised water, iodide or iodate, is about 1500 ohm (ii) the resistance of the pyrite particles conditioned with iodine is higher than 20,000 ohm and (iii) the resistance of the pyrite particles conditioned with selenite or selenate is even higher.

Voltammograms recorded using extremely slow scan rates (0.1 mV/s) allowed the electrochemical transformation of the complete electroactive matter immobilized at the working electrode. Therefore, after the electrooxidation of all the pyrite, species that have higher oxidation potentials can be detected. In this way it was found that: (i) after pyrite conditioning with deionised water, the voltammograms show only a main peak at about 0.95 V vs. SCE, (ii) after conditioning with iodine or iodate ions, this peak is followed by another at about 1.12 V vs. SCE, (iii) after conditioning with iodide, selenite or selenate ions, the main peak of pyrite is shifted to a lower potential by about 100 mV (0.85V).

XPS characterizations performed with extremely fine microparticles sampled after the reaction of FeS_2 with selenite or selenate ions in neutral and alkaline media revealed the presence of elemental selenium. The corresponding voltammograms show an additional

voltammetric signal at about -0.7 V vs. SCE. Experiments are in progress in order to confirm the absence of any photochemical origin for the observed selenium.

Dielectric measurements with dry pyrite microparticles during their stepwise exposure to air or pure oxygen

This study was initiated after an attempt to use dielectric spectroscopy to monitor in-situ the interactions of pyrite with soluble selenium and iodide species (and was continued after the end of the 4th reporting period). We have remarked that once dry pyrite was exposed to air for a short time its impedance rose rapidly. However, along its stay in a hermetically closed dielectric cell, its impedance progressively decreased and finally became almost the same as that before the exposure to air. It was as if pyrite had “repaired” the damage induced by its exposure to air. We considered that the observed phenomenon was worth being explored further: (i) because of the importance of the pyrite oxidation during the mining works in relation the underground installations construction and (ii) for avoiding the misinterpretation of dielectric data obtained during the in-situ monitoring of the interactions in liquid phase of pyrite with soluble selenium and iodide species.

The work performed using pyrite microparticles put in a dielectric cell under alternative flows of dry argon and ambient air (or dry oxygen) confirmed the preceding observation. The observed changes in the dielectric spectra are probably due to extremely fine transformations on the pyrite surface that cannot be detected with usual spectroscopic techniques (Raman microscopy). If the ambient air is used as the oxidizing agent, the presence of moisture renders the phenomena more complex. Even if this work was quite long, it must be considered as a preliminary approach; its main objective was to check the reproducibility of the measurements and if no artefacts occurred. The systematic study of other parameters as the particles size, the temperature, moisture degree... as well as the use of a well-suited and complementary technique would bring essential information in order to understand the observed phenomena.

Interactions of radionuclides with far-field solids

The work performed within this topic is focused on obtaining fundamental process understanding of the interaction of redox sensitive radionuclides such as Tc, U, Np and Pu with various far-field minerals.

The contribution of **CHALMERS** to ReCosy WP4 consists of an investigation of the redox state of groundwaters relevant to a crystalline rock environment (Äspö, Sweden) with the help of selected redox sensitive radionuclides.

The investigations are basically divided into two parts:

1. Synthetic groundwater
2. Synthetic groundwater with added crushed minerals ("batch" experiments)

In both parts we intend to look into aspects of the E_h agreement in a synthetic groundwater system containing the redox couples Fe(II)/Fe(III) with added redox-tracer e.g. radioactive Tc(IV)/Tc(VII), U(IV)/U(VI), Np(IV)/Np(V), Pu(III)/Pu(IV). Our aim

is to perform the studies under both oxic and anoxic conditions. Measurements with commercial redox electrodes as well as analysis and quantification of elemental oxidation states of redox tracer, using solvent-extraction, will be examined over time and discrepancies between these will be looked into.

Geological material and groundwater recipe are taken from the SKB Äspö LTDE-project (Long Term Diffusion Experiment), where results for in-situ adsorption of radionuclides onto rock surface and in-diffusion into the rock matrix is compared with laboratory results with crushed material.

During 2011 the experiments have continued with:

- 1) Production of An(IV) from An(V) or(VI) (An=U, Np) by catalytic reduction with H₂/Pt.
- 2) Spectroscopic measurement of redox state purity of 1mM solutions of An(IV) and its stability over time in inert atmosphere glove-box.
- 3) Separation of An(IV) from An(VI) by solvent extraction, using thenoyltrifluoroacetone (TTA), dibenzoylmethane (DBM) or 4-benzoyl-3methyl-1-phenyl-5-pyrazolinone (PMBP), for the purpose of quantification of ²³³U and ²³⁷Np in tracer concentrations (<1 µM).
- 4) Comparison of redox determination methods using synthetic groundwater of the LTDE type.

The reduction of 1mM solutions of U(VI) and Np(V) in 0.1M HClO₄ was followed with spectroscopy. 6 h of reduction was enough to convert U(VI) into U(IV), according to spectra. However, subsequent solvent extraction experiments were found to be more sensitive in the determination of redox state purity. Deviating results for extraction curves, where pH in aqueous phase was varied, was easily detected if traces of oxidized species was left after reduction. U(IV), U(VI) and Np(V) solutions were diluted to about 1-10µM and solvent extraction in the pH range 0.6 - 7 with three different systems were made: 0.5M TTA in xylene, 0.5M DBM in chloroform and 0.05M PMBP in xylene. Although the disappearance of characteristic peaks in Np spectra indicated that Np(V) could be reduced with H₂/Pt, the peaks for Np(IV) were not correspondingly enhanced. Solvent extraction also gave typical Np(V) extraction results. It was therefore concluded that Np reduction would need a more forceful method, such as a potentiostat, to be fully reduced to Np(IV). It was therefore decided to proceed with U reduction only, for the subsequent redox determinations. From the results for solvent extraction pH=2 was chosen for optimum separation of U(IV) and U(VI), using 0.5M DBM in chloroform. This method was used for comparison with a Pt/Ag/AgCl combination electrode in determining redox in synthetic LTDE groundwater. This water was prepared in glove-box (p(O₂)1 ppm) to pH=7.0, I=0.22M and with initial redox species [Fe²⁺]=12mM, [Mn²⁺]=6.5mM and [S²⁻]=3.1mM. Speciation calculations for this water gave a theoretical Eh=-167mV and should then be saturated with pyrite and quartz. However, it was found that the prepared water had an E_h=30mV when measured with a combined redox electrode. This is not surprising since the box atmosphere is not inert enough to maintain the initial conditions. A slow oxidation is therefore expected when reducing groundwaters are prepared and allowed to equilibrate with glove-box atmosphere. The prepared water was transferred to 100mL vessels, either with or without solid phase

additions of crushed pyrite and/or granite. These samples were spiked with U(IV) tracer and then measured with electrode and with the U(IV)/U(VI) determination method. The results gave about 280-340mV for electrode measurements, while U speciation gave about 30-70mV. If this measured discrepancy between the two methods indicates either: a tendency for conservation of initial redox conditions due to slow response to changed redox (U measurement) and a *de facto* further oxidation of solution (redox measurement) or: redox have actually not changed from what was as initially measured with electrode and the later electrode measurements were corrupted by some unknown disturbance, have not been established. A better control of initial redox is essential and some simple Fe(II)/Fe(III) strongly redox buffered systems may instead be used to establish: 1) whether the discrepancy between methods persist and 2) if possible, the cause for it. The inconclusive results were presented in the final workshop of ReCosy project. It is planned to publish more conclusive results in a full scientific paper, based on the S/T contribution (1) to the final ReCosy workshop.

FMTC carried out batch sorption experiments with ^{243}Am from NaNO_3 solutions onto wustite/magnetite, hematite and soil. ^{243}Am sorption onto wustite/magnetite and soil in static batch-type experiments showed a negative linear relationship within pH values (pH 2.15; pH 4.00; pH 6.95; pH 9.01), while the adsorption of ^{243}Am ions onto hematite increased with increasing pH values (correlation coefficient $R=0.83$, $R=0.92$, $R=0.90$, respectively). ^{243}Am distribution in the geosorbent column vertical profile under different pH values and 0.5 ml/h flow rate of 0.1 mol/L NaNO_3 aqueous solution was determined. Experimental results suggest ^{243}Am accumulation in the upper 2 cm layer regardless of geosorbent origin and aqueous solution pH value.

UMANCH is investigating the interactions between surfaces, humic acids and actinides in ternary systems, with the aim of developing a mathematical model to predict actinide chemistry and solid/solution partition.

During 2011, the partition of plutonium in oxidation states IV, V and VI between solid and solution phase has been studied in humic/quartz sand ternary systems as a function of time, both in the absence and presence of HA. The behaviour in the Pu(IV)/quartz sand ternary system appears simple, with the humic appearing to act largely as a competing solution phase ligand, and Pu sorption decreases with increasing HA concentration for all systems. The same type of behaviour was observed for the Pu(VI) system. For the Pu(V) system, the presence of humic at low concentrations enhances sorption, and so ternary complexes are very important. The Pu sorption in all systems is reversible to some extent, and in the Pu (IV) system, it seems fully reversible in the short-term. We have also augmented the database of humic-radionuclide binding constants for the WHAM speciation model.

Results:

Batch experiments with single oxidation states under controlled atmospheres the measured Pu concentration remaining in solution in ternary systems. To test reversibility, after equilibration, solid and solution were separated: fresh solid was added to the solution and fresh solution (Pu free) was added to the solid. These replacement experiments provide a more rigorous test of speciation models. They simulate processes that will take place as a Pu solution encounters fresh mineral surface

as it migrates, as well as the ability of humic acid to re-mobilise Pu that has been sorbed to a mineral surface.

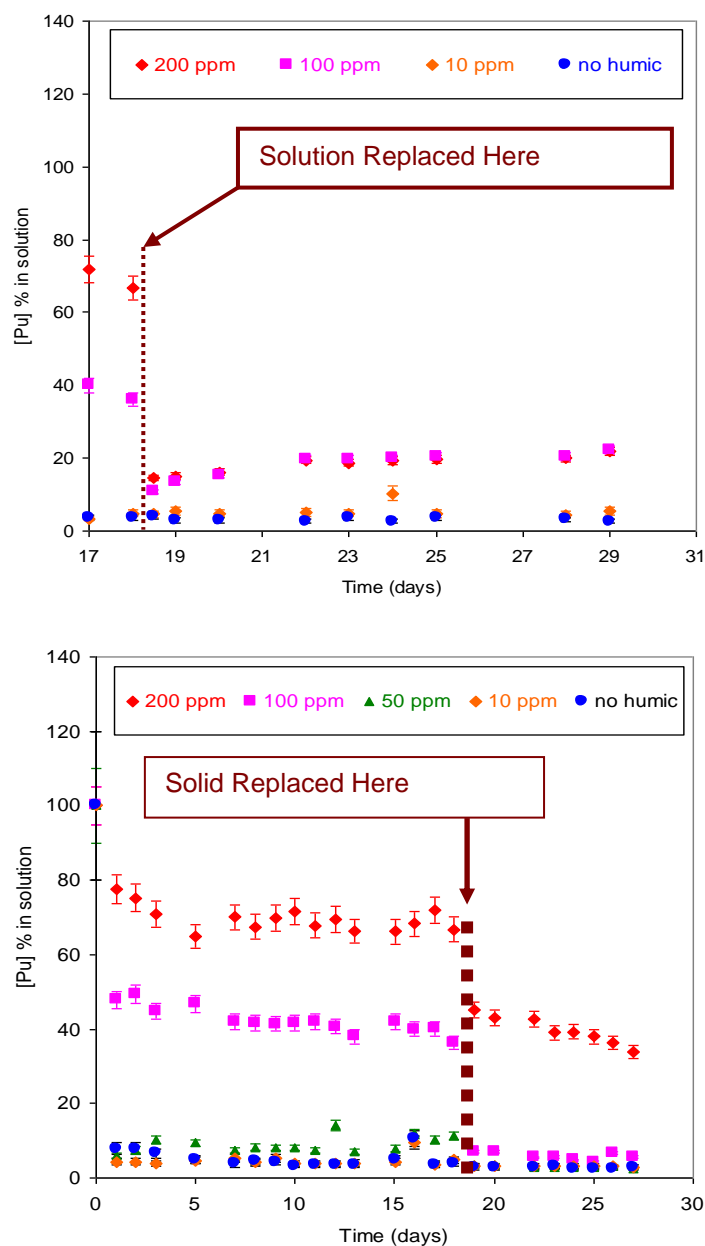


Figure 1: $^{239}\text{Pu(IV)}$, 1.22 kBq ml^{-1} , $I = 0.1$, $\text{pH} = 6$. **A (upper figure):** Pu concentration following exposure to 2 successive samples of mineral. **B (lower figure):** Pu concentration before and after replacement of the solution for the same sample of mineral.

Figure 1 shows the data for the Pu(IV) system, which shows simple, ‘classical’ ternary system behaviour. As [HA] increases, the amount of Pu sorbed decreases. The main apparent effect of the humic is to act as a competing solution phase ligand, which holds Pu(IV) in solution. There is no significant difference between the 10 ppm and humic free systems. The typical [HA] in the environment is $< 10 \text{ ppm}$, and so the results suggest that for the quartz sand system, the presence of humic at realistic concentrations

does not affect the solid/ solution partition. Further, the data show that this system is reversible, i.e., the data in Figure 1B may be predicted from that in Figure 1A. The Pu(V) system behaviour is much more complex, because low [HA] actually increases sorption. This can happen when the interaction with the humic is stronger than that with the mineral surface, which makes ternary complex formation (Quartz-HA-Pu) very significant. Hence, realistic [HA] may help prevent Pu(V) migration in quartz systems. Probably as a result of the these ternary complexes and the complex sorption behaviour, there is evidence for some irreversibility this time, and hence behaviour will be harder to predict for Pu(V). Pu(VI) is different to the Pu(V) in that the system appears largely reversible, which may be related to the fact that, like Pu(IV), the data show simple ternary behaviour (consistent increase in [Pu] with increasing [HA]). In the vicinity of a repository, the Eh may change. To test the effect, Pu(IV) was allowed to sorb before the experiment was exposed to oxygen (data not shown). Over a period of a few weeks, there was no significant effect. The data for the Pu (V/VI) systems are not shown here, but are available in the full S+T contribution.

In addition to the ternary system work, we have used linear free energy relationships to estimate WHAM/Model VII binding constants for Pd^{2+} , Sn^{2+} , U^{4+} , NpO_2^{2+} , Pu^{4+} and PuO_2^{2+} . The WHAM model has been widely applied to stable element speciation, but is lacking humic binding parameters for some radioisotopes. We have filled gaps in the binding constant database. When combined with the existing constants for inorganic species, this now allows the calculation of equilibrium distributions of important radionuclide species under a wide range of conditions. This has improved the applicability of the WHAM speciation model for radioactive isotope speciation and thus makes the model applicable to radiological performance assessment calculations. Full details of this work are available in Stockdale et al (2011).

It can be concluded that:

- HA/Quartz/Pu(IV)/(VI) systems show (short-term) reversible sorption;
- For quartz, realistic concentrations of HA have little effect on Pu(IV) solid:solution partition;
- Ternary complexes are very significant for Pu(V), and there is some irreversibility, making behaviour hard to predict;
- Exposure of a HA/Quartz/Pu(IV) system to oxygen does not seem to affect sorption in the short-term;
- We have extended the WHAM speciation model to include important radionuclides.

In the last ReCosy period, **KIT – INE** focussed its research towards the characterization of the Np, Pu, and Tc, which were sorbed on the clay surface after a long reaction time up to 8 months. The sorption and redox speciation of Np, Pu and Tc have been performed on crushed OPA and COx clay rocks with artificial pore water. The batch experiments were performed at the equilibrium pH 7.6 for OPA and pH 7.2 for COx under argon atmosphere (<1 ppm O_2) with 1% CO_2 conditions at room temperature. Four different solid to liquid ratios ($S/L = 10, 20, 50, 200$) have been regarded, at constant ionic strength (0.1 M NaCl). We have performed two series of sorption experiments, one at higher metal concentration of about 3.0×10^{-4} M and one at low metal concentration of 1.0×10^{-8} M. The higher concentration was necessary to get a

chance for characterizing the metal by spectroscopic methods like X-ray absorption fine structure (XAFS), UV-Vis absorption, X-ray photoelectron spectroscopy (XPS).

We observed at low concentration that more than 80% of Np, more than 90% of Pu and only 20-50% of Tc is sorbed on the OPA as well as on the COx. The amount of the sorbed metal ion depends on the different S/L ratio; the higher the S/L ratios the higher the sorption. Liquid-liquid extraction of the aqueous solution after separating the clay by ultrafiltration (10 kD) showed reduction of Np(V), Pu(V), and Tc(VII) to the tetravalent oxidation state. About 50% of the remaining metal ions are in the tetravalent state whereas the rest of the metal ion is still in the higher oxidation state. These findings qualitatively match with the results of thermodynamic calculation based on measured E_h values of the solutions in contact with the clay. The E_h was measured after 8 months to be 10 – 40 mV for the Np/Clay system, (-180) – 40 mV for the Pu/Clay system, and (-100) – (-80) mV for the Tc/Clay system.

To remind the results at higher metal concentration, the Np and Tc ions were not sorbed in the lower oxidation state after a reaction time of 1 week. Only Pu has been found in the tetravalent oxidation state after 1 week. However, after a reaction time of 4 or 8 months neither Np nor Tc sorbed on the clay has been found in the tetravalent oxidation state by XANES. Even the presence of hydroquinone (10^{-3} M) and magnetite (0.6 g/L) did not change the speciation as well as the E_h value that still is the same as in the solution without them. From the EXAFS we could show with the help of the measured Pu-Pu interaction with a distance of 3.75 Å that the Pu(IV) must be precipitated as a Pu-polymer species on the surface. For the Np(V) we assume that with increasing reaction time the Np(V) surface complex changes from an outer sphere complex after 1 week to a inner sphere complex after 8 months. This is proven by a weak third shell signal coming from Si/Al neighbours at 3.75 Å, which was not observed in the spectra of samples after one week.

The lack of reduction at high metal concentrations might be due to limited number of reducing sites on the clay presumably pyrite sites. The concentration of pyrite sites is estimated to be around 10^{-8} mol/g (Descostes et al. (2010)).

However, the experiments showed that under reducing conditions, the elements Np, Pu, and Tc, whenever they are released in the pentavalent or heptavalent oxidation state, are sorbed in the tetravalent oxidation state when a sufficient amount of reducing sites are available on the clay for the reduction process.

Redox processes under hyperalkaline conditions

The work performed within this topic aims to provide an understanding of the redox behaviour of redox-sensitive radionuclides such as Tc, U, Np under hyperalkaline conditions.

The contribution of **ULOUGH** to the Recosy WP4 consists of an investigation of the effect of ISA and picolinic acid on the redox chemistry of technetium. The current UK option for the management of ILW is to store it in a deep geological disposal facility (GDF). This may then be backfilled with a cementitious material. The GDF will develop highly alkaline porewater for *ca.* 10^5 years. Corrosion of steel canisters will lead to reducing conditions, so the chemistry of Tc in the waste must be understood in

the context of this chemistry. The aqueous chemistry of technetium is likely to be dominated by the highly mobile pertechnetate anion in aerobic waters, and by $\text{TcO}_2(\text{am})$, in anaerobic.

Organic complexing agents will be present in ILW, including decontamination agents such as EDTA and picolinic acid, as well as polyhydroxylated carboxylic acids like α -isosccharinic acid (ISA) and gluconic acid. Such ligands are often highly complexing and can cause significant increases in radionuclide solubility, especially at high pH. The GDF will not be homogenous so there will be areas of reducing and oxidising potential, which could mean both Tc(VII) and Tc(IV) are present. If TcO_4^- migrates into an area of reducing conditions, the organics may complex with Tc during reduction to form water-soluble species. Also of relevance, is the possibility of increased solubility when organics are in contact with reduced Tc. In other words, does the presence of organics affect the reduction of Tc(VII) to Tc(IV) ? Studies were undertaken in which TcO_4^- was reduced in the presence and absence of the four ligands, to determine whether there was an increase in Tc solubility when TcO_2 was contacted with the ligand.

Experiments were conducted in an N_2 glove box. Solutions were boiled, N_2 sparged and kept in presence of Fe filings to maintain reducing conditions. The ligands were added to NaOH(aq) in the form of solids at pH 13.3, to give concentrations between 0.4 and $0.001 \text{ mol dm}^{-3}$. NH_4TcO_7 was added and pH and Eh measured. Reduction was achieved by 3 methods, the addition of 0.7 g of SnCl_2 or FeCl_2 or electrochemically. Five replicates were used. Control experiments showed that reducing conditions were maintained for the requisite periods of time and that 14 days was sufficient for steady state to be established.

The red data points in figures 1 and 2 show the effect of ISA and picolinic acid concentration on Tc(IV) solubility. The slopes of close to unity for ISA and picolinate indicate that the increase in solubility of Tc is being controlled by the formation of a 1:1 Tc(IV) -ligand complex.

TcO_4^- reduction in presence of ligands

In the presence of ISA, a lowering of $[\text{Tc}](\text{aq})$ took place, showing that ISA did not prevent reduction taking place (Figure 2). If this reduction was to Tc(IV) , then the final $[\text{Tc}](\text{aq})$ should be the same as that produced by the addition of ISA to Tc(IV) solution, i.e. the Tc(IV) -ISA complex would again be formed, but by 2 different routes at steady state. For ISA, this would seem to be the case. The presence of PA again inhibited the reduction of pertechnetate by all three reduction methods tried, (Figure 3).

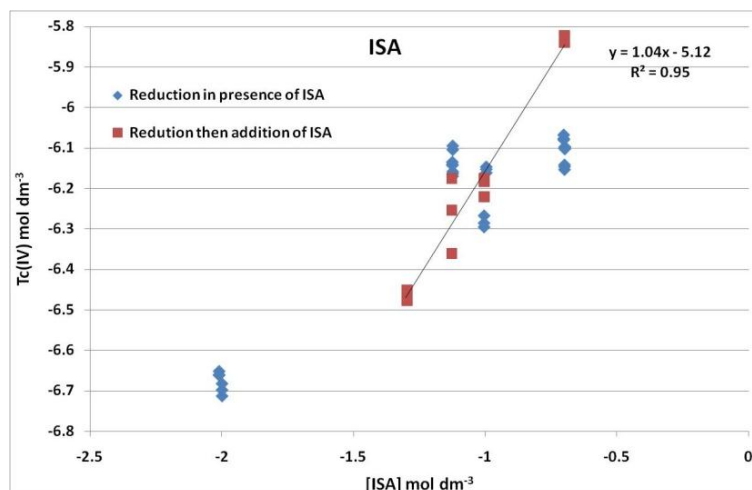


Figure 2: Comparison of final [Tc] in presence of ISA at pH 13.3, starting from TcO_4^- and $Tc(IV)$.

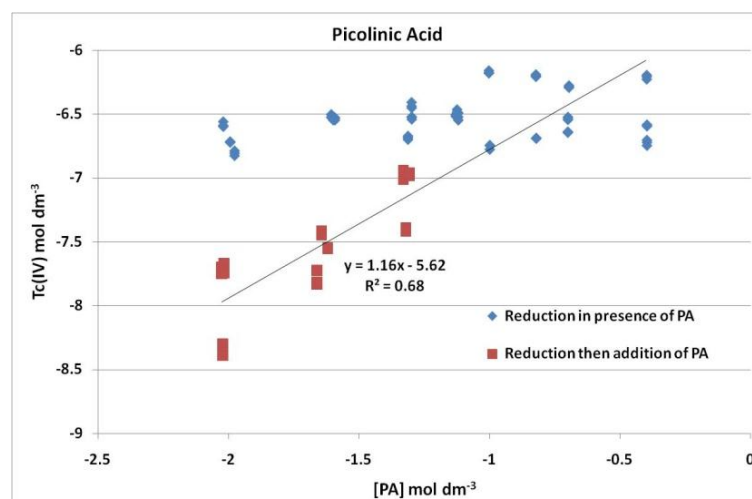


Figure 3: Comparison of final [Tc] with of PA at pH 13.3, starting from TcO_4^- and $Tc(IV)$.

AMPHOS has studied the solubility of uranium (IV) oxide in an alkaline environment (pH between 9-12) and using different anoxic / reducing conditions at 25° C in solutions without complexing ligands (carbonate, phosphate, silicate, etc.) where uranium oxides, oxyhydroxides or hydroxides are expected to be the solubility controlling solids (Riba et al. 2012). The proposed objectives of the project for the past year were to model solubility data of $UO_2(am)$ under alkaline pH and anoxic/reducing conditions under $H_2(g)$ atmosphere or by using dithionite as a reducing agent. Data used in the modelling exercise have been obtained during the previous years of the project and compared with data included in the literature. The objectives of the modelling exercise have been:

- To investigate the causes of the E_h - pH trend observed in the $UO_2(am)$ solubility experiments
- To study the mechanism determining the uranium concentration in solution.

The experiments performed under $H_2(g)$ atmosphere at $pH = 9.4$ and 11 and using $NaClO_4$ as electrolyte indicate that $H_2(g)$ behaves as an inert gas without reducing properties. The measured E_h is in agreement with the occurring uranium processes in the system. At low Na^+ concentration ($0.01\text{ M } NaClO_4$), the measured redox potential is in agreement with the oxidative dissolution process of $UO_2(am)$. However, at $0.1\text{ M } NaClO_4$ the measured redox potential responds to “redox-neutral” conditions (Neck et al., 2007) and measured uranium concentrations are in agreement with Na-uranate secondary phase ($Na_2U_2O_7 \cdot xH_2O$) controlling the solubility of U in solution (see Figure 4)

The experiments performed with Na-dithionite as a reducing agent (at $pH = 10, 11$ and 12 , $I = 0.1\text{ M } (NaClO_4)$) and using two different dithionite concentrations (0.001 and 0.01 M) demonstrate the E_h measurements respond to different dithionite processes of oxidation and decomposition as a function of dithionite concentration, pH and reaction time. Despite the variability in the redox potential, the measured uranium concentrations suggest that reducing conditions kept during the experiments are controlled by the formation of sulphide in solution, so that there is a limited oxidative dissolution process of $UO_2(am)$. The low concentrations of U measured in solution are in agreement with the low solubility $UO_2(am)$ under reducing conditions with an aqueous speciation scheme including U(IV) and U(VI) aqueous complexes but without any evidence of the formation of the anionic U(IV) species; $U(OH)_5^-$ and $U(OH)_6^{2-}$, proposed by Fujiwara et al (2005).

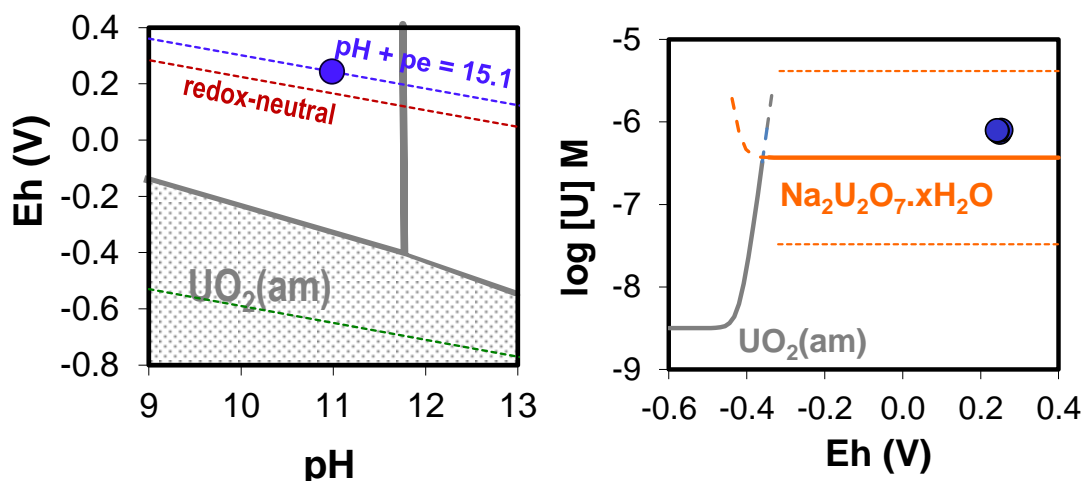


Figure 4: (Left). E_h/pH predominance diagram of uranium at uranium total concentration of $8 \cdot 10^{-7}\text{ M}$. The “redox neutral” conditions ($pH+pe=13.8$) have been represented as a dashed red line and the experimental $pH+pe=15.1$ is represented as a dashed blue line. The symbol represents the experimental data. **(Right)** Solubility curve of $UO_2(am)$ and $Na_2U_2O_7 \cdot xH_2O$ as a function of E_h at $pH = 11$ and $I = 0.1\text{ M}$. The dotted line represent the error associated to $Na_2U_2O_7 \cdot xH_2O$ solubility. The symbols represent the experimental uranium concentration and measured E_h .

The contribution of **PSI** to WP4 focuses on the influence of redox conditions on the immobilization of Neptunium in highly alkaline cementitious environments.

Neptunium is commonly believed to exist in oxidation states +IV and +V in a cementitious environment under reducing, respectively oxidizing conditions. However, the possible formation of anionic Np(VI) species ($\text{NpO}_2(\text{OH})_3^-$ and $\text{NpO}_2(\text{OH})_4^{2-}$) under oxidizing hyperalkaline conditions, in analogy to U(VI), may significantly limit the stability field of Np(V) in favour of Np(VI) species. Whereas experimental data concerning the sorption of Np(V) by cementitious materials are scarce, sorption data concerning Np(IV) and Np(VI) are non-existing in the literature. In many sorption databases these gaps are filled by proposing estimates for the missing sorption data based upon chemical analogies (e.g. Th(IV) – Np(IV) or U(VI) – Np(VI)) or based upon the electrostatic interaction energy (expressed by the effective charge, Z_{eff}) implying increasing sorption values in the series Np(V) ($Z_{\text{eff}}=2.2$) < Np(VI) ($Z_{\text{eff}}=3.0$) < Np(IV) ($Z_{\text{eff}}=4.0$) (e.g. Wieland & Van Loon, 2002). The PSI contribution to WP4 aims at validating these assumptions.

During the first 3 years of Recosy, emphasis was mainly put on the determination of the Neptunium redox speciation under hyperalkaline conditions and on the development of experimental procedures to control the redox conditions and measure the Np redox state during solubility and sorption experiments. Furthermore the sorption of Np(IV,V,VI) on CSH phases was investigated in detail. These latter studies showed that sorption distribution ratios (R_d values) measured for the Np(IV/V) sorption onto C-S-H phases are surprisingly high ($R_d=(6\pm4)\cdot 10^5 \text{ L kg}^{-1}$) and independent of the C:S ratio and the pH. The sorption of Np(VI) on C–S–H phases was found to be strong at low C:S ratios but decreased with increasing C:S ratios (increasing pH).

The sorption behaviour of Np(IV,V,VI) on C–S–H phases is influenced by the properties of the C–S–H phases (varying composition, varying structure and high recrystallisation rates) and by the aqueous speciation of Np(IV,V,VI). To determine the effect of the aqueous speciation on the Np(IV,V,VI) uptake, sorption experiments were carried out on TiO_2 , a stable solid phase with a constant composition and structure, and low recrystallisation rates. Overall, with progressing hydrolysis of Np the formation of anionic species, appeared to adversely affect the sorption of this radionuclide. In the case of Np(IV), $\text{Np}(\text{OH})_4$ is the sole species present in the pH range $10 \leq \text{pH} \leq 14$, resulting in constant sorption values for this tetravalent species (data not shown). In the case of pentavalent and hexavalent neptunium, the neptunyl moieties become progressively hydrolyzed with rising pH up to the formation of anionic hydroxy species ($\text{Np(V)O}_2(\text{OH})_2^-$, $\text{Np(VI)O}_2(\text{OH})_3^-$ and $\text{Np(VI)O}_2(\text{OH})_4^{2-}$) at the highest pH values. In parallel, the sorption of Np(V) and Np(VI) decreases significantly indicating a much weaker affinity of these anionic hydroxyl species for sorption sites of TiO_2 . The observed sorption reduction could be described in a satisfactory way assuming that the anionic species $\text{Np(V)O}_2(\text{OH})_2^-$ and $\text{Np(VI)O}_2(\text{OH})_4^{2-}$ are not sorbing and that the formation of these two anionic species in solution competes with the surface complexation reaction on the TiO_2 (Figure 5). Surprisingly, it has to be assumed that the $\text{NpO}_2(\text{OH})_3^-$ anionic species sorbs as strongly as the $\text{NpO}_2(\text{OH})_2$ species, to obtain a proper fit of the data.

For the modelling the following reduction factors were applied for Np(V) and Np(VI) respectively:

$$\text{Np(V):} \quad f = \frac{R_d}{R_d^0} = \frac{1}{1 + \frac{* \beta_2^0}{* \beta_1^0 \cdot [H^+]} \cdot \frac{1}{\gamma_- \cdot \gamma_+}} \quad (1)$$

$$\text{Np(VI):} \quad f = \frac{R_d}{R_d^0} = \frac{1}{1 + \frac{* \beta_4^0}{* \beta_3^0 \cdot [H^+]} \cdot \frac{\gamma_-}{\gamma_{2-} \cdot \gamma_+}} \quad (2)$$

β_1^0 and $*\beta_2^0$ are the stability constants for the formation of the hydroxy complexes $\text{NpO}_2(\text{OH})$ and $\text{NpO}_2(\text{OH})_2^-$, and $*\beta_3^0$ and $*\beta_4^0$ are the stability constants for the formation of the hydroxy complexes $\text{NpO}_2(\text{OH})_3^-$ and $\text{NpO}_2(\text{OH})_4^{2-}$. γ_- , γ_{2-} , and γ_+ are the activity coefficients for the monovalent and divalent anions, and for the monovalent cations in the SIT equation. SIT interaction parameters were taken from estimations presented by Hummel et al., (2009) assuming a NaCl matrix.

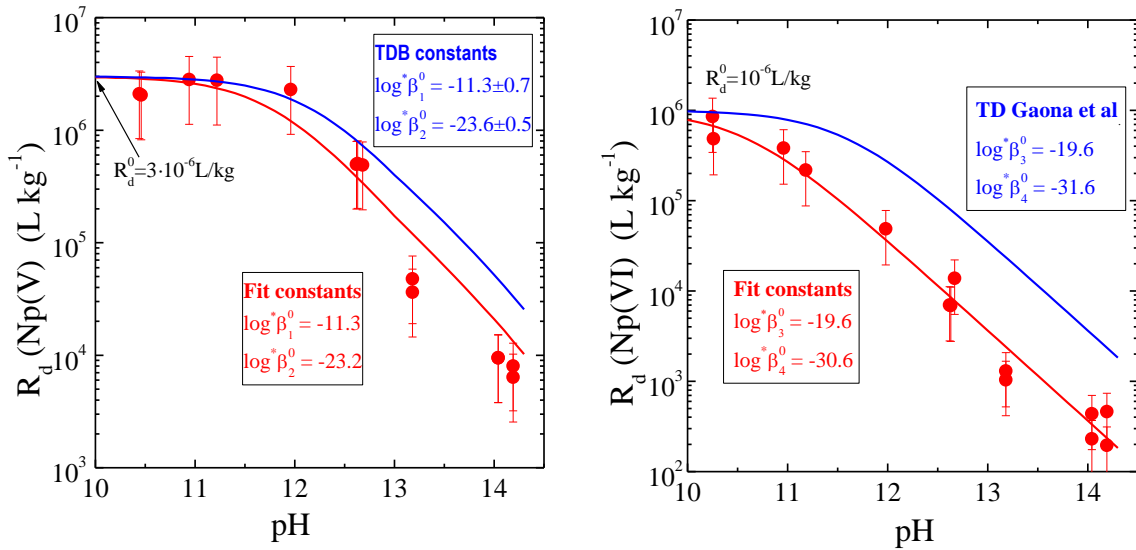


Figure 5: Effect of pH on the sorption of Np(V) (a) and Np(VI) (a) on TiO₂. The S:L ratio = $2 \times 10^{-4} \text{ kg L}^{-1}$. $[^{239}\text{Np}] = 1.5 \times 10^{-10} \text{ M}$. $I = 1.0$.

The values for these complexation constants were taken from the NEA thermodynamic database (Guillaumont et al., 2003) and from Gaona et al., 2011. The solid lines in Figure 5a and b are the model curves and the dotted lines are fitted curves with $\log * \beta_2^0$ and $\log * \beta_4^0$ taken as fitting parameters in equations 1 and 2 respectively. Figure 5a and b show that this model slightly overestimates the sorption values. However a comparison of the values for the thermodynamic complexation constants, $\log * \beta_2^0$ and $\log * \beta_4^0$, from the NEA TDB used in the models, with values obtained from a fit of the

data (Figure 5a and b) show that the difference between the model and the fit actually is quite small. Hence, it is concluded that the sorption of Np(IV,V,VI) on TiO₂ under hyperalkaline conditions can be explained satisfactorily assuming that anionic hydroxyl species are not sorbing.

The sorption behaviour of the tetravalent, pentavalent, and hexavalent actinides on C–S–H phases appears to be very similar to the sorption behaviour observed previously on TiO₂ up to a pH of 12.5 (Figure 4.9a) and can thus be explained by their speciation behaviour; i.e. with rising pH, negatively charged species increasingly dominate the aqueous speciation of the exavalent actinides, resulting in decreasing sorption. In the case of the tetravalent Np, the aqueous speciation is independent of pH in the pH range studied, resulting in constant sorption values with rising pH for this redox state. In the case of Np(VI), anionic species dominate the aqueous speciation starting from pH = 11 resulting in a decrease of the measured R_d values. The constant sorption values observed in the case of Np(V) are explained by its weaker hydrolysis with anionic Np(V)O₂(OH)₂[−] species appearing only above pH = 12.5. i.e. beyond the experimental pH range.

The similar sorption behaviour of the tetravalent, pentavalent and hexavalent neptunium on TiO₂ and C–S–H phases suggest that the variation in the C–S–H composition only has a marginal influence on actinide sorption.

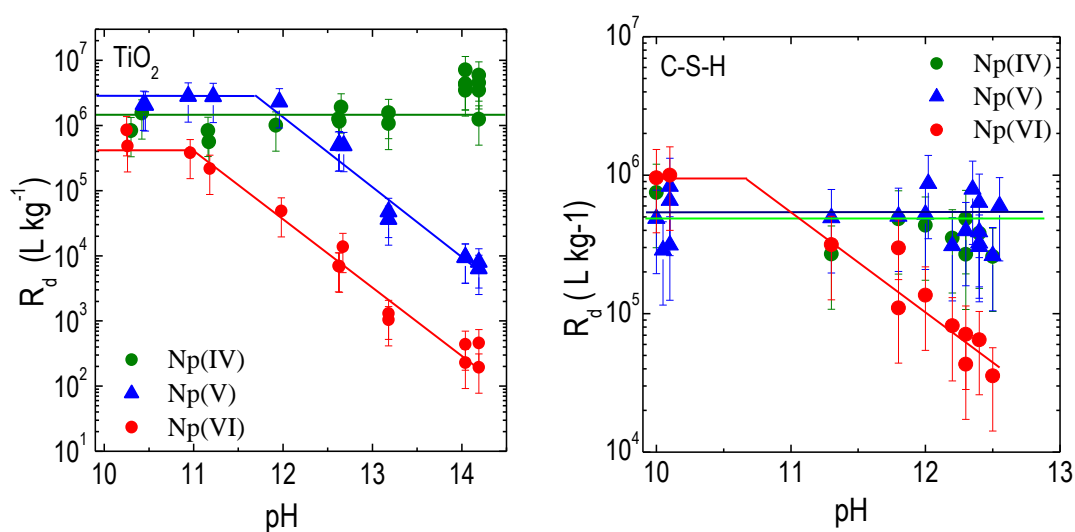


Figure 6: Effect of pH on the Np(IV,V,VI) sorption on TiO₂ (a) and on C–S–H phases (b). The S:L ratio = 2×10^{-4} kg L^{−1}. [239Np] = 1.5×10^{-10} M. I = 1.0.

Acknowledgements

Manchester university would like to thank the United Kingdom Engineering and Physical Sciences (DIAMOND Universities Consortium) and Natural Environment (BIGRAD Consortium) Research Councils for funding this work.

References

- Carbol, P., Cobos-Sabaté, J., Glatz, J.-P., Ronchi, C., Rondinella, V., Wegen, D.H., Wiss, T., Loida, A., Metz, V., Kienzler, B., Spahiu, K., Grambow, B., Quiñones, J. and Martínez-Esparza, A. (2005). The effect of dissolved hydrogen on the dissolution of ^{233}U doped $\text{UO}_2(\text{s})$, high burn-up spent fuel and MOX fuel. SKB Technical Report TR-05-09.
- Demoisson, F., Mullet, M., Humbert, B. (2008). Pyrite oxidation in acidic medium: overall reaction pathway. *Surf. Interface Anal.* 40: 343–348.
- Descostes, M., Schlegel, M.L., Eglizaud, N., Descamps, F., Miserque, F., Simoni, E. 2010. Uptake of uranium and trace elements in pyrite (FeS_2) suspensions. *Geochim. Cosmochim. Acta* 74, 1551 (2010).
- Fujiwara, K., Yamana, H., Fujii, T., Kawamoto, K., Sasaki, T., Moriyama, H. (2005) Solubility of uranium(IV) hydrous oxide in high pH solution under reducing conditions. *Radiochim. Acta.*, 93, 347-350.
- Gaona, X., Dähn, R., Tits, J., Scheinost, A., and Wieland, E. (2011). Uptake of Np(IV) by C–S–H phases and cement: an EXAFS study. *Environ. Sci. Technol.*, Submitted.
- Gaona X., Tits, J., Dardenne, K., Liu, X., Rothe, J., Denecke, M.A., Wieland, E., Altmaier, M. (2012). Spectroscopic investigations of Np(V/VI) redox speciation in hyperalkaline TMA-OH solutions. *Radiochim. Acta*. Submitted.
- Holgersson, S.: On the use of actinides as redox tracer elements in groundwater samples. S/T contribution to 4th ReCosy workshop, Karlsruhe 23rd-26th March, 2012.
- Hummel, W. (2009). Ionic strength corrections and estimation of DIT ion interaction coefficients. PSI Technical Report, TM-44-09-01, Paul Scherrer Institut, Villigen, Switzerland.
- Neck V., Altmaier M., Fanghänel T. (2007) Solubility of plutonium hydroxides/hydrous oxides under reducing conditions and in the presence of oxygen. *C. R. Chimie*, 959-977.
- Ollila K. (2002) Uranium solubility. In: Nuclear Waste Managements in Finland. Finalreport of Public Sector's Research Programme, JYT 2001 (Ed. K. Rasilainen), Ministry of Trade and Industry, Helsinki, Finland, pp. 77-79.
- Rai, D., Felmy, A. R., Ryan, J. L. (1990) Uranium (IV) hydrolysis constants and solubility product of $\text{UO}_2 \cdot x\text{H}_2\text{O}(\text{am})$. *Inorg. Chem.*, 29, 260-264
- Riba, O.; Montoya, V.; Grivé, M.; Duro, L. (2012). Uranium solubility under alkaline conditions using different reducing agents. Scientific and Technical Contribution, Recosy (in preparation).
- Ryan, J. L., Rai, D. (1983) The solubility of uranium(IV) hydrous oxide in sodium hydroxide solutions under reducing conditions. *Polyhedron*, 2, 947-952.
- Scholz, F., Meyer, B. (1998). Voltammetry of solid microparticles immobilized on electrode surfaces. In: *Electroanalytical Chemistry, A Series of Advances* (A.J. Bard, I. Rubinstein, ed.) Marcel Dekker, Vol. 20, pp. 1-86.
- Stockdale, A., Brian, N., Lofts, S. 2011. Estimation of model VII humic binding constants for Pd^{2+} , Sn^{2+} , U^{4+} , NpO_2^{2+} , Pu^{4+} and PuO_2^{2+} . *J. Environ. Monit.*, 2011, 13, 2946–2950.

Torrero, M. E. (1995) Estudio de la disolución del UO₂ como análogo Químico de la matriz del combustible nuclear gastado. Influencia de los principales parámetros fisicoquímicos que definen los repositorios en medios salino y granítico. Universidad de Barcelona, Thesis, Barcelona, Spain.

Wieland, E. and van Loon, L. R. (2002). Cementitious Near-Field Sorption Data base for performance Assessment of an ILW Repository in Opalinus Clay. PSI Report. Nr. 03-06, Paul Scherrer Institute, Villigen-PSI, Switzerland and Nagra Technical Report NTB 02-20, Nagra, Wettingen, Switzerland

Yajima, T., Kawamura, Y., Ueta, S. (1995) Uranium(IV) solubility and hydrolysis constants under reduced conditions. Sci. Basis Nucl. Waste Management XVIII, Symp. Proceedings, 353, 1137-1142

WP 4.2. CHEMICAL AND REDOX BEHAVIOUR OF THE INVESTIGATED RADIONUCLIDES IN THE DIFFERENT SYSTEMS

Introduction

Within WP 4.2 the participating institutes are focusing their work on the study of the microbial impact (**FTMC**) and on the uranium redox state in-situ in biofilms with emphasis on biologically mediated redox processes (**HZDR**). The studies are carried out on isolated microorganisms as well as on biofilms. Biofilms are composed of bacteria, fungi, algae, protozoa, exopolymeric substances (EPS), corrosion products and 50–95% water. They are ubiquitous and have to be considered as an important factor in natural biogeochemical processes influencing the redox state of radionuclides. They show a multiplicity of interactions with metals and contribute to metal mobility or immobilization.

Work performed by partners

The activities of **HZDR** during the third year of ReCosy were focused on biologically mediated redox processes of biofilms growing in the nuclear waste repository research tunnel ONKALO (Finland), which will be part of the nuclear waste repository in the future.

Introduction

Since most surface and subsurface environments are inhabited by microorganisms, natural microbial communities (= biofilms) are considered, along with minerals, as an important factor influencing the transport of radionuclides in the environment. Microsensor measurements of the oxygen concentration, redox potential and pH are helpful in interpreting in-situ microbial metabolic processes in biofilms. Since microbial processes are sensitive to metals and their speciation, the bioavailability of the metals changes with redox potential, pH, and oxygen in a complex manner. Massive biofilms are growing next to a fracture zone in a granitic rock environment. at site 777 m of the tunnel. They were described by Pedersen et al. (2008) as a pink and solid slime, consisting of *Pseudomonas anguilliseptica*, *Arthrobacter bergeri*, *Hydrogenophaga sp.*, *Methylobacter tundripaludum*, *Rhodoferrax ferrireducens*, and *Haliscomenobacter hydrossis*.

Experimental

Biofilm samples were removed from the tunnel wall at the 777 m position and exposed into a rectangular cell with an outer dimension of 121 x 42 x 15 mm. During the sensor measurements, 150 ml of the groundwater as a blank solution from the site was pumped

through the cell in a closed circuit with a flow velocity of approximately 4 mL/min. For the sensor measurements a miniaturized platinum redox microelectrode, oxygen microsensor of the Clark-type and a miniaturized conventional pH electrode, each with a tip diameter of 10 μm , were used. After the values were recorded, uranium was added in ecologically relevant concentrations (4×10^{-5} M) to the groundwater solution. Microsensor measurements were recorded 22 and 42 hours after the addition of uranium. Samples of the groundwater solution were taken before and after the addition of uranium as well as at the end of the experiments. The samples were acidified in-situ and analyzed for determination of the inorganic elements by Inductively Coupled Plasma Spectrometry. The anions were determined by Ion Chromatography. The analytical data of the groundwater sample was used for the calculation of the predominance fields of different uranium species in the pH-Eh diagram for the U-S-O-H-C system at 15°C by using the geochemical speciation code “Geochemist’s Workbench” Version 8.0.8 / ACT2 Version 8.0.8. For Energy-filtered Transmission Electron Microscopy (EF-TEM) and by electron energy loss spectroscopy (EELS) studies a biofilm sample was fixed in-situ with 1 % (vol/vol) glutardialdehyde at the end of the experiments and prepared afterwards following the routine embedding protocol with minor modifications as described by Lünsdorf et al. (2001). EF-TEM offers the possibility to systematically study and analyse the ultrastructure and elemental composition of nanoscale mater by electron energy loss spectroscopy (EELS).

Results

Several micropprofilings of the redox potential and pH were performed in the biofilm sample, placed in the flow cell. Before the addition of uranium to the groundwater, which was pumped through the biofilm in a closed circle, the results showed an average value of $+70 \pm 2$ mV, including a correction factor of + 239 mV after Stumm and Morgan (1996) and a pH of 5.37. The values measured in the groundwater differed significantly. The results showed a pH of 8.68 and a redox potential of +491 mV. The redox potential of the groundwater is approximately 420 mV lower than in the biofilm. The difference of the pH amounts more than 3.5 units. These results clearly demonstrate that the geochemistry inside a biofilm is totally different compared to the surrounding water/environment. With regard to the migration and the retention of radionuclides these differences are of great importance. In uranium contaminated waters the formation of possible uranium species are dependent on the redox potential and the pH. Changes of these parameters will have the consequence of the formation of solid uranium(IV) and uranium(VI) species as precipitates in the determined biofilm. In our experiments microsensor measurements were performed 42 hours after the addition of uranium, showing a significant change of the parameters. The redox potential within the biofilm decreased to -164 mV with an increase of the pH at the same time to 7.27. The low redox potential indicates that reducing conditions are present, probably catalyzed by microorganisms. For a better interpretation a pH-Eh diagram for the U-S-O-H-C system at 15°C was constructed by using the geochemical speciation code “Geochemist’s Workbench” Version 8.0.8 / ACT2 Version 8.0.8. The analytical data of the uranium contaminated groundwater was used for the calculation of the predominance fields of different uranium species. The default data base used was the thermo.dat accompanying code, supplemented by the most recent NEA database for uranium (Guillaumont et al., 2003), and by solubility data for Bayleyite from Gourman-Lewis et al. (2008). The theoretical predominance fields of solid uranium species under the ambient condition

found in the contaminated groundwater are defined clearly in geochemically different areas: The first area is characterized by a redox potential of approximately $< 1\text{ V}$ and a $\text{pH} > 4.0$. This area is dominated by the solid uranyl carbonate Rutherfordine (UO_2CO_3) and the magnesia bearing uranyl carbonate mineral Bayleite [$\text{Mg}_2(\text{UO}_2)(\text{CO}_3)3 \cdot 18(\text{H}_2\text{O})$] at a $\text{pH} > 4.2$. The second area is characterized by a redox potential of approximately $< +320\text{ mV}$ and a pH which varies between 0 and 5.8. Assuming reducing conditions, the formation of Uraninite, a uranium(IV) oxide (UO_2) mineral, was predicted. The results of the redox potential measurements of the biofilm 42 hours after the addition of uranium to the groundwater were plotted together with the pH into the calculated pH -Eh diagram for the U-S-O-H-C system. As shown in Fig. 3, the plots appear in the area of Bayleite, indicating that an uranium(VI) solid mineral may have been formed in the contaminated groundwater. For great importance is the localization of the measured biofilm plotted into the eh-pH diagram. Due to the fact that after the addition of uranium the redox potential inside the biofilm decreased and the pH increased the formation of a solid uranium(IV) mineral within the biofilm seems possible after thermodynamically calculations.

The retardation of uranium in the biofilm was determined by Energy-filtered Transmission Electron Microscopy (EF-TEM) and Electron Energy Loss Spectroscopy (EELS). Elongated particles of high electron density were observed in the cytoplasm of some rod shaped gram negative bacteria, which were often found associated with large rod shaped bacteria. Analysis of the elongated particles by EELS provided spectroscopic evidence for the presence of uranium immobilization, showing unequivocally uranium ionization intensity peaks of O4,5- and N6,7-edges. Distribution analysis of uranium, phosphorus and calcium clearly showed, that a solid uranium mineral has formed intracellular, which indicates the presence of a solid U-phosphate mineral similar to Autunite [$\text{Ca}(\text{UO}_2)_2(\text{PO}_4)_2 \cdot 10\text{-}12\text{H}_2\text{O}$].

The scientific activities of **FTMC** during the third year within ReCosy comprised the behaviour of $^{99}\text{Tc}(\text{VII})$ in the system iron-bearing mineral-Na brine-microorganism under aerobic conditions. In order to estimate the effect of minerals/mineral surface on redox, sensitive radionuclide (technetium) sorption has been studied. To explore the interactions of Tc with iron-bearing minerals, series of laboratory batch-type experiments were carried out. The effect of pH on the radionuclide transport/retention was taken into consideration as well as the exposure time and the microbial activity. The composition of two powdered iron oxides (purchased from FSU) was verified using Mössbauer spectroscopy. Mössbauer spectra indicated the presence of hematite (Fe_2O_3) (first sample) and wustite and magnetite (second sample). For wustite, Fe(II) and Fe(III) components of Mössbauer spectra in the ratio 18:82 were detected in agreement with wustite formula $\text{Fe}(1-x)\text{O}$. Two subspectra, which are attributed to tetrahedral and octahedral sublattices are characteristic of magnetite. The ratio of area of magnetite subspectra is 45:55. Tetrahedral sublattice of magnetite is occupied by Fe(III) ions while octahedral is occupied by Fe(II)+Fe(III) ions. Thus, Fe(II) may be found either in magnetite and wustite.

For the batch experiments under ambient conditions, 0.1 g of mineral hematite (ms) and 0.2 g of mixture of wustite and magnetite (resuspended in 0.08 M Na brine solution) were used. The colloidal mineral suspensions were obtained by adding the volume (V) of 5 mL of Na-brine solution to hematite. The volume to mass ratio was 50 in the series of experiments ($V/\text{ms}=50$) with hematite. The solution volume to mass ratio

(V/ms=250) was 250 in the experiments with mineral wustite/magnetite. After addition of ammonium pertechnetate to the suspension pH values reached 7.5 ± 0.5 . Bacteria and fungi, isolated from groundwater of two different boreholes and from soil of known physical-chemical properties, were tested under different conditions. Microbes (*Streptomyces sp.*, *Aspergillus niger*, *Arthrobacter globiformis*, *Cellulomonas cellulans*, *Bacillus mycoides*, *Fusarium oxysporum*, *Penicillium sp.*, *Rhodococcus sp.*, *Spicaria sp.*) were selected for batch-type experiments because of their more pronounced peculiarities: ability to reduce nitrate, H₂S formation, organic acid production and resistance to different pH values. The ability of selected microorganisms to participate in adsorption processes of ⁹⁹Tc(VII) on hematite and wustite/magnetite was investigated by batch experiments. Results of the combined effect of microorganisms and iron-bearing minerals on Tc(VII) sorption peculiarities using batch-type experiments have shown that bacteria isolated from fluided soil *Arthrobacter globiformis* and *Cellulomonas cellulans* practically did not have any influence on Tc(VII) sorption onto hematite under aerobic conditions, while *Micromicete Fusarium Oxysporum* of the same substrate altered sorption to approximately 85% compared to that in the system without microorganisms. Differences in Tc(VII) sorption processes onto hematite due to microbial activity of microorganisms isolated from the groundwater borehole were observed as well. Presence of microorganisms *Penicillium sp.*, *Rhodococcus sp.* and *Streptomyces sp.* in the tested system induced Tc(VII) sorption onto hematite up to 80-85%. The effect of microbial activity of *Bacillus mycoides*, *Aspergillus niger* and *Spicaria sp.* on Tc(VII) sorption onto hematite was lower 60%, 27% and 17%, respectively. Thus, we can state that mineral hematite at neutral or slightly alkaline pH under aerobic conditions is attributed to minerals which do not adsorb Tc(VII). Stimulation of Tc(VII) sorption onto hematite is achieved because of presence of specific microorganisms.

References

- Guillaumont R., Fanghänel T, Fuger J, Grenthe I, Neck V, Palmer DA, Rand MH (2003): Update on the chemical thermodynamics of uranium, neptunium, plutonium, americium and technetium. Chemical Thermodynamics Vol. 5 (OECD Nuclear Energy Agency, ed.), Elsevier, Amsterdam.
- Nguyen AN, Silvac RJ, Weed HC, Andrews JW (1992) Standard Gibbs free energies of formation at the temperature 303.15 K of four uranyl silicates: soddyite, uranophane, sodium boltwoodite, and sodium weeksite. Journal of chemical thermodynamics, Vol. 24 (4), 359-376.
- Pedersen K, Arlinger J, Eriksson S, Hallbeck M, Johansson J, Jägevall S, Karlsson L. "Microbiology of Olkiluoto Groundwater". Results and Interpretations 2007. POSIVA Working Report 2008-34. Olkiluoto, Finland.
- Stumm W and Morgan JJ. Aquatic Chemistry, Chemical Equilibria and Rates in Natural Waters. 3rd ed. John Wiley & Sons, Inc., New York, 1996.

WORK PACKAGE 5: REDOX PROCESSES IN RADIONUCLIDE MIGRATION

Juhani Suksi

University of Helsinki, Department of Chemistry, Laboratory of Radiochemistry,
Finland

Introduction

Work package 5 studies transport and retention properties of redox sensitive radionuclides to learn more of redox-reactions induced effects. Key question addressed is: does reduction of radionuclides explain retention and deposition observed in laboratory experiments and in natural environment? Practically all radionuclide redox couples relevant under natural conditions have been studied. Radionuclide behaviour has been studied in diffusion and sorption experiments with clay and fracture surface materials in various experimental designs. In natural-system studies (direct observations from nature) information has been derived by studying U behaviour in fracture network and in and around contaminated areas. Samples used in near-natural system studies were fracture surface material from Äspö HRL and Grimsel test site and claystone from Opalinus Clay, Callovo-Oxfordian argillite and Boda claystone. In natural-system studies samples were fracture surface material from the Olkiluoto study site, SW coast of Finland, various U containing phosphogypsum material from Cyprus and bottom sediments and surface waters from different Lakes of cascade of industrial basins at the Mayak site. Also methodology to determine redox-state of deposited U was developed. In the 4th project year most of the work was focused on finalizing experimental work, evaluating results and reporting. Results were presented in the 4th Annual Workshop in Karlsruhe.

Work performed by partners

Near-natural system studies

KIT-INE continued studies on radionuclide desorption kinetics from bentonite colloids and subsequent sorption onto fracture filling material. Batch-type experiments with a cocktail of strong and weak sorbing radionuclides as well as FEBEX bentonite colloids were used. Results show that tri- and tetravalent radionuclides, $^{232}\text{Th(IV)}$, $^{242}\text{Pu(IV)}$ and $^{243}\text{Am(III)}$ are clearly colloid associated in contrast to $^{233}\text{U(VI)}$, $^{237}\text{Np(V)}$ and $^{99}\text{Tc(VII)}$. Concentrations of colloid-borne $^{232}\text{Th(IV)}$, $^{242}\text{Pu(IV)}$ and $^{243}\text{Am(III)}$ decreased after ~ 100 h showing desorption from bentonite colloids while $^{233}\text{U(VI)}$ and $^{99}\text{Tc(VII)}$ concentrations remained constant over the entire experimental time of 7500 h thus showing no interaction neither to colloids nor to the fracture filling material. $^{232}\text{Th(IV)}$ and $^{242}\text{Pu(IV)}$ data yielded a slower dissociation from colloids compared to $^{243}\text{Am(III)}$ indicating stronger RN-colloid interaction. In the case of $^{237}\text{Np(V)}$, a decrease in

concentration after ~300 h was observed which can be explained either by slow reduction to Np(IV) and subsequent sorption to mineral surfaces in accordance with the evolution of pe/pH and/or by a slow sorption onto the fracture filling material. The driving force of the observed metal ion desorption from colloids is binding to fracture filling material surfaces being in multiple excess of the available colloid surface area. Synthetic montmorillonite colloids containing structurally bound Zn and Ni in its octahedral layer was used to perform radionuclide reversibility kinetic experiments similar to those on Febex bentonite derived bentonite colloids. No colloidal attachment occurred over 3500 h (~5 months) for both types of montmorillonite colloids on fracture filling material from Grimsel. Similar results were obtained for the FEBEX bentonite colloids. The ²³⁷Np concentration remaining after UC decreases clearly after ~300 h in both batch series. According to the experimental Eh-pH conditions, the initial Np(V) is probably reduced into Np(IV). Thus, Np(IV) may be present as Np(IV) colloids (“eigencolloids”) or may be attached to the montmorillonite colloids, which explains the concentration decrease after UC. Unfortunately, based on the data available so far one cannot differentiate which of the two explanations holds. Nevertheless, the Np does not sorb on the FFM since its concentration in the not-UC batch samples remains constant, which is a clear difference compared to the FEBEX colloid data. The ⁹⁹Tc behaves similarly to the ²³⁷Np. No reduction to Tc(IV) is observable which is in line with the measured redox potentials. After ~1000 h, differences in the concentration for UC and not-UC samples are detectable and explained as for the ²³⁷Np. According to the experimental Eh-pH conditions, a reduction of pertechnetate to the tetravalent Tc is feasible. In conclusion, the synthetic Ni- and Zn-montmorillonite colloids behave similarly as the natural FEBEX bentonite colloids used in previous studies but possess higher specific surface areas, which in turn influences the radionuclide desorption kinetics. In both systems slow reduction kinetics under glacial melt water conditions could be observed under Grimsel groundwater conditions and retention is higher in migration experiments compared to batch type studies (stop-flow experiments showed admixture of matrix pore water). This would also explain the strong bentonite colloid retention and associated tri- and tetravalent actinides observed (Ca-source for higher attachment probability is the working hypothesis).

CEA finalized experimental work by testing the effect of mineralogical heterogeneity on iodide retardation during diffusion in Callovo-Oxfordian claystones. Iodide concentrations were varied in the experiment. The retardation was still observed for the lowest concentration ($<10^{-4}$ M). A diffusive behaviour of iodide was underlined. A manuscript about iodide experiments was submitted to Journal of Contaminant Hydrology. Selenium reduction phenomena within the claystone sample could be demonstrated by means of XAS (Savoie et al. 2012).

II-HAS studied in collaboration with UH the redox-state of the sorbed uranium component. U oxidation states were determined using a dissolution technique where sorbed U was extracted in anoxic 4.5 M HCl extraction. U(VI) was found to be the predominant species. This measurement provided a direct proof that the sorption process is not linked simultaneous redox processes (Lázár et al., 2012).

Natural-system studies

UH continued development of chemical extraction method for U oxidation states in rock and sediment samples. Redox effects of the sample material itself were in

particular studied. These redox effects represent certain complexities while analyzing true U valent form composition in the original solid material. Possible impact of radiation induced defects in the sample material was studied in an annealing experiment, where sample material was heated at different temperatures at the range of 200-1000 °C. Heating is supposed to heal radiation defects and thus decrease considerably the intensity of redox effects which would give finer U⁴⁺ and U⁶⁺ forms distribution values. It was found that the reduction of ²³⁶U⁶⁺ tracer during the extraction decreased when annealing temperature was increased: no reduction of U occurred during the leaching when sample was annealed at 500 °C. At 1000 °C all original U⁶⁺ in material transformed to U⁴⁺. Most of the results obtained by wet chemistry were validated by XANES (Pidchenko et al., 2012).

UCyprus evaluated the data obtained in the 3rd project year and during the entire project and submitted a S&T contributin (Pashalidis and Suksi, 2012).

MSU studied speciation of actinides (U and Pu) in organic-rich bottom sediment from one of the industrial reservoirs at PA “Mayak” (Russia). These studies show only isolated uranium particles with no associations with other elements \geq Ca, neither evenly distributed within the particles nor as an agglomerate that would imply U sorption on a mineral surface that nucleated further growth of a U-containing precipitate on the surface. The XANES and the EXAFS spectra and curve-fit results unambiguously show that the particles consist of chemically homogeneous UO_{2+x}, U₃O₈, and schoepite ((UO₂)₈O₂(OH)₁₂)(H₂O)₁₂ with metrical parameters within the range exhibited by these compounds within the lab and other environmental and geological sources. There are no indications even after several decades of environmental exposure of any convergence of these species towards the most stable schoepite form. It can therefore be safely assumed that these species are the original source terms from multiple waste streams and that they unexpectedly were highly inert under these conditions.

References

- Kalmykov, S., 2012. Redox behavior of actinides in organic-rich industrial pond (PA “MAYAK”). 4th Annual Workshop Proceedings of the Collaborative Project “Redox Phenomena Controlling Systems” (7th EC FP CP RECOSY).
- Lázár, K., Máthé, Z., Megyeri, J., Széles, É., Mácsik, Zs. and Suksi, J., 2012. Redox properties of clay minerals and sorption of uranyl ions on Boda Claystone. 4th Annual Workshop Proceedings of the Collaborative Project “Redox Phenomena Controlling Systems” (7th EC FP CP RECOSY).
- Pashalidis, I. and Suksi, J., 2012. Redox Chemistry and Mobility of Uranium in Phosphogypsum. 4th Annual Workshop Proceedings of the Collaborative Project “Redox Phenomena Controlling Systems” (7th EC FP CP RECOSY).
- Pidchenko, I., Salminen-Paatero, S., Vitova, T. and Suksi, J., 2012. Study of U oxidation states in natural geological material. 4th Annual Workshop Proceedings of the Collaborative Project “Redox Phenomena Controlling Systems” (7th EC FP CP RECOSY).

Savoye, S., Schlegel, M., Frasca, B., Fayette, A. and Grenut, B., 2012. How mobile is selenite diffusing through the Callovo-Oxfordian claystones? Insights given by radiochemistry and x-ray absorption spectroscopy. 4th Annual Workshop Proceedings of the Collaborative Project “Redox Phenomena Controlling Systems” (7th EC FP CP RECOSY).

WORKPACKAGE 6: REDOX PROCESSES AFFECTING THE SPENT FUEL SOURCE- TERM

D. H. Wegen^{1*}, P. Carbol¹, A. Seibert¹, T. Gouder¹, T. Petersmann¹, R. Pehrman^{2,7},
M. Trummer², C. M. Lousada², M. Jonsson², A. Loida³, N. Müller³, V. Metz³, E.
Bohnert³, B. Kienzler³, D. Cui⁴, K. Spahiu⁶, D. Dobrev⁵, R. Červinka⁵, A. Vokál⁵

¹ Institute for Transuranium Elements (ITU), (DE)

² KTH Chemical Science and Engineering, Nuclear Chemistry, Royal Institute of
Technology, (SE)

³ Institut für Nukleare Entsorgung (INE), KIT, (DE)

⁴ Studsvik Nuclear AB, (SE)

⁵ Nuclear Research Institute Řež plc (NRI), (CZ)

⁶ Svensk Kärnbränslehantering AB (SKB), (SE)

⁷ University of Helsinki, (FIN)

Introduction

The source term from spent fuel dissolution is subject to considerable uncertainties, both with respect to the presence and extent of oxidative dissolution processes of the spent fuel itself and the coupling with processes associated with the iron canister. Related problems to be examined in this work package are the representativeness and reliability of laboratory data with respect to the impact of unavoidable minor concentrations of oxygen also in inert-gas boxes used, the potential reactivity and its outcome of hydrogen from container corrosion in combination with high burn-up spent fuel, possible galvanic coupling of spent fuel and container material and the retention of redox sensitive radionuclides by relevant minerals, especially by steel container corrosion products.

A set of investigations has been conducted with the aim of getting better insight into redox processes determining spent fuel and iron canister corrosion. The following summary covers the activities conducted between 2011 and 2012. In the last project year the main emphasis was on finalising experiments, on final evaluation of obtained results and on reporting. Therefore the WP summary focuses on the main achievements and conclusions obtained in the project. More detailed information is included in the ReCosy Final Report and in the annual workshop proceedings (Buckau et al. 2009, 2010, Altmaier et al. 2011). **ITU** reports on studies on spent fuel in presence of corroding Fe, on corrosion of spent fuel in presence of H₂ and on fuel corrosion studies on thin film model systems. The redox reactivity of doped UO₂ in view of effects on the reactivity towards H₂O₂ has been studied at **KTH**. The reductive trapping of actinides in container corrosion products during spent fuel corrosion is investigated by **INE**. **Studsvik** reports on the redox chemistry at the near field of repository and the

influences of iron canister material and hydrogen. Redox conditions near waste packages were studied by **NRI**.

Work performed by partners

Studies on Spent Fuel in Presence of Corroding Fe and on Thin Film Model Systems

Underground storage of spent nuclear fuel is a generally accepted strategy for final disposal. In many European countries the disposal concept foresees a storage of spent fuel in a cast iron, stainless steel or carbon steel container with an overpack of copper or carbon steel (Bennett and Gens, 2008, Feron et al. 2008). In such a container spent fuel is in direct contact with the cladding material e.g. Zircaloy and steel. The principle of galvanic coupling of spent fuel with metals has been discussed at the example of defect spent fuel electrodes immersed in synthetic groundwater and 5 M NaCl solution (Grambow et al. 2000). Studies on the effect of carbon steel and Zircaloy-4 in direct contact with UO_{2+x} have been carried out in salt brines and bentonite porewater under oxidising conditions. It was shown that in case of Zircaloy-4 UO_2 dominates the contact potential and the corrosion behaviour (Kupfer 2000) while in the pair carbon steel and UO_2 the steel is dominating. In the latter case the corrosion of UO_2 is reduced when in direct contact with steel. This effect is enhanced in cases where less iron corrosion products were detected which form a passive layer on the steel surface (Engelhardt and Marx, 1999). The stability of this passive layer is influenced by hydrogen (Yu et al. 2002). Hydrogen promotes the susceptibility of the passive film on iron to pitting corrosion especially under lower chloride ion concentrations. Therefore studies on the behaviour of UO_2 electrically connected to carbon steel in presence of hydrogen have been carried out.

The first experiments were conducted under Ar purging. Under these conditions the Pt-electrode of the redox combination electrode acts mainly as an oxygen electrode. The E_h is dominated by the oxygen activity. The OCP measured after pre-cathodisation of the samples show for the fully UO_2 coated steel a potential shift of 50 mV in anodic direction compared to pure steel. This shift is attributed to a galvanic coupling effect where UO_2 is the more anodic part. At the same time the OCP of the half UO_2 covered electrode was found to be 30 mV more cathodic than pure steel. This is explained by the facts that due to the surface ratio of UO_2 to steel in this case the influence of UO_2 decreases and is surpassed by decreased oxygen content in solution derived from a 30 mV lower E_h . Therefore the cathodic partial current densities governed by the oxygen reduction are smaller and the OCP is shifted cathodically.

The next experiment, now without pre-cathodisation, shows the opposite behaviour. The E_h is 200 - 300 mV higher indicating oxygen intrusion into the system and consequently also the OCP is shifted about 200 mV into anodic direction. As a result of the increasing cathodic processes also the anodic corrosion processes must increase and the sample shows heavy corrosion pattern combined with localised pitting attack.

Under $\text{Ar}/5\%\text{H}_2$ the Pt-electrode of the redox combination electrode acts mainly as a hydrogen electrode and E_h cannot be used as qualitative parameter for the oxygen content. Therefore oxygen was measured with an optical sensor. The partial pressure was during experiments always below (2 ± 2) mbar. Here a very low OCP of -550 mV_{SHE} was measured for a fully UO_2 coated steel sample. Consequently this

sample showed no major corrosion attack. The solution contained after the experiment approximately 100 times less uranium and 3000 – 14 times less iron in solution. Even the pH remains constant at pH 7 while in all other cases it dropped to ~pH 4.5 due to Fe(II) in solution.

In case of a pre-oxidised uranium oxide coated steel sample under Ar/5%H₂ the same final OCP of -270 mV_{SHE} was found as in the case of oxygen intrusion. Here the reason for this large potential shift must be different because no increase of the oxygen partial pressure could be detected. But differently to other experiments a Fe(III) (hydr)oxide layer was found by XPS. The reduction of this Fe(III) layer is coupled to the corrosion process and shifts as cathodic process the OCP into anodic direction and increases at the same time the metal corrosion (Smart et al. 2002).

Remarkable was the finding by XPS measurements that after all experiments the uranium oxide film on the steel surface was reduced to UO₂ and the UO₂ layer was in contact with steel stabilized even in the case of pre-oxidation.

The experiments have shown that the corrosion processes are ruled by iron corrosion and in contact with iron is a reduction of UO_{2+x} to UO₂ possible.

Thin Films as Spent Fuel Models for Surface Corrosion

In order to understand SNF corrosion the elucidation of the involved single processes is indispensable. In this context, the impact of individual fuel components on fuel corrosion has to be clarified. To achieve this, thin films are used as model systems for spent nuclear fuel, to investigate the surface reactions of these films in single effect studies (i.e. isolating one single parameter like fp, stoichiometry, etc.). In the present contribution, we investigated the inhibition of surface corrosion by molecular hydrogen, generated for example during corrosion of the iron canisters. We focussed on the contribution of the ϵ -particles to the activation of the hydrogen.

To investigate the catalytic properties of the noble metal particles in the single effect approach, we studied actinide oxide thin films (UO₂) doped with the pure noble metals. In this work, we concentrate on the Pd, which is a known hydrogenation catalyst and thus very efficient in activating hydrogen. We first determined the optimal conditions for thin film preparation. In particular we investigated, under what deposition condition U was oxidised to UO_{2+x}, while the metallic inclusions stayed reduced. Also, the size of the metallic particles as function of deposition temperature was an issue, Goal was to simulate the real ϵ -particles, which have a size of about 0.1 to 1 μm – being composed of smaller grains (Cui et al. 2004).

Thin film deposition study

First experiments of the co-deposition of U and Pd at room temperature in presence of oxygen showed that UO₂ films containing different Pd concentrations can be produced. For room temperature deposition, Pd is partially oxidized to PdO₂ at low Pd concentrations. Uranium obviously plays an active role in the oxidation of the Pd – which is probably related to the dispersion of Pd in the UO₂ oxide lattice.

XRD was used to check the formation of metallic particles and the presence of oxidic matrix. It was found that only above 70% Pd, characteristic Pd diffraction patterns appear, while simultaneously UO₂ diffraction lines disappear. The homogeneous dissolution of Pd in UO₂ is interpreted as a result of the method of sputter deposition.

Due to the low substrate temperature (\sim room temperature) U-Pd-O-clusters from the plasma are instantaneously cooled at the surface and the components are "frozen" in the deposited film.

To favour diffusion of the film components after deposition, and a relaxation of the system into a thermodynamically stable state, the substrate was heated (2 minutes at temperatures $\sim 150^{\circ}\text{C}$ to 200°C) during or after the deposition process (Stumpf et al. 2012). It was hoped, that Pd would segregate into larger metallic particles, more representative of the ϵ -particles. It was found that even at such low temperatures (compared to the substance melting points) diffusion and rearrangement of the film components is allowed. As a result Pd oxide transforms into a metallic Pd phase. Agglomerates of spherical particles with a diameter of $0.3\text{ }\mu\text{m}$ to $1\text{ }\mu\text{m}$ form on top of the film surface. Indeed these structures resemble very well the results of Cui et al. (2004) who investigated structure, morphology and composition of mixed alloy particles (ϵ -particles) extracted from spent fuel. In the cited study, the ϵ -particles are described as agglomerates of micrometer sized spheres ($\sim 0.7\text{ }\mu\text{m}$).

Electrochemical investigations

The thin film surface corrosion behaviour in aqueous environment was investigated by electrochemical tools. Two sets of experiments were performed: CV measurements under oxidizing conditions and open circuit potential measurements under oxidizing and reducing conditions. The influence of Pd on the surface corrosion behaviour was determined by comparing UO_2 to UO_2/Pd doped films.

CV measurements on UO_2 and UO_2 doped with 2% and 16% Pd (0.01 M NaCl , $\text{pH} \sim 5$, scan rate 10 mVs^{-1}) show on UO_2 , three stages of oxidation on the anodic scan. At low potentials (-1.0 to -0.4 V) a shoulder appears that can be attributed to a reversible oxidation process. With increasing Pd concentration new features appear in the oxidative as well as reductive path of the voltammogram. Without going into more detail, we note that Pd has an impact on the overall redox behaviour of UO_2 and propose, according to literature, dissociative sorption processes at Pd sites as being responsible for such effect. We observe a decreased current with increasing Pd concentration at $+0.25$ to $+0.3\text{ V}$. The current decrease indicates a less extensive oxidation of the matrix which is in good agreement with results described in [NAOHARA H., YE S., UOSAKI K. (2000)]. Assuming the adsorption and reaction of redox active species at the Pd particles as cited above, the activated components obviously couple more readily to recombination and reduction processes than to the oxidation of $\text{UO}_{2.33}$.

This interpretation of experimental data is supported by theoretical studies on the recombination of OH_{ads} to form $\text{H}_2\text{O}_{\text{ads}}$ on a Pd(111) surface performed by Cao and Chen (2006) who predict such reaction path as being very likely from an energetic point of view.

With increasing number of voltammetric cycles the electrode response resembles more and more the pure UO_2 case. Such effect indicates the passivation of Pd particles towards dissolution inhibition. Shoesmith et al. (1994, 2000) propose the formation of secondary phases as being responsible for the blockage of donor-acceptor sites at the UO_2 surface.

In a first set of experiments, the reactivity of SNF model surfaces (UO_2/Pd_x thin films) was investigated in electrochemical experiments under oxic conditions. The corrosion of UO_2 in (aerated) aqueous solution is decreased (lower anodic currents / less dissolution observed in cyclic voltammetry) when Pd is incorporated into the oxide surface. The formation of secondary phases on the UO_2 surface (built up in subsequent cathodic scans) disabled this inhibiting effect of Pd.

The influence of Pd doping on the OCP of UO_2 under air was investigated by using the freshly prepared films as working electrode. For a pure UO_2 film the OCP reaches a steady state after 6 hours at about 250 mV_{SHE} which is similar to results found for SIMFUEL (without ϵ -particles) under oxygen. With increasing palladium amount the open circuit potential increases, shifting closer to the value of a pure Pd metal electrode. Even the 2% doped film shows an increase of the potential (~50 mV_{SHE}) which is thought to be due to the noble metal doping.

The measured potential is always a combination of single potentials therefore the mixed potentials of UO_2/Pd are placed between pure UO_2 and pure Pd electrodes.

Experiments under reducing conditions were carried out under Ar/H_2 (5% H_2). For the pure UO_2 film a potential of around 0 mV_{SHE} is measured which is 250 mV lower compared to the one obtained under air. The absolute value is similar to measurements under Argon. This indicates a decrease of the corrosion potential due to very low concentrations of oxidants. A much stronger response to the presence of H_2 is shown by the UO_2/Pd electrodes. Here the potential after 4 h is still below the threshold for surface oxidation of UO_2 . These findings correspond to the trend reported in literature (the given absolute values are higher). Although the steady state was not reached during the experiment the clear effect of H_2 in presence of Pd could be demonstrated. The different possible explanation is that H_2 is activated on Pd, which is acting as galvanically coupled anode within the UO_2 matrix and is leading to a decrease of the corrosion potential and inhibition of UO_2 oxidation. But also reduction of dissolved oxidants or the surface itself by surface hydrogen is possible, as described in the introduction.

Gas adsorption experiments

In order to simulate one conceivable heterogeneous redox reaction, such as the oxide reduction by hydrogen, UO_2 -Pd thin films are exposed to H_2 gas. The U4f spectrum of UO_{2+x} is characterized by two main peaks with peak maxima at 380 eV and 391 eV binding energy. Two satellites at 7 eV higher binding energy are characteristic for the actinide dioxides. For the hyperstoichiometric oxide these satellites are broadened. The treatment with H_2 gas does not result in a change of the U4f electronic structure and the UO_{2+x} reduction can be therefore ruled out. This changes when doping the UO_{2+x} matrix with Pd. Already at very low pressures of about $1.3 \cdot 10^{-5}$ mbar H_2 (x 5 min), the treatment of the mixed film induces a narrowing of the main peaks as well as of the satellites. The calculation of the U/O ratio from the corresponding U4f and O1s spectra after 15 minutes H_2 treatment gives a stoichiometry of UO_2 . Obviously, the activation of H_2 is solely due to the presence of Pd. We conclude as a first result, that the catalytic properties of the uranium oxide matrix can be ruled out (at least at the H_2 pressure used) and that the activating effect is exclusively attributed to the noble metal incorporation instead. The activation of H_2 is consistent with a dissociative sorption process and with the formation of atomic H at Pd active sites. The only possible reaction path to further

reduce uranium oxide in the doped oxide films is the diffusion of hydrogen atoms at the UO_{2+x} -Pd surface. Such process is known in literature as spillover reaction (Teichner, 1990, Gorodetskii et al. 2009) which is defined as migration of a sorbed species, such as hydrogen, from one solid phase, such as a metal where it is easily adsorbed and dissociated, onto another solid phase, such as uranium oxide, in contact with the first.

Redox Reactivity of Doped UO_2

UO_2 has been used as a model for spent nuclear fuel in numerous experimental studies. Rates and rate constants for oxidation as well as dissolution of the oxidized UO_2 matrix of spent nuclear are derived from experiments on pure UO_2 powder or pellets (Roth and Jonsson, 2008). On the basis of these results the relative impact of radiolytic oxidants have been assessed and also employed in simulations of spent nuclear fuel dissolution under deep repository conditions (Ekeröth et al. 2006). One important conclusion from these studies is that H_2O_2 is the major oxidant responsible for radiation induced oxidative dissolution of spent nuclear fuel under deep repository conditions. H_2O_2 can react with UO_2 by catalytic decomposition and by oxidizing U(IV) to U(VI). Since spent nuclear fuel can be regarded as highly doped UO_2 , the effects of the presence of dopants in the UO_2 matrix should be regarded as key-knowledge in the field of spent nuclear fuel dissolution. To elucidate this we have studied the dissolution yield in reactions between H_2O_2 and doped UO_2 and the reactivity of a number of oxidants towards doped UO_2 materials. In parallel we have studied the catalytic formation of hydroxyl radicals (upon reaction with H_2O_2) on the doped UO_2 materials.

The experiments are described in detail in the publications (Trummer, 2011, Lousada et al. 2011)

Dissolution yield

Experiments performed at KTH have shown that the oxidative dissolution yield, i.e. the amount of dissolved uranium per consumed H_2O_2 varies dramatically between different UO_2 -based materials (Trummer et al. 2010, Nilsson and Jonsson, 2011). It has not been clear whether this variation can be attributed to changes in redox reactivity or in the catalytic ability of the material.

Rate of H_2O_2 consumption

The rate of H_2O_2 consumption has been measured in a number of previous studies (Roth and Jonsson, 2008, Trummer et al. 2010, Nilsson and Jonsson, 2011). The rate constant for UO_2 oxidation by H_2O_2 was obtained in experiments on UO_2 powder suspensions. This rate constant can be used to make fairly reasonable predictions of the rate of oxidation for UO_2 pellets as well as for doped UO_2 pellets. Hence, the overall rate of H_2O_2 consumption on UO_2 surfaces is relatively insensitive to the presence of dopants. However, noble metal particles have been shown to catalyze oxidation to some extent (Trummer et al. 2009).

Hydroxyl radical formation

Hydroxyl radicals formed as a primary product in metal oxide catalyzed decomposition of H_2O_2 can be detected using a modified version of the Hantzsch method [LOUSADA C. M., JONSSON M. (2010)]. In short, tris-buffer is added to the system. Upon reaction with hydroxyl radicals (or other hydrogen abstracting radicals), formaldehyde is produced. The formaldehyde concentration is the used to monitor the accumulated hydroxyl radical production in the system.

It can clearly be seen that the consumption of H_2O_2 is accompanied by production of OH. For UO_2 powder, the dissolution yield, expressed as the ratio between dissolved U(VI) and consumed H_2O_2 , has been determined to 80% (Jonsson et al. 2004). The present experiments on hydroxyl radical production confirms this as the hydroxyl radical production corresponds to ca 20% of the H_2O_2 consumption. The rate of hydroxyl radical production varies by less than 30 % for UO_2 , SIMFUEL, Y_2O_3 doped UO_2 , Pd-doped UO_2 and Y_2O_3 /Pd-doped UO_2 .

Reactivity of different oxidants towards doped UO_2

If differences in the ability to catalyze decomposition of H_2O_2 cannot explain the observed differences in dissolution yield, the rationale must be differences in the redox reactivity of the doped materials. In order to elucidate this possibility we performed experiments using pure oxidants that cannot undergo catalytic decomposition. In addition to H_2O_2 , which has already been studied quite extensively, we used IrCl_6^{2-} and MnO_4^- to monitor the redox reactivity of the doped UO_2 materials.

What can clearly be seen here is that the redox reactivity of the doped materials differs significantly for the weaker oxidant (MnO_4^-) while the reaction with the stronger oxidant (IrCl_6^{2-}) is much faster and the difference between the doped materials is also less pronounced. Furthermore, experiments (kinetics as a function of temperature) show that the activation energy for oxidation of UO_2 by MnO_4^- is lower than the activation energy for oxidation of SIMFUEL by MnO_4^- . The measured activation energies are 7.4 and 12.9 $\text{kJ}\cdot\text{mol}^{-1}$, respectively. This shows that the redox reactivity is significantly influenced by doping (Pehrman et al. 2011, 2012)

From our work we can conclude the following:

- The dissolution yield in the reaction between H_2O_2 and UO_2 decreases with rare earth oxide doping.
- The catalytic decomposition of H_2O_2 on UO_2 initially produces hydroxyl radicals (adsorbed)
- The overall rate constant for the reaction between H_2O_2 and UO_2 is fairly insensitive to rare earth oxide doping.
- The rate constant for the catalytic decomposition of H_2O_2 on UO_2 is fairly insensitive to rare earth oxide doping.
- The redox reactivity of UO_2 pellets decrease significantly with upon rare earth oxide doping. This effect is more pronounced for weaker oxidants than for strong oxidants.

Reductive Trapping of Actinides in Container Corrosion Products during Spent Fuel Corrosion

The source term from spent nuclear fuel (SNF) dissolution is highly dependent on oxidative dissolution of the fuel matrix. Various experimental data on the dissolution behaviour of the spent fuel matrix itself and in some cases in presence of container material (initial metallic Fe powder) as well, and the associated releases of radioelements were already obtained by extensive laboratory test programs and reported e.g. in Shoesmith, (2000), Ferry et al. 2005, Loida et al. (1996). The capacity of corroded canister iron phases to incorporate radionuclides is under investigation within the European collaborative project “ReCosy”. The stable corrosion product of steel canister material under reducing disposal conditions is magnetite. In the present study, it was intended to investigate the reductive trapping of actinides in metallic corrosion products, which may provide for a driving force for SNF dissolution. Over almost 10 years, an experiment (“denoted as K14Mt”) was carried out to study the effect of magnetite on the overall corrosion behaviour of SNF in NaCl solution. Unexpected was the measured rather high U solution concentration of $\sim 1 \cdot 10^{-4}$ M at the end of the experiment, in association with an at first unexplainable CO₂ content of 0.8 vol % in the gas phase. Additionally, first studies by means of optical microscopy (SNF sample, corroded magnetite), SEM/EDS (corroded magnetite), XPS (corroded magnetite), Raman spectroscopy were carried out. Further characterization work upon the corroded magnetite was focused on its mineralogical phase composition and on possible impurities by carbon. Additionally, the distribution of radioelements released from the SNF sample in the course of almost 10 years of corrosion over the magnetite, the container wall and the aqueous phase was determined.

The amounts of retained radionuclides upon the magnetite and the vessel wall were obtained after dissolution of 230 mg magnetite in 30% HCl and acid stripping of the vessel wall (5 M HNO₃) followed by radiochemical analysis of related aliquots. The results show that the total releases of Cs, Sr and Tc (in solution + on the vessel wall + on the magnetite) were measured at $1.48 \cdot 10^{-6}$ M, $3.04 \cdot 10^{-7}$ M and $1.52 \cdot 10^{-7}$ M, where parts of 95%, 99% and 98.5 % were found in the aqueous phase. U was released in total at $5.1 \cdot 10^{-5}$ Mol, where of 70% was found upon the magnetite. The total measured amount of Am was determined to be $3.56 \cdot 10^{-8}$ M, where a percentage of 95% upon the magnetite was encountered. The Pu release was measured to be $2.3 \cdot 10^{-8}$ Mol, whereof 90% was re-immobilized upon the magnetite. The retention of radioelements upon the glass vessel wall does not play a significant role except for plutonium.

In the glass vessel used for SNF corrosion experiments over almost 10 years the atmospheric conditions were not sustained. The presence of CO₂ and O₂ explained the observed U and Sr concentrations. Under these conditions, Sr cannot be used as indicator for SNF matrix dissolution.

The unexpected high CO₂ content in the gas phase at the end of the corrosion experiment might be explained by the carbon/carbonate content of the magnetite as fabricated, reacting with oxygen released during magnetite dissolution. The relevant carbon-containing phases are of minor concentration in the ALFA 012962 magnetite and could not be detected by XRD and Raman spectroscopy.

In spite of the accelerated release of radioelements in particular U due to the high CO₂ content in the gas phase, considerable amounts of radioelements were retained upon the

magnetite. With respect to Am, Pu, U and Np about 95, 87, 71 and 39 % of the released measured amounts were found to be re-immobilized upon the magnetite.

Due to the Raman findings, which are corroborated by XRD, a hematite layer is present onto the surfaces of this material. Therefore, the trapping of the actinides cannot be attributed to reductive process alone, but sorption reactions may influence the retention, too. The ALFA 012962 magnetite plays a significant role in retaining the redox sensitive actinides.

Corrosion of spent fuel in presence of H₂

The aim was to study the influence of dissolved H₂ on corrosion of the high burn-up rim fraction of spent nuclear fuel. The rim fraction was selected as it contains a higher concentration of Pu, as well as, fission products and the first water will contact in case of container penetration in a spent fuel disposal. The experimental conditions were selected to imitate crystalline rock disposal environment. A titanium autoclave is used to avoid presence of atmospheric oxygen and to study the interaction of spent fuel (UO₂ matrix, ϵ -particles, fuel gap inventory and grain boundaries), water (composition in respect to concentration of carbonate and α -radiolysis) and hydrogen (originating from corrosion of carbon steel containers). Titanium was selected to minimise the influence of iron which is known to react with oxidants formed by α -radiolysis. The final goal was to perform a mass balance of reductants and evolved oxidants.

This 1435-days long study aimed to investigate the corrosion of fragments isolated from the rim of high burn-up UO₂ in a slightly saline leachate containing 2 mM carbonate under a pressure of 14-41 bar H₂. The main task is to perform a mass balance in respect to reducing and oxidising species.

Despite the fact that 0.23 mol of atmospheric O₂ intruded the autoclave on day 63 (Fors et al. 2009) and additional O₂ was produced in the autoclave during the period of 0-313 days, as a result of α -radiolysis of water, low steady state concentration levels were reached for U and Pu of $1.5 \cdot 10^{-10}$ M and $7 \cdot 10^{-11}$ M, respectively. The release of Cs almost stopped which indicate an almost insignificant corrosion of grain boundaries and the UO₂ matrix (which contains 97 wt% of the total Cs).

Having exchanged the leachant during the rinse action, the Cs concentration was lowered by a factor of 1415, thus removing the instant release fraction, made it possible to monitor the spent fuel corrosion. During the period of almost 3 years of corrosion (442-1435 days) the Cs concentration increased by a factor of 5. The concentration of U and Pu remained, after a corrosion time of 1121 days (314-1435 das) at the same steady state level as during the initial period of $2 \cdot 10^{-10}$ M and $8 \cdot 10^{-12}$ M, respectively.

These results confirm that in the studied UO₂-H₂-H₂O system, within the range of 10-33 mM dissolved H₂, radiolytically induced UO₂ corrosion is inhibited by hydrogen and that the rim high burn-up structure of the 67 GWd/tHM fuel did not enhance fuel dissolution.

For the first time, to the knowledge of the authors, the variation of redox sensitive natural elements, present in the leachate as contaminants from the autoclave setup, are studied in order to confirm the redox state of redox sensitive actinides and fission products. Out of the inactive elements studied: Fe, Zn, Cu, Ti, Cr, Y, Mn, Mo, Ni, Sr, Cd and Rb, only Ti and Fe seems to be able to influence the redox conditions. The redox-sensitive natural elements; Fe, Ti, Mn, Mo behave more similarly to Pu than U.

After having identified the redox sensitive elements that influence the redox in the studied system made it possible to perform a mass balance of reducing and oxidising species during the corrosion experiment. The results of the mass balance calculation showed that during the period 0-313 days more than 10^6 times more oxidants were present in the autoclave and must have been reduced in the system since no O_2 or H_2O_2 could be detected and the U concentration was in the range of 10^{-10} M, which indicates a non-oxidised spent nuclear fuel. The discussion on different possible mechanisms are outside the scope of this work but are discussed elsewhere (Eriksen et al. 2012, Carbol et al. 2012, Metz et al. 2012).

Additionally, the co-variation of redox sensitive natural elements with redox elements originating from the fuel was used to support the measured redox potential in the bulk leachate which is coupled to the oxidative-dissolution process at the UO_2 - H_2O interface. The results presented gives a better understanding of the redox processes occurring at the UO_2 - H_2O interface and is crucial for the understanding of the spent fuel corrosion which is directly applicable to the conceptual model of the spent fuel corrosion used in safety assessments.

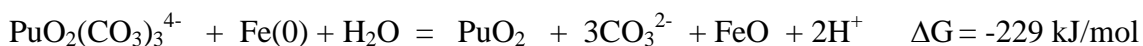
On the redox chemistry at the near field of repository, the influences of iron canister material and hydrogen

Pu reductive immobilization by iron canister material

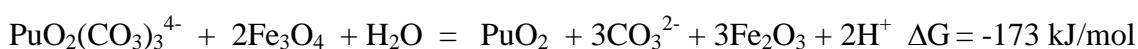
^{239}Pu is one of the most radiotoxic radionuclides contained in high level nuclear waste due to its long half live and chemical properties. The environmental behaviour of plutonium is the most difficult to predict due to its multi-valence state in the subsurface environment (Rondinella, 2011). Pu(III)/(IV) are the predominant valence states at low pH and strongly reducing conditions while Pu(V)/(VI) is favoured in oxidative and high pH systems.

Previous studies have shown that aqueous Pu(V) can be reduced to sorbed Pu(IV) by Fe(II) containing SRS sediments (Hixon et al. 2009). Pu(VI) reduction by Fe(0) and Fe(II) phases has been investigated (Lucchini et al. 2008), however, the authors did not show the stability of Pu(V)/(VI) in water solution, neither gave the ratio of Pu(V)/Pu(VI) in the solution.

A calculation of Gibbs free energy of redox reaction between Pu(VI) and metallic iron or Fe_3O_4 shows that the process is in both cases possible. The reaction of plutonyl carbonate with Fe gives, for a groundwater with pH 10 (25 °C);



and the reaction between plutonyl carbonate and magnetite;



The relative small negative values of ΔG for both reactions suggest that these two redox reactions may be feasible but the driving force is not very large. In comparison, ΔG for a very slow redox reaction between Se(VI) and Fe(0) at repository conditions (pH 8.5) is -278 kJ/mol (Cui et al. 2007).

The experiment started with preparation of a Pu(VI) carbonate solution. Speciation showed that $\text{PuO}_2(\text{CO}_3)_3^{4-}$ is stable at pH higher than 9. Without direct evidence if Pu exists as Pu(VI) in the solutions four indirect proofs were used as evidence for the existence of Pu(VI)-carbonate as the dominating Pu species. Firstly, only Pu as Pu(VI) is stable, for longer periods at a Pu-concentration of 10^{-5} M Pu in air atmosphere and in 20mM carbonate solution at pH 10. Normally, Pu(IV) precipitates as $\text{Pu}(\text{OH})_4(\text{s})$ at $\text{pH} > 5$. In highly concentrated carbonate solutions (1-2.5 M) tetravalent Pu can form $\text{Pu}(\text{CO}_3)_4^{4-}$ and $\text{Pu}(\text{CO}_3)_5^{6-}$ complexes (Morss et al. 2006).

Anyhow, in our experiment the formation of Pu(VI) was clearly visible during the Pu(IV) oxidation with fuming HClO_4 . Over a period of 114 days there were no changes of the Pu concentration in the reference solution indicating a stable Pu(VI) solution (at pH 10, $[\text{CO}_3^{2-}]$ of ~20mM). Secondly, the fact that all Pu-solutions, before the experiment start, were centrifuge-filtrated through a 3000 Dalton filter without reduction in Pu concentration indicate that if colloids are present they must consist of aggregates < 11 PuO_2 molecules. Thirdly, the TEM investigation of Pu-solution collected after experiment termination showed no Pu-particles (even at a size level of 10\AA). Fourthly, there were no evidence of larger Pu-agglomerates on the Fe coupon indicating Pu(VI) hydroxide precipitates.

The study of Pu(VI) reduction by Fe or Fe_3O_4 in 20 ml of a solution 0.1M NaCl + 0.084M Na_2CO_3 solution at pH 10 (with a CO_3^{2-} concentration of ~20mM) showed that Pu deposition occurred only on Fe_3O_4 surfaces. Despite the fact that the calculations give negative ΔG -values for the reactions between Pu(VI) and Fe or Fe_3O_4 , only approximately 1% of the added ^{239}Pu was found on the Fe_3O_4 surface after 114 days contact time.

The concentration of Fe was similar in all solutions including the reference. Calculations show that $\text{FeCO}_3(\text{s})$ is the solubility limiting phase at pH 10.

Mechanisms of the hydrogen influence on radionuclide migration by D/H isotope exchange method

a) It was observed that isotope exchange between D in D_2 gas (11 bar) and H in water solution does slowly occur with the presence of SIMFUEL pellet, (a spent fuel simulator containing UO_2 and noble metal fission product particles) through the reaction $\text{D}_2 + \text{H}_2\text{O} \Rightarrow \text{D}_2\text{O} + \text{H}_2$, but not significant occurs in the blank experiment.

b) An increase of N_2/O_2 ratio in the gas mixture of air and D_2 in autoclave containing water solution and the SIMFUEL pellet, but not in blank experiment without SIMFUEL.

c) The D/H ratio in water solution that interacted with a 11.3 bar gas mixture of D_2 + 0.14% O_2 with the presence of SIMFUEL pellet for 2 months was found to be (7157 dD per mil) 1270 ppm (isotopic ratio). It is about three times higher than the calculated value according to the O_2 added in the system. It proves that beside the deoxygenation reaction, $2\text{D}_2 + \text{O}_2 \Rightarrow 2\text{D}_2\text{O}$, there should be an isotope exchange reaction $\text{D}_2 + \text{H}_2\text{O} \Rightarrow \text{D}_2\text{O} + \text{H}_2$.

The Effect of Iron Corrosion on Redox Potential

Spent fuel dissolution and mobility of radionuclides in the near field of a deep geological repository is significantly affected by reactions of iron from disposal canisters with water. A large number of studies have been devoted to investigate iron reactions in repository conditions. The results are, however, often ambiguous. The problem is that reactions of iron with water are affected by a great variety of factors such as pH, temperature, water composition, radiation or the amount of oxygen in the water. The investigation conducted in the Nuclear Research Institute Rez (NRI) within the ReCosy project has been carried out to clarify some uncertainties concerning the effect of iron and carbon steel on redox conditions developed in or around spent fuel canisters.

To summarise the results obtained, it was found that the firmly adhering corrosion product layers formed on the carbon steel surface, containing a high amount of oxygen and carbon, have an important impact on the development of geochemical conditions in a repository. These layers protect the carbon steel against fast corrosion, but data about their long term stability are rare. No or very thin layers of corrosion products were formed on iron powder at very low E_h . This leads surprisingly to a higher corrosion rate of iron powder at lower E_h values. The presence of solid bentonite can lead to an increase of the corrosion rate of iron, possibly due to the faster sorption (exchange) of ferrous ions on the bentonite leading to a higher concentration gradient between the metal and the solution.

Laboratory experiments conducted in this work contributed to a deeper knowledge of the effect of iron corrosion on redox evolution, but did not remove all uncertainties concerning this issue. For reliable predicting and ascertaining the behaviour of canisters in a repository and their influence on the evolution of geochemical conditions in a repository a more systematic programme involving both laboratory and in situ experiments should be started in future to verify the results obtained.

Acknowledgement

The Swedish Nuclear Fuel and Waste Management Company (SKB) is gratefully acknowledged for financial support.

References

Altmaier M., Kienzler B., Duro L., Grivé M., Montoya V. (EDS.) (2011): 3rd Annual Workshop Proceedings of the Collaborative Project “Redox Phenomena Controlling Systems” (EC 7th FP CP RECOSY), Karlsruhe Institute of Technology, KIT Scientific Reports 7603, Germany.

Buckau G., Kienzler B., Duro L., Grivé M., Montoya V. (EDS.) (2009): Collaborative Project “Redox Phenomena Controlling Systems” - 1st Annual Workshop Proceedings, Forschungszentrum Karlsruhe, Wissenschaftliche Berichte, FZKA 7466, Karlsruhe, Germany.

Buckau G., Kienzler B., Duro L., Grivé M., Montoya V. (EDS.) (2010): 2nd Annual Workshop Proceedings of the Collaborative Project “Redox Phenomena Controlling Systems” (EC 7th FP CP RECOSY), Karlsruhe Institute of Technology, KIT Scientific Reports 7557, Germany.

Bennett D.G., Gens R. (2008): Overview of European concepts for high-level waste and spent fuel disposal with special reference waste container corrosion, J. Nucl. Mater. 379, 1-8.

Cao Y., Chen Z.-X. (2006): Theoretical studies on the adsorption and decomposition of H₂O on Pd(111) surface. Surf.Sci.600, 4572-4583.

Carbol P., Wegen D.H., Wiss T., Fors P. (2012): Spent Fuel as Waste Material. In: Konings R.J.M., (ed.) Comprehensive Nuclear Materials, volume 5, pp. 389-420 Elsevier, Amsterdam, Netherlands.

Cui D., Low J., Sjöstedt C.J., Spahiu K. (2004): On Mo-Ru-Tc-Pd-Rh-Te alloy particles extracted from spent fuel and their leaching behaviour under Ar and H₂ atmosphere. Radiochimica Acta, 92, 551.

Cui D., Puranen A., Scheidegger A., Grolimund D., Wersin P., Leupin O., SPAHIU K. (2007): On the interaction between iron canister material and fission products ⁷⁹Se and ⁹⁹Tc under simulated deep repository conditions. NF-PRO report Contract Number: FI6W-CT-2003-02389, RTDC 2-WP 2.5 Task 7.

Ekeröth E., Roth O., Jonsson M. (2006): The relative impact of radiolysis products in radiation induced oxidative dissolution of UO₂. J. Nucl. Mater. 355, 38-46.

Engelhardt J., Marx G. (1999): Contact corrosion measurements on the pair UO_{2+x} and carbon steel 1.0330 in brines and bentonite porewater with respect to direct waste disposal, J. Nucl. Mater. 264, 161-168.

Eriksen T.E., Shoesmith D.W., Jonsson M. (2012): Radiation induced dissolution of UO₂ based nuclear fuel –A critical review of predictive modeling approaches. J. Nucl. Mater. 420, 409-423.

Ferry C., Poinssot C., Broudique V., Cappelaere C., Desgranges L., et al. (2005): Synthesis of the Spent Fuel Long-Term Evolution, Rapport CEA-R--6084.

Féron D., Crusset D., GRAS J.-M. (2008): Corrosion issues in nuclear waste disposal, J. Nucl. Mater. 379, 16-23.

Fors P., Carbol P., Van Winckel S., Spahiu K. (2009): Corrosion of high burn-up structured UO₂ fuel in presence of dissolved H₂. J. Nucl. Mater. 394, 1-8.

Gorodetskii V.V., Sametova A.A., Matveev A.V., Tapilin V.M. (2009): From single crystals to supported nanoparticles in experimental and theoretical studies of H₂ oxidation over platinum metals (Pt, Pd): Intermediates, surface waves and spillover. Catalysis today, 144, 219-234.

Grambow B. et al. (2000): Source term for performance assessment of spent fuel as a waste form, Report No. EUR 19140, 82-101, Luxembourg.

Hixon A.E., Hu Y.-J., Kaplan D.I., Kukkadapu R.K., Nitsche H., Qafoku O., Powell B.A. (2009): Influence of iron redox transformations on plutonium sorption to sediments. Radiochimica Acta 98, 685-692. doi: 10.1524/ract.2010.1769.

- Jonsson M., Ekeröth E., Roth O. (2004): Dissolution of UO_2 by one- and two-electron oxidants. *Mat. Res. Soc. Symp. Proc.* 807, 77-82.
- Kupfer A. (2000): Radiochemische Korrosionsuntersuchungen an Urandioxid und Cladding-Materialien von Kernbrennstoffen in praxisrelevanten Salzlaugen als Beitrag zur direkten Endlagerung, Dissertation, Freie Universität Berlin, Berlin.
- Loida A., Grambow B., Geckeis H. (1996): Anoxic corrosion of various high burnup spent fuel samples. *J. Nucl. Mater.* 238, 11-22.
- Lousada C. M., Jonsson M. (2010): Kinetics, Mechanism and Activation Energy of H_2O_2 Decomposition on the Surface of ZrO_2 . *J. Phys. Chem. C.* 114, 11202-11208.
- Lousada, C. M., Trummer, M., Jonsson, M. (2011): Reactivity of H_2O_2 towards different UO_2 -based materials: The relative impact of radiolysis products revisited. *J. Nucl. Mater.* In press doi: 10.1016/j.jnucmat.2011.06.003.
- Lucchini J.F., Khaing H., Richmann M.K., Borkowski M., Reed D.T. (2008): Plutonium (VI) and Uranium (VI) reduction by iron (II) at high pH under subsurface conditions. Plutonium Futures Conference "The Science". Dijon, France, July 7-11, 2008, LA-UR-0808-04292.
- Metz V., Geckeis H., González-Robles E., Loida A., Bube C., Kienzler B. (2012): Radionuclide behaviour in the near-field of a geological repository for spent nuclear fuel. *Radiochimica Acta*, In press doi: 10.1524/ract.2012.1967.
- Morss L.R., Edelstein N.M., Fuger J. (2006): The chemistry of the Actinide and Transactinoid Elements. Springer, Dordrecht, the Netherlands.
- Naohara H., Ye S., Uosaki K. (2000): Electrocatalytic reactivity for oxygen reduction at epitaxially grown Pd thin layers of various thickness on Au(111) and Au(100). *Electrochimica Acta* 45, 3305-3309.
- Nilsson S., Jonsson M. (2011): H_2O_2 and radiation induced dissolution of UO_2 and SIMFUEL pellets. *J. Nucl. Mater.* 410, 89-93.
- Pehrman R., Trummer M., Lousada C. M., Jonsson M. (2011): Redox reactivity of doped UO_2 - Effects on the reactivity towards H_2O_2 , RECOSY 3rd Annual Workshop Proceedings of the Collaborative Project "Redox Phenomena Controlling Systems" (EC 7th FP CP RECOSY), Karlsruhe Institute of Technology, KIT Scientific Reports 7603, Germany, pp. 241 – 249.
- Pehrman R., Trummer M., Lousada C. M., Jonsson M. (2012): On the redox reactivity of doped UO_2 pellets – Influence of dopants on the H_2O_2 decomposition mechanism. Submitted to *J. Nucl. Mater.*
- Rondinella V. V. (2011): Failure mechanisms of high level nuclear waste forms in storage and geological disposal conditions. Handbook of advanced radioactive waste conditioning technologies. Edited by M. I. Ojovan, Woodhead Publishing Series in Energy: Number 12, Woodhead Ltd, Philadelphia, USA.
- Roth O., Jonsson M. (2008): Oxidation of $\text{UO}_2(\text{s})$ in aqueous solution. *Cent. Eur. J. Chem.* 6, 1-14.
- Shoesmith D.W., Sunder S., Hocking W.H. (1994): in *Electrochemistry of Novel Materials*, edited by J. Lipowski and P.N. Ross, VCH Publishers, New York, pp. 297-337

Shoesmith D.W. (2000): Fuel corrosion processes under waste disposal conditions. J. Nucl. Mater. 282, 1-31.

Smart N.R., Blackwood D.J., Werme L. (2002): Anaerobic corrosion of carbon steel and cast iron in artificial groundwaters: Part 1 – Electrochemical Aspects. Corrosion 58, 547-559.

Stumpf S., Seibert A., Gouder T., Huber F., Wiss T., Römer J. (2012): Development of fuel-model interfaces: Characterization of Pd containing UO₂ thin films. To be submitted to J. Nucl. Mater.

Teichner S.J. (1990): Recent Studies in Hydrogen and Oxygen Spillover and their Impact on Catalysis. Appl. Catalysis 62, 1-10.

Trummer M., Roth O., Jonsson M. (2009): H₂ Inhibition of Radiation Induced Dissolution of Spent Nuclear Fuel. J. Nucl. Mater. 383, 226-230.

Trummer M., Dahlgren B., Jonsson M. (2010): The effect of Y₂O₃ on the dynamics of oxidative dissolution of UO₂. J. Nucl. Mater. 407, 195-199.

Trummer, M. (2011): The effect of solid state inclusions on the reactivity of UO₂. A kinetic and mechanistic study. Doctoral Thesis in Chemistry, KTH, Stockholm, Sweden.

Yu J.G., Luo J.L., Norton P.R. (2002): Electrochemical investigation of the effects of hydrogen on the stability of the passive film on iron, Electrochimica Acta 47, 1527-1536.

S + T CONTRIBUTIONS

List of contributions

On the use of actinides as redox tracer elements in groundwater samples

S. Holgersson

Spectrophotometric and potentiometric investigation of iron (III) hydrolysis in chloride media

S. Hagemann, T. Scharge, B. Bischofer

Investigations on structural iron electrochemical properties in layered silicates using massive mica electrodes

J. Hadi, I. Ignatiadis, C. Tournassat, L. Charlet and E. Silvester

Mechanistic study of pyrite reduction by hydrogen in NaCl 0.1 M at 90 °C using electrochemical techniques

S. Betelu, C. Lerouge, G. Berger and I. Ignatiadis

Synthesis of fulvic acids-like compounds in alkaline media and their interactions with iodide ion

E. Pourtier, C. Nguyen-Trung, M. Perdicakis, F. Baros, D. Bordg, L. Richard

Reduction of Pu(VI) by Fe

P. Carbol, A. Nicholl, D. Wegen, T. Wiss, A. Janssen, B. Cremer, R. Malmbeck, S. Van Winkel, C. Apostolidis, R. Lavandera, J. Himbert, D. Cui

Reduction of iron oxides by S(-II) and its effect on uranium phase distribution

V. Alexandratos, T. Behrends

Speciation of reduced selenium species in hyperalkaline solutions: attempt at developing a specific analytical protocol

C. Landesman, C. Bailly, V. Baty, J. Vandenborre, B. Grambow

How mobile is selenite diffusing through the callovo-oxfordian claystones? Insights given by radiochemistry and x-ray absorption spectroscopy

S. Savoye, M. Schlegel, B. Frasca, A. Fayette, B. Grenut

Advances in multiplexed fiber-optical sensing for environmental applications

D. Steinbrück, F. Geißler and M. Kumke

Study of U oxidation states in natural geological material

I. Pidchenko, S. Salminen-Paatero, T. Vitova, J. Suksi

Redox properties of clay minerals and sorption of uranyl species on boda claystone

K. Lázár, Z. Máthé, J. Megyeri, É. Széles, Z. Mácsik, J. Suksi

Redox behavior of uranium in biofilms and groundwater seeps, sampled from the granitic rock walls in the onkalo tunnel (Finland)

E. Krawczyk-Bärsch, H. Lünsdorf, K. Pedersen, T. Arnold, F. Bok, R. Steudtner, A. Lehtinen, V. Brendler

Partial equilibrium-based redox estimations in groundwaters from crystalline systems

M. Gimeno, L. Auqué, P. Acero, J. Gómez, M. Asta

Nano-sized pyrite/greigite reactivity towards Se(IV) and Se(VI)

L. Charlet, M. Kang, F. Bardelli, A. Géhin, F. Chen

The effect of carbon steel corrosion on the evolution of conditions in a deep geological repository

D. Dobrev, R. Červinka, A. Vokál

Redox chemistry and mobility of uranium in phosphogypsum

I. Pashalidis, J. Suksi

Redox reaction of aqueous Se(IV) with pyrite: reaction products and pathway studies

M. Kang, L. Charlet, F. Bardelli, A. Géhin, A. Shchukarev, F. Chen

The effect of plutonium oxidation state on sorption and reversibility in humic acid-quartz sand ternary systems

R. Kay, N. Bryan, N. Evans, P. Warwick

Uranium solubility under alkaline conditions using different reducing agents

O. Riba, V. Montoya, M. Grivé, L. Duro

Investigations on Np(VI) in alkaline NaCl solutions: aqueous chemistry and solid phase characterization

X. Gaona, D. Fellhauer, J. Rothe, M. Altmaier

Dielectric monitoring of dry pyrite during its exposure to air or pure oxygen

M. Perdicakis, R. Thomahowski, C. Malhomme

An attempt for fabricating ultramicroelectrodes compatible with sodium chloride brines

M. Perdicakis, A. Chebil, M. Etienne, A. Cheikh-Ibrahim

U removal kinetics in the presence of magnetite and maghemite nanoparticles

F. Huber, D. Schild, T. Vitova, J. Rothe, R. Kirsch, T. Schäfer

ON THE USE OF ACTINIDES AS REDOX TRACER ELEMENTS IN GROUNDWATER SAMPLES

Stellan Holgersson*

Department of Chemical and Biological Engineering, Division for Nuclear Chemistry,
Chalmers University of Technology (SE)

*Corresponding author: stehol@chalmers.se

Abstract

Redox measurements in environmental samples are usually made with electrodes. However, these have certain weaknesses in terms of stability and memory effects. Alternative methods for determination of redox are therefore of interest and the use of radioactive tracer elements may be one such method, which was the subject of investigation. It is suggested that the actinides are particularly appropriate for use as indicators of redox, provided that their different redox states can be separated in a fast and reliable way. A literature survey show that solvent extraction is an established method for separation of tracer amounts of actinides into their redox states and three of the most commonly used extraction reagents of the beta-diketone type were investigated: thenoyltrifluoroacetone (TTA), dibenzoylmethane (DBM) and 4-benzoyl - 3-methyl-1-phenyl pyrazol-5-one (PMBP). U and Np were reduced to tetravalent state and extraction curves in the pH range 0.6-7 were measured. It was found that 0.5M DBM in chloroform and 0.05M PMBP in xylene gave the best separation factor for actinide (IV)/(VI) and (IV)/(V) oxidation states, respectively, when pH of aqueous phase was in the region 1-2. Actinide tracer was used for redox determinations of prepared samples with an artificial groundwater, with or without addition of grains of rock and pyrite. Comparison to redox measurements of a synthetic groundwater with an ordinary redox electrode (Pt/Ag/AgCl) gave values that were considerable lower: 30mV compared with about 300mV with electrode. Whether this reflects a preservation of an earlier state of the groundwater could not be established. However, the U redox speciation method also have a limited range of about $-100 > Eh < 100$ mV and in this investigated case an absolute correspondence between the methods may therefore be impossible to attain.

Introduction

The mobility of certain elements in the environment is usually dependent on the local chemical conditions. Controlling chemistry parameters are pH, Eh, concentrations of dissolved elements and gases and solid phases present that maybe in equilibrium with groundwater or else approach equilibrium. In addition to this, microbiological activity may also influence the chemical conditions. The local Eh or redox conditions of the site of investigation are one of the chemical parameters that are more difficult to obtain. This may have a number of reasons; the most obvious is the difficulty to preserve samples at original conditions of the site investigated. Samples usually have to be transported to surface level, or even further, to a laboratory for analyzes. Just taking samples from a borehole may be enough to upset the redox conditions. Another difficulty is methodological, where redox measurements are usually made with redox electrodes with their inherited weaknesses, such as slow approach to a stable reading and tendencies for memory effects. A third reason for the difficulty of redox measurement is of more fundamental type, because the systems investigated may not be at perfect equilibrium. In a more complex system with several redox participants, a perceived equilibrium with a net zero current, might in fact be a summation of potentials that results in pseudo-equilibrium. This is the case of non-buffered groundwater with typical redox couples O_2/H_2O , NO_3/N_2 , NO_3/NH_4^+ , SO_4/HS^- , CO_2/CH_4 , which all exhibit kinetically slow reactions and these couples will not give any measureable current and/or will probably not be in equilibrium. Attempts to measure redox equilibrium in such a system with ordinary redox electrode are therefore bound to fail. In the context of a deep repository for nuclear waste, located at approximately 500m depth in a granite rock formation, local chemical conditions include low O_2 and CO_2 concentration levels, high inert-gas levels and iron-containing solid phases together with dissolved Fe^{2+} apparently controlling Eh to between -250 and -150mV, the variation depending on depth and groundwater type (Laaksoharju *et al.* 2008). The problems experienced with redox electrodes can give highly diverging results when compared (Altmaier, *et al.* 2010). In order to have a complementary redox measurement method, redox couples of the actinides may be considered and their potential use for this purpose is the subject for this investigation. The investigation is directed to a radiotracer addition, preferentially below solubility limits, to available samples, and is not a determination on the actual actinide content of the samples. A number of reasons for the potential use of actinide redox tracers can be forwarded: 1) the redox pairs U(IV)/U(VI), Np(IV)/Np(V) and Pu(III)/Pu(IV) have their electrode potentials within a suitable redox and pH range of interest (Table 1), 2) their redox state will particularly influence their retention properties, 3) they are radiometrically detectable, ensuring low detection levels, 4) methods for redox state separations are well documented in the literature, and 5) the interconversion between actinyl (i.e. $U(VI)O_2^{2+}$, $Np(V)O_2^+$) and actinide ($U(IV)^{4+}$, $Np(IV)^{4+}$) ions is kinetically slow, which gives some freedom in how fast and in what way the separation have to be made to preserve the redox condition of the sample.

Table 1. *Electrode potentials at pH 8 (corrected for hydrolysis). From Allard et al. (1980).*

Redox couple	E at pH 8
U(IV)/U(VI)	- 0.07
Np(IV)/Np(V)	0.15
Pu(III)/Pu(IV)	-0.39

Literature survey

The crucial stage for the use of actinides as redox tracers is the separation of their oxidation states. They should be separated quantitatively, as quickly as possible and this should be accomplished without affecting the redox balance itself. Spectrophotometric methods would ideally be suited since the redox states of the each actinides show very distinctive spectra in the visual wavelength region. However, the high detection levels for ordinary spectrophotometric methods means that the use of tracer concentration levels ($<1\mu\text{M}$) is usually not possible. The separation of actinides according to their oxidation states has been reviewed in the literature (Choppin and Bond, 1996) and solvent extraction and laser-induced photoacoustic spectroscopy (LIPAS) seem to be the only suitable methods for tracer concentrations. More recent studies also include ion chromatography coupled with online scintillation detectors (Coates *et al.* 2001) or mass spectrometry (Röllin and Eklund, 2000) and the methods have been shown to be suitable for actinide tracer concentrations. Solvent extraction requires less hardware and can be made compact for the requirements of glove-box work. In this work, the focus will therefore be on existing solvent extraction methods documented in the literature.

The use of thenoyltrifluoroacetone (TTA), a β -diketone (see Figure.1a), for the selective extraction of An(IV) is a method that has been used for analytical purposes (Foti and Freiling 1964, Bertrand and Choppin 1982, Rai 1984, Kobashi et al. 1988, Nitsche et al. 1988, Schramke et al. 1989, El-Naggar et al. 2000). For a review of earlier work with TTA extraction of metals see Poskanzer and Foreman (1961). In the work by Foti and Freiling the optimum pH for separation of An(IV) was found at a pH value of 0.4, using 15 min. extraction with 0.4M TTA in benzene. An(III) can then be separated by increasing pH to 4.3 with 11M acetate solution and then again extracting with 0.4M TTA, where An(VI) is kept in aqueous phase by acetate complexation. In the work by Bertrand and Choppin the authors state an optimum separation of An(IV) at pH 0.6, using 5 min. extraction with 0.5M TTA in xylene. The separation factor was about 10^4 . At pH 4.0 both An(IV) and (VI) extracted, while An(V) were not extracted in the pH range 0-4. However, the pK_a of 6.38 for TTA limits its use to the acidic pH region.

To improve on this, another β -diketone, dibenzoylmethane (DBM, see Figure 1b) with pK_a of 9.35 has been used for actinide extraction in pH range 6-8 (Saito and Choppin, 1983). A separation scheme based on 0.5M DBM in chloroform was devised for neutral solutions: first an extraction step of 10min. which extracts An(III+VI) and leaves An(IV+V) in the aqueous phase. Here it is important to notice that An (IV) is actually sorbed on the glass walls of the extraction vessel and not dissolved in the water phase, which means that the organic phase has to be removed first. The mixed oxidation states can then be separated by adjustment of pH to about 5 in aqueous phases, and extracting again with DBM, where this time An(VI) and An(IV) will be retained in and extracted

to organic phase, respectively. Both TTA and DBM extraction methods have been used for Pu redox speciation in acetate (pH 4.7) and borax (pH 8) buffered solutions, respectively (Kobashi *et al.* 1988). When Pu(VI) was dissolved in the pH 4.7 solution, it was rapidly reduced to Pu(V) and consequently not extracted. The DBM method was assumed to preserve the Pu(VI) state better than TTA method, but from the stated results, which required an oxidant to support the (VI) state during extraction at pH 8, it is doubtful if the DBM method is better in this respect.

Extraction reagents commonly used in nuclear fuel reprocessing, such as tributylphosphate (TBP), di(2-ethylhexyl)phosphoric acid (HDEHP) or dibutylbutylphosphonate (DBBP) requires strongly acidic solutions, which makes them less suitable for preserving original redox speciation conditions (Choppin and Bond, 1996). However, 0.5M HDEHP in toluene was nevertheless used in pH range 0-1 and compared with 0.5M TTA in xylene in pH range 0-4 and methyl-isobutyl-ketone (MIBK) at pH 0 in three parallel extractions of a test solution of Pu, prepared in different oxidation states (Nitsche *et al.*, 1988). For HDEHP at pH 0 Pu(IV+VI) was extracted, while Pu(III+V) and polymeric Pu(IV) remained in aqueous phase. Increasing pH to 1 extracted also Pu(III). TTA showed the expected behaviour of Pu(IV) extracting at pH 0 (70-100% redox state purity), while increasing pH to 4 extracted Pu(III+IV+VI). Polymeric Pu or Pu(V) were not extracted with TTA. MIBK at pH 0 showed essentially the same extraction behavior as HDEHP at pH 0, but gave not as quantitative results. A separation scheme with parallel analyses was designed where also LaF₃ co-precipitation was used for separating Pu(III+IV+polymers) while Pu(V+VI) stayed in the supernatant. Information on individual species were then obtained as differential measurements, for example Pu(HDEHP-extracted, pH 0)-Pu(TTA-extracted, pH 0)=Pu(VI). In another work with Pu redox speciation, 0.5M TTA in xylene was used at pH 0.6 and "pH>3", where respectively Pu(IV) and Pu(V) should be separated from the rest of the oxidation states (Schramke *et al.* 1989). The results with Pu(IV) solutions in water and brines at pH 0.6 show 84-94% extraction of Pu, but some 5-11% were left in the aqueous phase, presumably by oxidation to Pu(V+VI) during extraction. Results with Pu(V) solutions at "pH>3" show 79-89% recovery of Pu in aqueous phase, but some 15% had been extracted, again presumably by oxidation to Pu(VI).

In later works TTA extraction was replaced with the more effective extraction reagent 4-benzoyl -3-methyl-1-phenyl pyrazol-5-one (PMBP, see Figure 1c) as 0.025M solution in xylene for Pu redox speciation (Nitsche *et al.* 1994, Neu *et al.* 1994). In the latter work comparison was made with LIPAS measurements and the agreement between the two methods was good. From this literature review it can be concluded that solvent extraction at pH range 0-1 with TTA or PMBP, in xylene should suffice to separate An(IV) from all other oxidation states. The method with DBM may also be considered since it promises lesser pH adjustments. However, for Pu, which is notorious for redox disproportionation, one of the full separation schemes maybe have to be considered. The results from the cited work with Pu and TTA/PMBP have shown that Pu redox speciation are in good agreement with results from non-intrusive methods, despite the shift of pH to acidic conditions (Nitsche *et al.* 1994, Neu *et al.* 1994). It can also be noted that in the cited work that were studying Pu, several different radiotracers were used, i.e. ²³⁸Pu, ²³⁹Pu and ²⁴²Pu, but ²⁴¹Pu have been avoided, presumably because its more intense alpha radiation, that may affect redox conditions and increase disproportionation.

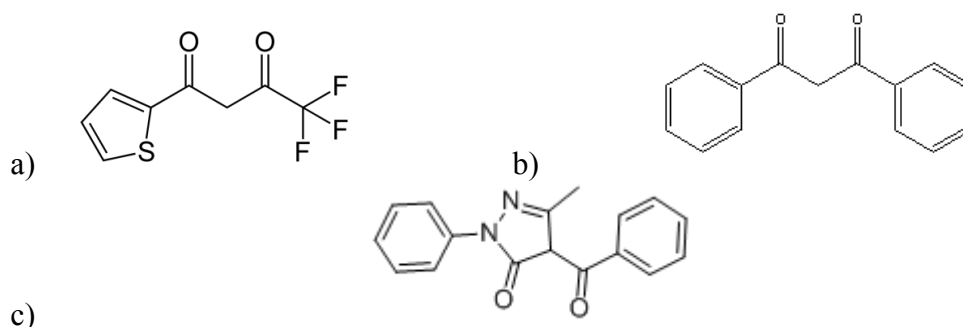


Figure 1. Extraction reagents of the β -diketone type: a) Thenoyltrifluoroacetone (TTA), b) Dibenzoylmethane (DBM), c) 4-Benzoyl-3-methyl-1-phenylpyrazol-5-one (PMBP).

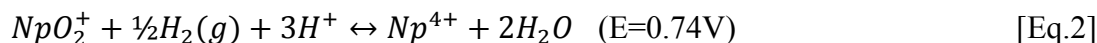
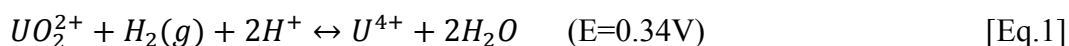
Objective and Scope

Within the EU-RECOSY project, Chalmers University was investigating the agreement of redox as measured with an ordinary redox electrode (Pt/Ag/AgCl) and the speciation determinations of actinides by solvent extraction. The systems studied were simple representatives of a final repository of radioactive waste in granitic bedrock: so-called batch experiments with crushed rock and synthetic groundwater under an inert-gas atmosphere. Redox control was made by addition of Fe(II). Three solvent extraction methods that use β -diketones for actinide separation were studied. The method with thenoyltrifluoroacetone (TTA) extraction is reported to give maximal separation from other oxidation states at pH 0.6 (Bertrand and Choppin, 1982). An alternative method that was tested is the extraction with dibenzoylmethane (DBM), the method is reported to extract hexavalent actinides at pH 7 and tetravalent actinides at pH 4 (Saito and Choppin, 1983). The third system that was studied utilizes 4-benzoyl -3-methyl-1-phenyl pyrazol-5-one (PMBP) which is reported to extract actinides similar to TTA, but with better efficiency (Nitsche et al. 1994, Neu et al. 1994). The work reported here is divided into three parts: 1) reduction of actinide solutions, 2) solvent extraction studies of actinide solutions for selecting optimized conditions for separation of different redox states of actinides, 3) application of the most successful solvent extraction method to redox measurements in synthetic groundwater systems and comparison with electrode measurements. The synthetic groundwater was based on analyses made at the Äspö Laboratory during the project Long Term Diffusion Experiment (LTDE) (Widestrand et al., 2010). Speciation calculations made with PHREEQC code indicated that the groundwater is saturated with pyrite and quartz. Samples were therefore prepared both with pyrite additions and crushed rock for the redox measurements. Initially U, Np and Pu were considered to be used for this work but problems with reduction of Np with Pt/H₂ arised (see below). Only Np(V) was used to obtain solvent extraction results, for use in future Np(IV)/Np(V) separation studies. In the end, Pu was left out altogether, expected to be even harder to reduce with Pt/H₂ than Np.

Experimental

Reduction of actinides

The reduction of actinides was accomplished by the immersion of a Pt net in 1mM actinide solutions in 0.1M HClO₄ and with H₂(g) bubbling around the net. The Pt net was previously cleaned in 4M HNO₃ (dilution of conc. p.A., Merck). The reduction method was selected for not leaving any residuals in the reduced solution. For checking the effectiveness of the reduction, the progress was followed by taking out samples for spectrophotometer (Perkin-Elmer Lambda 19) measurements in the visual wavelength region, to ordinary 1cm plastic cuvettes. The reactions taking place are:



The reduced solutions were immediately transferred to an N₂ gas-filled glove-box ([O₂(g)]~1ppm, MBraun UniLAB), for subsequent use in extraction experiments and redox measurements.

Preparation of synthetic groundwater

The composition of groundwater is shown in Table 2, which served as recipe for a synthetic groundwater. For the preparation of the synthetic groundwater, hereafter called LTDE-water, pre-concentrated (PC 1-7) solutions were made first. All salts were of p.A. quality, except Na₄SiO₄ (Alfa Aesar product 017568) and HCl (0.1M Fixanal, Fluka). Purified water was used in all applications (Milli-Q Plus185, Millipore).

PC 1) 0.7513g LiCl, 2.1928g KCl and 9.3416g SrCl₂·6H₂O were dissolved in water in a 100mL measure flask and diluted to the mark. *PC 2)* 4.0949g NaBr, 4.9564g NaHCO₃ and 0.3138g NaF were dissolved in water in a 100mL measure flask and diluted to the mark. *PC 3)* 21.6475g NH₄Cl, 0.3419g CsCl, 4.77g RbCl and 6.69g BaCl₂·2H₂O were dissolved in water in a 1000mL measure flask and diluted to the mark. 1mL of this solution was transferred to a 100mL flask and diluted to the mark. *PC 4)* a dissolution of 34.1g/L Na₄SiO₄ in water was prepared. *PC 5)* 0.3385g FeSO₄·7H₂O were dissolved in glove-box atmosphere saturated water in a 100mL measure flask and diluted to the mark. *PC 6)* 0.082g MnCl were dissolved in glove-box atmosphere saturated water in a 100mL measure flask and diluted to the mark. *PC 7)* 0.025g Na₂S were dissolved in glove-box atmosphere saturated water in a 100mL measure flask and diluted to the mark. For the LTDE-water, 1mL each of the PC 1-3 was added to about 750mL water in a 1000mL measuring flask. 1.18mL of the PC 4 was then added, followed by 4.3226g NaCl, 0.5092g MgCl₂·6H₂O, 6.2335g CaCl₂·2H₂O, 0.5295g Na₂SO₄ were added and dissolved, in sequence. The water was degassed with ultrasonic bath for 1h and then transferred to an inert-gas glove-box. 1mL each of PC 5-7 were added and pH adjusted to 7.0 with 0.1M HCl, using pH electrode and meter (Radiometer pH3006-9 and pHM240). Finally, the solution was diluted to the mark.

Table 2. Composition of Äspö groundwater (LTDE project, Widestrand et al. 2010). Also shown are the calculations results made here for pH, redox and ionic strength with PHREEQC code and LLNL.dat database.

Element	Conc (ppm)	Conc(mM)
Li⁺	1.23	0.177
Na⁺	1930	83.9
K⁺	11.5	0.29
Mg²⁺	60.9	2.51
Ca²⁺	1710	42.7
Sr²⁺	30.7	0.35
Rb⁺	0.0337	$3.94 \cdot 10^{-4}$
Cs⁺	0.00272	$2.05 \cdot 10^{-5}$
Ba²⁺	0.0856	$6.23 \cdot 10^{-4}$
NH₄⁺	0.073	$4.04 \cdot 10^{-3}$
Fe²⁺	0.68	0.0122
Mn²⁺	0.359	$6.53 \cdot 10^{-3}$
F⁻	1.42	0.0747
Cl⁻	5813	164
Br⁻	31.8	0.400
SO₄²⁻	359	3.74
Si	6.68	0.238
HCO₃⁻	36	0.590
S²⁻	0.10	$3.15 \cdot 10^{-3}$
pH (calculated)	7.0	
Eh (calculated)	-167mV	
Ionic strength (calculated)	0.223	
Saturated phases (calculated)	Pyrite, quartz	

Preparation of samples for redox measurements

The following 100mL samples were prepared: 1) LTDE-water, 2) LTDE-water with 1 g of grains of pyrite, 3) LTDE-water with 1g sample of crushed rock (size fraction 1-2mm), 4) LTDE-water with 1g of grains of pyrite and 1g sample of crushed rock. The pyrite specimen is from Skellefteå, Sweden and the rock from the drilling cores taken from Äspö during the LTDE experiments (Widestrand et al., 2010). Two separate series were made for measurements with electrode and tracer addition, respectively.

Solvent Extraction

The following organic phases were prepared: 1) a 0.5M solution of thenoyltrifluoroacetone (TTA) (99%, Acros) was made by dissolving 11.1g in 100mL xylene, 2) a 0.5M solution of dibenzoylmethane (DBM) (98%, Fluka) was made by dissolving 11.2g in 100mL chloroform, 3) a 0.05M solution of 4-benzoyl-3-methyl-1-

phenyl-5-pyrazolinone (PMBP) (98%, Alfa Aesar) was made by dissolving 1.39g in 100mL xylene. The organic phases were stored in light-shielded flasks. Aqueous phases in pH range 4-7 were buffered with non-complexing tertiary amines (Yu *et al.* 1997). The following aqueous phases were prepared: 1) for pH 0.6, a 0.25M solution of HClO₄ (p.A. 70-72%, Merck), 2) for pH 1, a solution of 0.1M HClO₄ and 0.12M NaClO₄ (p.A. Merck), 3) for pH 2, a solution of 0.01M HClO₄ and 0.21M NaClO₄, 4) for pH 3, a solution of 0.001M HClO₄ and 0.22M NaClO₄, 5) for pH 4, a solution of 5mM 1,4-piperazinebispropane sulfonic acid (PIPPS) (99%, Chemos) and 0.22M NaClO₄, pH adjusted with 1M NaOH (Fixanal, Fluka), 6) for pH 5, a solution of 5mM 1,4-diethylpiperazine (DEPP) (98%, Acros) and 0.22M NaClO₄, pH adjusted with 1M NaOH, 7) for pH 6 and 7, solutions of 5mM N,N,N,N-tetraethyl-ethylenediamine (TEEN) (98%, Aldrich) and 0.22M NaClO₄, pH adjusted with 1M NaOH. For each pH, 1.5mL aqueous phase of appropriate pH were transferred to a glass vial of 4mL size. 10μL of actinide solution was added and then 1.5mL organic phase. The actinide solutions were either a 1mM solution of a mixture of ²³⁸U and ²³³U or a 1mM solution of ²³⁷Np, both in 0.1M HClO₄. Reduced solutions were transferred to glove-box for the extraction. U(VI) and Np(V) solutions were pH adjusted to 3 with 1M NaOH. The choice of pH 3 was made to minimize an effect on the final pH in the aqueous phase and simultaneously minimize losses due to hydroxide precipitations. A similar pH adjustment to U(IV) was not made, due to hydroxide precipitations observed when adding NaOH. The extraction was made with shaking machine for 15 min. followed by 1 min. manual shaking. Thereafter, by leaving the samples standing, phase separation was achieved within 15 min. 0.2mL samples were taken from both aqueous and organic phase, transferred to 20mL Liquid Scintillation Counting (LSC) glass vials (High Performance, Perkin Elmer). 18mL of an alpha/beta discriminating LSC cocktail was added (Ultima Gold AB, Perkin Elmer) and the samples counted for alpha radioactivity on a LSC instrument (Wallac Guardian 1414, Perkin Elmer) for 10 min. Pulse Shape Analysis was used for alpha/beta discrimination. LSC quenching was tested with comparison of samples made by standard additions of U or Np radiotracer solutions to 200μL 0.22M NaClO₄, 0.5M TTA in xylene, 0.5M DBM in chloroform and 0.05M PMBP in xylene.

Redox Measurements

The measurements, except for LSC, were made in inert-gas glove-box. Four 100mL samples of groundwater were each "spiked" with 0.1mL of 1mM ²³³U+²³⁸U solution in 0.1M HClO₄ to give 1μM of U in the samples. Four other 100mL samples was measured with an Ag/AgCl/Pt electrode (Mettler-Toledo Inlab Redox) and pH meter (Radiometer pHM 240). The function of the electrode was checked with pH4 and pH7 buffers saturated with quinhydrone to give a response that was >97% of the theoretical 58.2mV/pH at 20°C. Redox in the prepared solutions was measured by immersing the electrode for about 2 minutes. The measurements were repeated after 1, 2 and 24 hours. Immediately before each measurement duplicate 1.5mL samples were taken from "spiked" samples to 4mL glass vials and 15μL 1M HClO₄ was added for the adjustment of pH to 2. Then 1.5mL 0.2M DBM in chloroform was added. Extraction was then made for 10min. with a shaking machine followed by 1 min. by hand. Samples of 20μL was taken and transferred to LSC vials and LSC cocktail was added and counted for alpha radioactivity, as described in previous section.

Results

Reduction of actinides

The results for reduction of 1mM U and Np solutions in 0.1M HClO₄, using Pt net with H₂(g) bubbling, are shown in Figs. 2 and 3, respectively.

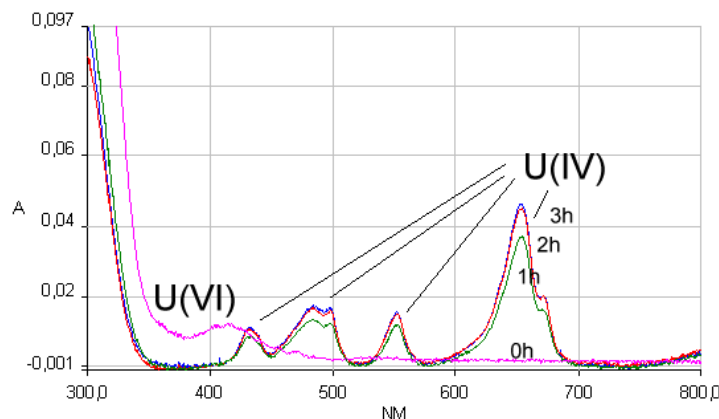


Figure 2. Spectra of U(VI) (cerise) and after reduction to U(IV) for 1h (green), 2h (red) and 3h (blue).

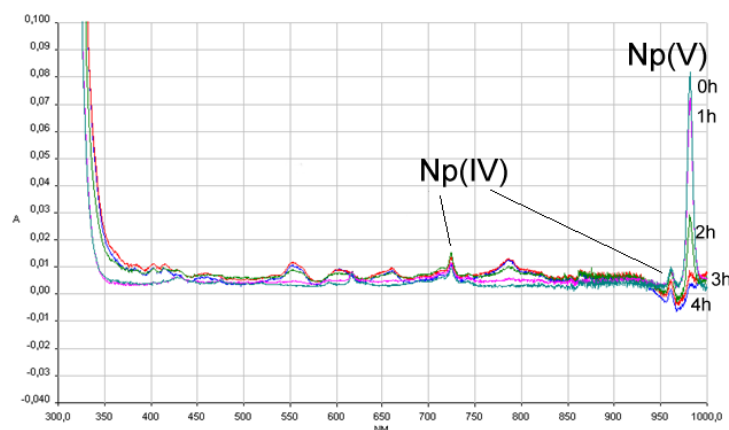


Figure 3. Spectra of Np(V) (cerise) and after reduction to Np(IV) for 1h (green), 2h (light green), 3h (red) and 4h (blue).

The six strongest absorption peaks of U(IV) in HClO₄ media in the visual region are: 425, 470, 490, 540, 650 and 670nm (only approximate values, from Katz *et al.* 1986). According to the same reference, U(VI) shows one complex multiple peak centered at about 415nm. The progress of reduction is therefore relatively easily followed with spectroscopic measurements, provided that the peaks in the 400-425nm region are resolved good enough. Figure 2 shows that the reduction of U(VI) to U(IV) is complete after 3 hours with no visual increase in the absorption from U(IV). However, effects on the extraction efficiency of U(IV) were still noticed when increasing the reduction time up to 6 hours, so at least 6 hours of reduction is recommended. The two strongest adsorption peaks in the visual-to-IR region of Np(IV) in HClO₄ media are one at 723

and one at 960nm. Np(V) has only one strong adsorption peak at 980nm (Katz *et al.* 1986) and the progress of reduction is therefore easily followed with spectroscopic absorption measurements. Fig. 3 shows that the reduction of Np(V) to Np(IV) is almost complete after 4 hours but, interestingly, the absorption peaks of Np(IV) do not correspondingly increase in size. Since subsequent extraction experiments indicated presence of Np(V) even after 6 hours of the reduction it was decided to not proceed with Np for redox state determinations. A more powerful reduction method with a potentiostat may be required to obtain pure Np(IV) solutions. The Np(V) solution was used here for solvent extraction curves to obtain separation factors for U(IV)/Np(V).

Solvent extraction

The results from the LSC quench test showed that the 0.5M TTA and 0.05M PMBP (both in xylene) gave a slight negative quenching (enhanced count rate: quench factor 1.1-1.3) relative to 0.22M NaClO₄. Results for these organic phases were therefore corrected with quench factors. DBM in chloroform gave no quench effect for LSC. The results for solvent extraction with 0.5M TTA in xylene of U(IV), U(VI) and Np(V) in 0.22M perchlorate at pH 0.6-8 are shown in Table 3 and Figure 4.

Table 3. Results for distribution coefficients, *D*, and separation factors, *SF*, for solvent extraction of U(IV), Np(V) and U(VI) in 0.22M (for pH 0.6 0.25M) perchlorate, using 0.5M TTA in xylene. Bold *SF*'s are maximum values. *D* and *SF* have no units.

pH	D U(IV)	D Np(V)	D U(VI)	SF U(IV)/U(VI)	SF U(IV)/Np(V)
0.6	5.8±0.6	2.2±1.2·10 ⁻¹	1.7±0.4·10 ⁻²	3.5·10²	2.6·10 ¹
1	5.4±0.6	1.4±0.2·10 ⁻¹	7.4±2.0·10 ⁻²	7.3·10 ¹	3.9·10 ¹
2	1.2±0.6·10 ¹	9.8±4.6·10 ⁻²	5.0±0.6	2.5	1.2·10 ²
3	1.3±0.9·10 ¹	7.5±0.9·10 ⁻²	4.8±1.1·10 ¹	2.7·10 ⁻¹	1.8·10 ²
4	6.2±3.3	7.8±1.7·10 ⁻²	9.1±0.0·10 ¹	6.7·10 ⁻²	7.9·10 ¹
5	3.9±1.0·10 ¹	1.1±0.3·10 ⁻¹	4.4±4.3·10 ²	8.8·10 ⁻²	3.5·10 ²
6	3.3±0.9·10 ¹	1.6±0.5·10 ⁻¹	1.5±1.1·10 ²	2.3·10 ⁻¹	2.1·10 ²
7	8.5±0.2·10 ¹	2.2±1.0·10 ⁻¹	1.2±0.3·10 ²	7.3·10 ⁻¹	3.8·10²

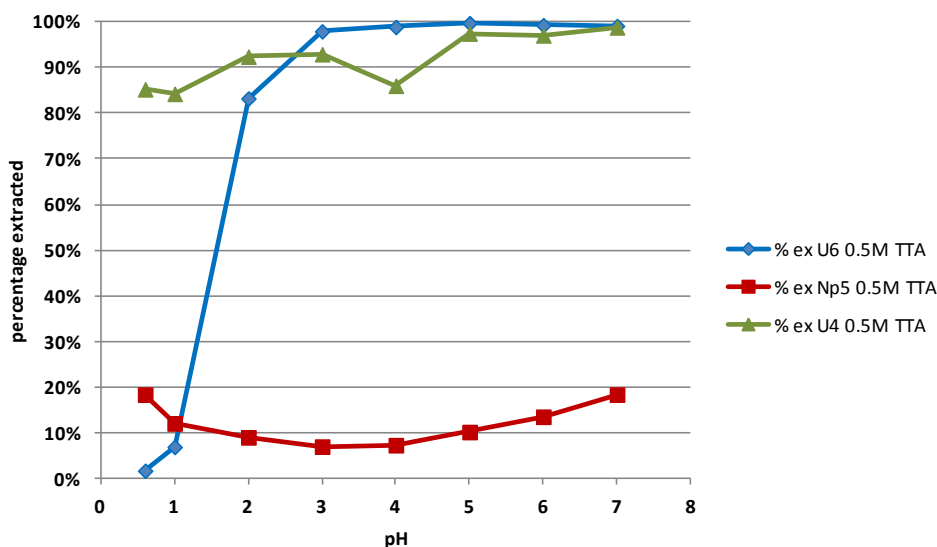


Figure 4. Percentage extracted of U(IV), Np(V) and U(VI) for the 0.5M thenoyltrifluoroacetone in xylene extraction system.

The results for solvent extraction of U(IV), U(VI) and Np(V) in 0.22M perchlorate at pH 0.6-8 with 0.5M DBM in chloroform are shown in Table 4 and Figure 5.

Table 4. Results for distribution coefficients, *D*, and separation factors, *SF*, for solvent extraction of U(IV), Np(V) and U(VI) using 0.5M DBM in chloroform. Bold *SF*'s are maximum values. *D* and *SF* have no units.

pH	D U(IV)	D Np(V)	D U(VI)	SF U(IV)/U(VI)	SF U(IV)/Np(V)
0.6	$9.0 \pm 0.2 \cdot 10^{-2}$	$7.6 \pm 0.3 \cdot 10^{-2}$	$2.6 \pm 1.0 \cdot 10^{-3}$	$3.5 \cdot 10^1$	1.2
1	$6.9 \pm 0.8 \cdot 10^{-1}$	$7.2 \pm 0.3 \cdot 10^{-2}$	$4.0 \pm 1.9 \cdot 10^{-4}$	$1.7 \cdot 10^3$	9.6
2	1.9 ± 0.4	$3.5 \pm 0.6 \cdot 10^{-2}$	$5.9 \pm 2.3 \cdot 10^{-3}$	$3.2 \cdot 10^2$	$5.4 \cdot 10^1$
3	1.7 ± 0.3	$3.6 \pm 1.0 \cdot 10^{-2}$	$5.8 \pm 0.5 \cdot 10^{-1}$	2.9	$4.5 \cdot 10^1$
4	$1.0 \pm 0.1 \cdot 10^1$	$5.0 \pm 0.0 \cdot 10^{-2}$	$1.8 \pm 0.5 \cdot 10^1$	$5.6 \cdot 10^{-1}$	$2.0 \cdot 10^2$
5	2.6 ± 0.5	$6.0 \pm 0.2 \cdot 10^{-2}$	$6.2 \pm 1.9 \cdot 10^1$	$4.2 \cdot 10^{-2}$	$4.4 \cdot 10^1$
6	2.7 ± 0.5	$5.4 \pm 0.0 \cdot 10^{-2}$	$7.0 \pm 1.6 \cdot 10^1$	$3.9 \cdot 10^{-2}$	$5.0 \cdot 10^1$
7	$1.2 \pm 0.6 \cdot 10^1$	$4.7 \pm 0.2 \cdot 10^{-2}$	$3.5 \pm 0.0 \cdot 10^1$	$3.6 \cdot 10^{-1}$	$2.6 \cdot 10^2$

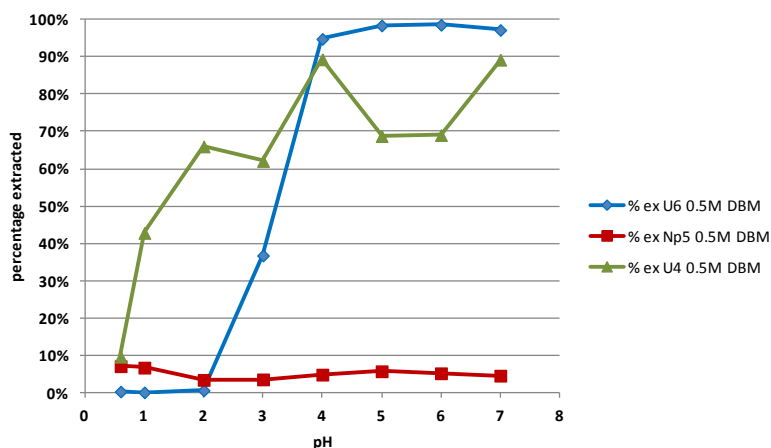


Fig.5. Percentage extracted of U(IV), Np(V) and U(VI) for the 0.5M dibenzoylmethane in chloroform extraction system.

The results for solvent extraction of U(IV), U(VI) and Np(V) in 0.22M perchlorate at pH 0.6-8 with 0.05M PMBP in xylene are shown in Table 5 and Fig.6.

Table 5. Results for distribution coefficients, D , and separation factors, SF , for solvent extraction of U(IV), Np(V) and U(VI) using 0.05M PMBP in xylene. D and SF have no units.

pH	D U(IV)	D Np(V)	D U(VI)	SF U(IV)/U(VI)	SF U(IV)/Np(V)
0.6	3.5 ± 0.4	$7.5 \pm 1.2 \cdot 10^{-2}$	$5.5 \pm 0.2 \cdot 10^{-2}$	$6.4 \cdot 10^1$	$4.6 \cdot 10^1$
1	4.9 ± 0.3	$3.9 \pm 0.2 \cdot 10^{-2}$	$3.1 \pm 0.3 \cdot 10^{-1}$	$1.6 \cdot 10^1$	$1.3 \cdot 10^2$
2	$6.1 \pm 2.0 \cdot 10^1$	$5.6 \pm 4.6 \cdot 10^{-2}$	$2.0 \pm 0.1 \cdot 10^1$	3.1	$1.1 \cdot 10^3$
3	$6.6 \pm 1.3 \cdot 10^1$	$8.8 \pm 0.9 \cdot 10^{-2}$	$6.4 \pm 0.0 \cdot 10^1$	1.0	$7.5 \cdot 10^2$
4	$9.0 \pm 5.5 \cdot 10^1$	$2.9 \pm 1.7 \cdot 10^{-1}$	$5.8 \pm 1.1 \cdot 10^1$	1.5	$3.1 \cdot 10^2$
5	$1.5 \pm 1.1 \cdot 10^2$	$1.3 \pm 0.3 \cdot 10^1$	$1.8 \pm 1.0 \cdot 10^2$	$8.3 \cdot 10^{-1}$	$1.1 \cdot 10^1$
6	$3.4 \pm 1.9 \cdot 10^1$	$2.2 \pm 0.5 \cdot 10^1$	$1.8 \pm 1.3 \cdot 10^2$	$1.9 \cdot 10^{-1}$	1.5
7	$9.7 \pm 5.5 \cdot 10^1$	$3.8 \pm 1.0 \cdot 10^1$	$1.8 \pm 0.1 \cdot 10^2$	$5.4 \cdot 10^{-1}$	2.5

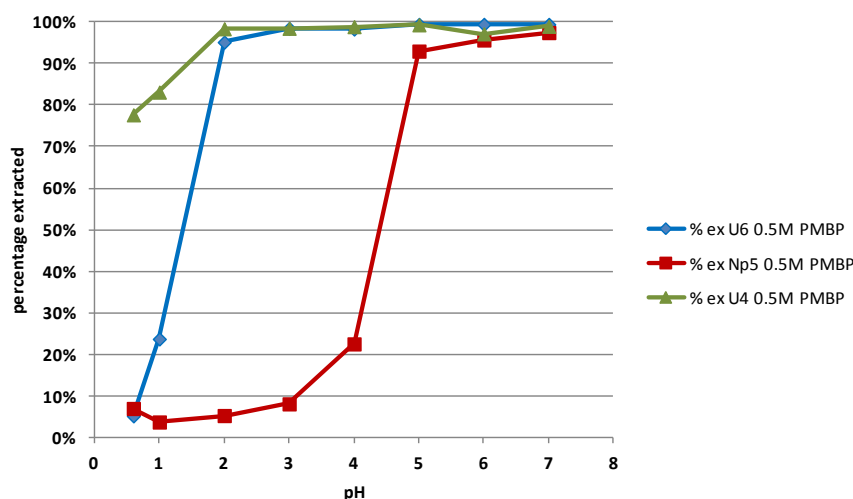


Fig.6. Percentage extracted of U(IV), Np(V) and U(VI) for the 0.05M 4-benzoyl-3-methyl-1-phenyl-5-pyrazolinone in xylene extraction system.

From the extraction results for separation factors it was concluded that optimum conditions for separation of the actinide (IV) and (VI) states are with the 0.5M DBM at pH 1 with a separation factor of over 1000. However, percentage extraction of (IV) with this system is only 40% (Fig.5), so the extraction results have to be compensated for this. For the separation of the actinide (IV) and (V) states, optimum conditions are found for 0.05M PMBP at pH 2 with separation factor of 1000 and where percentage extraction of (IV) with this system is 100% (Fig.6). However, if pH 2 is selected for both separations, the separation of (IV) and (VI) with the DBM system is then down slightly from 1000 to 320, but the extraction efficiency has, increased to 65% and extraction results are compensated with a factor of 1.5. By selecting the same pH value, sample handling is somewhat simplified since the same pH adjustment are made to the groundwater before extraction, irrespective if either U (IV)/(VI) or Np (IV)/(V) is to be measured. Although Np was not selected for the redox measurements here, due to problems with reduction to Np(IV) state, the data may be used in future studies. Alternatively, the TTA system at pH 0.6 can be selected for the (IV)/(VI) separation, where the separation factor is 350 and extraction efficiency is about 85%. Since the DBM system involves less pH adjustment (pH 2) for about the same separation performance, the DBM system was selected here for the (IV)/(VI) separation in the subsequent redox measurements. A comparison with some literature data for TTA, the percentage extraction of U(IV) at pH 0.6 is somewhat lower with 85% compared with the 95% obtained for U(IV) by Foti and Freiling (1964) and the 98% that was obtained for Th(IV) in Bertrand and Choppin (1982). For DBM, the percentage extraction of 70-90% in the pH range 4-5 is lower than the 93-95% measured for Th(IV) by Saito and Choppin (1983). Further data was given in the literature review, above.

Redox measurements

The results of redox measurements of the synthetic groundwater (LTDE water) with redox electrode and U radiotracer addition are shown in Tables 6-9. The correction factor +219mV (20°C) was used for converting Ag/AgCl ref. electrode measurements to

values versus Standard Hydrogen Electrode (SHE). For calculation of Eh from [U(IV)]/[U(VI)] the PHREEQC thermodynamic speciation code and LLNL.dat database was used. Input data was LTDE water composition (Table 2), [U]_{tot}=1μM, T=20°C with variable pO₂ to give the calibration curve shown in Fig. 6.

Table 6. Results for redox measurements with electrode and [U(IV)]_{tot}/[U(VI)]_{tot} measurements for the synthetic groundwater (LTDE water). U ratios were converted to Eh (vs SHE) by speciation calculations using PHREEQC and LLNL.dat.

Sample time(h)	Electrode Eh (vs SHE) (mV)	[U(IV)] _{tot} /[U(VI)] _{tot} measured	U(IV)/U(VI) derived Eh (vs SHE) (mV)
1	316	0.38±0.02	28
2	321	0.34±0.00	29
24	336	0.09±0.03	46

Table 7. Results for redox measurements with electrode and [U(IV)]_{tot}/[U(VI)]_{tot} measurements for the synthetic groundwater (LTDE water) with granite. U ratios were converted to Eh (vs SHE) by speciation calculations using PHREEQC and LLNL.dat.

Sample time(h)	Electrode Eh (vs SHE) (mV)	[U(IV)] _{tot} /[U(VI)] _{tot} measured	U(IV)/U(VI) derived Eh (vs SHE) (mV)
1	320	0.33±0.06	30
2	295	0.13±0.00	41
24	326	0.14±0.01	40

Table 8. Results for redox measurements with electrode and [U(IV)]_{tot}/[U(VI)]_{tot} measurements for the synthetic groundwater (LTDE water) with pyrite. U ratios were converted to Eh (vs SHE) by speciation calculations using PHREEQC and LLNL.dat.

Sample time(h)	Electrode Eh (vs SHE) (mV)	[U(IV)] _{tot} /[U(VI)] _{tot} measured	U(IV)/U(VI) derived Eh (vs SHE) (mV)
1	283	0.33±0.02	31
2	260	0.21±0.03	37
24	268	0.04±0.01	57

Table 9. Results for redox measurements with electrode and $[U(IV)]_{tot}/[U(VI)]_{tot}$ measurements for the synthetic groundwater (LTDE water) with granite and pyrite. U ratios were converted to Eh (vs SHE) by speciation calculations using PHREEQC and LLNL.dat.

Sample time(h)	Electrode Eh (vs SHE) (mV)	$[U(IV)]_{tot}/[U(VI)]_{tot}$ measured	U(IV)/U(VI) derived Eh (vs SHE) (mV)
1	286	0.23±0.02	34
2	260	0.07±0.03	49
24	310	0.01±0.01	69

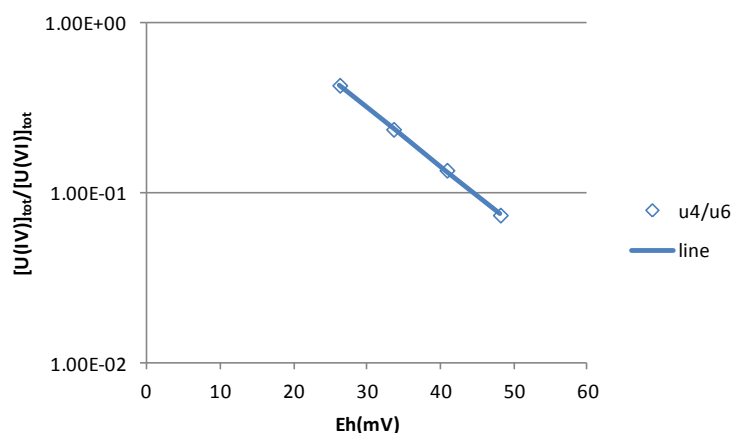


Figure 6. Calibration curve used for the conversion of measured ratios of U redox state to Eh .

Initial electrode measurements show that the prepared synthetic groundwater is not as reducing as the calculated value of $Eh = -167\text{mV}$ (Table 2). As soon as the synthetic groundwater is prepared, it will start to equilibrate with the glove-box atmosphere where $[O_2(g)]$ is about 1ppm. At equilibrium this will result in a theoretical $Eh = 757\text{mV}$. Therefore, any value between these two extremes is possible to measure in the artificial groundwater. The initially measured value when prepared was 30mV. However, when transferring 100mL portions of this water to the plastic vessels for parallel measurements with U radiotracer and redox electrode, it was found that the electrode Eh values had changed to 260-320mV (Tables 6-9). This increase was noted in all batches, whether a solid phase was present or not. The reason is probably increased mixing with gas-phase when transferring solution. The measured values with electrode may therefore be out of range for the $U(IV)/U(VI)$ determination method. At 300mV the extrapolation of the calibration line would give a $U(IV)/U(VI)$ ratio of $1 \cdot 10^{-10}$, which is clearly out of reach for the method. It is interesting that the measured Eh derived from $[U(IV)]/[U(VI)]$ corresponds very well with the initial electrode measurement of 30mV.

Conclusions

The measurement of actinide redox states may be used as a complementary method to electrode measurements. Results from U(IV)/U(VI) measurements show that the method is within the range of expected redox values in groundwater. However, absolute correspondence of measured values with electrode and U redox states was not possible to achieve in this work, probably because the U redox state method have a narrow measuring window and the measured electrode Eh values are too high in the example studied. The U redox values were about 30mV, which was about 300mV below values with electrode. Whether this reflects a preservation of redox condition from an earlier state of the water, where electrode measurements indeed gave 30 ± 4 mV, is at the moment not possible to say and further investigations are needed. Despite its limited range (Eh within about -100 to 100mV), the method of U(IV) addition, equilibration and redox state separation by solvent extraction is nevertheless a compact, quick and cost-effective method. Actinide redox states may also be of relevance, for example in the groundwater at waste repositories and mining facilities. The method may be extended to also include Np and Pu as possible redox tracers, but this needs further development.

Acknowledgements

PHREEQC Interactive 2.15.0 is a computer code developed at the United States Geological Survey. The thermodynamic database LLNL.dat was developed at the Lawrence Livermore National Laboratories, USA.

The research leading to these results has received funding from the European Union's European Atomic Energy Community's (Euratom) Seventh Framework Programme FP7/2007-2011 under grant agreement n° 212287 (RECOSY project) and SKB, the Swedish Nuclear Fuel and Waste Management Company.

References

- Allard, B., Kipatsi, H. and Liljenzin, J-O. (1980): Expected species of uranium, neptunium and plutonium in neutral aqueous solutions. J. Inorganic and Nuclear Ch. 42, 1015-1027.
- Altmaier, M. Gaona, X., Fellhauer, D. and Buckau, G.(eds.) (2010): Intercomparison of Redox determination methods on designed and near-natural aqueous systems. Karlsruhe Institute of Technology Scientific Report 7572.
- Bertrand, P.A. and Choppin, G.R. (1982): Separation of actinides in different oxidation states by solvent extraction. Radiochim. Acta 31, 135-137.
- Choppin, G.R. and Bond, A.H. (1996): Actinide oxidation speciation. J. Analytical Chemistry 51, 1129-1138.

- Coates, J.T., Fjeld, R.A., Paulenova, A. and DeVol, T. (2001): Evaluation of a rapid technique for measuring actinide oxidation states in a ground water simulant. *J. Radioanalytical and Nuclear Ch.* 248, 501-506.
- El-Naggar, H.A., Ezz El-Din, M.R. and Sheha, R.R. (2000): Speciation of neptunium migration in under groundwater. *J. Radioanalytical and Nuclear Ch.* 246, 493-504.
- Foti, S.C. and Freiling, E.C. (1964): The determination of the oxidation states of tracer uranium, neptunium and plutonium in aqueous media. *Talanta* 11, 385-392.
- Katz, J.J., Seaborg, G.T. and Morss, L.R. (eds.) (1986): The chemistry of the actinide elements, 2nd ed. Chapman and Hall.
- Kobashi, A., Choppin, G.R. and Morse J.W. (1988): A study of techniques for separating plutonium in different oxidation states. *Radiochim. Acta* 43, 211-215.
- Laaksoharju, M., Smellie, J., Tullborg, E.-L., Gimeno, M., Hallbeck, L., Molinero, J. and Waber, N. (2008): Bedrock hydrogeochemistry Forsmark, Site descriptive modelling, SDM-Site Forsmark. SKB Report R-08-47.
- Neu, M.P., Hoffman, D.L., Roberts, K.E., Nitsche, H., Silva, R.J. (1994): Comparison of chemical extractions and laser photoacoustic spectroscopy for the determination of plutonium species in near-neutral carbonate solutions. *Radiochim. Acta* 66/67, 251-258.
- Nitsche, H., Lee, S.C. and Gatti, R.C. (1988): Determination of plutonium oxidation states at trace levels pertinent to nuclear waste disposal. *J. Radioanalytical and Nuclear Ch.* 124, 171-185.
- Nitsche, H., Roberts, K., Xi, R., Prussin, T., Becraft, K., Al Mahamid, I.; Silber, H.B., Carpenter, S.A. and Gatti, R.C. (1994): Long term plutonium solubility and speciation studies in synthetic brine. *Radiochim. Acta* 66/67, pp 3-8.
- Poskanzer, A.M. and Foreman, B.M. (1961): A summary of TTA extraction coefficients. *J. Inorganic and Nuclear Ch.* 16, 323-336.
- Rai, D. (1984): Solubility product of Pu(IV) hydrous oxide and equilibrium constants of Pu(IV)/Pu(V), Pu(IV)/Pu(VI) and Pu(V)/Pu(VI) couples. *Radiochim. Acta* 35, 97-106.
- Röllin, S. and Eklund, U.-B. (2000): Determination of U(IV) and U(VI) by ion chromatography-ICPMS and its application to kinetic studies. *J. Chromatography. A.* 884, pp 131-141.
- Saito, A. and Choppin, G.R. (1983): Separation of actinides in different oxidation states from neutral solutions by solvent extraction. *Analytical Chemistry* 55, 2454-2457.
- Schramke, J.A., Rai, D., Fulton, R.W. and Choppin, G.R. (1989): Determination of aqueous plutonium oxidation states by solvent extraction. *J. Radioanalytical and Nuclear Ch.* 130, pp 333-346.
- Widestrand, H., Byegård, J., Selnert, S., Skålberg, S., Höglund, S. and Gustafsson, E. (2010): Long Term Sorption Diffusion Experiment (LTDE-SD) Supporting laboratory program – Sorption diffusion experiments and rock material characterisation. SKB Report R-10-66.

Yu, Q., Kandegedara, A., Xu, Y. and Rorbacher, D.B. (1997): Avoiding interferences from Good's buffers: a contiguous series of noncomplexing tertiary amine buffers covering the entire range of pH 3-11. *Anal. Bioch.* 253, 50-56.

SPECTROPHOTOMETRIC AND POTENTIOMETRIC INVESTIGATION OF IRON (III) HYDROLYSIS IN CHLORIDE MEDIA

Sven Hagemann*, Tina Scharge, Barbara P. Bischofer

Gesellschaft für Anlagen und Reaktorsicherheit (GRS) mbH (GER)

* Corresponding author: sven.hagemann@grs.de

Abstract

By means of spectrophotometric titrations with constant concentrations of NaCl, MgCl₂ or CaCl₂ but varying pH values, formation of hydroxo complexes of Fe(III) could be observed. At the same time, activity of Fe(III) was measured potentiometrically using a redox electrode. On the basis of the altered cell potential relative concentrations of hydroxo complexes could be derived. With this information it was possible to decompose the measured UV-spectra into single species spectra and to identify the principle type of hydroxo complexes in chloride media. The first detectable hydroxo complex to form is FeOH⁺ up to chloride concentrations of about 4 mol/kg and -log c_H below 4. Only at higher concentrations there are indications that another complex, possibly a mixed chloro hydroxo complex, is present as well.

Introduction

Recently Bischofer et al. (2009) and Scharge et al. (2010) investigated the influence of brines on measured redox potentials and developed a model which describes the medium induced bias on the instrument signal. The investigations were based on a new thermodynamic model for the calculation of activity coefficients for Fe(II) and Fe(III) salts in acidic electrolyte solutions (Hagemann et al. 2012a). In order to extend its applicability to slightly acidic and near neutral solutions, a better understanding of Fe(III) complex formation with Cl⁻ and OH⁻ in chloride media is needed.

The potential of a redox sensitive cell E_{Rx} may be expressed as

$$E_{Rx} = E_{Rx}^0 + 0.05916 \log \frac{a_{Fe^{3+}}}{a_{Fe^{2+}}} \quad (1)$$

in a solution whose redox state is determined by the redox couple Fe(III)/Fe(II). The formula is valid independently of the actual speciation of Fe(II) and Fe(III). In a series of solutions of constant media composition but increasing hydrogen (H⁺) concentration (-log c_{H+} between 4.2 and 0.8 by an addition of aq. HClO₄), the cell potential is expected to be constant at high H⁺ concentrations, where hydroxo complexation does not occur. At lower H⁺ concentrations Fe(III) hydroxo complexes become relevant, so that the activity of free Fe³⁺ will decrease. In the acidic solutions of our experiments,

Fe^{2+} hydroxo complex formation is negligible (Baes and Mesmer 1976). Taking the measurements at high H^+ concentration as a basis, the cell potential E'_{Rx} will be at lower H^+ concentrations:

$$E'_{\text{Rx}} = E_{\text{Rx}}^0 + 0.05916 \log \frac{c'_{\text{Fe}^{3+}}}{c_{\text{Fe}^{2+}}} + 0.05916 \log \frac{\gamma_{\text{Fe}^{3+}}}{\gamma_{\text{Fe}^{2+}}} \quad (2)$$

The difference ΔE_{Rx} between E_{Rx} and the cell potential E'_{Rx} at lower H^+ concentration is directly connected to the ratio of free Fe^{3+} concentrations because the constant ion activity coefficients are cancelled down.

$$\Delta E_{\text{Rx}} = E'_{\text{Rx}} - E_{\text{Rx}} = 0.05916 \log \frac{c'_{\text{Fe}^{3+}}}{c_{\text{Fe}^{2+}}} - 0.05916 \log \frac{c_{\text{Fe}^{3+}}}{c_{\text{Fe}^{2+}}} = 0.05916 \log \frac{c'_{\text{Fe}^{3+}}}{c_{\text{Fe}^{3+}}} \quad (3)$$

Since there is no change in the media composition beside the H^+ and ClO_4^- concentration, the decrease of free Fe^{3+} concentration may be directly attributed to an increase of hydroxo complex concentration. Consequently, redox potential measurements allow a quantification of the concentration ratio “ FeOH^+ ”/ Fe^{3+} in a broad range of solutions (cf. equation 4).

$$\log \frac{c'_{\text{FeOH}^+}}{c_{\text{Fe}^{3+}}} = \frac{\Delta E_{\text{Rx}}}{0.05916} \quad (4)$$

Unfortunately, this expression leads to nowhere because the free concentration of Fe^{3+} is a priori unknown, especially in solutions where most of Fe^{3+} is bound in chloro complexes. Without knowing the exact speciation it may be assumed that the free concentration of Fe^{3+} and the total concentration of iron (III) chloro complexes “ FeCl_n ” (with n , the average number of bound chloride ions in solution of defined and constant media composition) are related through

$$c_{\text{Fe}^{3+}} = k c_{\text{FeCl}_n} \quad (5)$$

The parameter k is a constant that is independent of the hydrogen concentration for a given electrolyte concentration. If hydroxo complexes become relevant the concentrations of Fe^{3+} and “ FeCl_n ” would be reduced proportionally. Then, equation 3 can be rearranged to

$$\Delta E_{\text{Rx}} = E'_{\text{Rx}} - E_{\text{Rx}} = 0.05916 \log \frac{k c'_{\text{FeCl}_n}}{c_{\text{Fe}^{2+}}} - 0.05916 \log \frac{k c_{\text{FeCl}_n}}{c_{\text{Fe}^{2+}}} = 0.05916 \log \frac{c'_{\text{FeCl}_n}}{c_{\text{FeCl}_n}} \quad (6)$$

and with

$$c_{\text{FeCl}_n} = c'_{\text{FeCl}_n} + c'_{\text{FeOH}^+} \quad (c_{\text{FeOH}^+} \cong 0) \quad (7)$$

$$\frac{c'_{\text{FeCl}_n}}{c_{\text{FeCl}_n}} = 10^{\frac{\Delta E_{\text{Rx}}}{0.05916}} \quad (8)$$

or

$$\frac{c'_{\text{FeOH}^+}}{c_{\text{FeCl}_n}} = 1 - 10^{\frac{\Delta E_{\text{Rx}}}{0.05916}} \quad (9)$$

Equation (9) allows to calculate the actual concentration of Fe(III) bound in hydroxo complexes c'_{FeOH} from the total Fe(III) concentration at high H^+ concentrations c_{FeCl_n} and the change of the cell potential ΔE_{Rx} during the experiment.

In fact, this equation is even valid in cases in which only part of Fe^{3+} is bound in chloro complexes because at any time during our titration experiments the law of mass action assures that the relative ratio of Fe^{3+} and its chloro complexes remains constant even if their total concentration decrease. Therefore, a change in cell potentials may always be attributed to an increase of the relative concentration of hydroxo complexes.

In order to make use of this approach, measurements were conducted in form of titrations in NaCl, MgCl_2 , and CaCl_2 solutions of different concentration.

Experimental Setup

UV-spectra of different electrolyte solutions containing Fe(II) and Fe(III) were measured with a double-beam UV-spectrometer (Shimadzu UV-2450) between 190 and 700 nm using 1 cm temperature-controlled flow-through cuvettes. The stock solutions were prepared and stored in an argon flushed glove box. The measurements were carried out in an argon atmosphere to avoid oxidation of Fe(II). All used salts (NaCl , $\text{CaCl}_2 \cdot 4\text{H}_2\text{O}$ and $\text{MgCl}_2 \cdot 6\text{H}_2\text{O}$) were purchased from Merck (Germany). NaCl and $\text{CaCl}_2 \cdot 4\text{H}_2\text{O}$ had the grade suprapur, $\text{MgCl}_2 \cdot 6\text{H}_2\text{O}$ had the grade p.a. FeCl_2 and FeCl_3 (purity of 99,99%, respectively 99,99+%) from Sigma Aldrich were used for the preparation of Fe(II) and Fe(III) containing solutions. Solutions were prepared with CO_2 -free Milli-Q water ($18.3\text{M}\Omega$) and for acidification HClO_4 (70%, suprapur, Merck) was used.

The measurements were conducted as pH titrations in which the pcH value (the negative logarithm (base 10) of the molar hydrogen concentration) varied between 4 and 1 in about 12 steps. This was achieved by titrating a starting solution containing $\text{Fe(II)} = \text{Fe(III)} = 5 \cdot 10^{-5} \text{ M}$ and a background salt with a titrant containing the same concentration of iron and background salt as well as 0.2 M HClO_4 . For each salt, measurements at five concentrations between 0.01 mol/kg and near saturation (maximum of 2 mol/kg for CaCl_2) were carried out.

Beside the UV-spectra also the redox potential was measured with a combined platinum ring electrode (Metrohm 6.0451.100) with a silver/ silver chloride/ 3M KCl reference. The measurements were conducted after 5 minutes time of stirring and 5 additional minutes equilibration time. Readings were only accepted if the signal during the measurement were within 0.3 mV in 120 sec. If this criterion was not fulfilled the measurements were repeated after further 5 minutes. The pH was measured with a Unitrode with Pt 1000 (Metrohm 6.0258.000) using three different calibration standards from Merck (pH 2.0, 4.0 and 7.0) according to the expected pH-values. The pcH value was calculated from the apparent pH value using the correction functions described in Hagemann et al. (2012b). All measurements were carried out at 25°C .

Results

Generally, the measured cell potentials followed a common pattern. With rising pcH the cell potentials in most cases stayed constantly until the hydrogen concentration fell

below a certain media specific value where the potential started to fall. Sometimes, at hydrogen concentrations above 0.1 mol/kg ($p\text{cH} < 1$), there was a slight decrease of cell potentials as well. The reason for this may be an influence of the hydrogen concentration on the platinum electrode or a slight change of liquid junction potential at the reference electrode. An example for this behaviour is given in Fig. 1. Here the results of a titration in a 3.58 mol/kg NaCl solution are illustrated.

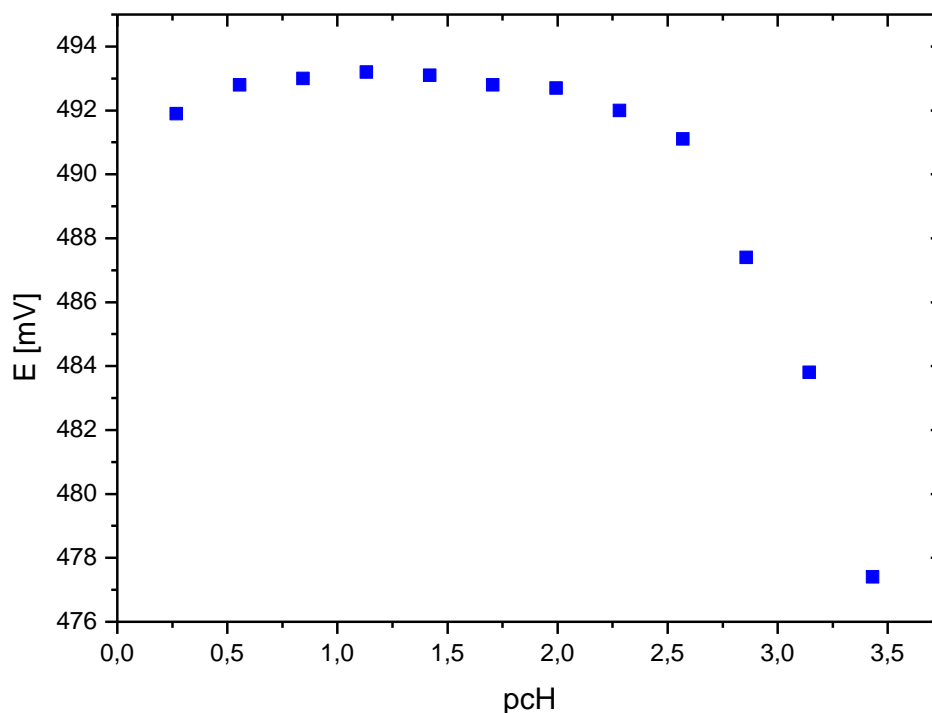


Figure 1: Cell potential in relation to $p\text{cH}$ in 3.58m NaCl with $\text{Fe(II)}=\text{Fe(III)}=5 \cdot 10^{-5} \text{ M}$

Based on these measurements the relative concentrations of hydroxo complexes were calculated according to equation 9. The results for MgCl_2 are summarized in Tab. 1, and Fig. 2. The value $p\text{H}_{\text{app}}$ listed in table 1 stands for the measured (biased) pH indicated by measuring the pH with a standard electrode.

Table 1: Experimental Results

$p\text{H}_{\text{app}}$	E [mV]	$p\text{cH}$	$c' \text{ "FeOH" } [\%]$	$p\text{H}_{\text{app}}$	E [mV]	$p\text{cH}$	$c' \text{ "FeOH" } [\%]$
0.00088 m MgCl_2				1.01 m MgCl_2			
3.784	429.3	3.722	97.2	3.537	457.7	3.861	79.4
3.491	446.1	3.429	94.6	3.301	468.2	3.625	69.0
3.253	460.0	3.191	90.7	2.983	478.3	3.307	54.1
2.913	478.4	2.851	81.0	2.668	484.4	2.992	41.8
2.684	489.7	2.622	70.5	2.357	488.8	2.681	30.9
2.428	499.1	2.366	57.4	2.110	491.1	2.434	24.4

pH _{app}	E [mV]	pCH	c' "FeOH" [%]	pH _{app}	E [mV]	pCH	c' "FeOH" [%]
0.0088 m MgCl₂				1.01 m MgCl₂			
2.158	506.6	2.096	43.0	1.839	493.9	2.163	15.7
1.852	512.9	1.790	27.1	1.541	495.4	1.865	10.7
1.570	516.9	1.508	14.9	1.267	497.8	1.591	1.9
1.330	519.8	1.268	4.7	0.941	498.4	1.265	<1
1.092	521.9	1.030	<1	0.644	498.7	0.968	<1
1.048	521.4	0.986	<1	0.575	496.3	0.899	<1
2.08 m MgCl₂				3.21 m MgCl₂			
3.063	481.0	3.968	35.4	2.419	483.1	3.952	10.9
2.783	486.3	3.688	20.6	2.098	484.8	3.631	4.8
2.525	489.0	3.430	11.8	1.805	485.6	3.338	1.8
2.180	490.9	3.085	5.0	1.440	486.0	2.973	<1
1.754	492.1	2.659	<1	1.100	486.2	2.633	<1
1.518	492.2	2.423	<1	0.912	486.0	2.445	<1
1.212	492.4	2.117	<1	0.610	485.8	2.143	<1
0.910	492.2	1.815	<1	0.345	485.5	1.878	<1
0.648	491.8	1.553	<1	0.014	484.4	1.547	<1
0.353	491.0	1.258	<1	-0.326	482.1	1.207	<1
0.036	488.4	0.941	<1	-0.597	480.6	0.936	<1
4.41 m MgCl₂							
1.924	478.1	4.133	1.4				
1.547	478.5	3.756	<1				
1.340	478.5	3.549	<1				
1.063	478.4	3.272	<1				
0.740	477.5	2.949	<1				
0.246	477.0	2.455	<1				
-0.099	476.2	2.110	<1				
-0.328	475.5	1.881	<1				
-0.561	474.2	1.648	<1				
-0.860	472.0	1.349	<1				
-1.092	470.9	1.117	<1				

Results from the redox measurements correspond well with calculated hydroxo complex formation that was derived by applying Lawrence Livermore National Laboratories dataset thermo.com.V8.R6 as delivered with the geochemical code Geochemist's

Workbench (version 9.0). Due to the lack of an appropriate activity model for Fe(III) chloro complexes at higher ionic strengths such a comparison was not feasible for other salt concentrations.

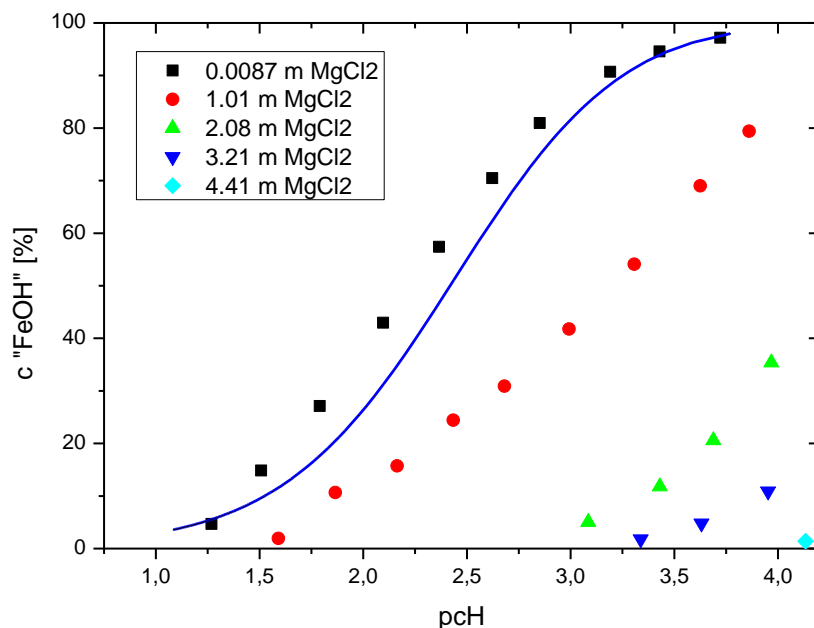


Figure 2: Calculated concentration of hydroxo complexes in MgCl_2 solutions based on redox measurements. Blue line describes the extent of hydroxo complex formation calculated by Geochemist's Workbench for 0.0087 m MgCl_2 .

For MgCl_2 solutions, the results were combined in a smoothed contour diagram (Fig. 3). It shows that the hydroxo complex formation is delayed with increasing MgCl_2 concentration.

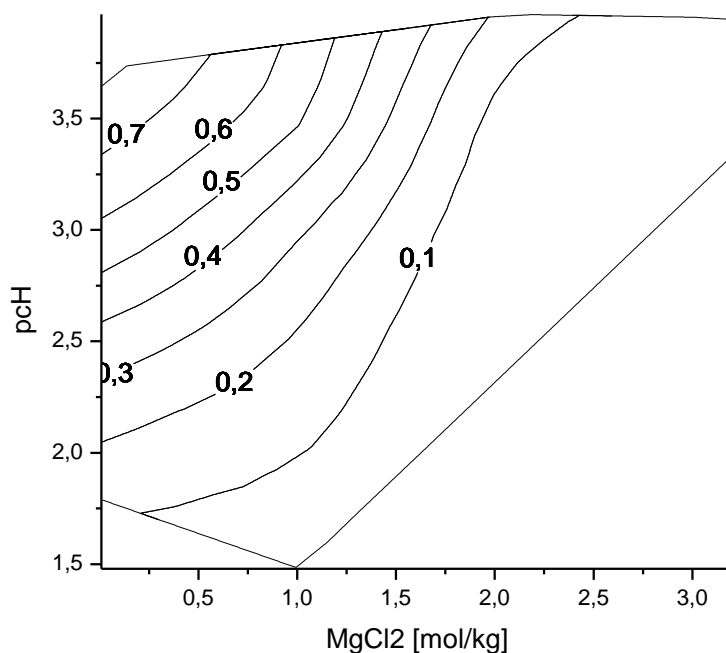


Figure 3: Calculated relative concentrations of hydroxo complexes in $MgCl_2$ solutions

Type and constitution of hydroxo complexes

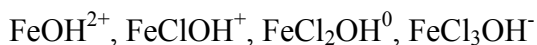
Although the potential measurements give quantitative information about how much Fe(III) is bound in hydroxo complexes the type of complexes has still to be determined. This can be done by evaluating der equilibrium condition

$$c_{Fe(OH)_n} = Kc_{OH}^n c_{Fe^{3+}}^n = Kc_{OH}^n k^* c_{FeCl_n}^n \quad (10)$$

That is valid in solutions of constant media composition. Here, k^* is the equilibrium constant for the formation of chloro complexes “ $FeCl_n$ ” from Fe^{3+} and Cl^- . By plotting

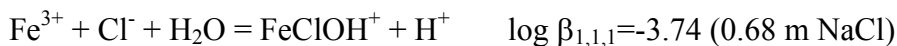
$\log \frac{c_{Fe(OH)_n}^n}{c_{FeCl_n}^n}$ over the hydrogen concentration (pCH) one gets n, the number of hydroxo

ions bound per Fe^{3+} cation. For high H^+ concentrations the ratio is zero. For all solution types and concentrations, the plotting resulted in a linear trend with a slope of one or slightly above one. The most important hydroxo complex must have an OH^-/Fe^{3+} ratio of 1. The following species are candidates:



At higher salt concentrations the slopes reached values of up to 1.3. An explanation for this could be that in these solutions the formation of hydroxo complexes starts at higher pCH values where the formation of dihydroxo complexes like $Fe(OH)_2^+$ or possibly $FeCl(OH)_2^0$ already becomes important. Thus, the average number of hydroxo ions bound to Fe^{3+} is higher than one.

FeOH^{2+} is a well known species (Byrne et al. 2005) that definitely is formed in dilute solutions. In solutions of high chloride concentrations mixed chloro hydroxo complexes may be expected. In the literature only one mixed complex has been described: FeClOH^+ (Koren and Perlmutter-Haymen 1972, Byrne and Kester 1981). The findings of these two studies differ significantly with regard to the complex formation constant. Byrne and Kester (1981) published the following two equilibrium constants:



Then, the reaction



has an equilibrium constant of $\log K = -1.03$.

A chloride activity of approximately 10 would be needed to bring the complex FeClOH^+ to the same concentration as FeOH^{2+} . Therefore, the mixed complex is expected only at higher chloride concentration. However, the authors did not investigate such solutions.

In order to get more insight into the type of the hydroxo complexes formed in concentrated chloride media spectrophotometric measurements were performed with same solutions that were measured potentiometrically. An example is given in Fig. 4. The graph shows that the spectrum of a mixture of chloro complexes is gradually altered due to the formation of hydroxo complexes. The spectrum of the mixture of hydroxo complexes could be separated from the spectrum of chloro complexes by applying the concentrations c_{FeCl_n} and c_{FeOH} derived from the potentiometric measurements.

At any time of the titration the resulting solution spectra A_{meas} is a combination of the spectra of free Fe^{3+} and its chloro complexes A_{FeCl_n} and the spectrum of the combination of hydroxo and chloro hydroxo complexes A_{FeOH} .

$$A_{\text{meas}} = c_{\text{FeCl}_n} A_{\text{FeCl}_n} + c_{\text{FeOH}} A_{\text{FeOH}} \quad (11)$$

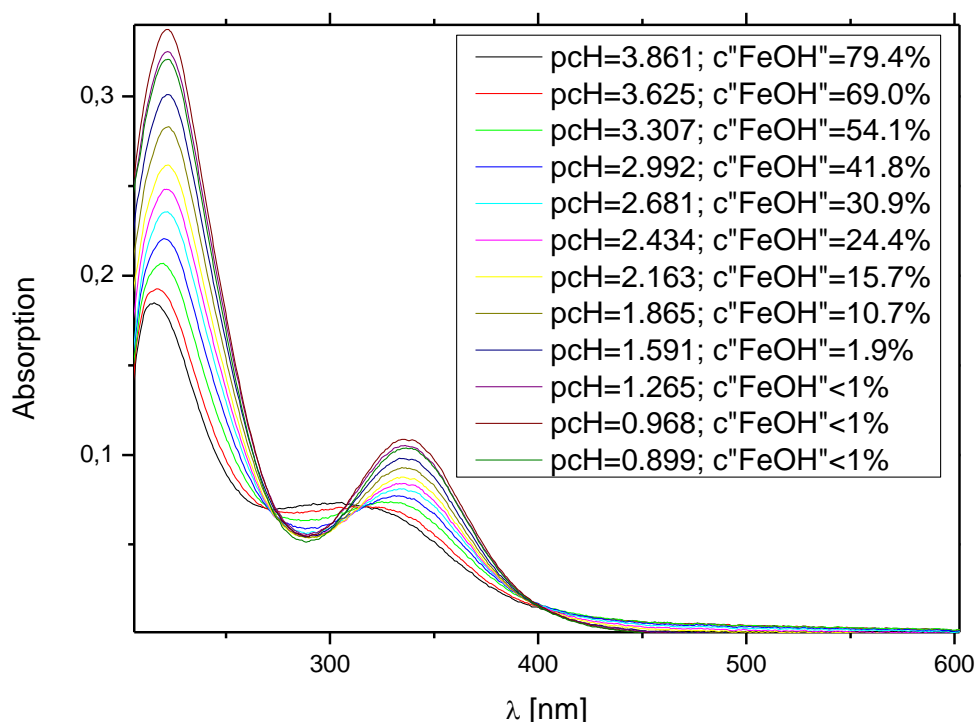


Figure 4: UV-spectra of solutions containing $Fe(II)=Fe(III)=5 \cdot 10^{-5} M$ and $1.01 m$ $MgCl_2$ at various pcH values

The spectrum of the combination of hydroxo and chloro hydroxo complexes may be easily derived by rearranging equation 11.

$$A_{FeOH} = \frac{A_{meas} - c_{FeCl_n} A_{FeCl_n}}{c_{FeOH}} \quad (12)$$

Most of the derived spectra have a maximum at 294 ± 3 nm (Fig. 5). The spectra are very similar to those that Knight and Silva (1975) found for the hydroxo complex $FeOH^{2+}$ (maximum at 297 nm). More recently, Perera and Hefter (2003) determined the maximum of the $FeOH^{2+}$ spectrum at 286 nm. But they have applied a model which included six mononuclear Fe(III) hydroxo complexes (up to $n_{OH}=6$) that is not well supported by other studies.

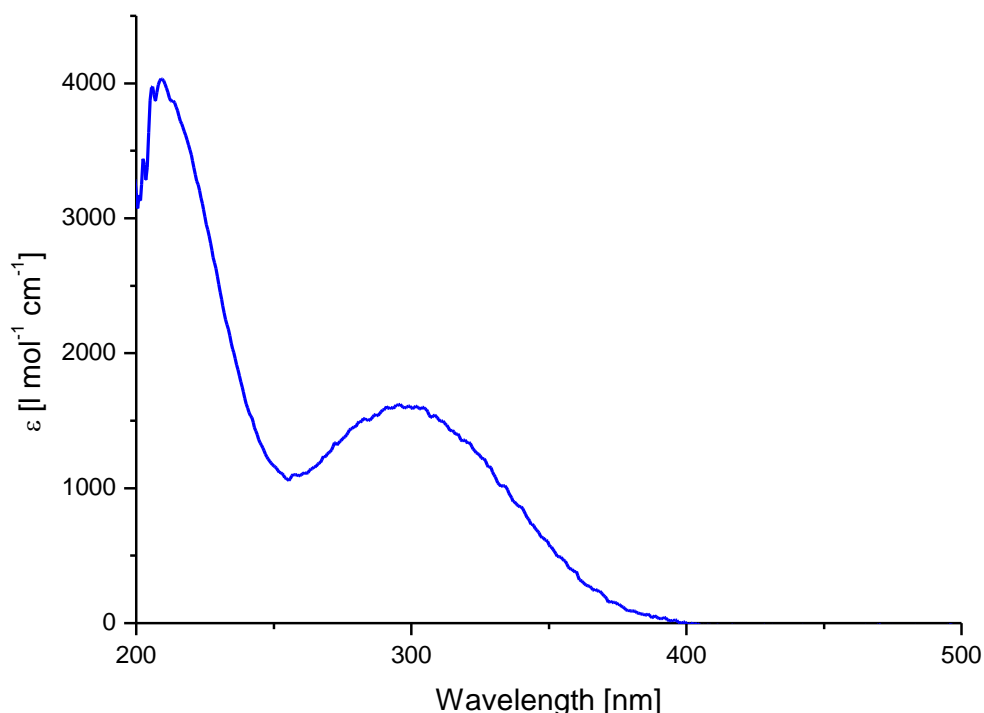


Figure 5: Example for the calculated UV-spectra of the hydroxo complexes at a pcH of 3.84, in 3.59 mol/kg NaCl

The maximum of the absorbance spectra is higher for solutions with a chloride concentration larger than 4 mol/kg and pcH near 4, indicating the formation of another hydroxo species. At concentrations around 0.02 mol/kg chloride the formation of a different hydroxo complex, probably $\text{Fe}(\text{OH})_2^+$ was observed.

We conclude that there is no evidence that another hydroxo complex forms below pcH 4 beside FeOH^{2+} in chloride concentrations of 1-4 mol/kg. A mixed complex may be formed at higher concentrations and pcH values. Calculation of the concentration dependend formation constant K for FeOH^{2+} would require knowledge of the extend of chloro complex formation (or k^* in eq. 10) at each chloride concentration in our experiments. Unfortunately, a model to describe the complex formation in all investigation solution systems is not available yet.

Further measurements are necessary to better understand the chloro and hydroxo complex formation at higher pH.

Summary and Conclusions

Combined spectrophotometric and potentiometric titrations of Fe(II) and Fe(III) containing solutions of NaCl, MgCl_2 and CaCl_2 allowed the quantification of Fe(III) hydroxo complexes in relation to Fe^{3+} and Fe(III) chloro complexes. With this information the UV-spectra were evaluated and the single species spectrum for the monohydroxo complex FeOH^{2+} was calculated. It was shown that FeOH^{2+} is in chloride concentrations between 1 and 4 mol/kg the only hydroxo complex. No evidence was found for mixed chloro hydroxo complexes.

Acknowledgements

The research leading to these results has received funding from the European Union's European Atomic Energy Community's (Euratom) Seventh Framework Programme FP7/2007-2011 under grant agreement n° 212287 (RECOSY project) and of the German Federal Ministry of Economics and Technology (BMWi), grant agreement 02 E 10075.

References

- Baes, C. F., Mesmer, R. E. (1976). The Hydrolysis of Cations, Wiley Interscience, New York. 489 p.
- Bischofer, B. P., Hagemann, S., Hühne, C., Schönwiese, D., Scharge, T. (2009): Influence of chloride concentrations on the signal of redox electrode and on UV-spectroscopic determination of Fe species, KIT Report FZKA 7466, December 2009, 83-91.
- Byrne, R. H., Kester, D. R. (1981). Ultraviolet spectroscopic study of ferric equilibria at high chloride concentrations, J. Solution Chem., 10, 51-67.
- Byrne, R. H., Yao, W., Luo, Y.-R., Wang, B. (2005). The dependence of Fe(III) hydrolysis on ionic strength in NaCl solutions, Mar. Chem., 97, 34-48.
- Hagemann, S., Bischofer, B. P., Scharge, T., Schönwiese, D., Hühne, C. (2012a). A new approach for determining redox potentials in solutions of high ionic strength, Z. Phys. Chem., in preparation.
- Hagemann, S.; Bischofer, B.; Scharge, T.; Schönwiese, D. (2012b). Entwicklung von Methoden und Modellen zur Bestimmung des Redoxpotentials salinarer Lösungen. Abschlussbericht zum Vorhaben 02 C 1244 Redoxprognose. GRS-Bericht 260 (in print).
- Knight, R. J., Sylva, R. N. (1975). Spectrophotometric investigation of iron(III) hydrolysis in light and heavy water at 25°C, J. Inorg. Nucl. Chem., 37, 779-783.
- Koren, R., Perlmutter-Hayman, B. (1972). The kinetics of the aquation of Iron(III)chloride. The role of water structure and of the intermediate FeOHCl^+ , Inorg. Chem., 11, 3055-3059.
- Perera, N. W., Hefter, G. (2003). Mononuclear Cyano- and Hydroxo-Complexes of Iron (III), Inorg. Chem., 42, 5917-5923.
- Scharge, T., Bischofer, B. P., Hagemann, S., Schönwiese, D. (2010): Spectrophotometric and potentiometric determination of the redox potential in solutions of high ionic strength, KIT Scientific Reports 7557, 147-159.

INVESTIGATIONS ON STRUCTURAL IRON ELECTROCHEMICAL PROPERTIES IN LAYERED SILICATES USING MASSIVE MICA ELECTRODES

Jebril Hadi^{1*}, Ioannis Ignatiadis¹, Christophe Tournassat¹, Laurent Charlet²
and Ewen Silvester³

¹ BRGM, BP 36009, 45069 Orléans CEDEX 2 (FR)

² ISTERre, BP 53, 34081 Grenoble CEDEX 9 (FR)

³ Latrobe University, PO Box 821, Wodonga VIC 3689 (AU)

* Corresponding author: j.hadi@brgm.fr

Abstract

It is occasionally admitted that the semiconducting properties of a wide range of minerals are often ignored in the study of their interfacial geochemical behaviour.

Iron is one of the most common redox species in soils and sedimentary rocks. Iron-bearing phyllosilicates play key roles in various biogeochemical processes. The complexity of the physical and chemical (along with structural) changes involving their structural iron makes the studies of its redox properties challenging. Most of the recent reported efforts were focused on probing Fe redox on finely powdered clay (and often micas) particles, and have been hampered by inadequate interactions between particles and electrodes. Moreover, such experiments usually involve redox probe ions, thus adding supplementary difficulties in the determination of structural iron redox parameters such as redox potential (Eh) and kinetics.

The present study aims at qualitatively investigating the above mentioned phenomena on minerals like iron-bearing micas. In the current work, we present initial insights regarding efforts to build a direct electrical interface between solid electrodes and conveniently shaped macroscopic mica crystals in order to investigate the redox properties of structural iron in dry and aqueous environments, in the presence of representative perturbations.

Results show that several aspects of the designs of such electrodes have at first to be improved for further experiments.

Introduction

Iron-bearing phyllosilicates, such as clays and micas, are extensively studied for their specific physical and chemical behaviour in natural environments, in particular in terms

of the redox activity of their structural iron sites. Their role of “electron sinks” (or electron “buffer”) has been demonstrated several times, especially by wet chemistry (Hofstetter *et al.*, 2006; Neumann *et al.*, 2008; White and Yee, 1985), but the mechanisms involving electron transfer inside and outside this type of crystal structure is still not fully understood. Hence, more comprehensive studies of this aspect would improve our understanding of many phenomenon implying clays and redox, such as accessibility of nutrient in agricultural soils or migration of pollutants in contaminated soils. The latter case is particularly relevant in modelling behaviour of clays, when envisioned as landfill barrier for long term nuclear waste repository.

Iron is one of the most common redox species in soils and sedimentary rocks. Oxidation and reduction reactions involving the Fe(II)/Fe(III) redox couple are usually kinetically fast (in solution?). Among the different Fe(II)/Fe(III) couples present in soils and sediments, thermodynamic properties of structural Fe(II)/Fe(III) in clay lattice are not well known, although they could give valuable information on the redox environment of a system when coupled to a detailed mineralogical analysis (Favre *et al.*, 2006). Experimental evidence shows that redox reactions involving structural iron affect many physical and chemical properties of the mineral. This is especially the case for smectites where Fe redox reaction induces major changes such as colour, layer charge, cation exchange capacity, or structural arrangement (Stucki, 2011). The understanding of redox properties of the structural iron relies partly on a clear understanding of the mechanisms for Fe(III)/Fe(II) oxidation or reduction.

Previous attempts to characterize the clay structural iron redox properties (Eh and kinetics), using electrochemical techniques, have been hindered by insufficient interactions between electrode material and iron sites in the solid mineral phases. One of the most promising electrochemical methods that is being developed implies homogenous catalysis with organic electron transfer mediators, using chronocoulometric measurement on dispersed and/or dissolved smectites particles (Gorski *et al.*, 2011). This technique aims at overcoming the issues encountered with the most common approaches, based on the use of clay modified electrodes (CME). Clear interpretations of iron redox activity have always been limited by the complex design usually obtained for this type of electrode, presenting different sites of interaction (pores, channels, adsorption sites, edge sites, direct access of electrolytes to the underling electrode...) in layered clay structures (Fitch *et al.*, 2002; Mousty, 2004). Moreover, most of these studies ignore the major structural changes that occur during redox reactions of this material and that are partially reversible, and are focused in measuring a single Eh value. Actually, the complex relationship that exist between the different structural iron sites should lead to consider that not only one but several Fe(II)/Fe(III) poles (classes) must exist in the structure, thus exhibiting gradually decreasing Eh values.

Hundreds of studies involving CME prepared from finely powdered smectites, or often micas, have been carried out but up to now, there is no documented effort about shaping of electrodes from macroscopic single mica crystals. Micas are widely used in electronic systems as efficient electrical insulators, owing to their high electrical resistivity and their thermal properties. Convenient crystals for this purpose consist of “high grade” muscovite and often end-member phlogopite (i.e. lowest iron-bearing phlogopite), used as thin sheets, exhibiting very high electrical resistivity. Nonetheless,

electrical conduction in micas has been demonstrated in several studies (Arii and Inuishi, 1968; Crine *et al.*, 1977; Davidson and Yoffe, 1968; Meunier *et al.*, 1983; Tolland and Strens, 1972). This property is strongly anisotropic (Rüscher and Gall, 1995; Tolland and Strens, 1972), resistivity measured parallel to the cleavage plan being 2 to 5 orders of magnitude lower than the one measured perpendicular to the cleavage plan. Also, along with temperature, applied electrical field and frequency dependencies, resistivity has been shown to also be linked to the crystal composition and it decreases with increasing iron content. Hence, in certain aspects, iron-bearing micas, such as biotite, could be classified as semi-conductors. The mechanism proposed for electrical conduction along the sheets consists in “small polarons” hopping between adjacent octahedral iron sites (Meunier *et al.*, 1983; Rosso and Ilton, 2003; Rosso and Ilton, 2005; Rüscher and Gall, 1995). Quickly, a polaron is a fermionic quasiparticle composed by an electron and an accompanying polarization field. This field is self induced by the conduction electron, producing a lattice distortion that lowers its energy to the point that the electron become self trapped. Term “small” refers to short range interactions, eg. a “small polaron” arises when the polarization field self induced by the electrons is in the order of magnitude of the lattice parameter. Participation of tetrahedral iron cannot be excluded as well. Even though most of these studies are focused on the behaviour of the mica crystals at high temperatures and in high electrical fields, electrical conduction has been demonstrated to occur in conditions of more environmental relevance, e.g. at room temperature and in presence of low electrical field. So far, although efforts for developing quantitative physical models have been made (Rosso and Ilton, 2003; Rosso and Ilton, 2005), there are no experimental studies trying to connect these observations with the numerous explorations of aqueous chemical reactions involving iron in layered silicates under environmental conditions.

Iron hydroxides and sulphides have been studied as electrode materials for decades. However, as outlined in previous studies (Rosso *et al.*, 2010; Yanina and Rosso, 2008), *“the semiconducting properties of a wide range of minerals are often ignored in the study of their interfacial geochemical behaviour”*. The first step in this direction has been focused on the hematite structure. Using macroscopic crystals, controlling their shape and the exposed surfaces, coupled reactions have been demonstrated involving distinct exposed surfaces, direction dependant and controlled by bulk electronic conductivity. According to the authors, this participation of the bulk crystal conduction is likely to be extended to other natural semi-conductors. Despite their several orders of magnitude lower conductivity relative to those of natural oxides and oxyhydroxides, micas should also be investigated in that manner.

Here, similarly to what has been done on hematite, we propose to use such an approach on the iron-bearing micas. This study presents first insights of our investigation on shaping of electrodes from single mica crystals, in order to obtain reactive uniform structure on which analytical methods provided by aqueous electrochemistry could be applied. The goal is to determine if phenomena involving electron transfers that occur on edge surfaces and also through macroscopic mica crystal can be observed under dry and wet conditions as well. If electrically conductive iron paths exist along sheets of ferruginous micas, it is worth trying to use well-oriented thin crystals as an interface between solid electrodes of known behaviour and/or identified solutions. By changing and/or monitoring the redox conditions on each sides of this interface, use of electrochemical techniques such as open circuit potential (OCP) measurement,

electrochemical impedance spectroscopy (EIS) measurements at fixed potential and chronocoulometry (CC) should provide new information on the redox behaviour of structural iron in presence of mild perturbations (such as few millivolts changes in redox potential or slight changes in pH). First efforts are focused on building an efficient electrical interface, and seeing how this interface could be isolated from direct interaction with ions from the solution.

Materials and methods

Description of mineral samples

Different di- and trioctahedral micas, with varying iron content, from several families (eg. muscovite, biotite, phlogopite, lepidolite), were selected. The chemical compositions of the samples were determined by microprobe analysis (model CAMECA SX50). Structural formulas given in table 1 have been calculated on the average of 30 measurements on a mm-sized piece. For biotite and muscovite, the deviation from the mean value is less than 3%. For lepidolite, since it contains a high Li^+ content, which cannot be analysed by microprobe, no clear formula has been determined. Other crossed analyses will be performed for the determination of the Li^+ content of this sample, as well as to determine $\text{Fe}^{2+}/\text{Fe}_{\text{tot}}$ ratio in all samples. However, lepidolite has been used as a test sample in the experiments since it has the lowest iron ratio measured among all the present samples.

Table 1: List of micas, geographic origins, and structural formulas

Specie	Origin	Structural formula	Iron content (% wt)
Biotite ¹	Bancroft, Ontario	$\text{K}_{1.74}\text{Na}_{0.17}[\text{Fe}^{2+}_{2.35}\text{Mg}_{3.18}\text{Mn}_{0.11}\text{Ti}_{0.18}](\text{Si}_{5.94}\text{Al}_{1.98}\text{Ti}_{0.07})\text{O}_{20}\text{OH}_{1.97}\text{F}_{2.04}$	14.42%
Muscovite ¹	Madras	$\text{K}_{1.72}\text{Na}_{0.19}[\text{Al}_{3.84}\text{Fe}^{3+}_{0.13}\text{Mg}_{0.04}](\text{Si}_{6.1}\text{Al}_{1.9})\text{O}_{20}\text{OH}_4$	0.94%
Lepidolite ²	Unknown	$\text{K}_2[\text{AlLi}]_3(\text{Si}_6\text{Al}_2)\text{O}_{20}(\text{OH,F})_4$	< 0.02%

1: obtained from Ward's Natural Science Establishment: ref 46V1194 (biotite) and ref 46V5474 (muscovite)

2: unknown origin

The biotite structural formula matches the formula determined in a previous study (Rancourt *et al.*, 1993) on this mineral. Given the high octahedral occupancy of the biotite sample, it might be a good candidate for testing the hypothesis of electrically conductive iron path along the sheets. On the contrary, no current flows should normally be observed on the lepidolite and muscovite samples.

Preparation of electrode materials

Electrode material consists of mm-sized slice of embedded mica exposing edge surface on both sides, as shown in figure 1. Samples are specially designed so as to check the hypothesis of possible conductive iron path along the octahedral sheets at room temperature. Small pieces were carefully cut from a large flake, in several steps, using

epoxy resin (Araldite 2020, Huntsman Advanced materials) as embedding medium. Slices with thickness of 1-1.5 mm and surfaces of 0.2-0.4 cm² were obtained with a diamond saw. Then one side was electrically wired and isolated. In the experiments presented in this study, silver paint SCP033 (Electrolube, Derbyshire, UK) on a copper plate has been used as the support electrode. If the covering of the copper plate is uniform, it results in a silver electrode.

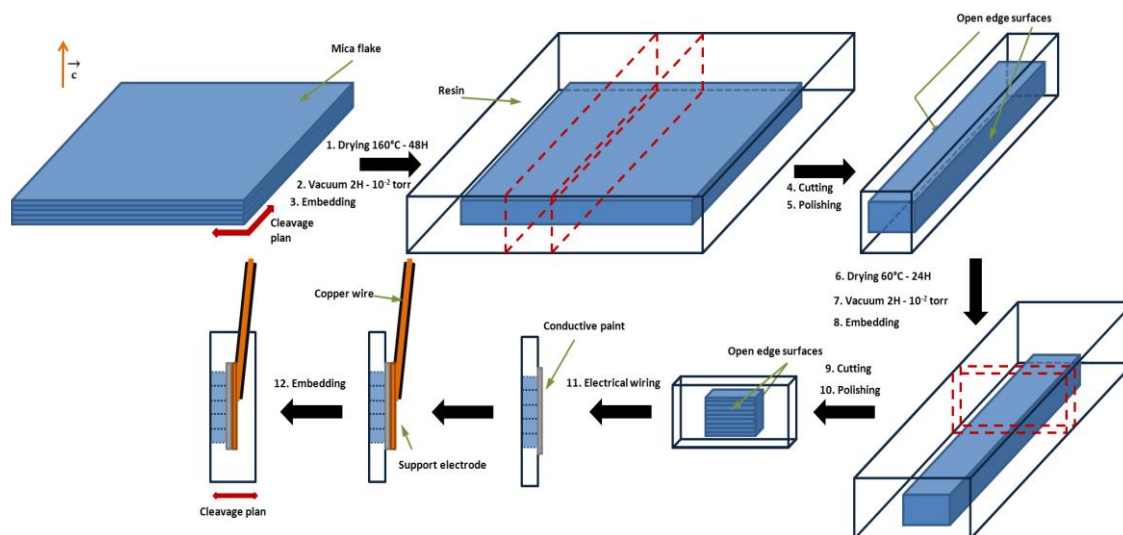


Figure 1: Steps in design of the massive electrodes made of micas

For the first trials, a choice of materials and techniques has been made in order to easily shape a large number of test electrodes from the different samples. In this design, the highest difficulty is in ensuring that electronic signals that might be measured in this type of junction would originate from iron present in the mica structure. Use of possibly electrochemically active wiring material, under wet conditions (copper and silver), is deliberate because it may indicate if diffusion of bathing electrolyte along defects was taking place. On some electrodes, defects have been made voluntarily to observe how direct contacts between the support electrode and the bathing electrolyte would affect the experiments.



Figure 2: Views of three different electrodes. From left to right: lepidolite, muscovite and biotite.

Electrochemical systems and methods

In following experiments, we present Open Circuit Potential (OCP) measurements and Cyclic Voltammetry (CV) realised with diverse electrochemical apparatuses. Three different models of potentiostats-galvanostats have been used: PGSTAT 12 (Metrohm, Herisau, Switzerland), PARSTAT 2273 and 273A (Princeton Applied Research, PAR, Tennessee, USA). Long term OCP measurements, along with pH and other parameters, are also provided by a digital multimeter and data acquisition system (Keithley instruments, model 2700, Cleveland, USA).

A classical three electrode system has been used for voltammetric measurements. Platinum plate (1cm²) was the counter electrode. Potentials have been measured against either silver-silver chloride electrode (Ag-AgCl/3M KCl) or Saturated Calomel Electrode (SCE/KCl_{sat}) as reference electrodes.

Bathing electrolyte

Most of the experiments discussed here have been conducted in unbuffered NaCl or KCl 0.1 M solutions, at 25°C. Anoxic conditions were maintained by first bubbling N₂ and then maintaining a gas layer in the head space of the reactor. Long term measurements showed that in these conditions, pH stays at a value around 8.9 and is stable for several weeks. Experiments realised in buffered solution, at pH 7.5, using 1 mM Piperazine-1,4-bis(2-ethanesulfonic acid) (PIPES) and 2 mM NaOH did not show any observable change. In some experiments, 5 mM ferricyanide (Fe(CN)₆³⁻) have also been used as a redox probe.

Preliminary results and discussion

High resistivities previously have been reported for this type of material, ranging from 10¹⁰ to 10¹⁵ Ω.cm at room temperature (Rüscher and Gall 1995). Given the current flows detection limit of the apparatus used for measuring (~nA), the mm-thick pieces used in first experiments should normally behave like insulating screens on silver (or maybe copper-silver) electrodes, e.g. no current could be measured across the sample with low iron content. Open circuit potential (OCP) measurement consists in measuring the electrode rest potential against a reference electrode, in absence of observable current. It provides a first indication on the type of material present on the support electrode; normally no potential should be measured in absence of an electrically conductive path. Unfortunately, first records showed that OCP can be measured immediately after the immersion of all the first electrodes prepared (Figure 3, left) even on muscovite and lepidolite, clearly indicating the presence of water in the different samples. However, signals obtained for lepidolite and muscovite are less stable and can only be conveniently recorded in absence of external perturbation around the electrode such as vibration or even air movement, whereas signals obtained for the different biotite samples are very stable. Changing parameters in the electrolyte such as pH (figure 3, right) removal of O₂, or change in Cl⁻ does not seem to affect the measured OCP of this type of electrode as it stay stable for days. Several week-long monitoring on ten biotite electrodes, dipped in unbuffered NaCl 0.1 M, showed that the OCP slowly decreases and stays stable, at values between 0.1 and 0.14 mV/NHE (data not shown), despite occasional pH oscillation between 4 and 9.

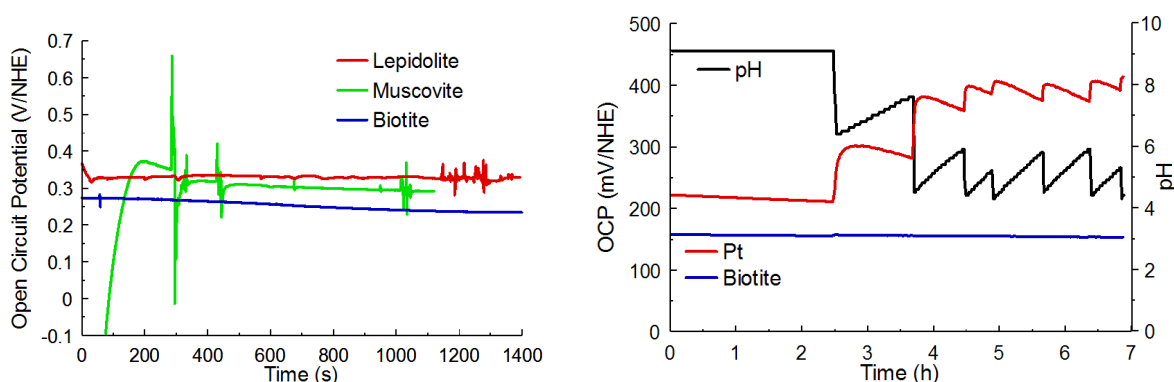
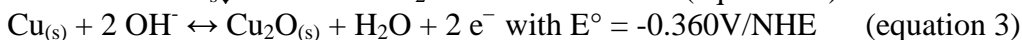
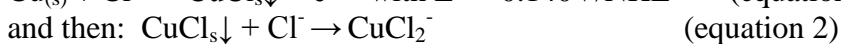
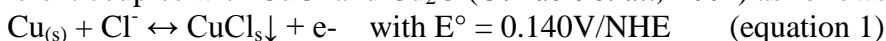


Figure 3: (left) OCP measurements recorded after immersion of various electrodes in NaCl 0.1M (pH 7.5). (right) Effects of HCl 0.1M repeated dropwise addition in the bathing electrolyte on a biotite electrode and on a platinum electrode.

From these observations, we can't preclude that water might participate in the electrical contact between the support electrode and the solution, but we can still hypothesize that it could be due to interlayer traces of water, offering a poorly electrically conductive path in lepidolite and muscovite, whereas another mechanism might participate in the biotite sample. In the pH region of the experiments, a copper electrode usually forms two different couples with CuCl and Cu₂O (Otmacic *et al.*, 2004) as follows:



Silver produced by oxidation in chloride solutions can produce AgCl (Hamdy *et al.*, 2010), as follows:



Over the time scale of the experiment, neither changes in [O₂], [Cl⁻] nor pH seem to induce observable OCP changes, showing that, as intended, the region sampled by this type of electrode might be limited to the vicinity of the interface between silver and mica, acting as a copper-silver electrode screened by a solid barrier where diffusion of ions from the solution is very limited.

Cyclic voltammetry (CV) has been performed on different types of electrodes in order to observe the effects of the suspected presence of water inside (or around) the crystals and to identify which electro active species might be present in the area of the silver-biotite junction. First information comes from the comparison between the 3 different samples (figure 4). Interestingly, while lepidolite electrodes give a flat signal, which is actually almost below the detection limit of the apparatus, muscovite electrodes exhibit somehow higher current exchanges and unclear voltammetric waves appear. The current range (~nA) of the voltammogram typically recorded on these two iron-poor samples is several orders of magnitude lower than what is obtained with the biotite electrodes (~μA).

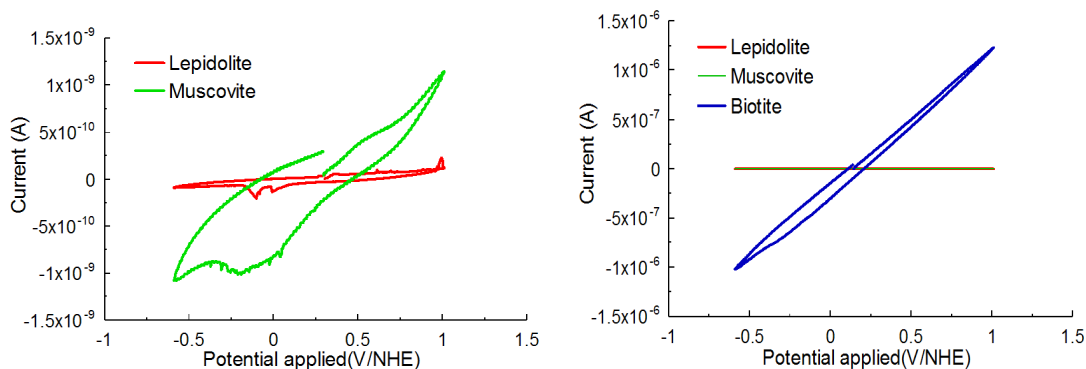


Figure 4: CV recorded at scan rate of 25 mV/s, at pH 7.5, in NaCl 0.1 M (left) muscovite and lepidolite electrode. (right) same overlaid with CV on a biotite electrode in the same conditions.

The voltammogram obtained with biotite electrodes suggests an ohmic-like behaviour, (a quasi-proportionality between I and V). If the much stronger signals obtained on biotite electrodes might be imparted to a higher water content in the sample (rather than to its much higher iron content), then CVs at slow scan rates should reveal typical voltammetric waves on each test electrodes. Figure 5 (left) shows a comparison between a biotite electrode exposing detectable defects (blue line) and a well-isolated biotite sample (red line). The presence of a well-shaped CV (with anodic and cathodic peaks) indicates interaction between silver from the support electrode and the bathing electrolyte (Cl^-), according to equation 4.

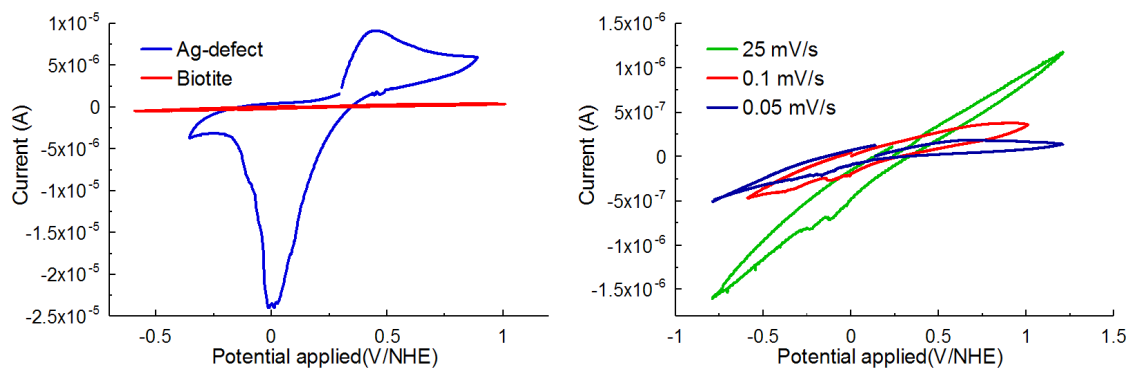


Figure 5: CV recorded in NaCl 0.1 M, pH 7.5. (left) a biotite sample and an electrode showing detectable defects at (0.1 mV/s) (right) CV recorded on the same biotite electrode as in (left), at various scan rates.

As shown on figure 5 right, lowering the scan rate slightly changes the shape of the voltammogram, revealing unclear voltammetric waves. Similarly to what was observed on muscovite (figure 4 left), these peaks could be due to interaction of silver with trace chloride present in the junction, leading to a very limited production of $\text{AgCl}_{(s)}$. Addition of 5 mM of ferricyanide to the bathing solution does not show any effect, e.g. no voltammetric waves that would identify the redox couple $\text{Fe(III)(CN)}_6^{3-}/\text{Fe(II)(CN)}_6^{4-}$ (with $E^\circ = 361 \text{ mV/NHE}$ at pH 7) can't be observed even after one week of

immersion (figure 6. left). Scanning over a larger potential domain, even larger than the domain of stability of water in this pH domain (roughly +0.7 V/NHE) shows that the ohmic-like behaviour is only partially conserved, with an increase in the capacitance (difference between anodic and cathodic current) and a slight change in the slope in the negative potential (< -2V/NHE). This could be due to a limited oxygen and hydrogen production from trace water present at the interface.

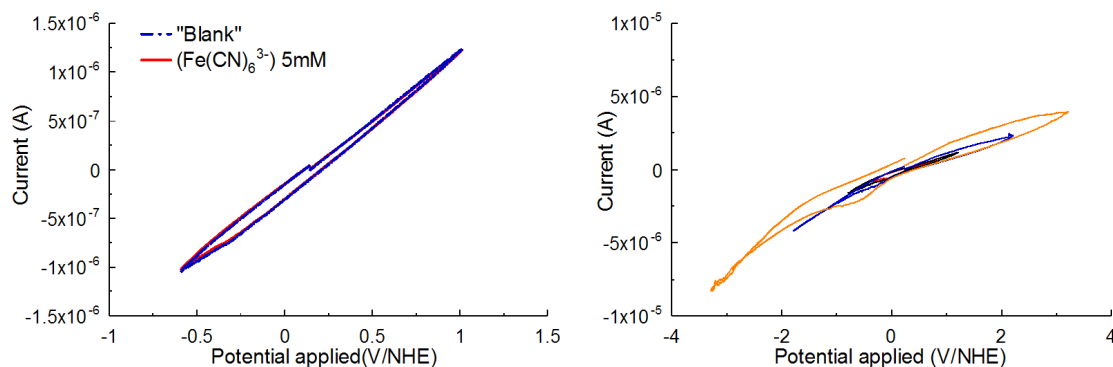


Figure 6: CV recorded on a biotite electrode at scan rate of 25mV/s, at pH 7.5, in NaCl 0.1M. (left) in absence (a) and in presence (b) of 5mM $(\text{Fe}(\text{CN})_6^{3-})$. (right) overlays of CV recorded on another biotite electrode, in the same condition as (a), with gradually increasing the potential domain.

Cyclic voltammetry measurements confirm the first observations made on open circuit potential measurements. The region sampled by the support electrode seems to be limited to the vicinity of the silver-mica junction. Despite a noticeable presence of water in the different minerals, its effects on the electrochemical response of this junction cannot be clearly identified. Moreover, the diffusion of chloride and ferricyanide ions from the solution is extremely limited. This suggests that the poor conduction pathways, indicated by OCP measurements on supposed insulating thick slices of low iron bearing samples (muscovite and lepidolite), might be assigned to interlayer traces of water, rather than channels along larger defects or around possibly not well embedded crystals. Assuming that the three different samples have been prepared the same way, biotite electrodes should also exhibit poor conduction pathways. But actually, observations of much higher currents with the latter sample brings additional support for our assumption that the higher and more stable response observed on OCP records with the biotite electrodes can be assigned to its much higher iron content.

Summary and Conclusions

Results of these experiments show that several aspects of the designs of such electrodes have to be improved for further experiments.

First, lowering of the water content in the mineral must be realised, using smaller crystals, longer drying and vacuuming time, and using more penetrating and impregnating resins. Platinum plates and evaporated platinum or carbon are envisioned

for the inert support electrode. Using thinner slices should reduce electrical resistivity of the whole bulk structure, allowing more convenient observations of the coupled electrons transfers that might occur at separated crystal surfaces. Hence, more suitable cutting techniques, such as wire sawing, should be planned to obtain thinner slices. More mica samples must also be selected, with higher and lower iron contents than the one used in the present experiments.

This first set of experiments in interfacing solid electrodes and conveniently shaped mica crystals offers hope that this could be a valuable technique for probing structural iron.

Acknowledgement

The research leading to these results has received funding from the European Union's European Atomic Energy Community's (Euratom) Seventh Framework Programme FP7/2007-2011 under grant agreement n° 212287 (RECOSY project).

References

- Arii, K. and Inuishi, Y. (1968) Electrical conduction in mica. Technical Reports of the Osaka University 18, 385-397.
- Crine, J.P.; Friedmann, M.R.; Wertheimer, M.R. and Yelon, A. (1977) The relationship between chemical composition and electrical conductivity of some North American micas. Canadian Journal of Physics 55, 270-275.
- Davidson, A.T. and Yoffe, A.D. (1968) Hopping electrical conduction and thermal breakdown in natural and synthetic mica. Physica Status Solidi 30, 741-754.
- Favre, F., Stucki J.W. and Boivin. P. (2006) Redox properties of structural Fe in ferruginous smectite. A discussion of the standard potential and its environmental implications. Clays and Clay Minerals 54, 466-472.
- Fitch, A., Amonette, J.E., Baker, S., Giannelis, E.P., Macha, S., Manias, E., Panagiotopoulos, A.Z., Villemure, G., Yamagishi, A. and Zax, D.B. (2002) CMS workshop lectures, volume 10: Electrochemical properties of clays.
- Gorski, C.A., Sander, M., Aeschbacher, M. and Hofstetter, T.B. (2011) Assessing the redox properties of iron-bearing clay minerals using homogeneous electrocatalysis. Applied Geochemistry 26, S191-S193.
- Hamdy H.H., Magdy A.M.I., Sayed S.A., Mohammed A.A. (2010) Comparative studies of the electrochemical behavior of silver electrode in chloride, bromide and iodide aqueous solutions. I. Journal of Electrochem. Science 5, 278-294.
- Hofstetter, T.B.; Neumann, A. and Schwarzenbach, R.P. (2006) Reduction of Nitroaromatic Compounds by Fe(II) Species associated with iron-rich smectites. Environmental Science and Technology 40, 235-242.

- Meunier, M., Currie, J.F., Wertheimer, M.R. and Yelon A. (1983) Electrical conduction in biotite micas. *Journal of Applied Physics* 54, 898-905.
- Mousty, C. (2004) Sensors and biosensors based on clay modified electrodes - new trends. *Applied Clay Science* 27, 159-177.
- Neumann, A.; Hofstetter, T.B.; Luřssi, M.; Cirpka, O.A.; Petit, S. and Schwarzenbach, R.P. (2008) Assessing the Redox Reactivity of Structural Iron in Smectites Using Nitroaromatic Compounds As Kinetic Probes. *Environmental Science & Technology* 42, 8381-8387.
- Otmacic H., Telegdi J., Papp K., and Stupnicek-Licak E. (2004). Protective properties of an inhibitor layer formed on copper in neutral chloride solution. *Journal of Applied Electrochemistry* 34, 545-550.
- Rancourt, D.G.; Tume, P. and Lalonde, A.E. (1993) Kinetics of the $(\text{Fe}^{2+} + \text{OH}^-)_{\text{mica}} \rightarrow (\text{Fe}^{3+} + \text{O}^{2-})_{\text{mica}} + \text{H}$ oxidation reaction in bulk single-crystal biotite studied by Mössbauer spectroscopy. *Physics and Chemistry of Minerals* 20, 276-284.
- Rosso, K.M. and Ilton, E.S. (2003) Charge transport in micas: The kinetics of $\text{Fe}^{\text{II/III}}$ electron transfer in octahedral sheet. *Journal of Chemical Physics* 119, 9207-9218.
- Rosso, K.M. and Ilton, E.S. (2005) Effects of compositional defects on small polaron hopping in micas. *The Journal of Chemical Physics* 122, 244709.1-244709.9.
- Rosso, K.M.; Yanina, S.V.; Gorski, C.A.; Larese-Casanova, P. and Scherer, M.M. (2010) Connecting observations of hematite ($\alpha\text{-Fe}_2\text{O}_3$) growth catalyzed by Fe(II). *Environmental Science and Technology* 44, 61-67.
- Rüscher, C.H. and Gall, S. (1995) On the polaron-mechanism in iron-bearing trioctahedral phyllosilicates: an investigation of the electrical and optical properties. *Phys. Chem. Minerals* 22, 468-478.
- Stucki, J.W. (2011) A review of the effects of iron redox cycles on smectite properties. *Comptes Rendus Geoscience* 343, 199-209.
- Tolland, H.G. and Strens, R.G.J. (1972) Electrical conduction in physical and chemical mixtures. Application to planetary mantles. *Physics of the Earth and Planetary Interiors* 5, 360-386.
- White, A.F. and Yee, A. (1985) Aqueous oxidation-reduction kinetics associated with coupled electron-cation transfer from iron-containing silicates at 25°C. *Geochimica et Cosmochimica Acta* 49, 1263-1275.
- Yanina, S.V. and Rosso, K.M. (2008) Linked reactivity at mineral-water interface through bulk crystal conduction. *Science* 320, 218-222.

MECHANISTIC STUDY OF PYRITE REDUCTION BY HYDROGEN IN NaCl 0.1 M AT 90 °C USING ELECTROCHEMICAL TECHNIQUES

Stephanie Betelu¹, Catherine Lerouge¹, Gilles Berger² and Ioannis Ignatiadis^{1*}

¹ BRGM, BP 36009, 45069 Orléans CEDEX 2 (FR)

² IRAP, Observatoire Midi-Pyrénées 14 av. E. Belin, 31400 Toulouse (FR)

* Corresponding author: i.ignatiadis@brgm.fr

Abstract

Nuclear waste repositories are being installed in deep excavated rock formations in some places in Europe to isolate and store radioactive waste. In France, the Callovo-Oxfordian formation (COx) is a potential candidate for a nuclear waste repository. The COx formation contains pyrite (FeS₂), which would, *a priori*, react with Hydrogen gas (H₂).

After the closure of the underground nuclear waste repository, aqueous corrosion of the steel canister and, to a lesser extent, radiolysis of water would produce significant amounts of H₂. This H₂ can interact with materials from the repository and with the surrounding clay host formation. This work aims at understanding these interactions. Given the mineralogical complexity of clay formation, this work focused on the study of the interaction of FeS₂ alone with H₂, using electrochemical techniques and the analysis of solutions and interfaces. After pyrite electrodes had been assembled, various electrochemical disturbances were applied to this material (and to platinum for comparison) while it was submerged in a partially reconstituted solution of COx pore water, enclosed in a **High Pressure Thermo-Reactor (HPTR)** at 90 °C, in the absence and in the presence of pyrite grains (particle size between 40 and 63 µm) and H₂ (0 partial pressure or 1 bar). In addition to the electrochemical behaviour of the platinum and the pyrite, the pH, temperature and pressure of the liquid medium were monitored.

The principal result of this work is the elucidation of the mechanism governing the reduction of the sulphur S⁰ of the FeS₂. Indeed, the S⁰ is reduced to sulphide (HS⁻/S²⁻), which is freed in solution, whereas the pyrite turns superficially into pyrrhotite (FeS_{1+x} with 0<x<0.125), forming a layer that slows down the reduction process. All of the measurements agree, and the qualitative exploitation of these data (open circuit electrode potential, Tafel curves, and electrochemical impedance measurements on platinum and pyrite electrodes) and surface analyses, made it possible to provide evidence of the reduction of pyrite into pyrrhotite and to create a large electrochemical database. The future exploitation of this electrochemical database will make it possible

to determine the kinetics of the reaction of reduction of pyrite by H₂ in a HPTR and, by extrapolation, to storage conditions.

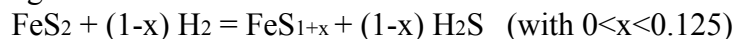
Key words: Callovo-Oxfordian, Redox, Electrochemistry, Kinetics, Pyrite, Hydrogen gas, Pyrrhotite, Radioactive waste, Storage.

Introduction

After the closure of the underground nuclear waste repository, aqueous corrosion of the steel canister and, to a lesser extent, radiolysis of water would produce significant amounts of H₂. Its chemical interaction with the surrounding material must be studied in order to assess possible transformations of thermodynamic conditions, especially redox potential. Redox reactions with iron and sulphur bearing minerals present in clay formations, e.g. Callovian-Oxfordian formation (COx), are expected: reactions with carbonate, sulphur-bearing minerals (celestite, pyrite) and aqueous sulphate are possible due to the accumulation of H₂. These reactions consume H⁺ ions, which will result in an increase in pH. The H₂ produced in the waste storage cells dissolves until it saturates the interstitial water in the near field and the excess gas will diffuse through the damaged zone until it reaches the galleries and the un-weathered argillite after the gas pressure has increased to a point that enables it to penetrate the rock. Hydrogen gas is weakly soluble (Crozier et Yamamoto, 1974), but under a H₂ pressure of 100 bars (maximum pressure expected in the repository) and at 25°C, the aqueous H₂ concentration will be around 0.08 mol.L⁻¹. The increase in the quantity of H₂ causes a decrease in the redox potential of the pore water, the redox potential at 25 °C of a solution under 100 bars of H₂ is -0.473 V/NHE at neutral pH, in agreement with the Nernst equation: $E_{eq}(H^+/H_2)=0 - 0.0591 \cdot pH - 0.0295 \cdot 2 = -0.473V$. The redox reactions with the formation's oxidized species such as sulphate are generally insignificant, although they are thermodynamically possible in the geological storage context, because the strength of the H-H bond (436 kJ/mol) imposes to overcome a high energy barrier to trigger an electronic transfer (Truche *et al.*, 2010). There are strong thermodynamic constraints associated with the reactivity of H₂ as a reducing agent.

The COx formation contains iron ores such as pyrite (FeS₂), which, although present in only small quantities, is a potential oxidant for H₂ due to the degree of oxidation of one of its sulphur atoms. Indeed, the S(0) of the pyrite might reduce to S(-II). This would transform the pyrite into pyrrhotite and produce H₂S, HS⁻, S²⁻, depending on the pH.

Experiments carrying out in disequilibrium in a Hastelloy reactor under slightly alkaline conditions (pH = 7.5-8.9) at mildly hyperthermal temperatures (90-180°C) and H₂ partial pressures P(H₂) of 8-18 bars have shown the reactivity of pyrite with H₂ (Truche *et al.*, 2010). These studies, which included both textural studies and measurements of species in solution, showed the partial reduction of FeS₂ into pyrrhotite (FeS_{1-x}), according to:



These results made it possible to improve our understanding of the mechanisms involved and evaluate the reaction kinetics involving FeS₂-H₂, but the experiments were done under disequilibrium conditions (90-180°C), which makes the extrapolation of the rate laws to temperatures of interest for storage (25 °C ≤ T ≤ 90 °C) difficult.

The objective of the work presented here was, therefore, to carry out new experiments that would enable us to understand the phenomenology and kinetics of the alteration of FeS₂ by H₂ in the 25 to 90 °C temperature range.

Given the mineralogical complexity of the CO_x formation, this study focused solely on the interaction of pyrite. After the pyrite electrodes had been assembled, various electrochemical disturbances were applied to this material while it was submerged in a partially reconstituted solution of CO_x pore water in a High Pressure Thermo-Reactor (HPTR) at 90 °C, at pH 8.7 and 9.7, in the absence and in the presence of pyrite grains (particle size between 40 and 63 µm) and hydrogen gas (H₂ partial pressure: 0 or 1 bar). The initial objective was to understand the basic mechanisms that occur on the pyrite-electrode. In addition to the customary electrochemical triplet, the pH, temperature and pressure of the liquid medium were monitored continuously. For pyrite, this involved studying, with regard to H₂, both its electrochemical behaviour and the kinetics of its reactivity. Various measurement apparatuses and electrochemical techniques were used to understand the various phenomena occurring on the pyrite under different conditions.

Materials and methods

Characterization of pyrite and electrode preparation

Pyrite characterization

Pure pyrite from Peru was used to build pyrite electrodes and prepare pyrite grains. The composition of this 96 %-pure Peruvian pyrite was determined by Atomic Absorption Spectroscopy (AAS) and Inductively Coupled Plasma (ICP) and is given in **Table 1**.

Table 1: Chemical composition of pyrite

Element	Co (%)	Cu (g.t ⁻¹)	Ni (g.t ⁻¹)	Fe (%)	S (tot %)	SO ₄ (%)
Concentration	< 0.01	2715	16	45.10	51.60	1.90
Element	S ₂ ²⁻ (%)	SiO ₂ (%)	Al ₂ O ₃ (%)	CaO (%)	MgO(%)	K ₂ O (%)
Concentration	50.90	0.95	< 0.01	<1.0	<1.0	<0.50
Element	MnO(%)	TiO ₂ (%)	V (g.t ⁻¹)	Cr (g.t ⁻¹)	Zn (g.t ⁻¹)	As(g.t ⁻¹)
Concentration	<0.01	<0.01	g.t ⁻¹	g.t ⁻¹	20	438
Element	Sr (g.t ⁻¹)	Ag (g.t ⁻¹)	Sn (g.t ⁻¹)	W (g.t ⁻¹)	Pb (g.t ⁻¹)	Bi (g.t ⁻¹)
Concentration	22	12.3	240	1101	< 10	515

Pyrite electrodes

The pyrite electrochemical sensor made out of massive pyrite, built using pure Peruvian pyrite (Fig. 1), is cylindrical, screwed onto a metal piece that ensures the contact, and is insulated with Teflon. It's active surface measures 22 mm². Prior to running any experiments, the electrode was polished to remove the oxidized layer of pyrite, washed in an ultrasonic cleaner with a HCl 0.1 M solution in order to remove all trace of silicate left by the polishing paper, rinsed with ethanol to minimize its oxidation by water, and then dried in an oven at 80 °C for 10 min.

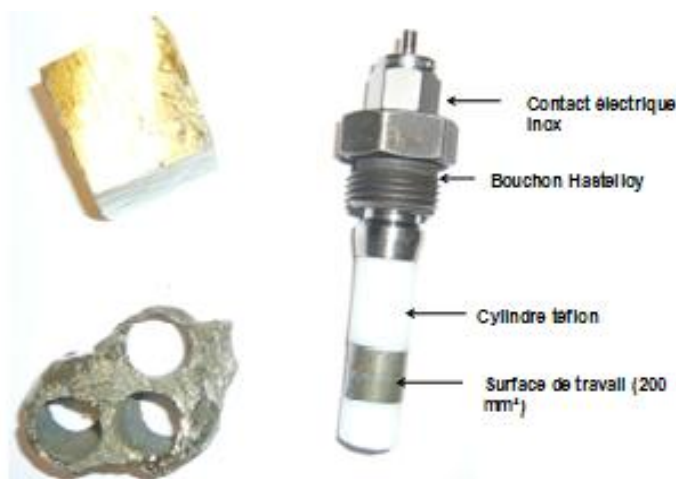


Figure 1: FeS_2 electrode made with "pure" Peruvian pyrite

Pyrite grains

For our experiments, we prepared grains with a specific particle size using a precise preparation protocol. After crushing, the pyrite grains were washed, and then separated, using various sieves, to separate the particle size fractions. The fraction that interests us is between 40 and 63 μm (corresponding to grinding limit conditions: grains stability during grinding and during limited contact with atmospheric conditions) as characterized with a CILAS 850HR particle size analyzer.

The experimental setup

Experimental setup

In order to confirm the mechanisms and the study of the physical-chemical phenomena at the interfaces, the experiment was carried out under a total pressure of 10 bars and at a temperature of 90 °C in a High Pressure Thermo-Reactor (HPTR).

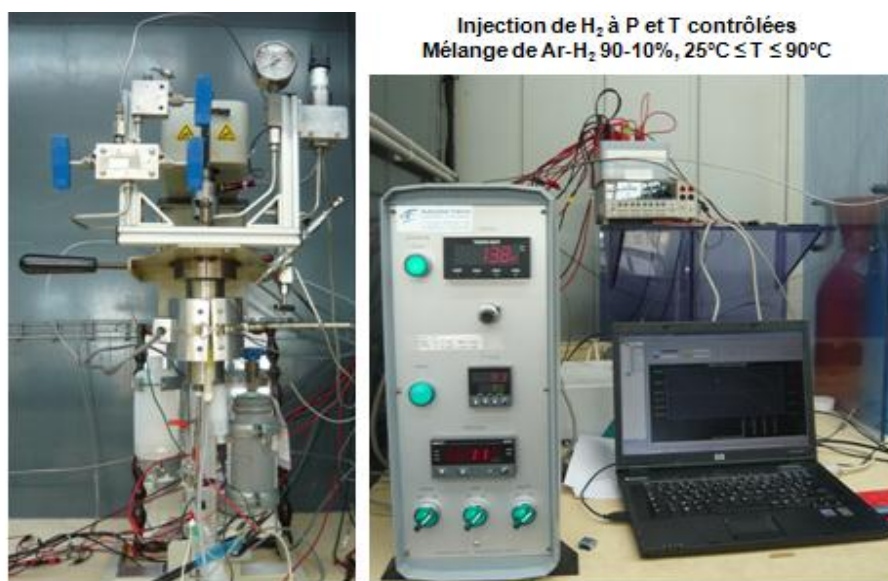


Figure 2: The Hastelloy High Pressure Thermo-Reactor, control unit and acquisition unit

The HPTR is a 300-mL hydrothermal reactor made by Autoclave Engineers®. It enables working with pressures up to 350 bars and temperatures of 400°C. It is built entirely of Hastelloy C276, whose exact composition (in % on a weight basis) is: Ni: 55 %; Mo: 15-17 %; Cr: 14.5-16.5 %; Fe: 4-7 %; W: 3-4.5 %; Co: 2.5 %; Si: 0.08 %; Mn: 1 %; C: 0.01 %. This Ni-Mo-Cr alloy, to which tungsten is added, offers an excellent resistance to corrosion in a wide variety of corrosive environments and is particularly resistant to pitting. This reactor has a built-in magnetic stirrer, several sampling ports and liquid and gas injection ports. The HPTR reactor is connected to an auxiliary line that enables the compression of the commercial gas mixture of Ar (90 %) and H₂ (10 %) (Alphagaz), used for the experiments. The reactor is equipped with three internal threads, making it possible to incorporate the pyrite, platinum and pH electrodes needed for electrochemical experiments. The pH electrode is a combination gel electrode (with pressure and temperature compensation) whose internal reference is Ag-AgCl/3M KCl. The latter was also used as a reference for the platinum and pyrite electrodes. The HPTR reactor was used as a counter-electrode for the electrochemical impedance measurements. The experiments were done in the presence and in the absence of pyrite grains with a particle size of between 40 and 63 µm, so that we could study the influence of the presence of pyrite grains in the reactor depending on the set potentials on the electrodes. The electrodes are hooked up to a data acquisition system, which is connected to a computer to record the data. (Fig. 2)

Experimental conditions

Four experiments were carried out in the HPTR at a constant temperature of 90°C (mimicking the temperature near the region of the container in the first years of storage) under intermittent stirring (about 200 rpm) and under a H₂ partial pressure of 1 bar (1 bar of PH₂ corresponds to $5.6 \pm 0.3 \cdot 10^{-4}$ mol.L⁻¹ of dissolved hydrogen), in NaCl 0.1 mol.L⁻¹, in NaHCO₃/Na₂CO₃ buffer solution (ionic strength in the range 0.05 to 0.1 mol.L⁻¹), under anoxic conditions (solution was degassed ten times with pure Argon, by successive cyclic pressurizations from 1 to 10 bars. It is worth noted that the successive cyclic pressurizations do not modify the pH of the solution). Two different solutions are prepared, in the absence and presence of pyrite grains, having pH values as follows:

- pH = 8.9 at 90 °C and pH = 9.7 at 90 °C; without pyrite grains.
- pH = 8.9 at 90 °C and pH = 9.7 at 90 °C; with 2 g of pyrite grains with a particle size between 40 and 63µm.
-

These conditions were chosen to imitate radioactive waste storage conditions ($25 < T < 90$ °C, $5.7 < \text{pH} < 11.7$), where the pH is controlled by CaCO₃ naturally present in the COx argillite.

Electrochemical techniques

Electrochemistry studies the relationship between chemical transformations and the passage of an electrical current. An electrochemical process is the set of phenomena associated with the production of a transfer of electrical charge between an electrode (solid) and an electrolyte (ionic solution). We used several techniques to characterize the electrochemical behaviour of platinum and pyrite. During the experiments carried

out under a total pressure of 10 bars and at a temperature of 90°C in the HPTR, the open circuit potential, E_{cor} , was monitored on the electrodes with respect to the Ag-AgCl/3M KCl reference electrode (results plotted against NHE). DC electrochemical techniques were carried out in Pyrite and Platinum electrodes using a potentiostat-galvanostat (Princeton Applied Research, PAR, Tennessee, USA) PAR model-2273, interfaced to a PC system with the PowerSuite v.2.58 software packages also from PAR. A platinum wire was used as auxiliary electrode. Working solution volume was 200 mL. The objective here was to monitor the evolution of the redox potential in solution with E_{Pt} and show the reactivity of the pyrite with E_{Py} . We also measured electrochemical impedance on pyrite FeS_2 and on platinum at E_{cor} and at imposed potentials: -0.7; -0.8; -0.9; -1.0 and -1.1 V/ E_{ref} (Ag-AgCl, 3M KCl). The objective here was to analyse the behaviour of the electrochemical interface at a given polarization point, calculate the variation in faradic current, i , (variation of the potential of the electrode, at pulsation ω) and study the mechanisms and kinetics of electrode reactions. Electrochemical Impedance Spectroscopy (EIS) measurements were realized over frequency range of 10 μHz to 1 MHz using perturbation signals with amplitude of 5 mV. The computer-aided evaluation of the impedance spectra was performed with the PAR-2273 impedance measurement system using an integrated data-acquisition and analysis system and the ZSimWin v.3.21 software (Echem Software, Bruno Yeum, Ann Arbor, Michigan, USA). The impedance was measured after the monitored potentials had stabilized, in the absence and presence of H_2 (partial pressure of 1 bar in the HPTR), in order to compare with the results of the interaction of the H_2 .

Solution and surface analyses

Potentiometric measurements were recorded continuously with a digital multimeter and data acquisition system (Keithley instruments, model 2700, Cleveland, USA). The pH value of all reactive solutions was monitored with a commercial glass electrode that was initially calibrated using commercial standard buffer solutions. The species of interest in solution (Fe^{2+} , S^{2-} , SO_4^{2-} , silicate,...) are determined by colorimetry using Merck Spectroquant kits with a Merck-Nova 60 spectrophotometer. After the experiments were completed, the pyrite electrodes were placed in flasks under N_2 in a glove box under N_2 without O_2 . The textural analyses were done on some of the pyrite electrodes with an environmental scanning electron microscope (SEM) and by electronic microanalysis with an EDS detector.

Results and discussion

Experiments at pH 8.9 and 9.7 at 90 °C without pyrite grains

Monitoring the potential of platinum E_{Pt} and pyrite E_{Py}

In the absence of H_2 , at pH 8.9 and 9.7, the potentials stabilize at the beginning at high values (Figs. 3 and 4). Although there are no strong redox couples in solution to control the redox potential, all of the electrodes reach an almost stable self-potential. E_{Pt} is the highest, followed by E_{Py} . At this stage for the pyrite electrode, the potential might be controlled by the redox couple S(-II)/S(0) in the pyrite. However, the thermodynamic redox potential determined by calculations using the PHREEQC computer code would

be -461 mV/NHE at pH 8.9 and -537 mV/NHE at pH 9.7. These values are lower than the value measured on E_{Pt} and E_{Py} because they are calculated for the S(-II)/S(VI) couple in solution. The calculation for a solid/solution couple is not included in the geochemical code. The pyrite electrode alone, by dissolution-precipitation equilibria, is therefore not able to control the redox potential in the solution.

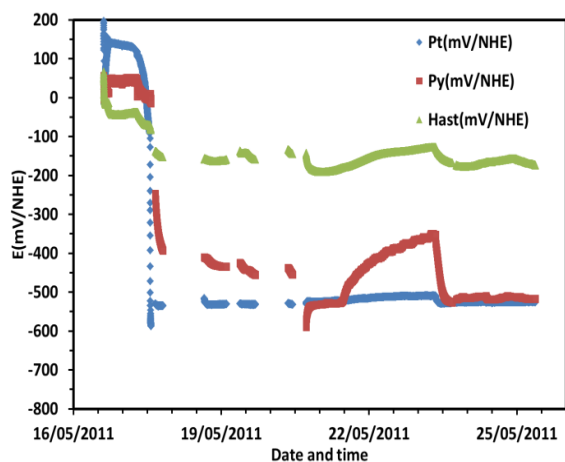


Figure 3: Monitoring electrode potential in the HPTR: pH=8.9 at 90 °C without pyrite grains, without and then with H_2 at $P(H_2)=1\text{bar}$ (experiment begun 16 May, 2011)

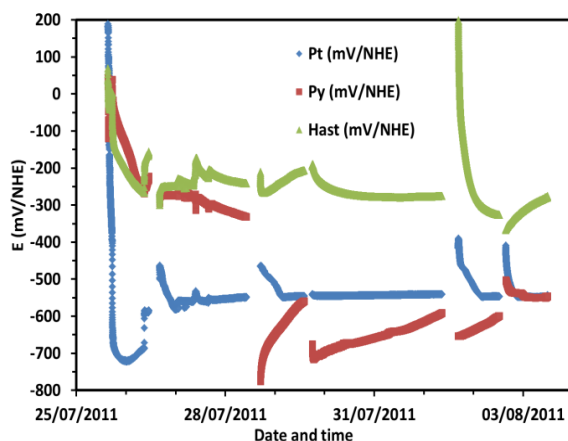


Figure 4: Monitoring electrode potential in the HPTR: pH=9.7 at 90 °C without pyrite grains, without and then with H_2 at $P(H_2)=1\text{bar}$ (experiment begun 25 July, 2011)

Following the injection of H_2 , at pH 8.9 and 9.7, with a partial pressure of 1 bar (for a total pressure of 10 bars), we observe that the electrode potentials, E_{Pt} and E_{Py} , decrease and stabilize, respectively, for pH 8.9 at -526 ± 1 mV/NHE and -525 ± 23 mV/NHE, and for pH 9.7 at -543 ± 1 mV/NHE and -654 ± 31 mV/NHE. However, the thermodynamic redox potential calculated under the same conditions using the PHREEQC is -543 mV/NHE for pH 8.9 and -697 mV/NHE for pH 9.7 (controlled by the H^+/H_2 couple). The values for E_{Pt} are in agreement with redox potential, which means that it is the H^+/H_2 couple that controls the E_{Pt} . Since E_{Py} is equal to or lower than E_{Pt} , seems to be controlled in some instances by the H^+/H_2 couple and in others by the S(-II)/S(V) couple.

Electrochemical impedance (EIS) measurements on platinum and pyrite electrodes

To investigate the elementary phenomena encountered at the electrolyte/electrode interfaces many EIS measurements were performed on the two working electrodes, under potentiostatic mode at the open circuit electrode potential (E_c) or at a cathodic potential imposed on the electrode in a quiescent electrolyte and at different cumulated exposure times. Some of the impedance diagrams are presented in fig. 5.

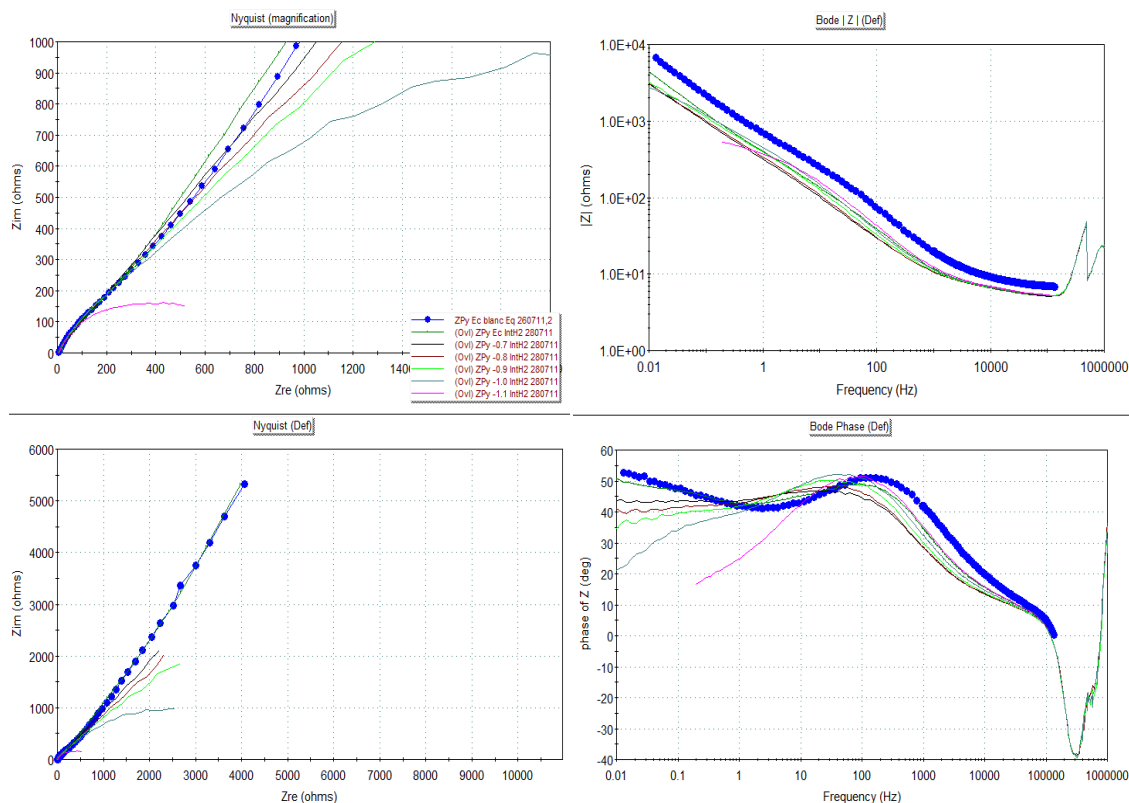


Figure 5: EIS diagrams in Nyquist mode (normal and with magnification in high frequencies) and in Bode mode (modulus and phase of Z), obtained with Pyrite immersed in $\text{NaCl } 0.1 \text{ mol L}^{-1}$, pH 9.7 at 90°C , in the absence of pyrite grains, and initially in the absence of H_2 , then in the presence of H_2 . The blue curve is in the absence of hydrogen gas at E_c , and all of the others are in the presence of hydrogen gas at E_c ; -0.7; -0.8; -0.9; -1.0 and -1.1V.

The key to interpreting impedance data is selecting an appropriate Equivalent Electrical Circuit (EEC). The simulation of the data acquired throughout these experiments will enable us to determine an equivalent electrical circuit. The EEC will be deduced from the shape of measured impedances and how we conceive the electrolyte/electrode interface system. The various parameters (component values) of these circuits will enable us to compare the results obtained in all of the environments. The EEC shown in figure 6 is taken into consideration in the models presented in table 2. The components of the EEC (presented in fig. 6 and Table 2) are explained below:

- R_e represents dc-resistance (in admittance $1/R$) of the electrolyte;
- R_t represents the charge transfer dc-resistance of the faradic reaction that takes places at the electrode surface;
- C represents capacitor (in admittance $i\omega C$)
- Q is a Constant Phase Element (CPE) or equivalent capacitance. Q is the impedance of the electrical double layer at the pyrite/solution interface and corresponds to a semi-infinite diffusion, or an imperfect (leaking) capacitor. Q (in admittance is $Y_o(i\omega)^n$) is characterized by two parameters, Y_o , which is the parameter of Warburg (W) element, and n . When $n=1$, Q is only a C (capacitor).

- R_c is a dc-resistance and C a capacitance both of them are connected to the electrode surface state and
- G , represents the impedance of diffusion (Gericher type), which is approaching the Warburg impedance W at high frequencies and a dc-resistance at low frequencies. W is a specific case of G , when $n=0.5$.

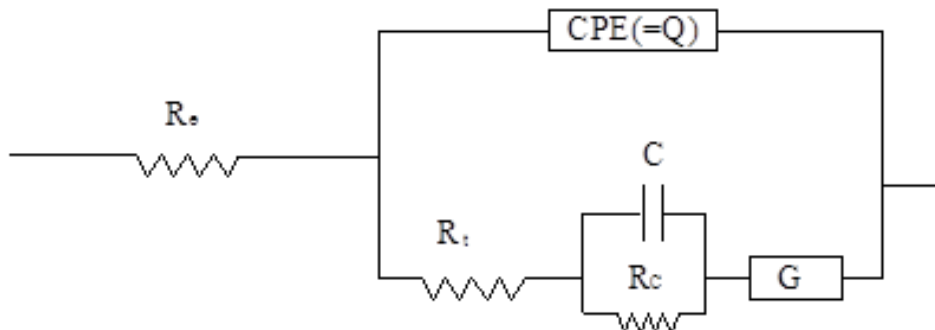


Figure 6: Electrical equivalent circuit (EEC) obtained from EIS diagrams conducted with pyrite in NaCl (0.1 mol L^{-1}) in pH 8.9 and 9.7 at 90°C in the absence and in the presence of pyrite grains and in the presence of H_2 .

For all of the impedance diagrams, the inductive portion was disregarded since, to date, it has not been elucidated and modelled.

In the presence of H_2 , at pH 8.9 and 9.7, the shapes of the impedance curves on platinum vary little with time, with or without stirring. Only R_t is of interest since it is 15 times lower on platinum than on pyrite. The adsorption of H_2 in the atomic form ($\text{H}-\text{H}$) within the Pt metal is well known and determines the behaviour of this electrode where there is no reduction, as opposed to what is observed on pyrite, nor diffusion of S^{2-} from the electrode to the solution, nor deposition of FeS on the electrode.

In the presence of H_2 , at pH 8.9 and 9.7, the shapes of the impedance curves on pyrite are identical to the selected EEC (Fig. 7 and Table 2). The impedance curves for the two pH values have the same shape. Therefore, it has not yet been determined that pH has any effect. R_t is much lower on platinum than on pyrite. The impedance curves for imposed cathodic potentials (that normally accelerate the reduction processes at the pyrite electrode), compared to those done at E_{corr} , have shapes that progressively slant towards the real z -axis: a) R_t first decreases, then increases with time; b) the diffusion processes (G parameters) accelerate from the electrode to the solution; c) the diffusion processes are hindered (R_c and C parameters) by increasingly thick FeS scale on the pyrite surface. R_t is much lower on platinum than on pyrite. R_c decreases markedly compared to pyrite without H_2 , but increases as the layer of scale grows thicker.

Table 2: Values of parameters of each component of the exposed EEC (fig. 6) $R(Q(R(CR)G))$, corresponding to electrode-solution interface for Pt and Py under different conditions (pH 9.7 at 90°C; NaCl 0.1 M; without grains of pyrite, in the absence of H₂; in the presence of 1 atm of H₂; impedance measurement at Ec, Ec-0.7V and Ec-1.1V) and immersion times. The test of Chi squared (χ^2), which was carried out for each simulation, makes it possible to check that the results given by the model are matched with the measured values (reduced values).

		Re (ohm)	Q-Yo (CPE, Yo)	Q-n (freq. power)	Rt (ohm)	C (F)	Rc (ohm)	G-Yo	G-K	χ^2
pH 9.7 90°C without Pyrite	Pt at Ec(-598mV/NHE) without H ₂ ; July 25, 2011	4.92	2.31E-03	0.67	1.30	8.22E-04	11710.00	1.33E-02	257.40	1.10E-04
	Py at Ec(-261mV/NHE) without H ₂ ; July 25, 2011	6.64	1.98E-04	0.66	581.20	1.80E-03	28680.00	5.86E-04	0.19	6.13E-04
	Pt at Ec(-550mV/NHE) with H ₂ ; July 28, 2011	4.89	3.55E-03	0.65	2.13	9.22E-04	12500.00	1.62E-02	188.10	1.70E-04
	Pt at Ec-0.7V with H ₂ ; July 28, 2011	4.84	2.81E-03	0.63	1.06	6.25E-04	1.51E+11	1.18E-02	199.80	1.90E-04
	Pt at Ec-1.0V with H ₂ ; July 28, 2011	4.91	1.10E-03	0.75	2.34	2.85E-04	183.70	5.49E-03	0.89	1.23E-03
	Py at Ec (-550mV/NHE) with H ₂ ; July 28, 2011	5.06	4.65E-04	0.63	354.80	1.16E-10	32.79	6.37E-04	1.11E-12	1.09E-03
	Py at Ec-0.7V with H ₂ ; July 28, 2011	4.81	9.18E-04	0.56	19.05	1.03E-05	914.50	5.96E-04	0.02	6.55E-04
	Py at Ec-1.1V with H ₂ ; July 28, 2011	5.08	3.49E-04	0.63	21.30	6.20E-06	450.50	4.87E-03	0.76	1.81E-04

Analyses of the black coating on some electrodes after experiments in the presence of H₂

Only the electrode used in the experiment at pH 8.9 and T = 90 °C in a NaHCO₃/Na₂CO₃ buffer solution without NaCl is shown here. The surface of the electrode in contact with the solution is highly altered. This is characterized by a general modification of the texture of the surface, micro-incrustations, micro-cracks, micro-deposits revealed by secondary electron imaging (SE) (Fig. 7 a, c, e, f) and by chemical modifications revealed by backscattered electron imaging (BSE) (Fig. 7 b, d). EDS analyses done on the base the electrode, which is not in contact with the solution, give the thickness of the surface of the electrode that reacted, and the transformation of the pyrite from a Fe/S ratio of 0.5 to a Fe-S phase with a Fe/S ratio of almost 1 (Fig. 8). Detailed observations of the surface of the electrode in contact with the solution show a relatively homogeneous chemical composition, whose EDS spectra are similar to spectra 1 and 2 done on the base of the electrode (Fig. 9). This suggests that the entire surface of the electrode in contact with the solution and H₂ was modified. The chemical differences between the light and dark areas do not seem to be related to the Fe/S ratio of the sulphur phase, but rather to the presence, more or less abundant, of silica scale (Fig. 9).

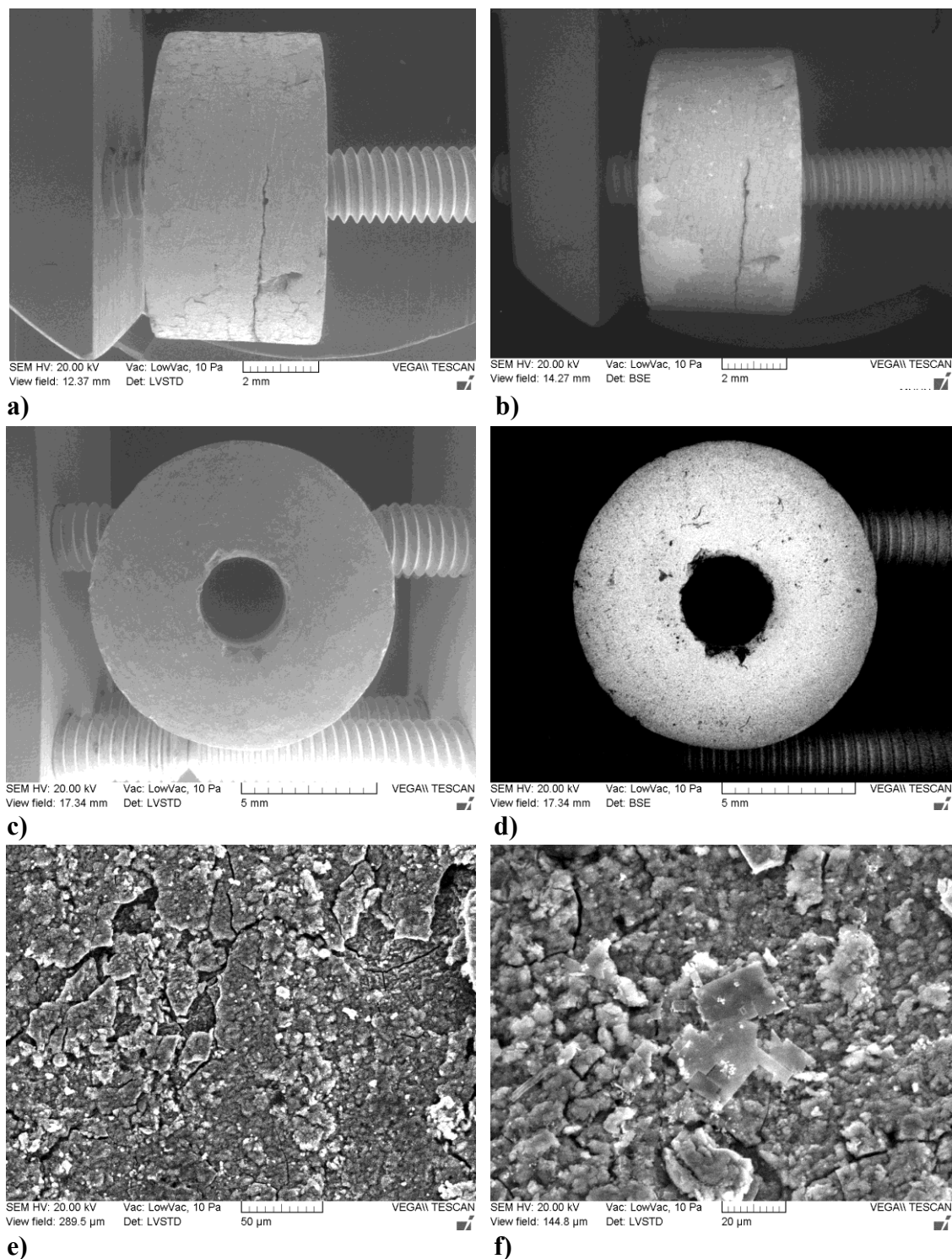


Figure 7: SEM images of the electrode after experimentation at pH 8.9 and $T = 90\text{ }^{\circ}\text{C}$ in the presence of an NaCl-free solution: a) state of the surface in contact with the solution (SE), b) chemical zonation of the same surface (BSE), c) the base of the electrode (SE), d) the same view with BSE showing the chemical modifications around the electrode and indicating the depth of penetration of the chemical modifications, e) surface incrustation (SE), f) modification of the texture and presence of scale on the surface of the electrode.

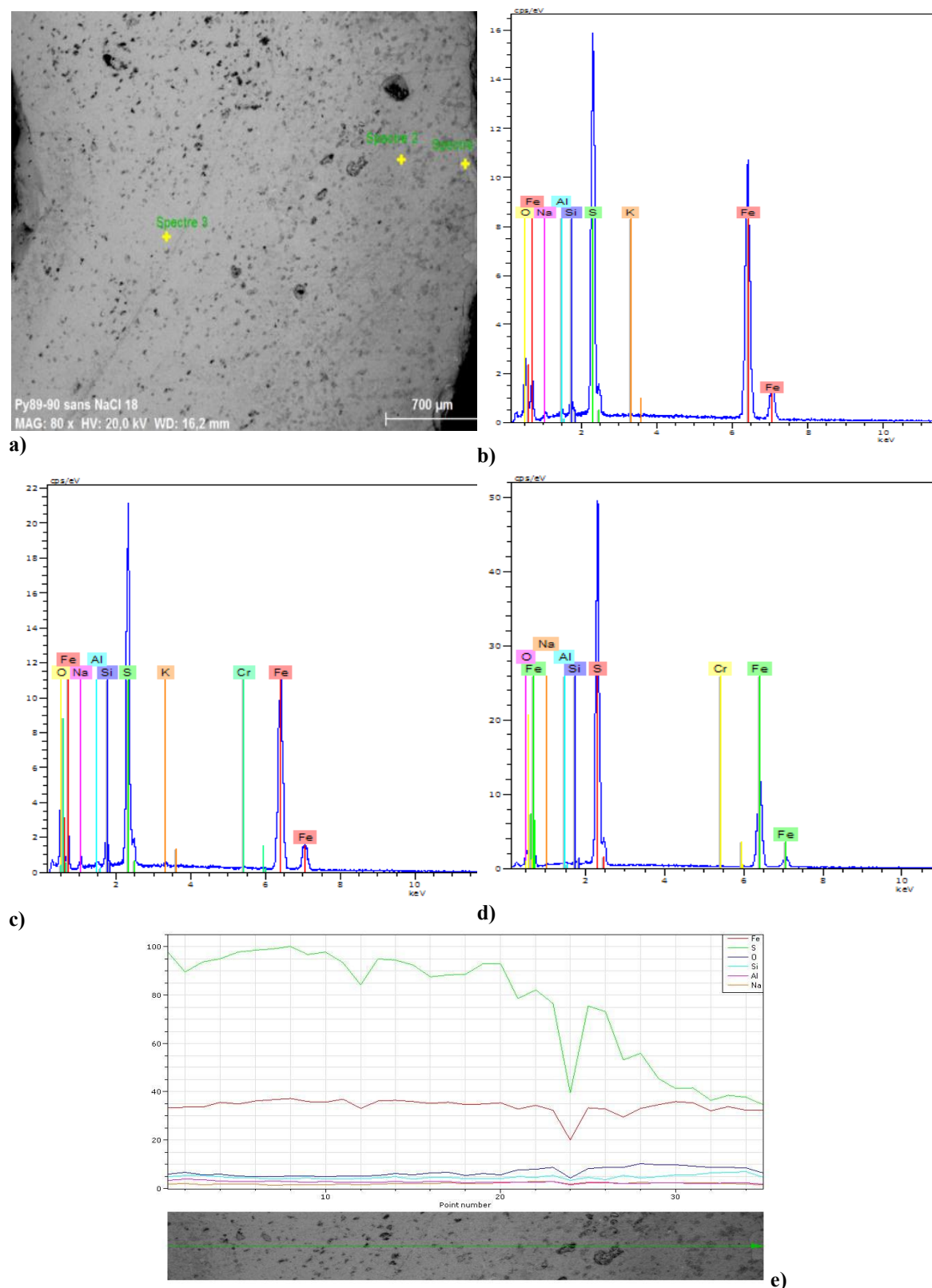


Figure 8: EDS analyses of the electrode after experimentation at pH 8.9 and $T = 90\text{ }^{\circ}\text{C}$ in the presence of an NaCl-free solution: a) the area where the spot analyses and the profile were done, b) EDS spectrum 1 on the edge of the electrode, c) EDS spectrum 2, near the edge, d) reference EDS spectrum 3 of pyrite, far from the edge, e) chemical profile of Fe (red) and S (green).

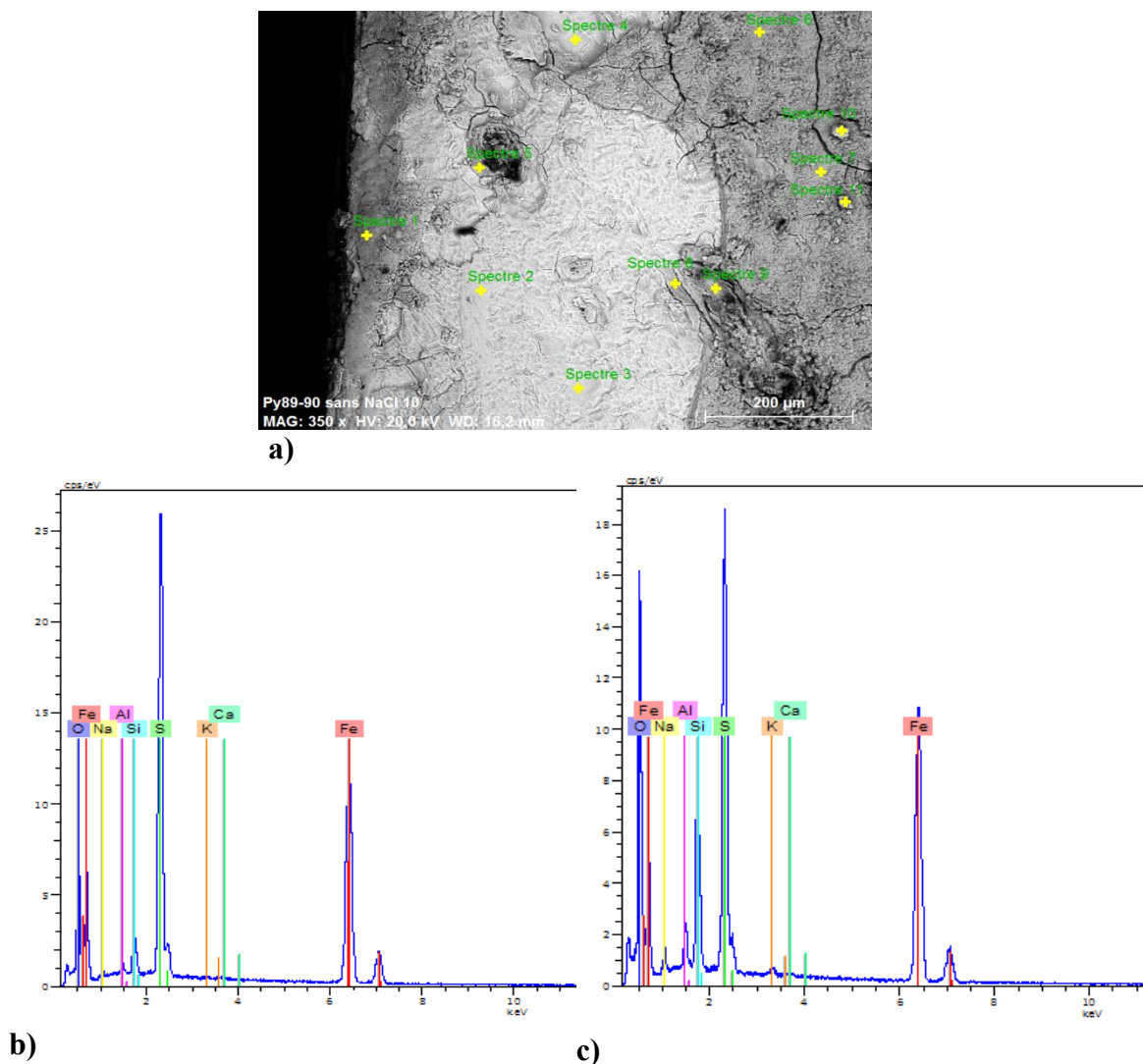


Figure 9: EDS analyses of light areas at the base and at the tip of the electrode:
a) BSE image of the analysed area, b) EDS spectrum 4 of the light area, poor in silica, c) EDS spectrum 6 of the dark area, rich in silicon. The two spectra have similar Fe/S peak ratios.

Experiments at pH 8.9 and 9.7 at 90 °C in the presence of pyrite grains

Monitoring the potential of platinum and pyrite

The peaks on the curves correspond to disturbances related to sample collection for sulphur, sulphate, dissolved iron and silicate analyses.

In the absence of H₂, at pH 8.9 and 9.7, the potentials stabilize at the beginning at high values and all of the electrodes reach an almost stable self-potential (Figs. 10 and 11). The pyrite grains in solution impose a certain potential on the platinum electrode (E_{Pt} at -332 ± 63 mV/NHE at pH 8.9 and at -304 ± 4 mV/NHE at pH 9.7) and on the pyrite electrode (E_{Py} at -234 ± 31 mV/NHE at pH 8.9 and at -263 ± 9 mV/NHE at pH 9.7). E_{Pt} is lower than E_{Py} and E_{Ha} for the two pH values, but whereas E_{Pt} increases when the pH increased from 8.9 to 9.7, E_{Py} decreases. At this stage for the pyrite electrode, the potential might be controlled by the redox couple S(-II)/S(0) present in the pyrite.

However, the potential determined by geochemical calculations using the PHREEQC computer code would be -461 mV/NHE at pH 8.9, and -537 mV/NHE at pH 9.7. These values are lower than those measured on E_{Pt} and E_{Py} because they are calculated for a couple in solution S(-II)/S(VI). The calculation for a solid/solution couple is not included in the geochemical code. The pyrite electrode alone, by dissolution-precipitation equilibria, is therefore not able to control the redox potential in the solution.

Following the injection of H_2 , at pH 8.9 and 9.7, at a partial pressure of 1 bar (for a total pressure of 10 bars), all of the electrode potentials, E_{Pt} , and E_{Py} , decrease and stabilize, respectively, for pH 8.9 at -655 ± 2 mV/NHE and -615 ± 23 mV/NHE, and for pH 9.7 at 677 ± 1 mV/NHE and -596 ± 3 mV/NHE. These values are lower than those obtained in the absence of pyrite grains. Also, E_{Pt} is lower than E_{Py} for the two pH values, but whereas E_{Pt} decreases when the pH increased from 8.9 to 9.7, E_{Py} increases. However, the potential determined under the same conditions using PHREEQC is -631 mV/NHE for pH 8.9, and -697 mV/NHE for pH 9.7 (controlled by the H^+/H_2 couple). The measured values for E_{Pt} (and E_{Py}) are in agreement with these values, which means that the H^+/H_2 couple controls E_{Pt} (and E_{Py}). This enables us to predict the adsorption of H_2 on platinum and probably on FeS_2 .

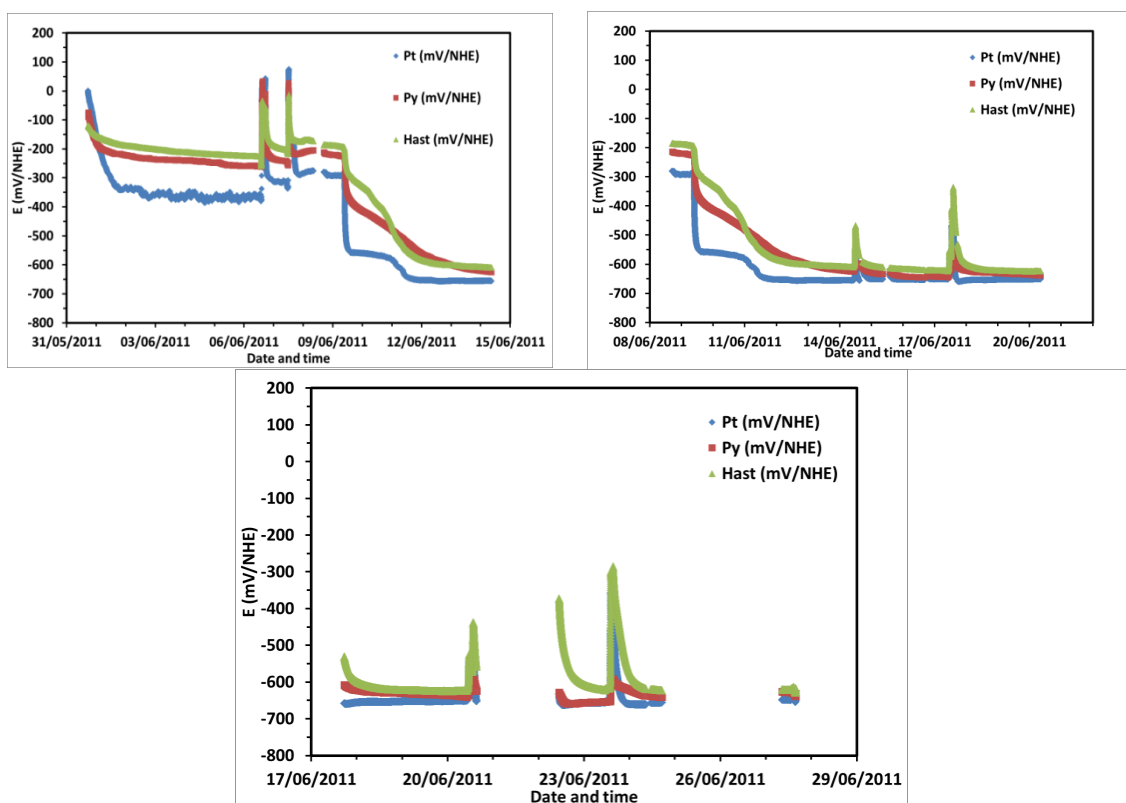


Figure 10: Monitoring electrode potential in the HPTR: pH = 8.9 at 90 °C in the presence of pyrite grains. Particle size between 40 and 63 μm ($mFeS_2 = 2$ g in 200 mL) (experiment begun May 31, 2011)

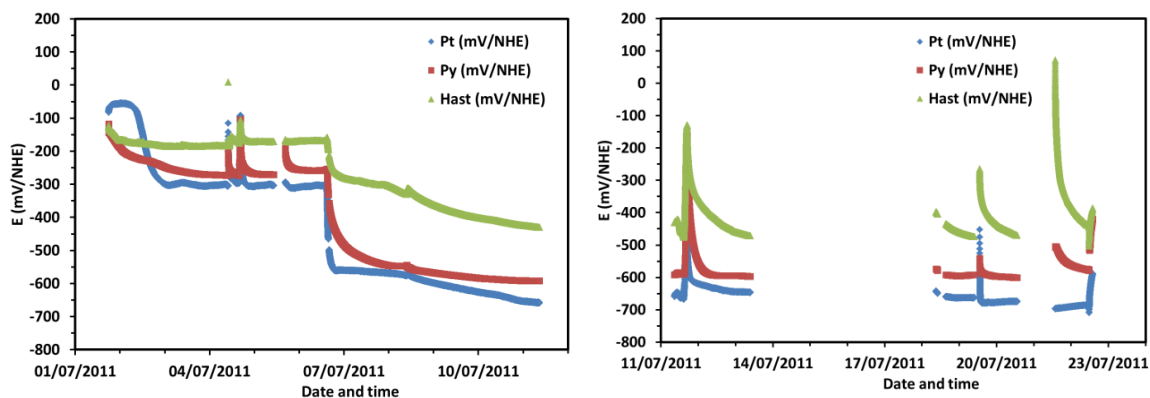


Figure 11: Monitoring electrode potential in the HPTR: $pH = 9.7$ at $90\text{ }^{\circ}\text{C}$ in the presence of pyrite grains. Particle size between 40 and $63\text{ }\mu\text{m}$ ($m\text{FeS}_2=2\text{ g}$ in 200 mL) (experiment begun July 1, 2011)

Electrochemical impedance on platinum and pyrite

The impedance diagrams for values measured in this medium are given in figure 12 and the results are given in table 3.

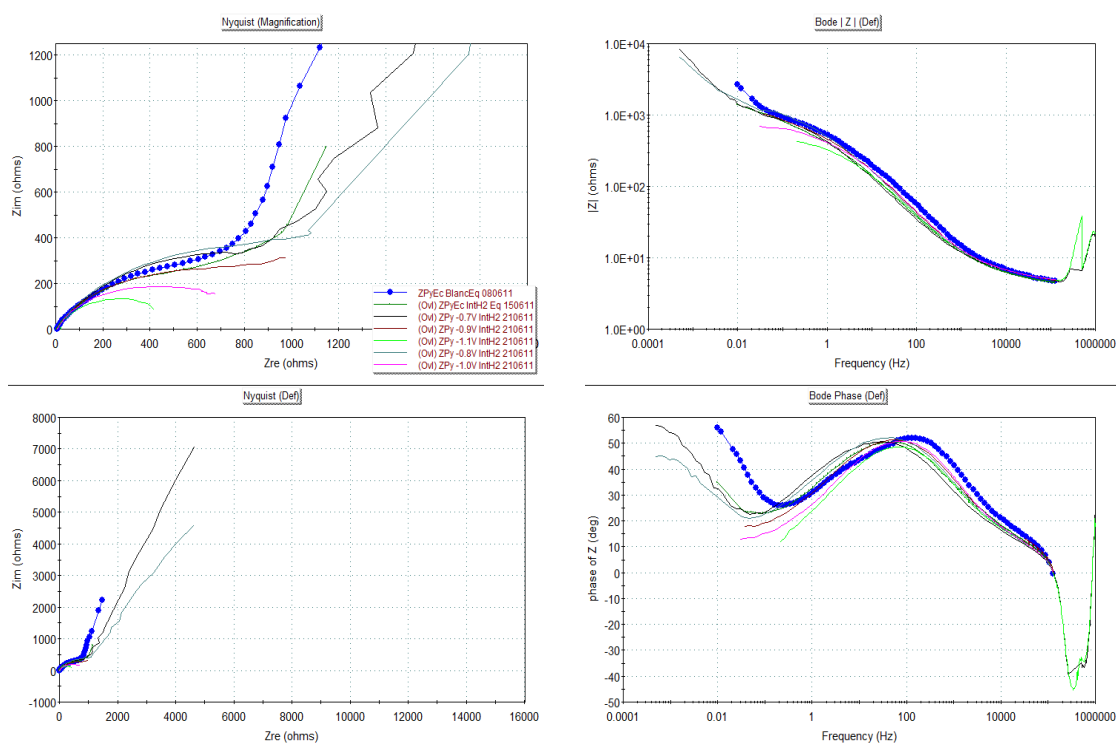


Figure 12: EIS diagrams in Nyquist mode (normal and with magnification in high frequencies) and in Bode mode (modulus and phase of Z), obtained with Pyrite immersed in $\text{NaCl } 0.1\text{ mol L}^{-1}$, $pH\ 8.9$ at 90°C , in the presence of pyrite grains, and initially in the absence of H_2 , then in the presence of H_2 . The blue curve is in the absence of hydrogen gas at E_c , and all of the others are in the presence of hydrogen gas at E_c ; -0.7 ; -0.8 ; -0.9 ; -1.0 and -1.1 V

Table 3: Values of parameters of each component of the exposed EEC (fig. 6) $R(Q(R(CR)G))$, corresponding to pyrite-solution interface under different conditions (pH 8.9 at 90°C; NaCl 0.1 M; with grains of pyrite, in the absence of H₂; in the presence of 1 atm of H₂; impedance measurement at Ec, Ec-0.7V, Ec-0.8V, Ec-0.9V, Ec-1.0V and Ec-1.1V) and immersion times. Explanation for Chi squared (χ^2) is the same as in Table 2.

		Re (ohm)	Q-Yo (CPE, Yo)	Q-n (freq. power)	Rt(ohm)	C (F)	Rc (ohm)	G-Yo	G-K	χ^2
pH 8.9 at 90°C with 2g of pyrite	Py at Ec(-207mV/NHE) without H ₂ ; June 8, 2011	4.62	3.58E-04	0.64	984.20	5.70E-03	14080.00	9.01E-03	0.10	1.11E-02
	Py at Ec (-640mV/NHE) with H ₂ ; June 15, 2011	4.44	5.47E-04	0.60	909.80	2.07E-02	6679.00	5.75E-03	0.19	1.82E-03
	Py at Ec-0.7V with H ₂ ; June 21, 2011	5.16	5.67E-04	0.62	1039.00	3.51E-02	21780.00	6.74E-03	0.01	1.69E-03
	Py at Ec-0.8V with H ₂ ; June 21, 2011	4.78	4.16E-04	0.62	33.81	6.98E-06	944.90	3.21E-03	4.19E-16	1.95E-03
	Py at Ec-0.9V with H ₂ ; June 21, 2011	4.55	4.30E-04	0.60	28.17	5.89E-06	828.80	4.92E-03	0.15	8.87E-04
	Py at Ec-1.0V with H ₂ ; June 21, 2011	4.46	6.99E-04	0.41	0.08	3.70E-05	880.40	1.30E-03	113.10	7.23E-04
	Py at Ec-1.1V with H ₂ ; June 21, 2011	5.93	7.39E-08	1.00	2.96	1.64E-04	57.51	1.36E-03	3.86	6.08E-02
	Py at Ec with H ₂ ; June 24, 2011	4.40	5.06E-04	0.58	32.99	4.10E-06	1464.00	1.04E-02	5.95E-19	2.26E-03

In the presence of H₂, at pH 8.9 and 9.7, the shapes of the impedance curves on platinum vary little with time, with or without stirring. Only R_t is of interest since it is several times lower for platinum than for pyrite. The adsorption of hydrogen gas in the atomic form (H-H) within the Pt metal is well known and determines the behaviour of this electrode where there is no reduction, as opposed to what is observed on pyrite, nor diffusion of S²⁻ from the electrode to the solution, nor deposition of FeS on the electrode.

In the presence of H₂, at pH 8.9 and 9.7, the shapes of the impedance curves on pyrite are identical to the selected EEC (Fig. 6 and Table 3). The impedance curves for the two pH values have the same shape. Therefore, it has not yet been determined that pH has any effect. However, the shape of the impedance curves is different from those of pyrite without grains: appearance of a loop at high frequencies followed by a diffusion segment towards low frequencies. The impedance curves for imposed cathodic potentials (that normally accelerate the reduction processes at the pyrite electrode), compared to those done at Ec, have shapes that progressively slant towards the real z-axis, with progressive loss of the diffusion segment: a) R_t, high without H₂, decreases progressively in its presence; b) the diffusion processes (G parameters) accelerate from the electrode to the solution; c) the diffusion processes are hindered (Rc and C parameters) by increasingly thick FeS scale on the pyrite surface. R_t is much lower on platinum than on pyrite. In general, R_t is much higher on pyrite with grains than without grains. Rc decreases markedly compared to pyrite without H₂, but increases as the layer of scale grows thicker.

Analyses of the black coating on some electrodes and, for information, the analytical monitoring of the solutions

The determination of Fe^{2+} , S^{2-} , SO_4^{2-} and SiO_2 in solution revealed the presence of species that can control the electrode potentials (presence, more or less pronounced, of sulphide), but also that can confirm the reduction of pyrite by hydrogen with the production of $\text{HS}^-/\text{S}^{2-}$. Sulphide content that increases with time and range between 0 and 19 μM is measured.

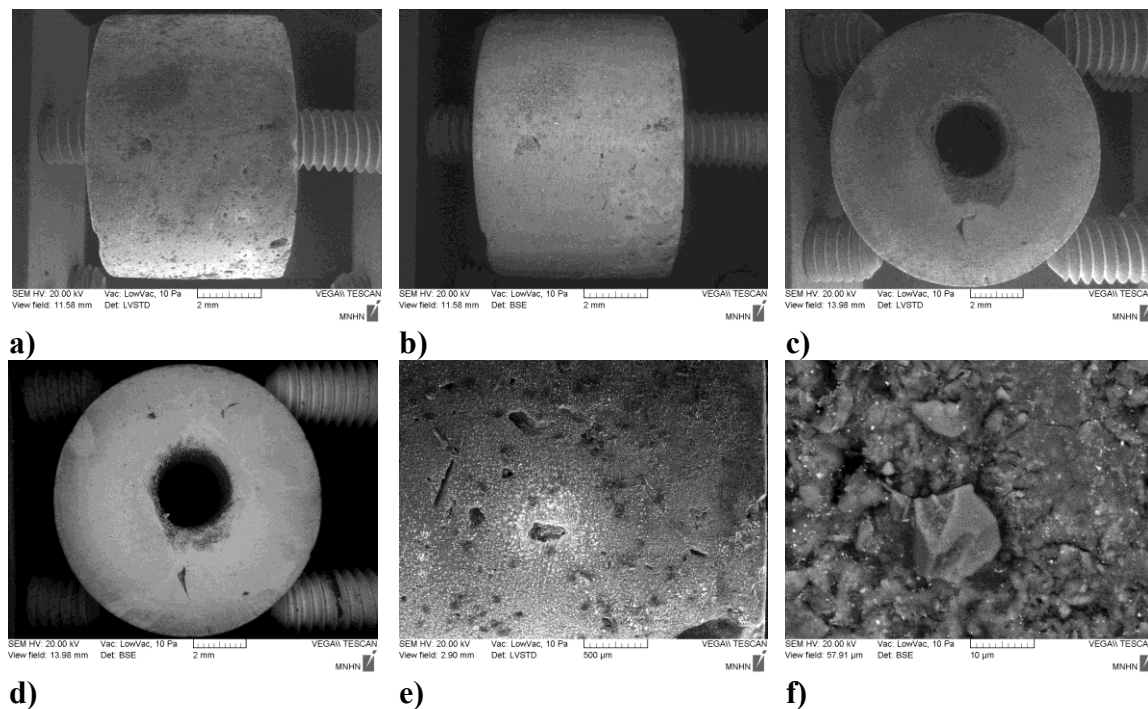


Figure 13: SEM images of the pyrite electrode + pyrite grains after experimentation at pH 8.9 and $T = 90^\circ\text{C}$ in the presence of an NaCl solution: a) state of the surface in contact with the solution (SE), b) same surface (BSE) showing chemical modifications, mostly at each end and, in particular, on the right-hand end, c) the base of the electrode (BSE), d) BSE image showing the general texture of the electrode, e) right-hand end of the electrode (SE) showing pyrite grains and fine precipitation at the surface, f) modified texture (granular aspect) and presence of small pyrite grains and white particles ($< \mu\text{m}$)

Textural analyses were done on some pyrite electrodes with an environmental scanning electron microscope (SEM) and by electronic microanalysis with an EDS detector. The electrode, after experimentation at pH 8.9 and $T = 90^\circ\text{C}$ in a NaCl solution, has a heterogeneously altered surface state (Fig. 13). The alteration is particularly visible at the ends of the electrode (Fig. 13b). It is marked by a change in the texture a bit more granular and the presence of nanoparticle deposits (Fig. 13e, f). The EDS analysis profile done on the end of the electrode that is not in contact with the solution shows no transformation of pyrite – the Fe/S ratio is constant and near 0.5 (Fig. 14). EDS analyses done on the surface of the electrode (right-hand edge), however, show the presence of an Fe-S phase with an Fe/S ratio of around 1, and the presence of white grains that are probably iron sulphate (Fig. 15). The observation and EDS analyses of pyrite grains do

not reveal any significant reactivity of the pyrite grains compared to the electrode. Some spot analyses might present Fe/S peak ratios a bit higher than those of the initial pyrite. Grains of quartz and calcite were also observed. Moreover, the almost systematic presence of silica associated with the Fe-S phase with an Fe/S ratio near 1 was observed, as well as the significant presence of Fe-Cr-Ni, Cr-Ni and W particles.

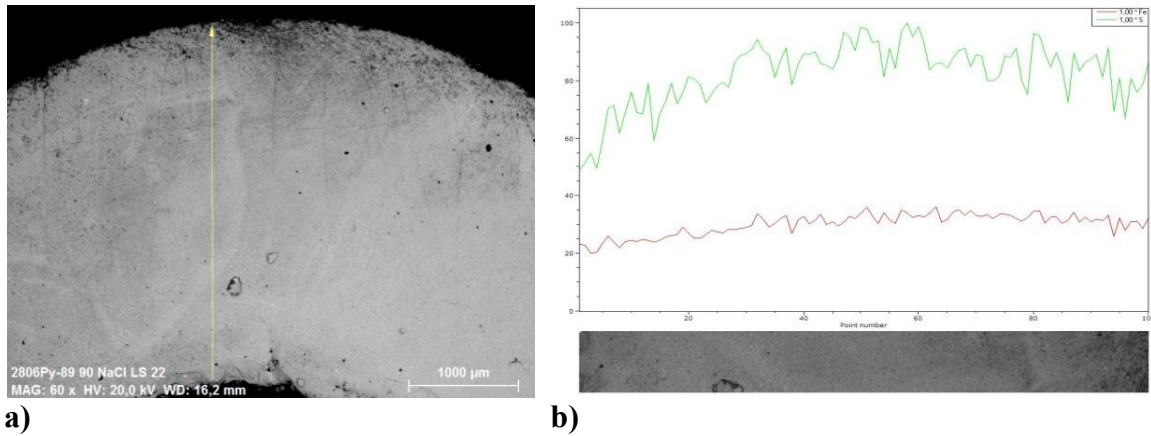


Figure 14: EDS analysis done on the base of the electrode: a) BSE image of the area on the electrode that was analysed, b) EDS profile of Fe and S done on the base of the electrode

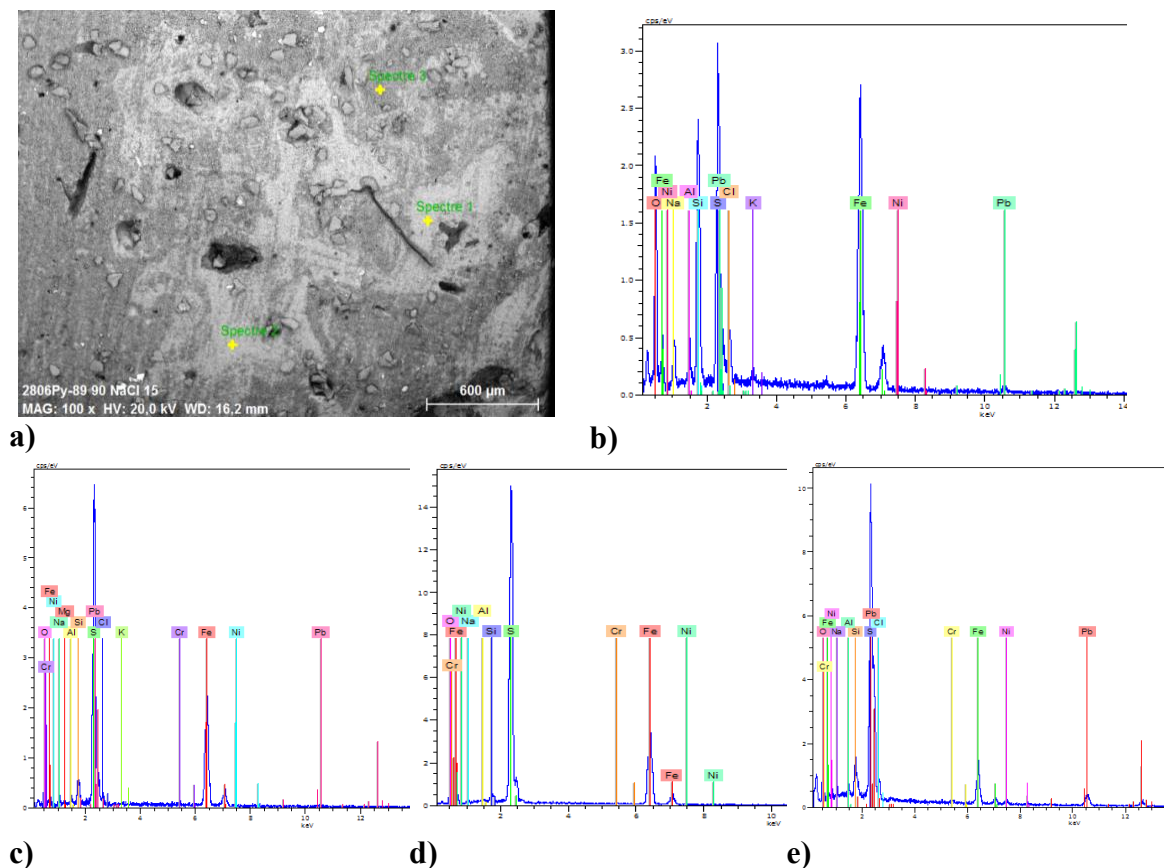


Figure 15: EDS analysis of the reactive surface of the electrode: a) EDS image showing the location of EDS analyses b) and c), EDS spectrum 3 of a Fe-S phase with an Fe/S ratio near 1 and of silica, c) EDS spectra 2 of pyrite that is little or not modified nearby, d) EDS spectra of an area of unmodified pyrite, e) EDS spectrum showing the presence of a Pb-S phase overlying the pyrite (probably iron sulphate)

Summary and Conclusions

The pyrite electrodes were subjected to the reactivity of H₂ under the following conditions:

- Temperature: 90 °C
- pH: i) 11.0 at 25 °C, which corresponds to 9.7 at 90 °C and ii) 10.0 at 25 °C, which corresponds to 8.9 at 90 °C
- absence and presence of pyrite grains (particle size between 40 and 63 μm)
- imposed initial ionic strength (0.1 M NaCl solution)
- absence and presence of a cathodic potential imposed on the pyrite electrode during impedance measurements

E_{Pt} and E_{Py} decrease in the presence of H₂ to reach a stable redox potential controlled by the H⁺/H₂ couple. However, E_{Pt} and E_{Py} drop lower, but less rapidly, in the presence of

pyrite compared to the case without pyrite grains. Pyrite goes through a period during which E_{Py} is greater than E_{Pt} . This period corresponds to the (alkaline dissolution, then) reduction of pyrite by H_2 , but without the pyrite's being entirely covered by pyrrhotite. E_{Pt} and E_{Py} are identical at this time. The corrosion currents are strong on pyrite in the presence of H_2 and increase with the imposed cathodic potentials. They are much stronger than those measured without pyrite grains. The initial reduction reaction rate is rapid due to the high reactivity of pyrite surface, hence the rapid increase in the sulphide content in the bulk solution, which seems to hinder the progress of the reaction up to a rapidly reached sulphide concentration plateau. Pyrite dissolution and pyrrhotite precipitation are coupled reactions. The fluid composition remains fairly steady when pyrite dissolution balances pyrrhotite precipitation, the iron content remaining very low in the solution.

The impedance curves are identical to the selected EEC. The effect of pH (8.9 or 9.7) has not yet been determined. Theoretically, pyrite is more soluble in alkaline solutions, and then the pH effect should be related to the chemical affinity effect of pyrite dissolution. May be an increase should be observed in the global rate under more alkaline conditions than pH 9.7. The EEC parameters modelled at different moments and under different conditions make it possible to follow the phenomena occurring on the electrolyte/pyrite interface. In general, the R_t is much higher on pyrite in the presence of grains than without grains. The impedance curves measured on pyrite with grains have a different shape than those without grains: appearance of a loop at high frequencies followed by a diffusion segment towards low frequencies. The impedance curves for imposed cathodic potentials (that normally accelerate the reduction processes at the pyrite electrode), compared to those done at E_c , have shapes that progressively slant towards the Zreal-axis, with progressive loss of the diffusion segment chronologically as follows:

- R_t , high without H_2 , decreases progressively in its presence (this means that the charge transfer of the reduction reaction progressively impeded by its consequences);
- the diffusion processes (G parameters) accelerate from the electrode to the solution (this means that produced S^{2-} progressively diffuses to the bulk solution);
- the diffusion processes are hindered (R_c and C parameters) by increasingly thick FeS scale that covers the pyrite surface.

Under these conditions far from equilibrium, three steps seem to control the kinetics of the pyrite reduction reaction:

- The diffusion of H_2 and $H_2S_{(aq)}$ between the reaction front and the reaction medium through the porous microstructures of the pyrrhotite
- The pyrite dissolution reaction at the surface
- The pyrrhotite precipitation reaction at the surface

Analyses of the surface and the inside (cross-section) of pyrite electrodes subjected to the reactivity of H_2 under the various conditions described above enable us to compare the alterations undergone by the pyrite. It is clear that the pyrite reacts with H_2 and that its alteration is indicated by the presence, at the surface of electrodes, of a black scale whose Fe/S ratio is near 1 (FeS), while the ratio within the pyrite is 0.5 (FeS₂). The growth of this iron sulphide scale in the pyrite dissolution pits, the proximity of the

source and the iron sulphide suggests that pyrrhotite easily forms a core and increases more rapidly than the pyrite dissolution. The intensity of the pyrite alteration by H₂ seems to increase with the imposed cathodic potential on the pyrite electrode.

The principal result of this work is the evincing of the reduction of the sulphur S^o of the FeS₂ to sulphide (HS⁻/S²⁻) with the superficial transformation of pyrite into pyrrhotite (FeS). All of the measurements agree and following the qualitative exploitation of these data (electrode potential and electrochemical impedance measurements on platinum and pyrite) and surface analyses, it was possible to:

- show the pyrite reduction by H₂ into an iron sulphide whose Fe/S ratio is near 1 (pyrrhotite) with the simultaneous release of hydrogen sulphide in solution.
- create a large electrochemical database

The future exploitation of this electrochemical database will make it possible to determine the kinetics of FeS₂ reduction by H₂ in a HPTR. The prospects for this work are, therefore, the exploitation of these data and their extrapolation to storage conditions. In this paper, the apparent consequences of FeS₂-H₂ interaction into a actual repository cannot yet be discussed, particularly the impact of HS⁻/S²⁻ freed in solution. Further investigations should be realized, notably at lower temperature and in the presence of CO_x, in order to determine the reactivity and competitiveness of other sources of sulphur.

Acknowledgement

The research leading to these results has received funding from i) the European Union's European Atomic Energy Community's (Euratom) Seventh Framework Programme FP7/2007-2011 under grant agreement n° 212287 (RECOZY project) and ii) the ANDRA under the BRGM-ANDRA partnership (TRANSFERT project, Dr. E. Giffaut).

References

- ANDRA, (2005), Référentiel du comportement des radionucléides et des toxiques chimiques d'un stockage dans le Callovo-Oxfordien jusqu'à l'homme, Dossier Argile 2005.
- Crozier T.E., Yamamoto S. (1974). Solubility of hydrogen in water, seawater and NaCl solutions. J. Chem. Eng. Data 19, 242-244
- Gaucher E., Blanc P., Bardot F., Braibant G., Buschaert S., Crouzet C., Gautier A., Girard JP., Jacquot E., Lassin A., Negrel G., Tournassat C., Vinsot A., Altmann S. (2006). Modelling the porewater chemistry of the Callovian-Oxfordian formation at a regional scale, C. R. Geoscience, 338, 917-930.
- OECD, Nuclear Energy Agency (2001). Reversibility and Retrievability in Geologic Disposal of Radioactive Waste: Reflections at the International Level, OECD, Paris.
- Truche L., Berger G., Destigneville C., Guillaume D., Giffaut E. (2010) - Kinetics of pyrite to pyrrhotite reduction by hydrogen in calcite buffered solutions between 90 and 180°C: implication for the nuclear waste disposal. Geochim. Cosmochim. Acta 74, 2894-2914.

SYNTHESIS OF FULVIC ACIDS-LIKE COMPOUNDS IN ALKALINE MEDIA AND THEIR INTERACTIONS WITH IODIDE ION

Emilie Pourtier¹, Chinh Nguyen-Trung^{1*}, Michel Perdicakis², Francis Baros³, David Bordg², Laurent Richard¹

¹ Géologie et Gestion des Ressources Minérales et Energétiques
UMR 7566 Nancy-Université – CNRS, 54506 Vandœuvre-lès-Nancy Cedex (FR)

² Laboratoire de Chimie Physique et Microbiologie pour l'Environnement
UMR 7564, Nancy-Université – CNRS, 54602 Villers-lès-Nancy Cedex (FR)

³ Laboratoire Réactions et Génie des Procédés
UPR 3349 CNRS, BP 20451 54001 Nancy Cedex (FR)

* Corresponding author: Chinh.Nguyentrung@g2r.uhp-nancy.fr

Abstract

Fulvic acid-like compounds (FALCs) containing only two functional groups, alcohol and ether, have been synthesized at pH 13 starting from catechol and acetic acid in view of the further investigation of the FALCs reactions with I_2 and IO_3^- oxidizing species. In this work, their interactions with the reduced form I^- have been investigated by studying the “KI–synthetic fulvic acid-like compounds– H_2O ” system as a function of iodide ion concentration and pH using optical spectrometric techniques. Results obtained from UV-visible and fluorescence measurements have indicated that iodide anion weakly interacts with synthetic fulvic acid-like compounds in the 4-12 pH range.

Introduction

Iodine is a fission product present in the spent fuel from nuclear power plants, but also in the final waste from reprocessing. The knowledge of the extent of its interactions with inorganic and organic species in aqueous solutions is of vital importance in modelling iodine release from irradiated nuclear reactor fuel elements stored in deep underground vaults. In general, underground vaults are surrounded by engineered barriers and argillites. The great majority of argillites contains approximately 1 wt% of organic compounds such as kerogen and low molecular mass substances. The infiltration of natural water into concrete walls of engineered barriers generates hyperalkaline solutions with pH up to 13. In contact with argillites, hyperalkaline solutions dissolve inorganic and some organic substances and degrade partly organic compounds (e.g. kerogen) into hydrophilic substances resembling fulvic acids (*Claret et al.*, 2003). In its turn, fulvic acid could form aqueous complexes with radionuclides

ions. The knowledge of interactions of radionuclides with natural inorganic and organic substances, therefore, is fundamental to modelling the physico-chemical behaviour of radionuclides in natural environment. Interactions of iodine and inorganic substances of the Callovo-Oxfordian argillites under alkaline conditions have been studied by several authors (*Devivier et al.*, 2004; *Bazer-Bachi et al.*, 2006; *Tournassat et al.*, 2007). Earlier works on interactions of iodine and natural fulvic acid in neutral aqueous solutions have been made by *Moulin et al.* (2001) and *Schlegel et al.* (2006) using ElectroSpray Ionisation–Mass Spectrometry and X-ray Absorption Spectroscopy respectively. Moulin et al. have reported the presence of covalent bond between iodine and natural fulvic acid whereas *Schlegel et al.* (2006) have characterized the molecular environment of iodine in iodinated natural humic substances. Both earlier works have been performed under uncontrolled redox conditions. Meanwhile, up to recently, valid data on the chemical behaviour of iodide anion in humate/fulvate aqueous solutions appear to be not available. Under these conditions, it is unclear if the incorporation of iodine in fulvic acids undergoes or not through a redox process involving the oxidized species I_2 and/or IO_3^- . Regarding organic compounds, it is difficult to study natural humic/fulvic acids due to the complexity of their chemical composition. The most effective approach would be to study synthesized humic/fulvic acids with determined chemical composition.

The present work was considered as essential prior to the further investigation of the interactions of I_2 and IO_3^- oxidized species with fulvic acid-like compounds (FALCs). It aimed to answer two questions: (i) Is it possible to synthesize fulvic acid-like compounds (FALCs) containing only two functional groups: alcohol and ether, in basic solution? (ii) Is the optical spectrometry can be an effective measurement technique to detect iodide complexes with fulvate ligands? In response to the two above cited questions, and in order to complete earlier works, an experimental study of interactions involved in the “KI–synthetic fulvic acid-like compounds–H₂O” system has been carried out as a function of two parameters: iodide concentration (0.01 and 0.1 mM) and pH (4-12), using UV-visible and fluorescence spectrometry under argon atmospheric condition at 25°C and 0.1 MPa. Synthesized fulvic acid-like compounds (FALCs) mainly contain two functional groups: alcohol and ether.

Experimental

Synthesis of fulvic acid-like compounds (FALCs) at pH 13

The synthesis procedure refined by *Nguyen-Trung et al.* (2006) is adopted in the present study. It is a modification of the synthesis reported by *Andreux et al.* (1980). FALCs are synthesized in highly alkaline media from an equimolar mixture of catechol and acetic acid, and therefore, are only composed of C, H and O. The synthesis reaction was made possible in a glove bag purged with argon, in the dark at ambient temperature and under atmospheric pressure. The initial chemicals mixture was homogenized using a magnetic stirrer according to the procedure as follows: in a 5 L beaker 56 g of NaOH was dissolved in a solution of 18 g acetic acid in 4 L of degassed water then, 33 g of catechol powder is subsequently added to the mixture. The solution turns immediately to brownish colour, probably resulting either to the catechol ionization or to polymerization reactions initiated by residual oxygen, or both. The volume of the solution is finally brought to 5 L with water. The added amount of NaOH was

calculated in order to completely neutralize acetic acid and catechol and to adjust the pH value of the aqueous mixture up to 13. After 50 days, the pH of the solution was stabilized after a gradual decrease due to the formation of humic and fulvic acids-like compounds and the reaction was stopped. At the end of the experiment, these two acids were separated and extracted from aqueous solution according to the procedure as follows: The solution was acidified to about pH 2 by addition of HCl. Under this condition, HALCs precipitate. The filtration of the solution with 0.1 μm filtration membrane allows separating solid HALCs from soluble FALCs. The yield of FALCs synthesis is approximately 5 wt%. Similar results have been obtained for HALCs. Both acids were recovered after lyophilisation at -90°C . FALCs were then characterized using elemental analysis (C, O and H), XRD and optical spectrometric techniques (UV-visible, infrared and fluorescence).

Iodination of synthetic fulvic acids-like compounds (FALCs)

The interactions between iodide anions and the synthesized FALCs have been studied at different pH values. For each pH, three different solutions have been prepared: (i) a reference solution of FALCs, (ii) a reference solution of iodide ion, and (iii) a solution containing a mixture of iodide ion and FALCs. All solutions have been prepared in a glove bag saturated with argon and the duration of each experiment was fixed at 24 hours. The pH of each solution was adjusted by addition of NaOH or $\text{CF}_3\text{SO}_3\text{H}$ (trifluoromethanesulfonic acid) and the ionic strength using $\text{CF}_3\text{SO}_3\text{Na}$ when necessary.

Chemicals

All chemicals were of analytical reagent grade and were used without any further purification. For all sample preparation and dilutions, ultra pure water was used (Milli-Q academic, $18.2 \text{ M}\Omega\cdot\text{cm}^{-1}$, Millipore S.A.S). For synthesis, glacial acetic acid (99.8 %) and catechol Reagent Plus ($\geq 99\%$) were supplied from Sigma-Aldrich and sodium hydroxide was a 0.1N NaOH Titrisol solution supplied by Merck. For the study of FALCs interactions with iodide ion, KI puriss. p.a., from Sigma-Aldrich was used.

Miscellaneous

Lyophilization was done using Lyotec 6L from Cryo Rivoire S.A.R.L. (Montpellier, France).

UV-visible spectra were recorded with a Cary 3E UV-Vis Spectrophotometer from Varian, equipped with a photo-multiplier detector having a resolution of 0.2 nm. All measurements were made in quartz cuvettes (Hellma) using pure water as the reference.

Fluorometry measurements were performed on a Fluorolog-3 fluorometer from Jobin-Yvon.

Infrared spectra were recorded using a Perkin-Elmer Spectrum One FTIR Spectrometer taking air as the reference. The scanner velocity was 10 kHz and the resolution 4 cm^{-1} .

Results and discussion

Characterization of the synthesized compounds

Elemental analysis

The synthesized FALCs have been analyzed in duplicate for C, H and O. Table 1 shows the elemental analysis for two synthesized FALCs. In both cases, the sums of the weight percentages for C, H, and O are close to 70 %. This is attributed to the presence of significant amounts of sodium chloride in the samples (about 30%) resulting from the addition of NaOH to adjust the initial pH of the reaction medium at 13 and then the addition of HCl to separate fulvic from humic acids. The elemental compositions of FALCs 1 and FALCs 2 approximately correspond to the formulas $C_8H_{10}O_{12}$ and $C_8H_{14}O_{13}$ respectively.

Table 1: Elemental analysis data for the synthesized of fulvic acid-like compounds (FALCs). The percentage of Na^+ is calculated by difference.

Compounds	C wt % (C mole %)	H wt % (H mole %)	O wt % (O mole %)	Cl ⁻ wt % (Cl ⁻ mole %)	Na ⁺ wt % (Na ⁺ mole %)
FALCs 1	21.39 (22.88)	2.19 (28.11)	42.54 (34.13)	20.56 (7.43)	13.32 (7.43)
	21.44 (22.17)	2.38 (29.53)	45.53 (35.30)	18.60 (6.50)	12.05 (6.50)
FALCs 2	20.53 (19.93)	2.97 (34.61)	45.37 (33.05)	18.89 (6.20)	12.24 (6.20)
	20.71 (19.99)	3.03 (35.09)	44.90 (32.50)	19.03 (6.21)	12.33 (6.21)

Attenuated Total Reflectance-Fourier Transform Infrared (ATR-FTIR)

ATR-FTIR spectra of initial compounds (catechol, sodium acetate) and synthesized FALCs are displayed in fig. 1.

Fig. 1A exhibits three characteristic absorption bands groups of catechol: (a) aromatic C-H group (3052 cm^{-1} (ν_{C-H}), 1039 and 1093 cm^{-1} (in-plane δ_{C-H}), 848 and 740 cm^{-1} (out-of-plane δ_{C-H})), (b) aromatic C=C group (1469 , 1513 and 1619 cm^{-1} ($\nu_{C=C}$)) and (c) C-OH phenolic group (3326 and 3445 cm^{-1} (ν_{O-H}), 1360 cm^{-1} (in-plane δ_{O-H}), 1279 and 1238 cm^{-1} (aromatic ν_{C-O})).

The spectrum of hydrated sodium acetate ($NaCH_3CO_2 \cdot 3H_2O$) (Fig. 1B) displays characteristic absorption bands of: (i) $-CH_3$ group (2976 cm^{-1} ($\nu_a CH_3$), 2868 cm^{-1} ($\nu_s CH_3$) and 2934 cm^{-1} (overtone of ν_{C-H})) (ii) $-COOH$ group (1716 cm^{-1} ($\nu_{C=O}$), 1395 - 1440 cm^{-1} (ν_{C-O}), 1568 cm^{-1} ($\nu_a CO_2$) and 1409 cm^{-1} ($\nu_s CO_2$)) (iii) $-C-C-$ group (1044 , 1011 , 924 and 810 cm^{-1} (ν_{C-C})) and (iiii) constitutional H_2O (3145 and 3420 cm^{-1} (ν_{OH})).

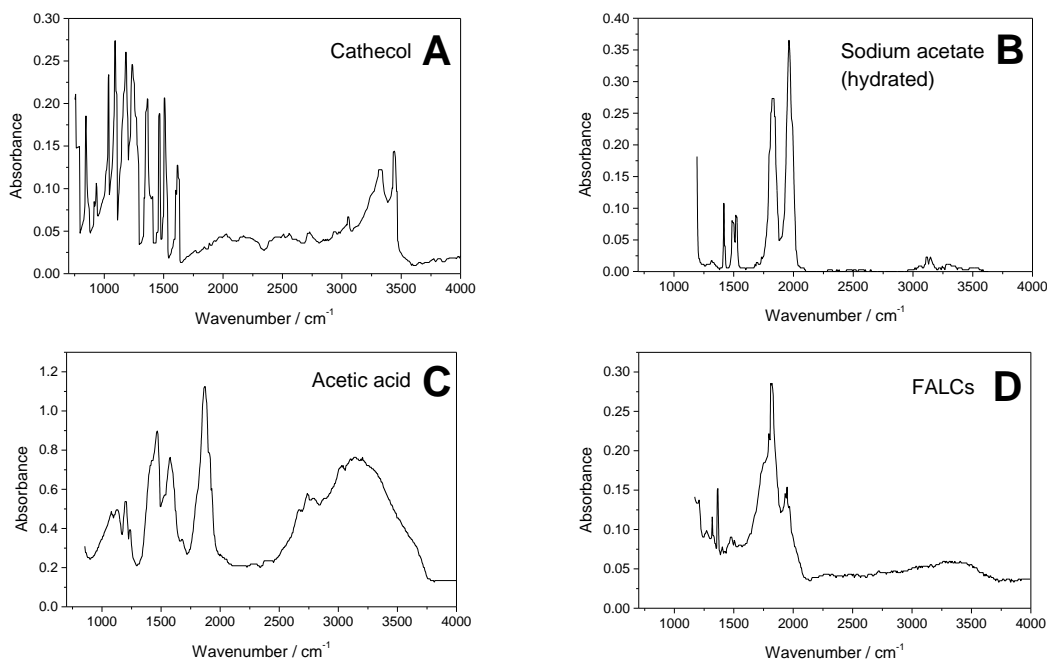


Figure 1: ATR-FTIR spectra of catechol (A), sodium acetate (B), acetic acid (C) and synthesized fulvic acid-like compounds (FALCs 1) (D).

Fig. 1D only shows the ATR-FTIR spectrum of FALCs 1 because its spectral characteristics are similar to those of FALCs 2. The FALCs 1 ATR-FTIR spectrum (Fig. 1D) is characterized by three bands groups: (i) A low intensity broadbands in the wavenumber range 3400-3000 cm⁻¹ including two types of bands: the ν OH stretching band of O-H alcohol functional group (3300-3400 cm⁻¹) and the ν CH stretching band of aromatic C-H (3030-3075 cm⁻¹), (ii) A series of bands ranging from 1700 to 900 cm⁻¹ with three intense and distinct bands at 1572, 1424 and 1336 cm⁻¹ and five small bands around 1620, 1250, 1040, 1020 and 950 cm⁻¹ (the bands at 1620, 1572 and 1424 cm⁻¹ correspond to the stretching ν C=C of the aromatic ring; the band at 1336 cm⁻¹ is assigned to the in-plane δ O-H of the alcohol of the aromatic ring; the two bands around 1250 and 1047 cm⁻¹ represent antisymmetric and symmetric ν C-O-C stretch of ether function. The weak broadband in the 950-1020 cm⁻¹ range results from the in-plane δ C-H bending mode of aromatics), and, (iii) The 900-500 cm⁻¹ region is composed of five weak bands at 850, 810, 779, 760 and 744 cm⁻¹. All these bands characterize the out-of-plane δ C-H bend of aromatic compounds containing one (744 cm⁻¹), two (760 cm⁻¹), three (779 cm⁻¹) and four (810 and 850 cm⁻¹) substitutional groups.

UV-visible absorption spectrophotometry

The absorption spectra for aqueous solutions of catechol (44 mg/L) and synthesized FALCs (200 mg/L) were recorded in slightly acidic and alkaline media and in the wavelength range 230-600 nm (fig. 2). Under these experimental conditions, acetic acid does not absorb. The spectra recorded at pH 4 (fig. 2A) show that catechol exhibits an absorption band at 275 nm corresponding to π - π^* electron transitions in phenolic compounds. FALCs continuously absorbs in the 220-600 nm range with a maximum around 261 nm. This continuous absorption probably results from the fact that FALCs

are composed of several series of individual fulvic acids. The spectra measured in alkaline media are shown in fig. 2B.

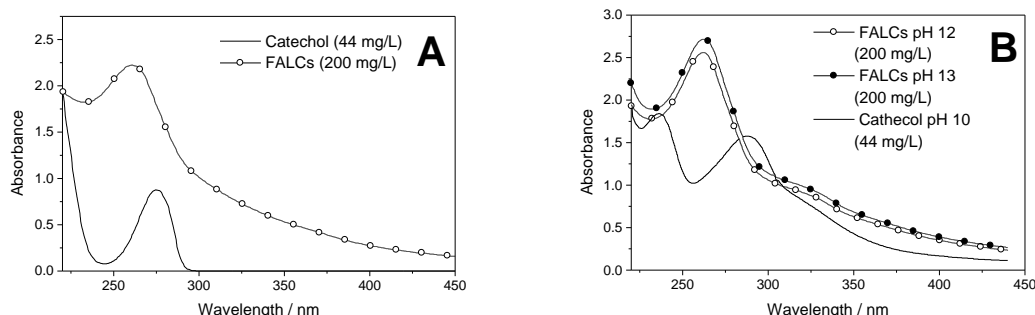


Figure 2: UV-visible spectra of catechol, and FALCs: (A) at pH 4 and (B) at basic pH. (10 mm light path quartz cuvette)

Fluorimetry

Fluorimetric spectra of a 20 mg/L FALCs solution in acidic and alkaline media are shown in fig. 3. Figure 3A displays two emission spectra that were recorded at pH 4 and were excited at 320 and 400 nm. The emission spectrum excited at 320 nm shows a broad signal including two maxima at about 450 and 620 nm. The second emission spectrum excited at 400 nm, is less intense and is composed of two maxima at about 550 and 620 nm and one intense band at 465 nm corresponding to the water Rayleigh scattering emission. The presence of two different emission spectra reveal that FALCs are composed of at least two different compounds.

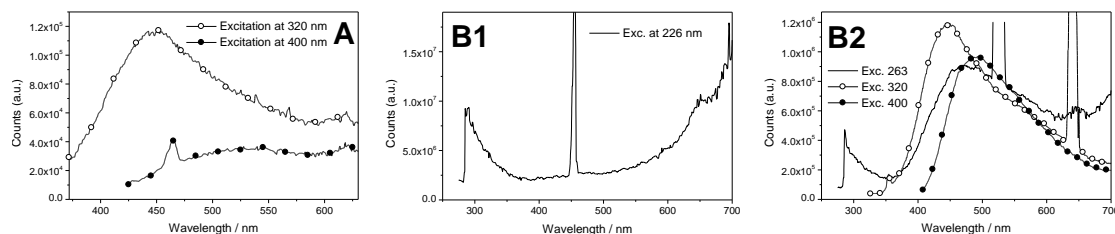


Figure 3: Emission spectra of the synthesized FALCs (20 mg/L): (A) at pH 4 (excitation at 320 and 400 nm), (B) at pH 12: excitation at 226 nm (B1), excitation at 263 nm, 320 nm, and 400 nm (B2).

Figures 3B depicts the emission spectra of the synthesized FALCs at pH 12 after excitation at 226 nm (B1) as well as at 263, 320 and 400 nm (B2) that respectively show fluorescence bands around 700, 450, 450 and 480 nm. The three intense and distinct bands at 400, 525 and 640 nm are due to the water Rayleigh scattering emission. The fact that excitations at four wavelengths 226, 263, 320 and 400 nm lead to different emission spectra confirms the presence of a mixture of individual fulvic acids.

Interactions of iodide with FALCs

The “FALCs–I[−]” interactions were successively analyzed by UV-visible spectrophotometry and the fluorimetry.

UV-visible spectrophotometry

Figure 4 shows the absorption spectra of 0.1 mM potassium iodide, 200 mg.L^{−1} FALCs and the “200 mg/L FALCs + 0.1 mM KI” mixture at pH 4.0 (5A), 7.5 (5B) and 12 (5C). If iodide does not interact with the synthesized FALCs, the spectrum of the mixture should be identical to the spectrum corresponding to the sum of the individual spectra. In order to effectively detect the eventual changes in the absorption spectra, a “difference spectrum” has been carried out by subtracting the spectrum corresponding to the “FALCs + KI” mixture from the sum of the spectra of potassium iodide and FALCs alone for each pH value (spectra not shown here).

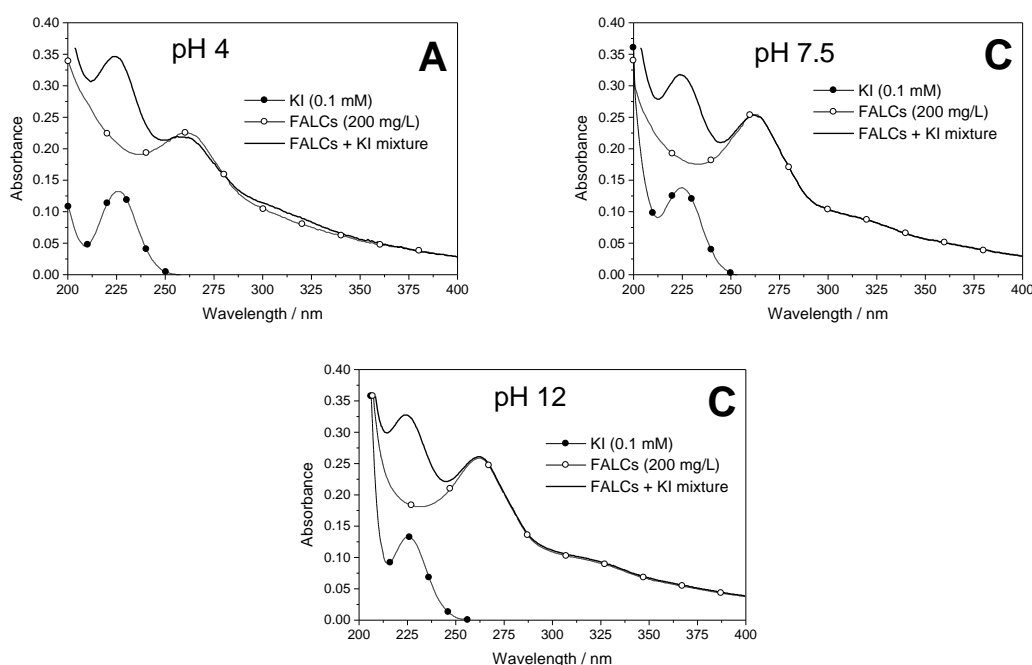


Figure 4: Interaction of iodide with synthesized FALCs at different pH values: UV-visible absorption spectra for 200 mg/L FALCs, 0.1 mM KI and the “200 mg/L FALCs + 0.1 mM KI” mixture at pH 4 (A), 7.5 (B) and 12 (C).

Potassium iodide: Given the fact that the spectra recorded for potassium iodide at pH 4, 7.5 and 12 remain unchanged, we can easily deduce that those spectra are independent of pH and show a maximum at 226 nm.

FALCs–iodide mixtures: The influence of pH on the absorption spectra of FALCs has already been commented in an above subsection. The absorption spectra of the mixtures of iodide ions and FALCs show two bands around 224 and 260 nm.

For the spectra recorded at pH 4 (fig. 4A) slight variations are observed in several regions of the UV-visible spectra after the addition of iodide. Indeed, the “difference spectrum” shows three characteristics: (i) a minimum at about 230 nm *i.e.* the

absorption intensity of the mixture is less important than that of the sum of the absorption values of the individual components, (ii) a maximum in the vicinity of 270 nm and (iii) a minimum around 315 nm. The first characteristic is probably due to the decrease of iodide ion concentration. The formation of a FALCs–iodide complex apparently absorbs at 268 nm and 315 nm more than initial FALCs. In addition, the intensity of the “difference spectrum” dramatically increases at wavelength below 206 nm.

At pH 7.5 there are no significant differences between the spectrum corresponding to the “FALCs + KI” mixture and the sum of the KI and FALCs individual spectra except for wavelengths below 206 nm where the “difference spectrum” intensity dramatically increases as at pH 4.

In basic solution (pH 12), the “difference spectrum” shows a minimum at about 230 nm and a minimal increase of absorption in the spectral range 250–400 nm. The former result is similar to that obtained at pH 4.

Fluorimetry

The emission spectra of initial potassium iodide and “FALCs + KI” mixtures are represented in fig. 5.

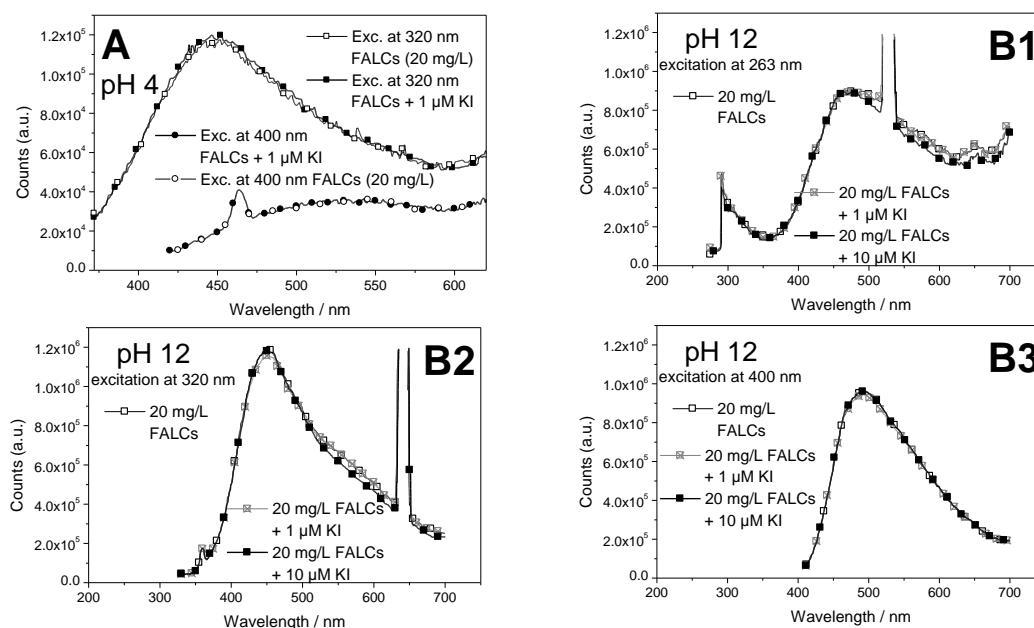


Figure 5: Interactions of iodide with FALCs at different pH values. Fluorescence spectra: (A) at pH 4 with excitation at 320 and 400 nm for 20 mg/L FALCs alone and for the “20 mg/L FALCs + 1 μ M KI” mixture. (B) at pH 12 with excitation at 263 nm (B1), at 320 nm (B2) and at 400 nm (B3): (i) for the 20 mg/L initial FALCs solution, (ii) the “20 mg/L FALCs + 1 μ M KI” and (iii) the “20 mg/L FALCs + 10 μ M KI” mixture mixtures.

Potassium iodide:

Measurements of 0.1 mM potassium iodide solutions at pH 4 and 12 using triangular or square cuvettes with excitation at 226 nm (maximum absorbance of I⁻ anion) revealed that KI has no fluorescence band.

FALCs-iodide mixtures at pH 4:

The emission spectra at pH 4 for 20 mg/L FALCs and the “20 mg/L FALCs + 1 μ M KI” mixture with excitation at 320 and 400 nm are shown in fig. 6A. The spectrum recorded for the mixture “FALCs + KI” with excitation at 320 nm is slightly more intense at 450 nm than that of initial FALCs. This result is an indication in favour of possible interaction of FALCs with iodide leading to the formation of a complex that is more fluorescent than initial FALCs. On the other hand, the two emission spectra measured with excitation at 400 nm are almost identical. This result indicates that the FALCs components that fluoresce with excitation at 400 nm do not interact with iodide.

FALCs -iodide mixtures at pH 12:

Figures 5B display emission spectra of three samples at pH 12: (i) the 20 mg/L initial FALCs solution, (ii) the “20 mg/L FALCs + 1 μ M KI” and (iii) the “20 mg/L FALCs + 10 μ M KI” mixture mixtures. The excitation was at 263, 320 and 400 nm. The spectra with excitation at 263 nm, 320 nm and 400 nm respectively show fluorescence bands around 475, 450 and 500 nm. For each excitation wavelength, emission spectra of the three above cited samples appear to be slightly increased with increasing iodide concentration. The differences between initial 20 mg/L FALCs solution and the two mixtures: 20 mg/L FALCs + 1 μ M KI and 20 mg/L FALCs + 10 μ M KI, are evidence of the existence of interactions between FALCs and iodide ions. Note that the three distinct bands of 460, 525 and 640 nm result from the water Rayleigh scattering emission for excitations at 226, 263 and 320 nm.

Summary and Conclusions

The approach taken in the present work is to use: (i) an initial mixture of catechol and acetic acid to synthesize humic and fulvic acids in NaOH solution (pH 13) under argon atmospheric condition. Synthesized FALCs were characterized using ATR-FTIR technique. (ii) a set of two UV-visible and fluorescence spectroscopies to detect the eventual complex formation of iodide ions with FALCs at different pH values.

Synthesized FALCs are composed of many molecules containing two functional groups: alcohol and ether. Due to the impossibility of a polyaromatic ion to interact with an acetate ion under argon atmosphere, of carboxylate-bearing FALCs could not be formed in the present work. From a practical point of view, the synthesis procedure has to be improved by passing the FALCs aqueous solution through ion exchange resins prior to the lyophilisation process in order to remove sodium chloride that is formed during the process.

To our knowledge, for the first time, the treatment of UV-visible and fluorescence spectra of aqueous solutions containing iodide ions and FALCs have showed that slight but significant differences are observed between the spectrum of the “FALCs + KI”

mixture and the sum of the spectra of initial potassium iodide and FALCs. However, the relative concentrations of FALCs and KI in the mixture are worth to be optimized in order to increase the amount of the FALCs–I⁻ complex formed.

Based on this work, several lines of research can be suggested in the following order of priority: (i) evaluation of redox interactions of elemental iodine and iodate ions towards humic/fulvic compounds (ii) determination of stability constants values of iodide–FALCs complexes, (iii) use of high-precision potentiometry as a complementary tool for the study of the formation of the above cited complexes. (iv) investigations on radioactive iodine and humic/fulvic substances, and (v) synthesis of humic and fulvic acids containing more functional groups (carboxylate, amine, thiol) and their interactions with iodide anion as a function of pH.

Acknowledgements

E. Pourtier and C. Nguyen-Trung wish to thank GdR PARIS (Physicochimie des actinides et radioéléments aux interfaces et en solution) for the financial support.

The research leading to these results has received funding from the European Union's European Atomic Energy Community's (Euratom) Seventh Framework Programme FP7/2007-2011 under grant agreement n° 212287 (RECOSY project).

References

- Andreux, F., Golebiowska, D., Metche, M., (1980). Oxidative polymerization of O-diphenols in presence or absence of amino-acids. Topics on (catechol-glycocolle) and (catechol-diglycylglycine). General Assembly of Polyphenols Group Report, Logrono (Spain), Bulletin 9, 178-188.
- Bazer-Bachi F., Tevissen E., Descostes M., Grenut B., Meier P., Simonnot M. O., Sardin M., (2006). Characterization of iodide retention on Callovo-Oxfordian argillites and its influence on iodide migration. Phys. Chem. Earth 31, 517-522.
- Claret F., Schaëfer T., Bauer A., Buckau G., (2003). Generation of humic and fulvic acid from Callovo–Oxfordian clay under high alkaline conditions. Sci. Total Environ. 317, 189-200.
- Devivier K., Devol-Brown I., Savoye S., (2004). Study of iodide sorption to the argillite of Tournemire in alkaline media. Appl. Clay Sci. 26, 171-179.
- Moulin V., Reiller P., Amekraz B., Moulin C., (2001). Direct characterization of iodine covalently bound to fulvic acids by electrospray mass spectrometry. Rapid Commun. Mass Spectrom. 15, 2488-2496.
- Nguyen-Trung C., Richard L., Kiprop A.K., Caumon M.C. (2006). Etude expérimentale des interactions entre l'uranyle (VI) et l'acide humique synthétisé à l'aide de la spectroscopie optique (UV-visible, fluorimétrie) et la potentiométrie à 25°C, 0.1 MPa. Réunion des Sciences de la Terre (RST), Dijon, France, 4-8 December 2006.

Schlegel M. L., Reiller P., Mercier-Bion F., Barré N., Moulin V., (2006). Molecular environment of iodine in naturally iodinated humic substances: Insight from X-ray absorption spectroscopy. *Geochim. Cosmochim. Acta* 70, 5536-5551.

Tournassat C., Gaucher E.C., Fattahi M., Grambow B., (2007). On the mobility and potential retention of iodine in the Callovian-Oxfordian formation. *Phys. Chem. Earth* 32, 539-551.

REDUCTION OF PU(VI) BY FE

Paul Carbol^{1*}, Adrian Nicholl¹, Detlef Wegen¹, Thierry Wiss¹, Arne Janssen¹, Bert Cremer¹, Rikard Malmbeck¹, Stefaan Van Winckel¹, Christos Apostolidis¹, Rafael Alvarez Sarandes Lavandera¹, Jerome Himbert¹, Daqing Cui²

¹European Commission, DG JRC, Institute for Transuranium Elements (DE)

²Studsvik AB (SE)

* Corresponding author: paul.carbol@ec.europa.eu

Abstract

The main purpose of this task (part of deliverable D6.1) is to study the immobilization/remobilization of Pu under simulated near-field conditions: Fe as iron coupon mimic the canister material, and magnetite as the relevant crystalline rock fracture filling Fe(II) minerals found at for example ÄSPÖ Hard Rock Laboratory.

In collaboration between ITU and Studsvik, solutions of hexavalent Pu were exposed to iron coupons, either freshly polished Fe(0) or pre-corroded and coated with Fe₃O₄, under anoxic conditions. Plutonium and Fe concentration in solution as a function of time was monitored by sector field inductive coupled plasma mass spectrometry (SF-ICP-MS) and γ -spectrometry. Plutonium precipitate on the iron phases were characterized by scanning electron microscope coupled with energy dispersive X-ray spectroscopy (SEM-EDX) and α -track analysis.

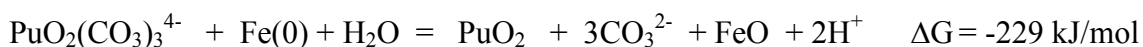
It can be concluded that only 1 % of the added amount of Pu(VI) was reduced by Fe₃O₄ after a contact time of 4 months. There was no Pu(VI) reduction on the Fe coupons. Considering the small negative ΔG -values and the small amount of Pu(VI) reduced on the magnetite surface it can be concluded that it is a relatively slow reduction reaction.

Introduction

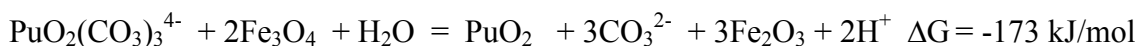
²³⁹Pu is one of the most radiotoxic radionuclides contained in high level nuclear waste due to its long half live and chemical properties. The environmental behaviour of plutonium is the most difficult to predict due to its multi-valence state in the subsurface environment [Rondinella, 2011]. Pu(III)/(IV) are the predominant valence states at low pH and strongly reducing conditions while Pu(V)/(VI) is favoured in oxidative and high pH systems.

Previous studies have shown that aqueous Pu(V) can be reduced to sorbed Pu(IV) by Fe(II) containing SRS sediments [Hixon et al., 2009]. Pu(VI) reduction by Fe(0) and Fe(II) phases has been investigated [Lucchini et al., 2008], however, the authors did not show the stability of Pu(V)/(VI) in water solution, neither gave the ratio of Pu(V)/Pu(VI) in the solution.

A calculation of Gibbs free energy of redox reaction between Pu(VI) and metallic iron or Fe₃O₄ shows that the process is in both cases possible. The reaction of plutonyl carbonate with Fe gives, for a groundwater with pH 10 (25 °C);



and the reaction between plutonyl carbonate and magnetite;



The relative small negative values of ΔG for both reactions suggest that these two redox reactions may be feasible but the driving force is not very large. In comparison, ΔG for a very slow redox reaction between Se(VI) and Fe(0) at repository conditions (pH 8.5) is -278 kJ/mol [Cui et al., 2007].

It is relatively difficult to convert Pu(IV), in mg-amount, to Pu(VI) in absence of NO₃⁻ and stabilise Pu at pH 8.2-8.5, for a time period of months. Only a relatively small number of publications exist which describe the conversion of Pu(IV) to Pu(VI) [Fedoseev et al., 2010; Tait et al., 1995; Reilly et al., 2006; Reilly et al., 2007; Newton et al., 1986; Ghosh et al., 1964].

Based on the publications concerning the oxidation of Pu(IV) to Pu(VI), the best method, which is also suitable for glovebox work, is to oxidise Pu with fuming HClO₄ and then add the Pu(VI) solution to 0.5 M Na₂CO₃ solution. The high Na₂CO₃ concentration was selected to ensure that there is enough of carbonate to form Pu(VI) carbonate. The pH should be in the range of 9-10 (Figure 1).

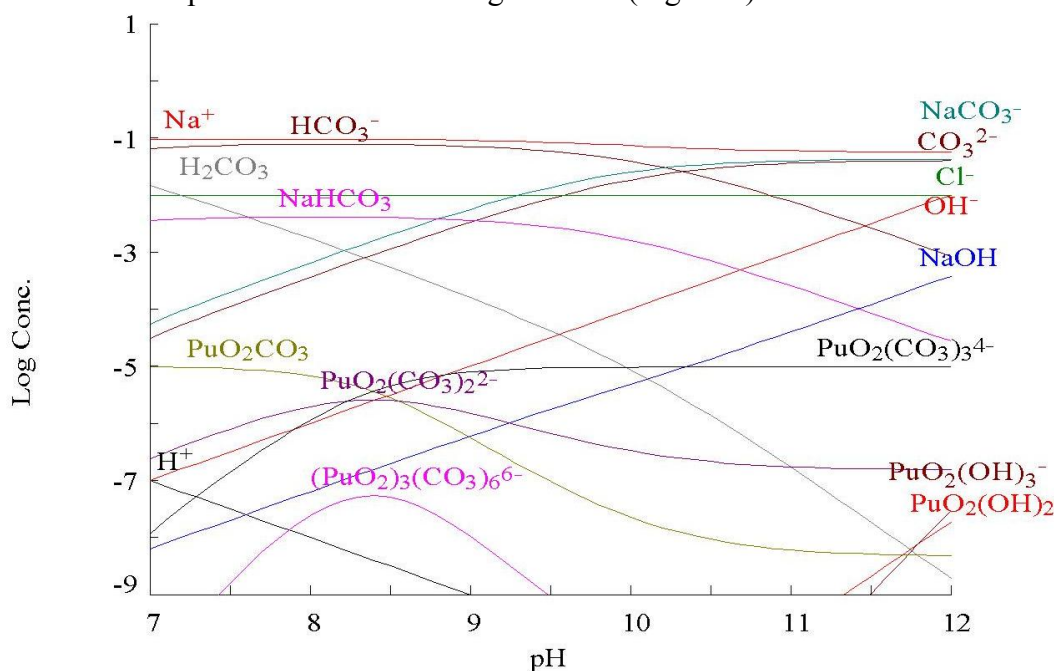


Figure 1: Pu speciation in 0.084M Na₂CO₃ solution under oxidative conditions. The total concentrations used for the speciation calculation were: [Na⁺]=0.1M, [CO₃²⁻]=0.084 M, [PuO₂²⁺]=10μM and [Cl⁻]=0.01 M.

The experiment aims are: a) to investigate the stability of 10^{-5} M Pu(VI) in a synthetic groundwater solution (a 10mM NaCl and 84mM Na₂CO₃ solution, a pH of 10 gives a [CO₃²⁻] of ~20mM, Figure 1) and b) to investigate the possibility of a redox reaction between Pu(VI) and iron canister surface, i.e. Fe(0) surface or Fe₃O₄ (magnetite) coated Fe(0) surface.

Experimental

The Pu(VI) reduction experiment is described in more or less chronological steps. Additional to the description of the experimental procedure also the analytical results are given in this section.

1.1 Conversion of Pu metal to Pu solution

The Pu was prepared from the reference material IMN10031, referred to as "MP2", consisting of 99.90±0.04 wt.% metallic Pu. The reference material contained 489 mg uranium/kg and 438 mg americium/kg on 12 April 2001. The isotopic composition of "MP2" is given in Table 1 and 2.

Table 1: Isotopic composition of reference material "MP2" at the reference date of 12 April 2001.

	Isotope mass ratios
$n(^{238}\text{Pu})/n(^{239}\text{Pu})$	0.000 033 15(41)
$n(^{240}\text{Pu})/n(^{239}\text{Pu})$	0.022 437 4(99)
$n(^{241}\text{Pu})/n(^{239}\text{Pu})$	0.000 298 0(17)
$n(^{242}\text{Pu})/n(^{239}\text{Pu})$	0.000 070 87(71)

Table 2: Isotopic composition of reference material "MP2" at the reference date of 12 April 2001. The molar mass of Pu was taken as 239.074 888(11).

	Mass fraction ($\cdot 100$)
$m(^{238}\text{Pu})/m(\text{Pu})$	0.003 227(40)
$m(^{239}\text{Pu})/m(\text{Pu})$	97.757 76(98)
$m(^{240}\text{Pu})/m(\text{Pu})$	2.202 62 (95)
$m(^{241}\text{Pu})/m(\text{Pu})$	0.029 38(17)
$m(^{242}\text{Pu})/m(\text{Pu})$	0.007 015(70)

The plutonium reference material "MP2" in an amount of 2 mg Pu metal was dissolved in 10 ml of 8 M HNO₃. A Pu purification step was made to reduce the relatively large amount of ²⁴¹Am in the reference material.

1.2 Pu-²⁴¹Am separation

The Pu-Am separation, performed in a ventilated glovebox, was initiated by filling two large Bio-Rad columns with 1.8 ml of TEVA resin (50-100 µm grain size). The columns were fitted with frits and conditioned with 10 bed volumes of 8 M HNO₃. A volume of 100 µl of 30 vol.% H₂O₂ was added to the Pu solution, to convert Pu(III) to Pu(IV), which was then mixed and left for 20 min at room temperature. The H₂O₂ treatment was repeated once. Finally, 1 ml of 2.5 M NaNO₂ was added to the Pu solution to further oxidise Pu to Pu(IV). The Pu sample (2 mg of total Pu in 11.1 ml of 8 M HNO₃) was split and 5.55 ml of the solution was added to each TEVA resin column. The Am and other trivalent actinides were washed off each column with 20 ml 8 M HNO₃. The Pu-fractions were eluted with 10 ml of 0.2 M Hydroxylamine nitrate in 2 M HNO₃ (with 4 mg of ascorbic acid added), a mixture that reduces Pu(IV) to Pu(III), into a 50-ml Erlenmeyer flask. The original Pu solution, the Am and Pu fractions were individually bulked together to determine the TEVA separation recovery. The recovery in the two Pu-fractions was 88.9% and the ²⁴¹Am reduction was >90%.

The purified Pu solution was transferred from the 50-ml Erlenmeyer flask into a 10-ml glass tube. The solution was taken to dryness and dissolved in 0.01 M HCl. This matrix conversion step, from HNO₃ to HCl matrix, was repeated three times. Finally, the dried sample was taken up with 2 ml of 0.01 M HCl.

1.3 Preparation of Pu(VI) carbonate solution

The preparation of the Pu(VI) carbonate solution, made in a ventilated glovebox, started by taking 1.8 ml of a $9.2 \cdot 10^{-4}$ M purified ²³⁹Pu(VI) solution in 0.01 M HCl and introducing it into a 12 ml borosilicate glass tube. An amount of 360 µl concentrated HClO₄ (70 wt.%) solution was added. The colourless Pu solution changed to a yellow colour. The mixture was carefully heated (boiling point 203 °C) and remained yellow while white HClO₄ fumes left the tube. The Pu solution was reduced to approximately 50 µl. Then a second batch of 360 µl concentrated HClO₄ was added to the Pu solution. Applying careful heating the solution was again reduced to 50 µl and was still slightly yellow, a colour verifying Pu(VI) formation (Morss et al., 2006). After cooling the solution became almost colourless.

The Pu solution was introduced drop-wise into a flask containing 18 ml of a 0.5 M Na₂CO₃ solution. The glass tube was washed three times with small volumes of 0.5 M Na₂CO₃ solution.

1.4 ²³⁹Pu(VI) solution stability test in air glovebox

The stability of the prepared Pu solution was investigated for 55 days through repeated α-spectrometry measurement of the 18 ml Pu solution. The results showed that the Pu concentration remained constant during the complete time period. As the solubility limit of Pu(IV) hydroxide, at pH 10, is $\sim 10^{-11}$ M the high Pu concentration is a evidence of Pu in hexavalent state present as PuO₂(CO₃)₃⁴⁻ (Figure 1). Determination of the ²³⁹Pu concentration, by α-spectrometry and spiking with ²⁴²Pu-tracer, gave a concentration of $5.8 \cdot 10^{-5}$ M. The Pu(VI) solution was diluted with 82 ml of a NaCl solution to yield a total amount of 103.18 g. The final composition of the Pu solution is given in Table 3.

Table 3: Calculated composition of 103.18 g $^{239}\text{Pu(VI)}$ solution used for the redox experiments.

Compound	Concentration (M)
^{239}Pu	$1.0 \cdot 10^{-5}$
ClO_4^-	0.006
Na^+	0.098
Cl^-	0.012
CO_3^{2-}	0.020

1.5 $^{239}\text{Pu(VI)}$ solution stability in N_2 -purged glovebox

After the stability test the Pu(VI) solution was divided into five 20ml glass liquid scintillation counting (LSC) vials yielding an amount of approx. 20 g in each vial (Table 4).

Table 4: Amount of ^{239}Pu in 20-ml LSC vials.

Denomination	Mass of Pu solution (g)	Amount of Pu (μg)
A: MP2 Pu-239, Fe coupon 1, Recosy Studsvik, 2011-06-28	19.80956	47.148
B: MP2 Pu-239, Fe coupon 2, Recosy Studsvik, 2011-06-28	20.39222	48.535
C: MP2 Pu-239, Fe magnetite 1, Recosy Studsvik, 2011-06-28	19.42700	46.238
D: MP2 Pu-239, Fe magnetite 2, Recosy Studsvik, 2011-06-28	20.61427	49.064
R: MP2 Pu-239, Reference, Recosy Studsvik, 2011-06-28	21.43751	51.023

The vials were transferred into the N_2 -purged glovebox 5, lab A132 (approximately 0.32 vol.% O_2 , 14 ppm H_2O). The solutions were left in the glovebox for a period of 10 days. During this time period an orange coloured precipitate was formed at the bottom of all vials (Figure 2).

The Pu-solutions were centrifuge-filtrated through 3000 Dalton filters, removing colloids consisting of $>11 \text{ PuO}_2$ agglomerates. The precipitate was collected and analysed by SEM-EDX.

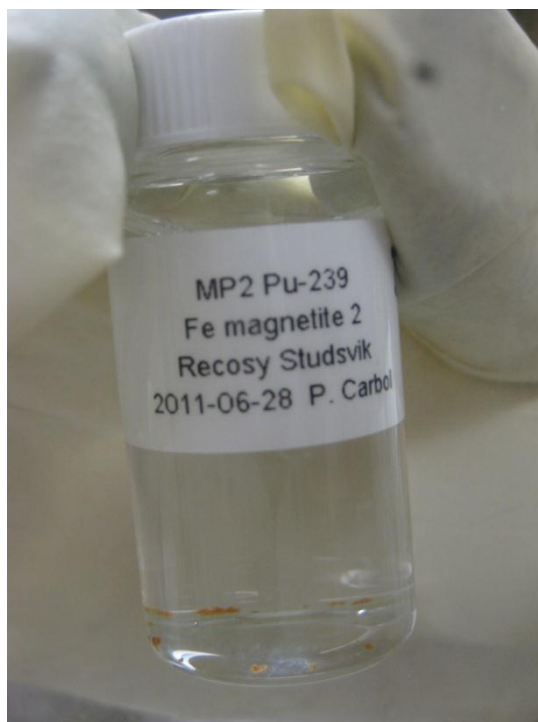


Figure 2: Precipitate at the bottom of LSC-vials after Pu(VI)-solution preparation but before experiment start.

1.6 SEM-EDX analysis of precipitate

The SEM-EDX analysis was performed on a Philips 40XL equipped with an EDX-analyser. The SEM is adapted for work with α -active samples. Thirteen different areas, both spots and overview areas of the precipitate were investigated and the following results were obtained (Table 5).

It can be concluded that the precipitate contained insignificant amounts of Pu. Co-variation analysis gave following composition; Na_2CO_3 , NaCl and traces of NaSiO_4 , FeCO_3 , FeOOH , CaCO_3 . A reasonable explanation is that the strongly acidic and oxidising conditions, during the oxidation of Pu(IV) to Pu(VI) with concentrated HClO_4 at 208 °C could have leached the borosilicate glass tube and thereby introduced these elements into the Pu-solution.

Anyway, measurement of the ^{239}Pu concentration in the solution containing the precipitate showed the same concentration as measured right after preparation of the Pu(VI) carbonate solution.

Table 5: Results of SEM-EDX analysis of 3kDa isolated precipitate. Values <0.1% are below detection limit.

Sample	Element (at-%)									
	C	O	Na	Si	S	Cl	Ca	Fe	U	Pu
1	52.7	43.9	1.4	0	0.1	0.1	1.7	0	0	0
2	67.3	30.1	2.3	0	0	0.2	0	0	0	0
3	67.0	32.6	0.4	0	0	0	0	0	0	0
4	64.4	35.0	0.5	0	0	0.1	0	0	0	0
5	12.7	72.0	2.8	0	0.3	0.1	11.9	0.2	0	0
6	59.5	37.9	1.6	0.3	0	0.1	0	0.5	0	0
7	58.8	39.7	0.8	0.1	0	0	0.3	0.3	0	0
8	57.4	41.8	0.6	0	0	0	0.1	0.1	0	0
9	68.5	24.2	1.0	0.8	0	0.6	0.2	4.7	0	0
10	58.5	31.4	7.2	0.2	0	2.2	0	0.5	0	0
11	65.0	33.0	1.3	0.2	0	0.1	0	0.1	0	0
12	68.5	30.6	0.8	0.1	0	0	0	0	0	0
13	65.3	32.9	1.5	0.1	0	0.1	0	0.1	0	0

1.7 Preparation of Fe and magnetite coupons

Four coupons with 99.9% purity were cut and polished with a 4000 mesh sand papers. Two of them were then stored in acetone in refrigerator while the other two coupons were pre-corroded for six months in distilled water at 80 °C. A thick black coloured corrosion layer formed on these two coupons. The fact that corrosion product particles fallen down to the bottom of the vessel could be moved by magnetic stir, suggests that magnetite (Fe₃O₄) is the dominant corrosion product. It was also confirmed by both Raman spectroscopy and XRD. The coupon materials (Fe and Fe covered by magnetite) were cut into pieces with similar surface area (Table 6).

Table 6: Preparation of iron and magnetite coupons.

Sample	Cut	Length (mm)	Depth (mm)	Thickness (mm)	Area (mm ²)	Weight (g)
Fe coupon 1	Middle	5.5	10.0	0.95	139.5	0.3640
Fe coupon 2	End	5.6	10.0	0.95	141.6	0.3638
Fe magnetite 1	End	8.4	7.2	1.00	152.2	0.4307
Fe magnetite 2	Middle	7.7	7.2	1.00	140.7	0.3901

1.8 Start of Pu(VI) reduction experiment

The reaction vessel, in N₂ purged glovebox, was equipped with a holder for the five LSC vials, and the oxygen trap was placed in the middle of the reactor, see Figure 3. The oxygen trap consisted of freshly mixed CaCO₃ and FeSO₄. MilliQ-water was added at the bottom of the reactor to get water vapour saturated atmosphere and thereby avoiding Pu-solution evaporation.



Figure 3: Start of the Pu(VI) reduction experiment. In foreground the reactor with five 20ml glass LSC vials (2x Fe coupon, 2x magnetite and one reference) and the oxygen trap in the middle of the reactor. In background the gas bubbling flask to determine the purging rate and act as water lock for oxygen intrusion.

The filtered Pu-solution was poured into new 20ml glass liquid scintillation counting (LSC) vials. The vials were placed in the holder in the reactor and the iron and magnetite coupons were added into labelled Pu-vials, respectively. The reactor was purged with a gas mixture (Basi Schröbert GmbH, Germany) of 0.0302 ± 0.0006 vol-% CO₂ (quality 4.5) and the rest Ar (quality 5.0) at high throughput for 20 minutes. After this time period the gas purging was set to 3 bubbles/s and kept at this purge-rate for the rest of the experiment. The experiment was run at a temperature of 23 ± 2 °C.

The Pu-solutions were sampled after 0, 1, 7, 37, 77, and 114 days. The sampling was made with a long steel cannula inserted through the rubber sealing located at the top of the reactor vessel. The solution was sucked up into a disposable 2-ml syringe. The syringes were exchanged between each sampled Pu-vial and the cannula cleaned. During sampling, additional surgical gloves were used on the inside of the glovebox to avoid contamination of the Pu-samples.

1.9 The Pu(VI) reduction experiment

The experiment was run continuously, without opening the reactor or gas supply interruption. The oxygen trap became darker with increasing experimental time. Optical inspection of the vials containing the Pu-solution and the coupons showed a reddish colour appearing on the vial bottom and surrounding each coupon. The first appearance occurred after approximately 50 days of experiment.

1.10 Termination of Pu(VI) reduction experiment

The experiment was terminated after 114 days (see Figure 4, 5). Still under gas purging and with an glovebox atmosphere of 0.32 vol-% O₂, 12 ppm H₂O and the rest N₂, the reactor was opened. The ²³⁹Pu-solution, in contact with the iron coupon, was transferred from 20ml glass vials, into new 20ml plastic LSC vials, leaving the iron coupon in the glass vial. The iron coupon was taken out of the vial, dried on a Kleenex and rinsed twice for 2 seconds in freshly prepared 10ml 10mM NaCl + 2mM NaHCO₃ solution. The coupon was dried in 0.03vol% CO₂ /Ar gas stream. The iron coupon was transferred to the original vials used before the start of the experiment.

Two of the coupons (Fe coupon 1 and Fe magnetite 1) were prepared for SEM-EDX analysis while the other two coupons (Fe coupon 2 and Fe magnetite 2) were bagged out from the glovebox and used for α -track analysis.

The ²³⁹Pu solutions obtained after terminating the experiment was used for different analyse: SF-ICP-MS analysis, γ -spectrometry, Transmission electron microscope coupled to energy dispersive Y-ray spectroscopy (TEM-EDX), pH measurement and absorption spectrometry.



Figure 4: Termination of the Pu(VI) reduction experiment.

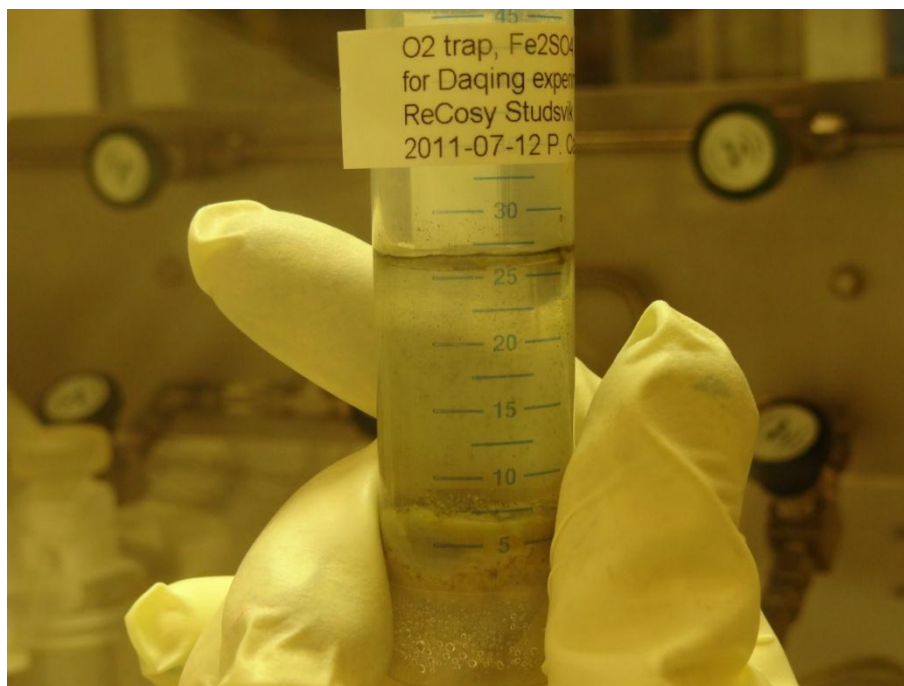


Figure 5: Oxygen trap, picture taken at the end of the experiment, which existed inside the reactor during the experiment. If there would have been oxidising condition inside the autoclave a reddish colored precipitation would be found in the trap.

1.11 α -track analysis of Fe and magnetite coupon surfaces

The α -track analysis was performed on both sides of the two iron coupons (Fe coupon 2 and Fe magnetite 2). The surface of the coupon was placed in contact with an α -sensitive cellulose nitrate film (CN85, Kodak, France). Four squares, with the dimensions similar to the coupons, were engraved in the film with a sharp-edge pincette. The individual squares were used for different pellet exposure times, varying between 10 sec and 1000 sec. The purpose of this procedure was to find an appropriate exposure time for each intensity of the α -spots since highly active α -spots made so many α -tracks that the tracks overlap each other. The background α -radiation in the glove box 3, lab A132 was monitored by observing the area beside the exposed squares.

After the exposure the film was etched in 6.5M NaOH at 60°C for 15min. Subsequently, the etched film was rinsed for 10min in milliQ-water. In order to identify the intensive α -radiation spots the etched film was investigated with an optical microscope (AxioPlan 2, Zeiss AG, Germany) equipped with a camera. In order to be able to count individual α -tracks the films were searched with a magnification of 5x, 10x, 20x, and 50x. An area of the same size as the iron coupon surface was searched for α -spots and average α -track density.

Four developed films were searched under the microscope: the exposed front (upper) and back of the coupons "Fe coupon 2" and "Fe magnetite 2". The maximal exposure time of 1000 s gave optimal α -track density and all of the following results are based on images for this exposure time.

Firstly, the optical inspection in the microscope showed that only the upper side of coupon "Fe magnetite 2" showed α -tracks. We assume that the upper surface received

more Pu-deposition than the one directed towards the bottom of the glass vial, as a consequence of restricted exchange of solution.

Secondly, the upper surfaces of Fe magnetite 2 showed 15 hotspots with different α -track density, here denominated as α -spots (Figure 6, 7 and 8). The α -track densities in the hotspots varied from 1 to 10 α -track/100 μm^2 (Table 7).

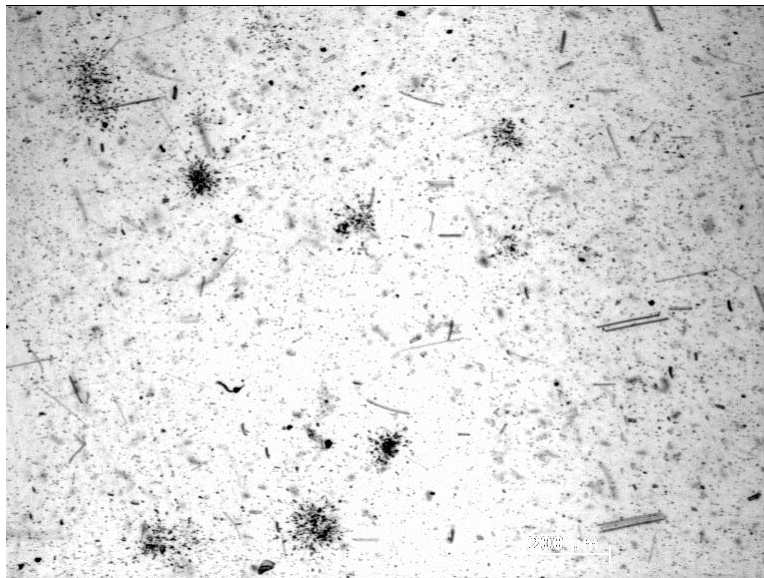


Figure 6: Distribution of α -tracks from film exposed to Fe Magnetite 2 coupon (exposure time 1000 s, magnification 5x). A number of α -spots (accumulation of α -tracks) are easily visible on the left side of the picture.



Figure 7: α -tracks from Fe Magnetite 2 coupon (exposure time 1000 s, magnification 20x). The picture is a zoom-in on the upper left corner of Figure 6.

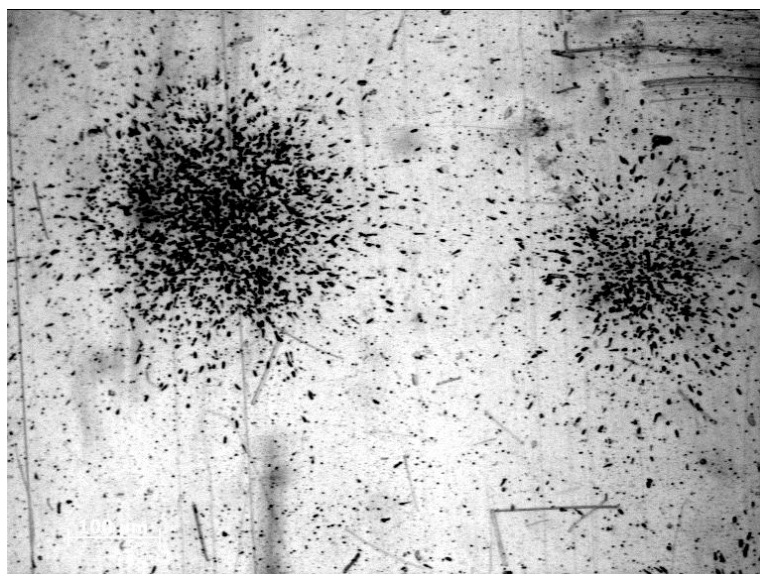


Figure 8: The image shows the most intensive α -spot observed on the Fe Magnetite 2 coupon (exposure time 1000 s, magnification 10x).

Using the α -track density on the exposed CN-85 film the surface deposition of ^{239}Pu could be determined (Table 8). The calculation shows that the ^{239}Pu activity in the 15 α -spots (0.17 Bq) is negligible in comparison to the average surface ^{239}Pu activity (1390 Bq) measured on the entire Fe magnetite coupon upper surface. The amount of ^{239}Pu deposited on the coupon was $2.5 \cdot 10^{-9}$ mol and should be compared to the amount of ^{239}Pu added to each 20ml LSC vial of $2.1 \cdot 10^{-7}$ mol.

Table 7: Results of the α -track analysis originating from ^{239}Pu decays on iron and magnetite coupons. The counting efficiency was set to 40% [Durrani et al., 1987].

Denomination	Average, excluding α -spots (Bq/ μm^2)	Minimum α -spot (Bq/ μm^2)	Maximal α -spot (Bq/ μm^2)
Fe coupon 2, front	$2.5 \cdot 10^{-8}$	n.d.	n.d.
Fe coupon 2, back	$2.5 \cdot 10^{-8}$	n.d.	n.d.
Fe magnetite 2, front	$2.5 \cdot 10^{-7}$	$2.5 \cdot 10^{-6}$	$2.5 \cdot 10^{-5}$
Fe magnetite 2, back	$2.5 \cdot 10^{-8}$	n.d.	n.d.
Background	$2.5 \cdot 10^{-8}$	n.d.	n.d.

n.d. means "not detected"

This means that approximately 1 % of the total amount of ^{239}Pu is deposited on the Fe magnetite 2 coupon surfaces. Assuming a homogenous coverage of the surface approximately 6 atomic $^{239}\text{PuO}_2$ layers were deposited and should be compared with 470 layers that could be formed in case all ^{239}Pu added to the 20ml LSC vial would have been precipitated. The absence of α -spots on the Fe coupon implies that there are no

larger colloidal PuO₂ aggregates formed and deposited during the duration of the experiment.

Table 8: Calculation of deposited amount ²³⁹Pu.

Denomination	Total amount ²³⁹ Pu, without α -spots (mol)	Total amount ²³⁹ Pu, in α -spots (mol)
Fe magnetite 2, front	$2.5 \cdot 10^{-9}$	$3.1 \cdot 10^{-13}$
Amount ²³⁹ Pu added at start	$2.1 \cdot 10^{-7}$	-
Deposited fraction of ²³⁹ Pu	$1.2 \cdot 10^{-2}$	-
Number of ²³⁹ Pu mono-layers	6 (470)	-

1.12 SF-ICP-MS and γ -spectrometry analysis of ²³⁹Pu(VI) samples

Sector field inductively coupled plasma mass spectrometry, SF-ICP-MS (Element2, Thermo Scientific, Germany), measurements were made on all samples, except for the sampling during termination of the experiment (114 days), to determine the concentration of Fe and Pu. The sampled ²³⁹Pu-solutions (approximately 1ml) from the on-going experiment were diluted 1:10 with 1M HNO₃. This low dilution factor was selected to be able to run the SF-ICP-MS in medium resolution so that ⁵⁶Fe can be resolved from the interference of ⁴⁰Ar+¹⁶O.

All samples were analysed in duplicates, one with and one without internal standard addition. The elements Co and Ho (0.30ml 20ppb Co and 0.15ml 20ppb Ho) were used as internal standards. All samples were acidified to 1 M HNO₃. At the start of each measurement, a multi-element calibration was made using certified standards (Agilent Life Sciences/Chemical Analysis GmbH, Germany). Calibration standards with the concentrations 0, 50, 200, 1000, 5000, 20000, 50000 and 100000 ppt were prepared. Two quality-check solutions, each containing 1 ppb of one of the multi-element standards plus 1 ppb of the internal standard, were run to monitor the ICP-MS performance. The estimated uncertainty in the SF-ICP-MS determination of the concentrations of ²³⁹Pu is ~10% and for Fe approximately 20%.

The elemental Fe results are based on the low resolution measurements of ⁵⁷Fe and the medium resolution measurements of ⁵⁶Fe and ⁵⁷Fe. Both ⁵⁷Fe results did confirm each other nicely and also the ⁵⁶Fe vs. ⁵⁷Fe results were in agreement with the natural isotopic composition.

The γ -measurements were made using a high-purity Ge-detector in 2 π -geometry (EG&G Ortec Inc., USA). The standard used for the γ -spectrometric measurement of un-separated dilutions was the mixed radionuclide standard solution PD954 (QSA Global GmbH, Braunschweig, Germany). The expanded uncertainty (k=2) on each radionuclide in this mixed standard is 5%. The mixed radionuclide standard solution is certified as shown in Table 9.

Table 9: *Certified calibration standard for γ -spectrometry, PD954 (reference date: 2007-06-01).*

Radionuclide	Energy (MeV)	Activity (Bq)
²⁴¹ Am	0.060	$3.21 \cdot 10^3$
¹⁰⁹ Cd	0.088	$1.73 \cdot 10^3$
⁵⁷ Co	0.122	$5.97 \cdot 10^3$
¹³⁹ Ce	0.166	$8.06 \cdot 10^3$
²⁰³ Hg	0.279	$1.78 \cdot 10^3$
¹¹³ Sn	0.392	$2.75 \cdot 10^3$
⁸⁵ Sr	0.514	$3.61 \cdot 10^3$
¹³⁷ Cs	0.662	$2.71 \cdot 10^3$
⁸⁸ Y	0.898	$5.93 \cdot 10^3$
⁶⁰ Co	1.173	$3.01 \cdot 10^3$
⁶⁰ Co	1.333	$3.01 \cdot 10^3$
⁸⁸ Y	1.836	$5.93 \cdot 10^3$

The samples collected after 114 days of experiment were measured with γ -spectrometry (reference date: 2011-06-01) without dilution, together with background samples. Contribution from the background measurement was negligible. The expended uncertainty ($k=2$), by γ -spectrometry, of the concentrations of ²³⁹Pu is <6%.

The results indicated that the Fe concentration is approximately the same in all samples (0-77 days), even though there is a certain spread, averaging at $5 \cdot 10^{-6}$ M (Figure 9). The Fe(II) concentration also suggested that our experiment was at well controlled reducing conditions.

The ²³⁹Pu concentration during the experiment is shown in Figure 10. The concentrations during the time period 0-77 days were measured by SF-ICP-MS while the last values (at 114 days) are measured by γ -spectrometry. It can be concluded that the ²³⁹Pu concentration is similar in all samples and independent of the measurement technique. Taking into account the measurement uncertainty there are no ²³⁹Pu concentration differences between the samples and the reference. The ²³⁹Pu concentration converges towards an average concentration of $0.9 \cdot 10^{-5}$ M.

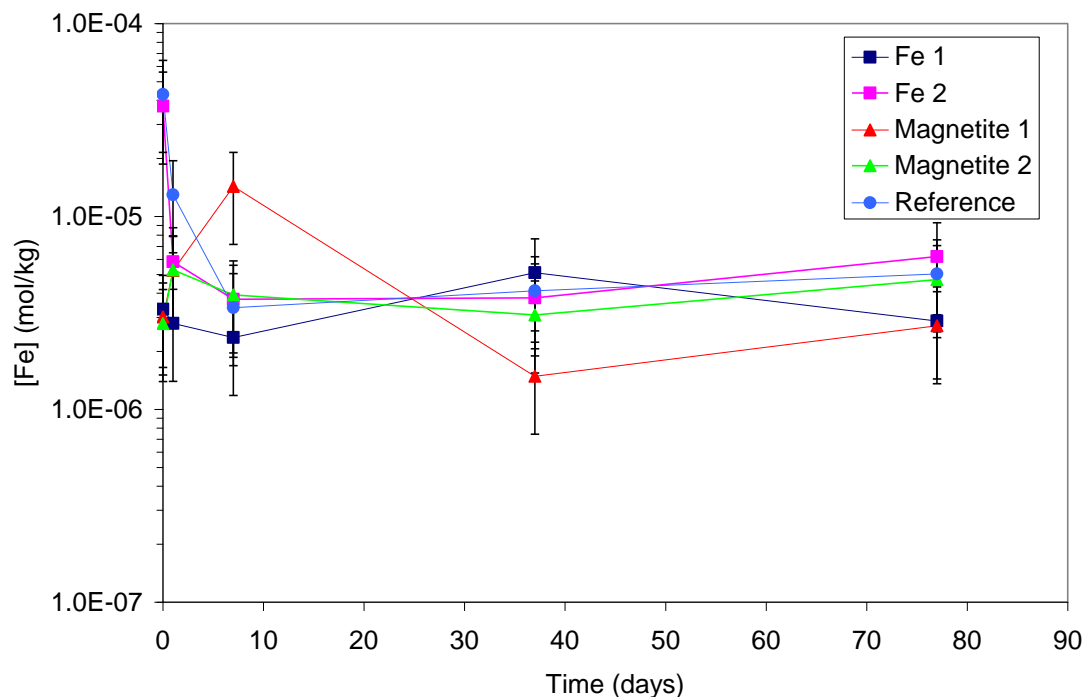


Figure 9: Concentration of Fe in Pu(VI)-solution during the experiment (0-77 days).

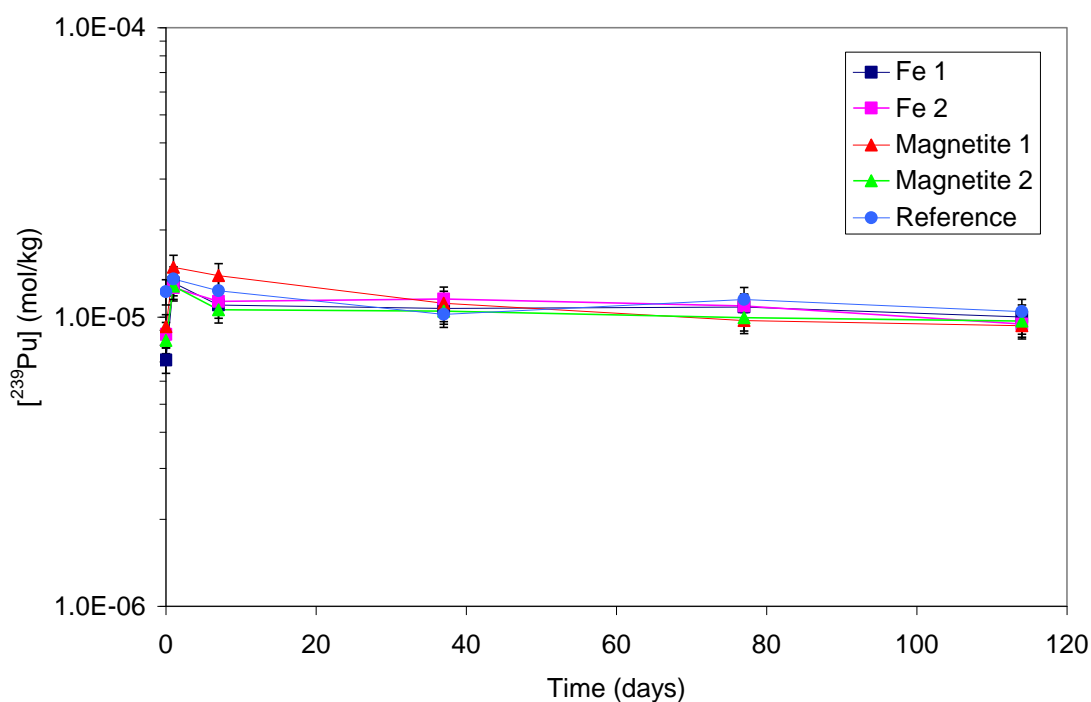


Figure 10: Concentration of ²³⁹Pu in Pu(VI)-solution during the experiment (0-114 days). The results during the time interval 0-77 days are measured by SF-ICP-MS and the last values (114 days) by γ -spectrometry.

1.13 SEM-EDX analysis of cross section of Fe and magnetite coupons

Both samples (Fe coupon 1 and Fe magnetite 1 (iron coupon covered with magnetite)) were mounted perpendicular in a Bakelite ring with a diameter of 25.4 mm (Figure 11). The position was fixed by embedding in epoxy resin (EPOTHIN, Buehler).

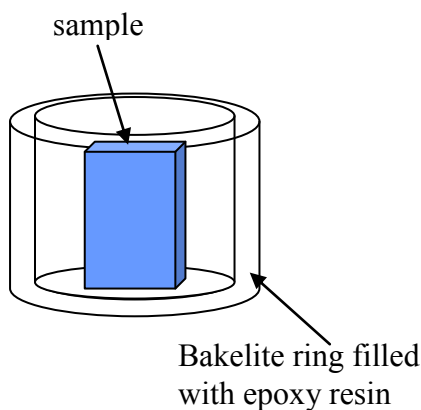


Figure 11: Embedding of iron coupon after termination of the experiment (114 days).

After curing the samples they were wet polished on the narrow side with SiC grinding paper (grit 400, 600, 1200, 2400). Thereafter they were rinsed and cleaned. They were transferred to the SEM-EDX. Here an electrical contact was made to the iron by conductive silver paint. No coverage with graphite or gold was necessary for the investigations.

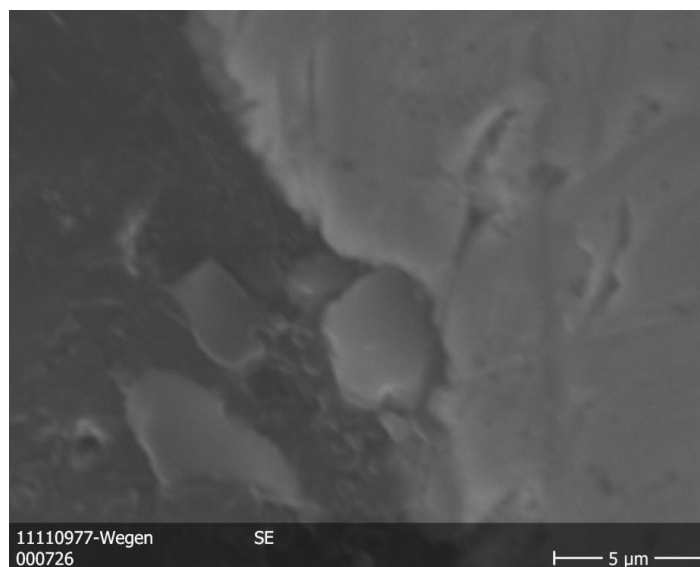


Figure 12: SEM picture of Fe magnetite 1 coupon after termination of the experiment (114 days). Light grey areas represent the metallic phase, dark grey areas are resin and magnetite is middle grey.

SEM and EDX examinations were performed at the interface between resin and sample and on the sample near the edges. Detailed pictures and spectra were compiled and in total 41 areas were investigated.

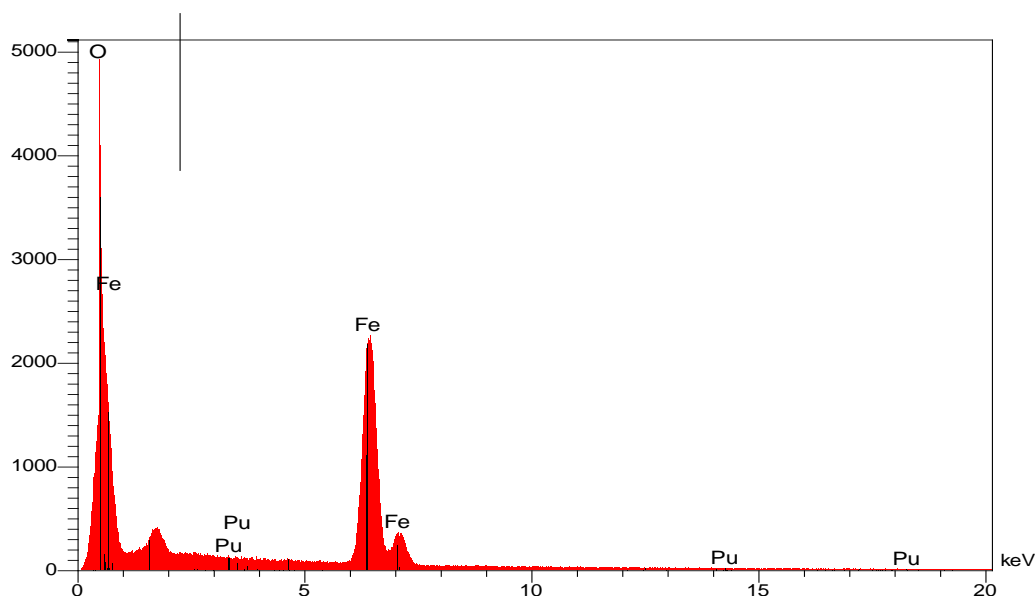


Figure 13: SEM-EDX spectra related to picture 726 (Figure 5) of Fe magnetite 1 coupon after termination of the experiment (114 days). The spectrum is taken from the left middle side of coupon.

An example of one of the analysis is shown in Figure 12, 13 and the corresponding SEM-EDX result in Table 10. In some cases SiC particles were identified. No significant signal was obtained by EDX for Pu. The Pu content is, if there is one, very low.

Table 10: SEM-EDX result related to picture 726 (Figure 12, 13) of Fe magnetite 1 coupon after termination of the experiment (114 days). The detection limit for Pu, by the used SEM-EDX, is above 0.5 at-%.

Element	Line	Intensity	Weight-%	Atom-%
Fe	K _α	519.1	99.48	99.88
Pu	M _α	2.1	0.52	0.12
			100.00	100.00

1.14 TEM-EDX analysis of ²³⁹Pu solution

For TEM analysis a drop of the Pu-solution “MP2 Pu-239, Fe magnetite 2, T114days, ReCosy Studsvik, 2011-11-04 P. Carbol” was dropped on a carbon filmed copper grid. TEM measurements were conducted with a FEI Tecnai G² F20 XT transmission electron microscope operating at 200 kV. The sample was analyzed by conventional transmission electron microscopy (TEM), scanning transmission electron microscopy

(STEM) and energy dispersive X-Ray analysis (EDX). However, Pu-particles or Pu as an amorphous film on the grid could not be detected with the TEM.

1.15 pH measurement of ^{239}Pu solution

pH in all five ^{239}Pu solutions, collected after termination of the experiment (114 days), was determined using pH indicator sticks (Merck, Germany). The pH indicator pH range is 7.0-14.0, in steps of 0.5 pH-units. There were no pH differences between the five solutions; they all showed a pH of 10.0 ± 0.5 . The relatively high pH, compared to a pH of 8.2-8.5 as expected in a solution buffered with 2mM NaHCO_3 and purged with 0.03 vol.% CO_2/Ar gas, is due to the preparation step where a 0.5M Na_2CO_3 solution was used to stabilize Pu(VI) (see section 1.3 and 1.4).

1.16 Absorption spectroscopy of ^{239}Pu solution

Three ^{239}Pu solutions, collected after termination of the experiment, were used for absorption spectroscopy to provide evidence that the Pu in the solution exists as Pu(VI) by detection of the Pu(VI) peak at 820nm. Different spectroscopy systems, installed in glovebox, were used (Ocean Optics: 1-cm cuvette coupled to USB4000 with the MicroPack UV-VIS-NIR light source DH 2000 BAL) and PerkinElmer spectrophotometer. Unfortunately, the detection limit for these systems, using a cuvette with a 1-cm path length, is $1 \cdot 10^{-5}$ M Pu. If there would have been more solution available a 10cm-path length could have been tried.

Summary and conclusions

The project started with preparation of a Pu(VI) carbonate solution. Speciation showed that $\text{PuO}_2(\text{CO}_3)_3^{4-}$ is stable at pH higher than 9. Without direct evidence if Pu exists as Pu(VI) in the solutions four indirect proofs were used as evidence for the existence of Pu(VI)-carbonate as the dominating Pu species. Firstly, only Pu as Pu(VI) is stable, for longer periods at a Pu-concentration of 10^{-5} M Pu in air atmosphere and in 20mM carbonate solution at pH 10. Normally, Pu(IV) precipitates as $\text{Pu}(\text{OH})_4(\text{s})$ at $\text{pH} > 5$. In highly concentrated carbonate solutions (1-2.5 M) tetravalent Pu can form $\text{Pu}(\text{CO}_3)_4^{4-}$ and $\text{Pu}(\text{CO}_3)_5^{6-}$ complexes (Morss et al., 2006).

Anyhow, in our experiment the formation of Pu(VI) was clearly visible during the Pu(IV) oxidation with fuming HClO_4 . Over a period of 114 days there were no changes of the Pu concentration in the reference solution indicating a stable Pu(VI) solution (at pH 10, $[\text{CO}_3^{2-}]$ of ~20mM, Figure 14). Secondly, the fact that all Pu-solutions, before the experiment start, were centrifuge-filtrated through a 3000 Dalton filter without reduction in Pu concentration indicate that if colloids are present they must consist of aggregates < 11 PuO_2 molecules. Thirdly, the TEM investigation of Pu-solution collected after experiment termination showed no Pu-particles (even at a size level of 10\AA). Fourthly, there were no evidence of larger Pu-agglomerates on the Fe coupon indicating Pu(VI) hydroxide precipitates.

The study of Pu(VI) reduction by Fe or Fe₃O₄ in 20 ml of a solution 0.1M NaCl + 0.084M Na₂CO₃ solution at pH 10 (with a CO₃²⁻ concentration of ~20mM, Figure 14) showed that Pu deposition occurred only on Fe₃O₄ surfaces. Despite the fact that the calculations give negative ΔG -values for the reactions between Pu(VI) and Fe or Fe₃O₄, only approximately 1% of the added ²³⁹Pu was found on the Fe₃O₄ surface after 114 days contact time.

The concentration of Fe was similar in all solutions including the reference. Calculations show that FeCO₃(s) is the solubility limiting phase at pH 10 (Figure 14).

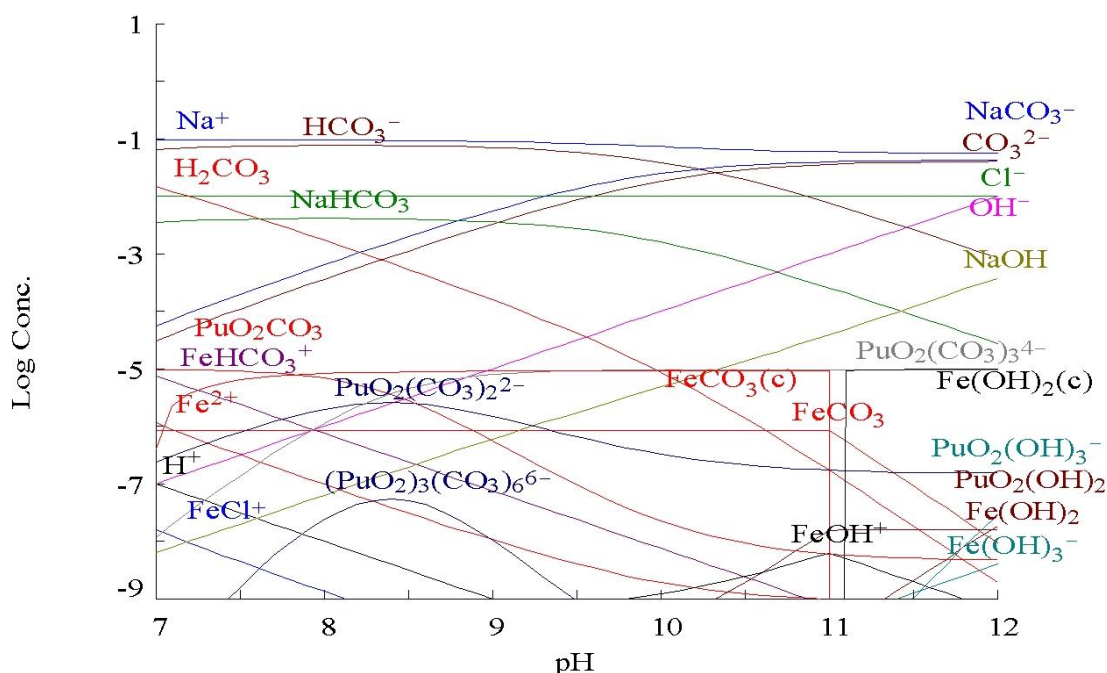


Figure 14: Speciation calculations of Fe and Pu in solution after termination of the experiment (114 days). The total concentrations used in the speciation were: $[Na^+] = 0.1M$, $[CO_3^{2-}] = 0.084M$, $[Fe^{2+}] = 10\mu M$, $[PuO_2^{2+}] = 10\mu M$ and $[Cl^-] = 0.01M$.

Acknowledgement

The authors acknowledge the valuable discussions with A. Morgenstern and M. Altmaier. The preparation and dissolution of the Pu metal was made by M. Vargas. The research leading to these results has received funding from the European Union's European Atomic Energy Community's (Euratom) Seventh Framework Programme FP7/2007-2011 under grant agreement n° 212287 (RECOSY project).

The participation of Daqing Cui in this research work was partly supported by SKB, Sweden (Project 19073 & collaboration agreement 30636) and ONDRAF/NAIRAS, Belgium (Project 2008009379/2008009381).

References

- Cui D., Puranen A., Scheidegger A., Grolimund D., Wersin P., Leupin O., Spahiu K. (2007). On the interaction between iron canister material and fission products ⁷⁹Se and ⁹⁹Tc under simulated deep repository conditions. NF-PRO report Contract Number: FI6W-CT-2003-02389, RTDC 2-WP 2.5 Task 7.
- Durrani S. A., Bull, R. K. (1987). Solid state nuclear track detection. In: Principles, Methods and Applications. Pergamon Press, Oxford, England.
- Fedoseev A. M., Shilov V. P. (2010). Oxidation of Am(III) to Am(IV) with ozone in solutions of heteropolyanions. Radiochemistry **52**(1), 40–42.
- Ghosh Mazumdar A. S., Sivaramakrishnan C. K. (1964). A study of the nitrate and the chloride complexes of plutonium(VI) by solvent extraction technique using TTA as the chelating agent. J. Nucl. Chem. Proc. Vol. **27**, pp. 2423-2427.
- Hixon A. E., Hu Y.-J., Kaplan D. I., Kukkadapu R. K., Nitsche H., Qafoku O., Powell B. A. (2009). Influence of iron redox transformations on plutonium sorption to sediments. Radiochim. Acta Vol. **98**, Issue 9-11, Migration 2009, pp. 685-692. doi: 10.1524/ract.2010.1769.
- Lucchini J. F., Khaing H., Richmann M. K., Borkowski M., Reed D. T. (2008). Plutonium (VI) and Uranium (VI) reduction by iron (II) at high pH under subsurface conditions. Plutonium Futures Conference "The Science". Dijon, France, July 7-11, 2008, LA-UR-0808-04292.
- Morss L. R., Edelstein N. M., Fuger J. (2006). The chemistry of the Actinide and Transactinide Elements. Springer, Dordrecht, the Netherlands.
- Newton T. W., Hobart D. E., Palmer P. D. (1986). The formation of Pu(IV)-colloid by the alpha-reduction of Pu(V) and Pu(VI) in aqueous solution. Radiochim. Acta **39**(3), 139-147.
- Reilly S. D., Neu M. P. (2006). Pu(VI) hydrolysis: Further evidence for a dimeric Plutonyl hydroxide and contrasts with U(VI) chemistry. Inorg. Chem. **45**, 1839-1846.
- Reilly S. D., Runde W., Neu M. P. (2007). Solubility of plutonium (VI) carbonate in saline solutions. Geochim. et Cosmochim. Acta **71**, 2672-2679.
- Rondinella V. V. (2011). Failure mechanisms of high level nuclear waste forms in storage and geological disposal conditions. Handbook of advanced radioactive waste conditioning technologies. Edited by M. I. Ojovan, Woodhead Publishing Series in Energy: Number 12, Woodhead Ltd, Philadelphia, USA.
- Tait C. D., Ekberg S. A., Palmer P. D., Morris D. E. (1995). Plutonium carbonate speciation changes as measured in dilute solutions with photoacoustic spectroscopy. Yucca Mountain Site Characterization Program, Milestone Report 3350, LA-12886-MS, UC-802, Los Alamos, National Laboratory, Los Alamos, New Mexico 87545, USA.

REDUCTION OF IRON OXIDES BY S(-II) AND ITS EFFECT ON URANIUM PHASE DISTRIBUTION

V.G. ALEXANDRATOS¹, T. BEHRENDTS^{1*}

¹ Faculty of Geosciences, Utrecht University, P.O.Box 80021, 3508 TA Utrecht, NL

* Corresponding author: behrends@geo.uu.nl

Abstract

Iron oxides are important sorbents for U(VI) in natural environments. The reaction of iron oxides with S(-II) and their transformation into iron sulphides can therefore potentially lead to the mobilization of adsorbed U(VI). In batch experiments, S(-II) containing solution was added to suspensions of lepidocrocite (γ -FeOOH) and hematite (α -Fe₂O₃) which contained adsorbed U(VI). The progress of the reaction with S(-II) was followed by monitoring the dissolved concentrations of S(-II) and the concentration of acid extractable Fe(II). The effect of the sulphide addition on uranium distribution was determined by measuring the concentration of dissolved uranium. Furthermore, the redox state of solid-bound uranium was determined by X-ray absorption spectroscopy. After addition of S(-II), release of adsorbed uranium occurred within minutes. Desorption of uranium was more pronounced in experiments with hematite than with lepidocrocite. The mobilization of uranium can be explained by the change in surface speciation of the iron oxides due to S(-II) adsorption and the transformation of iron oxides into iron sulphides with a lower tendency to adsorb U(VI). This instantaneous release of uranium was, in part, reverted when dissolved S(-II) was consumed. Additionally, reduction of U(VI) to U(IV) counteracted the release of uranium during the reaction. Under present experimental conditions, adsorbed U(VI) is a stronger oxidant than the Fe(III) in the iron oxides and U(VI) should become reduced to U(IV) and precipitate in the form of uraninite. One day after the addition of S(-II), however, reduction was incomplete and only 25% of the U(VI) became reduced in experiments with lepidocrocite while about 60 -70% was in the form of U(IV) in experiments with hematite. The difference in U(VI) reduction and desorption of uranium between hematite and lepidocrocite can be attributed to the different reactivity of the two minerals towards S(-II). Hematite reacts slower with S(-II) than lepidocrocite and the time period, before dissolved S(-II) is consumed, is longer. Dissolved S(-II) seems to be required for fast reduction of U(VI) and the longer presence of dissolved S(-II) can explain the larger extent of U(VI) in reactions with hematite. However, the longer presence also accounts for the more pronounced desorption of uranium as dissolved S(-II) is necessary for maintaining the pool of adsorbed S(-II). The results demonstrate that kinetics might be important when assessing uranium mobility in environments which

switch from oxic to sulphidic conditions and that the reactivity of the iron oxides plays an important role in these dynamic systems.

Introduction

Redox conditions exert important influence on the migration of uranium. At low redox potential, tetravalent uranium (U(IV)) is the thermodynamically favoured redox state of uranium, while U(VI) is the most stable redox state of uranium at high redox potential. Reduction of U(VI) to U(IV) is generally considered to provoke immobilization of uranium as U(IV) and can precipitate as uraninite (UO₂) which has a very low solubility. The mobility of U(VI) in porous media is predominately controlled by two antagonistic processes: formation of aqueous carbonate complexes and adsorption onto mineral surfaces. In particular, iron oxides are strong sorbents for U(VI). Based on thermodynamic considerations, a change from oxic to sulfidic redox conditions is expected to cause the transformation of iron oxides into iron sulphides and the reduction of U(VI) to U(IV). However, when the reaction of iron oxides with S(-II) proceeds faster than the reduction of U(VI), adsorbed U(VI) might become released from the iron oxide surface into solution when the system becomes sulphidic. Hence, the kinetics of processes controlling uranium phase distribution can be important in systems in which redox conditions are not constant but are changing from oxic to sulphidic.

In a previous study, we investigated the consequences of sulphide addition to suspension containing lepidocrocite (γ -FeOOH) with adsorbed U(VI) (Alexandratos, et al, 2009). Upon addition of sulphide, uranium was released into solution which was explained by the adsorption of sulphide onto the lepidocrocite surface. That is, dissolved sulphide competes with U(VI) for reactive surface sites. When S(-II) was not added in excess, only up to 25 % of the uranium was reduced to U(IV). When more S(-II) was added than required for complete reaction with lepidocrocite, about 50 % of the uranium was in the form of U(IV) after 24 h reaction time. This observation led us to the conclusion that lepidocrocite can inhibit or considerably retard complete reduction of U(VI) by acting as an more efficient oxidant for S(-II). Hence, in environments containing iron oxides with adsorbed U(VI) a flux of sulphide into the system, for example convectively with groundwater or produced in situ by sulphate reducing organisms can lead to temporary mobilization of uranium.

Here, we compare lepidocrocite with hematite regarding the consequences of adding sulphide on the phase distribution of uranium. Hematite has a lower reactivity towards sulphide and is therefore expected to be a weaker competitor for the reaction with S(-II) than lepidocrocite. The question is whether the lower reactivity of the iron oxide facilitates reduction of U(VI). A lower reactivity towards S(-II) implies that dissolved S(-II) is removed slower from solution which is expected to have an effect on uranium distribution as dissolved S(-II) competes with U(VI) for surface sites on the iron oxide surface. Hence, the second question addresses the differences between lepidocrocite and hematite regarding the desorption of uranium upon addition of S(-II).

Materials and Methods

Materials

Lepidocrocite and hematite were synthesized according to the procedures described in (Schwertmann and Cornell, 2000). After synthesis, the suspensions were dialyzed against deionized water and kept in aqueous suspension until used in experiments. The N₂-BET surface area of lepidocrocite was determined as 78 m² g⁻¹. From XRD measurements, the particle size of the hematite was determined from the peak width by using the Scherrer equation to be about 15 nm. This particle size corresponds to a specific surface area of about 80 m² g⁻¹ when assuming spherical particles. Stock solutions of U(VI) and S(-II) were prepared from uranyl acetate and Na₂S, respectively. All experiments were performed in a glove box under N₂ (95%) H₂ (5%) atmosphere. The glove box was equipped with a Pd catalyst and an O₂ monitor in order to maintain oxygen levels below 10 ppm. The temperature in the glove box was kept constant at 25 °C.

Reduction experiments

Hematite and lepidocrocite suspensions with a concentration of about 1 g L⁻¹ solid were prepared by diluting the stock suspensions with deionized water. Afterwards the suspension was purged with Ar to remove dissolved CO₂. The ionic strength in the suspensions was adjusted to 0.1 M by adding the required amount of NaCl. The pH in the experiments was kept constant at pH 8.0 by adding the buffer TAPS (0.04 M C₇H₁₇NO₆S) and by readjusting the pH with HCl or NaOH if necessary. Prior to the addition of S(-II), U(VI) solution was added to give a final concentration of about 13.5 µM and the suspensions were equilibrated for 24 h. The reaction with sulphide was initiated by adding S(-II) stock solution yielding concentrations of 1, 5, and 10 mM. The suspensions were stirred with a magnetic stir bar during the reaction. In order to monitor the progress of the reaction, aliquots were taken with a syringe. For determining dissolved S(-II) and U(VI), the suspension was filtered using 0.2 µm pore-size nylon membrane filters. For measuring the total concentration of Fe(II) in the suspensions, 0.5 mL of the suspension was added to 0.5 mL 6N HCl and extracted for at least 1 h. The concentration of Fe(II) in the HCl extracts was determined using the ferrozine method (Viollier, et al, 2000). After filtration, dissolved S(-II) was trapped in zinc acetate solution and the S(-II) concentration was determined by spectrophotometry using the methylene blue method (Cline, 1969). Uranium concentrations were determined by ICP-MS.

X-ray absorption spectroscopy

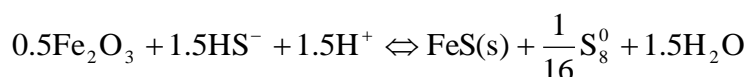
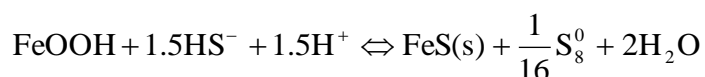
About 100 -150 mL of suspension were filtered over 0.2 µm pore-size filters (polycarbonate, Millipore) which were installed in a twist cap filter holder. The retained wet pastes were removed from the filter and placed into the cavity of a custom made sample holder (PTFE). The cavity was closed with Kapton tape and each holder was heat-sealed in LDPE bags. All samples were stored at -80 °C and transported on dry ice to the beamline. X-ray absorption spectra were collected at the DUBBLE beamline (BM26a) at the ESRF in Grenoble, France. The samples were installed in a cryostat (30 K) during measurement. Spectra were collected in fluorescence mode at the U L_{III} edge

around 17.17 keV. Energy calibration was performed by adjusting the first maximum of the first derivative of the yttrium foil spectrum to 17.038 keV. X-ray spectra were processed using the Athena software (Ravel and Newville, 2005). Factor analysis of the normalized X-ray spectra in the range between 17.10 and 17.25 keV was performed by using the ITFA software (Rossberg, et al, 2003). In addition to spectra obtained from the experiments with hematite and lepidocrocite, a spectrum from a U(IV) standard was used in the ITFA analysis. The U(IV) standard was produced by reducing U(VI) with Ti(III) in acidic solution and precipitating the solid in the presence of silica gel by adding NaOH. In this standard, U(IV) occurs predominately as a coprecipitate with titanium oxide. In the iterative target test, the relative concentration of the second component was constrained to one for the U(IV) standard. The concentration of the first component was set to one for spectra containing U(VI) adsorbed onto hematite.

Results

Reaction of iron oxides with sulfide

Concentrations of dissolved sulphide decreased rapidly after addition of sulphide stock solution (Fig. 1). Virtually all dissolved sulphide was consumed within 30 min of reaction time in experiments with lepidocrocite. The reaction of S(-II) with hematite was less vigorous than with lepidocrocite. Most of the dissolved sulphide was removed from solution within about 1h reaction time when 1mM or 5mM of S(-II) were added, but, in contrast to lepidocrocite, dissolved sulphide concentrations were still above 0.1 mM 24 h after sulphide addition. When 10 mM S(-II) were added, S(-II) concentrations were about 2.5 mM after 5 h and stayed constant until 24 h of reaction time (data not shown). In this experiment, consumption of S(-II) ceased although not all Fe(III) became reduced. Concentrations of Fe added in the form of hematite and lepidocrocite were about 12.2 mM and 9.3 mM, respectively. When 10 mM of S(-II) were added to hematite suspensions, concentrations of HCl extractable Fe(II) (Fe(II)_{HCl}) reached values of around 8mM. Hence, about one third of the initial Fe(III) still occurred in its oxidized state when consumption of dissolved S(-II) ceased after 5 h of reaction. In general, concentrations of Fe(II)Fe(II)stabilized and stayed constant over time. According to Poulton et al. (2004), the stoichiometry of the reaction of lepidocrocite and hematite with S(-II) at pH 8 is given by:



Based on this stoichiometry, Fe(II)_{HCl} concentrations of 6.6, 3.3, and 0.66 mM are expected when the reaction is completed after addition of 10, 5, and 1 mM of S(-II), respectively. Hence, the measured Fe(II)_{HCl} concentrations were in the range of those expected from the proposed stoichiometry in experiments with lepidocrocite. In experiments with hematite, Fe(II)_{HCl} concentrations were lower than the stoichiometric

values when 1 or 5 mM of S(-II) were added or higher when 10 mM of S(-II) was added.

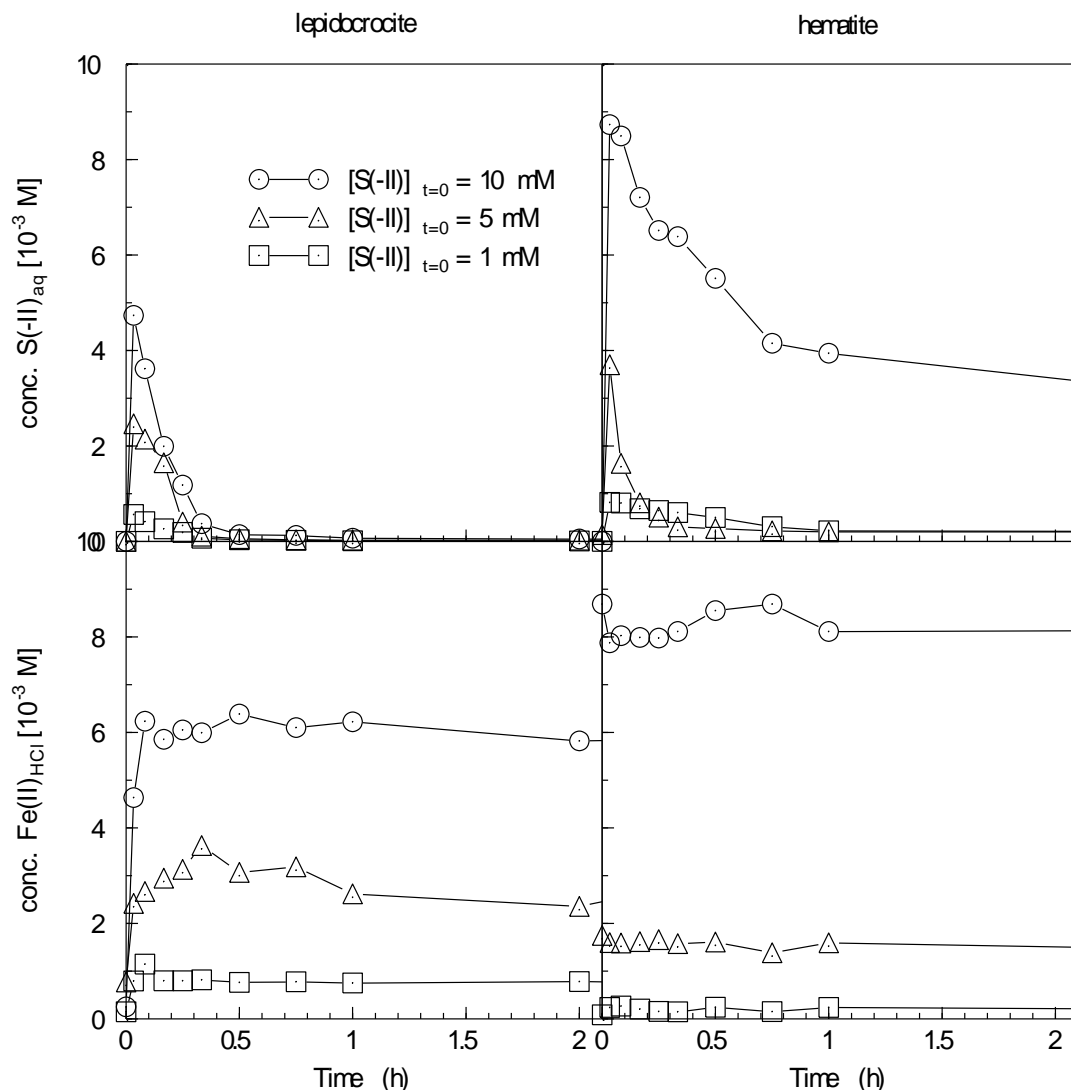
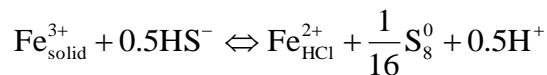


Figure 1: Time evolution of dissolved S(-II) and of HCl extractable Fe(II) in the experiments with lepidocrocite and hematite. Fe concentrations added in the form of hematite and lepidocrocite were 12.2 and 9.3 mM.

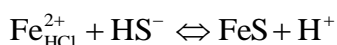
The time evolution of dissolved S(-II) and Fe(II)_{HCl} concentrations were in line with trends reported by Poulton (Poulton, et al, 2004). These authors also reported a lower reactivity of hematite towards sulphide compared to that of lepidocrocite. However, the relative difference between hematite and lepidocrocite regarding the time which was required to completely consume 5 or 1 mM of added sulphide was less than expected from results by (Poulton, et al, 2004) who obtained an about 9 times lower rate constant for S(-II) consumption by hematite than that by lepidocrocite.

Comparing the time evolution of dissolved S(-II) and Fe(II)_{HCl} shows that, after about 5 min of reaction time, S(-II) was removed from solution without accompanying production of Fe(II). This observation is in line with the experimental results of Poulton

et al. (2004) who reported that reduction of Fe(III) proceeded faster than the production of FeS. During the monitored time period of the reaction, solid bound Fe(II) accumulated which was not in the form of FeS. Thus, consumption of S(-II) was predominately coupled to Fe(III) reduction in the early stage of the reaction according to a simplified stoichiometry



Consumption of dissolved S(-II) without formation of Fe(II)_{HCl} can be attributed to the reaction of S(-II) with previously generated solid bound Fe(II) by forming FeS:



However, it cannot be excluded that part of the Fe(II)_{HCl} formed during acid extraction because the extraction vials were not purged with an inert gas to displace H₂S.

Phase distribution of uranium

Addition of sulphide caused an instantaneous increase in dissolved uranium (U(aq)) concentrations. In experiments with lepidocrocite, U(aq) concentrations quickly stabilized within 5-30 min after the abrupt increase. Concentrations of U(aq) after 2 hours reaction time were about 50 nM when 1mM of S(-II) was added and about 160 nM in experiments with higher S(-II) additions. In these experiments U(aq) concentrations decreased within the next 3 days to levels between 50 -100 nM. Only in experiments to which 10 mM of S(-II) were added, U(aq) concentrations temporarily increased further after 10 min reaction time to a maximum of about 320 nM and dropped back to the same level as in the experiment with 5 mM S(-II) addition after 30 min reaction time. Hence, the values and temporal dynamics of U(aq) concentrations in the experiments with 5 and 10 mM S(-II) addition differed predominately regarding the short-term spike of elevated U(aq) concentrations within the first 30 min of reaction with 10 mM S(-II). Afterwards, the amount of S(-II) addition appeared to be of minor importance for uranium release from the solid at these high S(-II) levels. When only 1 mM S(-II) were added, the amount of S(-II) had an effect on uranium release as U(aq) concentrations were significantly lower than with higher S(-II) loading.

The time evolution of U(aq) in experiments with hematite differed considerably to that of experiments with lepidocrocite (Fig. 2). The difference was most pronounced in the beginning of the experiment when release of uranium from the solid phase into solution was higher in experiments with hematite. Irrespective of the amount of added S(-II), maximum U(aq) concentrations reached values of about 4 µM. This concentration corresponds to about 30% of total uranium in the experiments and exceeded the concentration in experiments with lepidocrocite by about a factor of 20. In the first hour of reaction time, U(aq) concentrations followed the trend of dissolved S(-II) concentrations: After the initial increase, U(aq) decreased in parallel to the consumption of dissolved S(-II). Concentrations of U(aq) after 3 days were between 60-200 nM and

thus still higher than in experiments with lepidocrocite but the difference was less pronounced than at the beginning of the experiment.

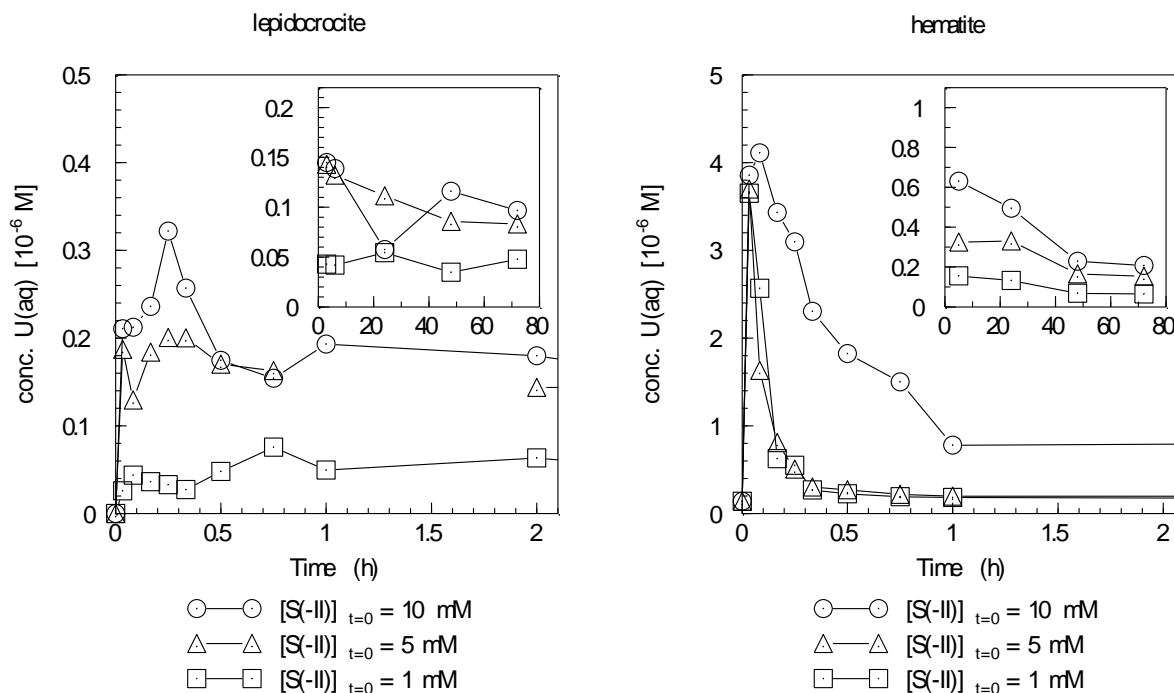


Figure 2: Time evolution of dissolved uranium ($U(aq)$) in the experiments with lepidocrocite and hematite. The insets show the time evolution after 2 hours reaction time. Total concentrations of uranium were 12 mM.

The different time evolution of $U(aq)$ concentrations on $S(-II)$ addition in experiments with hematite and lepidocrocite was also reflected in the uranium distribution when plotted against dissolved $S(-II)$ concentrations. The ratio between uranium associated with the solid phase ($U(solid)$) and $U(aq)$ did not show a pronounced dependency on dissolved $S(-II)$ concentrations in experiments with lepidocrocite (Fig. 3). The transient increase in $U(aq)$ concentrations in the first hour of reaction upon addition of 10 mM $S(-II)$ can hardly be recognized as a decrease in $U(solid)/U(aq)$ ratio at elevated dissolved $S(-II)$ concentrations. In contrast, the abrupt drop in $U(solid)/U(aq)$ ratios at highest $S(-II)$ concentrations and the concomitant increase of the ratios with decreasing dissolved $S(-II)$ concentrations can be clearly recognized for the experiments with hematite. However, the $U(solid)/U(aq)$ ratios were not a unique function of dissolved $S(-II)$ concentration. The described parallel dynamics of $U(solid)/U(aq)$ ratios and dissolved $S(-II)$ concentration occurred in all experiments with hematite irrespective of the total amount of $S(-II)$ addition.

The transformation of the two iron oxides into iron sulphides is expected to affect uranium distribution but $U(solid)/U(aq)$ ratios did not follow the extent of $Fe(II)_{HCl}$ formation in a simple manner (Fig. 3). In order to separate the effect of $S(-II)$ adsorption of that of iron mineral transformation reduction, only $U(solid)/U(aq)$ ratios were plotted when dissolved $S(-II)$ concentrations were below 0.1 mM or when the reaction had proceeded for more than 24 hours in the experiments with lepidocrocite and hematite,

respectively. In experiments with lepidocrocite, $U(\text{solid})/U(\text{aq})$ ratios were lower when $\text{Fe(II)}_{\text{HCl}}$ concentrations were larger than 2 mM. There was no significant difference between $U(\text{solid})/U(\text{aq})$ ratios measured after 5 mM or 10 mM S(-II) addition. A similar trend was observed in experiments with hematite.

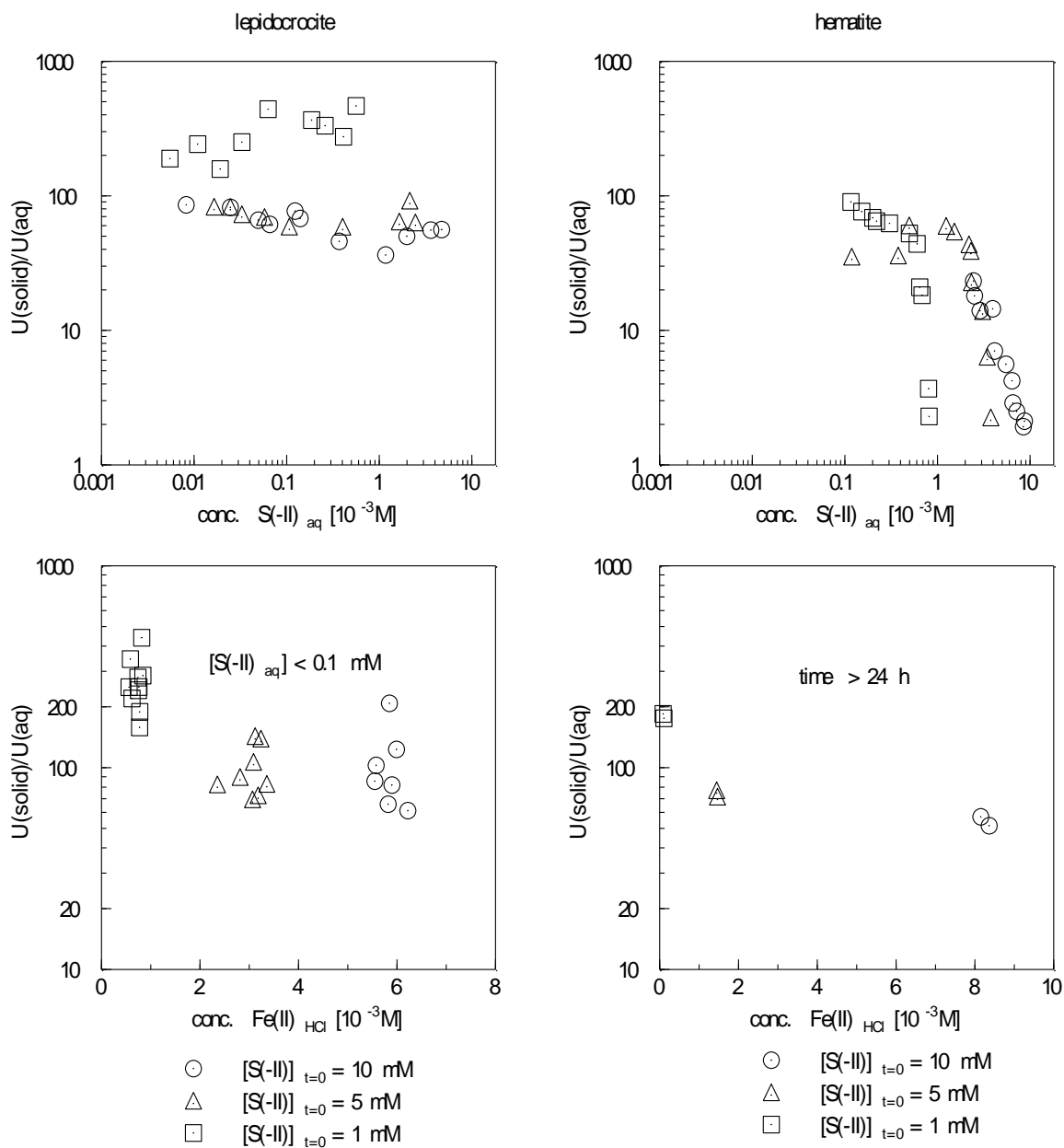


Figure 3: Ratios between solid bound uranium and dissolved uranium as a function of dissolved S(-II) concentration (upper two graphs) and as a function of HCl extractable Fe(II) (lower two graphs). In the lower graphs ratios were only plotted when the concentration of dissolved S(-II) was below 0.1 mM.

X-ray absorption spectroscopy

Upon addition of S(-II), the X-ray absorption spectra collected at the U L_{III} edge from the retrieved solids showed changes which are characteristic for reduction of U(VI) to U(IV). The edge position shifted to lower energies, the intensity of white line increased, and the shoulder at the high energy side of the main peak disappeared (Fig. 4). Component analysis revealed that two components were sufficient to account for more than 98% of the variance in all the spectra. The real spectra of the two component, extracted with the ITFA software, are similar to the spectra of U(VI) and U(IV) obtained from reference materials. Consequently, the concentration distribution of the two components for the different spectra was interpreted as the relative concentrations of U(VI) and U(IV) in the samples, respectively.

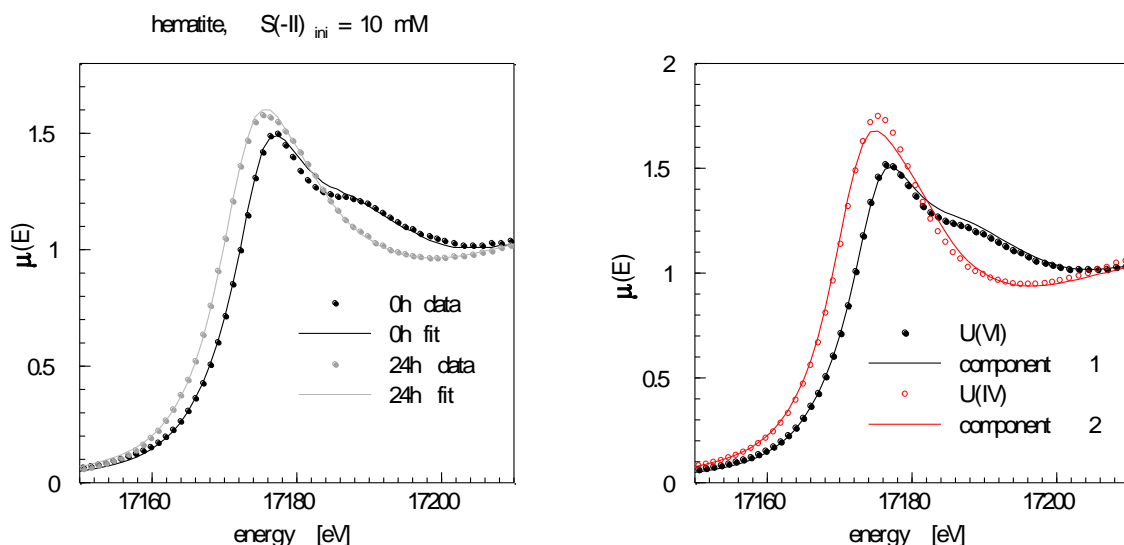


Figure 4: X-ray absorption spectra collected at the U L₃ edge. The left panel shows spectra obtained for solids from the experiment in which 10 mM S(-II) was added to hematite suspension. The dots are the data and the lines are the reproduction of the spectra by using two components derived from the ITFA analysis. The right panel compares the real spectra of the components obtained from ITFA analysis with those of reference materials: U(VI) adsorbed onto hematite and U(IV) which has produced by reducing U(VI) with Ti(III) in acidic solution and which was then precipitated together with the dissolved titanium in the presence of SiO₂ by addition of base.

After 24 h of reaction time, about 25 % of all U in the solid phase was reduced to U(IV) in the experiments with lepidocrocite (Fig. 5). The extent of U(VI) reduction was about the same irrespective of the added amount of S(-II). The fractions of U(IV) in the samples from experiments with hematite were significantly higher and about 70 % and 60 % of the initial U(VI) became reduced when 10 mM or 1 mM S(-II) were added, respectively. Already after 2 h of reaction time, the fraction of U(IV) was about 25 % in the experiments with lepidocrocite and stayed virtually constant over the next three days of reaction (Fig. 5). Also in the experiments with hematite no further reduction of U(VI) was observed after 24 h in the samples collected after two and three days (data not shown). Hence, fast reduction of U(VI) seemed to occur in the early phase of the

experiments and after this period U(VI) reduction apparently ceased or proceeded much slower. The extent of U(VI) did not vary considerably between experiments with different amounts of added S(-II) but U(IV) reduction was more than two times larger in the experiments with hematite than with lepidocrocite.

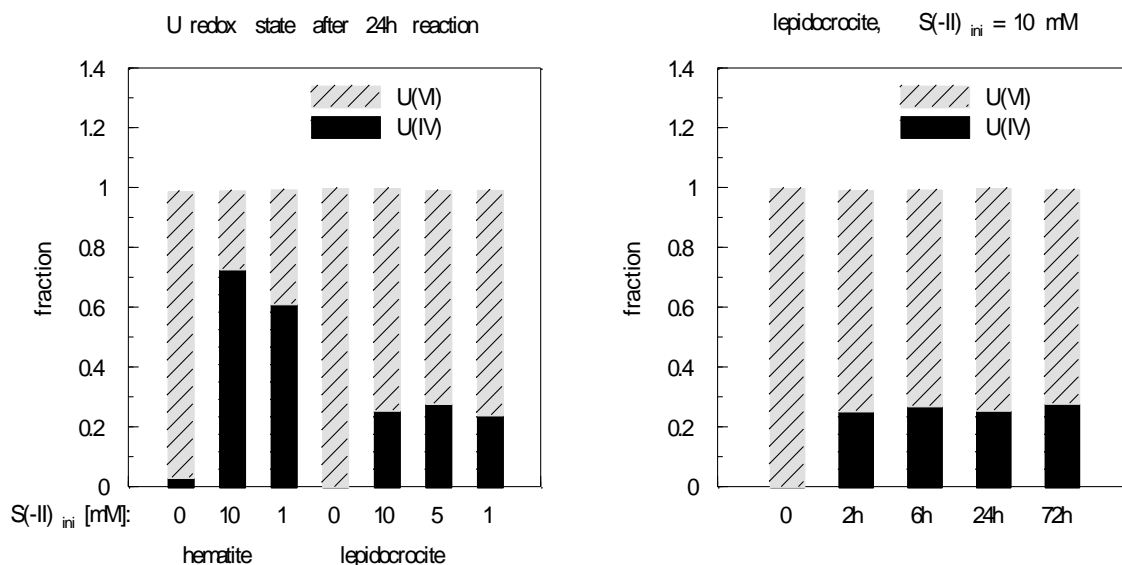


Figure 5: Fractions of U(VI) and U(IV) obtained from ITFA analysis. The left panel shows the fractions of uranium in the solids from the different experiments after 24 h reaction time. The right panel presents the time evolution of U(VI) reduction in the experiment with lepidocrocite to which 10 mM S(-II) was added

Discussion

Phase distribution of uranium

The phase distribution of uranium is controlled by several simultaneously acting processes in the different experiments. The transformation of the iron oxides into iron sulphide, the change in surface speciation of the solids, reduction of U(VI), and the formation of uranium containing precipitates, all exhibit influence on the phase distribution of uranium. Furthermore, the progress of the reaction of the iron oxides with sulphide is relatively fast so that U(aq) concentrations might not reach equilibrium with the iron phases which form intermediately during the reaction. Hence, the temporal dynamics of uranium distribution does not only reflect the kinetics of the reaction of sulphide with the iron oxides but also the kinetics of the interactions of uranium with the solids and solutes in the system. Due to this complexity an unambiguous interpretation of the results is not possible. Albeit this difficulty, some results are addressed in more detail in the following.

Effect of S(-II) adsorption on uranium distribution

The short-term release of uranium from the iron oxides upon addition of S(-II) and the reverse trend when dissolved S(-II) is consumed can be attributed to ligand exchange reactions at the solid surfaces. The first step in the reaction of S(-II) with iron oxide is the formation of inner sphere surface complexes between iron and sulphide at the surface of the iron oxides (Peiffer, et al, 1992). This step implies the exchange of hydroxide groups at the surface by thiol groups. Uranium has a strong affinity to bind to oxygen and to form complexes with oxo or hydroxide groups. To our knowledge no stability constants for complexes of U(VI) or U(IV) with sulphide or hydrogen sulphide have been reported so far which is, among other reasons, due to the low affinity of U for sulphur ligands. Hence, the initial release of uranium from the iron oxides due to sulphide addition can be understood as a competition between sulphide and uranium for hydroxide groups at the solid surface. When dissolved sulphide becomes consumed in the progress of the reaction, uranium readsorbs by forming inner sphere complexes with renewed hydroxide groups at the solid surfaces.

The more pronounced desorption and re-adsorption of uranium in experiments with hematite than with lepidocrocite can be explained by the different reactivity of the two iron oxides towards sulphide. Faster continuation of the reaction after the first step of sulphide adsorption implies that the half life of complexes between sulphide and iron on the surface of lepidocrocite is shorter than those at the surface of hematite. Therefore, sulphide is a less potent competitor for uranium adsorption onto lepidocrocite than onto hematite. This explanation is in agreement to results from our previous study in which we observed that release of adsorbed uranium from lepidocrocite was stronger after a second addition of sulphide when the consumption of dissolved sulphide was less vigorous (Alexandratos, et al, 2009). Although the main trends in U(aq) dynamics during the first hour of the reaction can be explained by changes in surface speciation of iron oxides in the presence of sulphide, several questions remain open. It is remarkable that approximately the same maximum U(aq) concentrations were reached in experiments with hematite although the amount of added S(-II) differed by a factor of ten. This could suggest that the maximum U(aq) concentration represents the maximum amount of adsorbed uranium which can be mobilized from the hematite surface due to adsorption of hydrogen sulphide. That is, some of the adsorbed uranium forms surface complexes in which the bridging oxygen cannot or can only partially be replaced by sulphide. It is also noticeable that U(aq) decreased after 1 h reaction of 10 mM S(-II) with hematite below 1 μ M although dissolved S(-II) concentrations were still about 4 mM. In comparison, addition of 1 mM of S(-II) was sufficient to raise U(aq) concentrations to about 4 μ M. This phenomenon could be explained by reduction and precipitation of uranium which also simultaneously occurs in this phase of the experiments and will be discussed in the following section.

Effect of iron mineral transformation on uranium distribution

Transformation of iron oxides into iron sulphides is expected to decrease U(VI) adsorption. Direct comparison of reported results on U(VI) uptake by iron sulphide phases and iron oxides is difficult due to differences in experimental conditions. When comparing the position of the adsorption edges, U(VI) uptake by iron sulphides such as

pyrite (Descostes, et al, 2010) seems to be less efficient than that by ferrihydrite (Waite, et al, 1994) or hematite (Liger, et al, 1999), although U(VI) reduction to U(IV) may contribute to uranium uptake by pyrite in addition to U(VI) adsorption. Hence, increase in U(aq) concentrations upon sulphidization of the iron oxides can be in part explained by the transformation of lepidocrocite and hematite into an iron sulphide with lower tendency to adsorb U(VI) than the iron oxides. The concentration of $\text{Fe(II)}_{\text{HCl}}$ is an indicator for the transformation of iron oxides into iron sulphides, although not all $\text{Fe(II)}_{\text{HCl}}$ is in the form of FeS but $\text{Fe(II)}_{\text{HCl}}$ reflects the maximum amount of FeS in the system. In order to separate the effect of S(-II) adsorption on uranium distribution from that of iron phase transformation, uranium distribution was plotted in Fig. 3 as a function of $\text{Fe(II)}_{\text{HCl}}$ only when S(-II)_{aq} concentrations were lower than 0.1 mM or when the reaction time was 24 h or longer. Under these conditions, the above described short-term dynamics of U(aq) concentrations due to S(-II)_{aq} adsorption is assumed to be of minor importance. The distribution of uranium is not a linear function of $\text{Fe(II)}_{\text{HCl}}$ which would be the case if uranium distribution was the result of a linear combination of U(VI) uptake by two end-member phases, and $\text{Fe(II)}_{\text{HCl}}$ reflects the concentration of one of these end-member phases. For lepidocrocite, uranium distribution decreases significantly when a small part of the total iron is in the form of $\text{Fe(II)}_{\text{HCl}}$. However, when more than about 25% of the total iron occurs as $\text{Fe(II)}_{\text{HCl}}$, uranium distribution does not change systematically with increasing $\text{Fe(II)}_{\text{HCl}}$ concentration. This trend is in agreement with our previous findings in experiments with lepidocrocite that partial transformation of the bulk lepidocrocite into iron sulphide causes the same change in uranium distribution as its complete transformation. This is not unexpected when the transformation of lepidocrocite proceeds from the surface of the lepidocrocite crystals towards their interior. Uranium distribution is controlled by the properties of the mineral surfaces exposed to the solution. Hence, formation of iron sulphide rims around the lepidocrocite crystals is sufficient to change the characteristics of the solid phase regarding uranium uptake from that of lepidocrocite to those of the iron sulphides. The formation of iron sulphide rims around lepidocrocite crystals upon the addition of sulphide has been shown by (Hellige, et al, 2012). The dependency of uranium distribution on $\text{Fe(II)}_{\text{HCl}}$ concentration in experiments with hematite follows the same trend as in experiments with lepidocrocite. Hence, transformation of the outer parts of the hematite crystals into iron sulphides can cause a decrease in uranium distribution to a similar extent as the bulk transformation of hematite. The observed decrease in uranium distribution upon the iron mineral transformation is, in part, compensated by reduction of U(VI) and the (co-)precipitation (use a non-braking hyphen by typing Shift Ctrl “minus”) of U(IV) with or incorporation into the forming iron sulphide phases.

Reduction of uranium

Equilibrium thermodynamics suggest that U(VI) can be quantitatively reduced to U(IV) and precipitate as uraninite in all experiments (data not shown), but XANES analyses reveal that U(VI) reduction was only incomplete. In our previous study, we proposed that lepidocrocite outcompetes U(VI) as an oxidant for S(-II) due to its faster reaction kinetics. When S(-II)_{aq} is present together with iron oxides and/or sulphides, U(VI) reduction is fast. After 2 h of reaction about 25% of the added U(VI) is reduced to U(IV) (Fig. 5). However, when all S(-II) is oxidized or bound in iron sulphides, the system reaches a metastable state and further reduction of U(VI) by solid bound Fe(II)

or S(-II) stops or proceeds on a longer time scale than the length of the experiments. In the case of experiments with lepidocrocite, the fraction of U(IV) remains practically constant after 2 h, when all S(-II)_{aq} is consumed, until the end of the experiments, 72 hours later. This suggests, that S(-II)_{aq} is the most reactive reductant for U(VI) in the system. Homogeneous reduction of U(VI) by S(-II) in aqueous solution in the time scale of a few hours has been reported by Hua et al. (2006). Another possibility is that S(-II)_{aq} is required for forming an effective reductant for U(VI). For example, iron-sulfide complexes which form in solution or at the solid surfaces in the presence of S(-II)_{aq} could be the most reactive species for the reaction with U(VI).

Hematite reacts slower with S(-II) than lepidocrocite so that the larger extent of U(VI) reduction in experiments with hematite is in line with the proposed explanatory model. That is, the length of the period with detectable amounts of S(-II)_{aq} in experiments with hematite is longer than in experiments with lepidocrocite and hence the time available for U(VI) reduction is also longer. Furthermore, the extent of desorption of uranium upon addition of S(-II) is higher in experiments with hematite. According to (Hua, et al, 2006) dissolved uranyl-hydroxide complexes are the reactive U(VI) species in the reaction with S(-II). Hence, the more pronounced U(VI) reduction in experiments with hematite might be a combination extended availability of S(-II)_{aq} and enhanced desorption of U(VI) followed by the formation of reactive uranyl-hydroxide complexes in solution.

Based on this explanation it is surprising that the amount of added S(-II) has only little effect on the extent of U(VI) reduction. In experiments with hematite, S(-II)_{aq} was still above 2 mM after 24 h reaction time when 10 mM S(-II) was added but nevertheless U(VI) reduction was not complete. Furthermore, the fraction of U(IV) is relatively similar to that in experiments which received only 1 mM S(-II). The low sensitivity of uranium reduction on the amount of added S(-II) could be explained by the formation of metastable uranium containing precipitates with mixed redox state. For example, precipitation of U₄O₉ is thermodynamically feasible in the system at suitable U(IV)/U(VI) ratios. That is, formation of solids containing uranium in mixed redox states might slow down reduction of U(VI) when U(VI) in the solids react slower with S(-II) than dissolved or adsorbed U(VI).

Summary and Conclusions

Uranium mobility is considered to be low in sulphidic environments because uranium is expected to occur in the form of uraninite when thermodynamic equilibrium is achieved. The results of this study demonstrate that U(VI) adsorbed to iron oxides is not instantaneously reduced to U(IV) when S(-II) emerges in the solution. Appearance of S(-II) in the solution can induce mobilization of adsorbed U(VI). This mobilization is caused by changes in surface speciation of the iron oxides due to adsorption of S(-II) and the transformation of iron oxides into iron sulphides with lower tendency to adsorb U(VI). The mobilization of uranium is counteracted by reduction of U(VI) to U(IV). Although reduction of U(VI) can occur in the time scale of hours the reaction does not reach completion within the time scale of days. This might be due to the temporal

limited availability of the reactive reductant for U(VI) or the formation of precipitates containing uranium in mixed redox state which slow down U(VI) reduction kinetics. Further research is required to unravel the detailed mechanisms involved in uranium mobilization and uranium reduction in these highly dynamic systems. However, it is shown that the kinetics of processes controlling uranium migration might become important in assessing uranium mobility in environments which are effected by a shift in redox condition from oxic to sulphidic.

Acknowledgement

We thank the team of the DUBBLE beamline at the ESRF, in particular Dr. S. Nikitenko, for their support during the collection of the XAS spectra. The research leading to these results has received funding from the European Union's European Atomic Energy Community's (Euratom) Seventh Framework Programme FP7/2007-2011 under grant agreement n° 212287 (RECOZY project).

References

- Alexandratos V., Behrends T. and Van Cappellen P. (2009) Effect of S(-II) driven conversion of iron oxides to FeS on uranium mobility. In: *4th Annual Workshop Proceedings of the Integrated Project "Fundamental Processes of Radionuclide Migration"* (6th EC FP IP FUNMIG) (eds. G. Buckau, L. Duro, B. Kienzler, V. Montoya and A. Delos). 205-212.
- Cline J. D. (1969) Spectrophotometric determination of hydrogen sulfide in natural waters. *Limnol. Oceanogr.* **14**, 454-458
- Descostes M., Schlegel M. L., Eglizaud N., Descamps F., Miserque F. and Simoni E. (2010) Uptake of uranium and trace elements in pyrite (FeS(2)) suspensions. *Geochim. Cosmochim. Acta* **74**, 1551-1562.
- Hellige K., Pollok K., Larese-Casanova P., Behrends T. and Peiffer S. (2012) Pathways of ferrous iron mineral formation upon sulfidation of lepidocrocite surfaces. *Geochim. Cosmochim. Acta* (in press)
- Hua B., Xu H., Terry J. and Deng B. (2006) Kinetics of Uranium(VI) Reduction by Hydrogen Sulfide in Anoxic Aqueous Systems. *Environ. Sci. Technol.* **40**, 4666-4671.
- Liger E., Charlet L. and Van Cappellen P. (1999) Surface catalysis of uranium (VI) reduction by iron(II). *Geochim. Cosmochim. Acta* **63**, 2939-2955.
- Peiffer S., Dos S. A., Wehrli B. and Gaechter R. (1992) Kinetics and mechanism of the reaction of hydrogen sulfide with lepidocrocite. *Environ. Sci. Technol.* **26**, 2408-2413.

Poulton S. W., Krom M. D. and Raiswell R. (2004) A revised scheme for the reactivity of iron (oxyhydr)oxide minerals towards dissolved sulfide. *Geochim. Cosmochim. Acta* **68**, 3703-3715.

Ravel B. and Newville M. (2005) ATHENA, ARTEMIS, HEPHAESTUS: data analysis for x-ray absorption spectroscopy using IFEFFIT. *J. Synchrotron Radiation* **12**, 537-541.

Rossberg A., Reich T. and Bernhard G. (2003) Complexation of uranium(VI) with protocatechuic acid-application of iterative transformation factor analysis to EXAFS spectroscopy. *Analytical and Bioanalytical Chemistry* **376**, 631-638.

Schwertmann U. and Cornell R. M. (2000) *Iron Oxides in the Laboratory, 2nd Edition*.

Viollier E., Inglett P. W., Hunter K., Roychoudhury A. N. and Van Cappellen P. (2000) The ferrozine method revisited: Fe(II)/Fe(III) determination in natural waters. *Appl. Geochem.* **15**, 785-790.

Waite T. D., Davis J. A., Payne T. E., Waychunas G. A. and Xu N. (1994) Uranium(IV) adsorption to ferrihydrite: application of a surface complexation model. *Geochim. Cosmochim. Acta* **58**, 5465-5478.

SPECIATION OF REDUCED SELENIUM SPECIES IN HYPERALKALINE SOLUTIONS: ATTEMPT AT DEVELOPPING A SPECIFIC ANALYTICAL PROTOCOL

Catherine Landesman^{*}, Céline Bailly, Véronique Baty, Johan Vandenborre, Bernd Grambow

Subatech Laboratory, UMR 6457, CNRS/IN2P3-Ecole des Mines de Nantes-University of Nantes, (FRA)

* Catherine Landesman : catherine.landelman@subatech.in2p3.fr

Abstract

Selenium(-II) speciation in hyperalkaline solution is characterized by the existence of both monomer (HSe^- , Se^{2-}) and polymer species (Se_2^{2-} , Se_3^{2-} , Se_4^{2-}). These species ions have formal oxidation states between -II and 0 and influence the redox behavior of selenium in high pH solution. Initially the aim of this work was to develop an analytical method in order to measure low concentrations of monomer and polymer species in hyperalkaline solution.

For that purpose, sodium selenide was electrochemically synthesized and characterized by XRD and XPS. Solutions of monomer and polymer selenium species were prepared in NaOH and KOH media and characterized by UV-visible spectrophotometry.

The main result of this work is the development of a specific analytical protocol aiming at measuring the monomer species HSe^- at a sub millimolar level (*ie* : $0,1 \cdot 10^{-3} \text{ mol/L}$) by using a speciation technique (ion chromatography). When coupled with a higher detector such as an ICP-MS spectrometer, this protocol leads to a quantitative determination of HSe^- at a submicromolar level. Unfortunately, this protocol is not efficient enough for quantitatively analyzing the other reduced selenium species altogether. Despite many analytical efforts, only partial separations were obtained for either the couple $\text{HSe}^-/\text{Se}^{2-}$ or the polymer species because of the too close interaction properties developed by those species towards the anion exchange columns which are commercially available. Nevertheless, because retention times of HSe^- and polymer species ($\text{Se}_3^{2-}/\text{Se}_4^{2-}$) are quiet different, it is still possible to consider using this protocol for separating these specific species.

Introduction

In the French and many others countries designs of a deep geological nuclear waste repository, cementitious materials are planned to be used for conditioning purposes

(containers) and for the construction of the engineered barrier system (buffer and backfill materials). Because of its chemical composition based on (Na, K and Ca), cement imposes a hyperalkaline environment (*ie* pH < 12) during a long period of time. The long-lived isotope ⁷⁹Se is present in nuclear waste as a potentially mobile fission product because of its ability to form anion species which generally interact weakly with the environment. In such a context, selenium interactions with cementitious materials are of great interest for detailed assessments of the long-term safety of nuclear waste repositories.

Laboratory experiments show that even at high Se concentrations over a wide range of pH, the Pt electrode is completely insensitive to the relative abundance of dissolved Se(VI) and Se(IV). Se speciation therefore cannot be deduced directly from Eh measurements with Pt electrodes and geochemical equilibrium calculations. This indicates that under certain conditions the Pt electrode measured Eh does not correspond to a "master variable" of the redox system. This clearly points to the need of direct measurement of solution speciation to assess the redox relevant for Se speciation.

Solution speciation in hyperalkaline solution will further be complicated by the formation of polyselenide species such as Se₂²⁻, Se₃²⁻ and Se₄²⁻. These ions have formal oxidation states between -II and 0 (figure 1)

It become obvious that polymer species play a large role under alkaline conditions and the presence of these species will strongly reduce the stability field for Se(0, triclinic). Essentially, in the interesting hyperalkaline pH range between pH 11 and 13, no Se(0, triclinic) will be formed. Even further reduced is the probability to form monoclinic Se(0) Oling *et al.* (2005).

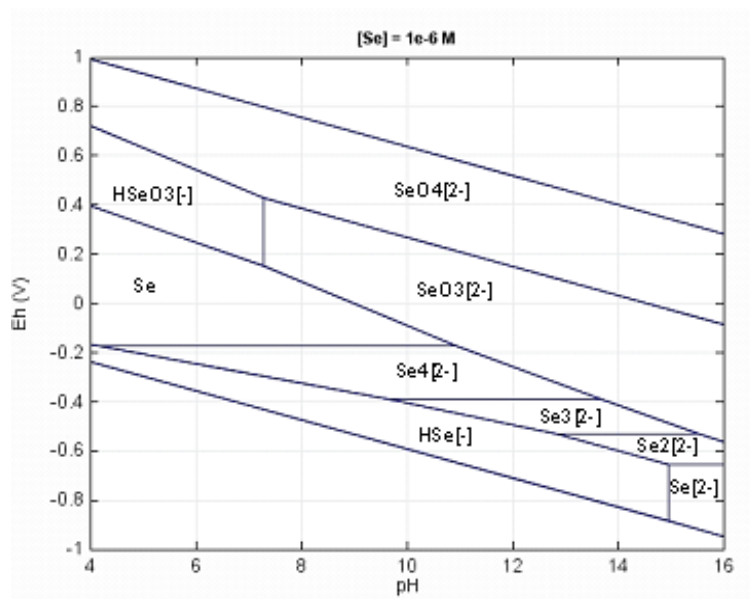


Figure 1 : Eh-pH diagram of selenium species (from Oling *et al.*, 2005)

The aim of this experimental work was then to determine low level concentrations of Se(-II) species in order to use the speciation of Se(-II) as a probe for redox state determination in hyperalkaline solutions. UV-visible spectrophotometry is the efficient

technique for the characterisation of Se(-II) species but its sensitivity is too low for determining concentrations lower than 10^{-4} M. The *in fine* analytical approach is then to use a speciation technique (ion chromatography) *off line* coupled with a very sensitive analytical technique (ICP-MS).

Synthesis of sodium selenide

The first step of the study was to synthesize a selenide source. As Se(-II) is not stable towards oxygen, the synthesis was performed in a glove box flushed with nitrogen ($O_2 < 100$ ppb) in order to maintain a non oxidative atmosphere. A specific electrochemical synthesis protocol for selenide ions was adapted from *Licht et al (1995)*.

This synthesis is based on the electrochemical reduction of a selenium(IV) solution in hyperalkaline media and the precipitation of the related alkaline selenide as a solid. The electroreduction of a sodium selenite solution (0,4 mol/L in NaOH 4 mol/L) was then carried out using a standard 3 electrode electrochemical cell. The very negative potential required for the reduction (-1.285 V/SHE) was imposed between a Pt wire electrode (counter electrode) and a mercury pool (working electrode). According to coulometric recordings, the reduction, from Se(IV) to Se(-II), is total. Moreover, UV spectra recorded *on line* during the synthesis show that, under our experimental conditions, Se(IV) is first reduced to the polymeric species Se_3^{2-} ($\lambda = 258, 328$ and 379 nm) then Se_2^{2-} ($\lambda = 251, 431$ nm). During the reduction, the solution becomes yellowish which is consistent with the presence of polymer species. A white frothy solid (sodium selenide) appears then as the solution turns more reddish. Finally a colorless solution is obtained and the aqueous species identified as Se^{2-} ($\lambda_{max} = 274$ nm). Figure 2 shows the progressive steps of the electrochemical reduction.

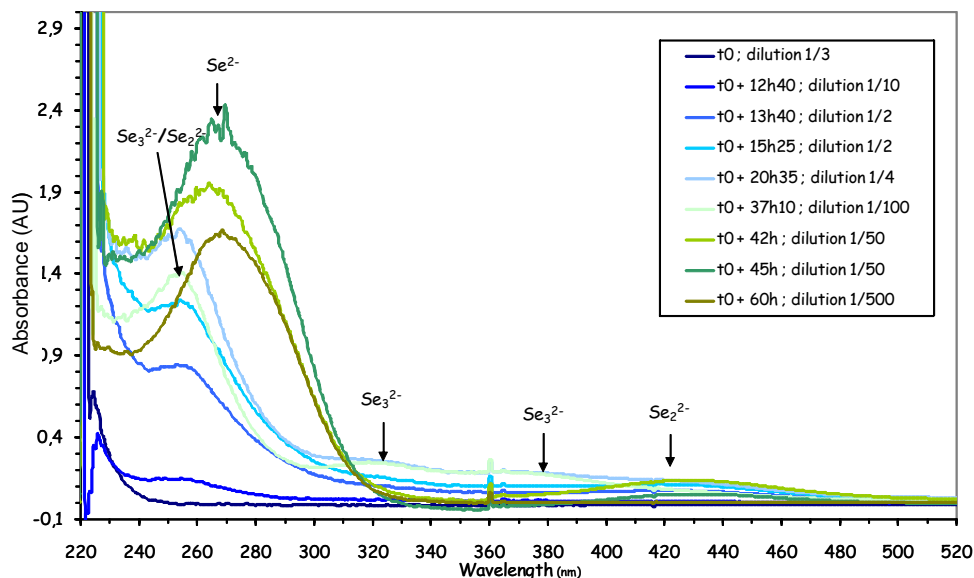


Figure 2 : Evolution of the Se species in solution during the electrochemical reduction

Characterization

Solid characterization

Bulk solid characterization by X-Ray Diffraction identified the synthesized solid as $\text{Na}_2\text{Se} \cdot 9\text{H}_2\text{O}$. A more precise characterization by X-Ray Photoelectron Spectroscopy (XPS) was undertaken to check the composition of the solid surface.

Selenium XPS analysis are performed on a Kratos Axix Ultra XPS spectrometer at the Institut des Matériaux de Nantes- Jean Rouxel (IMN, France) on an aged sodium selenide sample (*ie* : stored during 2 months in a glove box). The transfer of this sample from Subatech to IMN required the use of a specific “fully airtight transfer device” in order to maintain an anoxic atmosphere. Moreover, a specific feed of ultrapur N_2 ($\text{O}_2 < 100$ ppb) was connected to the spectrometer in order to provide a residual atmosphere with the lowest possible O_2 level. Figure 3 shows the XPS spectrum of a sodium selenide sample. The deconvolution of the XPS peaks shows two contributions at 52 and 52.9 eV which can be assigned to Se(-II), more precisely to the $3p_{5/2}$ and $3p_{3/2}$ transitions respectively. Nevertheless, a tiny contribution of Se(0) ($< 10\%$ of total Se analyzed) doublet lies at 53.7 and 54.25 eV has to be considered in order to fully interpret the spectrum. Since XPS technique analyses only the first layers of the solid surface (few nm of depth), this Se(0) contribution relies on a surface contamination probably due to traces of oxygen in the XPS spectrometer residual atmosphere. So the presence of tiny amount of Se(0) at the sodium selenide surface was not considered as an issue for this work. Moreover, this result proves that the storage conditions are airtight enough to keep the very reactive Se(-II) samples protected against oxidation during long period of time.

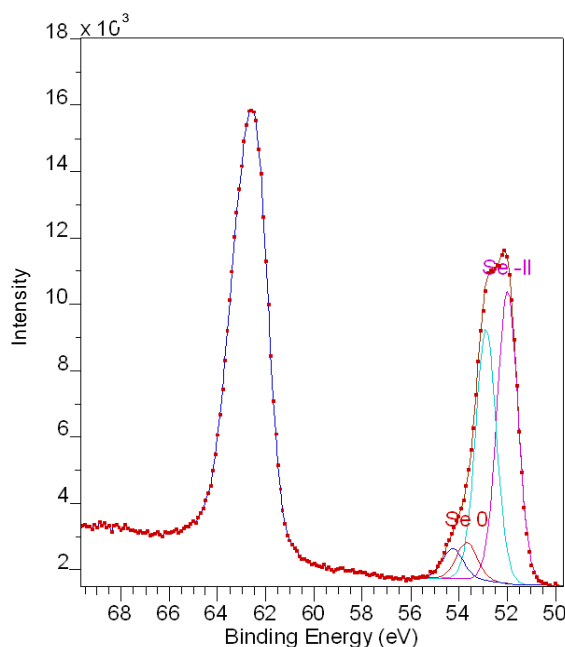


Figure 3: XPS spectrum of an electrochemically synthesised sodium selenide sample

Monomer Se(-II) solutions characterization

Solutions of sodium selenide ($6.2 \cdot 10^{-4}$ M) were then prepared, in a glove box, by dissolving a mass of solid in sodium hydroxide solutions ranging from 0.5 to 8 M in order to investigate the whole range of stability of Se(-II) monomer species. UV-visible spectra were systematically acquired for all these solutions. Results (figure 4) show that the major species is HSe^- ($\lambda_{\text{max}} = 245\text{nm}$) for NaOH concentrations lower than 1M and Se^{2-} ($\lambda_{\text{max}} = 274\text{nm}$) for concentrations higher than 2M. This agrees well with literature data (*Levy et al (1990), Iida et al, (2010)*). Moreover, redox measurements, carried out with a combined Pt-Ag/AgCl 3M redox electrode, show that our experimental conditions are efficient enough to keep these solutions stable towards oxidation over months.

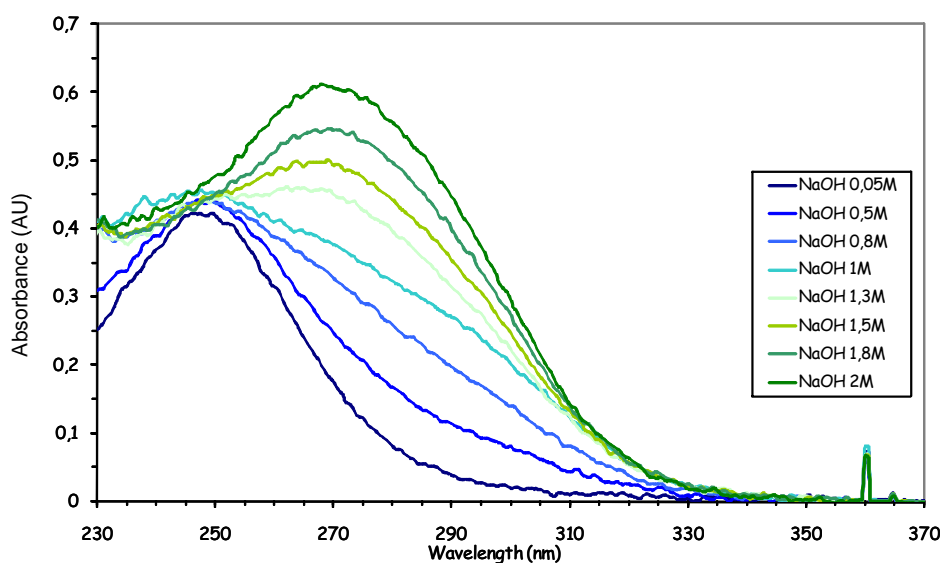


Figure 4 : Spectrophotometric evolution of Se(-II) solutions as a function of NaOH concentration ($\lambda_{\text{max}}(\text{HSe}^-) = 245\text{nm}$; $\lambda_{\text{max}}(\text{Se}^{2-}) = 274\text{nm}$)

Polymer species solution characterization

The preparation protocol is based on *Licht et al (1995)* work. Solutions of reduced polymer species were prepared by dissolving a certain mass of solid Se(0) in Se(-II) solutions in hyperalkaline KOH media (from 0.5 to 8M) in order to achieve molar Se(0)/Se(-II) ratios values of 1.0, 2.0 and 2.8. These molar ratios lead to the formation of a mixture of polymers species dominated by Se_2^{2-} , Se_3^{2-} and Se_4^{2-} respectively. These solutions are very stable towards oxidation when kept in the appropriate anoxic environment. Table 1 shows the stability of the redox potential of these solutions as a function of time.

Each species show several absorption peaks in UV-visible spectrophotometry (table 2). For some species such as Se_2^{2-} and Se_3^{2-} , main absorption wavelengths are very close. This tends to complicate the precise identification. Figure 5 shows an overall spectra of these species.

Table 1: Redox potential of selenium polymers solutions vs time and KOH concentration

[KOH] (mol/L)	Se(0)/Se(-II) ratio	Eh (/ESH) (mV) after 6 days	Eh (/ESH) (mV) after 14 months	Eh (/ESH) (mV) after 18 months
0.5	1.0	-577	-579	-582
	2.0	-471	-438	-459
	2.8	-438	-424	-427
1	1.0	-574	-593	-590
	2.0	-449	-457	-454
	2.8	-412	-390	-382
2	1.0	-578	-597	-595
	2.0	-432	-415	-411
	2.8	-419	-386	-398
4	1	-558	-524	-530
	2	-402	-447	-445
	2.8	-389	-447	-445

Table 2: Absorption wavelength of polymer Se species (main lines in bold) from [Licht et al]

Species	Wavelength (nm)
Se ₂ ²⁻	251, 431
Se ₃ ²⁻	258, 328 , 379, 529
Se ₄ ²⁻	219, 282 , 377, 469

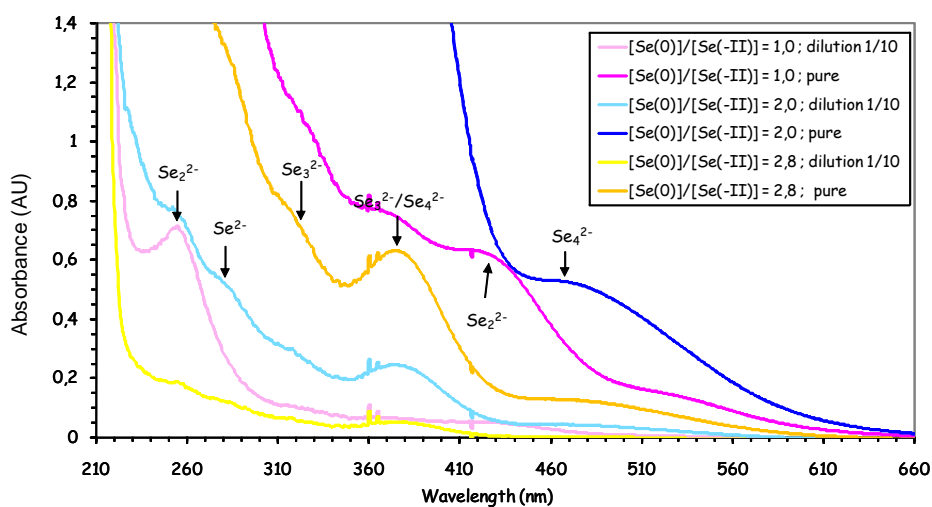


Figure 5: UV-visible spectra of Se polymer species mixture in KOH 2 mol/L media

Speciation experiments

Analysis of monomer HSe⁻ species

Speciation experiments are firstly performed on HSe⁻ solutions with a Dionex IC 2500 ion chromatograph using a hydroxide selective anion exchange column Dionex AS 16 (4 × 250 mm ; void volume = 2.59 mL) specifically optimized for determination of polarizable anions such as selenite, selenate and iodide (alkanol quaternary ammonium ions functional groups). The separation protocol was optimized for an *on line* detection of all Se species (HSe⁻, Se(IV) and Se(VI)) related to different redox states of selenium in order to get simultaneous information on a potential reoxidation of Se(-II) species during the analysis. For that purpose, two different detectors (an UV-visible single wavelength detector and a conductimetry cell detector) are connected in serie to the ion chromatograph because HSe⁻ can only be detected by UV-visible spectrometry at 245nm. For the other species (Se(IV) and Se(VI)), conductimetry detection is efficient. The elution mode is isocratic with a 20 mM KOH eluent. The entire chromatographic system was flushed continuously with ultrapur Helium in order to maintain an anoxic environment during the analysis. The flow rate and temperature are set at 1mL/min and 30°C respectively.

All selenium solutions are prepared in a glove box flushed with nitrogen. Previously to ion chromatography analysis, total selenium content is systematically measured with fibre-optic lines by UV spectrophotometry directly inside the glove box and by ICP-MS. Redox potential of the solution is also measured. Specific precautions were taken for the transfer of samples from the glove-box to the ion chromatograph and the injection of samples into the analytical apparatus in order to avoid interfering oxidation.

Figure 6 shows the two chromatograms obtained for the analysis of a HSe⁻ solution ($6.33 \cdot 10^{-4}$ mol/L) in NaOH 0.5 M. The redox potential of the solution is -0.655V/ESH. UV-visible detection shows only one peak at 12.6 min. which is assigned to HSe⁻. Because of the shifting, related to the coupling of the two detectors, the peak at 12.3 min can then be assigned to this species in conductimetric detection. The additional peak at 7.0 min. is due to the presence of some carbonate ions in the eluent.

The other peaks are assigned to Se(IV) and Se(VI) at 6.3 and 7.7 minutes respectively. The presence of these oxidized species show that, despite all the precautions taken, some traces of O₂ are still trapped in the ion chromatograph and lead to a partial re oxidation of HSe⁻. A fraction collector was then used to collect these oxidized species. An *off line* ICP-MS analysis of those fractions show that the contamination remains at a low level since Se(IV) and Se(VI) concentrations were measured less than 5 and 0.2 % of the total Se concentration respectively.

For a quantitative analysis of HSe species, a standardization curve absorbance = f(concentration) was determined in the submillimolar range of concentration (figure 7). Three concentrations were measured in triplicate at 245 nm. The results show a quiet good correlation indicating that a quantitative analysis is possible in our experimental conditions.

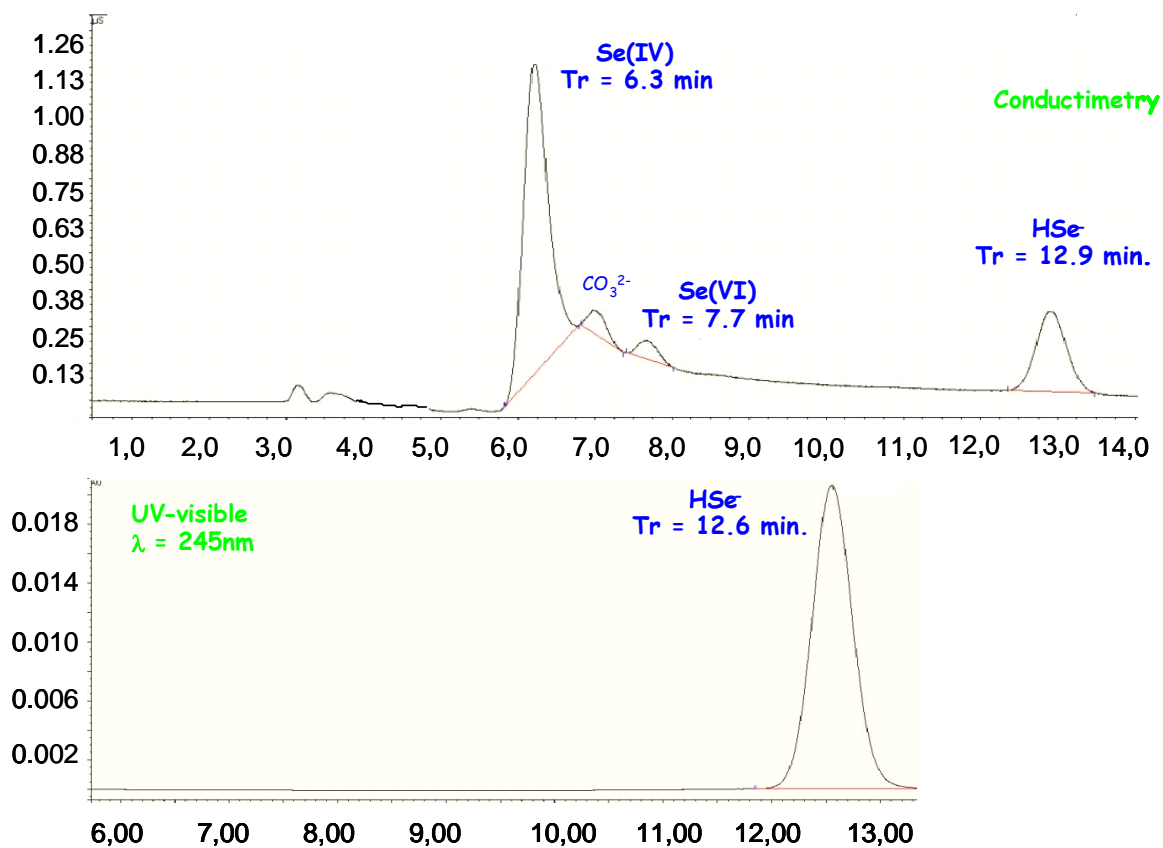


Figure 6 : Chromatograms (upper : conductimetry cell detection ; lower : UV-visible at 245nm detection) of a HSe^- solution in 0.5 M NaOH)

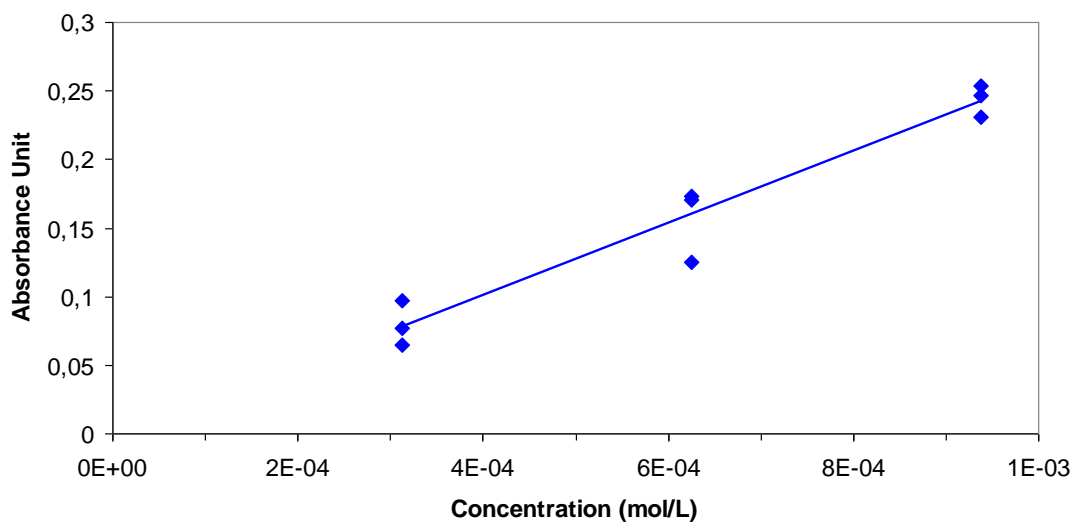


Figure 7 : Standardization curve for HSe^- species ; UV detection at 245 nm

As a conclusion, this separation protocol based on a conductimetry or spectrophotometry detection aims at measuring HSe^- at millimolar level. This protocol was coupled twice with a higher sensitivity *off line* detector (ICP-MS spectrometer) after fractions collection. The quantification limits obtained are of course much lower and HSe^- species can be measured at a sub micromolar level (*ie* : 0,1 $\mu\text{mol/L}$).

Analysis of monomer Se^{2-} species

This protocol was then adapted to analyze Se^{2-} solutions. Indeed, during the analysis, the sample is diluted by the eluent. The dilution factor depends on the separation conditions (efficiency of the separation, injected volume, flow rate,...) and therefore has to be kept low enough in order to preserve the existence of Se^{2-} species in the sample. Moreover, because of viscosity, the eluent concentration is limited to 0.5 mol/L. The best separation conditions were therefore obtained with a gradient elution (from 0.05 to 0.5 KOH). The flow rate and temperature were set at 0.4mL/min and 45°C respectively. Figure 8 shows the chromatogram of an initially $3 \cdot 10^{-3}$ mol/L Se^{2-} solution in 4M NaOH. Detection was performed by UV detection at $\lambda = 245$ nm.

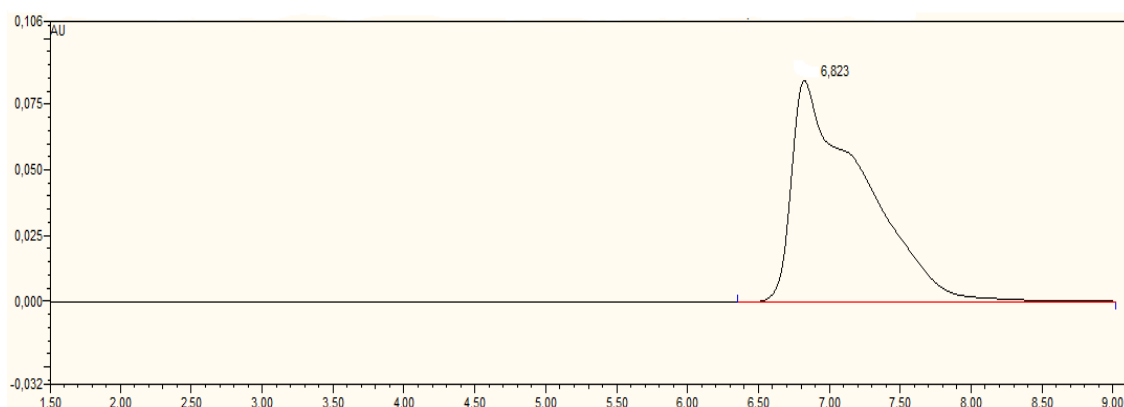


Figure 8 : Chromatogram of a $\text{HSe}^-/\text{Se}^{2-}$ mixture (elution conditions : see text)

The chromatogram shows two partially resolved peaks at 6.82 and 7.15 minutes. Injection of a HSe^- sample shows that the first peak can be attributed to this species. The second one should then be attributed to Se^{2-} which is consistent with the retention of a higher charged species. Unfortunately despite numerous analytical efforts, we were not able to improve separation of these two species.

Analysis of polymers species

The analysis was based on the previously described protocol. Improvements were obtained with an isocratic elution with 0.5 mol/L KOH. Nevertheless, we never succeeded in a total separation of a mixture of polymer species mostly Se_3^{2-} and Se_4^{2-} . Figure 9 shows the chromatogram of a mixture of polymer species synthesized with a 1:1 molar $\text{Se}(\text{-II})/\text{Se}(\text{0})$ ratio in KOH 4 mol/L. This chromatogram is representative of all results obtained with polymer species. The flow rate and temperature were set at

0.4mL/min and 45°C respectively. Detection was performed by UV detection at $\lambda = 360$ nm.

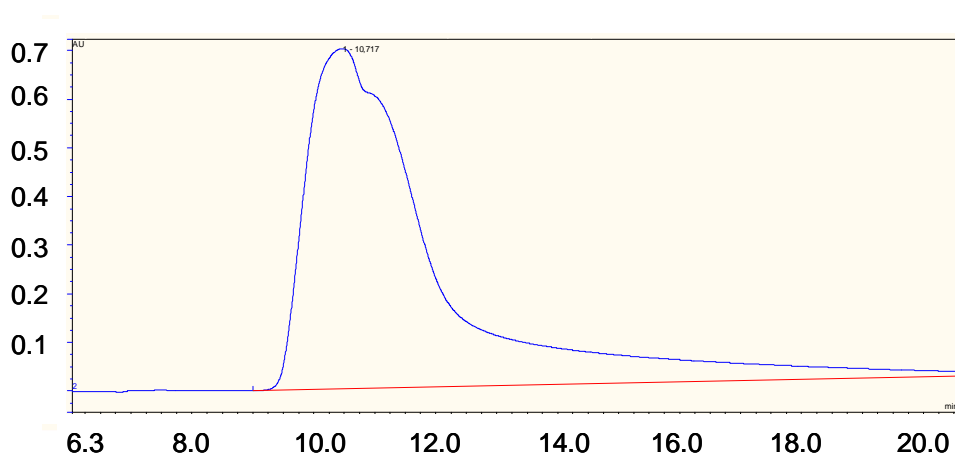


Figure 9 : Chromatogram of mixture of a 1:1 molar Se(-II)/Se(0) ratio polymer species

Two peaks can be distinguished at 10.72 and 11.31 minutes. That means that the analyzed species have a real chemical interaction with the functional groups of the column, but that the resolution is still too low for achieving a full separation. Attempts with another type of anion exchange column were also unsuccessful.

Summary and Conclusion

Selenium(-II) speciation in hyperalkaline solution is characterized by the existence of both monomer (HSe^- , Se^{2-}) and polymer species (Se_2^{2-} , Se_3^{2-} , Se_4^{2-}). These species ions have formal oxidation states between -II and 0 and influence the redox behavior of selenium in high pH solution. Initially the aim of this work was to develop an analytical method in order to measure low concentrations of monomer and polymer species in hyperalkaline solution.

For that purpose, sodium selenide was electrochemically synthesized and characterized by XRD and XPS. Solutions of monomer and polymer selenium species were prepared in NaOH and KOH media and characterized by UV-visible spectrophotometry.

The main result of this work is the development of a specific analytical protocol aiming at measuring the monomer species HSe^- at a sub millimolar level (*ie* : $0,1 \cdot 10^{-3}$ mol/L) by using a speciation technique (ion chromatography). When coupled with a higher detector such as an ICP-MS spectrometer, this protocol leads to a quantitative determination of HSe^- at a submicromolar level. Unfortunately, this protocol is not efficient enough for quantitatively analyzing the other reduced selenium species altogether. Despite many analytical efforts, only partial separations were obtained for either the couple $\text{HSe}^-/\text{Se}^{2-}$ or the polymer species because of the too close interaction properties developed by those species towards the anion exchange columns which are commercially available. Nevertheless, because retention times of HSe^- and polymer species ($\text{Se}_3^{2-}/\text{Se}_4^{2-}$) are quite different, it is still possible to consider using this protocol for separating these specific species.

Acknowledgement

The research leading to these results has received funding from the European Union's European Atomic Energy Community's (Euratom) Seventh Framework Programme FP7/2007-2011 under grant agreement n° 212287 (RECOSY project).

References

Iida Y., Yamaguchi T., Tanaka T., Nakayama, S. (2010) Solubility of selenium at high ionic strength under anoxic conditions, Journal of Nuclear Science and Technology, 47(5) 431-438

Levy D.E., Myers R. J. (1990) Spectroscopic determination of the second dissociation constant of H₂Se and the activity coefficients and spectral shifts of its ions, Journal of Physical Chemistry, 94, 7842-7847

Licht S., Forouzan, F. (1995). Speciation analysis of aqueous polyselenide solutions. Journal of the Electrochemical Society, 142, 1546-1551

Olin A., Nölang B., Osadchii, E.G., (2005) Chemical Thermodynamics of selenium (1), Chemical Thermodynamics vol. 7, F. J. Mompean (Eds), OECD Nuclear Energy Agency, Issy-les Moulineaux, France, Elsevier

HOW MOBILE IS SELENITE DIFFUSING THROUGH THE CALLOVO-OXFORDIAN CLAYSTONES? INSIGHTS GIVEN BY RADIOCHEMISTRY AND X-RAY ABSORPTION SPECTROSCOPY

Sébastien Savoye^{*,1}, Michel Schlegel², Benjamin Frasca^{1,3}, Agnès Fayette¹, Bernard Grenut¹

¹ CEA, DEN/DANS/DPC/SECR/Laboratoire de Mesures et Modélisation de la Migration des Radionucléides, F-91191 Gif-sur-Yvette, France

² CEA, DEN/DANS/DPC/SEARS/ Laboratoire de Réactivité des Surfaces et des Interfaces, F-91191 Gif-sur-Yvette, France

³ UMR “IDES” CNRS–Université de Paris-Sud, F-91405 Orsay, France

* Corresponding author: sebastien.savoye@cea.fr

Abstract

⁷⁹Se might be one of the key mobile fission products for nuclear waste disposal hosted in deep argillaceous formations due to its longevity and its anionic character. An in-depth understanding of the transport properties of selenium is therefore essential. However, because of its high sensitivity to redox condition, the mobility of such an element is highly related to its speciation forms. Therefore, the diffusive behaviour of selenite was studied through two rock samples originating from the Callovo-Oxfordian (COx) formation (France) and under physico-chemical conditions as close as possible to those prevailing in-situ, by means of the use of a N₂/CO₂ glove-box. A radiochemical approach using HTO, ³⁶Cl, and ⁷⁵Se, as tracers, was supplemented by a non-radioactive one, for which the solid was investigated by synchrotron-based spectroscopic methods. The two approaches led to mutually consistent results. While the observed selenium concentration in solutions could be roughly reproduced by a pure diffusion model with a reversible sorption ($De = 4 \times 10^{-12} \text{ m}^2 \text{ s}^{-1}$ and $R_d = 12 \text{ mL g}^{-1}$), the total selenium rock profiles exhibited irregular shapes, requiring more complicated models. The determination of the Selenium oxidation state by means of the spectroscopic analyses revealed, in the solid, (1) a relative regular diffusion profile for selenite and (2) the presence of some areas rich in selenium reduced forms (Se(red) ~ Se(0), S(-I) and/or Se(-II)), especially located at about 2 mm from the interface. This analysis allowed us to explain the shape of the ⁷⁵Se rock profile. Moreover, some correlations exist between some of the Se(red) hot-spots and the iron content, suggesting the role of iron-rich minerals, such as pyrite. However, the larger Se(red)-rich area (at 2 mm) could not be accounted for by mineralogical heterogeneities alone.

Other explanations have to be proposed, such as the existence of a reducing front located deeper in the sample because of some redox perturbations near the interface.

Introduction

⁷⁹Se might be one of the key mobile fission products for nuclear waste disposal hosted in deep argillaceous formations due to its longevity and its anionic character (Altmann, 2009; De Cannière *et al.*, 2010). The correct understanding of selenium migration behaviour through the clay barrier is therefore essential to support the transport parameters selected for the performance assessment calculations of a deep repository for high and intermediate-level, long-lived waste. However, up to now, it remains unclear under which predominant stable mobile species selenium would be capable of migrating from the nuclear wastes through these clayey media. Indeed, on one hand, ⁷⁹Se is generally assumed to be released from reprocessing wastes in an oxidized state (+VI or +IV) due to radiolysis processes, while thermodynamic calculations deduce that Se should be in lower oxidation states, Se(0, -II) under conditions prevailing in the geological barrier system such as the Callovo-Oxfordian formation (Altmann, 2009). On the other hand, selenium is a redox-sensitive element whose reduction rate can be hindered because it involves the transfer of multiple electrons along with multiple oxygen atoms between its various oxidation states (VI, IV, 0, -I, -II) (De Cannière *et al.*, 2010).

The reduction rate strongly varies with the oxidation number of the central atom in an oxyanion, and the higher the oxidation number, the slower the reaction (Shriver *et al.*, 1990). As a consequence, reduction of Se(+VI) can be very slow and it can therefore subsist in metastable conditions, far from thermodynamic equilibrium for undetermined periods of time. Conversely, selenite is more easily reduced. According to Bruggeman *et al.* (2005), the decrease in Se(+IV) concentration as a function of time seems proportional to the initial concentration of dissolved selenite and to the amount of solid FeS₂ present in the system. These authors observed that the Se(+IV) reduction rate slowed down when clay minerals and dissolved Boom Clay organic matter (OM) were present in the system. It was interpreted as a competition mechanism because SeO₃²⁻ also remained associated with illite by an inner-sphere complex or with organic matter by an iron bridge.

While several studies focused on the sorption behaviour of selenium on clay formations, especially the Boom clay, and their components (pyrite, calcite, clay minerals) by means of batch methods (Bruggeman *et al.*, 2005, Liu *et al.*, 2008, De Cannière *et al.*, 2010), only a few studies investigated the selenium diffusive behaviour. The former studies show that selenate is not solubility limited and selenite could precipitate as CaSeO₃ in cement environments only. Moreover, while selenate is not, or only weakly sorbed, under Boom clay conditions, selenite is the most reactive selenium species, capable of being sorbed on pyrite and illite edges. Lastly, among the more reduced selenium species (0, -I, -II), only selenide could be considered as a mobile element, even though its solubility limit is very low, especially in presence of iron (from 3 x 10⁻⁸ mol L⁻¹ to 4.5 x 10⁻¹⁰ mol L⁻¹). To our knowledge, diffusive data regarding selenate in hard clay rocks are only available for the Boom clay formation (De Cannière *et al.*, 2010). In this case, the diffusive parameters for selenate are very close to those of

sulfate. Descostes *et al.* (2008) deduced from through-diffusion experiments performed on clayey samples from the Callovo-Oxfordian formation, values for diffusive parameters of selenite that were one order of magnitude lower than those obtained for ³⁶Cl. The authors hypothesized that the chemical speciation of Se changed during the diffusion tests. Nevertheless, no monitoring of the Se speciation had been undertaken to verify such an assumption.

This non-exhaustive overview underlines the difficult task of predicting the fate of the selenium diffusing through such argillaceous media. The objective of this study was to investigate the diffusive behaviour of selenium, injecting under its one of several oxidized forms, *i.e.* +IV, through indurated clay rock samples originating from the Callovo-Oxfordian formation, under physico-chemical conditions as close as possible to those prevailing in-situ, by means of the use of a N₂/CO₂ glove-box. For this purpose, two complementary experimental approaches were used: (i) A more classical radiochemical approach using radiotracers, as HTO, ³⁶Cl, and ⁷⁵Se and enabling the determination of macroscopic data, *i.e.* evolution of radioactive selenite concentration in solution and in the solid and, (ii) a non-radioactive approach, for which the solid was investigated by synchrotron-based spectroscopic methods for acquiring more detailed data (selenium oxidation state, element mapping).

Materials and Methods

Sample Origin and Sample Preparation

The rock core used for the measurements was collected from the borehole OHZ1202, argon-drilled upwards in the Meuse/Haute Marne Underground Laboratory, located in the eastern portion of the Paris basin. The sedimentary host formation (152-160 Ma) is a ~130-m-thick clay-rich Callovo- Oxfordian formation and with a burial depth of ~420-550 m below ground level (bgl). According to Gaucher *et al.* (2004), the level from which the core originates (EST30471 core 480.7-481.7 m bgl) should contain 35-65% of clay minerals (with 27-38% of mixed layer Illite/smectite), 15-28% of carbonates, 21-31% of quartz, and accessory minerals. Just after the drilling, the core was inserted into an air-tight stainless-steel tank until its opening in a N₂ glove box (O₂ < 5 ppm) in the laboratory. Afterwards, two 1-cm-thick samples were sliced from the core under anoxic conditions, using a diamond wire saw (no lubricating fluid was used), each being then cut into a 38-mm-diameter disk.

Diffusion design

Figure 1 schematically represents the diffusion cells used in this study. The cells comprise two reservoirs in polypropylene (up and downstream: 175 and 130 mL, respectively), a polypropylene sample holder, two holed plates made of polyetheretherketone (Peek), the whole being assembled together. It is worth noting that the classical stainless steel filterplates were replaced by the more chemically-inert Peek plates. Each part of the diffusion cell was previously cleaned successively with HNO₃, water, isopropanol and ethanol and dried. All the preparations of the diffusion cells were made in a N₂ glove box (O₂ < 5 ppm).

Afterwards, the two experiments were carried out in an oxygen-depleted (~5 ppm O₂) glove box with a 99.6% N₂/0.4% CO₂ gas mixture and operated at ambient temperature (21 ± 1 °C). The CO₂ content was used to simulate the in-situ Callovo-Oxfordian claystone CO₂ partial pressure (Vinsot *et al.*, 2007), which controls the carbonate concentration and solution pH. That allows the chemistry of the solutions to be close to the equilibrium state with respect to the carbonate minerals (Beaucaire *et al.*, 2008). The rock disks in the diffusion cells were equilibrated over at 6 weeks, with the synthetic solutions of composition given by Table 1. This time was found to be sufficient to reach chemical equilibrium (Descostes *et al.*, 2008; Savoye *et al.*, 2011a).

Table 1: Composition of synthetic water used in this study

[Cl ⁻] (mmol L ⁻¹)	[SO ₄ ²⁻] (mmol L ⁻¹)	ΣCO ₂ (mmol L ⁻¹)	[Na ⁺] (mmol L ⁻¹)	[K ⁺] (mmol L ⁻¹)	[Ca ²⁺] (mmol L ⁻¹)	[Mg ²⁺] (mmol L ⁻¹)
41.00	15.6	2.57	51.9	1.04	6.44	4.48

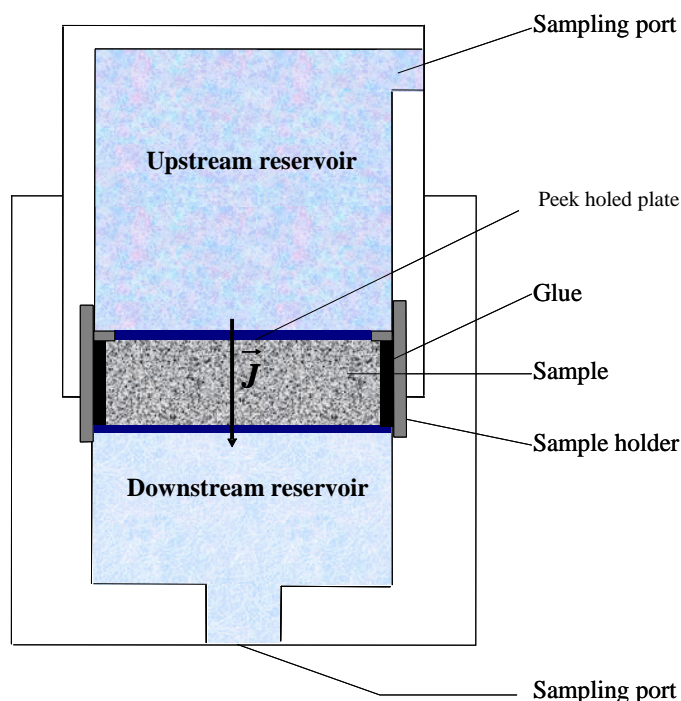


Figure 1: Experimental set-up for diffusion experiments

Diffusion stage

Diffusion cell used with radioactive tracers

After the equilibration stage, the solution in the upstream reservoir was replaced by a fresh one spiked with HTO (a water tracer) and ³⁶Cl. Their activities were set at 4.6 and 5.2 GBq m⁻³ (resp.). Both compartments were periodically sampled, the solution volume being renewed in each compartment either with the radiolabelled solution or with

synthetic water. The monitoring of the ^{36}Cl flux through the rock sample allows determination of the diffusion-accessible porosity of a non-reactive anionic tracer (ϵ_a). After completion of the first through-diffusion stage, an out-diffusion procedure was applied to the two cells in which the solutions in both reservoirs were replaced by synthetic solution without tracer, to drive HTO and ^{36}Cl diffusion out of the rock samples. At selected time intervals, the activity in the solutions was measured just before replacing them by fresh ones. This procedure was repeated until the activity measurement led to values close to the background activity values.

Then, an in-diffusion stage was performed by introducing into the upstream reservoir, both stable dissolved selenite (Na_2SeO_3 , Fluka) at a concentration of $1 \times 10^{-3} \text{ mol L}^{-1}$ and the ^{75}Se -labelled source (Eckert & Ziegler, Germany) at an activity of 5 GBq m^{-3} . As already mentioned by De Cannière *et al.* (2010), most of the $^{75}\text{Se}(+IV)$ sources supplied by the manufacturers were accompanied by $^{75}\text{Se}(+VI)$, because of the water radiolysis of the ^{75}Se stock solution. Therefore, using the ionic chromatography method described in Savoye *et al.* (2011b), we determined that 5.3% of the ^{75}Se stock was under selenate form.

For the through-diffusion stage with HTO and ^{36}Cl , careful attention was paid to keep a very low concentration in the downstream reservoir (not higher than 3% of the upstream reservoir concentration, renewed if higher) and in the upstream reservoir, a nearly constant concentration (not lower than 95% of its initial value).

In addition to the regular sampling used for monitoring the ^{75}Se activity evolution (*i.e.* 0.1 mL in the upstream), larger amounts of solutions (2 mL) were withdrawn four times throughout the selenium diffusion stage (240 days) in order to monitor any changes of the selenium speciation with the help of the ionic chromatography separation.

The activities for HTO and ^{36}Cl were counted by α - β liquid scintillation (Packard TRICARB 2500, USA) and by χ counter (Packard 1480 WIZARD, USA) in the case of ^{75}Se . The counting efficiency for each tracer was measured using synthetic water with known radioactivities. Background measurements were performed in a similar way using synthetic water without radiotracers. HTO, ^{36}Cl , and ^{75}Se data were corrected for radioactive decay with respect to the tracer injection time.

Diffusion cell used with stable selenite

Only an in-diffusion stage was carried out for selenium, directly after the equilibration stage, by introducing stable dissolved selenite (Na_2SeO_3 , Fluka) at a concentration of $2 \times 10^{-3} \text{ mol L}^{-1}$ into the upstream reservoir. This concentration value was chosen to be under the solubility limit of CaSeO_3 (Baur and Johnson, 2003), but sufficiently high so as to allow selenium detection by spectroscopic analysis. A regular sampling was performed for monitoring the decrease of the selenite concentration in solution. Analyses of stable selenite concentration were performed by ion exchange chromatography with an accuracy of about 7%. This analytical technique also allows the identification of selenate, if any.

Solid analyses

Radioactive cell: Acquisition of the ⁷⁵Se rock profiles in solid

After 240 days of selenium diffusion, the cell in which was injected radioactive selenium, was dismantled by removing the sample holder. This was roughly dried overnight in the dried atmosphere of the glove box, and afterwards in an oven at 70°C, out of the glove box, for 3 days. Then, the abrasive peeling technique developed by Van Loon and Eikenberg (2005) for Opalinus Clay, was applied to the rock sample, previously extracted from the sample holder and the glue. This technique enables the abrasion of a sample layer, thickness of which can vary from 10µm to 250 µm depending of the abrasion duration and the type of the grit grinding paper used (from P220 to P80). The choice of the thickness is directly related to the distance to the disk surface previously in contact with the upstream reservoir solution. This means that the closer to the disk surface the layer, the higher the specific ⁷⁵Se activity and the smaller the thickness.

The activities for ⁷⁵Se were counted by χ counter (Packard 1480 WIZARD, USA). ⁷⁵Se rock profile data were corrected with respect to the dismantling time.

Non-radioactive cell: X-ray Absorption Spectroscopic (XAS) analyses of the solid

After 508 days of selenium diffusion, the cell was dismantled and the rock sample was dried in the anhydrous atmosphere of an O₂-free glove box for 3 days, and then cut into a 2mm-thick section. The oxygen contamination was limited as much as possible (i) during the transportation to the synchrotron facility by using an air-tight tank and (ii) during the XAS analyses by inserting the sample into a vacuum chamber (~5 10⁻⁴ mBar).

Selenium K-edge X-ray Absorption Near-Edge Structure (XANES) and Extended X-ray Absorption Fine-Structure (EXAFS) spectra were collected at the Synchrotron Laboratory for Environmental Studies (Synchrotron Umwelt-Labor SUL) at ANKA (Karlsruhe, Germany).

Data analyses

The analysis of the results was based on Fick's second law for one-dimensional reactive transport:

$$\frac{\partial C}{\partial t} = D_a \frac{\partial^2 C}{\partial x^2} = \frac{D_e}{\alpha} \frac{\partial^2 C}{\partial x^2} = \frac{D_e}{\varepsilon_a + \rho R_D} \frac{\partial^2 C}{\partial x^2} \quad (1)$$

Where C is the concentration or activity per volume unit (mol m⁻³ or Bq m⁻³); t , the time (s); D_a , the apparent diffusion coefficient (m² s⁻¹); D_e , the effective diffusion coefficient (m².s⁻¹); α , the rock capacity factor; ε_a , the diffusion-accessible porosity; ρ , the bulk dry density (kg m⁻³); and R_D , the distribution ratio (m³ kg⁻¹).

According to van Brakel and Heertjes (1974), D_e can be written as follows:

$$D_e = D_p \varepsilon_a = \frac{\delta}{\tau^2} D_0 \varepsilon_a = \frac{D_0}{G} \varepsilon_a \quad (2)$$

Where D_0 is the free-solution (aqueous) diffusion coefficient ($\text{m}^2 \cdot \text{s}^{-1}$), δ represents the constrictivity factor (-), and τ is the tortuosity factor. G is the geometrical factor. Tortuosity and constrictivity are purely geometric factors, which, compared with a specific cross-section in free water, lengthen the diffusion pathway and reduce the diffusion cross-section, respectively (van Brakel and Heertjes, 1974).

For the through diffusion problem, the boundary and initial conditions are given by:

$$C(x, t) = 0, \quad t = 0 \quad (3)$$

$$C(x, t) = C_0, \quad x = 0, t > 0 \quad (4)$$

$$C(x, t) = 0, \quad x = L, t > 0 \quad (5)$$

Where L is the sample thickness (m), and C_0 is the concentration of the tracer in the upstream reservoir (Bq m^{-3}). For HTO and ^{36}Cl , which are non reactive tracers ($R_D = 0$), α is equal to ε_a .

The solution of Eq. (1), satisfying the boundary and initial conditions was given by Crank (1975), as the diffusive flux ($\text{Bq m}^{-2} \text{s}^{-1}$) in the downstream reservoir:

$$J(t) = D_e \frac{C_0}{L} \left[1 + 2 \sum_{n=1}^{\infty} (-1)^n \exp\left(\frac{-D_e n^2 \pi^2 t}{\varepsilon_a L^2}\right) \right] \quad (6)$$

For modelling the selenium in-diffusion data, a single reservoir method with decreasing source concentration for a semi-infinite case was used (Shackelford, 1991). The initial and boundary conditions are as follows:

$$C(x \leq 0, t=0) = C_0, \quad C(x > 0, t=0) = 0 \quad (7)$$

$$\frac{\partial C(x=0, t > 0)}{\partial t} = - \frac{D_e \alpha}{H_f \varepsilon_a} \frac{\partial C(x=0, t > 0)}{\partial x} \quad (8)$$

$$C(x=\infty, t > 0) = 0 \quad (9)$$

where the positive x -direction corresponds to the solid and H_f is the length of upstream reservoir (m). ε_a is the porosity accessible to a non reactive anionic species, *i.e.* ^{36}Cl , and α is the rock capacity factor determined for the selenite.

An analytical solution for these initial and boundary conditions is (Shackelford, 1991):

$$\frac{C(x, t)}{C_0} = \exp\left[\frac{\alpha x}{H_f} + \frac{\alpha D_e t}{H_f^2}\right] \times \text{erfc}\left(\frac{x}{2\sqrt{D_e t / \alpha}} + \frac{\sqrt{D_e \alpha t}}{H_f}\right) \quad (11)$$

Where $c(x, t)$ the concentration of the tracer in the pore water of the rock at distance x after time t (Bq m^{-3} or mol m^{-3}), and $\text{erfc}(z)$ is the complementary error function of argument z .

Results and Discussion

Diffusion of the non reactive tracers, HTO and ³⁶Cl

Figure 2 shows the instantaneous fluxes and the cumulative total activities obtained on the radioactive cell for HTO and ³⁶Cl. The best estimate of the diffusive parameters gave porosity values equal to 0.19, and 0.07 for HTO and ³⁶Cl (resp.), and effective diffusion coefficient values equal to $3.1 \times 10^{-11} \text{ m}^2 \text{ s}^{-1}$ and $4.8 \times 10^{-12} \text{ m}^2 \text{ s}^{-1}$ for HTO and ³⁶Cl (resp.). The values of the effective diffusion coefficient and the porosity for HTO and ³⁶Cl were in good agreement with those previously obtained on the same core by Savoye *et al.* (submitted) ($\langle \varepsilon(\text{HTO}) \rangle = 0.195 \pm 0.02$; $\langle \text{De}(\text{HTO}) \rangle = 2.9 \pm 0.4 \times 10^{-11} \text{ m}^2 \text{ s}^{-1}$; $\langle \varepsilon(^{36}\text{Cl}) \rangle = 0.086 \pm 0.015$; $\langle \text{De}(^{36}\text{Cl}) \rangle = 4.2 \pm 1.3 \times 10^{-12} \text{ m}^2 \text{ s}^{-1}$), and by Descostes *et al.* (2008) and Savoye *et al.* (2010) on nearby samples (less than 4 m away) ($\langle \varepsilon(\text{HTO}) \rangle = 0.195 \pm 0.045$; $\langle \text{De}(\text{HTO}) \rangle = 2.2 \pm 0.7 \times 10^{-11} \text{ m}^2 \text{ s}^{-1}$; $\langle \varepsilon(^{36}\text{Cl}) \rangle = 0.075 \pm 0.015$; $\langle \text{De}(^{36}\text{Cl}) \rangle = 3 \pm 2 \times 10^{-12} \text{ m}^2 \text{ s}^{-1}$).

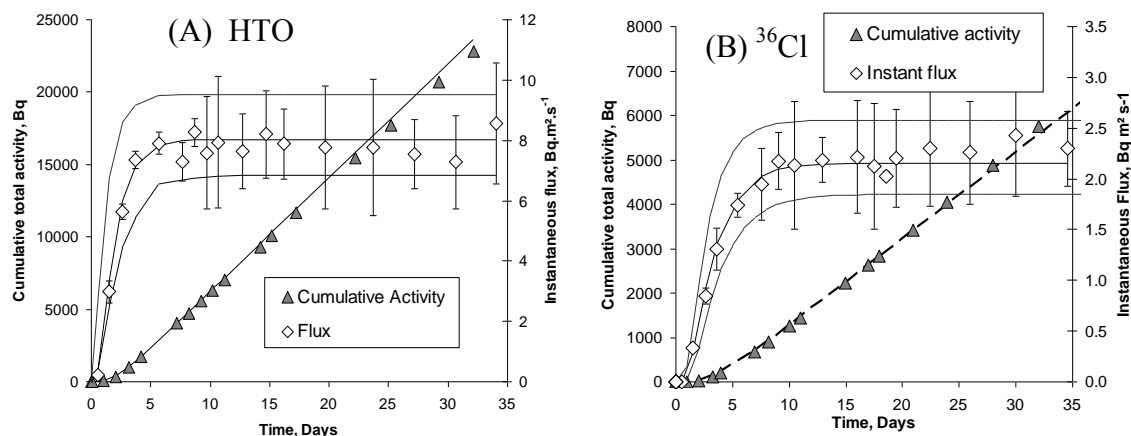


Figure 2: Cumulative total activity and instantaneous flux obtained on the radioactive cell for HTO (A) and ³⁶Cl (B). Curves were obtained from the analytical solution with the values of diffusive parameters given in the text.

Diffusion of selenite

The cell with radioactive tracers

Figure 3 shows the evolution of the ⁷⁵Se activity in the upstream reservoir as a function of time. A clear activity decrease was observed for the 240 days of the experiment. The results of the fractionation method indicated that the activity values originating from the active Se(+VI) remained quite constant throughout the duration of the experiment, while the evolution of the total measured activity can clearly be related to the decrease of the ⁷⁵Se(+IV) activity values.

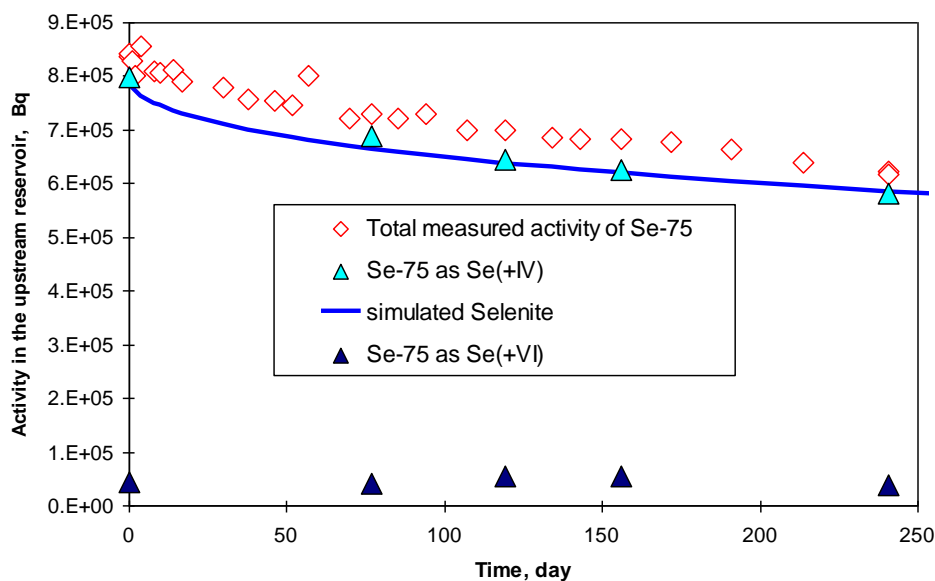


Figure 3: Evolution of the ^{75}Se activity in the upstream reservoir spiked with $\text{Se}(+\text{IV}) = 10^{-3} \text{ mol L}^{-1}$ as a function of time. The curve was calculated using the corresponding analytical solution with the parameters given in the text. Closed symbols denote the results of the fractionation. Open symbols denote the activity of total Se determined from the total radioactivity in the solution samples.

Figure 4 shows the concentration of ^{75}Se (in Bq g^{-1}) as a function of the diffusion distance in the solid. The poor quality of the experimental data fit, especially in the solid, using the equation (11) with D_e equal to $4 \times 10^{-10} \text{ m}^2 \text{ s}^{-1}$ and α equal to 28, underlines that the global pattern of the ^{75}Se profile cannot be accounted for only by a pure diffusion process with a reversible sorption. Other processes have to be proposed, related, for instance, to some possible redox phenomena.

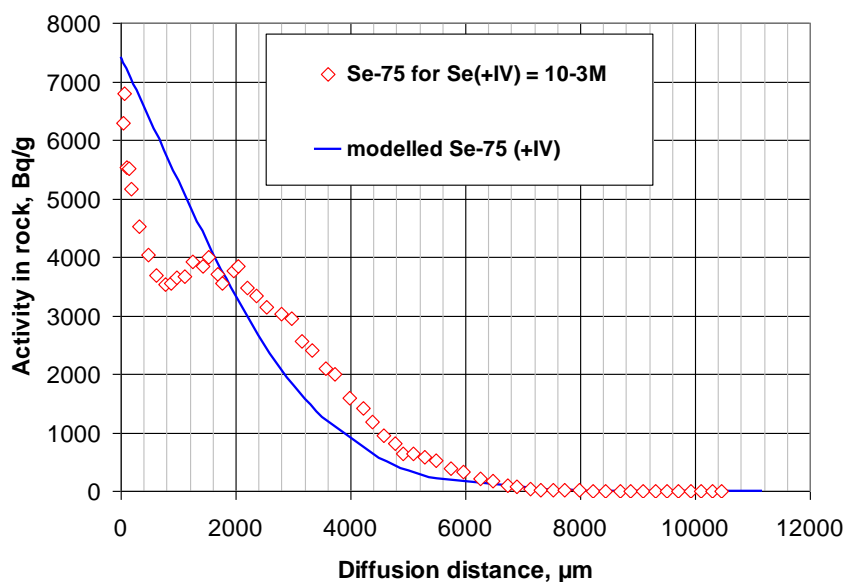


Figure 4: Concentration profile of ^{75}Se for. Symbols represent experimental data. The curve is the best fit with the parameters given in the text.

The cell with stable selenite

The evolution of the selenite concentration as a function of time in the upstream reservoir was given in the Figure 5. Even though the scattering is more pronounced than for the radioactive cell, the global tendency is quite the same, given the associated uncertainties.

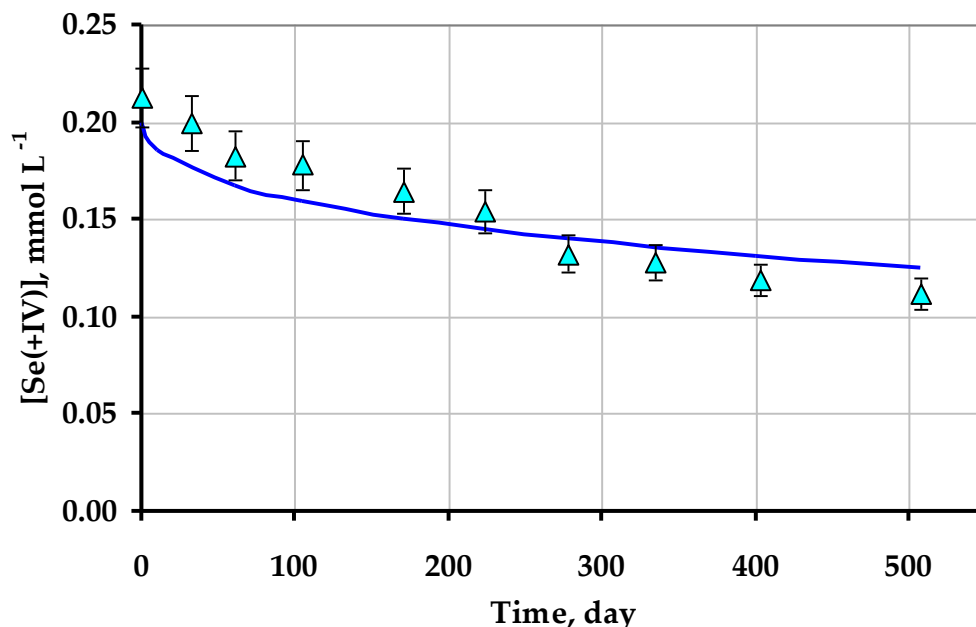


Figure 5: Evolution of the selenite concentration in the upstream reservoir. The curve was calculated using equation (11) with the same parameters than those used for the radioactive cell.

It is noteworthy that the simulated curve in Figure 5 was calculated with the same parameters as those used for the radioactive cell, indicating a relatively good consistency of the data set.

Based on the studies of Charlet *et al.* (2007) and Frasca (2011), the distribution of the total selenium content was acquired by means of μ XRF analyses at an energy of 12800 eV on some selected areas. An example is given in Figure 6 (A) showing a relative homogeneous decrease of the total selenium content from the upstream reservoir interface to the downstream reservoir, with, however, the occurrence of some isolated hot-spots.

The total Selenium profile calculated from this mapping (Figure 6(B)) exhibits a global pattern very similar to the ^{75}Se profile given in Figure 4, with a rapid drop down to 1 mm into the sample, an increase at about 2 mm, followed by a relatively regular decrease.

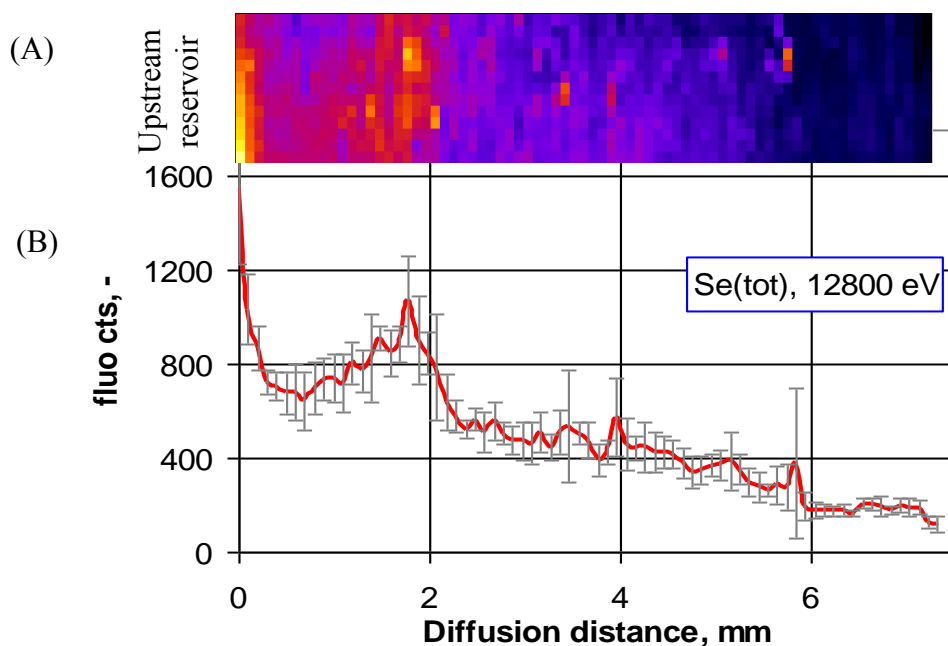


Figure 6: (A) μ XRF mapping of the selenium distribution concentration at 12800 eV. The resolution is for one pixel: 100 μ m in X-axis and 50 μ m in Y-axis. (B) Average values of total selenium as a function of the diffusion distance. Error bars correspond to the standard deviation.

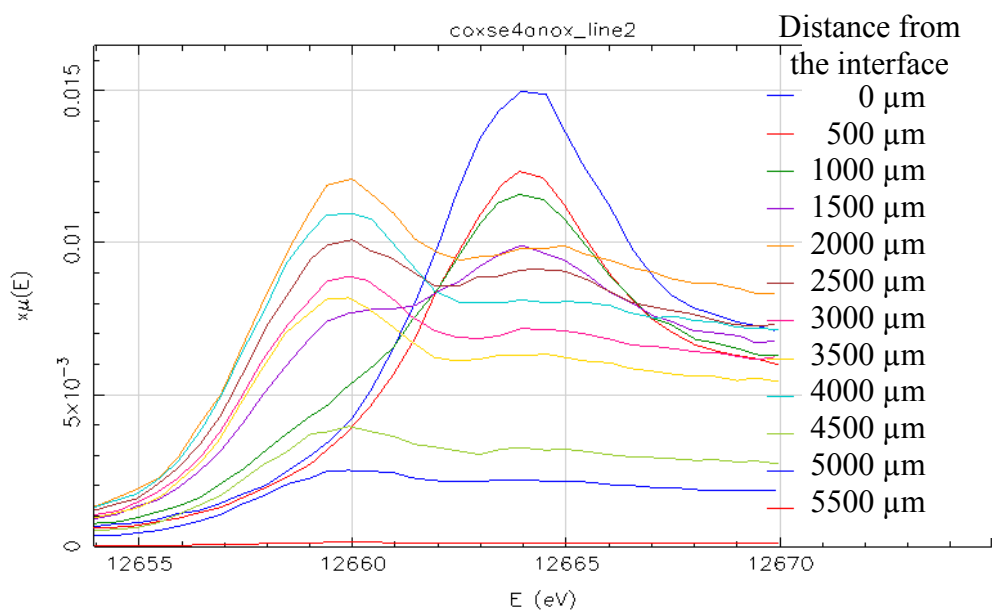


Figure 7: Selenium K-edge-XANES spectra acquired at an energy range from 12645 eV to 12670 eV, each 500 μ m, on a line from the interface with upstream reservoir to the downstream one.

To identify the evolution of the oxidation state of the selenium species into the sample, Se K-edge XANES spectra were acquired at an energy range from 12645 eV to 12670

eV (Charlet *et al.*, 2007; Frasca, 2011), each 500 μm , on a line from the interface with the upstream reservoir towards the direction of the downstream one (Figure 7). The spectra of the three first samples with respect to the interface are dominated by a strong line at 12664 eV, characteristic of Se(+IV). The spectrum acquired deeper in the profile shows a bigger contribution of a line at 12660 eV, characteristic of more reduced Selenium species, such as Se(0), S(-I) or Se(-II), called here Se(red). This profile demonstrates the occurrence of some reducing phenomena changing the oxidation state of the selenium during its diffusion through the indurated clay rock sample. The quantification of such a tendency would require a more detailed analysis of the spectrum data set, especially by reconstructing them with some reference spectra. However, a rough estimate can be obtained, assuming that (i) at the energy equal to 12.664 keV, the contribution from the reduced forms of selenium can be up to the half of the signal intensity acquired at 12.66 keV (Frasca, 2011) and (ii) at the energy equal to 12.660 keV, the contribution from selenite is quite negligible. Therefore, the μXRF mappings carried out at energies equal to 12.660 keV and 12.664 keV allowed us to build a map of the Se(red) from 12.660 keV (Figure 8(A)) and a map of the selenite by deducting the half of the intensity obtained at 12.660 keV to the signal intensity obtained at 12.664 keV (Figure 8(B)).

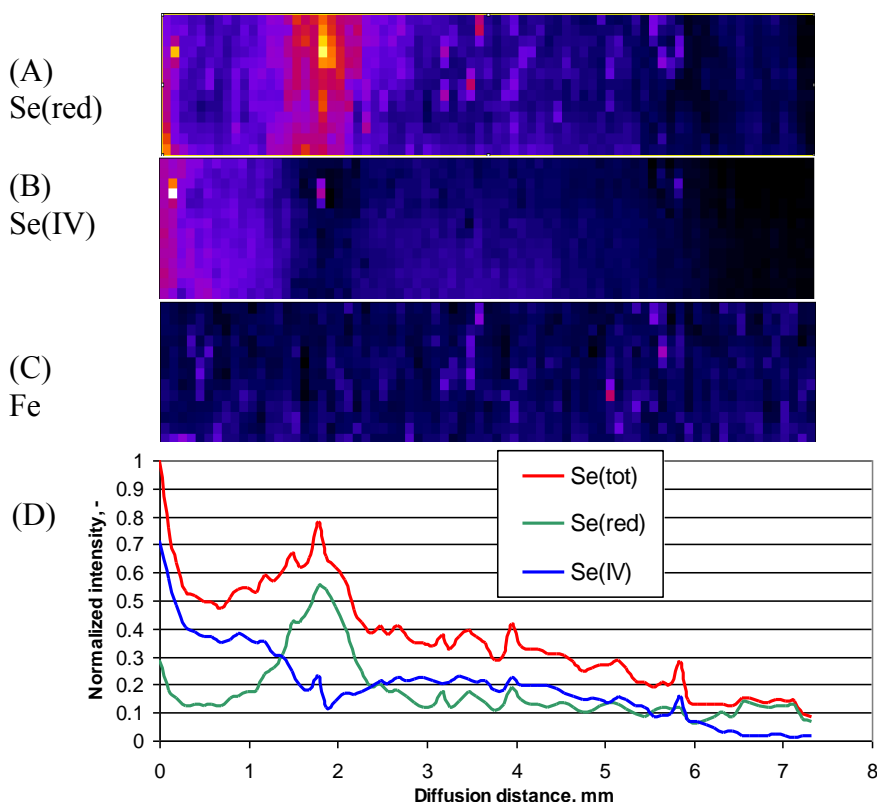


Figure 8: (A) μXRF mapping of the Se reduced forms acquired at 12.66 keV. (B) μXRF mapping of the selenite from the calculation given in the text. The investigated surface was the same than that in Figure 6. (C) μXRF mapping of Fe acquired at energies ranging from 6.1 to 6.7 keV. The resolution is for one pixel: 100 μm in X-axis and 50 μm in Y-axis. (D) Normalised average values as a function of the diffusion distance.

The Se(red) map exhibits several hot-spots, especially at about 2 mm from the interface (Figure 8(A)), while the selenite map shows a relatively smooth diffusion profile, if though the zone at 2 mm sounds selenite-depleted. Nevertheless, given the very rough approach we used, only the global pattern can be discussed. These tendencies were confirmed when considering the associated profiles built by averaging signals and normalizing by the signal acquired at 12.8 keV, i.e. the total selenium (Figure 8 (D)).

The occurrence of the large Se(red) hot-spot at 2 mm could be explained by some mineralogical heterogeneities, such as the presence of pyrite. To address this issue, the μ XRF mapping of Fe acquired for energies ranging from 6.1 to 6.7 keV is presented in Figure 8(C). The distribution of the iron is quite homogeneous over the investigated surface, infirming the assumption given above. However, other Se(red) hot-spots located deeper in the sample can be correlated with some Fe hot-spots (possible occurrence of pyrite).

Another explanation for accounting for the large Se(red) accumulation at 2 mm can be proposed, such as the occurrence of a reducing front located deeper than at the interface because of some redox disturbances related to the solution.

Summary and Conclusions

The diffusive behaviour of selenite was studied through two rock samples originating from the Callovo-Oxfordian (COx) formation (France) and lying in physico-chemical conditions as close as possible to those prevailing in-situ, by means of the use of a N₂/CO₂ glove-box. A radiochemical approach using HTO, ³⁶Cl, and ⁷⁵Se, as tracers, was supplemented by a non-radioactive one for which the solid was investigated by synchrotron-based spectroscopic methods.

The two approaches led to mutually consistent results. While the monitoring of the selenium concentration in solutions could be roughly reproduced by a pure diffusion model with a reversible sorption ($D_e = 4 \times 10^{-12} \text{ m}^2 \text{ s}^{-1}$ and $R_d = 12 \text{ mL g}^{-1}$), the total selenium rock profiles exhibited irregular shapes, requiring more complicated models. The determination of the Selenium oxidation state by means of the spectroscopic analyses revealed (1) a relative regular diffusion profile for selenite and (2) the presence of some areas rich in selenium reduced forms (Se(red) ~ Se (0), S(-I) and/or Se(-II)), especially located at about 2 mm from the interface. This analysis allowed us to explain the shape of the ⁷⁵Se rock profile. Moreover, some correlations exist between some of the Se(red) hot-spots and the iron content, suggesting the role played by the iron-rich minerals, such as pyrite. However, the larger Se(red)-rich area (at 2 mm) could not be accounted for by some mineralogical heterogeneities.

Other explanations have to be proposed, such as the existence of reducing front located deeper in the sample because of some redox perturbations near the interface.

Acknowledgement

The research leading to these results has received funding from the European Union's European Atomic Energy Community's (Euratom) Seventh Framework Programme FP7/2007-2011 under grant agreement n° 212287 (RECOSY project). The authors also thank Andra for providing the core used in this study.

References

- Altmann S. (2009). 'Geo'chemical research: A key building block for nuclear waste disposal safety cases. *J. Contam. Hydrol.* 102, 174-179.
- Baur I, Johnson C.A. (2003). Sorption of Selenite and Selenate to Cement Minerals. *Environ. Sci. Technol.* 37, 3442-3447.
- Beaucaire C., Michelot J.-L., Savoye S., Cabrera J. (2008). Groundwater characterisation and modelling of water-rock interaction in an argillaceous formation (Tournemire, France). *Appl. Geochem.* 23, 2182–2197.
- Bruggeman C., Maes A., Vancluysen J., Vandemussele P. (2005). Selenite reduction in Boom clay: Effect of FeS₂, clay minerals and dissolved organic matter. *Environ. Pollut.* 137, 209–221.
- Charlet L., Scheinost A., Tournassat C., Greneche J., Gehin A, Fernandezmartinez A, Coudert S., Tisserand D., Brendle J. (2007). Electron transfer at the mineral/water interface: Selenium reduction by ferrous iron sorbed on clay. *Geochimica et Cosmochimica Acta* 71(23), 5731-5749.
- Crank J. (1975). *The Mathematics of Diffusion*, second ed. Pergamon Press, Oxford.
- De Cannière P., Maes A., Williams S., Bruggeman C., Beauwens T., Maes N., and Cowper M. (2010) Behaviour of selenium in Boom Clay. Work performed under contract: SCK•CEN ref:CO 90 01 1467.01 1467 RP.W&D.037 – NIROND ref: CCHO2004/00/00 DS251-A44/2.1.
- Descostes M., Blin V., Bazer-Bachi F., Meier P., Grenut B., Radwan J., Schlegel M. L., Buschaert S., Coelho D., Tevissen E. (2008). Diffusion of anionic species in Callovo-Oxfordian argillites and Oxfordian limestones (Meuse/Haute-Marne, France). *Appl. Geochem.* 23, 655-677.
- Frasca B. (2011). Migration de l'iode et du sélénium au travers de roches argileuses. Thèse de L'Université Paris-Sud, Orsay.
- Gaucher E., Robelin C., Matray J.-M., Negrel G., Gros Y., Heitz J.-F., Vinsot A., Rebours H., Cassagnanere A., Bouchet A. (2004). ANDRA underground research laboratory: interpretation of the mineralogical and geochemical data acquired in the Callovian-Oxfordian formation by investigative drilling. *Phys. Chem. Earth* 29, 55-77.
- Liu X., Fattahi M., Montavon G., and Grambow B. (2008). Selenide retention onto pyrite under reducing conditions. *Radiochimica Acta* 96 (8), 473–479.

- Savoye S., Page J., Puente C., Imbert C., Coelho D. (2010). A new experimental approach for studying diffusion through an intact and unsaturated medium: A case study with Callovo-Oxfordian argillite. *Environ. Sci. Technol.* 44, 3698-3704.
- Savoye S., Goutelard F., Beaucaire C., Charles Y., Fayette A., Herbette M., Larabi Y., Coelho D. (2011a). Effect of temperature on the containment properties of argillaceous rocks: The case study of Callovo–Oxfordian claystones. *J. Contam. Hydrol.* 125, 102-112.
- Savoye S., Frasca B., Grenut B., Fayette F., Radwan J. (2011b). Study of the Diffusive behaviour of selenite and selenate through the Callovo-Oxfordian claystones (France): effect of the initial selenite concentration. 3rd Annual Workshop Proceedings of the 7th EC FP - Recosy CP, Balaruc-les-Bains (Sète - Languedoc - Roussillon, France).
- Savoye S., Frasca B., Grenut B., Fayette F. How mobile is iodide in the Callovo-oxfordian claystones under experimental conditions close to the in situ ones? Submitted to journal of Contaminant Hydrology.
- Schackelford C.D. (1991). Laboratory diffusion testing for waste disposal: A review. *Journal of Contaminant Hydrology* 7, 177-217.
- Shriver D.F., Atkins P.W., Langford C.H. (1990). *Inorganic chemistry*. 706 pp. Oxford University Press. Oxford, Melbourne, Tokyo.
- van Brakel J., Heertjes P. M. (1974). Analysis of diffusion in macroporous media in terms of a porosity, a tortuosity and a constrictivity factor. *Int. J. Heat Mass Transfer* 17, 1093–1103.
- Van Loon L.R., Eikenberg J. (2005). A high-resolution abrasive method for determining diffusion profiles of sorbing radionuclides in dense argillaceous rocks. *Appl. Rad. Isot.* 63, 11–21.
- Vinsot A., Mettler, S., Wechner, S. (2007). In-situ characterization of the Callovo-Oxfordian pore water composition. *Phys. Chem. Earth* 33, 75-86.

ADVANCES IN MULTIPLEXED FIBER-OPTICAL SENSING FOR ENVIRONMENTAL APPLICATIONS

Dörte Steinbrück, Felix Geißler and Michael U. Kumke*

Institute of Chemistry, University of Potsdam (GER)

* Corresponding author: kumke@uni-potsdam.de

Abstract

Within the last years we have developed a novel optode based on a time-resolved luminescence detection scheme for the determination of pH. The optode consist of a tailored proton permeable polymer (P1), in which a pH sensitive dye is embedded. This dye changes its photo physical properties based on the proton activity. We have tested different dyes, of which Carboxyfluorescein (CF) best matched the requirements for a decay time based determination of the pH-value [Steinbrück and Kumke (2009)]. In a second optode development an established oxygen sensor was significantly improved. We introduce a novel luminescence probe which improves the limit of detection (LOD) by two orders of magnitude [Steinbrück et al. (2010)]. Within the last project year we worked on the integration of both optodes into single probe for the simultaneous measurement of pH and oxygen content. Initial results of our efforts are presented.

Introduction

Fiber-optical chemical sensing (FOCS) may be a powerful alternative to electrochemical-based techniques for sensing of analytes such as oxygen or pH, especially for cases in which miniaturization potential or the simultaneous determination of several analytes (multiplexing) is a major request. A key factor in the design of novel multiplexed FOCS is the interplay between the fluorescence probes and the polymer matrix which is used for embedding. On the one hand a tailored polymer-matrix can enhance the selectivity of the optical sensor, but on the other hand it may also limit the performance in multiplexing approaches for one of the analytes. Currently available FOCS often use alterations in the luminescence intensity or spectral shifts for the qualitative and quantitative determination of the analytes. However, intensity-based measurements are prone to aging and matrix effects. Therefore, they require a tedious calibration procedure (often using additional dyes as internal reference). In contrast, sensing schemes that are based on measurements of the luminescence decay time are preferred – especially in environmental sensing applications – because their performance is less biased by such effects.

Our current research is focused on the evaluation and integration of decay-time based optical sensing schemes for the simultaneous determination of different chemical parameters. Recently Borchert et al. (2011), Kocincova et al. (2007), Schröder et al. (2007) and Tian et al. (2010) discussed the advantages of optical determination methods, especially with respect to multiparameter sensing and showed the successful implementation of optical-based simultaneous dual analyte sensing, which is intrinsically impossible to achieve with one electrochemical sensor. Applying frequency domain spectroscopy (FD-S) inexpensive, rugged diode lasers (DL) can be used as excitation source. Moreover, by modulating the DL in different frequency ranges (e.g., kHz and MHz) the simultaneous detection of different analytes can be established – without the necessity of a high spectral separation of the luminescence probes used in the detection scheme. In this contribution we present the progress made in the development of multiplexed optical sensor for the simultaneous determination oxygen and pH based on FD-S.

Experimental

The FD-S measurements were performed with the instrumentation described in [Steinbrück et al. (2010)]. The set-up was modified for the dual detection as shown in Figure 1. Briefly, for the oxygen determination a 405 nm LD was modulated with two frequencies $f_1 = 4.5$ kHz, $f_2 = 9.21$ kHz. The phase shift ϕ in the red spectral range (detector from Hamamatsu, type: H10723-20) was measured and the average decay time τ was calculated. For the pH determination the 405 nm LD was modulated with a frequency of 30 MHz and the phase shift ϕ was measured in the green spectral range (detector from Hamamatsu, type: H6780-20), and the average decay time τ was calculated. The fiber optical steady state emission measurements were carried out on a sec2000 system from ALS Co., Ltd.

The data were analyzed according to [Steinbrück et al. (2010)]. All measurements were performed at 20°C, unless otherwise stated. The NaCl was purchased from Aldrich; the solutions were prepared in buffered solutions (for details see [Rauscher et al. (1977)]).

Different polymers (P1, P2 and P3) were used for the immobilization of the pH- and oxygen sensitive probes. The pH sensitive CF was embedded in the water and oxygen permeable polymer P1. The polymers P2 and P3 have a high permeability for oxygen, but are impermeable for water, consequently only the oxygen sensitive dye was immobilized (see Figure 1), in this report only the results for P1 and P3 are shown.

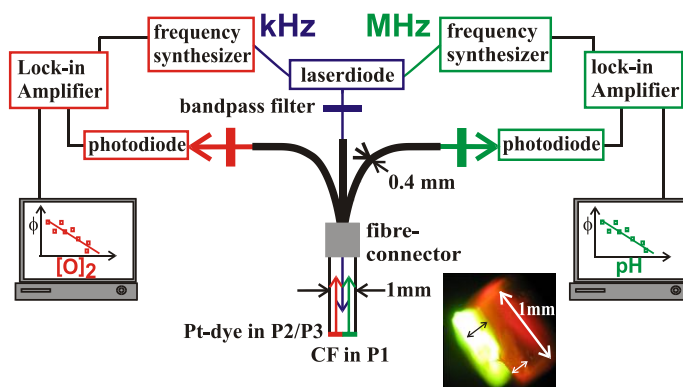


Figure 1: Schematic FD-S set-up for the simultaneous determination of two chemical parameters.

Characterisation of the pH-sensitive optode

Calibration, reversibility and long term stability in P1 Polymer

The pH-sensitive optode (CF immobilized in P1) was characterized with steady-state and FD spectroscopy. In Figure 2, pH dependent emission spectra of Carboxyfluorescein (CF) after excitation using a 450 nm laser diode are shown. The emission at $\lambda_{em} = 490$ nm decreases whereas the emission at $\lambda_{em} = 550$ nm increases with increasing pH. Consequently, from the fluorescence intensity variation the pH of the sample can be deduced based on spectral measurements, which could be applied in a very simple pH sensing scheme with all the benefits (e.g., miniaturization, distributed sensing) of FOCS. However, methods based on intensity alterations for the determination of pH are of limited use in biological, geological or medical samples because they are prone to artefacts cause by background fluorescence or scattering effects of the matrix. On the other hand, fluorescence decay time based detection schemes are less prone to such interferences.

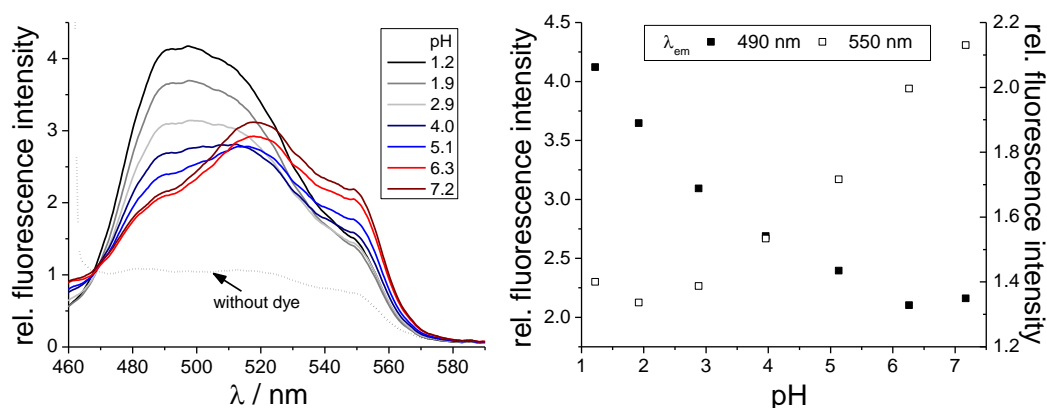


Figure 2: Fiber optical spectral and intensity measurements of CF at different pH in P1. ($\lambda_{ex} = 450$ nm).

The challenge to be met in FD-S based sensing of pH is that the fluorescence decay times of the available probes are mostly in the nanosecond time range, hence a MHz modulation scheme is required. Figure 3 (left) shows the change (relative to pH = 0.5) in the fluorescence decay time of CF immobilized in P1 polymer for the pH range $0.5 < \text{pH} < 7$ measured using FD-S. The inflection point is at $\text{pH} = 3.7 \pm 0.2$. From the data it can be seen that the change in the fluorescence decay time of CF may also be used for pH determination in the range between $1 < \text{pH} < 6$ (with highest accuracy around the inflection point at about pH 3.7).

The response time of the sensor depends on the direction of pH alteration. In Figure 3 (right) the measurement starts at pH = 1, after ten minutes the pH was changed to six, the equilibrium time (measured as t_{90}) of 5 min is much higher than it was observed by switching the pH from six to one. Here, t_{90} is determined to 30 s. A similar behaviour was also observed in an agarose based optical sensor by [Hashemi et al. (2008)]. Furthermore, the stability of the signal was measured over eight hours and only a slight change of ± 0.05 ns was found showing an excellent stability of the optode.

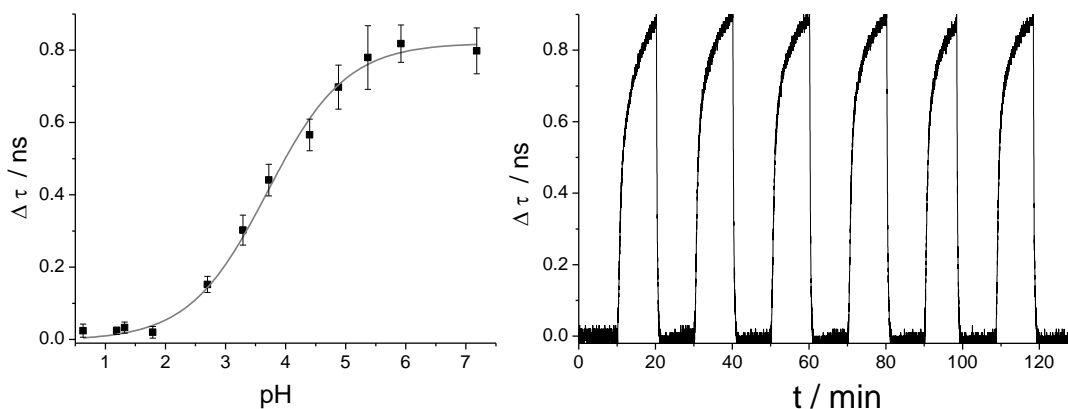


Figure 3: Calibration (left) and response behaviour (right) of the pH sensitive optode in P1 polymer switching the pH between 1 and 6 ($f = 30$ MHz, $\lambda_{ex} = 450$ nm).

Cross sensitivity FOCS based pH sensor

In environmental applications the ionic strength of the matrix can vary to a large extent. The pH sensitive optode contains a polymer matrix which is permeable for water but also other ions are able to diffuse into the polymer. Subsequently, the polarity of the polymer matrix is changed by those ions. Because the photo physical properties of the dye depend on it, the decay time is slightly shifted with the ionic strength of the medium. In Figure 4 the influence of the ionic strength is shown for different pH values.

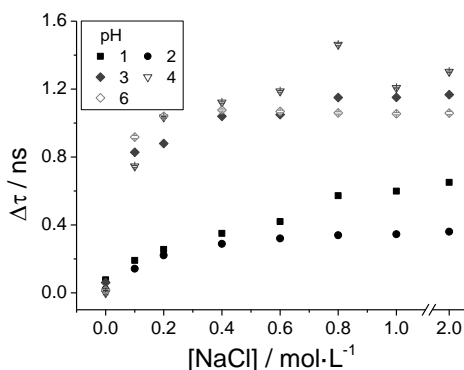


Figure 4: Change in decay time of an optode after addition of NaCl solution into an aqueous solution.

It can be seen, that the largest influence was found in the low ionic strength range of $I < 0.2$, at larger ionic strength the change in the fluorescence decay time is almost negligible. From the results it can be concluded that the optode i) can be used in media of different ionic strength but ii) it needs a proper calibration for the particular conditions of the medium in order to give proper readings.

In summary, the FOCS optode for pH based on a FD-S detection scheme is on hand and can be integrated into a first multiplexing FOCS scheme.

Characterization of FOCS for simultaneous pH and oxygen determination

Single polymer FOCS

The polymer matrix plays a key role in the performance of optodes. For the combination of oxygen and pH sensing the polymer matrix must be permeable for oxygen as well as for water. In the first show case presented here, the polymer material P1, which proved to be well suited for pH sensing, was tested, whether it also meets the requirement of good oxygen permeability. Therefore, in the first step the P1 polymer was tested for oxygen sensing only using the well-established luminescence probes (e.g., Pt-(tetrapentafluoro)phenylporphyrin).

In Figure 5 the performance of the oxygen sensitive optode at different pH is shown. Compared to the standard polymers used for the oxygen sensing the quenching efficiency and subsequently the resulting dynamic range for the detection of oxygen is decreased in the P1 polymer matrix. The observed decay time change for the oxygen concentration range of interest decreases to $\Delta\tau = 10 \mu\text{s}$ (immobilization in fluorinated polymer results in change of $\Delta\tau = 40 \mu\text{s}$). This was seen for all pH tested and the observed $\Delta\tau$ was almost independent of pH.

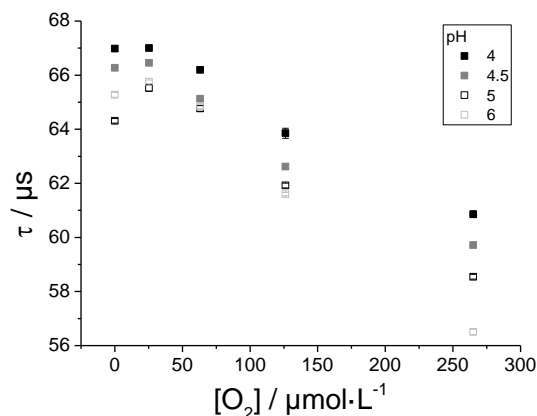


Figure 5: Calibration of a Pt-based oxygen optode (immobilized in P1) in aqueous solution with different proton concentrations (FD-S, $\lambda = 405$ nm and $f_1 = 4.5$ kHz, $f_2 = 9.21$ kHz).

In the next stage, CF was co-immobilized into the P1 matrix. First, the emission spectra of the FOCS containing the combined fluorescence probes were measured (see Figure 6). The steady state measurements showed that the two emission signals corresponding to CF fluorescence and to the Pt-dye luminescence are spectrally well separated yielding only a minimum of interference arising from bleed through contributions in the two detection channels (see Figure 1). Interestingly, in the intensity based measurements a much stronger effect of the pH on the luminescence intensity of the oxygen optode was observed.

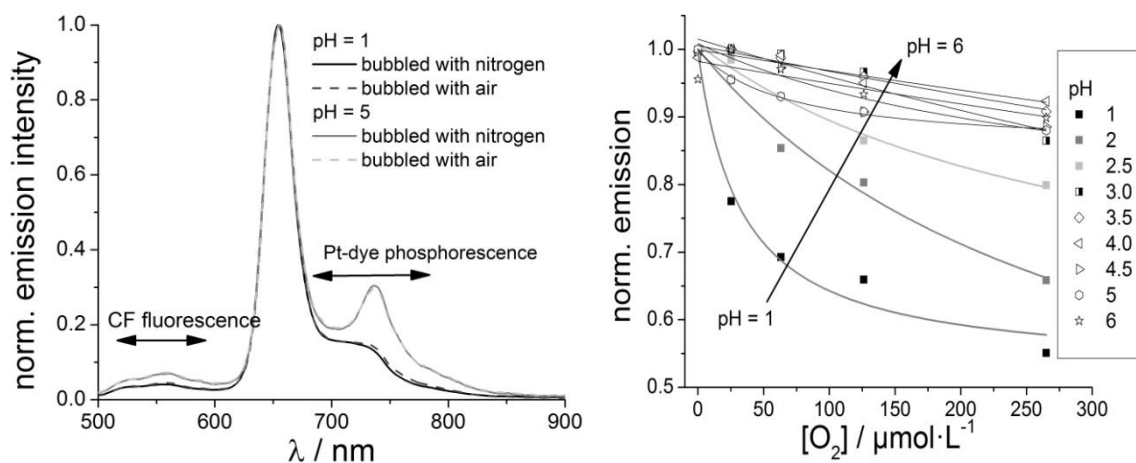


Figure 6: left: Emission spectra of the embedded Pt-dye and the CF in P1, $\lambda_{ex} = 405$ nm. Right: Normalised emission intensity ($620 \text{ nm} < \lambda_{em} < 740 \text{ nm}$) measured at different oxygen concentrations.

The influence of the oxygen concentration on the performance of the pH optode was also tested in FD-S measurements at a modulation frequency of 30 MHz. In Figure 7 the obtained change in the fluorescence decay time of CF (relative to pH 0.5) at different

oxygen concentrations is shown. It can be seen that for the pH range $1 < \text{pH} < 6$ basically no influence is observed (only a slight difference between oxygen free and “with” oxygen may be anticipated for the pH 6 measurement (see Figure 7)). These findings underline the superior performance of decay-time based detection schemes.

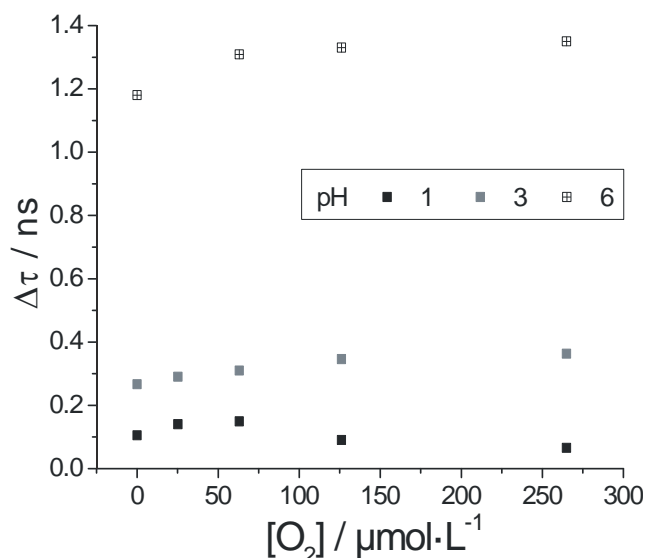


Figure 7: Results from FD-S by modulating a 405 nm laser diode 30 MHz, measuring the green fluorescence. The dye is immobilised in P1.

Dual polymer FOCS

In order to improve the overall performance of the combined sensor a second polymer for the oxygen probe, which allows also the combination with polymer P1 (optimized for pH sensing), was tested (see Figure 1). Of the different polymers tested, P3 showed the most promising results. P3 is not permeable for water; therefore protons did not interfere with the oxygen sensitive part of the probe, e.g., by altering the polymer matrix leaving the oxygen sensitive part of the optode unchanged or by avoiding direct interactions of the two probes.

In Figure 8 the performance of the dual FOCS sensor for the measurement of pH and of the oxygen concentration is shown. Compared to the other polymers the oxygen measurements are almost independent on the pH of the medium and also for the other way round, the pH measurements are not affected by the oxygen concentration present in the medium. For a high precision in the oxygen concentration determinations the pH of the solution could be considered in the data evaluation in the acidic pH range. Figure 9 shows that the influence of the pH on the oxygen determination is negligible at higher pH than 4.

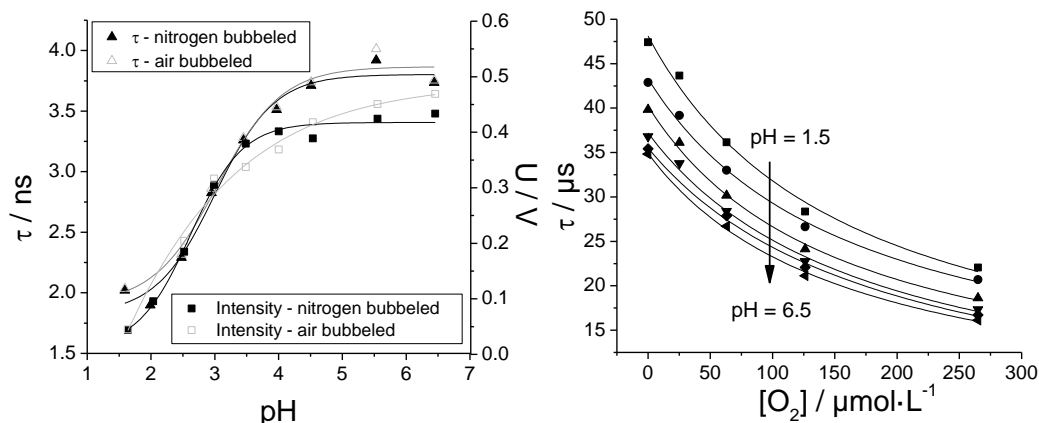


Figure 8: Results from FD-S by modulating a 405 nm laser diode with $f = 30$ MHz, measuring the green fluorescence (left), and $f_1 = 4.5$ kHz and $f_2 = 9.21$ kHz, measuring in the red spectral range (right). The pH sensitive dye is immobilised in P1, the oxygen sensitive dye is embedded in P3. Both were fixed on one optical fiber.

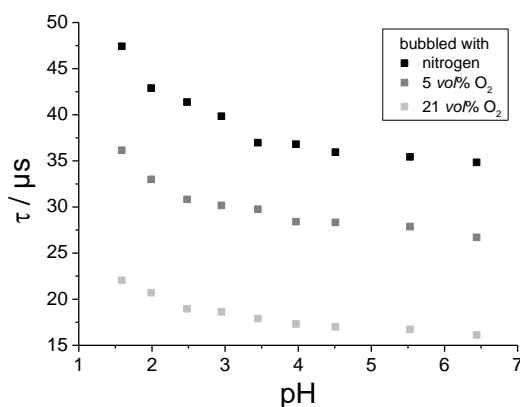


Figure 9: Measurements from Figure 8 (right side), for display the linearity of pH-dependent behaviour of the oxygen determination in the acidic range, and the almost constant decay time at $\text{pH} > 4$.

Summary and Conclusions

Within the ReCosy project we have worked on the development of FOCS for different chemical parameters. A key feature of the technique developed is the use of a time-resolved detection scheme for optical multiplexing of different chemical analytes, which is – compared to intensity-based approaches – less prone to interferences from the sample matrix.

In previous contributions we reported on the distinct improvement of the limit of detection for oxygen measurements in solution and in the gas phase as well as on the development of a FD-S based detection scheme for pH measurements. The sophisticated step during the development of the pH sensor was to find a polymer,

which did not affect the pH response of the sensitive dye and at the same time was capable of immobilizing the dye within the polymer. The last point depends on the solubility of the dye in the polymer matrix. The first point depends on the functional groups within the polymer. The complex interplay between functional groups of the polymer matrix and of the immobilized probe defines the overall performance of the pH optode. From the tested polymers P1 was selected because its hydrophilic groups show no or only minor blocking of the functional groups of the probe. The novel pH optode works reliable in aqueous solutions and in a next step more demanding matrices (e.g., clinical analytics, food production) will be tested for performance of the sensor.

As a logical continuation the two FOCS systems for oxygen and pH measurements were combined in one optical sensor. By using different frequency ranges as well as different spectral ranges in the detection scheme a dual FOCS optode was built. In the near future the performance of the dual optode is optimized with respect to i) cross sensitivity by testing additional polymer blends and ii) further improving optical components like filters for emission light selection.

Acknowledgement

The research leading to these results has received funding from the European Union's European Atomic Energy Community's (Euratom) Seventh Framework Programme FP7/2007-2011 under grant agreement n° 212287 (RECOSY project).

References

- Borchert N. B., Ponomarev G. V., Kerry J. P., Papkovsky D. B. (2011) O₂/pH Multisensor based on one phosphorescent dye, *Anal. Chem.*, 83, 18-22
- Hashemi P., Zarjani R. A. (2008) A wide range pH optical sensor with mixture of neutral red and thionin immobilized on an agarose film coated glass slide, *Sensors and Actuators B*, 135, 112-115.
- Kocincova A. S., Borisov S. M., Krause C., Wolfbeis O. S. (2007) Fiber-Optic microsensors for simultaneous sensing of oxygen and pH, and of oxygen and temperature, *Anal. Chem.*, 79, 8486-8493
- Rauscher, Voigt, Wilke (1977): *Chemische Tabellen und Rechentafeln für die analytische Praxis*, VEB Deutscher Verlag für Grundstoffindustrie Leipzig, Chapter 9.4, pp. 140-145.
- Schröder C. R., Polerecky L., Klimant I., (2007) Time-Resolved pH/pO₂ Mapping with Luminescent Hybrid Sensors, *Anal. Chem.*, 79, 60-70
- Steinbrück D., Kumke M. U. (2009) Development of multiparametric optical sensing for environmental applications, *Wissenschaftliche Berichte - Forschungszentrum Karlsruhe (FZKA 7466)* 103-110

Steinbrück D., Schmälzlin E., Kumke, M.U. (2010) Development of a fiber optical chemical sensor (FOCS) for the determination of low oxygen concentrations, wissenschaftliche Berichte - Karlsruhe Institut für Technologie, (KIT-SR 7557) 103-11

Tian C., Shumway B. R., Youngbull A. C., Li Y., Jen A. K.-Y., Johnson R. H., Meldrum D. R. (2010) Dually fluorescent sensing of pH and dissolved oxygen using a membrane made from polymerizable sensing monomers, Sensors and Actuators B, 147, 714-722

STUDY OF U OXIDATION STATES IN NATURAL GEOLOGICAL MATERIAL

IvanPidchenko^{1*}, Susanna Salminen-Paatero², Tonya Vitova³ and Juhani Suksi²

¹St. Petersburg State University (RU)

²University of Helsinki (FI)

³Karlsruher Institute of Technology

...

* Corresponding author:ivan.pidchenko@gmail.com

Abstract

A novel analytical procedure based on wet chemistry was developed to determine uranium oxidation states in low U content geological material. It is well known that U may change its redox state during acidic extraction of the material under study. To estimate degree U redox disturbances $^{236}\text{U}^{6+}$ and $^{232}\text{U}^{4+}$ redox tracers were prepared and used in the experiments. It was shown that during extraction no oxidation of U occurs; on the other hand, strong reduction of U was observed which was assumed to relate to Fe^{2+} released during the extraction. The possible role of radiation induced defects in the sample material in modifying redox-state of extraction solution was additionally studied using an annealing experiment. It was found that the reduction of $^{236}\text{U}^{6+}$ tracer during the extraction decreased when annealing temperature was increased: no reduction of U occurred during the leaching when sample was annealed at 500 °C. At 1000 °C all original U^{6+} in material transformed to U^{4+} . Most of the results obtained by wet chemistry were validated by XANES. Application of two independent methods can be utilized in controlled way to study U oxidation states in low U geological material.

Introduction

Spent nuclear fuel consists practically of UO_2 providing a large artificial source of U. A key property influencing the radioecological behavior of U and other actinides is their oxidation state [Silva, Nitsche (2001)]. Study of U oxidation states is important when assessing U release from and migration around a U source. Groundwater contains variable amount of U. It has been often observed using U series analyses that significant amount of U is moved from groundwater on fracture surfaces (Blomqvist et al. 2000). Whether this is due to sorption or co-precipitation or a result of U^{6+} reduction to U^{4+} is unclear. In order to study possible redox-impact it was considered necessary to have a simple and reliable method for determination of U oxidation state in fracture surface materials.

Study of U oxidation states consists of two basic approaches: wet chemistry (extraction and ion-exchange separation techniques) and instrumental, non-destructive, methods (XAS, XPS etc.). However, fracture surface samples have too low U concentrations to be reliably analyzed by instrumental methods [*Brown and Sturchio (2002)*]. Furthermore, the specific equipment for instrumental methods is unavailable in many laboratories. Reliable information about U oxidation state in a solid material can be obtained by means of wet chemistry, provided that original U oxidation forms composition is not disturbed during U extraction from the sample material. During extraction experiments U redox-balance may change and U oxidation states are affected by redox active elements, mainly Fe, extracted from ferric and ferrous mineral phases [*Ervanne and Suksi (1996)*, *Ervanne, (2003)*]. Radiation induced electron-hole defects in U ore components, e.g. quartz and mica, are also considered as possible redox centers.

In this work we have studied redox effects caused by the samples own components. These effects are measured using alpha-spectrometry technique by analyzing $U^{4+}/[U^{4+}+U^{6+}]$ ratio, further – U^{4+}/U_{total} , in both natural U and in artificial U isotope redox tracers. During the extraction procedure U can be reduced or oxidized depending on the conditions in the solution. These redox effects represent certain complexities while analyzing true U valent form composition in the original solid material. To increase understanding of possible impact of radiation induced defects in the sample material annealing experiment, where sample material was heated at different temperatures at the range of 200-1000 °C, was performed. Heating is supposed to heal radiation defects and thus decrease considerably the intensity of redox effects which would give finer U^{4+} and U^{6+} forms distribution values. Results are compared with those obtained from U L_{III} XANES. This study forms part of systematic investigation towards scientifically sound wet chemical method for U oxidation states determination in all types of low U concentration solid materials.

Material

Certified reference ore, known as DL-1a [*Steger and Bowman, 1980*] containing (uraninite UO_{2+x} ($0 < x < 0.25$) and brannerite $(U,Ca,Ce)(Ti,Fe)_2O_6$ as the main U minerals. It contains 0.0116% of U, 0.9% Fe and 0.45% S, the elements which may disturb U redox state. Main mineral components were identified as quart, muscovite (mica), pyrite and iron oxides.

Experimental

We focused on following issues of experimental design: (1) preparing of appropriate and reliable redox tracers; (2) quantitative U extraction from original untreated and annealed sample material (insoluble U is considered U^{4+}); (3) analyzing U^{4+}/U_{total} ratio, then for natural and tracer U fractions; (4) transfer of extraction experiment results to the original solid material; (5) comparison with XANES results.

1.1. Preparation of anoxic extraction solution

For the extraction of U from the sample material pure 4.5 M HCl and mixed with 0.03 M HF were prepared using commercial acids, and then bubbled with *Ar* gas during several minutes to remove dissolved oxygen.

1.2. Preparation of redox tracers

Two redox tracers $^{232}\text{U}^{4+}$ and $^{236}\text{U}^{6+}$ were prepared. $^{232}\text{U}^{4+}$ was prepared by adding a few drops of 15% TiCl_3 solution. Reduced U was expected to be oxidized back to U^{6+} after the reduction capacity of TiCl_3 has been used, the time depending mainly on concentrations of U, Fe and O [Hussonnois *et al.*, 1989]. The oxidation half-life time for U in the mixture of 4.5 M HCl + 0.03 M HF solution and 10^{-5} M U concentration was determined to be 292 h, equivalent to oxidation of <1% during the analysis time [Ervanne and Suksi(1996)]. Oxidation kinetics was monitored by taking samples from the $^{232}\text{U}^{4+}$ solution as a function of time and analyzing U^{4+} and U^{6+} fractions using ion-exchange chromatography as described in section 2. After ion-exchange separations some 2-3% of total ^{232}U was repeatedly found in the U^{6+} fraction. $^{236}\text{U}^{6+}$ solution was prepared by evaporating ^{236}U tracer solution to dryness and dissolving the evaporate into 4,5 M HCl. The amounts of $^{232}\text{U}^{4+}$ and $^{236}\text{U}^{6+}$ tracers used in experiments were 40 and 6-24 dpm respectively corresponding to U masses 0.8 pg and 0.04-0.16 μg , thus having from 2 to 7 orders of magnitude lower masses than it's of the natural U extracted (5-50 μg).

1.3. Annealing (heating)

Seven samples' aliquots were annealed at different temperatures 200-1000 $^{\circ}\text{C}$. For that a few grams of material were heated in quartz vessel under *Ar* gas flow during 1.5 hour.

1.4. Extraction of U

Ten original (untreated) and seven annealed samples (400 ± 10 mg) were extracted in 4.5 M HCl. After extraction of U supernatant was quickly filtered from solid residue using 0,2 μm Millipore membrane. Extraction and filtration of U was performed in *Ar*-atmosphere. Average extraction time was brought to 10 minutes. Redox tracers were added into the extraction solution just before the extraction.

1.5. Separation of U^{4+} and U^{6+} fractions (ion-exchange chromatography)

U^{4+} and U^{6+} fractions were separated from each other in an anion exchange column (Dowex 1 \times 4, 50-100 mesh) regenerated with 4.5 M HCl. Extraction solution was loaded into the column and U^{4+} was collected in the first 20 ml because it was not fixed in the column. U^{6+} which is fixed in the column was eluted with 20 ml of 0.1 M HCl. Both fractions were then purified by another anion exchange step. Purified U was then mounted on a plastic plate with CeF_3 precipitate for U isotope α -spectrometry.

1.6. Determination of U concentration

Uranium concentration was determined using α -spectrometry. Alpha activities were measured by PIPS-detectors of 450 mm² area with a nominal resolution of 20 keV. A counting time varied between one to five days.

1.7. XANES

Uranium L_{III} XANES spectra were measured for original (untreated) material, same material annealed at 300, 500 and 1000 °C and additionally for residue left after extraction in 4.5 M HCl. For the measurement samples were mixed with cellulose powder and pelletized for reliable measurements. UO₂ and schoepite (pure UO₂²⁺ containing mineral) were used as references. INEFFIT software [ANKA, *Karlsruher Institute of Technology*] was used to calculate U oxidation states distribution.

Results and Discussion

The amount of U left in the residue after extraction was 10-18% of the total and was considered U⁴⁺. XANES results (Table 3.) confirmed that U in residue is in U⁴⁺ state. U oxidation states distribution in the material was determined from samples of different masses for a view of possible redox perturbation during extraction. U⁴⁺ and U⁶⁺ were separated and the ratio U⁴⁺/U_{total} was determined (Table 1). The average value for U⁴⁺/U_{total} was 0.5, the small (~50 mg) samples having clearly lower values for the fraction of U⁴⁺ than for the large aliquots (~500 mg), which is rising to 0.8. U⁴⁺/U_{total} varies widely with small sample masses (low solid/solution ratio), whereas with large masses (high solid/solution ratio), a steady state appears. Different results obtained for varying sample masses indicate disturbance of redox balance which are related to different concentrations of redox active Fe²⁺ and Fe³⁺ fractions. The amount of Fe in U⁴⁺ and U⁶⁺ fractions measured by atomic absorption spectrometry showed that the amount of Fe²⁺ coming with U⁴⁺ fraction, is up to eight times higher than that for Fe³⁺, which is coming with U⁶⁺ fraction eluting with 0,1 M HCl [*Ion Exchange Separations in Analytical Chemistry*, O. Samuelson, 1963]. A much higher concentration of Fe²⁺ in extraction solution creates reducing conditions which become more reducing with larger sample amounts promoting faster U⁶⁺ reduction kinetics, according to Equation 1:



²³²U⁴⁺ and ²³⁶U⁶⁺ tracers behavior was studied using two different sample material and with varying masses. In the first experiments only the behavior of ²³²U⁴⁺ was studied. The results show that no significant oxidation of ²³²U⁶⁺ tracer occurred; less than 2% of total ²³²U was found in U⁶⁺ fraction irrespective of the samples material (Table 2.), i.e. extraction system is stable against U tracer oxidation. It has to be taken into account that U⁴⁺ and U⁶⁺ fractions have a slight overlap in the anion exchange step [*Hussonnois et al.*, 1989], which would explain 1-3% leak of “wrong” fraction. On the other hand, the reduction of U⁶⁺ to U⁴⁺ is quite dramatic at least with the largest sample mass. ²³⁶U⁶⁺ tracer is reduced up to 80% with 500 mg of the sample. Figure 1 shows the case for 500

mg sample: there is a $^{235+236}\text{U}$ peak in the spectra of the U^{4+} and U^{6+} fractions, indicating partial reduction of the tracer.

Table 1: U oxidation states in the sample material determined from 10 aliquots with different masses.

Sample mass, (mg)	$\text{U}^{4+}/\text{U}_{\text{total}}$, (%)
40	42
40	59
52	52
58	71
197	83
205	77
298	75
308	81
498	71
502	67

Table 2: Oxidation of $^{232}\text{U}^{4+}$ tracer during U extraction. **Table 3.** Reduction of $^{236}\text{U}^{6+}$ tracer during U extraction.

Sample description	Mass (mg)	$^{232}\text{U}^{4+}$ oxidation (%)
1 DL-1a	49	1.4
2 “	175	0.8
3 “	293	0.5

Sample description	Mass (mg)	$^{236}\text{U}^{6+}$ reduction (%)
1 DL-1a	51	18
2 “	205	42
3 “	501	80

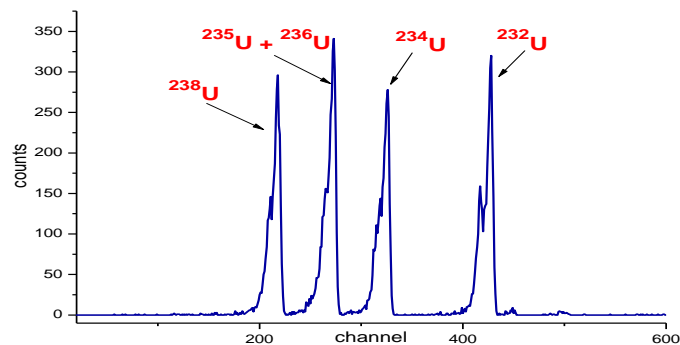


Figure 1: Example of U isotopes alpha-spectrum, including redox - ^{236}U and yield - ^{232}U tracers.

Extractions of annealed samples revealed significant change in U redox balance: amount of U extracted from the sample heated at 300 °C is comparable to that without annealing. No reduction of $^{236}\text{U}^{6+}$ tracer and, as expected, no reduction of the original U^{6+} occurred during the leaching of the sample material that was heated at 500 °C. The results from annealing experiments show that the radiation defects in the sample material can contribute to redox-state in extraction solution.

Less than 0.1 % of total U could be extracted from material annealed at 1000 °C (Figure 2a). All extracted U was found in U⁶⁺ state, which might represent uranium on the grain surface oxidized during material grinding. Hard U extraction may be explained as a result of U reduction to U⁴⁺ and probably vitrification by melted muscovite, which melts at 700 °C.

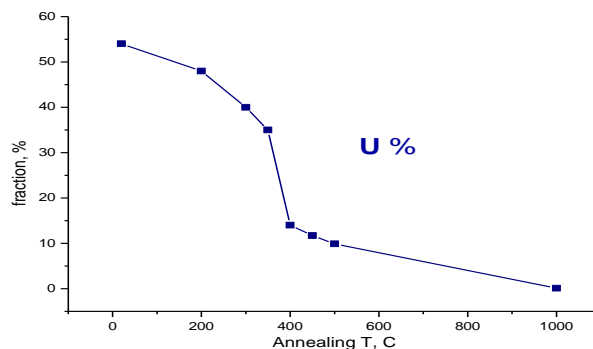


Figure 2a: Amount of extractable U from DL-1a samples, annealed at different temperatures.

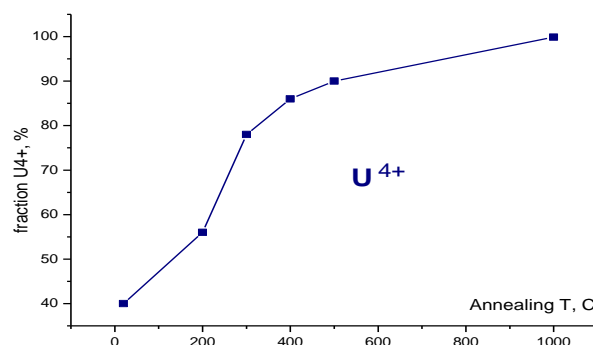


Figure 2b: Amount of U⁴⁺ fraction in annealed DL-1a determined by wet chemistry method.

It is reported [Balek, V., et al. *Ceramics – Silikaty* 53(1) 9-14 (2009)], that between 970-1020 °C occurs full recrystallization of metamict brannerite to original crystalline state where U is located in hardly extractable U⁴⁺ state. This observation is in agreement with XANES results for material annealed at 1000 °C where all U was found in U⁴⁺. Compared results are presented in Table 3.

Table 3: U oxidation state distribution measured by XANES and wet chemistry methods.

DL-1a	U(IV), % XANES	U(VI), % XANES	U(IV), % Wet Chemistry	U(VI), % Wet Chemistry
Original (untreated)	36 ± 3.5	64 ± 3.5	-	-
Residue left after extraction in 4.5 M HCl	97 ± 1.5	3 ± 3	63.5 ± 1 (extraction solution)	36.5 ± 1.5 (extraction solution)
Annealed at 300 °C, leached in 4.5 M HCl	54 ± 3	46 ± 4	55.4 ± 1.2	44.6 ± 0.8
Annealed at 500 °C, leached in 4.5 M HCl	85 ± 3	15 ± 4	92.2 ± 1.5	7.8 ± 2
Annealed at 1000 °C, leached in 4.5 M HCl	99.5 ± 1	0.5 ± 1.5	99.9 ± 2	0.1 ± 3.5

Summary and Conclusions

Wet chemistry methodology was developed to study U redox state in low U geological materials. New information of the influence radiation induced defects in modifying U redox-state during acidic extraction was obtained. U redox effects can be quantitatively estimated for a few minutes extraction time using ion-exchange chromatography. Application of U redox tracers made possible to transfer leaching experiment results to the original solid material. Results from the wet chemistry were to some extent in agreement with those obtained for XANES measurements. Application of synchrotron radiation methods for U oxidation forms analysis in U low samples can be complicated due to not enough sensitivity and thus, necessity of long measurement for enough statistics. However combination of wet chemical and physical methods can be done to get more or less validated values for wet chemistry method results.

References

- Balek, V., Zelenak, V., Benes, M., Subrt, J., 2002. Thermal behavior of brannerite ceramics and its natural analogue mineral brannerite. *Ceramics – Silikaty* 53(1) 9-14.
- Blomqvist, R., Ruskeeniemi, T., Kaija, J., Ahonen, L., Paananen, M., Smellie, J. T. A., Grundfelt, B., Pedersen, K., Bruno, J., Pérez del Villar, L., Cera, E., Rasilainen, K., Pitkänen, P., Suksi, J., Casanova, J., Read, D. and Frape, S., 2000. The Palmottu natural Analogue Project–Phase II: Transport of radionuclides in a natural flow system at Palmottu. European Commission, Report EUR 19611 EN, 192 p.
- Brown, G.E. and Sturchio, N.C., 2002. An overview of synchrotron radiation applications to low temperature geochemistry and environmental science. *Reviews in mineralogy&Geochemistry* 49,1.

Ervanne, H., 2003. Interferences in uranium oxidation states during dissolution of solid phases. J. Radioanal. Nucl. Chem. 256, 497-500.

Ervanne, H. and Suksi, J., 1996. Comparison of Ion-Exchange and Coprecipitation Methods in Determining Uranium Oxidation States in Solid Phases. Radiochemistry 38, 306.

Hussonnois, M., Guillamont, R., Brillard, L., Fattahi., 1989. A method for determining the oxidation state of uranium at concentration as low as 10^{-10} M, in: W. Lutze and R.C. Ewing (Eds.), Mater. Res. Soc. 127, 979-984.

Samuelson, O., 1963. Ion-exchange Separations in Analytical Chemistry, 474 pp.

Silva R.J., Nitsche H., 2001. Environmental actinide science. MRS bull;26;707-713.

Steger, H.F. and Bowman, W.S., 1980. Reference Uranium-thorium Ore DL-1a, Certificate of analysis, CANMET Report 80-10E, CANMET, Energy, Mines and Resources Canada.

REDOX PROPERTIES OF CLAY MINERALS AND SORPTION OF URANYL SPECIES ON BODA CLAYSTONE

Károly Lázár ^{1*}, Zoltán Máthé ², János Megyeri ¹, Éva Széles ¹, Zsuzsanna Mácsik ¹,
Juhani Suksi ³

¹ Institute of Isotopes, Hungarian Academy of Sciences (HU)

² Mecsekérc Environmental Plc. (HU)

³ University of Helsinki (FI)

* Corresponding author: lazar@iki.kfki.hu

Abstract

Redox and sorption properties of clay minerals in Boda Claystone samples were investigated. The possibility of $\text{Fe}^{2+} \rightarrow \text{Fe}^{3+}$ transitions were revealed in clay minerals by following a transition from a stratum formed under reducing conditions to oxidizing ones, and in another case of tracing weathering processes. In contrast, $\text{Fe}^{2+} \rightarrow \text{Fe}^{3+}$ oxidation process could not be observed upon treating the minerals by oxidizing agents in aqueous media. An opposite process however, the reductive dissolution of hematite was detected by treating the samples with dithionite solution. Strong sorption of uranyl species was demonstrated on the borecore samples in break-through experiments. From the combination of results it is concluded that the sorption of uranium is not correlated with simultaneous redox processes, i.e. the $\text{Fe}^{2+} \rightarrow \text{Fe}^{3+}$ and $\text{U(VI)} \rightarrow \text{U(IV)}$ processes are not simultaneously coupled to the observed strong sorption. Instead, probably complex formation with (hydro)carbonate facilitated the strong sorption of uranium species on the claystone.

Introduction

Boda Claystone Formation is considered as a perspective geological media for high level nuclear waste depository in Hungary (Szűcs *et al.* (2004)). Layered clay minerals are important constituents of the rock (Árkai *et al.* (2000)). These clays usually contain iron, in most of cases simultaneously both in ferrous and in ferric states (Lázár, Máthé *et al.* (2010), Lázár, Máthé, Földvári *et al.* (2009)).

Among the constituents of the high level nuclear waste long half life multivalent elements and their isotopes also occur, which are able to change their valency depending on the Eh – pH conditions of their actual geological environment (^{79}Se , ^{99}Tc , $^{235,238}\text{U}$, ^{237}Np , etc.). Migration of these redox sensitive elements depends on their actual valency state, which determines the actual charge of the migrating species. In most

cases sorption-desorption processes are dominant in these interactions. Further on, the actual oxidation state may also depend on closer interactions with the minerals of geological media, among which redox processes may also occur.

One long life-time representative component of the high level waste is uranium. Earlier studies account for significant sorption of U(VI) on clay minerals (*Tsunashima et al. (1981)*, *Akçay (1998)*), regardless to their iron content. Moreover, there are few specific studies which report on the sorption of uranium on clay minerals containing iron (*Hiemstra et al. (2009)*). In particular, sorption of uranium can be promoted by coupled $\text{Fe}^{2+} \Rightarrow \text{Fe}^{3+}$ redox processes taking place on surfaces of minerals (*Bruggeman et al. (2012)*). This process can be promoted by presence of hydrocarbonate (*Regenspurg et al. (2009)*). Conventional sorption measurements were also carried out on Boda Claystone samples (*Kovács, (1999)*), K_d values fall within the region of 50-60. These values had not been correlated to the iron content or to the oxidation state of iron in the respective clay minerals.

In a series of measurements we have performed similar studies in order to reveal whether migration of U(VI) through Boda Claystone borecore samples can be coupled with simultaneous $\text{Fe}^{2+} \Rightarrow \text{Fe}^{3+}$ oxidation taking place in the layered clay minerals of the rock. For that purpose four types of measurements were carried out. First, occurrence of $\text{Fe}^{2+} \rightarrow \text{Fe}^{3+}$ changes in claystone minerals were tracked proceeding during diagenetic and post-diagenetic processes (*Lázár, Máthé, Földvári (2009)*). Secondly, attempts were performed to induce similar $\text{Fe}^{2+} \leftrightarrow \text{Fe}^{3+}$ processes by treating the minerals with reducing and oxidizing agents in aqueous media (*Lázár, Máthé, Megyeri (2010)*). Break-through of uranium was attempted in a third study, in corresponding measuring cells through borecore samples of Boda Claystone (*Lázár et al. (2011)*). Fourth, „post mortem” analysis of these samples were performed, the concentration profile of uranium was determined along with parallel determination of the $\text{Fe}^{2+}/\text{Fe}^{3+}$ ratios of the clay minerals (*Lázár et al. (2011)*). In the present contribution a summary of these studies and an interpretation of results are provided.

Results

Occurrence of $\text{Fe}^{2+} \leftrightarrow \text{Fe}^{3+}$ redox transformations in clay minerals in diagenetic and post-diagenetic processes

An example is shown for the continuous $\text{Fe}^{2+} \Rightarrow \text{Fe}^{3+}$ transition in clay minerals of Boda Claystone in Fig. 1. The Mössbauer spectrum of sample obtained from a stratum formed under reducing conditions is compared with spectra collected on samples originated from deeper layers formed under oxidizing conditions (Fig. 1). In the sample representing the layer located at 83.7 m distance from the commencement of a borehole, iron is present exclusively in ferrous form (Fig. 1a). The dominant component is Fe^{2+} in chlorite as it can be derived from the corresponding parameters (isomer shift = 1.13 mm/s, and quadrupole splitting = 2.62 mm/s). Moving deeper in the borehole, the effect of oxidation becomes apparent. First hematite appears besides the Fe^{2+} -containing chlorite, as the sextet of the hematite displays with ca. 50 % contribution in the spectrum of sample collected in 1.5 m distance from the previous layer (Fig. 1b). Deeper, at 91.8 m distance from the commencement of the borehole, Fe^{3+} can already

be detected in the chlorite mineral together with a minor amount of Fe^{2+} . Further details are described in (Lázár, Máthé, Földvári (2009)).

Effects of secondary diagenetic processes, e.g. weathering, are also reflected in the change of $\text{Fe}^{2+}/\text{Fe}^{3+}$ ratios determined in clay minerals. For instance, the influence of weathering, namely oxidation of Fe^{2+} to Fe^{3+} in clay minerals can be followed in a series of Mössbauer spectra (Fig. 2). The contribution of Fe^{2+} increases as the samples are taken from deeper layers down to ca. 12 meters, from where the equilibrium $\text{Fe}^{2+}/\text{Fe}^{3+}$ ratio is stabilised. The effect can be clearly followed by the inspection of the change in the intensity of the far-right peak at 2.4 mm/s, which is a part of the Fe^{2+} doublet. (The peaks marked with H belong to hematite, and in the central, $-0.7 \div 1.2$ mm/s region are superpositions of Fe^{2+} and Fe^{3+} components). More details can be found in (Lázár, Máthé, Földvári (2009)).

The change of the $\text{Fe}^{2+}/\text{Fe}^{3+}$ ratio in the clay minerals can be monitored and can be correlated with diagenetic and post-diagenetic redox processes as the two examples in this paragraph demonstrate.

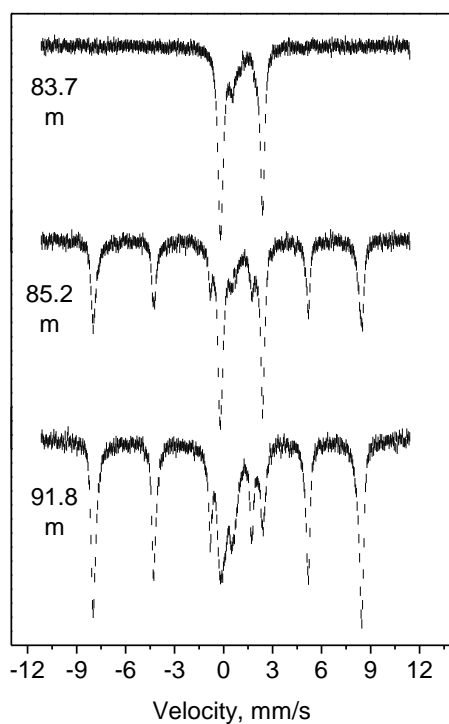


Figure 1. Mössbauer spectra obtained on samples taken from a borehole crossing a reductive stratum

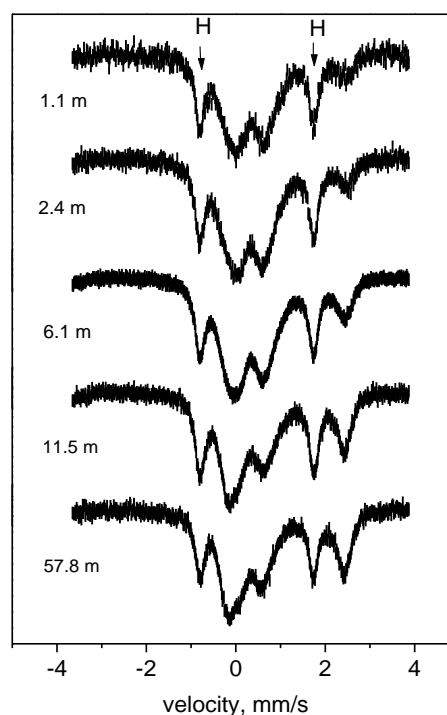


Figure 2. Mössbauer spectra obtained on samples taken from different depths from the surface

Redox processes in aqueous media

Considering the apparent changes in the $\text{Fe}^{2+}/\text{Fe}^{3+}$ ratios in clay minerals shown in the previous paragraph it can be hypothesized that similar changes might also be generated

by treating the Boda Clastone samples with reducing or oxidizing agents in aqueous media. These treatments may be considered as processes, analogous to the expected interactions taking place among migrating multivalent radionuclides capable of undergoing redox reactions with the iron species of the minerals.

In correspondence, in one side, samples containing iron exclusively in ferrous form in chlorite mineral were exposed to oxidizing agents (perchlorate, hydrogen peroxide and hypochlorite). On the contrary, in another series, samples with dominating presence of ferric components were exposed to reducing agents (hydroxyl amine, hydrazine and formaldehyde). Neither oxidizing nor reducing treatments resulted in detectable change in the original $\text{Fe}^{2+}/\text{Fe}^{3+}$ ratios of the clay minerals. There was one exception, namely by using sodium dithionite as reducing agent. In that particular case ferric iron was dissolved from the hematite component and relocated as a reduced iron species in the solid phase as a novel intercalated constituent (Fig. 3). Curiously, the $\text{Fe}^{2+}/\text{Fe}^{3+}$ ratios in the original clay minerals were not affected by the treatment, only the hematite component was altered as a closer analysis of spectra reveals (**Lázár, Megyeri, Máthé (2010)**). It is worth noticing here, that from the point of view of iron, the observed process, the reductive dissolution of hematite by dithionite is just the opposite process of the expected oxidation, mentioned in the Introduction ($\text{U}^{(\text{VI})} \rightarrow \text{U}^{(\text{IV})}$ coupled with $\text{Fe}^{2+} \rightarrow \text{Fe}^{3+}$).

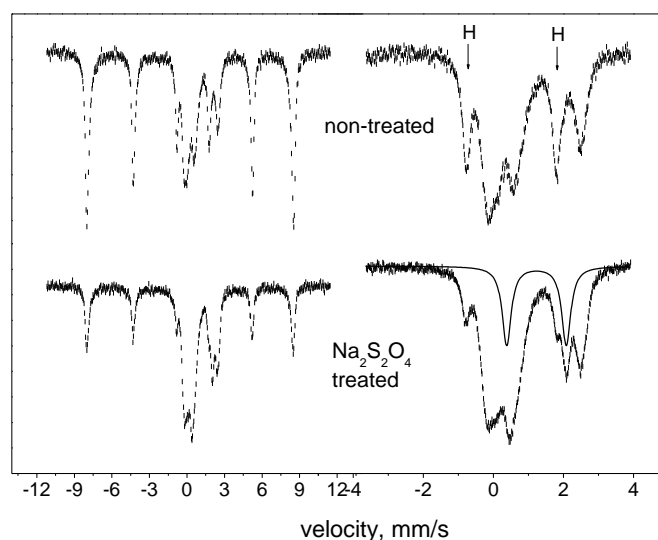


Figure 3. Mössbauer spectra of the non-treated and the dithionite-treated samples recorded in full (left) and central (right) velocity ranges. *H* indicates the positions of lines originated from hematite. The solid line in the right bottom spectrum displays the doublet of a newly formed Fe^{2+} component.

Migration of uranium through bore-core discs – break-through measurements

Direct information on the migration of uranyl species through Boda Claystone media were obtained from break-through measurements. A migration cell was applied, as used in earlier studies to determine the effective diffusion constants of $^{125}\text{I}^-$, $^{99}\text{TcO}_4^-$, $\text{H}^{14}\text{CO}_3^-$ anions and self-diffusion of HTO (**Lázár, Megyeri, Parneix (2009)**). The

break-through process of uranyl species from saturated uranyl acetate solution (7.7 g /100 ml - ~ 0.02M) was followed through c.a. 8 mm thick bore core samples. Detectable break-through was not observed, uranyl species could not penetrate the borecore disc during a long period (five years). Uranyl species were sorbed, their concentration in the original acetate solution decreased as periodic activity measurements showed. At the same time uranyl species did not appeared on the opposite side of the bore core discs in the ground water (Fig. 4 and *Lázár et al. (2011)*). Thus the experiments prove that the migration of U(VI) is retarded and very slow in comparison to the previously mentioned anions in the claystone media.

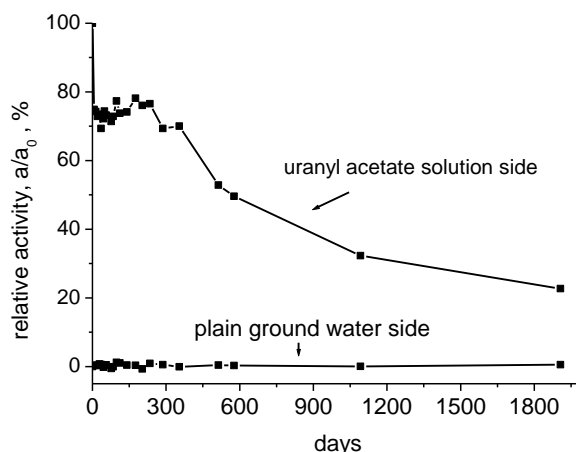


Figure 4. Decrease of the concentration of uranium in the uranyl acetate solution in the break-through cell (top curve) and lack of break-through in the opposite compartment (bottom curve).

At this stage the sequence of experiments can be summarised that Fe^{2+} vs. Fe^{3+} redox changes can be observed in clay minerals, dominantly in diagenetic and post diagenetic processes. Further, it is also obvious that the migration of uranyl ions is extremely retarded in claystone media compared to that of anionic species. At this stage the information collected is not sufficient yet to prove or disprove the starting hypothesis, namely that $\text{U(VI)} \rightleftharpoons \text{U(IV)}$ processes can be correlated with parallel $\text{Fe}^{2+} \rightleftharpoons \text{Fe}^{3+}$ processes, since either plain sorption of uranyl cations or precipitation of reduced uranyl in form of UO_2 may result in the retarded migration of uranium.

Post mortem analyses

Three types of „post mortem” analyses were carried out in order to prove or disprove the starting hypothesis. Namely, i/ the $\text{Fe}^{2+}/\text{Fe}^{3+}$ ratios in the surface layers of bore core samples were compared, ii/ the in-depth concentration profile of uranium was measured by laser ablation ICP-MS in the spent samples, and iii/ the oxidation state of the sorbed uranium was determined.

$\text{Fe}^{2+}/\text{Fe}^{3+}$ ratios - Mössbauer spectroscopy

The $\text{Fe}^{2+}/\text{Fe}^{3+}$ ratios in the 2 mm thick surface layers on both sides of the spent borecore samples were determined by Mössbauer spectroscopy. These studies revealed that there

are no apparent changes in the $\text{Fe}^{2+}/\text{Fe}^{3+}$ ratios in the clay minerals, the spectra are the same within the accuracy of measurements for the both sides of the discs, regardless whether the sample was taken from the surface layer of the disc, having contacted with the saturated uranyl acetate solution or from the surface layer on the opposite side, in contact only with the plain ground water. Further, these spectra were also the same as that of the one recorded on the starting plain borecore before immersing it to any aqueous media.

Uranium concentration profile - laser ablation ICP- MS measurements

In this analysis the concentration profile of the uranium was determined across the sample, along the direction of migration, i.e. perpendicular to the plane surface of the discs. The concentration profiles of uranium isotopes (^{235}U and ^{238}U) exhibit a logarithmic decrease. They can simply be described by $C = C_0 e^{-kx}$, (C_0 is the concentration of uranium at the outermost layer, x is the distance from the surface exposed to the uranyl acetate solution, k is constant – Fig. 5).

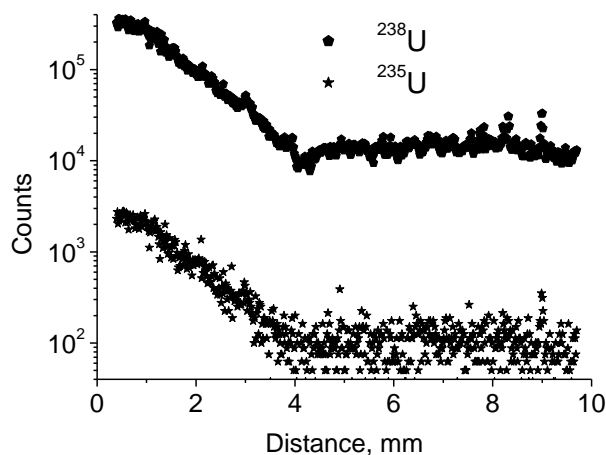


Figure 5. Concentration of uranium in logarithmic scale along the migration path perpendicular to the surface of the borecore disc.

Value of C_0 , the uranium concentration in the surface layer having kept in contact with the the saturated uranyl acetate solution for five years, was also determined in a few samples. The surfaces were gently scraped by drilling and the powder material obtained was extracted in 4.5 M HCl to dissolve sorbed U. As a medium value 1.85 wt % was obtained.

In order to estimate the amount of the sorbed uranium on clay minerals, a rough approximation can be attempted as follows. The total amount of the sorbed uranium is ca. 0.13 g ($\sim 5 \cdot 10^{-4}$ moles) on the borecore of 47 mm diameter. This amount is c.a. 0.5 milliequivalent assuming the sorbing species is mono valent. The surface layer involved dominantly in the sorption is ca. 1 mm thick, it corresponds to ca. 7 g claystone. In other words 0.5 milliequivalent uranium is sorbed on 7 g claystone. This value can be compared with sorption capacity values, reported for clay minerals, typically for

montmorillonite (in an average, ca. 50 milliequivalent / 100 g montmorillonite (*Tsunashima et al. (1981), Akcay (1998)*)). Further, assuming 20 % as an underestimated value for the amount of layered clay minerals (~montmorillonite) present in Boda Claystone, and disregarding the sorption of uranium on the other mineral components, the commensurable amount of the uranium sorbed on the 100 g equivalent of the sample discs is finally 36 milliequivalent. This value is unambiguously smaller than the 50 milliequivalent referred in the literature. It should be mentioned that in this latter value interactions with iron species are not involved. Thus, this rough comparison shows that plain sorption may result in the fixation of uranium, regardless to the presence or absence of iron.

Nominal comparison can also be made with the total potential reductive capacity of the sample as well. Considering 20 % presence of clay minerals (chlorite) and considering ca 30% Fe^{2+} content related to the total amount of iron present in it, 100 milliequivalent reductive capacity of 100 g stone can be estimated (*Lázár et al. (2011)*).

The sorbed species is probably not bare uranyl(VI) ion. In this case the break-through would probably be much faster, it would fall probably into a similar range as found for another monovalent, ^{137}Cs or two-valent ion, e.g. ^{85}Sr . In these instances dominant break-through was observed on similar Boda samples already within ~200 days (*Mell, (2006)*).

The determining role of another process, complexation with hydrocarbonate ions should also be considered. In this Eh-pH region neutral UO_2CO_3 , or anionic $\text{UO}_2(\text{CO}_3)_2^{2-}$ components may also exist (*Brookins (1988), Hiemstra et al. (2009)*). Thus, regardless to the $\text{Fe}^{2+} \Rightarrow \text{Fe}^{3+}$ process, there exist probably an interaction between the (hydro)carbonate component and the uranyl ions by forming (bi)carbonate complexes, and thereby increasing the strength of the sorption of uranium. In Boda Claystone calcite/dolomite are permanent constituents (1-5 %) and hydrocarbonate ions are also present in significant concentrations in the ground water ($1\text{-}2 \times 10^{-2}$ mol/L).

Direct determination of the redox-state of sorbed U

The powder material drilled from the borecore surface contacted with the uranyl solution was extracted in 4.5 M HCl in anoxic condition for 10 min and the solution obtained was loaded in an anion exchange column for U(IV) and U(VI) separation. Over 99 % of U dissolved in extraction was found in the U(VI) form. This direct measurement unambiguously demonstrates that $\text{Fe}^{2+} \Leftrightarrow \text{Fe}^{3+}$ redox processes do not play primary role in sorption of uranium.

Summary

In a series of experiments it was demonstrated that $\text{Fe}^{2+} \Leftrightarrow \text{Fe}^{3+}$ redox changes may proceed in clay minerals of Boda Claystone during diagenetic and post diagenetic processes. Further on, in Fe^{2+} and Fe^{3+} ions in clay minerals are not affected by treatments performed in aqueous media, either by various reducing or by oxidizing agents. At the same time however, reductive dissolution of ferric iron present in another mineral, hematite, can be observed by sodium dithionite. Break-through of U(VI)

through 8 mm thick borecore samples could not be observed in five year long experiments. Concentration profiles of uranium and $\text{Fe}^{2+}/\text{Fe}^{3+}$ ratios were determined in surface layers of sample discs in post mortem analyses. Strong sorption of uranium is revealed, which can be described by an exponential decrease of concentration inside from the surface in contact with uranium. The strong sorption is not connected with changes in $\text{Fe}^{2+}/\text{Fe}^{3+}$ ratios of clay minerals, since the latter effect cannot be detected, these ratios are the same, regardless to sorption processes. Direct determination of oxidation state of uranium by wet chemical method showed that sorbed U is in U(VI) form. Thus, it can be concluded that sorption of uranium on Boda Claystone is not promoted by redox processes, i.e. the expected coupled simultaneous redox processes $\text{U(VI)} \rightleftharpoons \text{U(IV)}$ and $\text{Fe}^{2+} \rightleftharpoons \text{Fe}^{3+}$ do not take place during sorption. Instead of the redox processes most probably complexation of uranium with carbonate component plays an important role in promoting the strong sorption.

Acknowledgement

The research leading to these results has received funding from the European Union's European Atomic Energy Community's (Euratom) Seventh Framework Programme FP7/2007-2011 under grant agreement n° 212287 (RECOSY project).

References

- Akcaý, H., (1998), Aqueous speciation and pH effect on the sorption behaviour of uranium by montmorillonite, J. Radioanalytical and Nuclear Chemistry, 237, 133-137.
- Árkai P., Balogh K., Demény A., Fórizs I., Nagy G., Máthé Z., (2000), Composition, diagenetic and post-diagenetic alterations of a possible radioactive waste repository site: the Boda Albitic Claystone Formation, southern Hungary, Acta Geologica Hungarica, 43 (2000) 351-378.
- Brookins, D.G., (1988), Eh-pH Diagrams for Geochemistry, Springer, p. 153.
- Bruggeman, C., Maes, N., Christiansen, B.C., Stipp, S.L.S., Breynaert, E., Maes, A., Regenspurg, S., Malström, M.E., Liu, X., Grambow, B., Schäfer, Th., (2012), Redox-active phases and radionuclide equilibrium valence state in subsurface environments – New insights from 6th EC IP FUNMIG, Applied geochemistry, 27, 404-413.
- Hiemstra, T., Van Riemsdijk, W.H., Rossberg, A., Ulrich, K.O., (2009), A surface structural model for ferrihydrite II: adsorption of uranyl and carbonate, Geochimica and Cosmochimica Acta, 73, 4437-4451.
- Regenspurg, S., Schild, D., Schäfer, Th., Huber, F., Malström, M.E., (2009), Removal of uranium(VI) from the aqueous phase by iron(II) minerals in presence of bicarbonate. Applied Geochemistry, 24, 1617-1625.
- Kovács L., (editor), (1999), Digest on the results of the short term characterisation programme of the Boda Claystone Formation, Mecsekérc-PURAM, p. 34.

Lázár K., Máthé Z., Földvári M., (2009), Redox transitions in Boda Albitic Claystone under natural conditions as reflected in the change of the $\text{Fe}^{2+}/\text{Fe}^{3+}$ ratios in clay minerals, in: 9. EURATOM EC-7, CP, „Redox Phenomena Controlling Systems”, 1st Annual Workshop Proceedings, Eds: G. Buckau et al., Forschungszentrum Karlsruhe, Wissenschaftliche Berichte, 7466, 131-137.

Lázár K., Máthé Z., Földvári M., (2010), Various redox conditions in Boda Claystone as reflected in the change of $\text{Fe}^{2+}/\text{Fe}^{3+}$ ratio in clay minerals, Journal of Physics: Conference Series, 217, 012053.

Lázár K., Máthé Z., Földvári M., Németh T., Mell P., (2009), Various stages of oxidation of chlorite as reflected in the Fe^{2+} and Fe^{3+} proportions in the Mössbauer spectra of minerals in Boda Claystone, Hyperfine Interactions, 190, 129-133.

Lázár K., Megyeri J., Mácsik Zs., Széles É., Máthé Z., (2011), Migration of uranyl ions in Boda Claystone samples, 3rd Annual Workshop Proceedings CP „Redox Phenomena Controlling Systems”, Eds: M. Altmaier et al., KIT Scientific Reports, 7603, 91-97.

Lázár K., Megyeri J., Máthé Z., (2010), Lack of redox response in some cases on Boda Claystone samples as reflected in the $\text{Fe}^{2+}/\text{Fe}^{3+}$ ratio in minerals, in: 2nd Annual Workshop Proceedings CP „Redox Phenomena Controlling Systems”, Eds: G. Buckau et al., KIT Scientific Reports, 7557, 193-200.

Lázár K., Megyeri J., Parneix, J-C., Máthé Z., Szarvas T., (2009), Diffusion of anionic species ($^{99}\text{TcO}_4^-$, $\text{H}^{14}\text{CO}_3^-$) and HTO in Boda Claystone borecore samples, in: 4th Annual Workshop Proceedings, FUNMIG, Eds: G. Buckau et. al, Forschungszentrum Karlsruhe, Wissenschaftliche Berichte, FZKA 7461, 199-204.

Mell P., Megyeri J., Riess L., Máthé Z., Hámos G., Lázár K., (2006), Diffusion of Sr, Cs, Co and I in argillaceous rock as studied by radiotracers, Journal of Radioanalytical and Nuclear Chemistry, 268, 411-417.

Szücs, I., Csicsák J., Óvári Á., Kovács L., Nagy Z., (2004), Confinement performance of Boda Claystone Formation, Hungary, in: Stability and Buffering Capacity of the Geosphere for long-term isolation of Radioactive waste, NEA 5303, OECD 2004, pp. 209-224.

Tsunashima A., Brindley G.W., Bastovanov M., (1981), Adsorption of uranium from solutions by montmorillonite; compositions and properties of uranyl montmorillonites, Clays and Clay Minerals, 29, 10–16.

REDOX BEHAVIOR OF URANIUM IN BIOFILMS AND GROUNDWATER SEEPS, SAMPLED FROM THE GRANITIC ROCK WALLS IN THE ONKALO TUNNEL (FINLAND)

Evelyn Krawczyk-Bärsch^{1*}, Heinrich Lünsdorf², Karsten Pedersen³, Thuro Arnold¹,
Frank Bok¹, Robin Steudtner¹, Anne Lehtinen⁴, Vinzenz Brendler¹

¹ Helmholtz-Zentrum Dresden-Rossendorf e.V., Institute of Radiochemistry, P.O. Box
510119, 01314 Dresden (D)

² Helmholtz Centre for Infection Research, Department of Vaccinology and Applied
Microbiology, Inhoffenstr. 7, 38124 Braunschweig (D)

³ University of Gothenburg, Department of Cell and Molecular Biology, Box 462,
40530 Gothenburg, (SE)

⁴ POSIVA OY, 27160 Eurajoki (FIN)

* Corresponding author: E.Krawczyk-Baersch@hzdr.de

Abstract

At a depth of 70 m of the ONKALO tunnel in Finland, 771 m from the tunnel entrance, massive biofilms were observed attached to the tunnel walls where groundwater was seeping from bedrock fractures. During a sample campaign 2010 samples of the biofilms and of the groundwater seeps were taken for laboratory experiments. Microelectrode measurements in the biofilms and in the groundwater seeps indicated that the studied biofilms constituted their own microenvironments, which differed significantly from that of the groundwater seeps. A pH of 5.37 was recorded inside the biofilm, approximately 3.5 units lower than the pH observed in the groundwater seeps. Similarly, the E_h of +73 mV inside the biofilm was approximately 420 mV lower than the E_h measured in the groundwater seeps. In flow cells with detached biofilms uranium was added to the circulating groundwater with a final uranium concentration of 4.25×10^{-5} M. After 42 h the pH increased in the biofilm to 7.27 and the E_h was reduced to –164 mV. The changes of E_h and pH influenced the bioavailability of uranium. EF-TEM investigations indicated that uranium in the biofilm was immobilized intracellularly in microorganisms by the formation of metabolically mediated uranyl phosphate, similar to needle-shaped Autunite $[\text{Ca}(\text{UO}_2)_2(\text{PO}_4)_2 \cdot 2-6 \text{H}_2\text{O}]$ or meta-Autunite $[\text{Ca}(\text{UO}_2)_2(\text{PO}_4)_2 \cdot 10-12 \text{H}_2\text{O}]$.

In contrast, TRLFS studies of the uranium-contaminated groundwater identified aqueous uranium carbonate species, likely $(\text{Ca}_2\text{UO}_2[\text{CO}_3]_3)$, formed due to the high concentration of carbonate in the uranium contaminated circulating groundwater. The results agreed with thermodynamic calculations of the theoretically predominant field of

uranium species, formed in the uranium-contaminated groundwater at the measured geochemical parameters.

Introduction

A final nuclear-waste repository for spent nuclear fuel (SNF) is planned at the underground rock characterization facility tunnel ONKALO. It is situated near the nuclear power plants of Olkiluoto approximately 300 Km northwest of Helsinki (Finland). The tunnel in the granitic bedrock is interspersed with numerous fractures (Nordbäck et al., 2008). Analysis of the groundwater, which is seeping through these fractures, indicated an average total number of 3.9×10^5 cells mL⁻¹ in the shallow groundwater (at depths of 0–20 m) and 5.7×10^4 cells mL⁻¹ in the deep groundwater (at depths of 100–800 m) (Pedersen et al., 2008). The results show that microbial activity is ongoing in groundwater, down to depths of at least 800 m in Olkiluoto. At a depth of 70 m of the ONKALO tunnel, massive biofilms were observed attached to the tunnel walls where groundwater was seeping from bedrock fractures (Fig. 1).



Figure 1: Slimy, massive biofilms, attached to the fractured bedrock at a depth of 70 m (771 m from the tunnel entrance) in the underground rock characterization facility tunnel ONKALO (Finland).

As described by Stroes-Gascoyne and Sargent (1998), microorganisms can influence the performance of SNF repositories by corroding the nuclear waste containers and mobilizing radionuclides in groundwater in the event of canister failure. Specific interactions between microorganisms and radionuclides are known and can be distinguished as biosorption, bioaccumulation, biotransformation, biomineralization, and bioreduction (Lloyd and Macaskie, 2002), with potential for the substantial retention of radionuclides. Interactions of radionuclides with biofilms probably differ

from interactions with suspensions of individual cells of single microorganism species. Biofilms are known to provide a sink for dissolved heavy metals (Späth et al., 1998) because the extra cellular polymeric substance (EPS), cell walls, cell membranes, and cell cytoplasm can serve as sorption sites (Flemming, 1995).

In the present work, biofilm samples were taken from the walls of the ONKALO tunnel and used for experiments in a laboratory on the surface. Laboratory experiments were performed under aerobic conditions thought to represent exceptional conditions over the lifetime of a deep geological repository. Uranium concentrations in the range of those expected from a damaged and leaking waste canister in the far-field were employed in these experiments to simulate the fate and behavior of this radionuclide in the event of canister failure in a SNF repository. Both biofilm and groundwater were used in studies employing different methods to find evidence of the possibility of uranium retention. The studies aimed to improve our understanding of the mechanisms by which biofilms respond to exposure to uranium with respect to safety assessments in the far-field of SNF repositories.

Experimental

1.1 Sampling

During the sampling campaign massive biofilms were observed attached to the fractured bedrock (Fig. 1) at a depth of 70 m (771 m from the tunnel entrance) in the ONKALO tunnel. The biofilms were removed from the tunnel wall using a knife and collected in sterile boxes. The groundwater seeping over the biofilms was sampled in 2 × 250-mL boxes. The boxes were transported together with the biofilm to the laboratory for further studies.

1.2 Microelectrode measurements

For microelectrode measurements a rectangular flow cell with outer dimensions of 121 × 42 × 15 mm and inner dimensions of 77 × 27 × 10 mm was used. 150 mL of circulating groundwater was pumped through the flow cell in a closed circuit, where the biofilm was positioned in. The pH was measured using a miniaturized conventional pH electrode (PH-10). The redox potential was determined by a miniaturized platinum electrode (RD-10; Unisense, Aarhus, Denmark). Both were characterized by a very small tip diameter of 8–12 µm. The pH and redox potential electrodes were connected via a high-impedance millivoltmeter to a separate reference electrode (REF-50), an open-ended Ag/AgCl electrode with a gel-stabilized electrolyte (Unisense). The pH electrode was calibrated against commercially available buffers for pH 4.008, 6.86, and 9.18 (WTW GmbH & Co. KG, Weilheim, Germany). The redox potential electrode function was checked against the defined redox buffers of 470 mV (pH 4 buffer) and 295 mV (pH 7 buffer) using a prepared quinhydrone redox buffer solution (MERCK, Darmstadt, Germany) as described by Unisense (Aarhus, Denmark). Since the oxidation reduction potential was measured, the values were corrected for the hydrogen electrode potential (+239 mV, after Cammann and Galster, 1997). After the pH and E_h values in the biofilm and the circulating groundwater were recorded, a uranium concentration of

4.2×10^{-5} M was obtained in the groundwater by adding 0.64 mL 1×10^{-2} M $\text{UO}_2(\text{ClO}_4)_2$ to 150 mL of the circulating groundwater. The uranium-contaminated groundwater was pumped through the flow cell over the biofilm in a closed circuit for 42 h.

1.3. Analysis

For analysis, samples were taken from the groundwater seeps and from the groundwater after uranium addition and after the experiments, each with a volume of 10 mL. The samples were acidified and analyzed for cation determination by means of inductively coupled plasma spectrometry (ICP-MS) using both an ELAN 9000 ICP-MS spectrometer (PerkinElmer, Überlingen, Germany) and an AXIOM ICP-MS spectrometer (VG Thermo Elemental, Winsford, UK). The anions were determined by means of ion chromatography (IC) using the 732/733 IC system (Metrohm, Filderstadt, Germany). In addition, the circulating groundwater used in our experiments was analyzed both after uranium addition and after the experiments. The biofilm was taken after the experiment and ultra centrifuged (Ultracentrifuge Optima XL100K, Rotor: SW 32Ti; Beckman Coulter) for 1 hour with $187000 \times g$. The formed pellet was freeze-dried (ALPHA 1-4 LSC, Christ), refined and decomposed for analysis of the uranium concentration.

1.4. Time-resolved laser fluorescence spectroscopy (TRLFS)

For the measurements, aliquots of contaminated groundwater were placed in quartz cuvettes without further sample preparation. The U(VI) luminescence was measured after excitation with laser pulses at 266 nm (Minilite high-energy solid-state laser; Continuum, Santa Clara, CA) and an average pulse energy of 300 μJ . The emitted fluorescence light of the solutions was recorded using an iHR550 spectrograph (HORIBA Jobin Yvon, Edison, NJ) and an ICCD camera (HORIBA Jobin Yvon) in the 371.4–664.3-nm wavelength range by accumulating 200 laser pulses and using a gate time of 20 μs . Data were analyzed using Origin software, version 7.5 (OriginLab Corporation, Northampton, MA), including the Peak Fit module, version 4.0. For comparison with the analytical data, solutions dominated by the uranyl carbonate species $(\text{MgUO}_2(\text{CO}_3)_3)^{2+}$ and $\text{Ca}_2\text{UO}_2(\text{CO}_3)_3$ were prepared as described in detail by Geipel et al. (2008) and Bernhard et al. (2001).

1.5. Energy-filtered transmission electron microscopy (EF-TEM) and electron energy-loss spectroscopy (EELS)

Biofilm samples from the experiments were prepared for EF-TEM and EELS studies by fixing them with 1% (vol/vol). In the TEM laboratory, portions of the biofilm were excised and processed further, following the routine embedding protocol, with minor modifications, described by Lünsdorf et al. (2001). Ultrathin sections of the biofilm samples, 30 nm thick, were analyzed by means of electron spectroscopy using an in-column filter EF-TEM (LIBRA 120 PLUS; Zeiss, Oberkochen, Germany) at magnifications ranging from $4000\times$ to $50,000\times$, and micrographs were registered using a bottom-mount 2048×2048 CCD camera (SharpEye; Tröndle, Moorenweis, Germany). Overall ultrastructure in the elastic bright field-mode was acquired from 90-nm sections. The following hardware settings were generally used for EELS

acquisition: objective aperture, 60 μm ; acceleration voltage, 120 kV; energy slit width, 10–15 eV; spectrum magnification, 100 \times . The following settings were used for specific ESI image acquisition: U-O₄₅ ESI acquisition, 10 s at 112 eV, 90 eV, and 77 eV with energy slit width set to 10 eV, 0.5 mrad illumination aperture, 1 μA beam current; P-L₂₃ ESI acquisition: 15 s at 153 eV, 121 eV, and 110 eV with energy slit width set to 10 eV, 0.63 mrad illumination aperture, 1 μA beam current; and Ca-L_{2,3} ESI acquisition, 20 s at 348 eV, 336 eV, and 320 eV with energy slit width set to 10 eV, 1.0 mrad illumination aperture, 1 μA beam current. Net elemental maps of Ca, P, and U were calculated after background correction according to the three-window method and iTEM software instructions (OSIS, Münster, Germany); 20-nm Spot-WR-PEELS registration from 50 eV to 1062 eV was performed using three integration cycles/frame of 10-s registration time, with a final total of five frames and an emission current set to 1 μA .

Results and discussion

Microelectrodes with a very small tip diameter made it possible to determine the E_h and pH inside the biofilm. The results indicated that the biofilm from the ONKALO site was characterized by pH and E_h values that differed significantly from those of the surrounding circulating groundwater. A pH of 5.37 ± 0.1 was recorded in the biofilm, which was approximately 3.5 units lower than that of the circulating groundwater. Similarly, the E_h of $+73 \pm 20$ mV measured in the biofilm differed by approximately +420 mV from that of the circulating groundwater. The geochemical parameters of the biofilm differed significantly from those of the circulating groundwater, clearly indicating that the biofilm had built up its own microenvironment. At the end of the experiment, 42 h after adding uranium to the circulating groundwater, the E_h in the biofilm had decreased to $-164 \text{ mV} \pm 20 \text{ mV}$ while the pH had increased to 7.27 ± 0.1 . The analytical data for the circulating groundwater after uranium addition (Table 1) were used to calculate the predominance fields of various uranium species at 25°C. Therefore, a pH– E_h diagram was constructed using the geochemical speciation code Geochemist's Workbench, version 8.0.12/Act2.

The database used was the thermo.dat accompanying the code, supplemented by the most recent NEA database for aqueous uranium species (Guillaumont et al., 2003) and by solubility data for the minerals Rutherfordine (Guillaumont et al., 2003), Uranophane (Nguyen et al., 1992), Bayleyite (Amayri, 2002), Haiweeite (Hemingway, 1982), and Uraninite (Guillaumont et al., 2003) and for the aqueous species $\text{Ca}_2\text{UO}_2(\text{CO}_3)_3(\text{aq})$ (Bernhard et al., 2001) and $\text{MgUO}_2(\text{CO}_3)_3^{2+}(\text{aq})$ (Amayri, 2002). Under the ambient conditions found in the uranium-contaminated circulating groundwater, several theoretical predominance fields of solid and aqueous uranium species can be defined. When plotting the measured pH and E_h values of the contaminated circulating groundwater in the pH– E_h diagram, the formation of this aqueous uranium carbonate species is predicted (Fig. 2). We assume that after the addition of uranium to the circulating groundwater, aqueous uranium carbonate species, likely calcium uranyl carbonates species $[\text{Ca}_2\text{UO}_2(\text{CO}_3)_3]$, were formed using the large available amount of carbonate in the water (Table 1).

Table 1. Mean concentration of cations and anions in the groundwater seeps and in the circulating groundwater after adding uranium, and after the experiments.

groundwater seeps			CGW after adding U		CGW after the experiment	
	mean value	range [in mol/L]	mean value	range [in mol/L]	mean value	range [in mol/L]
Na	9,10E-03	9,05E-03 - 9,18E-03	9,31E-03	9,18E-03 - 9,40E-03	1,02E-02	1,01E-02 - 1,03E-02
Mg	5,64E-04	5,60E-04 - 5,72E-04	5,83E-04	5,80E-04 - 6,05E-04	6,21E-04	5,93E-04 - 6,50E-04
Si	2,76E-04	2,61E-04 - 2,95E-04	2,80E-04	2,78E-04 - 2,82E-04	3,05E-04	3,01E-04 - 3,10E-04
Ca	9,38E-04	9,18E-04 - 9,88E-04	9,84E-04	9,75E-04 - 9,93E-04	1,04E-03	1,01E-03 - 1,05E-03
U	< 4,20E-09	< 4,20E-09	4,25E-05	4,20E-05 - 4,29E-05	1,61E-05	1,59E-05 - 1,64E-05
Al	9,27E-07	7,78E-07 - 1,00E-06	3,15E-06	3,03E-06 - 3,22E-06	4,23E-06	3,59E-06 - 5,04E-06
Mn	1,13E-06	1,00E-06 - 1,19E-06	1,12E-06	1,11E-06 - 1,12E-06	1,22E-06	1,22E-06
Fe	< 1,79E-07	< 1,79E-07	< 1,79E-07	< 1,79E-07	< 1,79E-07	< 1,79E-07
Cr	< 1,92E-07	< 1,92E-07	< 1,92E-07	< 1,92E-07	< 1,92E-07	< 1,92E-07
Co	1,95E-09	1,69E-09 - 2,95E-09	2,97E-09	2,88E-09 - 3,05E-09	< 1,69E-09	< 1,69E-09
Ni	< 1,70E-08	< 1,70E-08	< 1,70E-08	< 1,70E-08	< 1,70E-08	< 1,70E-08
Cu	4,63E-08	1,80E-08 - 6,22E-08	5,76E-08	5,38E-08 - 6,40E-08	1,16E-07	7,74E-08 - 1,39E-07
As	< 1,33E-07	< 1,33E-07	< 1,33E-07	< 1,33E-07	< 1,33E-07	< 1,33E-07
Br	8,15E-06	7,98E-06 - 8,46E-06	8,02E-06	7,98E-06 - 8,06E-06	1,07E-05	9,44E-06 - 1,14E-05
Sr	4,28E-06	4,24E-06 - 4,33E-06	4,31E-06	4,27E-06 - 4,36E-06	4,69E-06	4,42E-06 - 4,86E-06
Cd	< 8,89E-10	< 8,89E-10	< 8,89E-10	< 8,89E-10	< 8,89E-10	< 8,89E-10
Cs	2,20E-09	2,11E-09 - 2,29E-09	2,22E-09	2,18E-09 - 2,23E-09	2,78E-09	2,73E-09 - 2,80E-09
Cl ⁻	4,82E-03	4,77E-03 - 4,91E-03	5,39E-03	5,36E-03 - 5,47E-03	6,18E-03	6,18E-03 - 6,21E-03
NO ₃ ⁻	1,05E-05	1,00E-05 - 1,13E-05	3,23E-06	3,23E-06	3,16E-04	3,13E-04 - 3,24E-03
PO ₄ ³⁻	5,27E-06	5,27E-06	5,27E-06	5,27E-06	2,73E-05	2,73E-05 - 2,74E-05
SO ₄ ²⁻	8,09E-04	8,05E-04 - 8,20E-04	1,02E-03	1,01E-03 - 1,02E-03	1,27E-03	1,26E-03 - 1,30E-03
CO ₃ ²⁻	5,88E-03	5,87E-03 - 5,92E-03	6,17E-03	6,15E-03 - 6,18E-03	6,47E-03	6,43E-03 - 6,50E-03

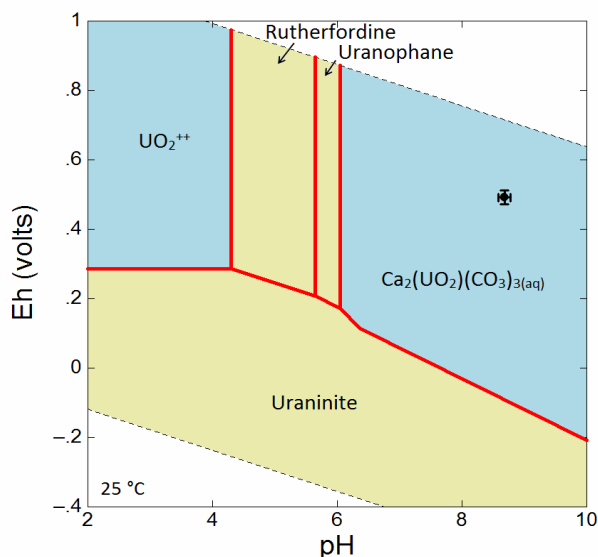


Figure 2: pH-E_h predominance diagram for the uranium contaminated circulating groundwater after thermodynamic calculation using the geochemical speciation code Geochemist's Workbench Version 8.0.12/Act2. The plotted pH and E_h data (including error bars) correspond to the measured values in the fracture water.

The results of the TRLFS studies are in excellent agreement with the thermodynamic calculations of the theoretical predominance fields of the uranium species formed in the uranium-contaminated circulating groundwater. The measured emission spectrum of the contaminated circulating groundwater is characterized by five emission bands at 465.2, 483.9, 503.6, 525.1, 549.8 with a decay time of 56.0 ± 1.8 ns (Fig. 3).

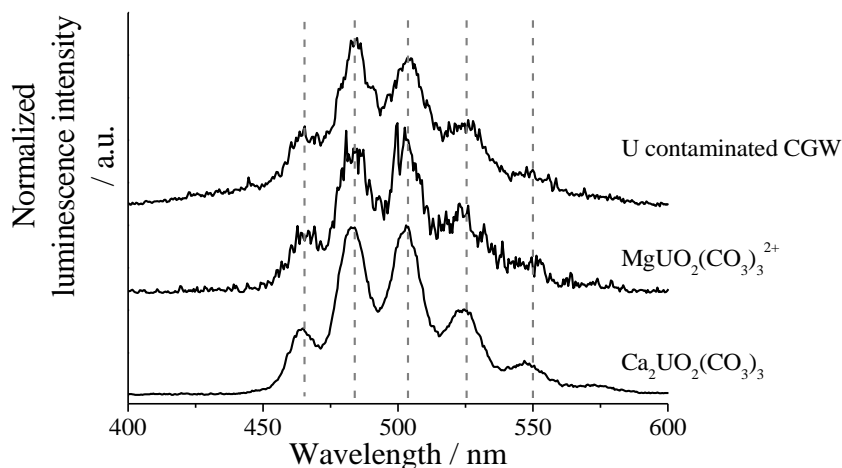


Figure 3: Fluorescence spectra and luminescence emission bands of the uranium contaminated circulating groundwater at 283 K in comparison to the spectra of aqueous alkaline earth uranyl carbonate species, which were described in the literature. For clarity, the spectra were normalized to the same maximum intensities and offset along the vertical axis.

In addition, the spectra of aqueous alkaline earth uranyl carbonate species were obtained for comparison displayed similar luminescence emission bands. The results were compared with the luminescence properties of the uranyl carbonate species $\text{Ca}_2\text{UO}_2(\text{CO}_3)_3$, described in Bernhard et al. (2001), which displays band positions similar to those of our studied groundwater. In addition, the luminescence spectrum of the $\text{MgUO}_2(\text{CO}_3)_3^{2+}$ species, described in Geipel et al. (2008), can be considered possible species as well. The considerable amounts of magnesium and calcium in the groundwater (Table 1) suggest that aqueous calcium and aqueous magnesium uranyl carbonate species could have formed in the contaminated circulating groundwater during the experiments.

In the cytoplasm of numerous small rod-shaped microorganisms ($\varnothing = 0.4 \mu\text{m}$), needlelike crystals with high electron density could be observed (Fig. 4a). EELS analysis of these crystals unequivocally identified uranium as a main constituent (Fig. 4b), based on ionization intensity peaks of O- and/or N-edges ($\text{O}_{4,5} = 93.5$ eV; $\text{N}_{6,7} = 380.0$ eV; Reimer et al., 1992). In addition, intensity peaks of phosphorus and calcium L2,3 edges were obtained as well. The presence of these elements in one crystal is clearly indicated in the elemental distribution analysis of uranium, phosphorus, and calcium, which was performed over a selected area of the biofilm. The results provide spectroscopic evidence for the existence of a U-phosphate mineral, similar to Autunite

($\text{Ca}[\text{UO}_2]_2[\text{PO}_4]_2 \cdot 2-6\text{H}_2\text{O}$) or meta-Autunite [$\text{Ca}(\text{UO}_2)_2(\text{PO}_4)_2 \cdot 10-12\text{H}_2\text{O}$], which formed intracellularly in the small rod-shaped microorganism cells during the experiment.

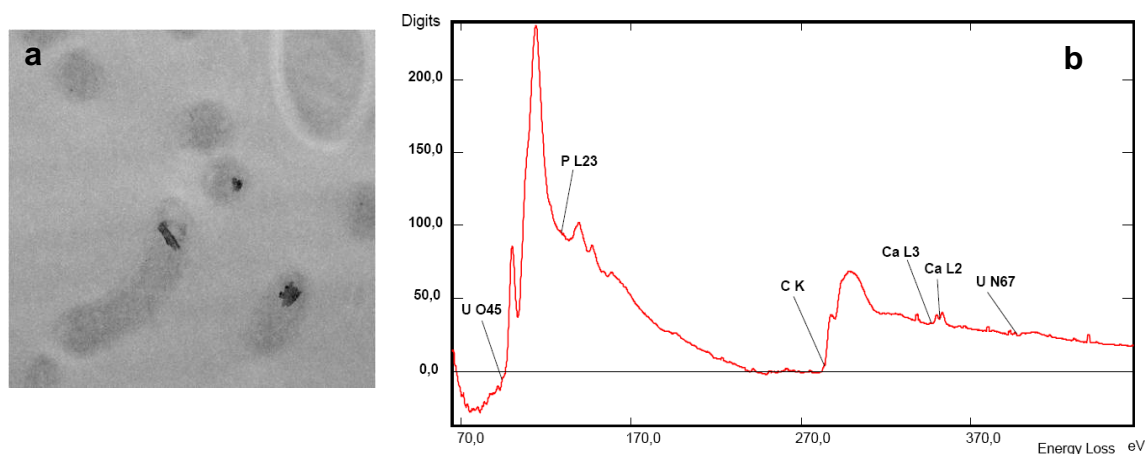


Figure 4: a) Particles of high electron density in the cytoplasm of some rod shaped gram negative bacteria of the U contaminated biofilm. b) EELS analysis showing intensity peaks of O- and N-edges of uranium, L-edges of Ca and L-edges of P.

Previous studies have described the formation of meta-Autunite as precipitates on the cell surface of numerous microorganism strains isolated from extreme habitats such as uranium waste piles and groundwater from radioactive waste depositories (e.g., Merroun et al., 2006; Jroundi et al., 2007; Nedelkova et al., 2007). The formation of intracellular polyphosphate-mediated Autunite or meta-autunite was detected in microorganisms isolated from uranium mine wastes as electron-dense granules (Merroun et al., 2006). The literature explains the formation as the cells' response to the heavy metal stress caused by the release of inorganic phosphate (H_2PO_4^-) from the cellular polyphosphate and the subsequent precipitation of uranium as uranyl phosphate ($\text{UO}_2[\text{H}_2\text{PO}_4]_2$) (Francis et al., 2004). Microorganisms are known to possess several uranium-resistance mechanisms, often involving precipitation to reduce toxicity (Hu et al., 2005). We found that the potential toxicity of uranyl was avoided by the uranium forming solid phases with phosphate in the cytoplasm of these strains of microorganisms. The phosphate released from the cellular polyphosphate was used, since analysis of the original groundwater indicated negligible amounts of phosphate. Under the given condition (pH, E_h) we assume that these Autunite minerals will be stable also in the absence of living organisms since the solubility constant is low (Gorman-Lewis et al., 2009). Analysis of the biofilm's dry mass show that approximately 17 % of the uranium added to the experiment was immobilized in biofilm microorganisms, probably by forming these stable U-phosphate minerals.

Summary and Conclusions

The combination of microelectrode measurements, EF-TEM/EELS and TRLS investigations, and theoretical calculation of the predominance fields of aqueous and solid species succeeded in differentiating between the mechanisms proceeding in the biofilm and the groundwater. The geochemical parameters of the biofilm differed significantly from those of the groundwater, clearly indicating that the biofilm had built up its own microenvironment. Uranium was removed from solution and immobilized exclusively in biofilm microorganisms in the form of the U-phosphate minerals Autunite or meta-Autunite. In contrast, aqueous calcium uranyl carbonates species formed in the groundwater contribute to the migration of U(VI) and consequently to environmental hazard. The results clearly indicate that biological systems must be considered part of natural systems that can significantly influence radionuclide behavior. Improved understanding of the mechanisms of biofilm response to actinides is very important, since microbial metabolic processes are sensitive to metals and their speciation. Consequently, changes of E_h and pH will influence the bioavailability of actinides. The present study improves our understanding of the mechanisms of biofilm response to radionuclides with respect to safety assessments of the far-field in high-level waste repositories. Although interest in microbial processes involving actinides has increased in recent years, research such as the present study is still rare and little is known of the microbial diversity in possible radioactive waste repository sites.

Acknowledgement

The research leading to these results has received funding from the European Union's European Atomic Energy Community's (Euratom) Seventh Framework Programme FP7/2007-2011 under grant agreement n° 212287 (RECOSYproject). We thank Posiva Oy for their cooperation in biofilm and water sampling. We thank Ursula Schaefer and Carola Eckardt (HZDR Dresden) for analysis. Inge Kristen's (HZI Braunschweig) skilfull work on sample preparation for analytical EF-TEM is gratefully acknowledged.

References

- Amayri S. (2002) Synthese, Charakterisierung und Löslichkeit von Erdalkaliuranylcarbonaten $M_2[UO_2(CO_3)_3] \cdot xH_2O$; M: Mg, Ca, Sr, Ba. Wissenschaftlich-Technische Berichte/ Forschungszentrum Rossendorf; FZR-359.
- Bernhard G., Geipel G., Reich T., Brendler V., Amayri S., Nitsche H. (2001) Uranyl(VI) carbonate complex formation: Validation of the $Ca_2UO_2(CO_3)_3$ (aq.) species. Radiochim. Acta 89, 511-518.
- Cammann K., Galster H. (1997) Das Arbeiten mit ionenselektiven Elektroden: Eine Einführung für Praktiker. Springer-Verlag, Berlin, Heidelberg, New York, Barcelona, Budapest, Hongkong, London, Mailand, Paris, Santa Clara, Singapur, Tokio, pp. 296.

- Flemming H.-C. (1995) Sorption sites in biofilms. *Wat. Sci. Tech.* 32, 27-33.
- Francis A. J., Gillow J. B., Dodge C. J., Harris R., Beveridge T. J., Papenguth H. W. (2004) Uranium association with halophilic and non-halophilic bacteria and archaea. *Radiochim. Acta* 92, 481–488.
- Geipel G., Amayri S., Bernhard G. (2008) Mixed complexes of alkaline earth uranyl carbonates: A laser-induced time-resolved fluorescence spectroscopic study. *Spectrochimica Acta Part A* 71, 53-58.
- Gorman-Lewis, D., Shvareva, T., Kubatko, K.-A., Burns, P. C., Wellman, D. M., McNamara, B., Szymanowski, J. E. S., Navrotsky, A., Fein, J.B. (2009) Thermodynamic Properties of Autunite, Uranyl Hydrogen Phosphate, and Uranyl Orthophosphate from Solubility and Calorimetric Measurements. *Environ. Sci. Technol.* 43, 7416–7422.
- Guillaumont R., Fanghänel T., Fuger J., Grenthe I., Neck V., Palmer D. A. Rand, M. H. (2003) Update on the chemical thermodynamics of uranium, neptunium, plutonium, americium and technetium. *Chemical Thermodynamics*, vol. 5, ed. OECD Nuclear Energy Agency, Elsevier, Amsterdam.
- Hemingway B.S. (1982) Thermodynamic properties of selected Uranium compounds and aqueous species at 298.15K and 1 bar and at higher temperatures - Preliminary models for the origin of Coffinite deposits: U.S.G.S. Open-file Rep. 82-619, 90 p.
- Hu P., Brodie E., Suzuki Y., McAdams H. H., Andersen G. L. (2005) Whole-genome transcriptional analysis of heavy metal stresses in *Caulobacter crescentus*. *J Bacteriol.* 187, 8437–8449.
- Lloyd J. R. and Macaskie L. E. (2002) Biochemical basis of microbe-radionuclide interactions. In *Interactions of microorganisms with radionuclides*. Ed. Miranda J. Keith-Roach and Francis R. Livens, Elsevier Sciences, Oxford, UK, 313-342.
- Lünsdorf H., Strömpfle C., Osborn A. M., Bennasar A., Moore E. R. B., Abraham W.-R., Timmis, K. N. (2001) Hydrophobic Substrates, and Soil Colloids Leading to Formation of Composite Biofilms, and to Study Initial Events in Microbiogeological Processes. *Methodes in Enzymology* 331, 317-331.
- Macaskie L. E., Bonthron K. M., Yong P., Goddard D. T. (2000) Enzymically mediated bioprecipitation of uranium by a *Citrobacter* sp.: a concerted role for exocellular lipopolysaccharide and associated phosphatase in biomineral formation. *Microbiology* 146, 1855-1867.
- Merroun M., Nedelkova M., Rossberg A., Hennig C., Selenska-Pobell S. (2006) Interaction mechanisms of bacterial strains isolated from extreme habitats with uranium. *Radiochimica Acta* 94, 723-729.
- Nguyen A. N., Silvac R. J., Weed H. C., Andrews J. W. (1992) Standard Gibbs free energies of formation at the temperature 303.15 K of four uranyl silicates: soddyite, uranophane, sodium boltwoodite, and sodium weeksite. *Journal of chemical thermodynamics* 24(4), 359-376.
- Nordbäck N., Engström J., Kemppainen K. (2008) Outcome of the Geological Mapping of the ONKALO Underground Research Facility Access Tunnel, Chainage 0-990. POSIVA Working Report 2008-84, Olkiluoto, Finland.

Pedersen, K., Arlinger, J., Hallbeck, A., Hallbeck, L., Eriksson, S. and Johansson, J. (2008) Numbers, biomass and cultivable diversity of microbial populations relate to depth and borehole-specific conditions in groundwater from depths of 4 to 450 m in Olkiluoto, Finland, *The ISME Journal* 2, 760–775.

Reimer L, Zepke U, Moesch J, Schulze-Hillert S, Ross-Messemer M, Probst W, Weimer E. (1992) *EELSpectroscopy. A Reference Handbook of Standard Data for Identification and Interpretation of Electron Energy Loss Spectra and for Generation of Electron Spectroscopic Images*. Institute of Physics, University of Münster, Germany, and Carl Zeiss, Electron Optics Division, Oberkochen, Germany.

Späth R., Flemming H.-C., Wuertz S. (1998) Sorption properties of biofilms. *Wat. Sci. Technol.* 37, 207-210.

Stroes-Gascoyne S. and Sargent F. P. (1998) The Canadian approach to microbial studies in nuclear waste management and disposal. *Journal of Contaminant Hydrology* 35, 175-190.

PARTIAL EQUILIBRIUM-BASED REDOX ESTIMATIONS IN GROUNWATERS FROM CRYSTALLINE SYSTEMS

Maria J. Gimeno¹, Luis F. Auqué^{1*}, Patricia Acero¹, Javier B. Gómez¹ and Maria Pilar Asta¹

¹ GMG, Geochemical Modelling Group, Earth Sciences Department, Faculty of Science, University of Zaragoza, Pedro Cerbuna 12, 50009 Zaragoza (Spain)

*Corresponding author: Luis F. Auqué: lauque@unizar.es

Abstract

An integrated methodology has been developed and applied to the study of the Laxemar-Simpevarp area (SE Sweden), which has been extensively investigated as a part of the Swedish program for the characterisation of the candidate sites for the deep geological disposal of spent nuclear fuel. The results from mineralogical studies, hydrochemical data and potentiometric Eh measurements have been interpreted with the assistance of different types of geochemical calculations (Eh calculations for homogeneous and heterogeneous redox couples, saturation index calculations with respect to key minerals and partial equilibrium calculations). The proposed conceptual model has helped to understand the behaviour of the redox processes active in this deep crystalline rock system and to find the limitations associated with it. This model will also allow improving the accuracy of geochemical predictive calculations focused on the long-term behaviour of this deep geologic environment after the construction and closure of a prospective spent nuclear fuel repository. Moreover, the developed comprehensive methodology used in this study is fully applicable to other studies focused of the redox behaviour of other natural systems.

1. Introduction

One of the most important issues for the long-term disposal safety of the radioactive wastes is the reducing capacity of the surrounding materials against the input of oxygen-rich waters. For the accurate evaluation of this reducing capacity, the main redox features and processes in the target systems must be identified and quantified.

The determination of the effective redox processes in an aquifer is usually an intensive task that needs the integration of very different types of data, including the analysis of dissolved redox indicators and mineralogical and microbiological determinations. These studies are even more complex when dealing with heterogeneous fractured systems, especially when reducing environments are investigated. Moreover, in these cases,

borehole drilling operations and sampling from different depths may result in the alteration of the pristine conditions. With the objective of proposing a conceptual model that allows improving our understanding of redox features and processes and the accuracy of predictive calculations for performance assessment, an integrated methodology has been developed and applied to the study of a deep groundwater system for which a wide range of all the required data is available, the Laxemar-Simpevarp area (SE Sweden). This area has been extensively studied during the last decade as part of the Swedish program for the characterisation of the candidate sites for the deep geological disposal of spent nuclear fuel. Following the integrated methodology, the results from comprehensive mineralogical studies, hydrochemical data and potentiometric Eh measurements from Laxemar-Simpevarp will be combined here with different types of geochemical modelling calculations, including redox pairs and saturation index calculations with respect to key minerals.

Moreover, since many of the redox features in the groundwater system of Laxemar-Simpevarp are controlled by the hydrogeochemistry of iron and sulphur and this is mainly determined by processes of microbial iron and sulphate reduction, a good understanding of the links between the activity of iron and sulphate reducing bacteria is mandatory to evaluate the relationship between both redox systems. In order to clarify their influence and to infer the effects of the stability of Fe(III)-oxyhydroxides on the predominance of iron and sulphate reduction processes, partial equilibrium calculations for iron and sulphate reduction have been performed and the obtained results are presented in the section 2.3.

2. Results and discussion

2.1. General hydrochemistry of the Laxemar-Simpevarp site

The general description of the Laxemar-Simpevarp candidate site has been provided elsewhere (Ström et al., 2008; Laaksoharju et al., 2008; Acero et al., 2009). The site is hosted in crystalline rocks in which most of the water-conducting pathways correspond to fracture networks (Tullborg et al., 2008). The present hydrochemistry of the Laxemar-Simpevarp groundwaters is the result of a complex mixing process driven by the input of different recharge waters, at least, since the last glaciation. As a general rule, there is a more or less clear trend towards more saline waters with depth from the shallowest and more dilute groundwaters to intermediate brackish groundwaters and, finally, to the deepest and more saline (Laaksoharju *et al.*, 2008). pH values range between 7.2 and 8.6.

2.2. Redox characterisation of the groundwater system and results from Eh and speciation-solubility calculations

Three types of data have been collected and are considered for the explorative analysis and for the modelling of the redox systems in Laxemar-Simpevarp: 1) potentiometrically measured Eh; 2) hydrochemical data, including microbiological determinations, obtained from several hundred groundwater samples taken at different depths in 23 drilled boreholes; and 3) chemical and mineralogical study of rock samples, including both bulk rock and fracture fillings from drillcores.

Groundwater redox conditions are clearly reducing, ranging all the potentiometrically measured values from -200 to -310 mV. Neither the distribution of Eh nor the dissolved contents of redox-sensitive elements (iron, sulphur, manganese and carbon) show any clear variation trend with depth (Gimeno *et al.*, 2008, 2009a). For Fe(II), most dissolved contents below 200 m depth are below 2 mg/L. Dissolved contents for S(-II) are usually low, although values up to 2.5 mg/L have sometimes been measured. However, the mere presence of S(-II) in the studied groundwaters has important implications, since it provides evidence of microbiological sulphate reduction in any low-temperature groundwater system (Hallbeck and Pedersen, 2008a). In the case of manganese, the concentrations of this element in the deep groundwaters vary from very low (below the detection limit) to more than 2.5 mg/L. Finally, methane content is very low, being always below 1 mL/L and usually below 0.1 mL/L.

Iron and sulphate reducing bacteria (IRB and SRB, respectively) have been identified in the microbiological studies (methanogens are barely present in the Laxemar area) though the relationship or the exclusion between both metabolisms is not clear yet (Hallbeck and Pedersen, 2008b).

Mineralogical studies indicate the presence of both Fe(II) and Fe(III) minerals widely distributed in the studied systems. In the shallowest part of the systems (upper 80-100 m), clay minerals and goethite are especially abundant in fracture fillings, whereas at greater depths the main iron oxide is hematite (Tullborg *et al.*, 2008). Besides the presence of hematite, the occurrence of Fe(II)-bearing minerals (mainly chlorite and pyrite) has been described in the fracture fillings, including those at shallow depths (Drake and Tullborg, 2009). This suggests that neither old nor recent oxidising episodes have been intense enough to exhaust the reducing capacity of fracture filling minerals, even in the shallowest part of the system. The identification of old, low temperature goethite down to 80 m depth indicates the possible maximum penetration depth of oxygenated groundwaters in the past (within the last 300,000 years; Drake and Tullborg, 2009), whereas the shallow location of recent, low temperature Fe-oxyhydroxides indicates that the present redox front is located at about 15-20 m depth, which is in agreement with the results of previous studies using different methodologies (Puigdomènech, 2001; Tullborg *et al.*, 2003). Moreover, manganese oxyhydroxides have not been identified at depths higher than 10 m, which is consistent with the existence of reducing conditions and with the presence of dissolved Fe(II) and S(-II), which are known to diminish the stability of manganese oxyhydroxides (Appelo and Postma, 2005).

The results obtained from Eh calculations¹ indicate that the calculated potentials (for the dissolved $\text{SO}_4^{2-}/\text{HS}^-$ and CO_2/CH_4 redox pairs and for the heterogeneous couples $\text{Fe}^{2+}/\text{Fe}(\text{OH})_3$, $\text{SO}_4^{2-}/\text{FeS}_{\text{am}}$ and $\text{SO}_4^{2-}/\text{pyrite}$) agree within a range of ± 50 mV with the potentiometrically measured Eh values. Finally, among the results obtained by means of saturation indices calculations, one of the most relevant for the redox characterisation of the deep groundwater system is the existence of equilibrium situations with respect to “amorphous” and crystalline ferrous iron monosulphides down to 600 m depth or even 900 m depth, in some cases. This equilibrium point towards a continuous and present

¹ Speciation-solubility and redox pair calculations have been performed with PHREEQC (Parkhurst and Appelo, 1999) and a modified version of the WATEQ4F thermodynamic database (as described, in detail, by Gimeno *et al.*, 2009a).

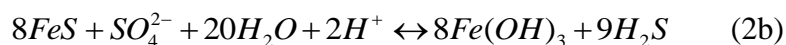
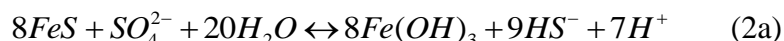
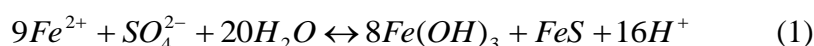
supply of Fe(II) and, most importantly, of S(-II), which is an indicator of the activity of sulphate reducing bacteria in low-temperature systems.

2.3. Partial equilibrium calculations

One of the most important issues in the understanding of the iron and sulphur redox hydrogeochemistry is related to the possibility that the corresponding bacterial metabolisms (i.e. IRB and SRB) be either mutually exclusive or concomitantly active. In the classical redox zonation scheme proposed by Berner (1981), a competitive exclusion between different metabolic groups is assumed. Although useful and widely used to identify and describe the redox evolution in a variety of aquatic systems (sediments, soils, aquifers), this sequential scheme of redox or biogeochemical zonation is not always observed to hold (e.g. Postma and Jakobsen, 1996; Jakobsen and Postma, 1999; Thornton *et al.*, 2001; Park *et al.*, 2006; Jakobsen and Cold, 2007). Therefore, the applicability of the classic redox sequence of metabolic reactions needs to be checked for any single studied system in order to propose a general conceptual model for the redox features in each particular natural environment

Following the work by Postma and Jakobsen (1996), some simple thermodynamic calculations have been used to discriminate between redox processes, assuming a partial equilibrium² between them and analysing their implications for what has been observed in Laxemar-Simpevarp system. This approach is especially useful for iron and sulphate reduction coupled to organic matter oxidation. The assumption of equilibrium between both processes implies that their energy yield is the same and, then, the effects of different iron oxyhydroxides on the favourability of Fe(III) and sulphate reduction can be easily explored.

For a groundwater system such as Laxemar-Simpevarp and based in earlier studies (Postma and Jakobsen, 1996; Appelo and Postma, 2005 and references therein), the following reactions can be written for Fe²⁺-dominated environments (reaction 1) and for sulphidic environments at pH higher and lower than 7 (reactions 2a and 2b, respectively):



According to these reactions, the dominance of Fe(III) or sulphate reduction processes under different conditions has been assessed. A logK= -3 has been assumed for the ferrous iron monosulphide dissolution from the review performed by Gimeno *et al.* (2009a). Calculations have been carried out at two different SO₄²⁻ concentrations (10⁻² and 10⁻⁴ M), which cover the range found in the Laxemar groundwaters. Moreover,

² In the degradation sequence of organic matter, molecular H₂ and simple organic molecules are continuously produced by fermentative bacteria from complex organic compounds that, in turn, are metabolised by other microorganisms using different terminal electron acceptors (TEAs). The overall sequence can be described as a partial equilibrium process, where fermentation represent the irreversible process (e.g. the rate-limiting step) and equilibrium is approached by TEAs and their reduction products (see Jakobsen and Postma, 1996).

different types of ferric oxyhydroxides have been considered in the calculations (Table 1): the less crystalline hydrous ferric oxides –HFO- or ferrihydrites, the more crystalline phases (e.g. hematite) and another two phases with intermediate crystallinity (a poorly crystalline phase, after Banwart, 1999, and a crystalline variety, after Grenthe et al., 1992).

Table 1: Types of ferric oxyhydroxides considered in the partial equilibrium calculations (referred as $Fe(OH)_3$) and their corresponding equilibrium constants.

Mineral phase	Reaction	logK	Reference
Amorphous Ferrihydrite	$Fe(OH)_3 \rightarrow Fe^{3+} + 3 OH^-$	-37	Nordstrom et al. (1990)
Crystalline Ferrihydrite		-39	
Iron oxyhydroxide with intermediate crystallinity		-40.9	Banwart (1999)
Crystalline oxyhydroxide (similar to goethite or hematite)		-43.1	Grenthe et al. (1992)
Hematite		-44.0	Macalady et al. (1990)

The main results are shown in Figures 1 and 2, for Fe(II) and sulphide-dominated environments, respectively. In these graphs, Laxemar-Simpevarp groundwaters are plotted together with the different equilibrium equation lines (with different grey intensities) according to the oxyhydroxide they represent. The range indicated by two parallel lines corresponds to the two sulphate concentrations used in calculations, which depict a region equally favourable for Fe(III)-reduction and sulphate reduction. In Figure 1, on the left side of the equilibrium zone, iron reduction is favoured for a given oxyhydroxide (reaction 1 tends to proceed to the left) whereas sulphate reduction would be thermodynamically favoured on the right side of the equilibrium zone. Similarly, in the areas above the equilibrium zone for a given oxyhydroxide in Figure 2, sulphate reduction is favoured (reactions 2a and 2b shift to the right), while below the equilibrium zones iron reduction is favoured over sulphate reduction.

Both plots show the minor influence of sulphate concentration on the equilibrium and the major influence of pH on the relative stability of iron and sulphate reduction. Moreover, the strong effect of the stability (and/or the specific surface) of iron oxyhydroxides on the prevalence of iron or sulphate reducing environments is also clearly shown. Whereas iron reduction is favoured under most aquatic conditions in the presence of ferrihydrite or similar poorly crystalline ferric phases, sulphate reduction is often more favourable if hematite or goethite are present (Postma and Jakobsen, 1996; Peiffer, 2000; Appelo and Postma, 2005). That is, as the stability of iron oxyhydroxides increases (and/or surface area decreases), sulphate reduction is comparatively favoured.

These diagrams also show the relative stability of the different oxyhydroxides considered in the calculations. In Fe(II)-dominated environments (Figure 1), their equilibrium zones are pH-dependent. For most waters with pH > 7 and with detectable amounts of dissolved iron, only the crystalline oxyhydroxides (i.e. hematite and/or goethite) are stable...Similar observations can be made for sulphidic environments, even though their equilibrium zones for ferric oxyhydroxides are less sensitive to pH (Figure 2). Poorly crystalline phases (ferrihydrites) are not stable for dissolved sulphide

concentrations around the sulphur detection limit (0.01 mg/L) and only more crystalline oxyhydroxides could be stable under these conditions.

According to these interpretations and to the detailed mineralogical characterisation of ferric oxyhydroxides at depth in the system (Dideriksen *et al.*, 2007, 2010), sulphate reduction is more favourable than iron reduction in most Laxemar-Simpevarp groundwaters (Figures 1 and 2). Another interesting result is related to the fact that Laxemar-Simpevarp groundwater samples are widely distributed throughout the field between the microcrystalline ferric oxides and the crystalline phase defined by Grenthe *et al.* (1992) and thus, simultaneous reduction of iron oxides and sulphate in these waters would need the existence of a broad spectrum of iron oxyhydroxides with different solubilities or surface areas, which has neither been identified in the fracture fillings nor expected in waters with such long residence time.

In the light of the results obtained and consistently again with the mineralogical observations, the presence of poorly crystalline Fe(III)-oxyhydroxides is not feasible under the pristine reducing conditions of Laxemar-Simpevarp groundwaters, given their long residence time and their generalised reducing character. Although these phases could have formed under oxygen intrusion events, they must have recrystallised over the time to more crystalline phases not easily bioavailable for the IRB. This is also consistent with the results obtained by Banwart (1999) and Trotignon *et al.* (2002) in the large-scale redox experiment carried out at the Äspö Hard Rock Laboratory. On top of that, the presence of dissolved Fe(II) in the groundwaters has noticeable catalytic effects on this process, increasing the transformation rates (Pedersen *et al.*, 2005). This means that the Fe(II) initially produced by a hypothetical reduction of ferrihydrite by IRB (or any other inorganic process) would cause an autocatalytic transformation of the remaining poorly crystalline Fe(III)-oxyhydroxides into less reactive phases.

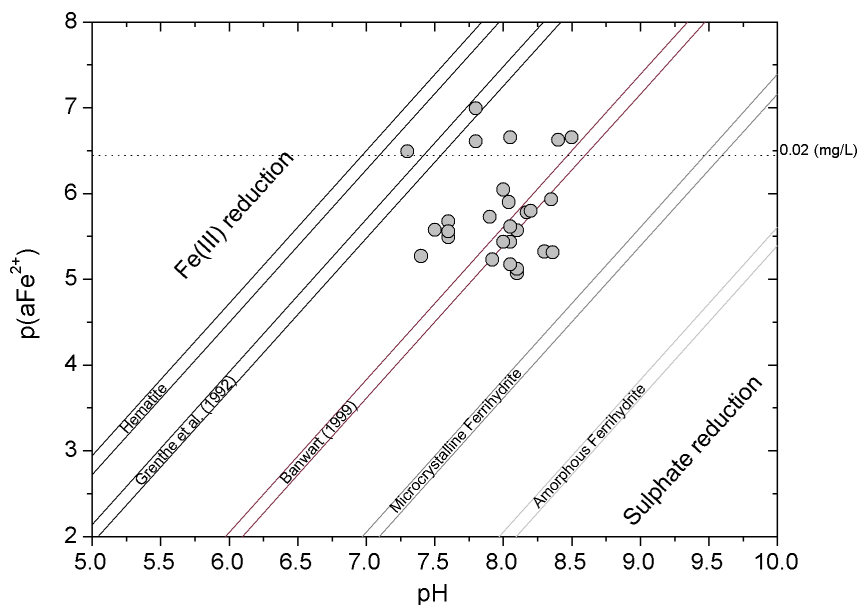


Figure 1. Fe^{2+} activity vs. pH diagram showing the stability relations for simultaneous equilibrium between Fe(III) and sulphate reduction at equilibrium with FeS in Fe^{2+} -dominated environments. Detection limit (0.02 mg/L) for analytical concentrations of dissolved Fe^{2+} is shown for reference. See text for details.

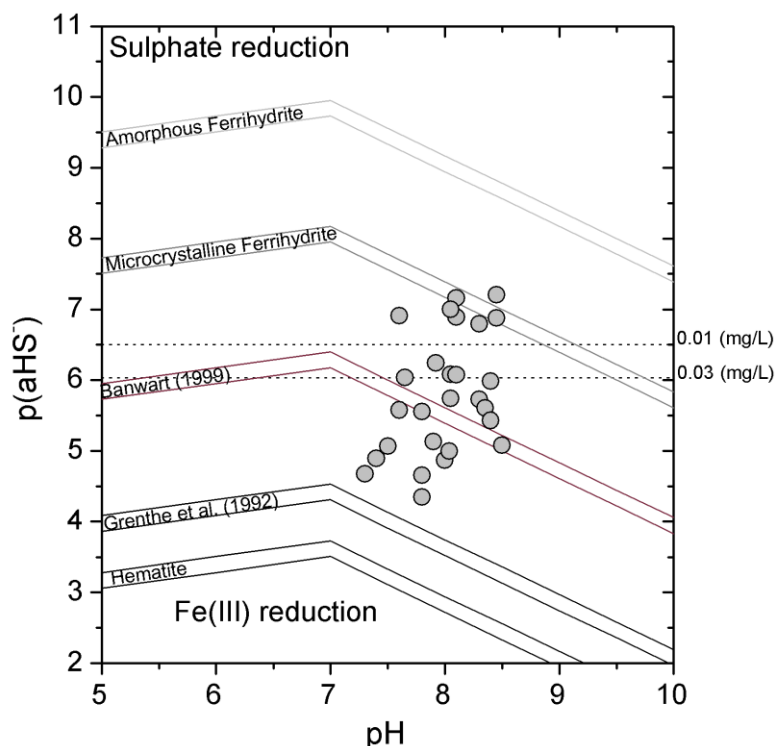


Figure 2: HS^- activity (a_{HS^-}) vs. pH diagram showing the stability relations for simultaneous equilibrium between $Fe(III)$ and sulphate reduction at equilibrium with FeS in sulphidic environments. Detection (0.01 mg/L) and reporting limit (0.03 mg/L) for analytical concentrations of dissolved sulphides are indicated for reference. See text for details.

Summary and Conclusions

As shown in the previous S+T communications (Gimeno et al., 2009b, 2010), redox pairs calculations for the Laxemar-Simpevarp groundwaters have shown that potentiometrically measured Eh values, clearly reducing, are consistent with the calculated redox potentials with the $Fe^{2+}/Fe(OH)_3$ redox couple, with most of the feasible sulphur redox pairs and with the CO_2/CH_4 couple. Moreover, the widespread presence of S(-II) (although low) in many of the sampled sections at different depths provides evidence of microbiological sulphate reduction.

These observations are consistent with the described mineralogy in the bulk rock and in the fracture fillings from the Laxemar-Simpevarp deep bedrock system and are indicative of the important role played by the iron and sulphur redox systems in the buffering of the redox conditions of this system.

As presented here, the results obtained by means of equilibrium calculations have allowed appreciating the importance of the crystallinity, particle size and surface area of ferric oxyhydroxides on the predominance of iron or sulphate reduction processes and, therefore, in the development of segregated redox zones in natural systems. The less crystalline ferric oxyhydroxides (e.g. ferrihydrite) constitute the primary source for IRB

activity and, therefore, their absence must be an important limitation in the activity of these microorganisms under the pristine highly-reducing conditions of the Laxemar-Simpevarp deep groundwater system. Thus, all the available data and interpretations suggest that present IRB activity in the Laxemar-Simpevarp groundwaters is restricted to the shallower levels, where a broad spectrum of Fe-oxyhydroxides (including poorly crystalline phases) exists. At deeper levels, the characters of Fe-oxyhydroxides and clays in the fracture fillings do not seem to be suitable to support the active presence of this type of microorganisms. However, this conceptual model also suggests that the presence of IRB is, at least, temporally feasible during oxygen intrusion scenarios, when low crystalline iron oxyhydroxides can be formed.

Overall, the partial equilibrium approach used here to analyse the sulphur and iron systems seems to confirm the preliminary results obtained by Gimeno et al. (2009a) from the bioenergetic calculations performed in the Laxemar-Simpevarp system. These calculations (based on the energetics of the possible terminal electron accepting processes) would allow incorporating the rest of the detected metabolic activities in the groundwaters and, thus, the bioenergetic approach must be further explored.

Acknowledgements

This study forms part of the SKB site investigation program, managed and supported by the Swedish Nuclear Fuel and Waste Management Company (SKB), Stockholm. The presentation of this work here is partly funded by the European Atomic Energy Community Seventh Framework Program [FP7/2007-2013] under grant agreement No 212287, Collaborative Project Recosy.

References

- Acero, P., Auque, L.F., Gimeno, M.J. and Gomez, J.B. (2009). Evaluation of mineral precipitation potential in a spent nuclear fuel repository. *Environ. Earth Sci.* (in press).
- Appelo, C.A.J. and Postma, D. (2005). *Geochemistry, Groundwater & Pollution*. Balkema, Rotterdam, The Netherlands, 2nd edition, 649 p.
- Banwart, S.A. (1999). Reduction of iron (III) minerals by natural organic matter in groundwater. *Geochim. Cosmochim. Acta*, 63, 2919-2928.
- Berner, R.A. (1981). A new geochemical classification of sedimentary environments. *J. Sediment. Petrol.*, 51, 359-365.
- Dideriksen, K., Christiansen, B.C., Baker, J.A., Frandsen, C., Balic-Zunic, T., Tullborg, E.-K., Mørup, S. and Stipp, S.L.S. (2007). Fe-oxide fracture fillings as a palæo-redox indicator: Structure, crystal form and Fe isotope composition. *Chemical Geology*, **244**, 330–343.
- Dideriksen, K., Christiansen, B.C., Frandsen, C., Balic-Zunic, T., Mørup, S. and Stipp, S.L.S. (2010). Paleo-redox boundaries in fractured systems. *Geochim. Cosmochim. Acta*, **74**, 2866-2880.

Drake, H. and Tullborg, E.-L. (2009). *Fracture mineralogy. Laxemar. Site Descriptive Modeling. SDM-Site Laxemar.* . SKB-R-08-99, Svensk Kärnbränslehantering AB, Stockholm, Sweden.

Gimeno, M.J., Auqué, L.F., Gómez, J. and Acero, P. (2008). *Water-rock interaction modelling and uncertainties of mixing modelling.* SDM-Site Forsmark. SKB-R-08-86, 212 pp.

Gimeno, M.J., Auqué, L.F., Gómez, J. and Acero, P. (2009a). *Water-rock interaction modelling and uncertainties of mixing modelling.* SDM-Site Laxemar. SKB-R-08-110, Svensk Kärnbränslehantering AB, Stockholm, Sweden.

Gimeno, M.J., Auqué, L.F., Gómez, J., Acero, P. and Laaksoharju, M. (2009b). *General characterisation of the redox systems in the Swedish candidate sites for deep disposal of nuclear waste.* 1st Annual Workshop Proceedings of the Collaborative Project “Redox Phenomena Controlling Systems” (7th EC FP CP RECOSY). Forschungszentrum Karlsruhe in der Helmholtz-Gemeinschaft Wissenschaftliche Berichte FZKA 7466, pp 111-120.

Gimeno, M.J., Auqué, L.F., Acero, P., Gómez, J. and Asta, M.P. (2010). *Distribution of redox elements and speciation-solubility results as a first approach to the general characterisation of the redox systems in the swedish candidate sites for deep disposal of nuclear waste.* 2nd Annual Workshop Proceedings of the Collaborative Project “Redox Phenomena Controlling Systems” (7th EC FP CP RECOSY). KIT Scientific Reports 7557, pp.219-228.

Grenthe, I., Stumm, W., Laaksoharju, M., Nilsson, A.-C. and Wikberg, P. (1992). Redox potentials and redox reactions in deep groundwater systems. *Chemical Geology*, 98, 131-150.

Hallbeck, L. and Pedersen, K. (2008a). Characterization of microbial processes in deep aquifers of the Fennoscandian Shield. *Applied Geochemistry*, 23(7), 1796-1819.

Hallbeck, L. and Pedersen, K. (2008b). *Explorative analysis of microbes, colloids and gases.* SDM-Site Laxemar. SKB-R-08-109, Svensk Kärnbränslehantering AB, Stockholm, Sweden.

Jakobsen, R. and Cold, L. (2007). Geochemistry at the sulfate reduction–methanogenesis transition zone in an anoxic aquifer. A partial equilibrium interpretation using 2D reactive transport modeling. *Geochim. Cosmochim. Acta*, 71, 1949–1966

Jakobsen, R., and Postma, D. (1999). Redox zoning, rates of sulfate reduction and interactions with Fe-reduction and methanogenesis in a shallow sandy aquifer, Rømø, Denmark. *Geochim. Cosmochim. Acta*, 63, 137–151.

Laaksoharju, M., Smellie, J., Tullborg, E.-L., Gimeno, M.J., Molinero, J., Gurban, I. and Hallbeck, L. (2008). Hydrogeochemical evaluation and modelling performed within the Swedish site investigation programme. *App. Geochem.* 23: 1761-1795.

Macalady, D.L., Langmuir, D., Grundl, T. and Elzerman, A. (1990). Use of model-generated Fe³⁺ ionactivities to compute Eh and ferric oxyhydroxide solubilities in anaerobic systems. In: D.C. Melchior and R.L. Bassett (Editors), *Chemical Modeling of Aqueous Systems II*. A.C.S. Symp. Ser. 416. Amer.Chem. Soc., Washington, D.C., pp. 350–367.

- Nordstrom, D.K., Plummer, L.N., Langmuir, D., Busenberg, E., May, H.M., Jones, B.F. and Parkhurst, D. (1990). Revised chemical equilibrium data for major water-mineral reactions and their limitations. In: Melchior, D.C. and Basset, R.L. (Eds.), *Chemical Modeling of Aqueous Systems II*. ACS Symp. Ser. pp. 398–413.
- Park, J., Sanford R.A., and Bethke C.M. (2006). Geochemical and microbiological zonation of the Middendorf aquifer, South Carolina. *Chem. Geol.*, 230, 88–104.
- Parkhurst, D. L. and Appelo, C.A.J. (1999). *User's Guide to PHREEQC (Version 2), a computer program for speciation, batch-reaction, one-dimensional transport, and inverse geochemical calculations*. Water Resources Research Investigations Report 99-4259, 312 p.
- Pedersen, H., Postma, D., Jakobsen, R. and Larsen, O. (2005). Fast transformation of iron oxyhydroxides by the catalytic action of aqueous Fe(II). *Geochim. Cosmochim. Acta*, 16, 3967-3977.
- Peiffer, S. (2000). Characterization of the redox state of aqueous systems—towards a problem oriented approach. In: Schuering, J., Schulz, H.D., Fischer, W.R., Boettcher, J., Duijnesveld, W.H.M. (Eds.), *Redox—Fundamentals, Processes and Measuring Techniques*. Springer Verlag, Berlin.
- Postma, D., and Jakobsen, R. (1996). Redox zonation: Equilibrium constraints on the Fe(III)/SO₄-reduction interface. *Geochim. Cosmochim. Acta*, 60, 3169–3175.
- Puigdomènech, I. (2001). Hydrochemical stability of groundwaters surrounding a spent nuclear fuel repository in a 100,000 year perspective. SKB Technical Report 01-28, 83 p.
- Ström, A., Andersson, J., Skagius, K. and Winberg, A. (2008). Site descriptive modelling during characterization for a geological repository for nuclear waste in Sweden. *Applied Geochemistry*, 23 (7): 1747–1760.
- Thornton, S.F., Quigley, S., Spence, M.J., Banwart, S.A., Bottrell, S. and Lerner, D.N. (2001). Processes controlling the distribution and natural attenuation of dissolved phenolic compounds in a deep sandstone aquifer. *Journal of Contaminant Hydrology*, 53, 233–267.
- Trotignon, L., Michaud, V., Lartigue, J-E., Ambrosi, J-P., Eisenlohr, L., Griffault, L., de Combarieu, M. and Daumas, S. (2002). Laboratory simulation of an oxidizing perturbation in a deep granite environment. *Geochim. Cosmochim. Acta*, 66, 2583-2601.
- Tullborg, E-L., Smellie J.A.T. and MacKenzie A.B. (2003). The use of natural uranium decay series studies in support of understanding redox conditions at potential radioactive waste disposal sites, *MRS, Scientific basis for Nuclear Waste Management XXVII* vol. 807, pp. 571–576.
- Tullborg, E.-L., Drake, H. and Sandstrom, B. (2008). Palaeohydrogeology: A methodology based on fracture mineral studies. *Applied Geochemistry*, 23 (7): 1881-1897.

NANO-SIZED PYRITE/GREIGITE REACTIVITY TOWARDS SE(IV) AND SE(VI)

Laurent Charlet ^{1,2,*}, Mingliang Kang ^{1,3,4}, Fabrizio Bardelli ¹, Antoine Géhin ¹, Fanrong Chen ^b

¹Environmental Geochemistry Group, ISTERre, Grenoble - 38041 (FR).

²Institute Universitaire de France, Paris - 75005 (FR).

³Guangzhou Institute of Geochemistry, Guangzhou - 510640 (CH).

⁴Graduate University of Chinese Academy of Sciences, Beijing - 100049 (CH).

*Corresponding author: charlet38@gmail.com

Abstract

Nano-pyrite was synthesized upon reaction of FeCl₃ and NaHS in the ratio of 1:2. Following this protocol, 28% of greigite (Fe²⁺Fe³⁺₂S₄) was found in the solid phase. Greigite is an important precursor for pyrite formation, and its occurrence in the present study may originate from HS⁻ loss during the synthesis. Batch reactor experiments were performed upon adding selenite or selenate to the nano-sized pyrite-greigite suspension at different pH values and with or without the addition of extra Fe²⁺. XANES-EXAFS spectroscopy revealed, for the first time, the formation of ferroselite (FeSe₂), the thermodynamically most stable species, as the predominant reaction product along with elemental Se. The nucleation and growth of FeSe₂ is believed to occur at the nano-pyrite/greigite surface via several steps and reaction kinetics and aging time may play a significant role. The present study demonstrates that, in Fe²⁺/sulfide-bearing environment, Se can be immobilized in its most insoluble form, which leads to its reduced mobility in the environment.

Introduction

Selenium has attracted extensive attention due to its implications in human health and its relevant role in management of radioactive nuclear waste (Chen et al., 1999; Grambow, 2008). Concerning human health, problems of both Se deficiency and excess occur in several geographic areas all over the world (Fordyce et al., 2000; Rayman, 2008). In general, soils originating from volcanic rocks and granite contain small

amounts of selenium, whereas soil developed from shale, sandstone, limestone, or claystone have higher selenium contents (Glazovskaya, 1996; Winkel et al., 2011). Recent safety evaluations on nuclear waste disposal have demonstrated that anionic ⁷⁹Se ($t_{1/2} = 2.95 \times 10^5$ y), together with ¹²⁹I, ³⁶Cl, and ⁹⁹Tc radionuclides contribute mostly to the ultimate dose (Dossier Argile, 2005; Jiang et al., 2001) because these anions are assumed to diffuse almost freely through the clay confinement barriers.

Selenium solubility and mobility in the environment largely depends on its oxidation state: Se species with higher oxidation states (4 and 6) are more soluble, and thus more mobile in the environment, whereas lower oxidation states species, such as elemental Se, or iron selenides (0, -1, and -2), are less soluble (Chen et al., 1999; Scheinost et al., 2008a; Scheinost et al. 2008b). The occurrence of a specific chemical form is controlled by the surrounding E_h-pH conditions. The occurrence of Se(VI) is limited to high redox potentials with moderate to alkaline pH values, while Se(IV) is the main selenium species in moderate environmental conditions. Due to the negligible sorption of Se(IV) and Se(VI) on natural minerals, in particular on granite and claystone minerals, reductive precipitation is considered to be the most effective way to immobilize Se.

Reductive environments are generally rich in Fe²⁺-bearing minerals, such as sulfides, and the same occurs in underground nuclear waste disposal repositories, due to the corrosion of steel containers and structural elements. For this reason, numerous studies have focused on the identification of the selenium reaction products in the Se/Fe²⁺-bearing minerals interaction process (Scheinost et al., 2008a; Scheinost et al., 2008b, Chakraborty et al., 2010; Missana et al., 2009; Charlet et al., 2007; Loyo et al. 2008). In most experiments, elemental selenium was identified as the main reaction product (Chakraborty et al., 2010, Charlet et al., 2007; Myneni et al. 1997; Liu et al. 2008), although the prevalence of elemental Se in these short term laboratory experiments is in obvious contrast to the prevalent occurrence of iron selenide phases in soils, sediments, and ore deposits (e.g. ferroselite, dzharkenite, and Se-substituted pyrite) (Howard et al., 1977; Xiong et al., 2003; Ryser et al., 2005; Belzile et al., 2000). This may be due to the formation of metastable S⁰ nano-particles in laboratory experiments (Winkel et al., 2011). Recently, a few investigations have observed iron selenides formation after selenite reduction by mackinawite, magnetite, and green rust (Scheinost et al., 2008a, Scheinost et al. 2008b). However, until now, no one reported the abiotic formation of ferroselite (FeSe₂), which is the most stable species from a thermodynamic point of view.

Pyrite (FeS₂) is the most frequent sulfide mineral in geological environment (granite and claystone) and is also presents in bentonites, which are widely considered as optimal candidates for buffer material in nuclear waste repositories (Metz et al., 2003; Vaughan et al., 1991; Baeyens et al., 1985). Among the many studies which focused on the reduction of selenite by pyrite, no one yet reported the formation of iron selenides. For example, Breynaert et al. (2008) found crystalline Se⁰ as the only reaction product with pyrite at pH values in the range 6.5 – 8.5, Se⁰ was also observed by Liu et al. (2008) as the reaction product of pyrite with HSe⁻ at pH 6.6 (Liu et al. 2008).

Greigite, which has the empirical formula Fe²⁺Fe³⁺₂S₄, is an authigenic ferrimagnetic mineral that grows as a precursor of pyrite during early diagenetic sedimentary sulfate reduction (Roberts et al., 2011). It often occurs in lacustrine sediments with clays, silts, and arkosic sand in varved sulfide-rich clays. The associated minerals include

montmorillonite, chlorite, calcite, veatchite, sphalerite, pyrite, marcasite, galena, and dolomite.

In this study, in order to better understand the immobilization mechanism of selenium by reaction with iron sulfides, we investigate the reduction of selenite and selenate by nano-sized pyrite containing a certain amount greigite as a function of pH and Fe²⁺ concentration. The reaction products are characterized by X-ray Absorption Spectroscopy (XAS) and solution analysis.

1. Materials and methods

1.1 Pyrite-greigite Composition Synthesis

Nano-sized pyrite was synthesized in a glove-box (O₂ < 2ppm), according to the protocol mentioned by Wei et al. (1996) and Liu et al. (2008). A solution of 250ml of 0.2 M NaHS·xH₂O was poured into 250 ml of 0.1 M FeCl₃·6H₂O solution and stored in a 500ml bottle under persistent stirring. The mixed-solution immediately turned black. The pH was continuously monitored, and a 0.5M NaOH solution was used to adjust the value to ~4.8, due to large amount of protons produced during the reaction process. The black suspension precipitated in a few tens of minutes and was aged for 20 days. After decanting the supernatant, the black precipitate was washed with degassed water followed by 0.1M HCl, and then washed several times with degassed water. The above experiment was repeated 5 times to obtain ~15g of material. Eventually, 100ml of degassed water were added to the washed precipitate. To characterize the synthesized material, 3 ml of the suspension were filtered on a porous membrane (0.2 μm) and used for Mössbauer spectroscopic analysis. Results indicated that the synthesized material is composed by 72±2% of pyrite and 28±2% of greigite (Table 1).

Table 1: Mössbauer parameters attributed to the pyrite and greigite contributions.

	IS (mm·s ⁻¹)	QS (mm·s ⁻¹)
pyrite	0.40	0.59
greigite	0.59	0.60

All manipulations were performed in the glove-box and all chemicals used in the experiments were of analytical grade or higher. The water used was deionized (18.3 mΩ), boiled, and cooled under an argon flux, before its introduction in the glove box.

1.2 Sorption Experiments

The pyrite-greigite suspension was shaken before the experiment, and 5ml of this stock suspension were added to 160ml of a 0.4 mM Na₂SeO₃ or ~ 0.5 mM Na₂SeO₄ solution. Due to the loss of HS⁻ during the synthesis, the pyrite-greigite solid phase concentration was estimated to be ~4.28g/L. Two series of sorption experiments were conducted: one with ~ 0.05M of CH₃COOH-CH₃COONa in order to keep the pH stable around 6, and another without the addition of the buffer solution. In both series of experiments, 0.02

M NaClO₄ solution was used as electrolyte background. To study the effect of Fe²⁺ on the reaction products, Fe²⁺ was initially added to two reactors in each series of experiments (Table 2).

Table 2: Solution analysis of the batch experiments (ICP-AES). nd = not determined; bdl = below detection limit.

Sample	Selenium species	pH	Time (h)	extra Fe ²⁺ (mM)	buffer	[Se] _{tot} (mM)	[Fe] _{tot} (mM)	[S] _{tot} (mM)
A-1	Se(IV)	Nd	0	0	Yes	0.4	0.0788	bdl
		6.19	0.5			0.031	0.6006	0.001
		6.21	24			nd	nd	nd
		6.27	336			bdl	0.6343	0.002
A-2	Se(IV)	Nd	0	0.1	Yes	0.4	0.0788	bdl
		6.18	0.5			0.015	0.7358	0.001
		6.22	24			nd	nd	nd
		6.28	336			bdl	0.7176	0.001
A-3	Se(IV)	Nd	0	0	No	0.4	0.0788	bdl
		8.99	0.5			0.25	bdl	0.001
		10.1	24			nd	nd	nd
		10.31	336			bdl	bdl	0.071
A-4	Se(IV)	Nd	0	0.08	No	0.4	0.0788	bdl
		8.8	0.5			0.17	bdl	0.002
		9.8	24			nd	nd	nd
		9.78	336			bdl	bdl	0.014
B-1	Se(VI)	Nd	0	0	Yes	0.5	0.0788	bdl
		5.9	0.5			0.46	0.2076	0.031
		5.89	336			0.38	0.3388	0.017
B-2	Se(VI)	Nd	0	0.1	Yes	0.5	0.0788	bdl
		5.9	0.5			0.45	0.3314	0.010
		5.9	336			0.37	0.4958	0.009
B-3	Se(VI)	Nd	0	0	No	0.45	0.0788	bdl
		8.12	0.5			0.41	0.0160	0.004
		8.73	24			nd	nd	nd
		8.84	336			0.33	0.0016	0.011
B-4	Se(VI)	Nd	0	0.08	No	0.45	0.0788	bdl
		8.18	0.5			0.39	0.0386	0.004
		9.35	24			nd	nd	nd
		8.46	336			0.27	0.0013	0.005

The reactors were manually shaken several times each day and at given time intervals the solution pH was measured with a Metrohm 6.0233.100 pH electrode connected to an Orion (525A) pH meter. Five pH buffer solutions were used to calibrate the electrodes. 6 ml of suspension aliquot from the reactors were sampled and filtered on a 0.2 µm pore size membrane (Millipore), and the total Se, Fe and S concentrations in the filtrate were

analyzed by Inductively Coupled Plasma - Optical Emission Spectrometry (ICP-OES), using a Varian 720-ES apparatus with a quantification limit of 3.80×10^{-7} , 8.95×10^{-8} , and 5.21×10^{-7} mol.L⁻¹ for Se, Fe, and S, respectively.

1.3 X-ray Absorption Spectroscopy

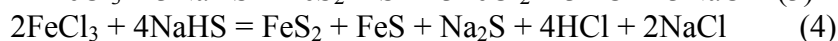
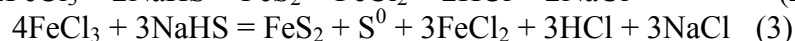
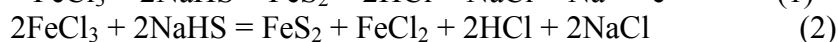
XAS measurements were performed at the Se K-edge (12,658 eV) on the Italian beamline (BM8-GILDA) at the European Synchrotron Radiation Facility (ESRF) in Grenoble (France). Two weeks aged reaction suspensions (15 ml) were filtered on porous membranes (Millipore, pore size 0.2 µm), and the solid deposited on the membranes was dried with silica gel, sealed with Kapton tape, and mounted on the sample holder. All the above operations were conducted inside the glove box to avoid samples' oxidation. The samples were then brought to the synchrotron facility in an anaerobic jar, transferred to the experimental chamber, and measured in vacuum at low temperature (77K) in order to avoid beam induced redox reactions and to enhance the EXAFS signal at high k. A Se⁰ reference spectrum was simultaneously acquired at each energy scan for accurate energy calibration. Principle Component Analysis (PCA) and Least Square Fitting (LSF) were applied to the XANES spectra to obtain quantitative information on the sample speciation. PCA and LSF were performed using the IFEFFIT and SIXPACK packages, respectively (Ravel et al., 2005; Webb 2005). Local structure around Se was obtained through quantitative refinements on the EXAFS signal up to ~ 3.5 Å. Fits were performed in the back-transformed reciprocal space (k) in the range 4–12 Å⁻¹, using a dedicated software package based on MINUIT routines from CERN libraries (James et al., 2005). The ATOMS package (Ravel et al., 2001) was used to generate the atomic clusters centered on the absorber atom (Se), which were used as reference structures for calculating theoretical amplitude and phase back-scattering functions with the FEFF8 package (Ankudinov et al., 1998).

2. Results and discussion

2.1 Reaction path

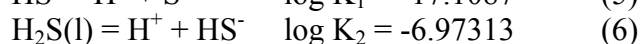
Schoonen et al. (1991) reported that greigite (Fe₃S₄) is an important precursors in the formation of pyrite and it is absent in highly reduced environments (Wei et al., 1997; Schoonen et al., 1991a; Schoonen et al., 1991b; Schoonen et al., 1991c). Sulfidation of the precursor proceeds through progressively more sulfur-rich, Fe-S phases: amorphous FeS (Fe_{1.11}S-Fe_{1.09}S) → mackinawite (FeS_{0.93}-FeS_{0.96}) → greigite (Fe₃S₄) → pyrite/marcasite FeS₂. Thus it is not uncommon to find greigite associated with pyrite.

The presence of greigite may also originate from HS⁻ loss during the reaction process. The possible reactions between NaHS and FeCl₃ are:



The above reactions indicate that in all cases a large amount of protons is produced. This can explain the sharp drop of the pH after the addition of NaHS·xH₂O to the FeCl₃ solution. Though 0.5M NaOH was added to neutralize the released protons, pH remained low enough to form gaseous H₂S, and the resulting excess of Fe³⁺ in solution favored the formation of greigite.

According to the recent thermodynamic data (Table 3) (Chivot, 2004), the following equilibrium equations apply to solution sulfide species:



The above equations indicate that H₂S(l) and HS⁻ are the predominant species at pH < 6.97 and pH > 6.97, respectively. Therefore, in the present study, as the reaction pH is around 4.8, the formation of H₂S gas is thermodynamically favorable. A further evidence for the development of H₂S gas is that the oxygen detector of the glove-box quickly decreased to < 0 ppm during the reaction process, since sulfide gases like CS₂, SO₂, and H₂S can poison the Cu-based catalyst of the glove-box. Considering the composition of the final product, ~10.71% (e.g. 26.77mmol) of the HS⁻ reactant is estimated to have been volatilized in the form of H₂S(g).

Table 3: Thermodynamic data used for sulfide species ($\Delta_f G^\theta$ /kJ/mol).

	S ²⁻	H S ⁻	H ₂ S (l)	H ₂ S (g)
Δ_f	109.	1	-	-
G^θ	85	2.2	27.6	33.44

2.2 Aqueous phase analyses

Batch experiments were labeled as following: A-1, A-2 refer to the reaction of the nano-pyrite/greigite suspension with Se(IV) at pH ~ 6.2, A-3, A-4 to the same reactants at pH > 8.0. An extra amount of Fe²⁺ was added to reactors A-2 and A-4. Reactions of nano-pyrite/greigite with Se(VI) at pH ~5.9 and pH >8.0, with and without the addition of extra Fe²⁺, were labeled B-1 to B-4, using the same scheme. The experiments conditions are summarized in Table 2.

In reactors A-1 and A-2, which contained ~0.05M of CH₃COOH-CH₃COONa at pH around 6.2, more than 90% of the added Se(IV) was reduced within 30 minutes. The buffer solution was not added to reactors A-3 and A-4, and the higher pH values in these reactors resulted in slower Se(IV) reduction (~50% reduction within 30 minutes). All reactors with Se(IV) showed an increasing pH trend, especially A-3 and A-4, which turned to strong alkaline conditions, indicating that the reaction process consumes protons. The iron concentration in reactors A-1 and A-2 highly increased during the reaction, while it remained under ICP-OES detection limit in reactors A-3 and A-4. Sulfur concentration in reactors A-3 and A-4 showed a slight increase, while in A-1 and A-2 the release of sulfur was negligible. The sulfur deficit in solution may originate from the formation of other sulfur species like S⁰, as observed in the oxidation of nano-

sized mackinawite by Se(IV) (Scheinost et al., 2008a), where surface S^{2-} was oxidized to S^0 rather than to sulfate.

In contrast to the rapid reduction of Se(IV), aqueous Se(VI) in reactors B-1 to B-4 showed extremely slow reduction kinetics. After 336 hours reaction, only 20% – 40% of the added Se(VI) was reduced. The slow reduction kinetics of aqueous Se(VI) by iron sulfides is in line with previous studies (Bruggeman et al., 2002; Han et al., 2011). Possible reasons for the inertness of selenate are discussed in more detail in a companion paper in preparation.

Comparing the selenite concentration in A-1 and A-2 (pH ~ 6.2), and A-3 and A-4 (pH > 8) it is clear that, upon adding extra Fe^{2+} to the solution, a larger amount of Se(IV) was reduced after 0.5h. This was also case of selenate in reactors B-3 (no Fe^{2+}) and B-4 (extra Fe^{2+}) (pH > 8), while the effect of Fe^{2+} on the reaction kinetics is less obvious when we compare reactor B-1 and B-2 (pH ~ 5.9).

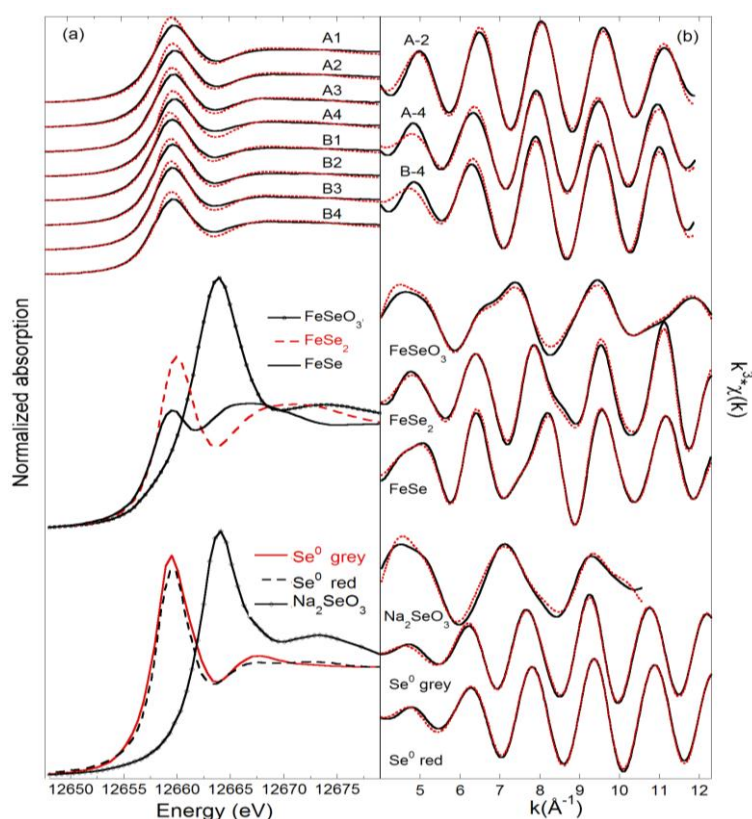
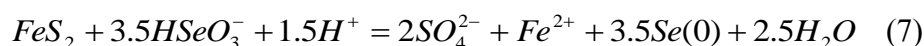
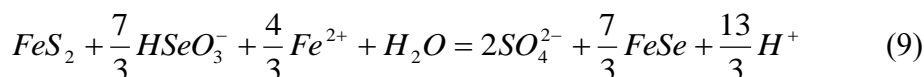
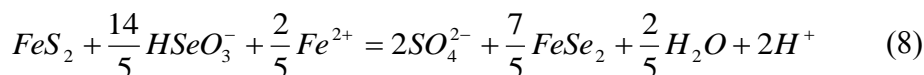


Figure 1: (a) Se K-edge XANES of all samples and reference compounds measured. For samples curves, continuous lines are experimental data and dotted lines are linear square fits using the amorphous Se(0) and FeSe₂ references, as reported in Table 6. (b) Back-Fourier transformed EXAFS signals of references and selected samples. Continuous lines are experimental data, dotted lines are fits.

Assuming that sulfate is the only reaction product, the possible electrochemical reactions between pyrite and aqueous Se(IV) are:





Equations (7), (8), and (9) indicate that the formation of Se(0) consumes protons and releases Fe^{2+} , while the formation of FeSe or FeSe_2 , produces protons and consumes Fe^{2+} . Therefore, the extra Fe^{2+} added can be either oxidized by Se(IV), due to the fast surface Fe^{2+} oxidation (Chakraborty et al., 2010, Charlet et al., 2007), or involved in the formation of iron selenides (equation (8) and (9)), and both reactions lead to an increase of the reaction rate.

2.3 Characterization of the reaction products

The XANES spectra of nano-pyrite/greigite reacted with Se(IV) or Se(VI) at different pH, with and without the addition of Fe^{2+} , are reported in Figure 1 together with the spectra of the reference compounds measured in the same experiment (FeSeO_3 , NaSeO_3 , amorphous (red) Se(0), crystalline (grey) Se(0), FeSe, and FeSe_2).

The comparison of the energy position of the absorption edges of the samples with that of the reference standards clearly shows that, in all the samples, the initially added Se(IV) or Se(VI) was reduced to Se(0) after reaction with nano-pyrite/greigite. Nevertheless, the presence of lower oxidation states Se species (-I and -II) cannot be confirmed from the position of the absorption edge, because the energy shift between the Se(0) and Se(-I, -II) references is about the same of the energy resolution of XANES spectra (0.5 eV). For this reason, PCA and LSF were applied to XANES spectra to help discerning the reaction products. PCA reported a minimum in the IND parameter in correspondence to two components, suggesting that up to two chemical species contribute to the XANES spectra. In addition, target transformation using the reference spectra suggested amorphous (red) Se(0) and FeSe_2 as the best candidates. The goodness of fit values for the target transformation procedure are reported in Table 4.

Table 4: Goodness of fit values for target transformation procedure: χ^2 is the traditional sum of the squared differentials, whereas the r is a measure of the percent misfit. Both values indicate amorphous (red) and crystalline (grey) Se^0 , and FeSe_2 as the best candidates, while FeSe and NaSeO_3 reported the bad matches.

Target	r	χ^2
Se(0) red	0.0010	0.43
FeSe_2	0.0029	1.10
FeSe	0.0123	4.54
FeSeO_3	0.1039	55.0

Linear square fits based on the candidates suggested by PCA (Se(0) and FeSe_2) are reported in Table 5. The results indicate that at pH ~ 6.2 (Se(IV)) and ~ 5.9 (Se(VI)), the Se(0) vs FeSe_2 ratios is roughly 30:70, while, with the exception of sample B-3, the Se(0)/ FeSe_2 ratios is about 50:50 for both selenite and selenate reacted at pH > 8.0 . LSF also suggested that the extra Fe^{2+} added to the solution does not increase the amount of

FeSe₂ in the final products. A possible reason is that the extra Fe²⁺ is firstly oxidized by Se(IV) to form ferric (oxyhydr)oxides (Chakraborty et al., 2010, Charlet et al., 2007). To confirm the XANES results, structural refinements around the Se atom were performed. The extracted structural parameters of samples A-2, A-4, and B-4, and of all reference compounds are reported in Table 6. The back-Fourier transformed EXAFS oscillations and the corresponding fit curves are reported in the panel (b) of Figure 1. Shell fitting were performed in the back transformed k-space. The structure of reference compounds was refined up to 4 Å from the absorber. On the contrary, since the aim was to confirm the presence of iron selenides, first shell fits were performed on samples' spectra by Fourier filtering contributions from higher coordination shells (see SI for details on the fitting strategy). This reduced the correlation between free parameters, and allowed more stable and reliable fits.

Table 5: Relative concentration of Se⁰ and FeSe₂ as derived from LSF. Also reported is the concentration sum (Σ), which is close to 100% for all samples, and the value of the reduced χ square (χ_v^2), both indicating good matches to the experimental spectra. The error on the determination of the concentrations is estimated to be in the range 5-15%.

sample	pH	Se	extra Fe ²⁺ (mM)	Se ⁰ -red (%)	FeSe ₂ (%)	Σ (%)	χ_v^2 x10 ³
A-1	~ 6.2	+4	0	31	69	100	1.4
A-2			0.1	34	67	101	1.6
B-1	~ 5.9	+6	0	30	71	101	1.9
B-2			0.1	35	64	99	1.2
A-3	> 8.0	+4	0	50	50	100	1.6
A-4			0.08	50	50	100	1.3
B-3	> 8.0	+6	0	27	72	99	1.3
B-4			0.08	48	53	101	1.0

The first coordination shell of sample A-2 can be fitted with a contribution from Se at ~2.3 Å and one from Fe at ~2.4 Å. The first one is close to the value of the first shell Se-Se distance in elemental Se (its slight reduction with respect to the Se⁰ reference could be attributed to the nanometric size of the crystallites. The distance of the Fe contribution is in agreement with both FeSe and FeSe₂ references and is a strong evidence for the formation of iron selenides. Therefore, the observed structure is compatible with the co-presence of amorphous Se⁰ and crystalline FeSe₂, in accordance with XANES results. In addition, a weight parameter was introduced to account for the relative abundance of the two structures. In final refinements, the weighting factor reached the value of 73 ± 23% for the FeSe₂ species, in excellent agreement with XANES results. The same strategy applied to samples A-4 and B-4 did not allow discerning between the Se-Fe and Se-Se contributions. For this samples, the first shell can be fitted with two Se atoms at a distance in agreement with the amorphous Se⁰ structure (~2.3 Å). This is probably due to the lower amount of FeSe₂ present in these samples, estimated by XANES to be ~50%.

Table 6: Structural parameters obtained from EXAFS refinements (CN: coordination numbers; R: atomic distances; σ^2 : Debye-Waller factors). Standards were fitted fixing the CNs to their crystallographic values. The numbers within parenthesis represent the error on the last digit.

standard	CN 1 st shell	R (Å)	σ^2 (Å ² ·10 ³)	CN 2 nd shells	R (Å)	σ^2 (Å ² ·10 ³)	S_0^2	χ_v^2
Se ⁰ red	2 Se	2.346(3)	3.6(3)	0.7(5) Se	3.77(4) 4.00(9)	8(5) “	1.1(1)	0.87
FeSe ₂	3 Fe	2.376(2)	4.5(1)	1 ^ˆ 1 ^ˆ 1 ^ˆ Se 4 Se 4 Se 2 Se 2 Se 1 Fe 2 Fe	2.558(4) 3.13(1) 3.29(1) 3.43(2) 3.58(4) 3.81(7) 3.97(2)	4.5(1) 4(1) “ 4(1) “ 3(2) “	0.9(1)	0.99
FeSe	4 Fe	2.399(4)	2.4(4)	8 Se 4 Se	3.74(2) 3.94(2)	8.4(2) 2.4(8)	0.7(1)	0.87
sample								
A-2	0.6(2) Se	2.31(5) 2.39(3)	6.1(9)				0.7(1)	1.12
A-4	2.1(2) 2 Se	2.33(4)	7.4(5)				0.9(1)	0.82
B-4	2 Se	2.32(3)	6.8(4)				0.9(1)	1.93

Summary and Conclusions

Thermodynamic calculations and experimental observations indicate that pyrite can significantly attenuate the mobility of Se by reductive precipitation. This study reports the abiotic formation of FeSe₂ in laboratory experiments for the first time, suggesting that stabilization of selenium in its most insoluble form is possible in Fe²⁺/sulfide-bearing environments.

Acknowledgment

The research leading to these results has received funding from the European Union's European Atomic Energy Community's (Euratom) Seventh Framework Programme FP7/2007-2011 under grant agreement n° 212287 (RECOSY project).

References

- Ankudinov A. L., Ravel B., J.J. Rehr J. J., Conradson S. D. (1998) Real space multiple scattering calculation and interpretation of XANES. *Phys. Rev. B* 58, 7565-7576.
- Baeyens B., Maes A., Cremers A., Henrion P. N. (1985) Radioactive waste management, Harwood Academic: Amsterdam, 1985, 6, 391-408.
- Belzile N., Chen Y. W., Xu R. R. (2000) Early diagenetic behaviour of selenium in freshwater sediments. *Appl. Geochem.* 2000, 15, 1439-1454.
- Breynaert E., Bruggeman C., Maes (2008) A. XANES-EXAFS analysis of solid-phase reaction products formed upon contacting Se(IV) with FeS₂ and FeS. *Environ. Sci. Technol.*, 42, 3595-3601.
- Bruggeman C., Vancluysen J., Maes A. (2002) New selenium solution speciation method by ion chromatography plus gamma counting and its application to FeS₂-controlled reducing conditions. *Radiochim Acta*, 90, 629-635.
- Chakraborty S., Bardelli F., Charlet L. (2010) Reactivities of Fe(II) on Calcite: Selenium Reduction. *Environ. Sci. Technol.*, 44, 1288-1294.
- Charlet L., Scheinost A. C., Tournassat C., Grenéche J. M., Gehin A., Fernandez-Martinez A., Coudert S., Tisserand D., Brendle J. (2007) Electron transfer at the mineral/water interface: Selenium reduction by ferrous iron sorbed on clay. *Geochim. Cosmochim. Acta*, 71, 5731-5749.
- Charlet L. (2008) X-ray absorption and photoelectron spectroscopy investigation of selenite reduction by Fe-II-bearing minerals. *J. Contam. Hydrol.*, 102, 228-245.
- Chen F. R., Burns P. C., Ewing R. C. (1999) ⁷⁹Se: geochemical and crystallo-chemical retardation mechanisms. *J. Nucl. Mater.*, 275, 81-94.
- Chivot J. (2004) Thermodynamique des produits de corrosion. Sciences et Techniques Series, ANDRA.
- Évolution phénoménologique du stockage géologique. Dossier Argile (2005). Collection Les Rapports, 1-523.
- Fordyce F. M., Zhang G. D., Green K., Liu X. P. (2000) Soil, grain and water chemistry in relation to human selenium-responsive diseases in Enshi District, China. *Appl. Geochem.*, 15, 117-132.
- Glazovskaya M. A. (1996) Global dispersion of natural and technogenic selenium and the risk of selenium accumulation in soils. *Eurasian Soil Sci.*, 28, 305-319.
- Grambow B. (2008) Mobile fission and activation products in nuclear waste disposal. *J. Contam. Hydrol.*, 102, 180-186.
- James F., Roos M. (1975) Minuit: A System for Function Minimization and Analysis of the Parameter Errors and Correlations. *Computer Physics Communications*, 10, 343-367.
- Han D. S., Batchelor B., Abdel-Wahab A. (2011) Sorption of selenium(IV) and selenium(VI) to mackinawite (FeS): Effect of contact time, extent of removal, sorption envelopes. *J. Hazard. Mater.*, 186, 451-457.

- Howard J. H. (1977) Geochemistry of selenium: formation of ferroselite and selenium behavior in the vicinity of oxidizing sulfide and uranium deposits. *Geochim. Cosmochim. Acta*, 41, 1665-1678.
- Jiang S.-S., Diao L.-J., Guo J.-R., Wu S.-Y. (2001) Remeasurement of the Half-Life of ⁷⁹Se with the Projectile X-Ray Detection Method. *Chin. Phys. Lett.*, 18, 746-749.
- Liu X., Fattahi M., Montavon G., Grambow B. (2008) Selenide retention onto pyrite under reducing conditions. *Radiochim. Acta*, 96, 473-479.
- Loyo R. L. D., Nikitenko S. I., Scheinost A. C., Simonoff M. (2008) Immobilization of selenite on Fe₃O₄ and Fe/Fe₃C ultrasmall particles. *Environ. Sci. Technol.*, 42, 2451-2456.
- Metz V., Kienzler B., Schussler W. (2003) Geochemical evaluation of different groundwater-host rock systems for radioactive waste disposal. *J. Contam. Hydrol.*, 61, 265-279.
- Missana T., Alonso U., Scheinost A. C., Granizo N., Garcia-Gutierrez M. (2009) Selenite retention by nanocrystalline magnetite: Role of adsorption, reduction and dissolution/co-precipitation processes. *Geochim. Cosmochim. Acta*, 73, 6205-6217.
- Myneni S. C. B., Tokunaga T. K., Brown G. E. (1997) Abiotic selenium redox transformations in the presence of Fe(II,III) oxides. *Sci.*, 278, 1106-1109.
- Olin Å., Noläng B., Osadchii E. G., Öhman L.-O., Rosén E. (2005) Chemical Thermodynamics 7: Chemical Thermodynamics of Selenium, OECD Nuclear Agency/Elsevier: Amsterdam.
- Parkhurst D. L., Appelo C. A. (1999) J. User's guide to PHREEQC (Version 2)-A computer program for speciation, batch-reaction, one-dimensional transport, and inverse geochemical calculations, Water-Resources Investigations Report 99-4259, U.S. Geological Survey, U.S. Department of the Interior: Denver, CO.
- Ravel B. (2001) ATOMS: crystallography for the X-ray absorption spectroscopist", *J. Synchrotron Rad.*, 8, 314-316.
- Ravel B., Newville M. (2005) ATHENA, ARTEMIS, HEPHAESTUS: Data analysis for X-ray absorption spectroscopy using IFEFFIT. *J. Synchrotron Radiat.*, 12, 537-541.
- Rayman M. P. (2008) Food-chain selenium and human health: emphasis on intake. *Br. J. Nutr.*, 100, 254-268.
- Roberts A. P., Chang L. A., Rowan C. J., Horng C. S., Florindo F. (2011) Magnetic properties of sedimentary greigite (Fe₃S₄): an update. *Rev. Geophys.*, 49, 1-46.
- Ryser A. L., Strawn D. G., Marcus M. A., Johnson-Maynard J. L., Gunter M. E., Moller G. (2005) Micro-spectroscopic investigation of selenium-bearing minerals from the Western US Phosphate Resource Area. *Geochem. Trans.*, 6, 1-11.
- Schoonen M. A. A., Barnes H. L. (1991) Reactions forming pyrite and marcasite from solution: I. Nucleation of FeS₂ below 100°C. *Geochim. Cosmochim. Acta*, 55, 1495-1504.
- Schoonen M. A. A., Barnes H. L. (1991) Reactions forming pyrite and marcasite from solution: II. Via FeS precursors below 100°C. *Geochim. Cosmochim. Acta*, 55, 1505-1514.

- Schoonen M. A. A., Barnes H. L. (1991) Mechanisms of pyrite and marcasite formation from solution: III. Hydrothermal processes. *Geochim. Cosmochim. Acta*, 55, 3491-3504.
- Scheinost A. C., Kirsch R., Banerjee D., Fernandez-Martinez A., Zaenker H., Funke H., Charlet L. (2008) Selenite reduction by mackinawite, magnetite and siderite: XAS characterization of nanosized redox products. *Environ. Sci. Technol.*, 42, 1984-1989.
- Vaughan D. J., Lennie A. R. (1991) The iron sulfide minerals - Their chemistry and role in nature. *Sci. Prog.* 75, 371-388.
- Webb S. M. (2005) SIXpack: a graphical user interface for XAS analysis using IFEFFIT. *Phys. Scr.* 1011.
- Wei D. W., OsseoAsare K. (1996) Particulate pyrite formation by the $\text{Fe}^{3+}/\text{HS}^-$ reaction in aqueous solutions: Effects of solution composition. *Colloid Surf. A-Physicochem. Eng. Asp.*, 118, 51-61.
- Wei D. W., OsseoAsare, K. (1997). Aqueous synthesis of finely divided pyrite particles. *Colloid Surf. A-Physicochem. Eng. Asp.*, 121, 27-36.
- Winkel L. H. E., Johnson, C. A., Lenz, M., Grund, T., Leupin, O., Amini, M., Charlet, L. (2011). Environmental selenium research from microscopic process to global understanding. Submitted to *Environ. Sci. Technol.*.
- Xiong Y. L. (2003). Predicted equilibrium constants for solid and aqueous selenium species to 300 °C: applications to selenium-rich mineral deposits. *Ore Geol. Rev.*, 23, 259-276.

THE EFFECT OF CARBON STEEL CORROSION ON THE EVOLUTION OF CONDITIONS IN A DEEP GEOLOGICAL REPOSITORY

David Dobrev^{1*}, Radek Červinka¹, Antonín Vokál^{1*}

¹ Nuclear Research Institute Rez (Czech Republic)

* Corresponding author:

Abstract

This article summarises the results of an investigation into the effects of corrosion of thin wire and plates of carbon steel and iron powder on the evolution of geochemical conditions around or inside canisters with spent fuel assemblies. The Eh and pH have been measured discontinuously to avoid the impact of corrosion product layers from the corrosion of carbon steel or iron powder precipitated on the surface of the electrodes as a result of the measurements. The corrosion potential of carbon steel wires was determined using electrochemical noise methodology. The extent of corrosion was determined by measuring hydrogen generated during anaerobic corrosion of iron and by measuring the weight loss of carbon steel plates. The nature of the corrosion layers formed on the surface of the carbon steel plates was determined using X-ray diffraction, Raman spectroscopy and analyses of the elemental composition of the carbon steel surface layers using ESCA electron spectroscopy. It was shown that after immersing the carbon steel or iron powder in the solution, Eh decreases to negative values and then slowly increases. The greater the ratio of surface of the iron metal to the volume of solution, the greater is the initial decrease of Eh of water in contact with the iron metal. The evolution of pH is different depending on whether carbon steel or iron powder was used in the experiments. In all the experiments with carbon steel plates the pH decreased during the 30-day experiments, but in experiments with the iron powder it remained constant. After an initial decrease, the Eh increases over time due to the oxidation of ferrous ions and the precipitation of iron-bearing minerals. Using an ESCA probe, it was found that firmly adhering corrosion product layers containing a high amount of oxygen and carbon were formed during the corrosion of carbon steel plates in bentonite water under anaerobic conditions. These layers have an important impact on hydrogen evolution rates. Under strongly reducing conditions, created by adding iron powder with a high surface to the solution, the protective effect of the corrosion layers could disappear, leading to an increase of hydrogen generation rates and consequently corrosion rates. Geochemical calculations were performed for the experiments with carbon steel plates and iron powder using the geochemical code PHREEQC. For experiments with carbon steel plates the modelled values (Eh, pH) showed large

discrepancies with the experimental data, but were close for the iron powder experiments.

Introduction

The conditions in a deep geological repository can be affected by the corrosion of the metal canisters, which can in turn affect the mobility of radionuclides, the properties of engineered barriers and in the end the rate of corrosion of the metal canisters themselves. In particular, the solubilities of phases containing multi-valent radioelements (Tc, U, Pu) are sensitively related to Eh (OECD, 1993). A large number of studies (e.g. Jelinek, Neufeld, 1982, Simpson, 1984, Simpson et al., 1985, Anantamula et al. 1987, Marsh and Taylor, 1988, Schenk, 1988, Grauer et al., 1991, Hara et al., 1992, Honda et al., 1991, Fujisawa et al. 1997, Fujiwara et al. 2000, Johnson and Smith, 2000, Xia et al., 2005, Smart et al., 2001, 2002, 2004, 2008, de Combarieu et al., 2007) have therefore been devoted to investigating metal reactions in repository conditions. The results are, however, often ambiguous. The problem is that the corrosion of metals is affected by a great variety of factors such as pH, temperature, the composition of the water, radiation and the amount of oxygen in the water. Because of the variety of values of these factors, a very wide range of results can easily be found. Another important issue is that for metals in aqueous solutions, the barrier that prevents inherently reactive metals from dissolving is a thin insoluble compound on the surface between the reactive metal and the chemical environment (Staehle, 2011). The formation of these passivating layers on metals significantly depends on the chemical conditions surrounding the metals. Even small changes in the water composition, the content of oxygen or temperature can change the stability of these passivating layers. The content of oxygen or more exactly the Eh of the solution at the beginning of corrosion has the most important effect. The higher the Eh, the thicker the passivating layer on the surface of the metal. This also strongly depends on the pH of the water. At low pH values, passivating layers could not be created at all, but at high values there is a very great tendency to create passivating layers. The strong effect of oxygen on the corrosion process was found by Hara et al., 1992 and later Fujiwara et al., 2001. They found that the hydrogen generation rate increases significantly with the amount of oxygen in the water. Hara et al., 1992 conducted the experiments in synthetic sea-water and Fujiwara et al., 2001 at cement equilibrium water. Hara et al., 1992 have found that with a high amount of oxygen (1, 3 or 10 ppm) dissolved in water, the hydrogen evolution rate ranges between 20 to 30 mol H₂ m⁻² yr⁻¹, but low values (0.5 mol H₂ m⁻² yr⁻¹) were reported for a very low amount of dissolved oxygen (0.01 ppm). A systematic study of the effect of the pH ranging from 11.5 to 14 and the amount of oxygen was conducted in the work of Fujiwara et al., 2001. The amount of oxygen (1 x 10⁻³ to 1 x 10⁵ ppm) in the solution was controlled by the amount of oxygen in the nitrogen gas flowing through the solution. They also found that hydrogen generation increases with the content of oxygen in the water. The important finding of Fujiwara et al., 2001 was that at very low oxygen values, hydrogen generation tends to be higher than with medium concentrations of oxygen. This was explained by the fact that under a very low concentration of oxygen passive films on the surface of carbon steels cannot be reproduced sufficiently and therefore the corrosion rate becomes higher.

The conditions selected for the experiments in this work were based on the Czech repository concept of disposing of spent fuel assemblies in multilayer canisters with a thick carbon steel overpack surrounded by compacted bentonite in a granite host rock structure. The experiments conducted mostly under anaerobic conditions focused on investigating the effect of carbon steel on the evolution of Eh and pH in the water simulated bentonite porewater in contact with the carbon steel waste packages. In some of the experiments iron powder was used instead of carbon steel for comparison. This paper summarises the main results achieved in the Nuclear Research Institute Rez in the 7th EC FP Project RECOSY. The more detailed results achieved in the first years of the RECOSY project have already been published as KIT-INE reports (Dobrev et al., 2009, 2010).

Experimental

Materials

The composition of carbon steel of Czech ISO standard 11321 is given in Table 1.

Table 1: Carbon steel composition.

Carbon steel	C [%] - max	Mn [%] - max	P [%] - max	S [%] - max
11 321	0.10	0.45	0.035	0.035

The dimension of the carbon steel plates was 70x70x1 mm with an 8 mm diameter circle cut out in the centre. Before the experiment the carbon steel plates were polished with sandpaper (grid 600) and washed with ethanol. The surface of the carbon steel plates was 99.7 cm²/plate.

The iron powder was Alfa Aesar A Johnson Matthey Company (< 10 micron, 99.9+% (metal basis), surface 0.205 m² g⁻¹).

The synthetic bentonite pore water was prepared according to the proposal of Bradbury and Bayens, 2003. The pH of this water was 7.5, conductivity 2100 mS m⁻¹ and ionic strength 0.29 mol. L⁻¹.

One of the experiments was conducted in contact with solid Na bentonite Volclay KWK 20-80 (Volclay Co. Südchemie, Germany). The solid bentonite was immersed in the solution in a permeable bag, which prevented the release of solid bentonite into the solution.

Eh and pH

A combined platinum electrode ORC 103–BAZ (Theta '90, Czech Republic, a 4 mm diameter platinum disc) was used to measure Eh in the system with steel plates (measuring period 1 day). The same platinum electrode and an additional XCL 101 XB2 platinum electrode (Gryf HB, Czech Republic, 2 mm diameter platinum disc) were used to measure the redox potential in the corrosion system with iron powder. An HC 113 electrode (Theta '90, Czech Republic) was used to measure pH and in the system with iron powder and also a pH PCL 321 XB2 electrode (Gryf HB, Czech Republic).

Corrosion potential

An electrochemical noise measurement system with three home-made electrodes, two steel working electrodes (3 mm diameter carbon steel rod, Czech standard 11321, mechanically polished by SiC paper (grid 320)) and one reference electrode RE403 (Theta '90, Czech Republic) were used to measure corrosion potentials. Before the electrodes were immersed in the corrosion cell, the cell was purged with nitrogen for 30 minutes. An ECM 8 Electrochemical Multiplexer Analyser with evaluation software ESA 400 Electrochemical Signal Analyser version 2.01 from Gamry Instruments was used to evaluate the results. The experiments were carried out at various temperatures controlled by a TDC 2 Temperature Controller with a Watlow series 988 PID control unit.

Corrosion cell and hydrogen generation

The experiments were conducted in the corrosion cells shown in Fig. 1. For most of the experiment the corrosion cells were emplaced in an anaerobic box (MBrown, Germany) with an argon atmosphere and less than 0.1 ppm oxygen content.

The corrosion rate was determined by measuring the hydrogen evolved from the corroding iron using equipment developed in NRI (Fig. 1). This device allows hydrogen evolution to be continuously measured at different temperatures and at a constant pressure in the water. The source of pressure is a heavy piston, moving in mutually interconnected pressurized cylindrical vessels with a rolling membrane (Brůha and Pelech, 1989). The volume measurement is based on detecting the piston position, which depends on the medium volume.

Corrosion products

Corrosion products on the carbon steel plates were measured by Raman spectrometer LabRam (Horiba – Jobin Yvon, France) with two lasers (He – Ne and Ar), by X-ray diffraction Philips-Xpert PRO (PANalytical, Netherlands) and by ESC Probe P (Omikron Nanotechnology, Germany) in the CAE mode (Constant Analyser Eberg).

Concentration of iron in the solution

The concentration of Fe^{2+} and S^{2-} ions in the solution after the experiments was measured by UV/Vis spectrometer Specord 205 – 222A358 (Analytic Jena Co., Germany), Fe^{2+} by the modified ferozzine method (Viollier et al., 2000) and for sulphide detection by a Spectroquant test kit (No. 167, Merck). The total iron concentration in the solution was measured by atomic absorption spectroscopy Varian SpectrAA 200 (Varian, U.S.A).

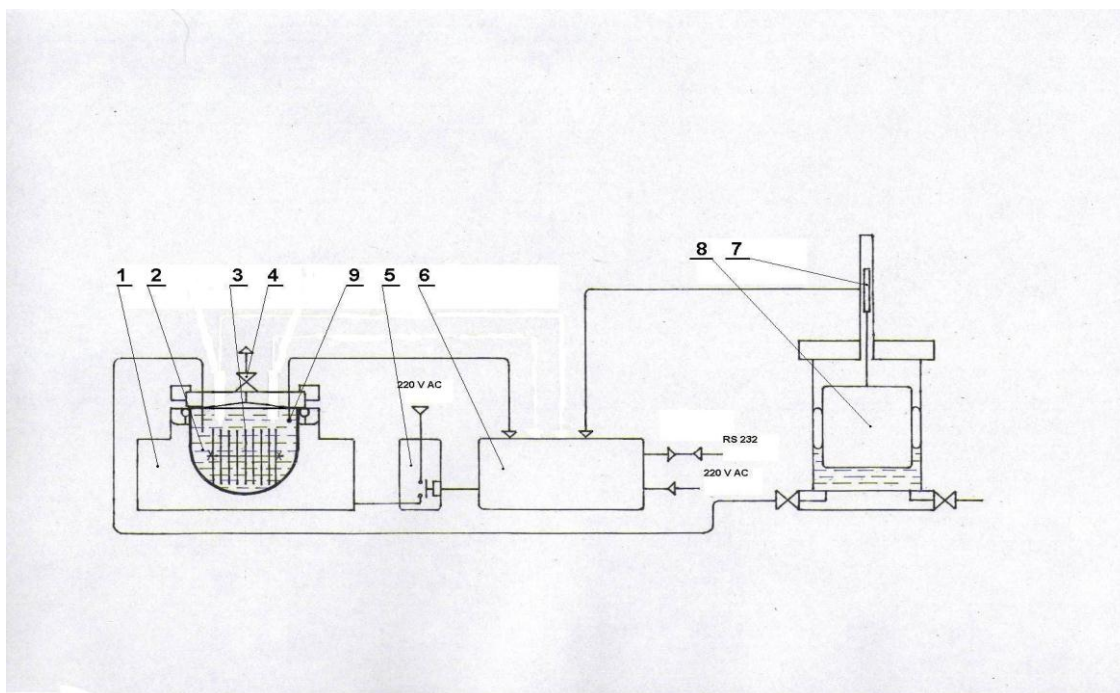


Figure 1: The hydrogen evolution measurements device. 1 – Heater, 2 – Constant pressure chamber, 3 – Samples, 4 – Gas sampling valve, 5 – Temperature regulator, 6 – Data acquisition equipment, 7 – Volume change detector, 8 – Source of constant pressure, 9 – Temperature sensor

Results and Discussion

Eh evolution

In all the experiments after immersing the carbon steel plates in the bentonite water solution, Eh significantly decreased. This is illustrated in Fig. 2 where the dependence of Eh over time is shown for one carbon steel plate in 2 litres of the synthetic bentonite water. Eh decreases from values above 0 mV in the anaerobic box to values below -100 mV. It can be seen that the extent of the initial decrease depends on the temperature of the corrosion. After a rapid initial decrease, Eh increases over time due to the oxidation of iron (II) ions to iron (III) ions and the precipitation of iron oxides on the surface of the carbon steel plates. The nature of these corrosion products will be discussed further. The extent of the Eh decrease depends primarily on the ratio of the metal surface to the volume of the solution. Details of this work can be found in our previous paper (Dobrev

et al., 2011).

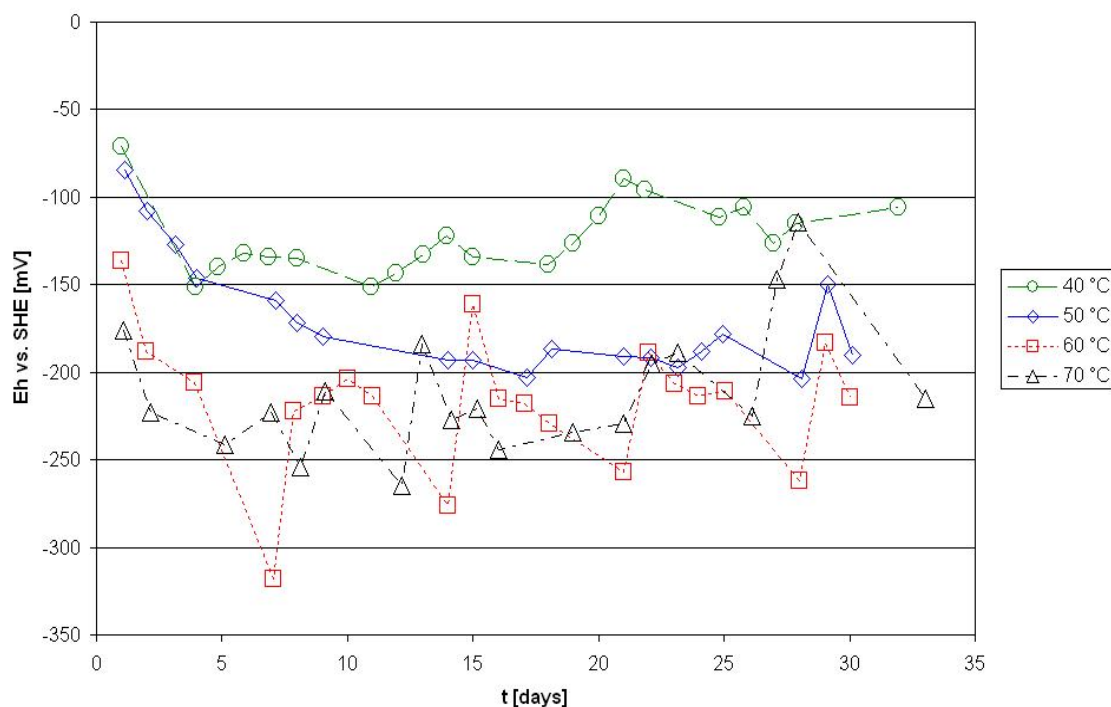


Figure 2: The Evolution of Eh after immersing one carbon steel plate in 2 l of synthetic bentonite water solution

pH evolution

A noticeable decrease of pH over time was observed in all the experiments with carbon steel (Fig. 3). However, no such decrease was observed after immersing pure iron powder in the solution (Fig. 4). The reason for this difference can be seen in the behaviour of carbon steel impurities. The surface of the carbon steel samples was investigated using Electron Spectroscopy for Chemical Analyses (ESCA) to determine the elemental composition of the surface layers. It was found that after corrosion, the corrosion layer created on the surface of carbon steels is composed mainly of carbon, oxygen and iron (Table 2). The migration of carbon to the surface and then to the water could explain this decrease of pH.

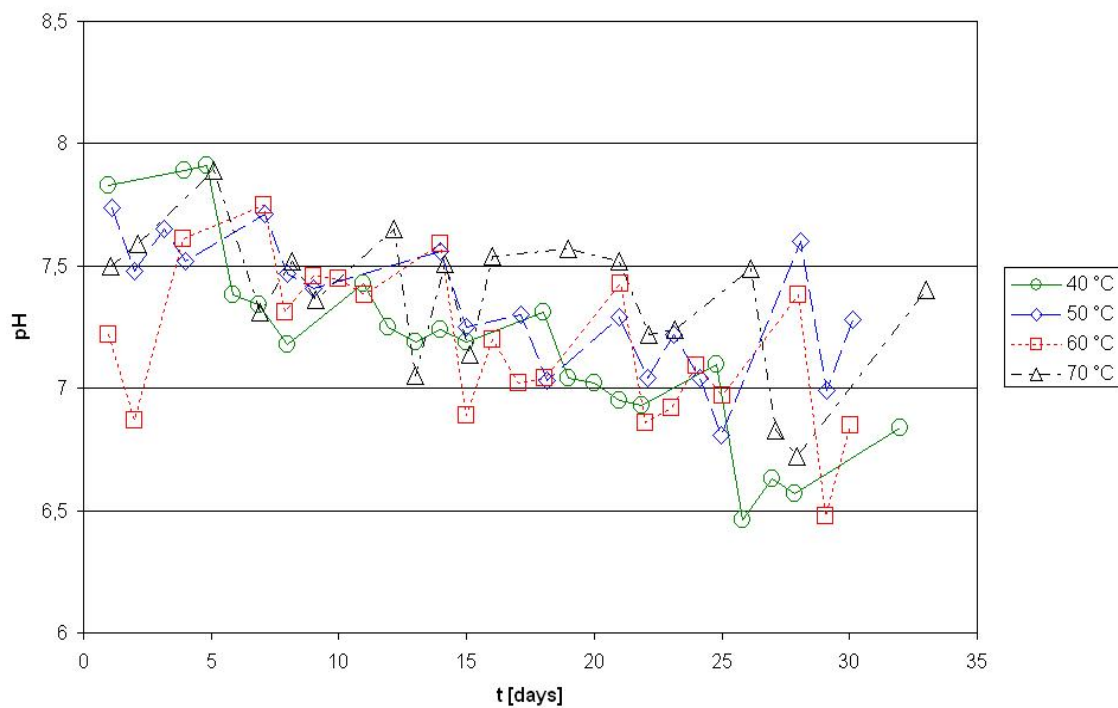


Figure3: Change of pH in the corrosion system with one carbon steel plate

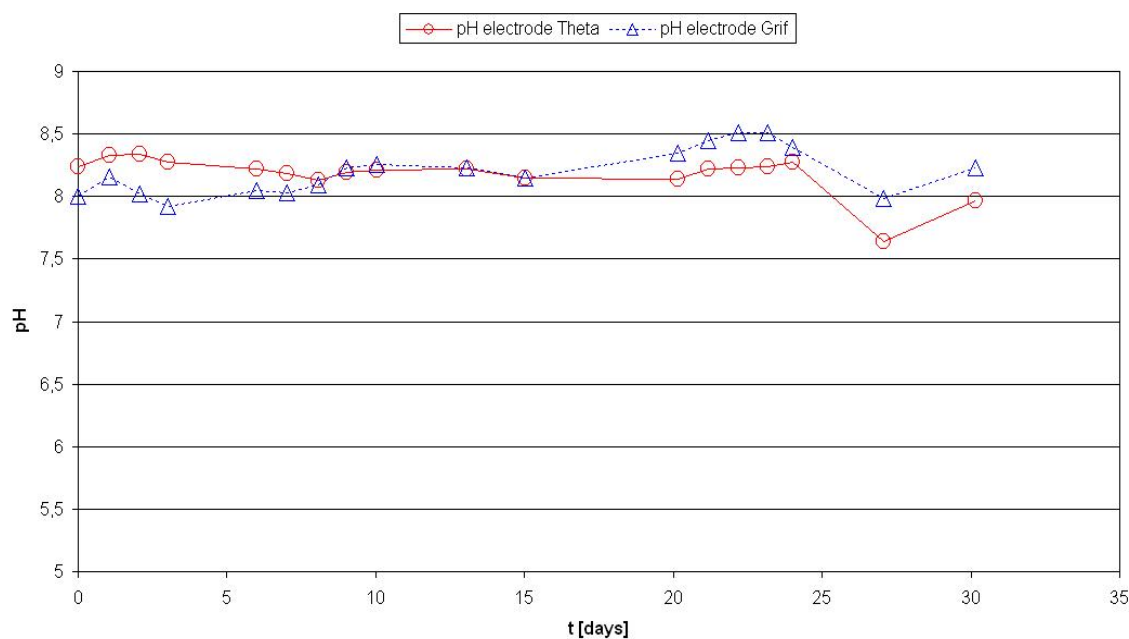


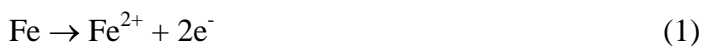
Figure 4: Change of pH after immersing iron powder in synthetic bentonite water

Table 2: Composition of a thin layer determined by ESCA before and after corrosion at various temperatures and before and after removal of the thin corrosion product layer

Element	Content (%) before corrosion	Content (%) 40 °C	Content (%) 50 °C	Content (%) 60 °C	Content (%) 70 °C
C 1s	7.4	53.2	19.7	4.9	13.0
O 1s	6.4	19.5	33.6	52.7	50.1
Fe 2p	86.2	9.8	26.0	21.1	14.6

Corrosion potential

The corrosion potential is the potential at which the anodic current density of iron dissolution (1) is equal to the cathodic current density of the depolarization reactions (2, 3):



The corrosion potential between the carbon steel electrodes and the reference electrodes was measured during electrochemical noise measurements, which allowed the corrosion process to be monitored in free corrosion conditions without imposing external polarization. The measurements were conducted with and without the addition of iron powder, which was added to the solution to simulate very low Eh values that should evolve in the near field of a repository. The results are given in Figs 5 and 6.

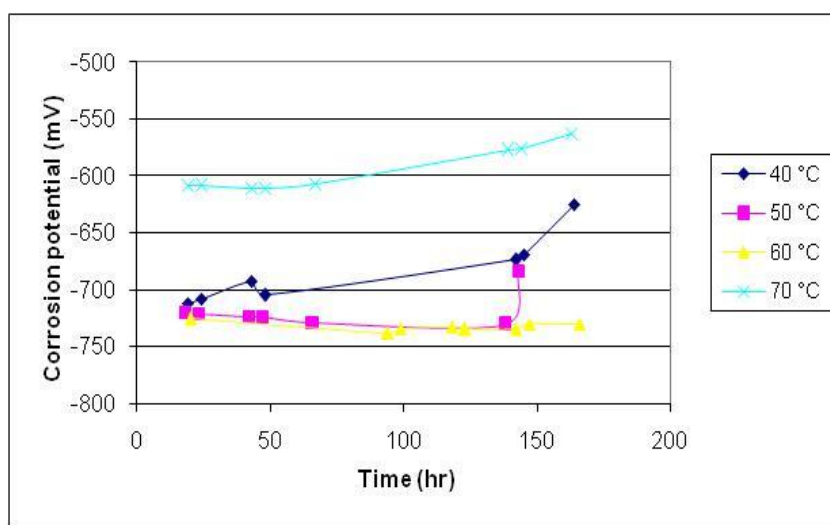


Figure 5: Carbon steel electrodes corrosion potential in a solution without iron powder

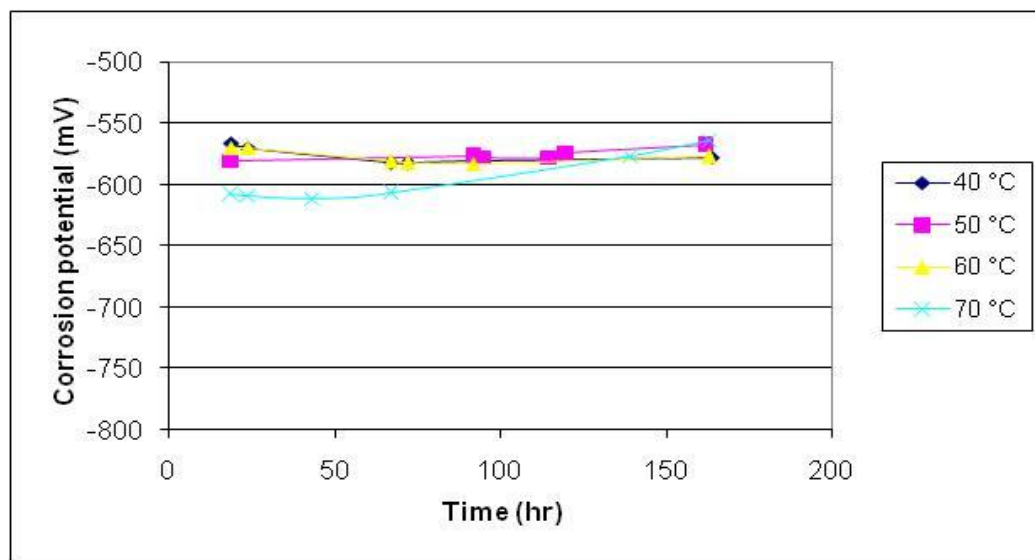


Figure 6: Carbon steel electrodes corrosion potential in a solution with iron powder

Fig. 5 shows that without adding iron powder, the corrosion potential of carbon steel at 70 °C is higher than the corrosion potential at lower temperatures. This indicates that at the same rate of cathodic reactions (2) and (3), given by the level of Eh slightly above 0 mV, the rate of carbon steel anodic reaction (1) at 70 °C is higher than the anodic reaction of carbon steel corroded from 40 °C to 60 °C. By adding iron powder to the solution, Eh is decreased to values lower than – 500 mV and accordingly the rate of cathodic reactions decrease. Primarily, the reaction (3) does not participate in the cathodic reactions because there is practically no free oxygen in the system. Despite this, the corrosion potential of carbon steel electrodes increased. This indicates that the corrosion rate of carbon steels at very low values of Eh can be higher than at a higher level of Eh, probably due to the loss of the protective character of the corrosion product layers.

Hydrogen generation

The typical picture of hydrogen generation from one carbon steel plate in 2 l of water in an anaerobic box with an oxygen content of less than 0.1 ppm is shown in Figure 7. It can be seen that after fast hydrogen generation at the beginning of corrosion, the hydrogen generation rate slows down over time. This decrease is presumably connected with the formation of passivating corrosion product layers formed on the surface of the metal discussed above.

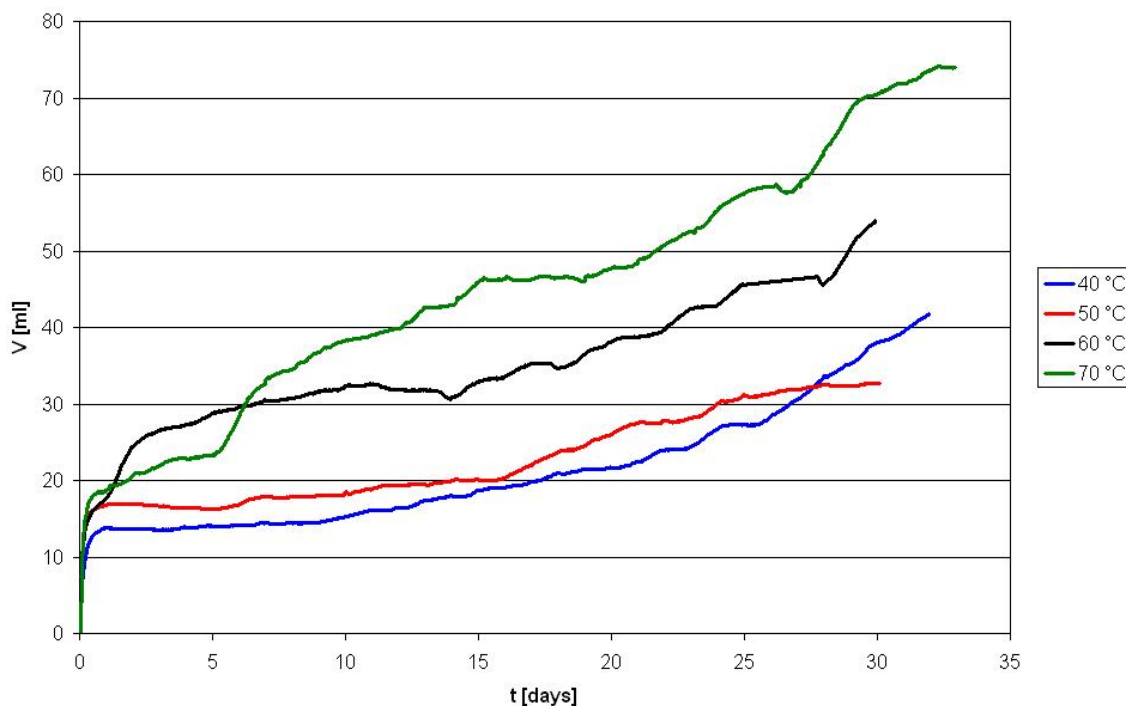


Figure 7. Hydrogen evolution rate under anaerobic conditions (one carbon steel plate in 2 l of water)

Character of the corrosion products

In addition to ESCA measurement (Table 2) the character of the corrosion product layers on the surface of the metal was investigated by Raman spectroscopy and X-ray diffraction. The corrosion product layers on the surface of the carbon steel plate samples corroded at 40 °C and 50 °C were under the detection limit of Raman spectroscopy and X-ray diffraction. This suggests that these layers were very thin. This result is consistent with ESCA measurements where practically no iron was detected after carbon steels were corroded 40 °C and 50 °C.

The corrosion product layer on the samples from the experiment carried out at 60 °C and 70 °C was also under the detection limit of X-ray diffraction but by Raman spectroscopy magnetite/maghemite (band 676 cm^{-1}), maghemite (1430 cm^{-1}) and hematite (band 220 cm^{-1}) was detected (Fig. 8).

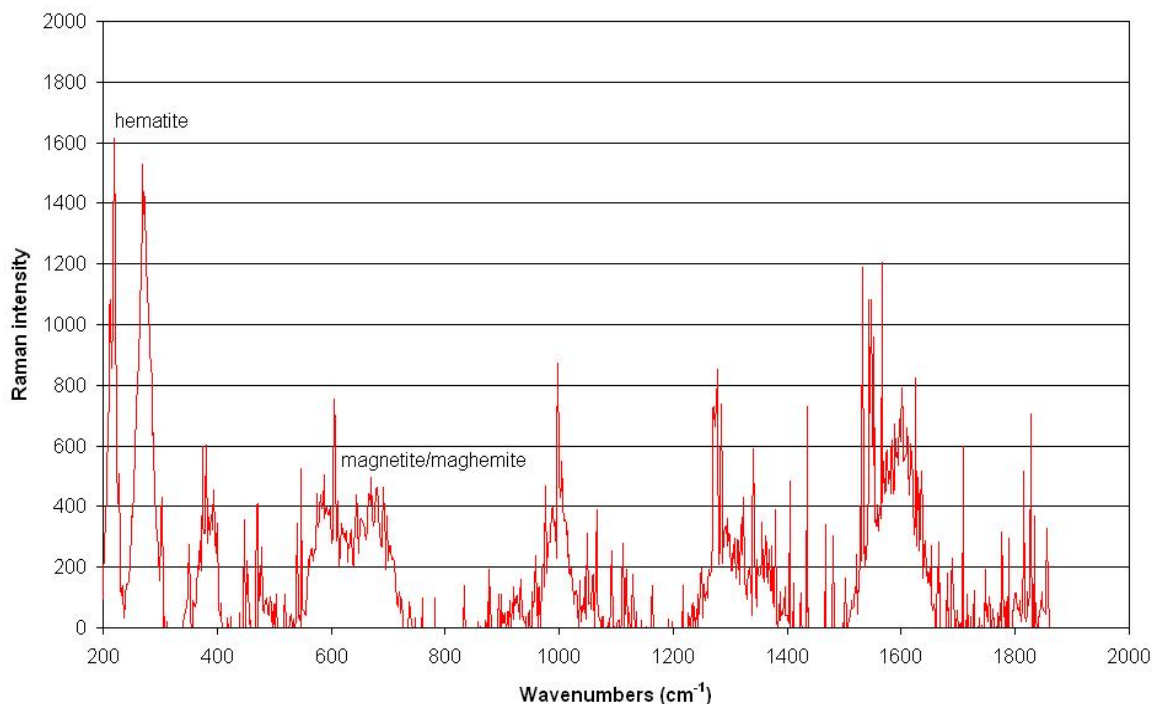


Figure 8 Raman spectroscopy of the carbon steel sample corroded at 60 °C

Iron powder corrosion

As mentioned in the introduction, iron powder with a large surface was used to accelerate the corrosion process. Carbon steel differs from iron mainly by the presence of some impurities (Table 1). These impurities could be leached out from the carbon steel so that after some time carbon steel could consist of iron only.

The first experiments with iron powder were not conducted in an anaerobic box but only under normal laboratory conditions in a bentonite water solution bubbled with nitrogen to remove free oxygen. No Eh was measured at that time, but it can be assumed that under these conditions oxygen could penetrate the corrosion cells. The hydrogen generation accumulation curve obtained under these conditions (Fig. 9) was similar to the curves obtained with carbon steels (Fig. 7). After a very fast period of hydrogen generation at the beginning of corrosion, hydrogen generation slows down over time. It can be assumed that some corrosion layer was formed on the surface of the iron powder due to the reaction of iron with oxygen.

Further experiments with iron powder were conducted in an anaerobic box with an oxygen content less than 0.1 ppm. Bentonite water was put in the anaerobic box 14 days before the experiment to remove oxygen from the solution. The Eh and pH were measured during the experiments. The results of the experiments in which 30 g and 15 g of iron were immersed in 2 l of bentonite water are shown in Fig. 10 and Fig. 11. It can be seen that a very different character of hydrogen accumulation curves compared to the curve shown in Fig. 9 occurred. This could be explained by the hypothesis that at the beginning of corrosion the corrosion rate is affected by a thin corrosion layer formed under atmospheric conditions on the surface of the iron powder. Under strongly reducing conditions, after adding 30 g of iron powder to the solution, this layer is

reduced to pure iron and no further protective layer can be reproduced under these conditions. After adding 5 g of iron powder to the solution in the anaerobic box, the Eh decreases less than in the previous case (Fig. 11) and hydrogen generation rate recalculated to unit of iron powder surface is lower than in the previous experiment with 30 g of iron powder (Fig. 12). The oxygen present is sufficient to form a protective layer on the iron powder under these Eh values.

The effect of solid bentonite on the corrosion rate and geochemical evolution of the conditions near to a repository was simulated by adding solid bentonite in a permeable bag to the solution of synthetic bentonite water. No difference in the change of Eh or pH of solution was observed. A comparison of the results of hydrogen generation with and without bentonite is also shown in Fig. 12. It can be seen that the presence of bentonite could increase the corrosion rate of carbon steel and thus change the geochemical conditions in a repository. The acceleration of the carbon steel corrosion rate in the presence of bentonite has been observed before, for example in the paper of Smart et al., 2004. The explanation was seen in the movement of ferrous ions into the bentonite.

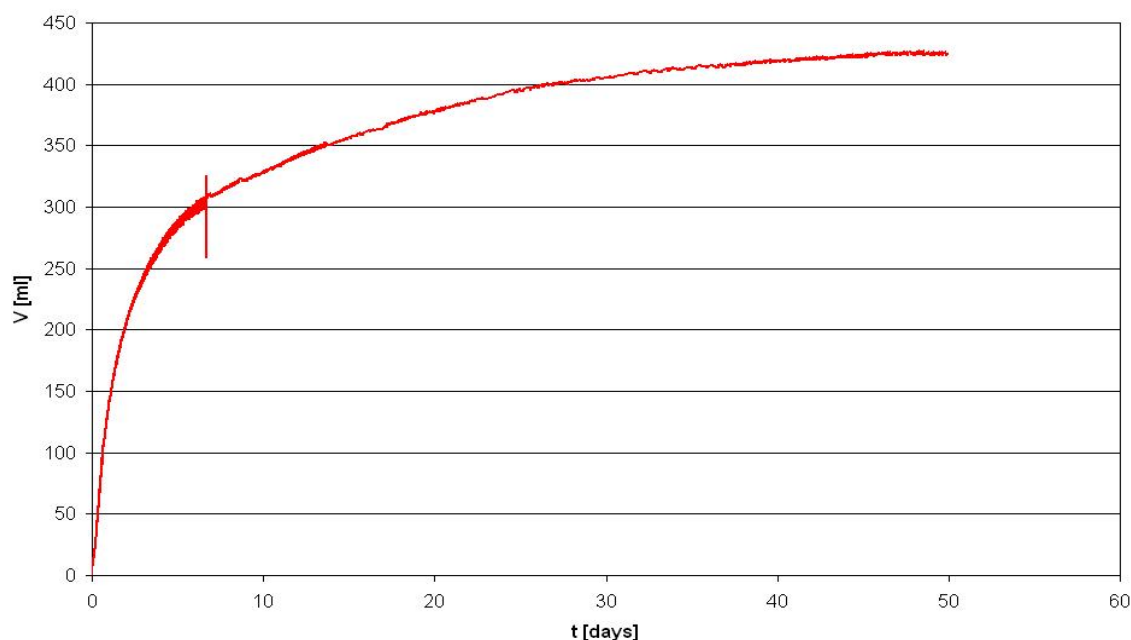


Figure 9: *Hydrogen evolution curve with iron powder under laboratory conditions*

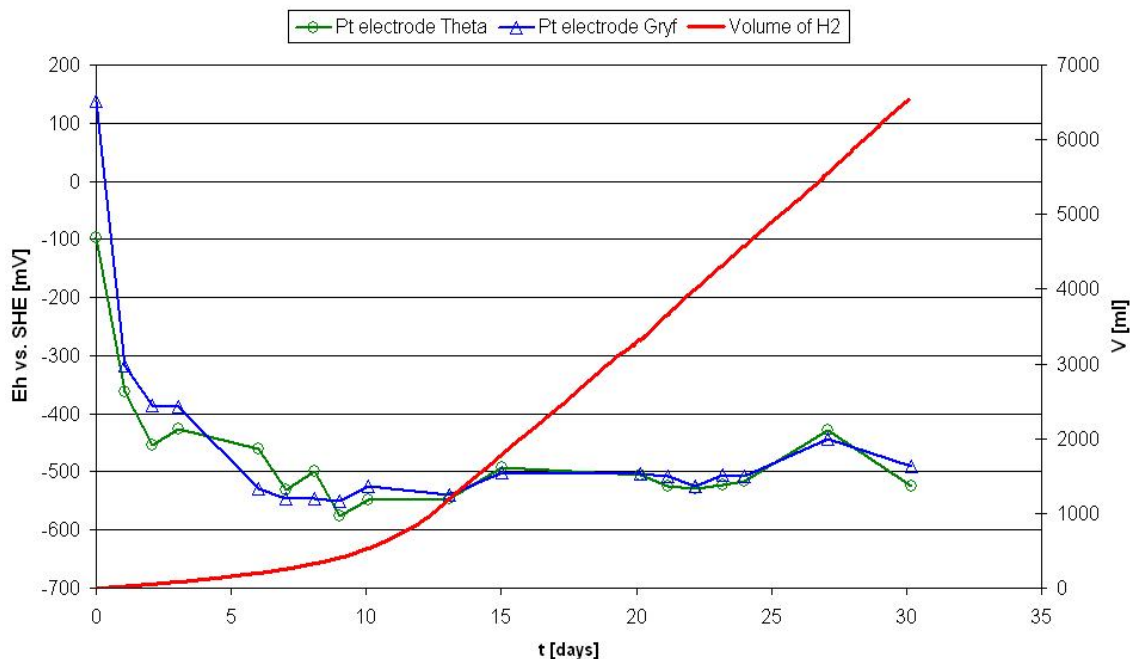


Figure 10 Hydrogen generation curve and Eh of the solution after adding 30 g of iron powder to the solution.

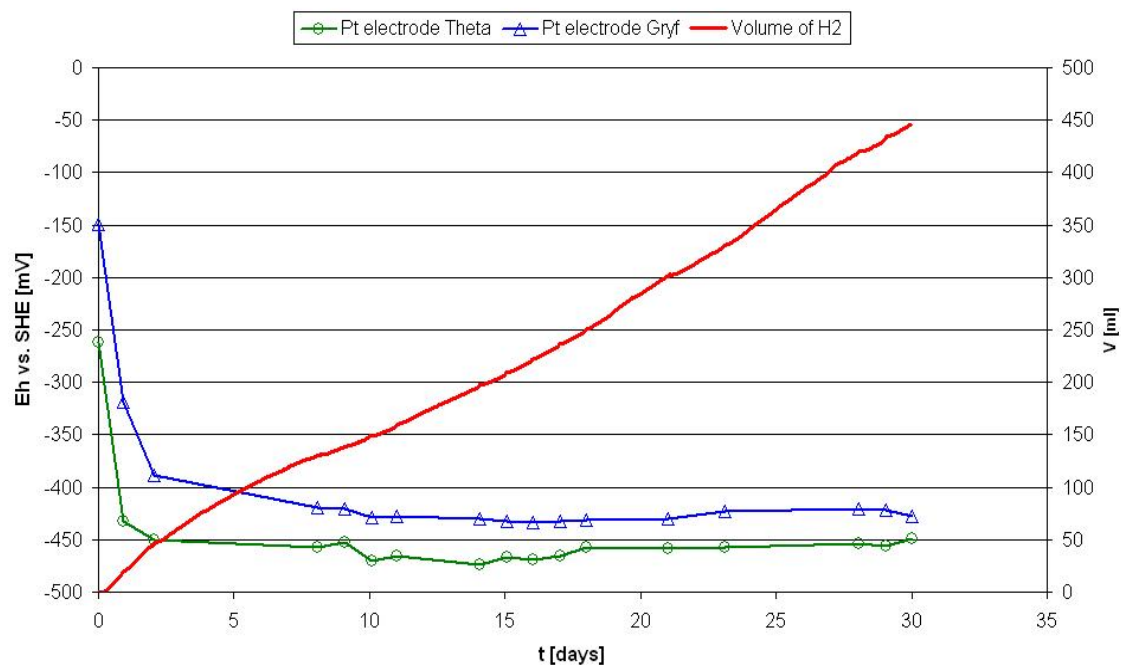


Figure 11. Hydrogen generation curve and Eh of the solution after adding 5 g of iron powder to the solution

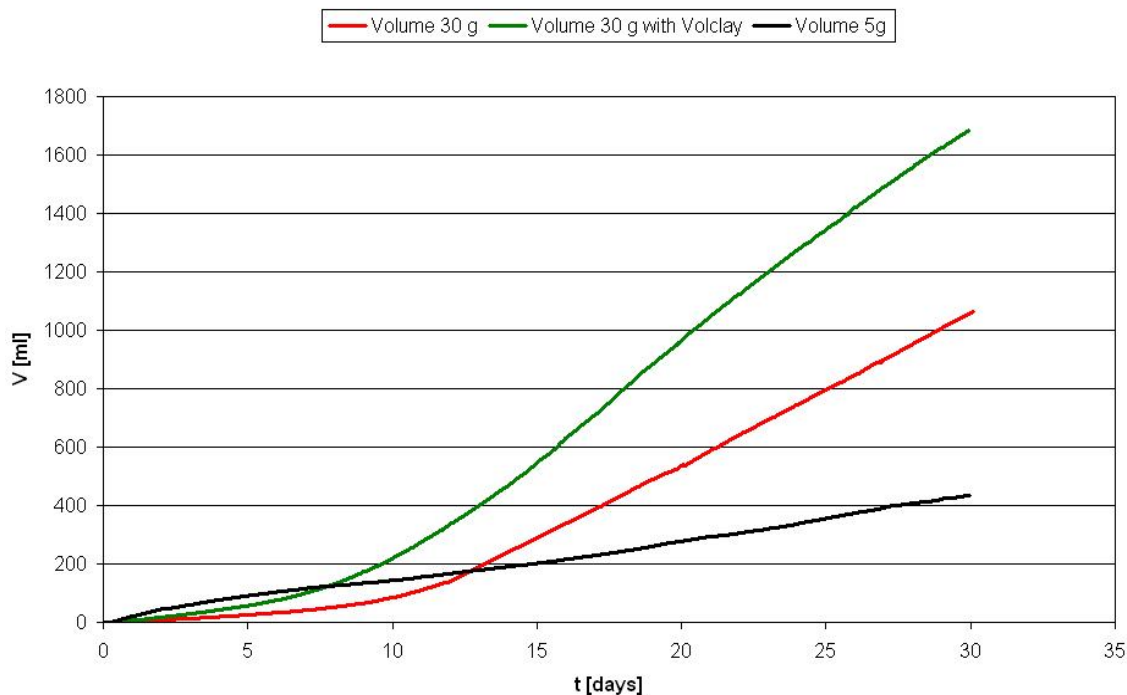


Figure 12 Comparison of the hydrogen generation rate recalculated per m^2 of iron

Summary and Conclusions

It was shown that the greater the surface of iron metal in the solution, the greater the initial decrease of Eh of the water in contact with the iron metal. The evolution of pH is different depending on whether carbon steel or iron powder was used in the experiments. In all the experiments with carbon steel it was found that pH decreases over time contrary to the experiments with iron powder. This could be explained by the presence of impurities, particularly carbon in carbon steel, which migrates to the surface of the carbon steel, as confirmed by ESCA measurements and could be released to the water.

After an initial decrease, the Eh increases over time due to the oxidation of ferrous ions and the precipitation of iron-bearing minerals. Using an ESCA probe, it was found that the firmly adhering corrosion product layers containing a high amount of oxygen and carbon were formed during the corrosion of the carbon steel plates in bentonite water under anaerobic conditions. These layers have an impact on hydrogen evolution rates. Under strongly reducing conditions, created by adding iron powder with a great surface to the solution, the protective effect of the corrosion layers could disappear, leading to an increase of hydrogen generation rates and consequently corrosion rates.

It was also shown that the presence of solid bentonite can increase the corrosion rate of iron. This could be because of the faster sorption (exchange) of ferrous ions on the bentonite leading to a higher concentration gradient between the metal and the solution.

Laboratory experiments could significantly differ from the actual conditions in a repository. For reliable predicting and ascertaining the behaviour of canisters in a

repository and their influence on the evolution of geochemical conditions in a repository a more systematic programme involving both laboratory and in situ experiments should be started in the future to verify the results obtained.

Acknowledgement

The research leading to these results has received funding from the European Union's European Atomic Energy Community's (Euratom) Seventh Framework Programme FP7/2007-2011 under grant agreement n° 212287 (RECOSY project) and the Ministry of Education, Youth and Sports of the Czech Republic

References

Anantamula R.P., Delegard C.H., Fish R.L., (1984). Corrosion behaviour of low-carbon steels in Grande Ronde Basalt groundwater in the presence of basalt-bentonite packing, Scientific Basis for Nuclear Waste Management VII, Mat. Res. Soc. Symp. Proc. Vol. 26, p.113

Brůha P., Pelech I., (1989). Czechoslovak patent no. 259785, Int. Cl. F 16 J 3/00.

de Combarieu G., Barboux P., Minet Y., (2007). Iron corrosion in Callovo-Oxfordian argillite: Form experiments to thermodynamic/kinetic modelling, Physics and Chemistry of the Earth 32, p. 346-358

Dobrev D., Bruha P., Vokal A. (2009): The effect of iron corrosion on conditions inside waste packages, 7466, p. 93, December 2009.

Dobrev D., Cervinka R., Vokal A., (2011). Redox potential in the near field of a deep geological repository containing carbon steel waste packages, KIT Report FZKA, will be published.

Fujisawa R., Cho T., Sugahara K., Takizawa Y., Horikawaa Y., Shiomi T., Hironaga M., (1997). The corrosion behaviour of iron and aluminium under waste disposal conditions, Scientific Basis for Nuclear Waste Management XX, MRS Symp. Proc. vol. 465, p. 675

Fujiwara A., Yasutomi I., Fukudome K., Tateishi T., Fujiwara K., (2001). Influence of Oxygen Concentration and Alkalinity on Hydrogen Gas Generation by the Corrosion of Carbon Steel, Mat. Res. Soc. Symp. Vol. 663, MRS 2001, Sci Basis XXIV, Sydney, p. 497

Grauer R., Knecht B., Kreis P., Simpson J.P., (1991). Hydrogen evolution from the corrosion of iron and steel in intermediate level waste repositories, Mat. Res. Soc. Symp. Proc. Vol.212, MRS, Sci. Basis XIV, Boston, p.295

Hara K., Ishikawa H., Honda A., Sasaki N., (1992). Influence of Dissolved Oxygen on the Generation Rate of Hydrogen Gas with the Corrosion of Carbon Steel, Proceeding of Workshop Gas Generation and Release, OECD Paris, p. 120

- Honda A., Teshima T., Tsurudome K., Ishikawa H., Yusa Y., Sasaki N., (1991). Effect of compacted bentonite on the corrosion behaviour of carbon steel as geological isolation overpack, Mat. Res. Soc. Symp. Proc. Vol.212, MRS, Sci. Basis XIV, Boston, p. 287
- Jelinek J., Neufeld P. , (1982). Kinetics of Hydrogen Formation from Mild Steel in Water under Anaerobic Conditions, Corrosion, Vol. 38, No.2, February
- Johnson L.H., Smith P.A.,(2000). The interaction of radiolysis products and canister corrosion products and the implications for spent fuel dissolution and radionuclide transport in a repository for spent fuel, Nagra Technical Report 00-04, February 2000
- Marsh, G.P., and Taylor, K.J., (1988). An assessment of carbon steel containers for radioactive waste disposal: Corrosion Science, v. 28, p. 289-320
- Smart N.R., Blackwood D.J., Werme L., (2001). The anaerobic corrosion of carbon steel and cast iron in artificial groundwaters, SKB Technical Report TR 01-22
- Smart N.R., Bond A.E., Crossley J.A.A., Lovegrove P.C., Werme L., (2001). Mechanical properties of Oxides Formed by Anaerobic Corrosion of Steel, Mat. Res. Soc. Symp. Vol. 663, MRS, Sci Basis XXIV, Sydney 2000, p. 477
- Smart N.R., Rance A.P., Fennell P, Werme L., (2002). Expansion due to anaerobic corrosion of steel and cast iron: experimental and natural analogue studies, In: Prediction of long term corrosion behaviour in nuclear waste systems. Proceedings of an int. Workshop, Cadarache, France , p. 280-294
- Smart N. R., Rance A.P., Werme L.O. (2004)., Anaerobic Corrosion of Steel in Bentonite, Mat. Res.Soc.Symp.Proc. Vo.807, Materials Research Society, p. 441
- Smart, N.R.R., Rance A. P.;Werme, L. O., (2008). The effect of radiation on the anaerobic corrosion of steel: Journal of nuclear materials, v. 379, p. 97-104.
- Staehle R.W., (2011). Lifetime Prediction of Materials in Environments, Uhlig's corrosion handbook, third edition, The electrochemical society, Inc, Wiley Publication.
- Xia X., Idemitsu K., Arima T., Inagaki Y., Ishidera T., Kurosawa S., Iijima K., Sato H., 2005, Corrosion of carbon steel in compacted bentonite and its effect on neptunium diffusion under reducing condition, Applied Clay Science 28, p. 89-100

REDOX CHEMISTRY AND MOBILITY OF URANIUM IN PHOSPHOGYPSUM

Ioannis Pashalidis¹ and Juhani Suksi²

¹ Chemistry Department, University of Cyprus (Cy)

² Laboratory of Radiochemistry, Department of Chemistry, University of Helsinki (Fi)

* Corresponding author: pspasch@ucy.ac.cy

Abstract

The present study aims to assess the effect of redox conditions existing within a phosphogypsum disposal site on the redox stability and mobility of uranium in the disposed material. Phosphogypsum sampling and in-situ measurements were carried out at a coastal stack in Vasiliko, Cyprus. pH, E_H and solubility experiments were performed in-situ and in laboratory systems. Generally, in the open stack oxidizing conditions predominate stabilizing uranium in its hexavalent oxidation state. On the other hand, after the application of a soil/vegetative cover and in the presence of natural organic matter, anoxic conditions prevail ($E_H < -70$ mV) enabling U(VI) reduction to U(IV). Uranium concentration measurements as well as $^{230}\text{Th}/^{238}\text{U}$ ratios show higher uranium retention under anoxic conditions, which could be ascribed to the lower solubility and mobility of U(IV).

Introduction

Phosphogypsum (PG) is an acidic by-product of the phosphate fertilizer industry, produced during the production of phosphoric acid from phosphate rock. Worldwide, large amounts of phosphogypsum have been produced up to now and it is estimated that if historic trends continue, production will increase to several hundred million metric tonnes annually. However, because of economic constraints (e.g. the price of the land) and pressing environmental issues the development of a safe disposal procedure is necessary. It is primarily the presence of toxic trace elements, as well as the radioactivity of radium (Ra) and uranium (U), which make this material a disposal and storage concern and have restricted its use in agriculture and construction industry (Rutherford et al. (1994); Burnett and Elzerman (2001)). Although, the best option for dealing with the PG problem appears to be the commercial use of this material in the agriculture (e.g. amelioration of acid soils) and construction industry (building/road construction), only a relative small portion of the phosphogypsum produced (14%) is reprocessed, a significant part is dumped into water bodies (28%) and the main part of

the material is accumulated in large sludge ponds and retaining stockpiles (Rutherford et al. (1994)).

Regarding the geochemistry of PG there are several studies on acidic runoff and hazardous material dispersion in the near-field of PG stacks. These studies show that in some situations groundwater pollution under a phosphogypsum stack is possible (Rutherford et al. (1994)).

Modelling of the environmental radiochemistry of uranium of Florida phosphogypsum showed that within the stacks uranium exists mainly in the form of complexes with sulphate and phosphate, which are relatively mobile as uncharged or negatively charged solution species. However, with increasing pH below the stack, precipitation of multi-component solid phases occurs preventing large-scale migration of uranium to the underlying aquifer (Burnett and Elzerman (2001); Lysandrou and Pashalidis (2008)).

Among the physicochemical parameters such as pH, E_H , ionic strength, chemical composition (**Papanicolaou et al. (2009)**), the redox potential (E_H) may significantly affect the chemistry and hence stability and leachability of phosphogypsum, because changes in E_H favour different oxidation states of a chemical species (e.g. sulfate or sulfide; U(VI) or U(IV)) which behave differently with respect to their solubility and mobility in the geosphere. Dramatic changes in E_H within a phosphogypsum stack may occur after application of a vegetative cover on the top of the stack. Generally, an enormous drop in the redox potential takes place due to restricted oxygen diffusion within the stack, organic matter disintegration and concomitant microbial activity, which leads eventually to the reduction of sulfate (S(+VI)) to sulfide (S(-II)) (**Luo et al. (2007)**); **Papanicolaou et al. (2010)**).

Recently, a soil/vegetative cover has been applied to an open stack in Cyprus, which has been extensively studied with respect to phosphogypsum characterisation and its radio-environmental impacts. In this respect the impact of the redox conditions existing within the phosphogypsum stack after application of a soil/vegetative cover has been investigated to assess the impact of changes in the redox potential on redox sensitive chemical species (e.g. sulfate and uranium). In this study we have focused on the mobility/leachability of uranium under oxic and anoxic conditions by means of uranium concentration measurements and isotopic ratio determinations. The redox speciation of uranium under oxic and anoxic conditions was also performed.

Materials and Methods

1.1 Study area and sampling description

The research reported here covers the phosphogypsum stack (about 50 000 m²) at the Vasilikos site, which is a coastal area in front of a former fertilizer plant in Cyprus. Several observation boreholes have been drilled into the stack (to a maximum depth of 5 meters) and stack solutions were sampled from the boreholes using a submersible pump and filtered in the field immediately after collection. Sample preparation and analysis as well as data of the physico-chemical characterisation of the phosphogypsum and the stack solution are given elsewhere (Lysandrou and Pashalidis (2008)). Since spring 2008, the stack is covered by 1-meter topsoil and dense vegetative cover, which is going to affect the redox conditions within the stack. Because the cover is relatively young, the effects due to the soil/vegetative cover are observed only close to

the soil-phosphogypsum interphase. Therefore, solid material samples were obtained from phosphogypsum adjacent to the topsoil and affected by organic run-offs. The respective samples have in contrast to non-affected phosphogypsum (PGypsum), which is white coloured, pale-brown to dark-brown colour (PGypsumNOM).

1.2 Uranium Concentration and Isotopic Ratio ($^{230}\text{Th}/^{238}\text{U}$) Measurements

Uranium series nuclides ^{238}U , ^{234}U and ^{230}Th were analysed to obtain information on U behaviour in the system. Sample materials were extracted in *aqua regia* and U series nuclides were analysed using ion exchange chromatography and α -spectrometry.

Table 1: U series nuclide concentrations and activity ratios in sample materials.

Sample material	U [mg/kg]	$\pm\delta$	$^{234}\text{U}/^{238}\text{U}$	$\pm\delta$	$^{230}\text{Th}/^{234}\text{U}$	$\pm\delta$
PGypsum	4.9	0.2	0.97	0.04	9.62	0.49
PRock	73	2	1.04	0.03	1.05	0.05
PGypsumNOM	12.5	0.4	1.03	0.04	4.46	0.22

As was expected the highest U concentration was found in phosphate rock (PRock). Nuclide activity ratios show also radioactive equilibrium in this material. PGypsumNOM shows an elevated U concentration compared to PGypsum. If the latter acts as a U source for U leaching and PGypsumNOM collects the released U, the observed decrease in the $^{230}\text{Th}/^{234}\text{U}$ activity ratio from around 10 in PGypsum to 5 explains the process. It is also possible that fixing the phosphogypsum stack with the soil/vegetative cover may have added some U in phosphogypsum which can explain the decrease in the $^{230}\text{Th}/^{234}\text{U}$ activity ratio as well.

1.3 Uranium Redox Speciation Experiments

Uranium oxidation states were determined by measuring the U(IV) and U(VI) fractions extracted from the sample materials in anoxic 4.5 M HCl. U(IV) and U(VI) form stable chloro complexes and can be separated by using anion exchange chromatography (*e.g.* Hussonnois et al. 1989; Ervanne and Suksi, 1996). The extraction solution was filtered (0.45 μm) and passed through a Dowex 1x4 anion exchange column regenerated to 4.5 M HCl. U(IV) goes through the column whereas U(VI) is fixed. For quantitative determination separated U(IV) and U(VI) fractions were spiked with the known amount of ^{236}U isotope. α -spectrometry was used for measuring U isotope concentrations.

Table 2: U oxidation state distribution in sample materials.

Sample	U(IV) [mg/kg]	$\pm\delta$	$^{234}\text{U}/^{238}\text{U}$	$\pm\delta$	U(VI) [mg/kg]	$\pm\delta$	$^{234}\text{U}/^{238}\text{U}$	$\pm\delta$	% U(IV)
PRock1	35.3	0.7	0.92	0.02	33	1	1.08	0.03	51
PRock2	41.0	0.6	0.92	0.02	31	1	1.09	0.03	57
PGypsum NOM	0.20	0.02	0.99	0.09	11.2	0.4	1.03	0.02	1.8

Non-affected phosphogypsum did not contain U(IV) whereas some 50 % of U in the phosphate rock (duplicate samples) occurs in U(IV) fraction. The lower $^{234}\text{U}/^{238}\text{U}$ activity ratio of U(IV) is explained by transfer of ^{234}U from the U(IV) pool to U(VI) pool due to radioactive decay which causes ^{234}U to be born in the higher oxidation (VI) state. Different $^{234}\text{U}/^{238}\text{U}$ activity ratios in U(IV) and U(VI) can also be considered a kind of success in oxidation state separation. Some U(IV) was found in NOM containing phosphogypsum suggesting U(VI) reduction to U(IV) during U accumulation in this material.

Results and Discussion

Figure 1 shows the uranium concentration determined in the raw/starting material (phosphate rock, PRock) and in two different types of the by-product material PGypsum and PGypsum NOM. The latter is phosphogypsum from the same charge/disposal area, but contains relatively increased amounts of natural organic matter ([NOM]~ 3%). The uranium concentration in the PR (73 mg kg^{-1}) is much higher than in the PGypsum samples because during the phosphoric acid production process the uranium remains basically in the liquid phase (phosphoric acid). However, there is significant difference in the uranium concentration between the two different PGypsum samples. Specifically, the PGypsum NOM (12 mg kg^{-1}) contains higher uranium than the PGypsum sample (5 mg kg^{-1}) and this is attributed to the NOM content of the material. The NOM could lead to a higher uranium concentration in the PGypsum NOM sample due to the retardation of the radionuclide in the material by complexation or reduction of U(VI) to U(IV), which is less mobile.

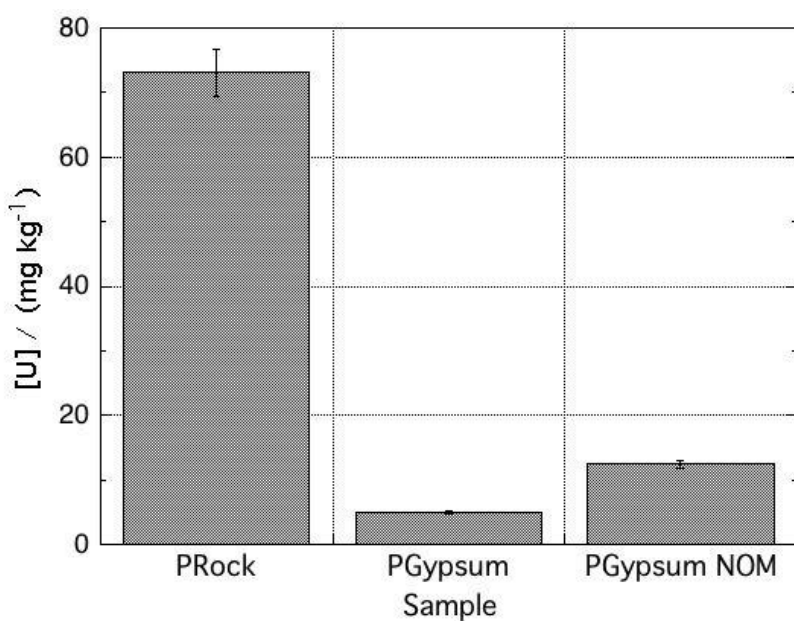


Figure 1: Uranium concentration in the raw material (phosphate rock, PRock), and two different types of phosphogypsum

According to Figure 2, which shows the isotopic ratios $^{230}\text{Th}/^{238, 234}\text{U}$ in PRock, PGypsum and PGypsum NOM, in the raw material the radioactive equilibrium between ^{230}Th and $^{238, 234}\text{U}$ does exist. As expected because of the production process this equilibrium is disturbed in the by-product (e.g. PGypsum), since thorium becomes enriched in the solid phase (e.g. phosphogypsum) compared to uranium, which is rather stabilized in the liquid phase (e.g. phosphoric acid). However, the $^{230}\text{Th}/^{238, 234}\text{U}$ ratio differs significantly also between PGypsum and PGypsum NOM. The $^{230}\text{Th}/^{238, 234}\text{U}$ ratio is almost twice as high in PGypsum compared to PGypsum NOM. The lower value of the $^{230}\text{Th}/^{238, 234}\text{U}$ ratio in PGypsum NOM, indicates U addition to the system. Whether this is due to reduction of U(VI) present in PGypsum to U(IV) in the presence of NOM, supported most probably by bacterial activity (Luo et al. (2007)), or due to sorption on NOM is not clear.

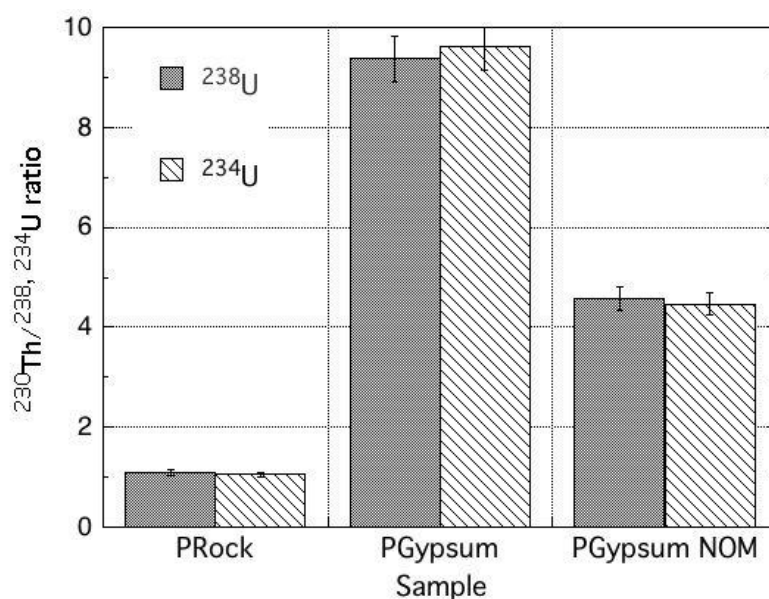


Figure 2: $^{234}\text{U}/^{238}\text{U}$ ratio concentration in the raw material (phosphate rock, PRock), and two different types of phosphogypsum

The experimental investigations to determine the U(IV) content of the studied samples resulted in about ~50% U(IV) in PRock, 0% U(IV) in PGypsum and ~2% U(IV) in PGypsum NOM. The U(IV) amount determined in the samples could be higher, since partial oxidation of the U(IV) in the material could happen during storage of the samples under oxic conditions before analysis. Nevertheless, these results are in agreement with previous experimental and calculated results, which have shown possible reduction of U(VI) under anoxic conditions existing in a phosphogypsum disposal site after application of a vegetative cover and contamination of the material with NOM.

Summary and Conclusions

Experimental and theoretical results obtained from this study lead to the following conclusions:

- the uranium concentration in NOM contaminated phosphogypsum (PGypsum NOM) is significantly higher than in corresponding non-contaminated phosphogypsum, because of higher uranium retardation in the former matrix
- the value of the isotopic ratio $^{230}\text{Th}/^{238, 234}\text{U}$ in PGypsum NOM is significantly lower than in the in PGypsum, indicating U immobilisation in the former system, probably due to U(VI) reduction to U(IV) in the presence of NOM
- The determination of U(IV) only in PGypsum NOM samples indicates clearly reduction of U(VI) to U(IV) in the presence of NOM under suboxic conditions.

Acknowledgement

The research leading to these results has received funding from the European Union's European Atomic Energy Community's (Euratom) Seventh Framework Programme FP7/2007-2011 under grant agreement n° 212287 (RECOSY project).

References

- Burnett, W.C., Elzerman, A.W. (2001), Nuclide migration and the environmental radiochemistry of Florida phosphogypsum. *J. Environ. Radioact.*, 54, 27-51.
- Carbonell-Barrachina, A., DeLaune, R.D., Jugsujinda, A. (2002), Phosphogypsum chemistry under highly anoxic conditions, *Waste Manage.*, 22, 657–665.
- Ervanne, H. and Suksi, J. (1996). Comparison of Ion-Exchange and Coprecipitation Methods in Determining Uranium Oxidation States in Solid Phases. *Radiochemistry* **38**, 306-309.
- Hussonnois, M., Guillamont, R., Brillard, L., Fattahi, M. (1989). A method for determining the oxidation state of uranium at concentration as low as 10⁻¹⁰ M, in: W. Lutze and R.C. Ewing (Eds.), *Mater. Res. Soc.* 127, 979-984.
- Luo J., Weber F.-A., Cirpka O. A., Wu W.-M., Nyman J. L., Carley J., Jardine P. M., Criddle C. S., Kitanidis P. K. (2007), Modeling in-situ uranium(VI) bioreduction by sulfate-reducing bacteria, *J. Contam. Hydrol.*, 92, 129-148.
- Lysandrou M., Pashalidis I. (2008), Uranium chemistry in stack solutions and leachates of phosphogypsum disposed at a coastal area in Cyprus, *J. Environ. Radioact.*, 99, 359-366.

Papanicolaou, F., Antoniou, S., Pashalidis, I. (2009), Experimental and theoretical studies on physicochemical parameters affecting the solubility of phosphogypsum, J. Environ. Radioact., 100, 854-857.

Papanicolaou, F., Antoniou, S., Pashalidis, I. (2010), Redox chemistry of sulphate and uranium in a phosphogypsum tailings dump, J. Environ. Radioact., 101, 601-605.

Rutherford, M.J., Dudas, P.M., Samek, R.A. (1994), Environmental impacts of phosphogypsum, Sci. Total Environ., 149, 1-38.

REDOX REACTION OF AQUEOUS SE(IV) WITH PYRITE: REACTION PRODUCTS AND PATHWAY STUDIES

Mingliang Kang ^{1,2*}, Laurent Charlet ^{2,3}, Fabrizio Bardelli ², Antoine Géhin ², Andrey Shchukarev ⁴, Fanrong Chen ¹

¹ Guangzhou Institute of Geochemistry, Chinese Academy of Sciences, Guangzhou, 510640, P.R.China.

² Environmental Geochemistry Group, ISTERre, University of Grenoble I, 38041 Grenoble, France.

³ Institute Universitaire de France, 75005, Paris, France.

⁴ Department of Chemistry, Umeå University, Umeå SE-901 87, Sweden.

* Corresponding author: kangmingliang@gmail.com

Abstract

Interaction of aqueous Se(IV) with natural pyrite was investigated in the pH range 5.05 – 8.65. Thermodynamic calculations, x-ray absorption spectroscopy (XAS) and x-ray photoelectron spectroscopy (XPS) indicate that red Se(0) is the unique or predominant reaction product at $\text{pH} \leq 5.65$, while at $\text{pH} \sim 6.1\text{--}8.65$, XAS and solution analysis results suggest the presence of small amount of FeSeO_3 , and/or iron selenides (or its precursors). At pH 6.94 and 8.65, however, due to the relatively high redox potential when Se(IV) is present, the formation of Fe(III)-(oxyhydr)oxide is kinetically favored. This precipitation consumes nearly all the aqueous ferrous iron, and limits the amounts of iron selenides or its precursor. The speciation studies demonstrate a strong kinetic dependence on the reaction products, which lead to severe redox disequilibrium in short-term laboratory experiments.

After pyrite oxidation, large amount of elemental sulfur along with sulfite on pyrite surface are detected. These observations indicate that thiosulfate is an important intermediate for pyrite dissolution. In this study, its decomposition follows the reaction: $8\text{S}_2\text{O}_3^{2-} + 8\text{H}^+ = \text{S}_8 + 8\text{HSO}_3^-$. Nevertheless, the significant deficit in detected sulfur suggests that pyrite dissolution is non-congruent. Possible mechanisms accounted for the non-congruency include gas formation or other undetected surface species that originate from either arsenic-impurity leaching or other dissolution pathway.

The experiments carried out in this study reveal that pyrite can significantly attenuate the mobility of Se by reductive precipitation, and that the reaction process does not produce acid under acidic to neutral condition.

Introduction

Selenium is essential to human life, and both Se excess and deficiency occur all over the world (Fordyce et al., 2000; Rayman, 2008). In addition, the radioactive isotope ^{79}Se , with a half-life of 2.95×10^5 years (Jiang et al., 2001), is presently considered as the key mobile fission product for the disposal of spent fuel and high-level radioactive waste (Chen et al., 1999; Grambow, 2008). For these reasons, Se mobility and bioavailability is of major interest in soil and environmental sciences, and an important concern for the safe disposal of radioactive waste.

The solubility of selenium is significantly controlled by its oxidation state, which in turn depends on the redox conditions of the surrounding environment. Tetravalent and hexavalent Se are very soluble and mobile aqueous oxyanions, while Se species with 0, -I, and -II oxidation states are low solubility solids (Scheinost and Charlet, 2008; Scheinost et al., 2008). Due to the weak adsorption of Se(IV) and Se(VI) on natural minerals, in particular on granite or claystone minerals, which are considered as host rocks for nuclear waste disposals, reductive precipitation is considered to be the most effective way to immobilize ^{79}Se . Pyrite (FeS_2) is the most widely distributed metal sulfide mineral in the geological environment, and it is also present in bentonites, which are considered as buffer materials for nuclear waste repository (Baeyens et al., 1985; Metz et al., 2003; Vaughan and Lennie, 1991). Owing to its strong reducing capacity and stability under anoxic condition, pyrite is expected to be the major reductive component within these geological medium, to immobilize redox-sensitive radionuclides like ^{79}Se on a geological time-scale.

Selenium speciation on pyrite surface has been the major interest in many studies, but conflicting results have been reported. For example, Breynaert et al. (2008) found crystalline Se^0 was the only reaction product of the pyrite-Se(IV) reaction between pH 6.5 to 8.5. Se^0 was also observed by Liu et al. (2008) as the reaction product between pyrite and HSe^- at pH 6.6. On the other hand, Naveau et al. (2007) excluded the formation of $\text{Se}(0)$, suggesting either Se(-I) or Se(-II) solid as the reaction products when aqueous Se(IV) and Se(-II) reacted with pyrite at pH 3.0. The disagreement among these experimental results suggests that Se speciation on pyrite surface may be significantly affected by the physico-chemical conditions under which the reactions occur. In this study, the redox reaction between natural pyrite and aqueous Se(IV) were conducted from pH 5.05-8.65 and the results were interpreted in light of thermodynamic calculations, X-ray Absorption Spectroscopy (XAS) and X-ray Photoelectron Spectroscopy (XPS).

Materials and Methods

Chemicals

Natural pyrite from the Jiguanshan ore mine located in Tongling, China, was used in this study. Large pyrite crystals were crushed, and fractions of 90 – 120 μm size were selected by sieving. Magnetic separation was employed to remove any pyrrhotite and iron oxide impurities. Then pyrite was ultrasonically washed using degassed water,

0.2M HCl, ethanol, and acetone, and finally dried and stored in O₂-free glove box (O₂ < 2 ppm). Before introduction in the reaction solution, pyrite grains were further ground in the glove box using agate mortar. The specific surface area of the ground pyrite powder was measured to be 0.48 m²·g⁻¹ by BET N₂-absorption method. XRD and Mössbauer characterization confirmed the sample to be a high purity pyrite, and its stoichiometric ratio (S/Fe = 2.08) was measured by SEM-based Energy Dispersive Spectroscopy (EDS). ICP-OES analysis, after aqua regia dissolution showed that this natural pyrite contains 2.56% arsenic (i.e. FeS_{2.08}-As_{0.043}), while no other elements (B, Co, Cu, Ni, Pb, Si) were detected using this method.

All other chemicals used were of analytical grade. The water used was deionized (18.2 MΩ) and boiled purging with argon before introduction in the glove box. Seven references were used as XAS standards: amorphous red Se(0) was synthesized via chemical reduction of Na₂SeO₃ by glutathione following the procedure by Huang et al. (Huang et al., 2003), while FeSe₂ was synthesized according to the protocol mentioned by Liu et al. (Liu et al., 2006). Commercial Na₂SeO₄ (MERCK), Na₂SeO₃·5H₂O (Sigma Aldrich), grey Se(0) (Sigma Aldrich), and FeSe (Alfa Aesar) were used as Se(VI), Se(IV), Se(0) and Se(-II) references, respectively. FeSeO₃ reference was the same of that used in a previous work (Kang et al., 2011).

Kinetic redox experiments

Kinetic redox studies were conducted in two series of experiments. In the first one, experiments were performed in three continuously stirred batch reactors in O₂-free (< 2ppm) glove box at pHs of 5.05, 5.65, and 6.10. In each reactor, 10.5 g of pyrite powder were equilibrated for 4 days with 1000ml of 0.01M NaCl solution before adding 4.2, 4.6, and 5.0 ml of 0.1M Na₂SeO₃ solution, respectively. A buffer solution of CH₃COONa-CH₃COOH (~ 0.05 M) was used to adjust the pH to the desired values.

In the second series of experiments, 0.4 mM of Se(IV) was added to 5.5 g/l pyrite suspension which was equilibrated for 2 days within a 0.02 M NaCl ionic background solution in a 250 ml reactor. Initial pHs were set equal to 6.94 and 8.65. No buffer solution was used in this series of experiments. The reactors were manually shaken several times everyday.

During the reaction process, the solution pH in all reactors was left free to vary. At a given time, the solution pH and redox potential (Eh) were measured with a Metrohm 6.0233.100 pH electrode and a Crison redox electrode (nb.5261) connected to an Orion (525A) pH meter. Five pH buffers and one Eh buffer were used to calibrate the electrodes. Meanwhile, an aliquot of 6 ml suspension from each reactor was sampled and filtered using 0.2 μm pore size membranes (Millipore). Total iron, sulfur, selenium, and arsenic concentrations in the filtrate were analyzed by ICP-OES (Varian 720-ES), with detection limits of 8.95×10^{-8} , 5.21×10^{-7} , 3.80×10^{-7} , and 1.33×10^{-7} mol/L, respectively. The Fe²⁺/Fe³⁺ concentrations were determined by the phenanthroline method, with and without a reduction step by hydroxylamines (Viollier et al., 2000).

The elemental sulfur formed at the pyrite surface after oxidation by Se(IV) was quantitatively measured by perchloroethylene extraction and subsequent quantitative analysis by high-performance liquid chromatography (HPLC), following the method developed by McGuire et al. (2000) (McGuire and Hamers, 2000).

X-ray Absorption Spectroscopy

Pyrite suspensions 15ml aliquots reacted with Se(IV) were sampled at different reaction times (Table 1) and filtered using 0.2 μm porous membranes (Millipore). The filter cake was dried with silica gel, sealed with Kapton tape, and mounted on the sample holder. All manipulations were conducted inside the glove box. The samples were then brought to the synchrotron facility in an anaerobic jar and transferred in the experimental vacuum chamber.

XAS measurements were performed at the Se K-edge (12,658 eV) on the Italian beamline (BM8- GILDA) at the European Synchrotron Radiation Facility (ESRF) in Grenoble (France). In order to avoid beam-induced redox reactions all samples and references were measured in vacuum at low temperature (77K), using a nitrogen cryostat. A Se(0) reference was simultaneously acquired at each energy scan for accurate energy calibration.

Principle Component Analysis (PCA) and Least Square Fitting (LSF) were applied to the XANES spectra to obtain quantitative information on samples' speciation (Ravel; and Newville., 2005). PCA and LSF were performed using the SIXPACK and IFEFFIT packages, respectively (Ravel; and Newville., 2005).

X-ray Photoelectron Spectroscopy

XPS measurements were performed on samples reacted at pH 5.05, 5.65, and 6.10 for 220 days, and samples reacted at pH 6.94 and 8.65 for 70 days. To avoid possible oxidation, all samples were dried in the glove box with silica gel, sealed in glass bottles with rubber stoppers, and brought to Umeå University (Sweden) in an anaerobic jar for XPS analyses. Fe(OH)₂ reference was prepared in the same way and showed no oxidation. Before measurements, samples were reduced in pellets in Argon atmosphere and immediately transferred to the XPS chamber. XPS spectra were recorded with Kratos Axis Ultra electron spectrometer equipped with a delay line detector. The monochromated Al K α source operated at 150 W, a hybrid magnetic lens system, and a charge neutralizer provided an analysis area of 0.3 \times 0.7 mm. The binding energy (BE) scale was referenced to the C 1s line of aliphatic carbon (285.0 eV). Processing of the spectra was accomplished with the Kratos software.

Results and Discussion

X-ray Absorption Spectroscopy

The XANES spectra of eleven samples (Table 1) reacted at different pH for different reaction times and of reference compounds (FeSeO₃, Na₂SeO₃, amorphous (red) Se(0), crystalline (grey) Se(0), FeSe, and FeSe₂) are reported in Figure 1.

Spectra of samples obtained at pH > 5.65 (C, D, and E) show different features compared to that of samples (A and B) obtained at lower pH, suggesting formation of different reaction products or variations in their proportions. The absorption edge energy position indicate that in all samples, Se(IV) was reduced to Se(0) after reaction

with pyrite, regardless the experimental reaction conditions (pH and reaction time). Nevertheless, the presence of lower oxidation states (-I and -II) cannot be excluded from the analysis of the edge positions, because the energy shift in the edge positions of Se(0) and Se(-I, -II) references is lower than the resolution of XAS data: 0.5 eV. For this reason, PCA and LSF were applied to XANES spectra to unravel the reaction products. PCA reported a minimum of the indicator function (IND) corresponding to three components, while the spectra were found to be satisfactorily reconstructed using two components only. In addition, the eigenvalues and the variance indicate that one single component is mainly responsible for the variation of the spectra. This information suggests that up to three chemical species contribute to the XANES spectra, but one is largely predominant on the others. Target transformation using the reference spectra suggested amorphous Se(0), FeSe₂, and FeSeO₃ as the best candidates (Figure 1), while the same procedure indicates that FeSe and Na₂SeO₃ can be ruled out.

Table 1: Summary of the XANES and XPS results. Compositional values are derived from LSF results on XANES spectra. The error is estimated to be around 10%.

Sample	pH	reaction time (days)	XANES					XPS		
			Se ⁰ red	FeSeO ₃ %	FeSe ₂ %	Σ %	χ _v ² × 10 ³	Se ⁰	Se ⁴⁺	Fe ³⁺
A1	5.05	7	100	0	0	100	0.99	Yes	No	No
A2		21	100	0	0	100	0.97			
A3		34	100	0	0	100	1.17			
		220								
B1	5.65	7	100	0	0	100	1.05	Yes	No	No
B2		21	100	0	0	100	1.12			
B3		34	100	0	0	100	0.96			
		220								
C1	6.10	7	95	7	0	102	0.85	No	No	Yes
C2		21	96	5	0	101	0.79			
C3		34	92	9	0	101	0.73			
		220								
D	6.94	44	91	11	0	102	0.29	Yes	No	Yes
		70								
E	8.65	44	95	7	0	102	0.31	Yes	No	Yes
		70								

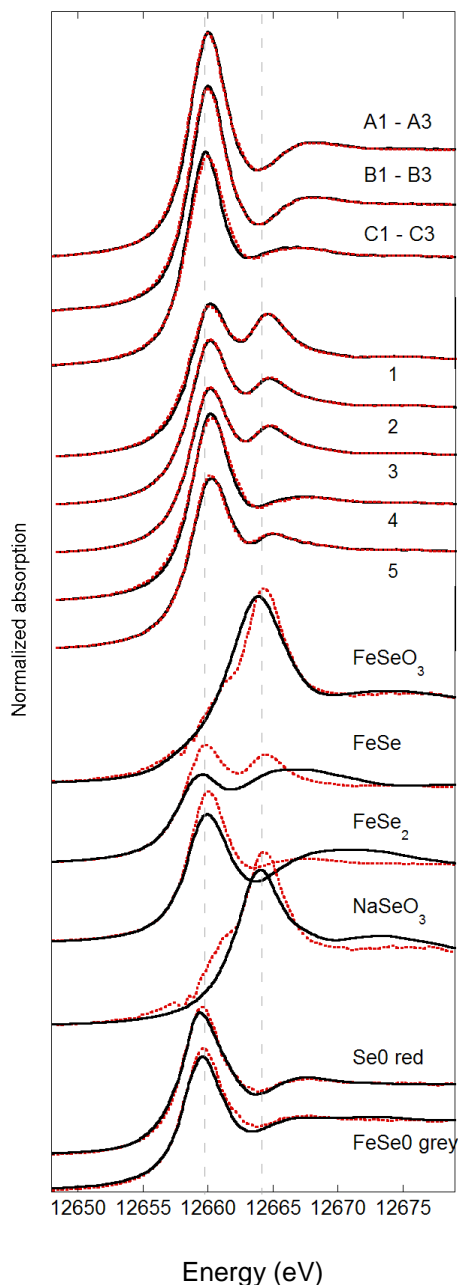


Figure 1: XANES spectra of pyrite reacted with Se(IV) samples and of the reference compounds (continuous lines are experimental data; dotted lines are PCA reconstruction of the samples' spectra using two components; for reference samples dotted lines represent target transformation curves).

Linear square fits (not shown) based on three reference compounds confirmed amorphous Se(0) as the main species, while possible presence of FeSeO₃ is estimated to be between 5 and 11% on samples C, D, and E (Table 1). Nevertheless, since the error on the relative compositions calculated from LSF is around 10%, the actual presence of Se(IV) is uncertain. In fact, in all reaction systems, FeSeO₃ ($K_s = 10^{-9.99}$ (Seby et al., 2001)) is always below saturation ($SI < -0.3$ at pH 6.1, while $SI < -1.1$ at pH 6.94). Nevertheless, since pyrite surface is negatively charged at pH > 2.0 and thus can adsorb

aqueous Fe^{2+} (Fornasiero et al., 1992; Descostes et al., 2010), precipitation of FeSeO_3 is possible due to the much higher interface Fe^{2+} concentration. Our recent studies further indicate that SeO_3^{2-} can bond to the surface hydrated Fe^{2+} sorbed on pyrite surface, and the reaction starts from Fe^{2+} oxidation through $\text{Fe}(\text{HSeO}_3)_2$ structure (Kang et al., unpublished). For this reason, XANES can detect the FeSeO_3 structure. In addition, since XAS is insensitive to species occurring in small amounts (lower than about 10%), the presence of FeSe_2 in smaller amounts cannot be ruled out. This applies in particular to samples C, D, and E, for which LSF leads to good fits only when using at least two reference spectra. A small amount of iron selenides (<10% wt) may account for the number of components suggested by PCA (3).

Surface analysis by XPS

The Fe 2p (or Fe 3p), S 2p, and Se 3d XPS spectra of initial pyrite and pyrite reacted with Se(IV) are shown in Figure 2. Initial pyrite spectrum exhibits intense peaks at 708.0 eV and 163.3 eV, in the $\text{Fe}(2p_{3/2})$ and $\text{S}(2s_{3/2})$ regions, characteristic of stoichiometric FeS_2 . The high energy tail of the $\text{Fe}(2p_{3/2})$ spectrum can be fitted with the component at 709.5 eV, which matches the $\text{Fe}(2p_{3/2})$ component of Fe(II)-O (708.5–709.5 eV) (McIntyre and Zetaruk, 1977) and the multiplet peaks (709.1–711.4 eV) of Fe(III)-S (Schaufuss et al., 1998). The Fe(II)-O feature can be assigned to surface hydroxylation processes (Eggleston et al., 1996), or to hydrated Fe^{2+} sorbed at the pyrite surface (Descostes et al., 2010), while the presence of Fe(III)-S may originate from the breaking of Fe–S bonds at the surface, with an electron being transferred from iron to sulfur, and inducing the formation of Fe^{3+} surface sites.

After reaction with Se(IV), additional Fe 2p and S 2p peaks appear at lower energies. Note that XPS detected significant amount of silica (SiO_2) on the pyrite surface (data not shown), originating from the prolonged stir in the glass reactor. The C 1s spectra show that all samples consist of two phases of different conductivity (data not shown), so-called inhomogeneous surface charging. Thus, the split pyrite phase can be ascribed to the silica precipitate on the pyrite surface.

Compared to the initial pyrite, an extra peak at 711.8 eV occurs on pyrite samples reacted with Se(IV) at pH 6.1, while an extra peak rises at 711.2 eV on samples pH 6.94 and 8.65. These peaks can be attributed to oxygen-bonded ferric ion, and suggests the formation of a $\text{Fe(III)-(oxyhydr)oxide}$ precipitate after reaction. This is in agreement with the lack of aqueous iron in these reactors after reaction (Table 2).

The S 2p spectrum was fitted with S $2p_{3/2}$ and S $2p_{1/2}$ spin orbit doublets, with a fixed 2:1 intensity ratio and 1.18 eV energy separation. Sample pH 6.94 shows three types of pyrite doublets. It appears that surface charge create a more complicated situation on this sample. This sample also shows S $2p_{3/2}$ peak at 165.2 eV, which is compatible with the binding energy range of sulfite (Swartz et al., 1971). In another work for Se(IV) reacted with pyrite at pH 4.37 (Kang et al., unpublished), an intense signal at 165.3 eV was detected. Therefore, we can conclude that sulfite is formed in the present experiments. Apart from the S 2p peak from disulfide in pyrite, no others S species were detected on other samples.

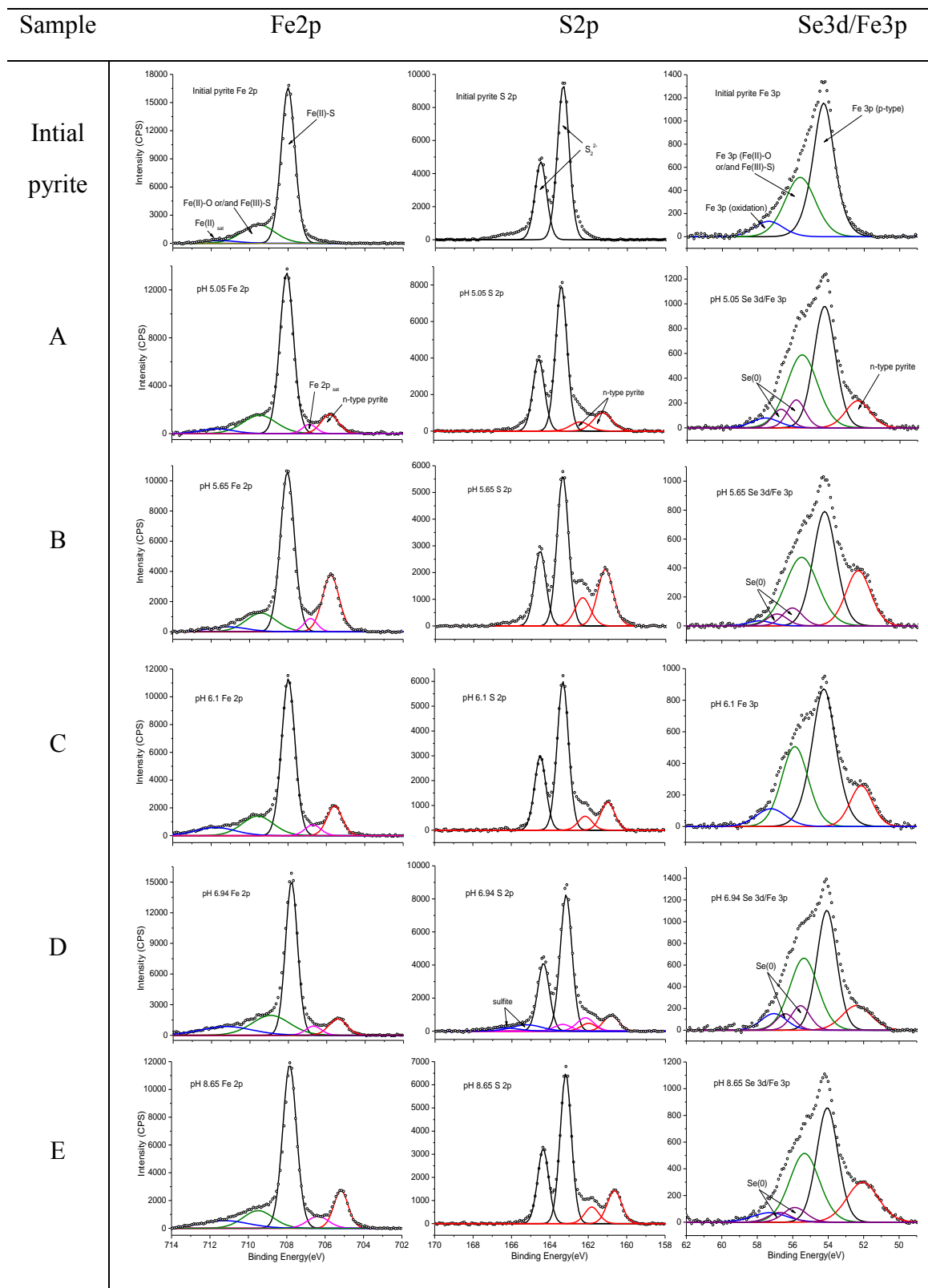


Figure 2: Fitted Fe 2p, S 2p and Se 3d (or Fe 3p) spectra for the initial pyrite and Se(IV)-reacted pyrite at pH 5.05, 5.65, 6.10, 6.94 and 8.65. N-type pyrite represents the split pyrite phase due to the inhomogeneous surface charge.

Since the photoelectrons of selenium with low oxidation state (0, -I and -II) interfere with the photoelectrons of iron, we chose to de-convolute the Se 3d spectra in Se 3d and Fe 3p peaks. In samples reacted at pH 5.05, 5.65, 6.94, and 8.65, the Se 3d 5/2 peaks occur at 55.8, 56.0, 55.5, and 55.9 eV, respectively, well matching the Se(0) reference at 55.6 eV (data not shown). Note that there is no Se 3d 5/2 contribution on samples obtained at pH 6.94 and 8.65 at 59.2 ± 0.1 eV corresponds to Se(IV) (data not shown). Since Fe 3p contribution cannot interfere with this energy position, it is easy to distinguish Se(IV) on Fe-mineral by XPS. Therefore, the residual Se(IV) on these two samples suggested by linear square fits for XAS data (Table 1) may be uncertain, and the XANES shape difference between spectra D and E (higher pH) and spectra A and B (lower pH) depicted in Figure 1 may also originate from selenium species other than Se(0) and Se(IV). This new phase with amorphous or nanocrystalline nature may be a precursor for the final stable species, FeSe₂. Due to the interference from Fe 3p, Se(0) signal on sample pH 6.1 is too weak to determine. Therefore, possible presence of a small amount of iron selenides on this sample cannot be confirmed by XPS technique as well.

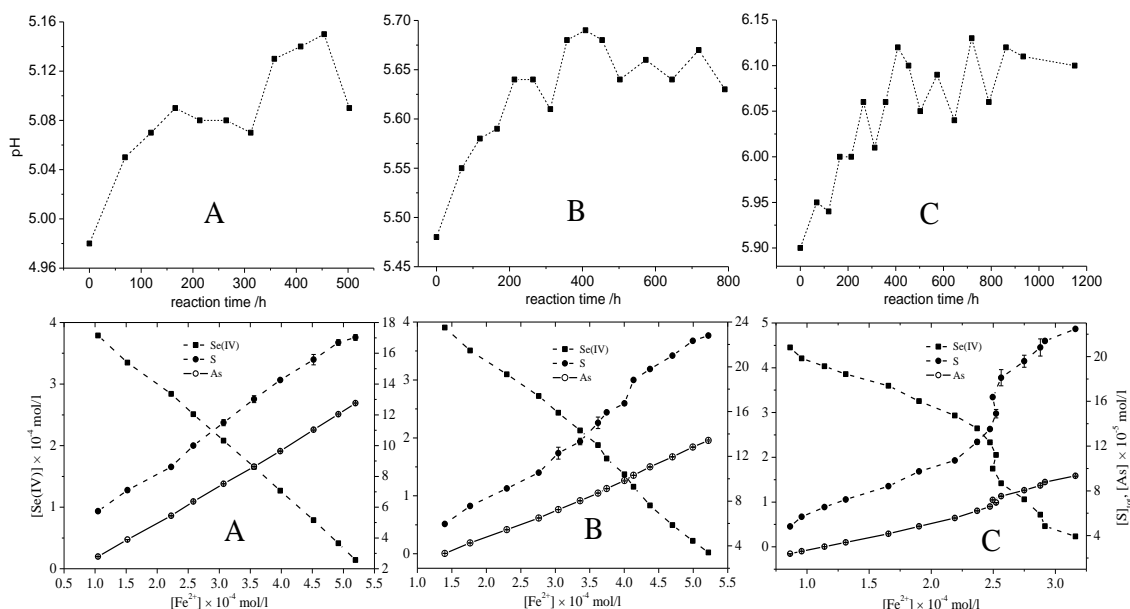
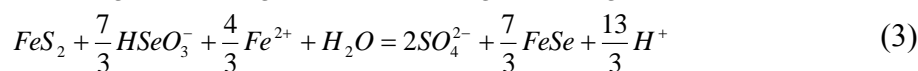
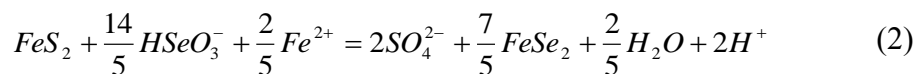
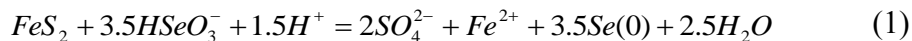


Figure 3: Upper panels show the variation of the solution pH; nether panels report the variation of [Se(IV)], [S]_{tot}, and [As] versus [Fe²⁺].

Reaction pathway

Oxidative dissolution of pyrite by dissolved oxygen and ferric iron has intensively been studied (Moses and Herman, 1991; Rimstidt and Newcomb, 1993; Rimstidt and Vaughan, 2003; Williamson and Rimstidt, 1994) and results demonstrated that the oxidation process does not oxidize iron but S(-II). Since the iron concentration determined by phenanthroline method with and without the reduction step by hydroxylamines resulted in the same value, this work demonstrates that this is also true for pyrite oxidation by Se(IV),

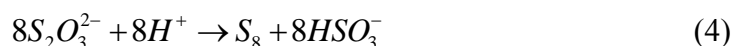
Assuming that sulfate is the only sulfur product, the possible electrochemical reactions between pyrite and aqueous Se(IV) are:



During the experiments ran at pH 5.05 and 5.65, aqueous iron and sulfur increased, and the pH slightly increased as well (Figure 3). These observations are consistent with the reduction of Se(IV) to Se(0). The $\Delta[S]_{tot}/\Delta[Fe]_{tot}$ ratios were calculated to be 0.28 and 0.47, while $\Delta[Se]_{tot}/\Delta[Fe]_{tot}$ were 0.88 and 1.04, at pH 5.05 and 5.65, respectively. The $\Delta[S]_{tot}/\Delta[Fe]_{tot}$ ratios are much lower than the values reported in previous works. Descostes et al (2004) reported a value ranging from 1.25 at pH = 1.5 to 1.6 at pH = 3 for pyrite oxidation by oxygen, while the ratio was calculated to be in the range of 0.93 - 2.00 for pyrite oxidation by oxygen at pH 5.7 ± 0.3 in the study conducted by Kamei et al (2000). The low $\Delta[S]_{tot}/\Delta[Fe]_{tot}$ ratio measured in the present study leads to lower ratios of $\Delta[Se]_{tot}/\Delta[Fe]_{tot}$ compared to the theoretical value of 3.5 according to reaction (1).

The significant sulfur deficit in the solution may be ascribed to the formation of solid or gaseous sulfur species (Descostes et al., 2004). In the present study, perchloroethylene extraction and subsequent quantitative analysis by high-performance liquid chromatography (HPLC) were employed to check the presence of S^0 . Results revealed that 0.156, 0.178, and 0.074 mmol of elemental sulfur were formed at pH 5.05, 5.65, and 6.1, close to the detected total aqueous sulfur amounts (0.146, 0.201, and 0.203 mmol at pH 5.05, 5.65, 6.1, respectively). Solution sulfur deficit during pyrite dissolution was reported by many authors (Descostes et al., 2004; Kamei and Ohmoto, 2000; Paschka and Dzombak, 2004), but they did not observe S^0 as a reaction product.

Furthermore, since Luther (1997), Kelsall et al. (1999), and Rimstidt and Vaughan (2003) proposed a pathway for pyrite oxidation involving thiosulfate ion ($S_2O_3^{2-}$), capillary electrophoresis method was used to check for $S_2O_3^{2-}$. However, the high instability of thiosulfate prevented its detection, and extra $S_2O_3^{2-}$ added to the solution was found to be oxidized to SO_4^{2-} within a few minutes. Therefore, the total sulfur concentration measured by ICP-OES is in the form of SO_4^{2-} or SO_3^{2-} as suggested by XPS surface analysis. Indeed, thiosulfate can disproportionate into either tetrathionate, or elemental sulfur and sulfite in acidic conditions, following the reactions (Williamson and Rimstidt, 1993; Xu and Schoonen, 1995):



Williamson and Rimstidt (1993) pointed out that ferric iron is a critical factor on these two reactions. Equation (4) indicates that elemental sulfur accounts for 50% of the total reacted thiosulfate through the decomposition reaction, which can explain the observed formation of S^0 at pH 5.05 and 5.65. Moreover, XPS surface analysis on samples at pH

6.94 (Figure 2) shows the sulfite species, confirming that reaction (4) occur in the present study. However, thiosulfate pathway alone cannot adequately describe the dissolution process in our experiments, since the sum of aqueous sulfur and solid S^0 is observed to be much less than the released Fe^{2+} , significantly deviating from the pyrite stoichiometric ratio. Thus, other sulfur species that were not detected may be formed in the present experiments.

McGuire et al. (2001) reported that greater than 50% of the reacted sulfur was in elemental form after arsenopyrite oxidation by ferric iron at pH = 1, and suggested that nucleation of S^0 lattice, arising from the leaching of Fe and As, could account for the formation of stable S_8 rings. Note that the pyrite used in this study contains 2.56%wt arsenic impurity ($FeS_{2.08}As_{0.043}$), and excessive arsenic leaching was observed in this study, with aqueous As/S ratios equal to 0.85, 0.56 and 0.38, at pH 5.05, 5.65, and 6.1, respectively (Figure 3). The significant As-impurity leaching suggests that a similar mechanism may apply to the present study as well. In addition, formation of elemental sulfur may occur independently from the thiosulfate pathway (Holmes and Crundwell, 2000), which likely involves an intermediate such as polysulfide formation at the oxidizing pyrite surface (Druschel and Borda, 2006; Flatt and Woods, 1995). In both pathways, sulfur species apart from S^0 and sulfate can be formed, leading to the metal-deficit and sulfur-rich surface observed by XPS analysis.

At pH 6.1, the $\Delta[S]_{tot}/\Delta[Fe]_{tot}$ and $\Delta[Se]_{tot}/\Delta[Fe]_{tot}$ ratios are 0.77 and 1.82, respectively. Note that the iron concentration slightly decreased after 502.5 h, although considerable amount of Se(IV) was reduced during this process. The decrease of the iron level was coupled with a decrease in $\Delta[Se]_{tot}/\Delta[S]_{tot}$ ratio (Figure 4), implying that more pyrite was oxidized. Therefore, $Fe(OH)_3$ cannot fully account for the iron decrease, since oxidation of the released Fe^{2+} would lead to less pyrite consumption. Similarly, homogeneous precipitation, like $FeSeO_3$, cannot account for the Fe^{2+} decrease as well. Considering that more pyrite was consumed during this process, it is reasonable to deduce that a new selenium species with lower valence state, like Se(-I) and/or Se(-II), other than Se(0), might be formed at pH 6.1, in agreement with reactions (2) and (3) which consume Fe^{2+} . On the other hand, at pH 6.94 and 8.65, relatively large amount of Se(IV) remains in the solution and the formation of Fe(III)-(oxyhydr)oxide is kinetically favored (Figure 2). The precipitation of Fe(III)-(oxyhydr)oxide consumes nearly all the aqueous ferrous, and limits the formation of iron selenides or the amorphous precursor, as suggested by the XAS and XPS spectroscopic data.

It appears that there are multiple complex concurrent reactions involved in the reduction of aqueous Se(IV) by pyrite. Due to the formation of Se(0) and the non-congruent dissolution of pyrite, the reaction is expected to consume protons. This can explain the pH increase, even when Fe(III)-(oxyhydr)oxide is formed at pH 6.94 (Table 2 and Figure 2).

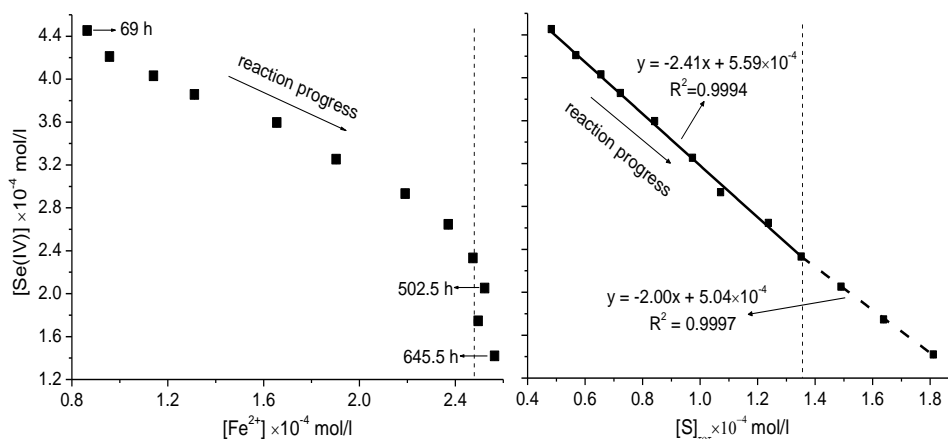


Figure 4: *Se(IV) concentration versus $[Fe^{2+}]$ (left panel) and $[S]_{tot}$ (right panel) at pH 6.1.*

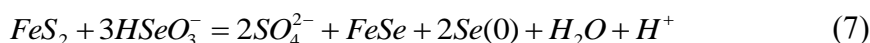
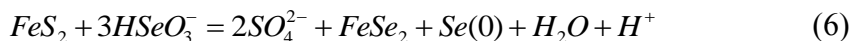
Table 2: *Analytical results for the experiments D and E.*

Sample	pH	Time	pH	$[Se]_{tot} \times 10^{-4}$	$[Fe]_{tot} \times 10^{-6}$	$[S]_{tot} \times 10^{-6}$	$[As] \times 10^{-6}$
		hours		mol/L	mol/L	mol/L	mol/L
D	6.94	0	6.94	4.50	nd	nd	nd
		24	6.95	4.19	0.98	3.6	2.7
		192	6.72	4.12	1.6	4.9	3.0
		720	7.54	3.53	im	16.3	9.5
		1056	7.57	3.15	im	29.7	10.0
E	8.65	0	8.65	4.50	im	nd	nd
		24	8.55	4.33	im	6.4	3.0
		192	8.33	4.32	im	8.1	3.5
		720	8.38	4.09	im	13.3	7.8
		1056	8.28	3.75	im	18.0	8.6

* nd, not determined; im, immeasurable (below detection limit).

Thermodynamic calculations

Reactions (1), (2), and (3), based on the stoichiometric dissolution of pyrite, point out that formation of Se^0 consumes protons and releases Fe^{2+} , while formation of iron selenides produces protons and consumes Fe^{2+} . Therefore, if no extra Fe^{2+} is added, $Se(IV)$ cannot be completely reduced to $FeSe_2$ or $FeSe$ by pyrite, and the reaction products are mixture of Se^0 , $FeSe$ and $FeSe_2$. In this case, $FeSe_2$ can account for up to 50% of the reaction products, and $FeSe$ up to 33%, according to:



Assuming an initial $pe = 4$, PHREEQC calculations suggest that under acidic to neutral condition $Se(0)$ is the unique/predominant reaction product at equilibrium, while in the neutral to slightly alkaline range, the formation of $FeSe_2$ becomes possible with up to equal molar fraction of $Se(0)$. In strongly alkaline conditions, part of the $Se(0)$ can further be reduced to HSe^- , leading to $FeSe_2$ as the predominant solid species (Figure 5). Therefore, the formation of iron selenides at pH 6.1, 6.94 and 8.65 are thermodynamically feasible, while $Se(0)$ is expected to be the predominant species at pH 5.05 and 5.65. Nevertheless, due to the low reactivity of natural pyrite, the system redox potential after $Se(IV)$ addition is relatively high, thus $Se(0)$ and $Fe(OH)_3$ formation is favored at the early stage of the reaction. This means that high concentration in $Se(IV)$ and low concentration in Fe^{2+} can hinder the formation of iron selenides. Upon $Se(IV)$ decrease and Fe^{2+} increase, the formation of iron selenides will occur afterwards. Note that the low solubility of bulk $Se(0)$ can kinetically prevent the dissolution required for the further transformation into more stable species ($FeSe_2$), leading the system to suffer redox disequilibrium in short-term laboratory experiments. Ongoing experiments on a more reactive nanosized pyrite revealed the formation of large amounts of the thermodynamic stable species $FeSe_2$ (L. Charlet et al., unpublished), which evidently confirm the effect of reaction kinetics on the reaction products.

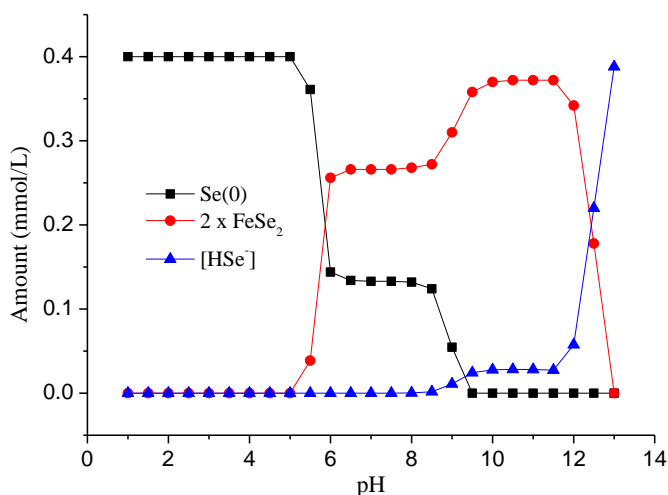


Figure 5: PHREEQC calculation for Se speciation distribution in the pyrite- $Se(IV)$ system as a function of pH. $[Se]_{tot} = 0.4$ mmol/L, $[Fe^{2+}]_{initial} = 0$, initial $pe = 4$. Goethite is allowed to precipitate if saturated.

Summary and Conclusions

In the present study, aqueous $Se(IV)$ was added to pyrite solution inducing its reduction to $Se(0)$ at pH 5.05 and 5.65, while at pH ~6.1-8.65, XANES and XPS spectra suggested the presence of small amount of $FeSeO_3$, and/or iron selenides (or its

precursor). Thermodynamically, higher pH favors the formation of iron selenides. However, due to the relatively high redox potential when Se(IV) is present, the formation of Fe(III)-(oxyhydr)oxide was kinetically favored. This precipitation consumes nearly all the aqueous ferrous iron, and limits the amounts of iron selenides or its precursor.

After pyrite oxidation, perchloroethylene extraction and subsequent quantitative analysis by HPLC reveal the formation of large amount of solid S⁰, which represents 51.5%, 47.0%, and 26.7% of the total detected sulfur (aqueous S + solid S⁰) at pH 5.05, 5.65 and 6.1, respectively. Meanwhile, XPS surface analysis show the presence of sulfite. The simultaneous occurrence of surface S⁰ and sulfite indicate that thiosulfate is an important intermediate for pyrite dissolution. In the present study, its decomposition follows the reaction: $8\text{S}_2\text{O}_3^{2-} + 8\text{H}^+ = \text{S}_8 + 8\text{HSO}_3^-$. The significant deficit in detected sulfur species with respect to Fe²⁺ released in solution suggests that pyrite dissolution is non-congruent. Possible mechanisms accounted for the non-congruency include gas formation or other undetected surface species that originate from either arsenic-impurity leaching or other dissolution pathway.

The results obtained in this work also showed that, when aqueous Se(IV) is used as oxidant under acidic condition, the formation of Se(0) consumes protons, and due to non-congruent dissolution of pyrite, the reaction does not produces acid as well under nearly neutral conditions. This implies that pyrite can be a good geological reductant, to immobilize the redox-sensitive radionuclides like ⁷⁹Se in the long-term nuclear waste repository.

Acknowledgement

The research leading to these results has received funding from the European Union's European Atomic Energy Community's (Euratom) Seventh Framework Programme FP7/2007-2011 under grant agreement n° 212287 (RECOSY project). In addition, we are grateful to Italian beamline (BM8 - GILDA) at the European Synchrotron Radiation Facility (ESRF) of Grenoble (France) for providing beamtime and assistance for XAS measurements.

References

- Baeyens, B., Maes, A., Cremers, A., Henrion, P.N. (1985). Insitu physicochemical characterization of Boom clay. In: Radioactive waste management and environmental restoration 6. Harwood Acad Publ GmbH, pp. 391-408.
- Breynaert, E., Bruggeman, C., Maes, A. (2008). XANES-EXAFS analysis of se solid-phase reaction products formed upon contacting Se(IV) with FeS₂ and FeS. Environmental Science & Technology, 42, 3595-3601.
- Chen, F.R., Burns, P.C., Ewing, R.C. (1999). Se-79: geochemical and crystallo-chemical retardation mechanisms. Journal of Nuclear Materials, 275, 81-94.

- Descostes, M., Schlegel, M.L., Eglizaud, N., Descamps, F., Miserque, F., Simoni, E. (2010). Uptake of uranium and trace elements in pyrite (FeS_2) suspensions. *Geochimica et Cosmochimica Acta*, 74, 1551-1562.
- Descostes, M., Vitorge, P., Beaucaire, C. (2004). Pyrite dissolution in acidic media. *Geochimica et Cosmochimica Acta*, 68, 4559-4569.
- Druschel, G., Borda, M. (2006). Comment on "Pyrite dissolution in acidic media" by M. Descostes, P. Vitorge, and C. Beaucaire. *Geochimica et Cosmochimica Acta*, 70, 5246-5250.
- Eggleston, C.M., Ehrhardt, J.J., Stumm, W. (1996). Surface structural controls on pyrite oxidation kinetics: An XPS-UPS, STM, and modeling study. *American Mineralogist*, 81, 1036-1056.
- Flatt, J.R., Woods, R. (1995). A voltammetric investigation of the oxidation of pyrite in nitric-acid solutions-relation to treatment of refractory gold ores. *Journal of Applied Electrochemistry*, 25, 852-856.
- Fordyce, F.M., Zhang, G.D., Green, K., Liu, X.P. (2000). Soil, grain and water chemistry in relation to human selenium-responsive diseases in Enshi District, China. *Applied Geochemistry*, 15, 117-132.
- Fornasiero, D., Eijt, V., Ralston, J. (1992). An electrokinetic study of pyrite oxidation, *Colloids Surfaces*, 62, 63-73.
- Grambow, B. (2008). Mobile fission and activation products in nuclear waste disposal. *Journal of Contaminant Hydrology*, 102, 180-186.
- Holmes, P.R., Crundwell, F.K. (2000). The kinetics of the oxidation of pyrite by ferric ions and dissolved oxygen: An electrochemical study. *Geochimica et Cosmochimica Acta*, 64, 263-274.
- Huang, B., Zhang, J.S., Hou, J.W., Chen, C. (2003). Free radical scavenging efficiency of Nano-Se in vitro. *Free Radical Biology and Medicine*, 35, 805-813.
- Kamei, G., Ohmoto, H. (2000). The kinetics of reactions between pyrite and O_2 -bearing water revealed from in situ monitoring of DO, Eh and pH in a closed system. *Geochimica et Cosmochimica Acta*, 64, 2585-2601.
- Kang, M.L., Chen, F.R., Wu, S.J., Yang, Y.Q., Bruggeman, C., Charlet, L. (2011). Effect of pH on aqueous Se(IV) reduction by pyrite. *Environmental Science & Technology*, 45, 2704-2710.
- Kelsall, G.H., Yin, Q., Vaughan, D.J., England, K.E.R., Brandon, N.P. (1999). Electrochemical oxidation of pyrite (FeS_2) in aqueous electrolytes. *Journal of Electroanalytical Chemistry*, 471, 116-125.
- Liu, A.P., Chen, X.Y., Zhang, Z.J., Jiang, Y., Shi, C.W. (2006). Selective synthesis and magnetic properties of FeSe_2 and FeTe_2 nanocrystallites obtained through a hydrothermal co-reduction route. *Solid State Communications*, 138, 538-541.
- Liu, X., Fattahi, M., Montavon, G., Grambow, B. (2008). Selenide retention onto pyrite under reducing conditions. *Radiochimica Acta*, 96, 473-479.

- Luther, G.W. (1997). Confirmation of a sulfur-rich layer on pyrite after oxidative dissolution by Fe(III) ions around pH 2 - Comment. *Geochimica et Cosmochimica Acta*, 61, 3269-3271.
- McGuire, M.M., Banfield, J.F., Hamers, R.J. (2001). Quantitative determination of elemental sulfur at the arsenopyrite surface after oxidation by ferric iron: mechanistic implications *Geochemical Transactions* 2, DOI: 10.1186/1467-4866-1182-1125.
- McGuire, M.M., Hamers, R.J. (2000). Extraction and quantitative analysis of elemental sulfur from sulfide mineral surfaces by high-performance liquid chromatography. *Environmental Science & Technology*, 34, 4651-4655.
- McIntyre, N.S., Zetaruk, D.G. (1977). X-ray photoelectron spectroscopic studies of iron-oxides. *Analytical Chemistry*, 49, 1521-1529.
- Metz, V., Kienzler, B., Schussler, W. (2003). Geochemical evaluation of different groundwater-host rock systems for radioactive waste disposal. *Journal of Contaminant Hydrology*, 61, 265-279.
- Moses, C.O., Herman, J.S. (1991). Pyrite oxidation at circumneutral pH. *Geochimica et Cosmochimica Acta*, 55, 471-482.
- Naveau, A., Monteil-Rivera, F., Guillon, E., Dumonceau, J. (2007). Interactions of aqueous selenium(-II) and (IV) with metallic sulfide surfaces. *Environmental Science & Technology*, 41, 5376-5382.
- Paschka, M.G., Dzombak, D.A. (2004). Use of dissolved sulfur species to measure pyrite dissolution in water at pH 3 and 6. *Environ Engineer Science*, 21, 411-420.
- Ravel, B., Newville, M. (2005). Athena, artemis, hephaestus: Data analysis for X-ray absorption spectroscopy using ifeffit. *Synchrotron Radiation*.
- Rayman, M.P. (2008). Food-chain selenium and human health: emphasis on intake. *British Journal of Nutrition*, 100, 254-268.
- Rimstidt, J.D., Newcomb, W.D. (1993). Measurement and analysis of rate data – the rate of reaction of ferric iron with pyrite. *Geochimica et Cosmochimica Acta*, 57, 1919-1934.
- Rimstidt, J.D., Vaughan, D.J. (2003). Pyrite oxidation: A state-of-the-art assessment of the reaction mechanism. *Geochimica et Cosmochimica Acta*, 67, 873-880.
- Schaufuss, A.G., Nesbitt, H.W., Kartio, I., Laajalehto, K., Bancroft, G.M., Szargan, R. (1998). Incipient oxidation of fractured pyrite surfaces in air. *Journal of Electron Spectroscopy and Related Phenomena*, 96, 69-82.
- Scheinost, A.C., Charlet, L. (2008). Selenite reduction by mackinawite, magnetite and siderite: XAS characterization of nanosized redox products. *Environmental Science & Technology*, 42, 1984-1989.
- Scheinost, A.C., Kirsch, R., Banerjee, D., Fernandez-Martinez, A., Zaenker, H., Funke, H., Charlet, L. (2008). X-ray absorption and photoelectron spectroscopy investigation of selenite reduction by Fe-II-bearing minerals. *Journal of Contaminant Hydrology*, 102, 228-245.
- Seby, F., Potin-Gautier, M., Giffaut, E., Borge, G., Donard, O.F.X. (2001). A critical review of thermodynamic data for selenium species at 25 degrees C. *Chemical Geology*, 171, 173-194.

S.S. Jiang, M. He, L.J. Diao, J.R. Guo, S.Y. Wu. (2001). Remeasurement of the Half-Life of ⁷⁹Se with the Projectile X-Ray Detection Method. Chinese Physical Letters, 18, 746-749.

Swartz, W.E., Wynne, K.J., Hercules, D.M. (1971). X-ray photoelectron spectroscopic investigation of group-VI-A elements. Analytical Chemistry, 43, 1884-1887.

Vaughan, D.J., Lennie, A.R. (1991). The iron sulfide minerals – their chemistry and role in nature. Science Progress, 75, 371-388.

Viollier, E., Inglett, P.W., Hunter, K., Roychoudhury, A.N., Van Cappellen, P. (2000). The ferrozine method revisited: Fe(II)/Fe(III) determination in natural waters. Applied Geochemistry, 15, 785-790.

Williamson, M.A., Rimstidt, J.D. (1993). The rate of decomposition of the ferric-thiosulfate complex in acidic aqueous-solutions. Geochimica et Cosmochimica Acta, 57, 3555-3561.

Williamson, M.A., Rimstidt, J.D. (1994). The Kinetics and Electrochemical Rate-Determining Step of Aqueous Pyrite Oxidation. Geochimica et Cosmochimica Acta, 58, 5443-5454.

Xu, Y., Schoonen, M.A.A. (1995). The stability of thiosulfate in the presence of pyrite in low-temperature aqueous-solutions. Geochimica et Cosmochimica Acta, 59, 4605-4622.

THE EFFECT OF PLUTONIUM OXIDATION STATE ON SORPTION AND REVERSIBILITY IN HUMIC ACID-QUARTZ SAND TERNARY SYSTEMS

Rajiv Kay¹, Nick Bryan^{1*}, Nick Evans², Peter Warwick²

¹ Centre for Radiochemistry Research, School of Chemistry, University of Manchester,
Oxford Road, Manchester, M13 9PL (U.K.).

² Department of Chemistry, University of Loughborough (U.K.)

* Corresponding author: nick.bryan@manchester.ac.uk

Abstract

The partition of plutonium in oxidation states IV, V and VI between solid and solution phase has been studied in humic/quartz sand ternary systems as a function of time, both in the absence and presence of Humic Acid (HA). Data have been recorded under an inert (O₂ and CO₂ free) atmosphere. The behaviour in the Pu(IV)/quartz sand ternary system appears simple, with the humic appearing to act largely as a competing solution phase ligand, and Pu sorption decreases with increasing HA concentration for all systems. The same type of behaviour was observed for the Pu(VI) system. For the Pu(V) system, the effects are more subtle. Here, the presence of humic at low concentrations actually enhances sorption, and so ternary complexes are shown to be very important. The Pu sorption in all systems is reversible to some extent, and in the Pu (IV) system, it seems fully reversible in the short-term. Pu(IV) reduced systems were allowed to equilibrate before they were exposed to oxygen. Upon exposure, there are small changes to the solid/solution partition. By comparison with the other experimental data, it seems that the Pu has not converted quantitatively to Pu(V), although it cannot be ruled out that some small part of the Pu has been oxidised. A simple mathematical kinetic model has been developed to interpret the behaviour of Pu ions and humic acid. The model shows that even in the systems that appear to show simpler ternary behaviour, i.e. Pu(IV) and Pu(VI), ternary complexes are significant, and that the surface humic ternary complexes are significantly stronger than the binary solution phase complexes.

Introduction

Humic substances are naturally occurring organic ligands that bind most metal ions very strongly. As a result, they have the capacity to compete with mineral surfaces for radionuclides (RN), increasing RN solubility, and hence mobility. Therefore, it is

essential to understand the effects of humic substances on RN behaviour if we are to predict accurately the migration of RN in the vicinity of a radioactive waste repository. However, humic ternary systems (HA + mineral + RN) can show highly complex behaviour, because the HA itself can sorb to the mineral surface, and RN can bind to these sorbed humics forming “ternary complexes”. Further, humic substance interactions with both mineral surfaces and RN are prone to significant kinetic effects (slow reactions and processes).

Plutonium can exist in a variety of oxidation states: III; IV; V; and VI, and (depending upon the pH and Eh) these multiple oxidation states can co-exist. Further, their chemistry can make data very difficult to obtain. In particular, the actinide IV oxidation state is hard to study, because these ions are generally sparingly soluble and very prone to hydrolysis and sorption to vessel walls. Therefore, Pu ternary system experimental data are very rare. However, these data are required to calibrate models of chemical speciation and solid/solution phase partition that may be used in the Radiological Performance Assessment of Radioactive Waste Repositories.

During this project, we have been studying radionuclide ternary complexes, starting with well behaved and less challenging systems (e.g. ¹⁵²Eu(III)) and progressively moving to more challenging systems: Th(IV); U(VI); U(IV) (Kay et al 2011). The final aim of the work was to study the most complex and challenging ternary systems that involve the various oxidation states of Pu. Here, we present data and initial modelling studies for systems of Pu (IV), (V) and (VI).

Experimental Methods

Commercially available humic acid from the Aldrich Chemical Company (Germany) was used in the experiments. Natural quartz sand (Aldrich) was also used without pre-treatment. All reagents used in the experiments were of analytical grade. Fresh Millipore de-ionized water (18 MΩ) was used in the preparation of all solutions.

A series of batch experiments were performed at room temperature. Because Pu can exist in a number of oxidation states, and transfer between the states is relatively easy, all experiments were performed under ‘inert atmosphere’ conditions in a Perspex glovebox that was flushed with O₂ free N₂ to exclude oxygen. E_h measurements in the box confirmed the absence of O₂. Also, the N₂ gas was passed through 2 Dreschel bottles with sintered frits containing concentrated NaOH solutions to remove traces of CO₂. The gas was then passed through a further Dreschel bottle containing water to remove any aerosols of NaOH solution before it entered the glove box. In the case of one experiment, part of the way through the experiment the sample tubes were removed from the glovebox, and CO₂ free O₂ was bubbled through the solution. This was to study the effect of a change from anaerobic to aerobic conditions on the partition of Pu between the solid and solution phases.

²³⁹Pu radiotracer solutions were treated so that they would contain a single oxidation state. Pu(IV) was synthesised by reducing a plutonium stock solution, using 8 M HNO₃ with a small amount of NaNO₂ (10 mg in 15 ml), with gentle heating. A Pu(VI) solution

was synthesised by the addition of 0.5 g of sodium chlorate to a Pu(IV) solution (10 ml). The penta-valent state was made by converting Pu(VI) to Pu(V) by adding 0.1 ml of 1 M hydroxylamine hydrochloride solution to 10 ml of Pu(VI) stock at 25°C. The oxidation states of the Pu in these solutions were checked before the experiment progressed further using the solvent extraction technique of Saito *et al.* (1985). In this technique, a small amount of the Pu stock solution was added to 1.5 ml of HNO₃ and 3 ml of 0.5 M thenoyltrifluoroacetone in cyclohexane. Pu(IV) is extracted quantitatively into the cyclohexane, whilst Pu(V) and Pu(VI) remain in the aqueous phase. The tracer solutions were tested before they were used further. If the test failed, then the solutions were discarded. Unfortunately, tests showed that the presence of humic acid prevented the extraction from working, and so it could not be used once the ternary system experiments had started.

The solid to solution ratio in all batch sorption experiments was 500 g L⁻¹. Known amounts of ²³⁹Pu solution in the required oxidation states (see above) were added to electrolyte solutions (total volume 100 ml) containing humic concentrations in the range 0 – 200 ppm in polypropylene containers to give final ²³⁹Pu concentrations of 1.22 or 0.6125 kBq ml⁻¹, which correspond to molar concentrations of 2.22x10⁻⁶ and 1.12 x10⁻⁶ mol dm⁻³, respectively. The solutions were adjusted to the required pH by adding appropriate quantities of NaOH or HNO₃. The actinide and humic were allowed to equilibrate for 24 hours before known masses of mineral phase were added to the system, and the pH readjusted. The containers were placed in an automatic shaker. At regular intervals, they were removed from the shaker, and the solution phase separated from the solid by double centrifugation (3500 rpm, 5 minutes, twice). This will remove all of the sand from the water column, but none of the humic acid species. Tests showed that the procedure gave the same separation results as 0.45 µm filtration, but without the risk of losses due to sorption. Therefore, colloidal species are not be removed from the solution. 0.5 ml of the supernatant were removed, so that the solution metal concentration could be measured. As soon as the sample had been removed from the polypropylene container, the mineral phase was resuspended and the system returned to the shaker. This sampling procedure was repeated over a period of up to several weeks. For some systems, once (apparent) equilibrium was reached, the supernatant was separated from the mineral phase and replaced with a fresh electrolyte solution containing the same concentration of humic. The solution that had been removed was added to a fresh sample of mineral. For both new systems, the distribution of metal between solid and solution was then monitored as before with time.

Results and Discussion

Pu(IV)

Figure 1 shows the uptake of Pu(IV) at a concentration of 0.6125 kBq ml⁻¹ in the presence of humic substances. The data are presented as the solution phase concentration, expressed as a percentage of the total Pu added to the system at the start of the experiment.

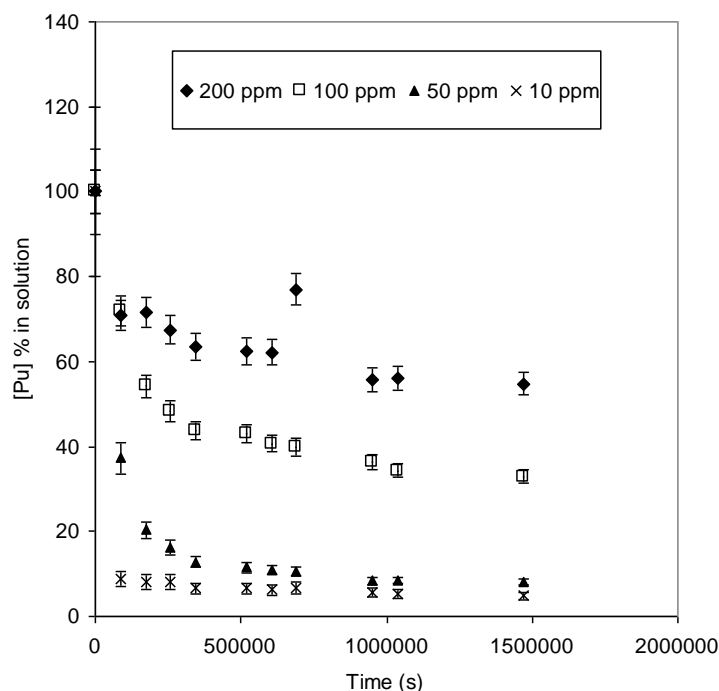


Figure 1: results for ternary humic acid/quartz sand system/ $^{239}\text{Pu(IV)}$, $0.6125 \text{ kBq ml}^{-1}$, $I = 0.1$, $\text{pH} = 6$, as a function of total humic concentration.

The Pu(IV) shows fairly simple, ‘classical’ ternary system behaviour. As the concentration of the humic increases, the amount of Pu sorbed to the mineral surface decreases. Hence, in this system, the main apparent effect of the humic is to act a competing solution phase ligand, which holds Pu(IV) in solution.

Figure 2A shows the results of an experiment where Pu(IV), 1.22 kBq ml^{-1} , was allowed to sorb to the quartz sand, but after 18 days, the solid phase was removed and a fresh sample added. Beyond 18 days, the plots show the further removal of Pu from the original solution, whilst Figure 2B shows the release of Pu into solution when a fresh solution of humic acid (containing no Pu) was added to the original mineral sample. In Figure 2B, so that the effect of changing the solution is clear, the last few data points from the first stage (shown in full in Figure 2A) are reproduced.

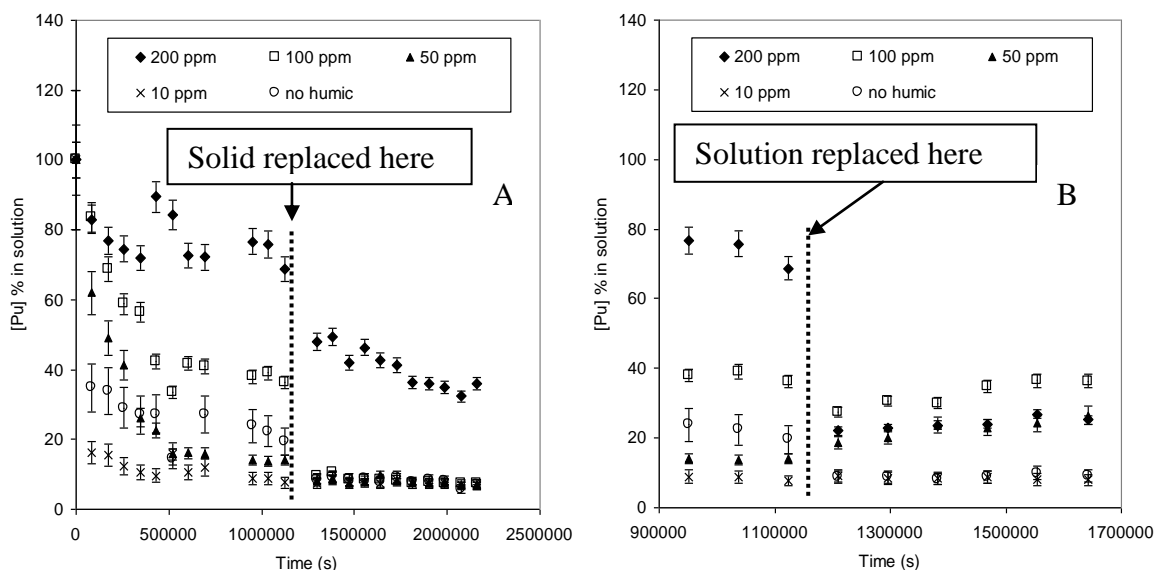


Figure 3: results for ternary humic acid/quartz sand system/ $^{239}\text{Pu(V)}$, $0.6125 \text{ kBq mL}^{-1}$, $I = 0.1$, $\text{pH} = 6$, as a function of total humic concentration. **A:** Pu concentration in solution following exposure to 2 successive samples of mineral. **B:** Pu concentration in solution before and after replacement of the solution for the same sample of mineral.

For the replacement experiment shown in Figure 3B, there is evidence of some reversibility, since at least some of the Pu has been brought back into solution. In a reversible system, the Pu concentrations that would be expected in solution following the change of solution are 20, 24, 12 and 8% for the 200, 100, 50 and 10 ppm systems, respectively, whereas the values at the end of the experiment are 25, 36, 26 and 8%. Therefore, although there is clearly some reversibility, the Pu(V) system is much harder to predict, probably because of very significant ternary complex formation.

Pu(VI)

Figure 4 shows the replacement data for the Pu(VI) system (1.22 kBq mL^{-1}). For this system, if sorption were reversible, then the concentrations that would be expected after exchange of the solutions (Figure 4B) would be, 18, 25, 8 and 5% for the 200, 100, 50 and 10 ppm systems, respectively, while the observed values are 22, 25, 25 and 6%. Therefore, in the 200, 100 and 10 ppm systems, the concentrations in solution after solution replacement are of the order that would be expected for a fully reversible system. The origin of the discrepancy in the 50 ppm system is unclear, but it seems unlikely that this system would not be reversible too, given that the systems with higher and lower concentrations of humic are.

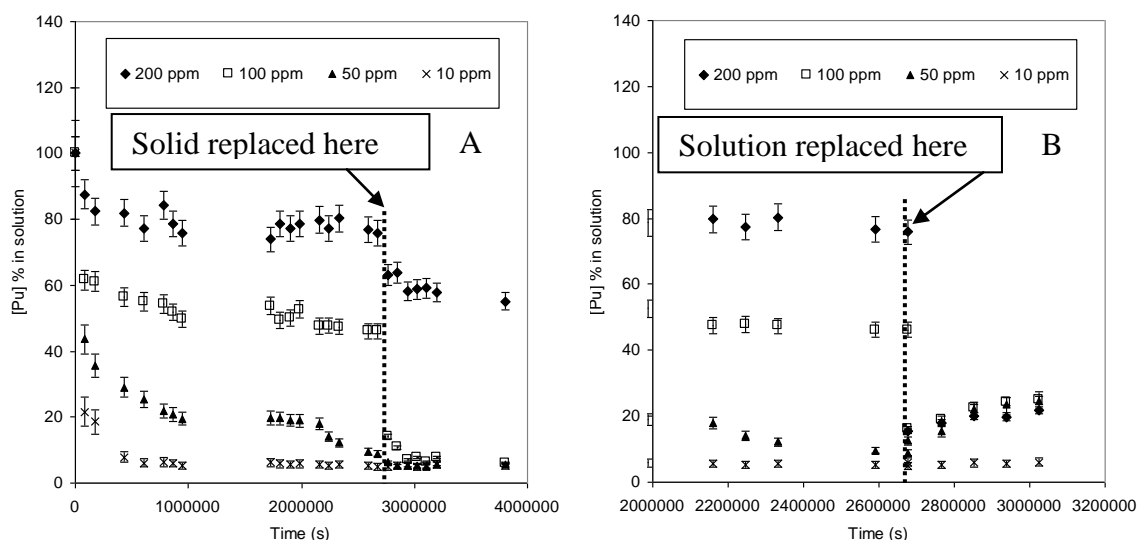


Figure 4: results for ternary humic acid/quartz sand system/ $^{239}\text{Pu}(\text{VI})$, 1.22 kBq ml^{-1} , $I = 0.1$, $\text{pH} = 6$, as a function of total humic concentration. **A:** Pu concentration in solution following exposure to 2 successive samples of mineral. **B:** Pu concentration in solution before and after replacement of the solution for the same sample of mineral.

It is possible that Eh values could change in the vicinity of a radioactive waste repository. Therefore, two experiments were attempted where Pu(IV) ($0.6125 \text{ kBq ml}^{-1}$) was allowed to sorb to the quartz surface before the system was 'oxidised'. The initial attempt used the addition of sodium chlorate. However, the concentration of chlorate required to raise the E_h , also increased the ionic strength significantly, and this could affect the interaction of the Pu with the humic and the mineral surface. Therefore, a second attempt involved bubbling O_2 (CO_2 free) through the solutions to raise the E_h , which did not change the ionic strength significantly. The results of this experiment are shown in Figure 5.

There is a small change in behaviour following exposure to oxygen. At the end of the experiment, the approximate concentrations left in solution are 70, 46, 12, 4 for the 200, 100, 50 and 10 ppm systems, respectively. The pattern of sorption after the change does not match with the Pu(V) because of differences in the concentrations and the order of sorption with humic concentration. There is a closer match to the Pu(VI) system, which shows 75, 46, 9 and 5% sorption. However, given the relatively small differences between the concentrations in Figure 5 before and after O_2 exposure, it is hard to tell whether the Pu has been oxidized or not. Certainly, a change in E_h results in very little change to the solid/solution partition.

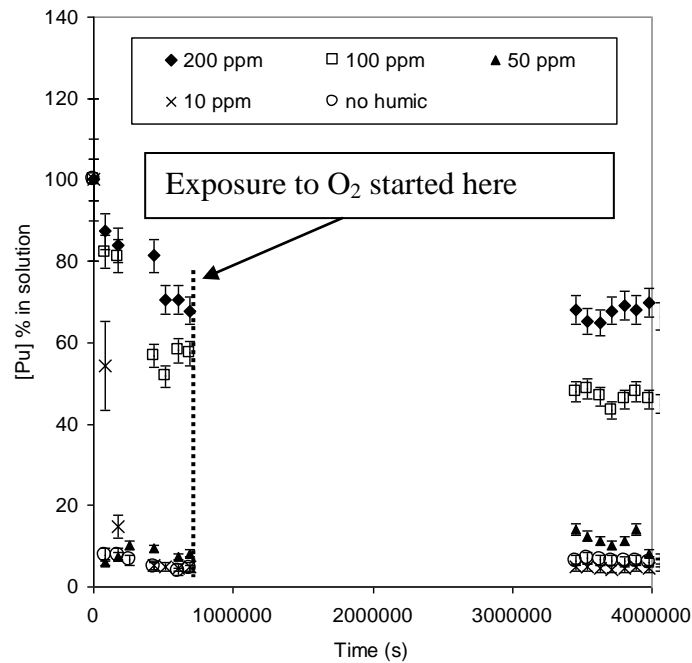
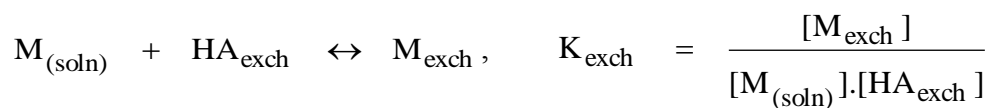


Figure 5: results for ternary humic acid/quartz sand system/²³⁹Pu(IV), 0.6125 kBq ml⁻¹, $I = 0.1$, pH = 6, as a function of total humic concentration. Samples exposed to O₂ during the experiment.

Modelling

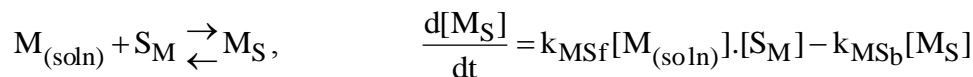
The results of the experiments have been compared with the predictions of a simple ternary system model. In this model, the interaction of metal, M, with the humic (HA) is described using two components, with initial uptake to an exchangeable fraction, M_{exch}, which is assumed to be instantaneous,



where HA_{exch} is the humic exchangeable binding site, and K_{exch} an equilibrium constant for the process. Subsequent transfer to and from the non-exchangeable fraction, M_{non-exch}, is a first-order kinetic (slow) process.

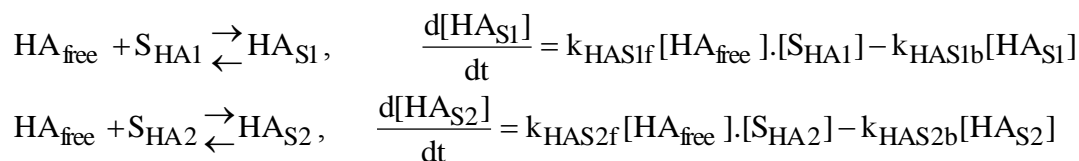
$$M_{exch} \xrightarrow{k_f} M_{non-exch}, \quad \frac{d[M_{non-exch}]}{dt} = k_f[M_{exch}] - k_b[M_{non-exch}]$$

where k_f and k_b are the forward and backward rate constants, respectively. These have been found to be approximately constant for all humic samples and metal ions previously (Bryan *et. al* 2012). The values are k_f = 1.1x10⁻⁸ s⁻¹ and k_b = 1x10⁻⁷ s⁻¹. The interaction of metal with the quartz surface is described with a single reaction,



where S_M is a metal binding site on the quartz sand surface, M_S is metal ion sorbed to the surface and k_{MSf} and k_{MSb} are the forward and backward rate constants, respectively.

The modelling work described here assumes that the surface is the source of the heterogeneity (a companion approach has also been applied that contains HA heterogeneity, but that is not described here). The model assumes a single type of humic species in solution and two surface sites:



where: S_{HA1} and S_{HA2} are surface binding sites, type 1 and 2, respectively; HA_{S1} and HA_{S2} are humic bound to surface sites, type 1 and 2, respectively; and k_{HAS1f} , k_{HAS1b} , k_{HAS2f} and k_{HAS2b} are rate constants. Note, $M_{(\text{soln})}$ is the total solution concentration of the metal ion, i.e., the constants involving $M_{(\text{soln})}$ are conditional (k_{MSf} , K_{exch}).

The behaviour of the humic itself has been modelled previously (Kay *et. al* 2011). That fit was very close (Kay *et. al* 2011) and so many of the parameters have been defined already (k_{HAS1f} , k_{HAS1b} , k_{HAS2f} and k_{HAS2b}). The parameters used in this study are given in Table 1.

Table 1: parameter values used in the modeling

	k_{HAS1f} (ppm ⁻¹ s ⁻¹)	k_{HAS1b} (s ⁻¹)	k_{HAS2f} (ppm ⁻¹ s ⁻¹)	k_{HAS2b} (s ⁻¹)	$[S1]_T$ (ppm)	$[S2]_T$ (ppm)	$[S_T] \cdot k_{MSf}$ (s ⁻¹)	k_{MSb} (s ⁻¹)	$[HA_{\text{exch},T}] \cdot K_{\text{exch}}$
Pu(IV)	1.4×10 ⁻⁶	2×10 ⁻⁵	2×10 ⁻⁸	6×10 ⁻⁷	20	30	2.0×10 ⁻⁵	7.5×10 ⁻⁷	42
Pu(VI)							1.0×10 ⁻⁵	5×10 ⁻⁷	100

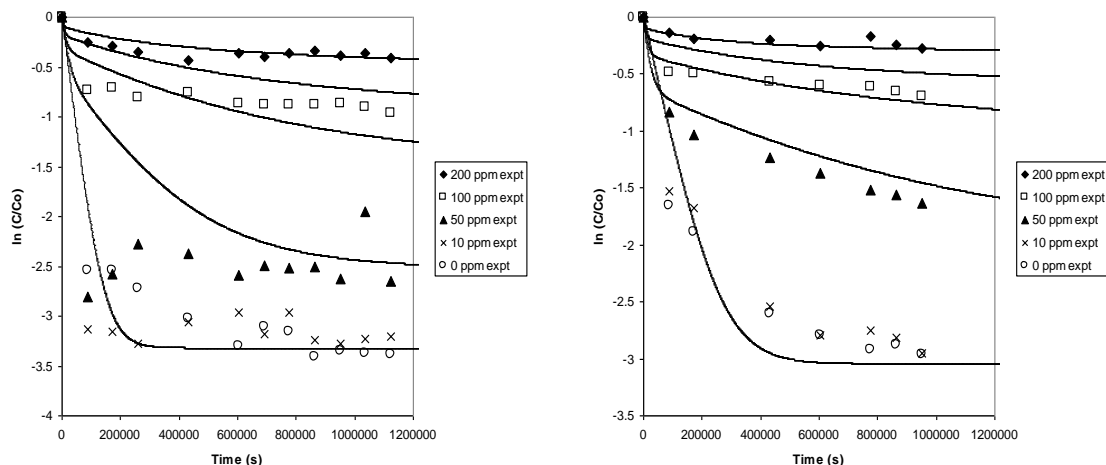


Figure 6 (left): results for ternary humic acid/quartz sand system/ $^{239}\text{Pu(IV)}$, 1.22 kBq ml^{-1} , $I = 0.1$, $\text{pH} = 6$, as a function of total humic concentration and Model fit to data.

Figure 7 (right): results for ternary humic acid/quartz sand system/ $^{239}\text{Pu(VI)}$, 1.22 kBq ml^{-1} , $I = 0.1$, $\text{pH} = 6$, as a function of total humic concentration and Model fit to data. In both figures, the lower model line corresponds to the 0 ppm system, following vertically by the 10, 50, 100 and 200 ppm systems (in that order).

The simple single stage sorption of the Pu(IV) and Pu(VI) have been modelled: the fits are shown in Figures 6 and 7, respectively. The data are plotted as $\ln(C/C_0)$, where C is the concentration of Pu in solution at any time, and C_0 is the Pu concentration at the start of the experiment. These systems were chosen, because they appeared (at least) to show relatively simple behaviour, i.e., sorption decreases with increasing humic concentration for all systems. It has been shown previously that systems where sorption increases in the presence of small concentrations of humic, compared to a humic free system cannot be explained with this simple model, because the sorbed and solution phase humic species have different binding strengths, but the model assumes that they are the same (Kay *et. al* 2011). The Pu(V) systems show this sort of complex behaviour.

The modelling results show that the behaviour in the Pu(IV) and Pu(VI) systems is not as simple as it seems. Although the model can fit the data in the 100 ppm and humic free systems, the match to the other humic concentrations is much less good. The reason for the poor fit is that the ions have different affinities for solution phase and sorbed humic species, because of fractionation. In both cases, the surface humic ternary complexes are stronger than the simple binary complexes in solution, and this is responsible for the poor fits, because the model assumes a single binding strength for all humic molecules.

Summary and Conclusions

Experimental data have been measured for the sorption of Pu (IV), (V) and (VI) in quartz sand/humic acid ternary systems. In all cases, higher concentrations of humic

substances reduce sorption. The Pu sorption in all systems is reversible to some extent, and in the Pu (IV) system, it seems fully reversible.

The Pu(V) system is complex, and there is direct evidence from the experimental data that ternary complexes are very significant. Although they are less obvious in the Pu(IV) and Pu(VI) systems, the modelling suggests that they are present.

The simple ternary model is not able to reproduce the Pu sorption data, and further work will concentrate on developing a model that has different binding strengths for sorbed and solution phase humic species.

Acknowledgement

The research leading to these results was funded by the United Kingdom EPSRC (DIAMOND consortium - EP/F055412/1) The authors are also grateful to the U.K. NERC for funding as part of the BIGRAD project.

References

Bryan N.D., Abrahamsen L., Evans N., Warwick P., Buckau G., Weng L., Van Riemsdijk W.H.. (2012) The Effects of Humic Substances on the Transport of Radionuclides: Recent Improvements in the Prediction of Behaviour and the Understanding of Mechanisms, *Applied Geochemistry*, 27, 378–389.

Kay R., Abrahamsen L., Bryan N.D., Warwick P, Evans N. (2011) Actinide Partition in Humic Colloidal Ternary Systems: experiments and preliminary modelling, *Proceedings of the 3rd Recosy Workshop*, 21st – 24th March 2011, Balaruc-les-Bains, France.

Saito A., Roberts R.A. and Choppin G.R. (1985), *Anal. Chem.*, 1985, 57, 390-392.

URANIUM SOLUBILITY UNDER ALKALINE CONDITIONS USING DIFFERENT REDUCING AGENTS

Olga Riba¹, Vanessa Montoya¹, Mireia Grivé^{*1}, Lara Duro¹

¹ Amphos 21 (ES)

*Corresponding author: mireia.grive@amphos21.com

Abstract

The UO₂(am) solubility has been assessed in this work by performing different batch experiments at alkaline pH (9-12) and in presence of H₂(g) or a reducing agent (Na-dithionite).

The systems have been studied by measuring pH, Eh and uranium concentration at different reaction times. The experimental data show the poor capability of H₂(g) in maintaining reducing conditions in absence of a catalyst. The used of Na-dithionite has proven to minimize the oxidative dissolution of UO₂(am), despite the measured Eh seems to be determined by different redox processes occurring to dithionite.

Introduction

Concrete (cement) based barriers are one of the main materials used in High and Low and Intermediate Level Waste repositories (HLW and LILW). These materials do not only offer high mechanical capacity and low hydraulic conductivity but also radionuclide retention capacity by sorption processes and the precipitation of solid phases as a result of the imposed alkaline conditions. The presence of important amounts of steel in this type of repositories used as reinforcement material and as a waste container (canister) can generate large amounts of hydrogen mainly due to the corrosion of the metallic canister or in minor extend due to the radiolysis of water by the spent fuel. Also, near the canister the redox potential can be actively controlled by these corrosion products (mainly magnetite and goethite) giving very reducing conditions. Consequently, the influence of high pH conditions, redox potential and hydrogen generation on uranium solubility and its potential transport to the biosphere are important factors to take into account when modelling uranium release in waste repositories.

The solubility of uranium(IV) oxide under alkaline conditions is highly dependent on the redox conditions of the system. Very reducing conditions are needed to minimise

the extent of oxidative dissolution process. Therefore, the assessment of the redox potential in repository conditions is considered one of the main parameters to be known in order to predict the migration of uranium and other radionuclides in the studied systems. Due to the uncertainties involved in redox potential measurements in complex systems, one of the main objectives of ReCosy project is to understand the coupling between redox processes and the redox measurements with the aim to apply the results to Performance Assessment. The present work gives an understanding of $\text{UO}_2(\text{am})$ solubility under alkaline conditions and using different anoxic / reducing conditions at 25° C in solutions without complexing ligands (carbonate, phosphate, silicate, etc.) where uranium oxides, oxyhydroxides or hydroxides are expected to be the solubility controlling solids. The redox potential measurements have been contrasted with predicted redox potential considering thermodynamic equilibrium.

Experimental

Material

All experiments are performed under N_2 atmosphere in a glove box. The chemicals used in this study are of analytical grade ($\text{UO}_2(\text{NO}_3)_2 \cdot 6\text{H}_2\text{O}(\text{s})$, $\text{NaOH}(\text{s})$, HClO_4 (3 M), $\text{NaHCO}_3(\text{s})$, $\text{NaClO}_4(\text{s})$ and $\text{Na}_2\text{S}_2\text{O}_4(\text{s})$). All solutions have been prepared using Milli-Q purified water (resistivity $>18.2 \text{ M}\Omega \text{ cm}$).

The $\text{UO}_2(\text{s})$ has been either freshly prepared or provided by ENRESA. The freshly prepared $\text{UO}_2(\text{s})$ has been synthesized by addition of saturated NaOH solution free of carbonates to a $\text{U}(\text{IV})$ solution. The $\text{U}(\text{IV})$ dissolution is previously obtained by dissolving 2 g of $\text{UO}_2(\text{NO}_3)_2 \cdot 6\text{H}_2\text{O}(\text{s})$ under acidic conditions and reducing the $\text{U}(\text{VI})$ solution to $\text{U}(\text{IV})$ by bubbling $\text{H}_2(\text{g})$ activated with Pd. The reaction has been followed by UV-Vis and fluorescence until $\text{U}(\text{VI})$ aqueous species were not detected. The $\text{UO}_2(\text{am})$ has been characterized by X-Ray Diffraction (XRD), previous and after the solubility experiments. On the other hand, 1g of $\text{UO}_2(\text{s})$, provided by ENRESA, has been used in the solubility experiment in presence of high PH_2 once it has been cleaned with HClO_4 (pH 3) followed with water and with 0.01M NaHCO_3 followed with water in order to minimize the possibility of the presence of oxidized phases on the surface. The $\text{H}_2(\text{g})$ is commercialized by Linde and it is specified as 99.999% of purity ($< 2 \text{ ppm O}_2$, $< 3 \text{ ppm N}_2$, $< 5 \text{ ppm H}_2\text{O}$, $< 0.5 \text{ ppm C}_n\text{H}_m$, CO_2 and CO are not specified).

Analytical techniques

ICP-MS analyses have been performed with an Agilent 7500cx. The solutions have been analysed after suitable dilution and acidification (using 2% nitric acid) to measure the concentration of uranium. For the time-resolved laser-induced fluorescence (TRFLS) measurements a Nd:YAG laser (20 Hz, 4–6 ns pulse duration, $\lambda = 266 \text{ nm}$, $E_{\text{max}} = 5 \text{ mJ}$, Polaris II, New Wave Research) is used. The hydrogen ion activity (pH) of the reacted solutions is measured with a CRISON 52-22 electrode. The Eh are measured with a conventional combined electrode CRISON 52-62 of Pt using Ag/AgCl as a reference. The reading time was around 30 minutes with a tolerated drift of 10mV in 10 minutes.

Results and Discussion

Thermodynamic database and ionic strength correction

The thermodynamic database used to model the experimental data is the ThermoChimie (Parkhurst and Appelo, 1999) and the constants have been corrected to the experimental ionic strength using the Specific Ionic Theory (SIT). Thermodynamic data for the $\text{Na}_2\text{U}_2\text{O}_7 \cdot x\text{H}_2\text{O}$ solid phase (not included in ThermoChime) have been selected from Yamamura et al. (1998).

Redox properties of the reducing agents used in this study

Two anoxic / reducing conditions have been used in this work (hydrogen and dithionite):

Hydrogen: $\text{H}_2(\text{g})$ is thermodynamically able to generate highly reducing conditions if reaction (1) is taken into account (see also Figure 1). However, it has been demonstrated in the literature (Shoesmith, 2008) the slow kinetics of this reaction in the absence of any catalyst (e.g. Pd, Pt, Mo). In cases where no catalyst is present, $\text{H}_2(\text{g})$ will act as inert gas providing anoxic instead of reducing conditions. Such conditions of inert atmosphere in aqueous solutions without additions of reducing or oxidising agents are described by Neck et al. (2007) as “redox-neutral” corresponding a value of $(\text{pH} + \text{pe}) = 13.8$.

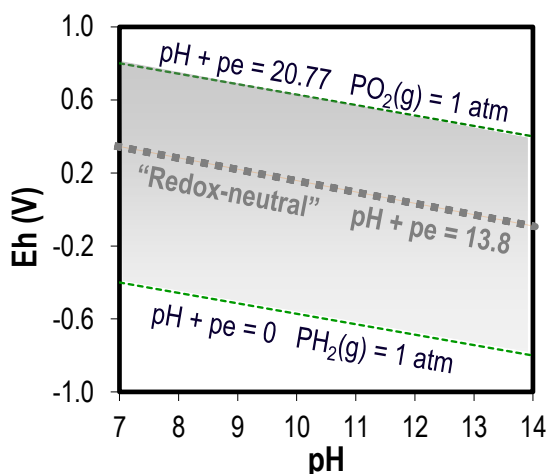
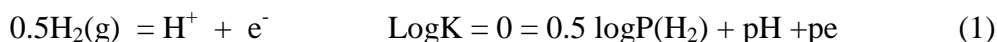


Figure 1. pH-Eh Predominance diagram of water stability (grey shadowed). The “redox-neutral” conditions are represented with grey dashed line.

Na-dithionite: To study the redox chemistry of dithionite in aqueous solution is important to understand the thermodynamic system of sulphur. Sulphur system under aqueous solution presents a rather complex chemistry mainly due to the formation of metastable species. A metastable diagram of sulphur system can be produced by eliminating the +VI oxidation state species (see Figure 2), which have a large activation energy barrier associated with their formation from lower oxidation state species (Kelsall and Thompson, 1992). However, some sulphur species have no areas of

predominance in the potential-pH diagrams even in metastable sulphur-water systems. These include dithionite species, which may be produced by electrochemical reduction of sulphite species, in neutral/slightly alkaline electrolytes.

It is widely reported in the literature (Chao et al. 1986, Ryan and Rai, 1983) the reducing properties of $S_2O_4^{2-}$ in aqueous solution, following the reaction (2). As shown in the predominance diagram of Figure 2 (right) water is not stable under the redox potential of the couple $S_2O_4^{2-}/SO_3^{2-}$

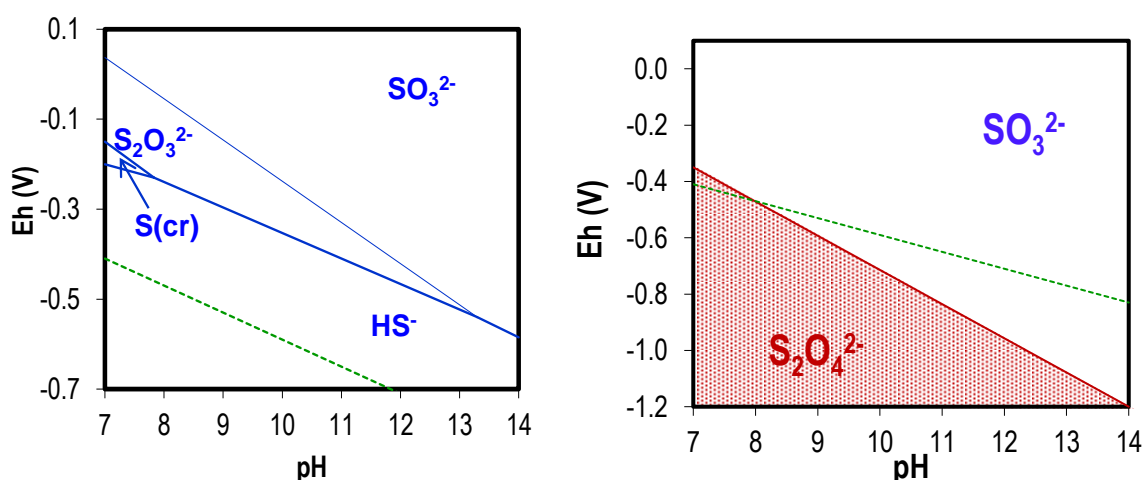
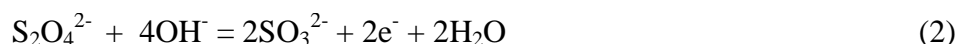


Figure 2. (left) Predominance diagram of sulphur system considering that the thermodynamic stable species SO_4^{2-} and HSO_4^- are not formed. Total concentration of sulphur used in the calculations is 0.01M. The green dashed line represent the water stability limit at $P_{H_2(g)} = 1 \text{ atm}$. **(Right)** Predominance diagram of sulphite/dithionite system excluding elemental sulphur and HS^- . Dithionite stability represented as red shadow. The green dashed line represent the water stability limit at $P_{H_2} = 1 \text{ atm}$.

The decomposition of $S_2O_4^{2-}$ has also been reported by several authors and despite being more favourable under acidic conditions it has been also proven to occur under alkaline conditions (Lister and Garvie, 1959; Szecsody et al., 2004). Carvalho and Schwedt (2001) performed polarographic measurements and determined that the decomposition products of $S_2O_4^{2-}$ in agreement with the mechanism (3) – (5) (mechanism also reported by Cermák and Smutek, 1975) were $S_2O_3^{2-}$, SO_3^{2-} , S^{2-} and $S(s)$ as shown in Figure 3 (left). The occurrence of reaction (6) instead of (5) under alkaline conditions has been reported by Siu, 1999.

Decomposition under alkaline conditions has been studied by Kilroy (1980). Kinetic investigations of Kilroy (1980) on $S_2O_4^{2-}$ decomposition under different pH conditions indicated that the kinetics of the process depend on the ratio $[NaOH]/[S_2O_4^{2-}]$. The kinetics of decomposition process of $6.5 \times 10^{-3} \text{ M}$ of $S_2O_4^{2-}$ under 0.1 and 1 M NaOH is shown in Figure 3 (right) and indicate that most of $S_2O_4^{2-}$ decomposes in 24 hours. The author also reported that in order to minimize decomposition at $pH > 12$, an excess of

alkali versus dithionite was preferable, however large excess of alkali (> 10-fold), enhanced the rate of dithionite decomposition.

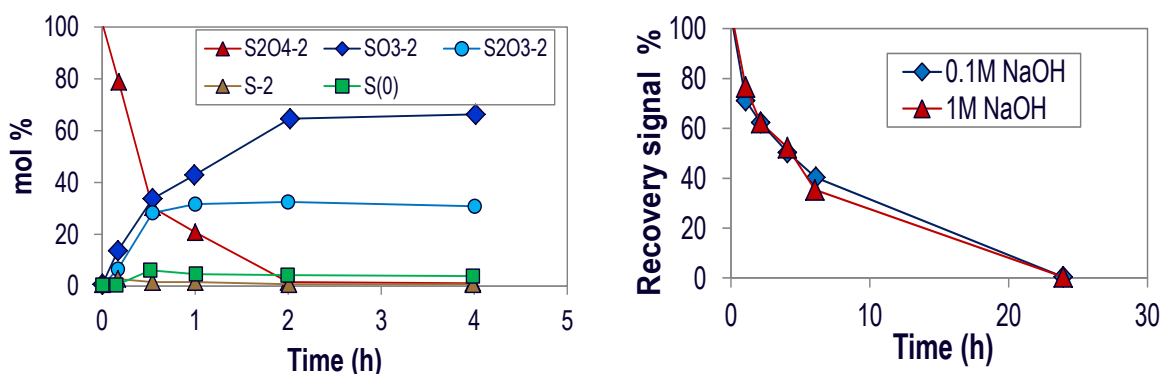
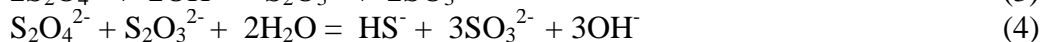
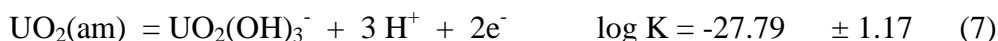


Figure 3. (Left) Decomposition of $6.5 \times 10^{-3} \text{ M}$ dithionite ($\text{pH} \sim 7.2$) and generated dithionite disproportion products with time. (Right) Decomposition of $6.5 \times 10^{-3} \text{ M}$ dithionite in 0.1 and 1 M of NaOH solution (previously deaerated with N_2) determined by polarographic signal intensity assigned to dithionite. Measurements performed with polarographic cell (Carvalho and Schwedt (2001)).

Solubility of $\text{UO}_2(\text{am})$ in presence of $\text{H}_2(\text{g})$

The $\text{UO}_2(\text{am})$ solubility has been studied under anoxic conditions in presence of different $\text{H}_2(\text{g})$ pressures at two different pH (9.4 and 11). In order to maintain a constant ionic strength, in all the cases, NaClO_4 has been used as inert electrolyte. Two different concentrations of NaClO_4 have been used depending of the experimental pH (0.01 M and 0.1 M in the case of experiments at $\text{pH} = 9.4$ and $\text{pH} = 11$, respectively).

For the solubility experiments performed in an autoclave at $\text{pH} = 9.4$ during 40 days in anoxic conditions with a constant overpressure of $\text{H}_2(\text{g})$ (1.8 bar) and using 0.01M NaClO_4 as electrolyte, the measured Eh with a Pt electrode was 0.2 ± 0.05 . This value is much higher than the expected one if considering the reducing properties of $\text{H}_2(\text{g})$ (see reaction (1) and Figure 1). The remaining question is what controls the measured Eh. As shown from the uranium predominance diagram (Figure 4), the measured redox potential seems to respond to oxidation of $\text{UO}_2(\text{am})$ following reaction (7).



The total uranium concentrations measured by ICP-MS after filtrating the solution with 2 nm pore size filter were $4.0 (\pm 0.2) \cdot 10^{-7} \text{ M}$. The uranium concentrations attributed to the aqueous species $\text{UO}_2(\text{OH})_3^-$ was quantified as $3.8 (\pm 0.7) \cdot 10^{-7} \text{ M}$ by fluorescence technique connected on-line to the autoclave. Taking into account the measured

uranium concentrations, the calculated Eh for the oxidative dissolution $\text{UO}_2(\text{am})$ following reaction (7) is 0.2 ± 0.04 V, in agreement with the measured Eh in the system.

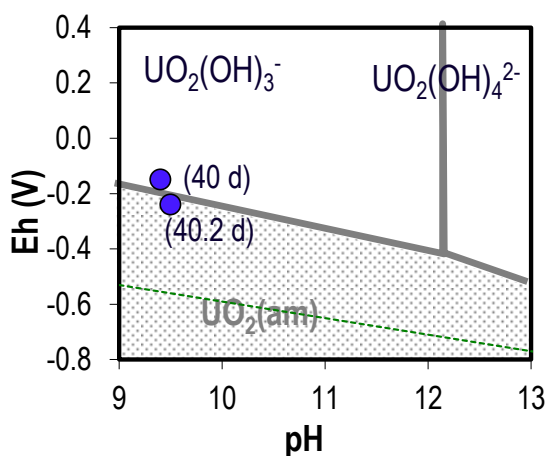
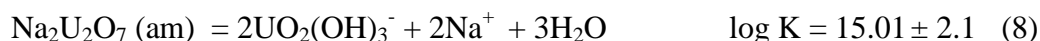


Figure 4. Eh/pH predominance diagram of uranium at the total uranium concentration measured at 40.2 days ($4 \cdot 10^{-7}$ M). Symbols represent measured pH / Eh data at reaction times of 40 and 40.2 days.

The $\text{UO}_2(\text{am})$ solubility has been also assessed under high $\text{H}_2(\text{g})$ pressure conditions and at $\text{pH} = 11$. The solution is initially set up at $\text{pH} = 11$ with NaOH and NaClO_4 (0.1 M) is used as electrolyte. With such an aim, the solubility of washed unirradiated- UO_2 pellet is performed in autoclave reactor using an initial $\text{H}_2(\text{g})$ pressure of 10 bars. The system is periodically sampled and at each sampling point the $\text{H}_2(\text{g})$ pressure was allowed to drop. The final $\text{H}_2(\text{g})$ pressure after six sampling operations is 6 bars (the final reaction time is 14 days).

The pH measurements indicated the pH is constant throughout the experiment and the Eh stabilized at ~ 0.25 V after 24 hours reaction time, despite the change of the total $\text{H}_2(\text{g})$ pressure. This measured Eh is well above the corresponding to H_2O in equilibrium with $\text{H}_2(\text{g})$ at the experimental pressure and also to the one characteristic of the redox pair U(IV)/U(VI) at the measured pH. Actually, the measured Eh is close to “redox-neutral” conditions (Neck et al., 2007) (see Figure 5, left).

The total measured U concentration after filtration is $7.8(\pm 0.4) \cdot 10^{-7}$ M, which is not in agreement with the oxidative dissolution of UO_2 at the measured Eh (see Figure 5 (right)). The fact that neither the measured Eh nor the U concentrations in solution are in agreement with the oxidative dissolution process of $\text{UO}_2(\text{am})$ led us to explore the possibility of secondary phase formation controlling the uranium concentrations in solution ($\text{Na}_2\text{U}_2\text{O}_7 \cdot x\text{H}_2\text{O}$). The solubility of $\text{UO}_2(\text{am})$ and $\text{Na}_2\text{U}_2\text{O}_7 \cdot x\text{H}_2\text{O}$ at $\text{pH} = 11$ are presented in Figure 5(right) as a function of Eh. It can be seen that the measured uranium concentration agrees with $\text{Na}_2\text{U}_2\text{O}_7 \cdot x\text{H}_2\text{O}$ (Yamamura et al. (1998)) governing the solubility of uranium according to reaction (8).



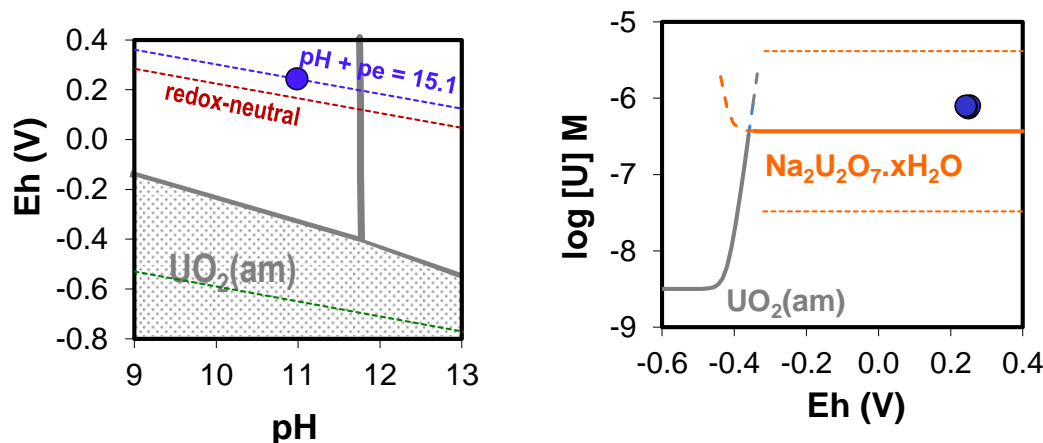


Figure 5 (Left). Eh/pH predominance diagram of uranium at uranium total concentration of $8 \cdot 10^{-7}$ M. The “redox neutral” conditions ($pH+pe=13.8$) have been represented as a dashed red line and the experimental $pH+pe=15.1$ is represented as a dashed blue line. The symbol represents the experimental data. **(Right)** Solubility curve of $UO_2(am)$ and $Na_2U_2O_7 \cdot xH_2O$ as a function of Eh at $pH = 11$ and $I = 0.1$ M. The dotted line represent the error associated to $Na_2U_2O_7 \cdot xH_2O$ solubility. The symbols represent the experimental uranium concentration and measured Eh.

Therefore, the thermodynamic study of $UO_2(am)$ solubility performed under alkaline conditions and different $H_2(g)$ pressures corroborate the poor performance of $H_2(g)$ to keep uranium as a tetravalent state in the absence of a catalyst (Trummer et al. 2008). The formation of an oxidized secondary phase of uranium suggests that a minimal part of U(VI) remained in the solid surface allowing a further precipitation of sodium uranate, which is the responsible of the measured uranium concentrations.

Solubility of $UO_2(am)$ in presence of dithionite.

Sodium dithionite has been widely used as a reducing agent to perform UO_2 solubility experiments under alkaline conditions (Ryan and Rai, 1983; Yajima et al., 1995; Fujiwara et al., 2005). These studies show that dithionite is able to keep reducing conditions although a complete investigation of the processes determining the redox potential of the system has not been performed. In this work, the solubility of freshly prepared $UO_2(am)$ has been measured at $pH = 10, 11$ and 12 and ionic strength of 0.1 M ($NaClO_4$) using two different dithionite concentrations (0.001 and 0.01 M).

The experimental pH and Eh measurements obtained from $UO_2(am)$ solubility experiments under 0.001 M of dithionite and initial pH 10 and 12 are presented in Figure 6 (left) overlapping the uranium and metastable-sulphur predominance diagram. The initial pH in the reactor ($pH_i = 10$) was periodically adjusted with NaOH. The corresponding uranium in solution was measured after 18 days reaction time and it is shown in Figure 6 (right). The figure shows that while measured Eh is near to redox-neutral conditions where uranium is expected to be present as U(VI), the measured total U concentration is characteristic of only mildly oxidized uranium system. The increase of the redox potential with time in both reactors suggests that the system is not in

equilibrium. These experimental data suggest that the decomposition of dithionite takes place (reaction (3)-(6)). As it can be seen in Figure 6 (right), the concentration of uranium in solution is apparently in agreement with the redox couple $\text{HS}^-/\text{S}_2\text{O}_3^{2-}$ maintaining $\text{pH} + \text{pe} = 3.7$, following reaction (9)

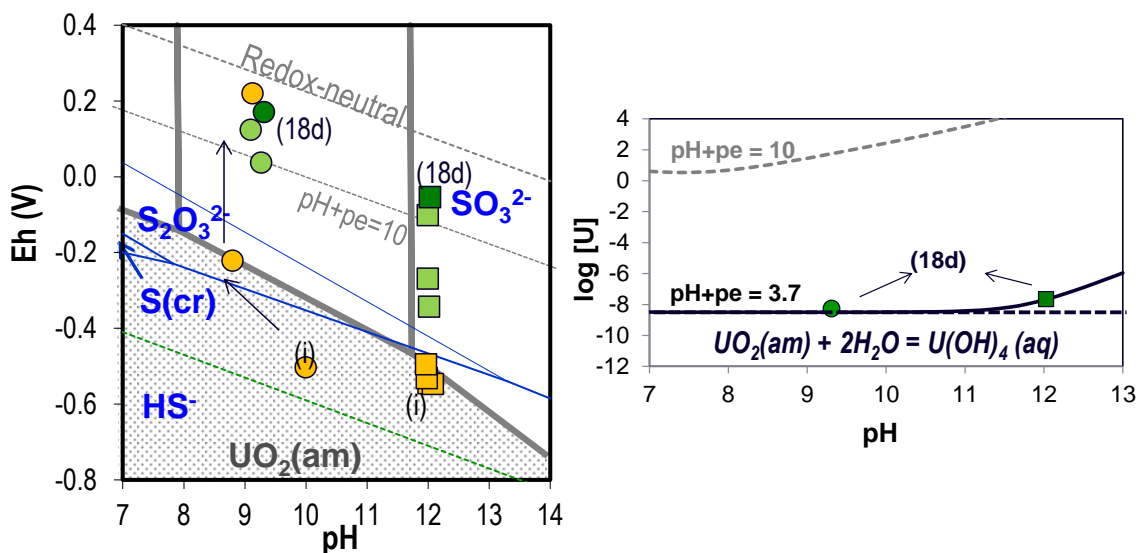
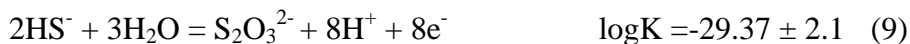


Figure 6. (Left) Eh/pH predominance diagram of uranium at $[U] = 1 \cdot 10^{-8} \text{ M}$ (grey solid lines) and sulphur at $[S] = 0.001 \text{ M}$ (blue solid lines). The green dashed line represents the water reduction at $P_t = 1 \text{ atm}$ and the grey dashed line represent the “redox-neutral” conditions. Symbols represent measured Eh and pH: circles represent data from reactor at initial pH 10 and squares represent data from reactor at initial pH 12. Yellow symbols represent reaction (RT) time < 7 and green symbols represent RT from 10 to 17, the deep green symbols represent RT = 18 days. **(Right)** $\text{UO}_2(\text{am})$ solubility calculated at $(\text{pH}+\text{pe}) = 3.7$, represented with solid line, and at $(\text{pH}+\text{pe}) = 10$, represented with grey dashed line. The symbols represent measure U in solution at RT = 18 days in the reactor $\text{pHi} = 10$ (round symbol) and in the reactor $\text{pHi} = 12$ (square symbol).

After 18 days period of reaction, 0.01M of Na-dithionite is added to each reactor. In Figure 7 (left), it is shown the measured pH and Eh of: a) solubility experiments performed at $\text{pHi}=10$ and $\text{pHi}=12$ after the addition of 0.01M $\text{S}_2\text{O}_4^{2-}$ (indicated with arrows) and reaction time < 10 days, b) solubility experiment performed at $\text{pHi}=11$ (reaction time < 10 days) and c) measurements performed in ICE exercise with cement solutions and using 0.005M Na-dithionite at reaction times ≤ 3 days (Tits and Gaona, (2011)). As it can be seen, the Eh in both reactors dropped to values characteristics of water reduction (see reaction (1)) and the pH also decreased. Figure 7 (right) indicates an increase of U in solution in both reactors after the addition of 0.01 M dithionite. Moreover, in reactor with $\text{pHi}=10$, it is detected the formation of a yellowish solid after 20 hours of the addition of dithionite. This solid has been characterized by SEM-EDX, confirming that the solid corresponds to $\text{S}(\text{s})$. These observations agreed with the fact

that the addition of $\text{S}_2\text{O}_4^{2-}$ produces $\text{H}_2(\text{g})$ (reaction (2) and (1)), which might have been activated in the Pt tip of the electrode, lowering the Eh to values characteristics of water reduction. On the other hand, the newly produced SO_3^{2-} by dithionite oxidation (reaction 2) shifts the equilibrium of reactions (5) and (6), depending on the pH, consuming the sulphide in solution, which seems to be the responsible of the limited oxidative dissolution of $\text{UO}_2(\text{am})$.

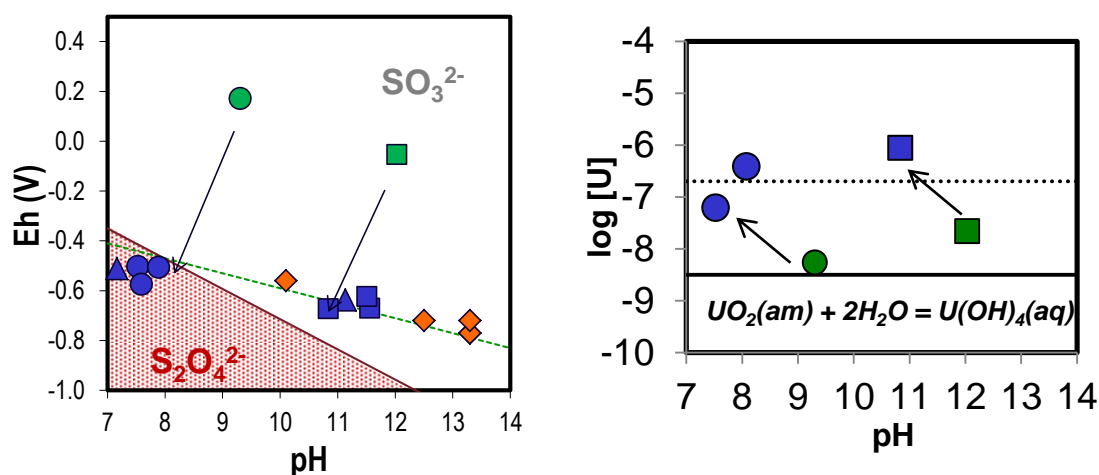


Figure 7. (Left) Eh/pH predominance diagram of dithionite. Symbols represent measured Eh and pH: circles represent data from reactor at pHi 10, triangles represent data from reactor at pHi 11, squares represent data from reactor at pHi 12. Green color correspond to RT = 18 days in 0.001M $\text{S}_2\text{O}_4^{2-}$ and blue color correspond to RT < 10 days in 0.01M $\text{S}_2\text{O}_4^{2-}$. Diamonds represent data obtained in ICE exercise. **(Right)** Solid and dashed line represent the $\text{UO}_2(\text{am})$ solubility calculated at $(\text{pH}+\text{pe}) = 0$ corresponding to no-oxidative dissolution and the associated error, respectively. The symbols represent measured U in solution in reactor pHi=10 (round symbol) and in the reactor pHi=12 (square symbol) at RT = 18 days (green color) and after the addition of 0.01M $\text{S}_2\text{O}_4^{2-}$ (blue color).

The study of the system in the reactor at pHi=12 with increasing reaction time is show in Figure 8 overlapping the uranium and metastable-sulphur predominance diagram. As mentioned above, the pH had a tendency to decrease during the first 10 days but after being adjusted with NaOH it maintains stable from 10 to 120 days. The representation indicates a progressive increase of the Eh and the measured data agree with the predominance of different redox pairs (Figure 8 left).

In Figure 8 (right, top) is presented the evolution of the measured Eh with reaction time in the reactor set up at pHi=12 together with the different redox pairs which can govern the Eh of the system at different RT. The graph indicates from 60 days up to the end of the experiment the measured Eh corresponds to the redox couple $\text{S}_2\text{O}_3^{2-}/\text{SO}_3^{2-}$. In Figure 8 (right, bottom) is presented the evolution of uranium concentration in solution together with the calculated uranium in equilibrium with the different sulphur redox pairs. The U in solution decreases and equilibrates with the redox pair $\text{HS}^-/\text{S}_2\text{O}_3^{2-}$ at reaction times higher than 30 days. Therefore, subsequent to the addition of 0.01M

dithionite sulphur speciation evolves with the different decomposition processes and sulphide is regenerated in solution decreasing the U concentration down to equilibrium with the redox pair $\text{HS}^-/\text{S}_2\text{O}_3^{2-}$.

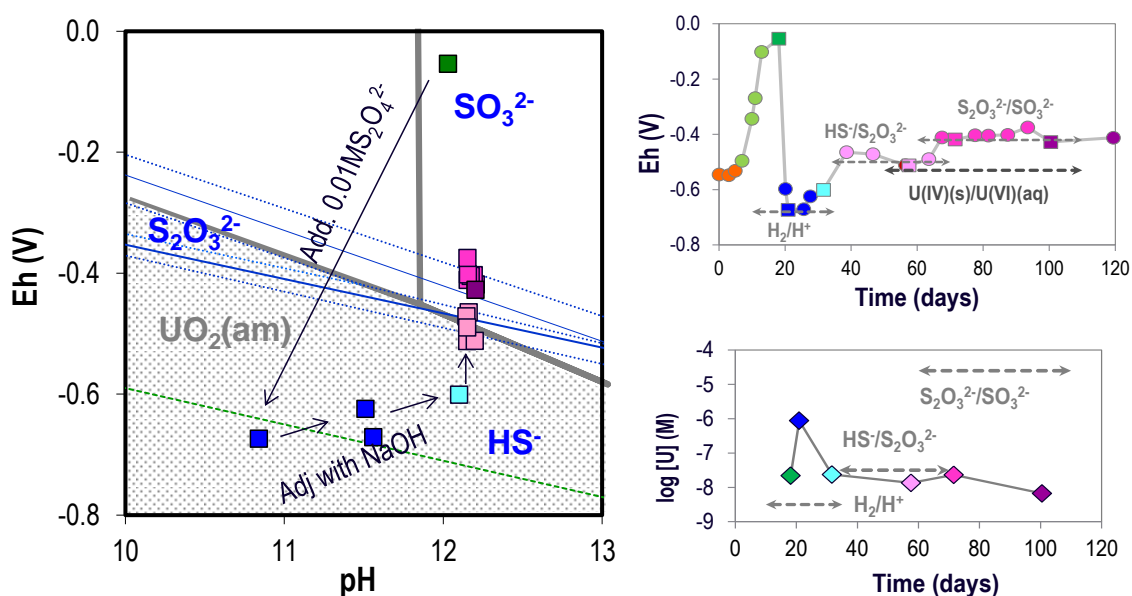


Figure 8 (Left). Eh/pH predominance diagram of uranium and sulphur (grey and blue solid lines, respectively). **Figure 8 (Right) (Top)** Evolution of measured Eh with reaction time in reactor $\text{pHi} = 12$ (represented as symbols) together with the different redox pairs able to govern the Eh of the system at different RT. **(Bottom)** Evolution of U in solution with the calculated uranium in equilibrium with the different redox pairs.

The experimental results obtained from $\text{UO}_2(\text{am})$ solubility experiment set up at $\text{pHi}=11$ in presence of 0.01M Na-dithionite indicated decrease of pH with time (pH was periodically readjusted with NaOH) and progressive increase of Eh suggesting that both the oxidation and the disproportion process of $\text{S}_2\text{O}_4^{2-}$ are taking place (reaction 2 and reaction 3-6) (figure not shown). By the end of the experiment, the measured Eh can be assigned to the redox pair $\text{S}_2\text{O}_3^{2-}/\text{SO}_3^{2-}$ and the U concentration in solution close to the equilibrium with the redox pair $\text{HS}^-/\text{S}_2\text{O}_3^{2-}$, in agreement with the experiments performed at $\text{pH} = 10$ and 12.

Comparison with literature data

For comparison exercise, uranium concentrations measured in this work have been plotted among other values reported in the literature from similar uranium solubility studies. As it can be seen measured concentrations in this work are in agreement with the ones measured in literature under similar redox conditions (see Figure 9).

The Eh measurements obtained in this study have also been compared with Eh measurements of other solubility studies performed with dithionite as reducing agent (see Figure 10). Fujiwara et al. (2001) measured after 3 months reaction time ($\text{pH}+\text{pe}$) = 10 in $\text{PuO}_2 \cdot x\text{H}_2\text{O}(\text{s})$ solubility experiments performed at pH 4 to 9 in presence of 0.001M of $\text{S}_2\text{O}_4^{2-}$. Also, redox measurements of Np(IV) hydrous oxide suspensions containing 0.05M dithionite as reducing agent after about 8 days of equilibration were

(pH+pe) = 4 (Rai and Ryan, 1984), characteristic of the sulphur redox pair $\text{S}_2\text{O}_3^{2-}/\text{SO}_3^{2-}$ at pH ~ 12 and in agreement with this work. As it can be seen in Figure 10, redox measurements depend on both reaction time and dithionite concentration used in the experiments.

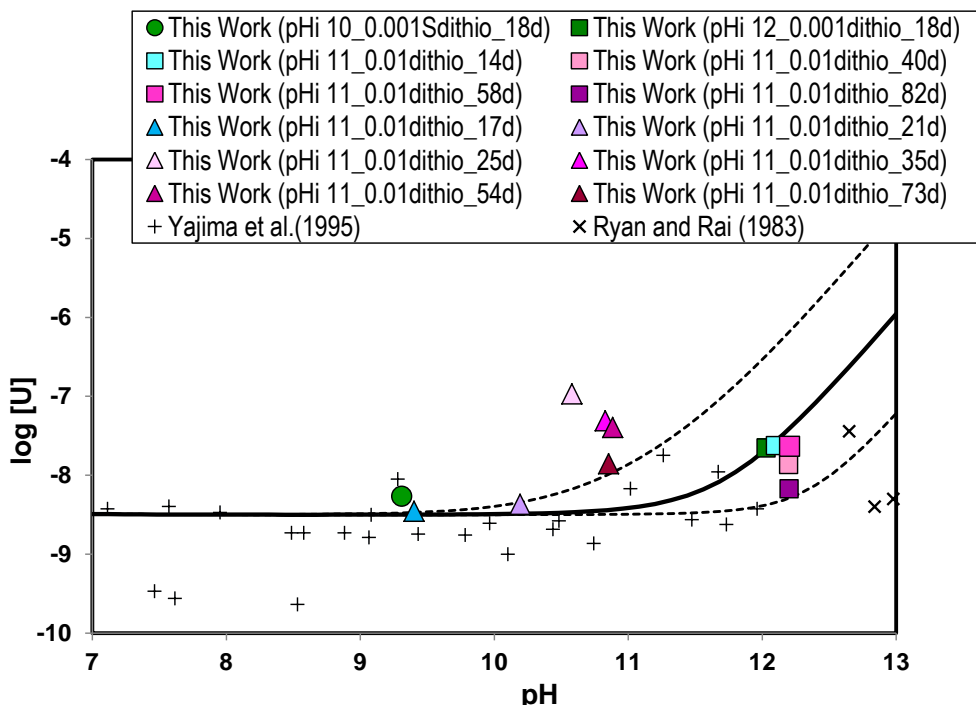


Figure 9. The symbols represent the $\text{UO}_2(\text{am})$ solubility data obtained in this work and reported in the literature in presence of dithionite as reducing agent and $I=0.1\text{M}$. (Left) Solid and dashed line (error) represent the $\text{UO}_2(\text{am})$ solubility calculated at $(\text{pH}+\text{pe}) = 3.7$, determined by the redox pair $\text{HS}^-/\text{S}_2\text{O}_3^{2-}$, and corresponding to the oxidative dissolution process and its associated error, respectively.

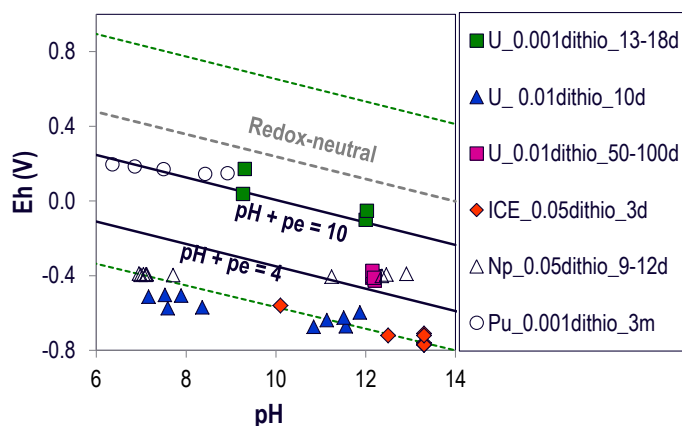


Figure 10. Measured pH-Eh in the $\text{UO}_2(\text{am})$ solubility experiments performed in this study at $\text{pHi}=12$ and in ICE exercise together with pH-Eh measurements reported in the literature from $\text{PuO}_2 \cdot x\text{H}_2\text{O}(\text{s})$ (Fujiwara et al. 2001) and $\text{NpO}_2 \cdot x\text{H}_2\text{O}(\text{s})$ (Rai and Ryan, 1984) solubility experiments.

Summary and conclusions

Despite the presence in the literature a whole bunch of studies dealing with $\text{UO}_2(\text{s})$ solubility under alkaline and reducing conditions, most of them lack of experimental measurements of redox potential. From the current study, the following conclusions can be drawn:

- (1) The experiments performed under $\text{H}_2(\text{g})$ atmosphere indicate that $\text{H}_2(\text{g})$ behaves as an inert gas without reducing properties. The measured Eh is in agreement with the occurring uranium processes in the system. At low Na concentration (0.01 M NaClO_4), the measured redox potential respond to the oxidative dissolution process of $\text{UO}_2(\text{am})$. However, at 0.1M NaClO_4 the measured redox potential corresponds to redox-neutral conditions and measured uranium concentrations are in agreement with a Na-uranate secondary phase controlling the U in solution.
- (2) The experiments performed with Na-dithionite as a reducing agent demonstrate the Eh measurements give response to different dithionite processes of oxidation and disproportion as a function of dithionite concentration, pH and reaction time.
- (3) Despite the variability in the redox potential, the measured U concentration in solution under the different studied conditions suggest that sulphide is controlling the oxidative dissolution process of $\text{UO}_2(\text{am})$.
- (4) It is necessary to properly understand the studied system in order to determine the redox couple responding to the measured Eh. In complex systems more than one redox pair can lead the redox measurement and it might not be in agreement with the redox pair controlling the uranium solubility.

Acknowledgement

The research leading to these results has received funding from the European Union's European Atomic Energy Community's (Euratom) Seventh Framework Programme FP7/2007-2011 under grant agreement n° 212287 (RECOSY project). AMPHOS 21 acknowledges Sandra Meca and Joan de Pablo from CTM Centre Tecnològic for their valuable contribution to the experimental studies.

References

- Carvalho, L.M and Schwedt, G. (2001) Polarographic determination of dithionite and its decomposition products: kinetic aspects, stabilizers, and analytical application. *Analytica Chimica Acta*, 436, 293-300
- Cermák, V. and Smutek, M. (1975) *Collect. Czech. Chem. Commun.* 40, 3241.
- Chao, M.S. (1986) The sulfite/dithionite couple: its standard potential and pourbaix diagram. *J. Electroche. Soc.: Electrochemical science and Technology*, 954.

- Fujiwara, K., Yamana, H., Fujii, T., Kawamoto, K., Sasaki, T., Moriyama, H. (2005) Solubility of uranium(IV) hydrous oxide in high pH solution under reducing conditions. *Radiochim. Acta.*, 93, 347-350.
- Fujiwara, K., Yamana, H., Fujii, T., Moriyama, H. (2001) Solubility product of plutonium hydrous oxide, *J. Nucl. Fuel Cycle Environ. (Jpn)*, 17
- Kelsall, G.H and Thompson, I. (1992) Redox chemistry of H₂S oxidation in the British Gas Stretford Process Part I: Thermodynamics of sulphur-water systems at 298 K.
- Kilroy, W.P. (1980) The iodometric determination of dithionite, thiosulphate and sulphite in the presence of alkali and/or cyanide. *Talanta*, 27, 343-347.
- Lister, M. W. and Garvie, R. C. (1959) Sodium dithionite, decomposition in aqueous solution and in the solid state. *Can. J. Chem.*, 37, 1567 – 1574.
- Neck V., Altmaier M., Fanghänel T. (2007) Solubility of plutonium hydroxides/hydrous oxides under reducing conditions and in the presence of oxygen. *C. R. Chimie*, 959-977
- Guillaumont, R., Fanghänel, J., Neck, V., Fuger, J., Palmer, D.A., Grenthe, I., Rand, M.H. (2003) *Chemical Thermodynamics 5. Update on the Chemical Thermodynamics of Uranium, Neptunium, Plutonium, Americium and Technetium*. NEA OECD, Elsevier.
- Parkhurst, D.L. and Appelo, C.A.J. (1999) PHREEQC v. 2.17.5: User's guide to Phreeqc (version 2) - A computer program for speciation, batch-reaction, one-dimensional transport, and inverse geochemical calculations. *Water-Resources Investigations Report 99-4259*.
- Ryan, J. L., Rai, D. (1983) The solubility of uranium(IV) hydrous oxide in sodium hydroxide solutions under reducing conditions. *Polyhedron*, 2, 947-952.
- Rai, D. and Ryan, J.L. (1984) Neptunium(IV) Hydrous Oxide Solubility under Reducing and Carbonate Conditions, 24, 3, 1985.
- Shoesmith, D.W. (2008) The Role of Dissolved Hydrogen on the Corrosion/Dissolution of Spent Nuclear Fuel Nuclear Waste Management Report, NWMO TR-2008-19.
- Siu, T. (1999) Kinetic and mechanistic study of aqueous sulfide-sulfite-thiosulfate system, Degree of Master, University of Toronto.
- Szecsody, J. E., Fruchter, J. S.; Williams, M. D.; Vermeul, V. E.; Sklarew, D. (2004) In situ chemical reduction of aquifer sediments: Enhancement of reactive iron phases and TCE dechlorination. *Env. Sci. Technol.* 38, 4656-4663.
- Tits J. and Gaona, X. (2011) Measurement of redox potentials in reference solutions with a combined redox electrode. Effect of measurement time. Comparison with thermodynamic calculations. In: *Intercomparison of redox determination methods on designed and near-natural aqueous systems*. Eds: Altmaier, M., Gaona, X., Fellhauer, D, Buckau, G, KIT Scientific report 7572
- Trummer, M., Nilsson, S., Jonsson, M. (2008) On the effects of fission product noble metal inclusions on the kinetics of radiation induced dissolution of spent nuclear fuel. *Journal of Nuclear Materials*, 378, 55.

Yajima, T., Kawamura, Y., Ueta, S. (1995) Uranium(IV) solubility and hydrolysis constants under reduced conditions. Sci. Basis Nucl. Waste Management XVIII, Symp. Proceedings, 353, 1137-1142.

Yamamura, T., Kitamura, A., Fukui, A., Nishikawa, S., Yamamoto, T., Moriyama, H. (1998) Solubility of U(VI) in highly basic solutions. Radiochimica Acta, 83, 139 – 146.

INVESTIGATIONS ON Np(VI) IN ALKALINE NaCl SOLUTIONS: AQUEOUS CHEMISTRY AND SOLID PHASE CHARACTERIZATION

Xavier Gaona^{1*}, David Fellhauer^{2,3}, Jörg Rothe¹, Marcus Altmaier¹

¹ Institut für Nukleare Entsorgung, Karlsruhe Institute of Technology, Karlsruhe (DE)

² European Commission, Joint Research Centre, Institute for Transuranium Elements
(EU)

³ Institut für Physikalische Chemie, Universität Heidelberg, Heidelberg (DE)

*Corresponding author: xavier.gaona@kit.edu

Abstract

Solubility experiments with Np(VI) were conducted in NaCl solutions ($0.1 \text{ M} \leq I \leq 5.0 \text{ M}$) to assess the thermodynamic properties of the aqueous species and solid compounds forming under alkaline conditions. The solubility controlling solid phases were characterized by XRD, chemical analysis and SEM-EDS, which indicated the prevalence of a solid phase with a Na:Np ratio 1:1, likely $\text{NaNpO}_2\text{O}(\text{OH})(\text{cr})$ (or $\text{Na}_2\text{Np}_2\text{O}_7 \cdot \text{H}_2\text{O}$). EXAFS further indicated the predominance of a neptunate-like structure with significantly short Np–O_{ax} and Np–O_{eq} distances ($1.76 \pm 0.02 \text{ \AA}$ and $2.12 \pm 0.03 \text{ \AA}$, respectively). In all cases, the solubility curve can be divided into three different regions: a: $\sim 7 \leq -\log[\text{H}^+] \leq \sim 9.5$, showing a steep decrease in the Np solubility with a slope between -2 and -3 ; b: $\sim 9.5 \leq -\log[\text{H}^+] \leq \sim 11$, with a nearly pH-independent [Np] and c: $\sim 11 \leq -\log[\text{H}^+] \leq \sim 13.5$, showing an increase in the solubility with a well-defined slope of $+1$. The slope analyses of these solubility data, together with the stoichiometries determined for the solid phases as well as direct analogies with U(VI), led to the definition of the equilibrium reactions $\text{NaNpO}_2\text{O}(\text{OH})(\text{cr}) + \text{H}_2\text{O} \rightleftharpoons \text{Na}^+ + \text{NpO}_2(\text{OH})_3^-$ and $\text{NaNpO}_2\text{O}(\text{OH})(\text{cr}) + 2\text{H}_2\text{O} \rightleftharpoons \text{Na}^+ + \text{NpO}_2(\text{OH})_4^{2-} + \text{H}^+$ to prevail in the regions “b” and “c” of the solubility curves. The equilibrium reaction controlling Np(VI) solubility in region “a” remains unclear, although it is suspected that reduction to Np(V) may have occurred under the $-\log[\text{H}^+]$ and E_h conditions of the experiment.

Introduction

The chemistry of Np(VI) under alkaline conditions remains largely unknown. In the aqueous phase, the formation of anionic species (e.g. $\text{NpO}_2(\text{OH})_3^-$ and $\text{NpO}_2(\text{OH})_4^{2-}$) has been proposed (Lemire et al., 2001), although no thermodynamic data are currently

selected in the NEA reviews (Guillaumont et al., 2003). The same thermodynamic data gap applies to Pu(VI), for which only first and second hydrolysis products ($\log^*\beta_{1,1}$ and $\log^*\beta_{1,2}$) are currently selected by the NEA. In analogy to U(VI), the precipitation of Na- and Ca-neptunates and plutonates is also expected to occur. The formation of these aqueous species and solid compounds may significantly limit the stability field of Np(V) and Pu(IV) in cementitious and saline environments, and therefore deserves further attention. In this work, solubility experiments were performed to determine the thermodynamic properties of Np(VI) aqueous species and solid compounds forming in alkaline NaCl solutions.

Experimental

Sample preparation and characterization

All samples were prepared and handled inside an inert gas (Ar) glovebox at $22 \pm 2^\circ\text{C}$. A $^{237}\text{Np(VI)}$ stock solution (with ~ 200 mg of Np) was obtained by electrochemical oxidation of Np(V) in HCl. By addition of the Np(VI) stock solution to alkaline 2.5 M NaCl solution ($-\log[\text{H}^+] \sim 12$), an immediate precipitation of a brownish solid phase occurred. After two months of equilibration in the same matrix solution, the resulting solid phase was characterized by XRD, chemical analysis and SEM-EDS, and distributed in 5 experimental series of increasing I (0.1 M, 0.5 M, 1.0 M, 2.5 M and 5.0 M NaCl), with $7 \leq -\log[\text{H}^+] \leq 14$. The amount of Np in each sample was ~ 5 mg. Oxidizing conditions ensuring the stability of Np(VI) were achieved by addition of 5×10^{-3} M NaClO. Samples were equilibrated for ~ 300 days; pH, E_h and [Np] were systematically monitored during this period.

Redox potentials were measured with a Pt combined electrode with Ag/AgCl reference system (Metrohm). A combined glass pH electrode (type ROSS, Orion), freshly calibrated against dilute standard pH buffers (pH 1–13, Merck), was used to determine the molal H^+ concentration $[\text{H}^+]$. In salt solutions of ionic strength $I \geq 0.1 \text{ mol}\cdot\text{kg}^{-1}$, the measured pH value (pH_{exp}) is an operational apparent value, which is related to $[\text{H}^+]$ by $-\log[\text{H}^+] = \text{pH}_{\text{exp}} + A$ (Altmaier et al., 2003a).

The aqueous concentration of Np was measured after 10 kD ultrafiltration (Pall Life Sciences) by liquid scintillation counting (LSC). Previous test (Altmaier et al., 2005) had shown the correct performance of these membrane filters (non sorption of neutral and negatively charged species). Solid phase was characterized by XRD, chemical analysis, and SEM-EDS in selected samples. For this purpose, a small amount (~ 1 mg) of the solid phase was separated from the solution and washed 5 times with ethanol (2 mL) under Ar-atmosphere to remove the matrix solution (NaCl). The largest fraction of the resulting solid was considered for XRD analysis. A second fraction was characterized by scanning electron microscope – energy disperse spectrometry (SEM-EDS), using a CamScan FE44 SEM equipped with a Noran EDS unit. After the XRD measurement, the solid phase was dissolved in 2% HNO_3 , and analyzed for neptunium and sodium concentration by LSC and ICP-OES, respectively.

XAFS measurements

XANES/EXAFS spectra were recorded at the INE–Beamline for Actinide Research at ANKA, KIT Campus Nord (Dardenne et al., 2009). The ANKA storage ring was operated at 2.5 GeV electron energy, with a mean electron current of 120 mA. Tuneable monochromatic beam was delivered by the Ge(422) crystal pair in the Lemonnier–type double crystal monochromator (DCM). Higher harmonics were rejected from the two mirrors in the optics of the INE–Beamline and by detuning the second crystal at a constant, controlled 70 % from the rocking curve maximum (Denecke et al., 2005).

At least four scans were performed for each Np sample, and the spectra were averaged for XANES/EXAFS data analysis. Spectra were recorded at $22 \pm 2^\circ\text{C}$ in fluorescence mode using a 5–pixel low energy Ge solid–state detector (Canberra–Packard Ultra–LEGe, Rüsselsheim, Germany) and Ar–filled ionization chamber to record the incident beam intensity. All spectra were energy calibrated using the first inflection point in the K–edge spectrum of a zirconium metal foil (17998 eV).

XANES/EXAFS data reduction was performed with the ATHENA package following standard procedures (Ravel and Newville, 2005). Structural information was obtained using the multi–shell approach for EXAFS data fitting implemented in the feffit code (v2.98, Stern et al. 1995). The fit yields parameters describing the Np coordination to surrounding oxygen and neptunium atoms (neighbouring atomic distances (R), EXAFS Debye–Waller factors (σ^2), coordination numbers (N) and relative shift in ionization energy E_0 (ΔE_0)). EXAFS spectra were Fourier transformed (FT) in the k–range between ~ 2.7 and 15 \AA^{-1} using symmetric square windows with Hanning sills. Theoretical single scattering paths (SS) were calculated with FEFF8.4 (Rehr and Albers, 2000) using the structure of $\beta\text{-Na}_2\text{UO}_4$ (Gasperin, 1985), where the central U atom was substituted by Np.

Results and discussion

Solid phase characterization

Portions of the solid phase taken from the initial material (before distributing it to the solubility samples) and from five selected batch samples after 200–300 days of equilibration were characterized by the methods described above. Chemical analysis and SEM–EDS indicate a Np:Na ratio ~ 1 in those solid samples characterized (see Table 1). Moreover, XRD data collected for these samples clearly indicate that the same solid phase is controlling the solubility in these systems (Figure 1), and further that the initially added solid is stable under the given conditions (no indications for a transformation). A relatively good agreement of these data has been obtained with XRD patterns reported elsewhere for $\text{Na}_2\text{Np}_2\text{O}_7$ (Keller et al., 1965). The agreement is very good in terms of peak position, but incomplete in terms of relative intensities of these peaks, thus indicating slight structural differences between the solid phases obtained in this work and reported in Keller et al. (1965). It is worth mentioning that Keller and co–workers obtained $\text{Na}_2\text{Np}_2\text{O}_7$ after mixing Na_2O and NpO_3 with a 1:1 ratio at 400°C . An additional increase of the temperature led to the formation of $\alpha\text{-Na}_2\text{NpO}_4$ ($T > 500^\circ\text{C}$) and $\beta\text{-Na}_2\text{NpO}_4$ ($T = 800^\circ\text{C}$). The further heating of the Na–Np(VI) solid (for any

initial Np:Na ratio) to 1000°C directly resulted in NpO₂ without the formation of any intermediate Np(V) compound.

Table 1: Ratio Np:Na in the solid phase determined by chemical analysis and SEM–EDS.

I [M]	$-\log[H^+]$	Np:Na (chemical analysis)	Np:Na (SEM–EDS)
0.1	12.8	1.1	n.m.
1.0	12.3	1.2	n.m.
2.5	12.6	1.1	0.95

Figure 2 shows experimental and theoretical k^2 –weighted Np L_{III}–edge EXAFS spectra and corresponding Fourier transforms obtained for the Np(VI) solid phase at $I = 2.5$ M NaCl and $-\log[H^+] = 12.6$. The structural parameters resulting from the fit are provided in Table 2.

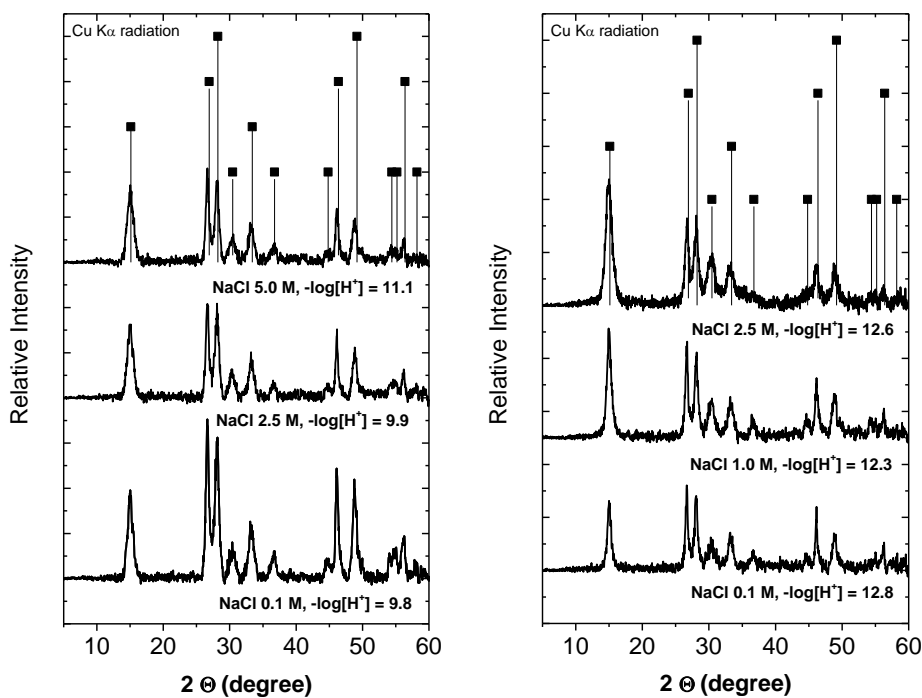


Figure 1: XRD spectra of selected solid phases from solubility experiments at $I = 0.1$ M, 1.0 M, 2.5 M and 5.0 M NaCl. Squares mark peak positions and relative intensities reported in Keller et al. (1965) for Na₂Np₂O₇.

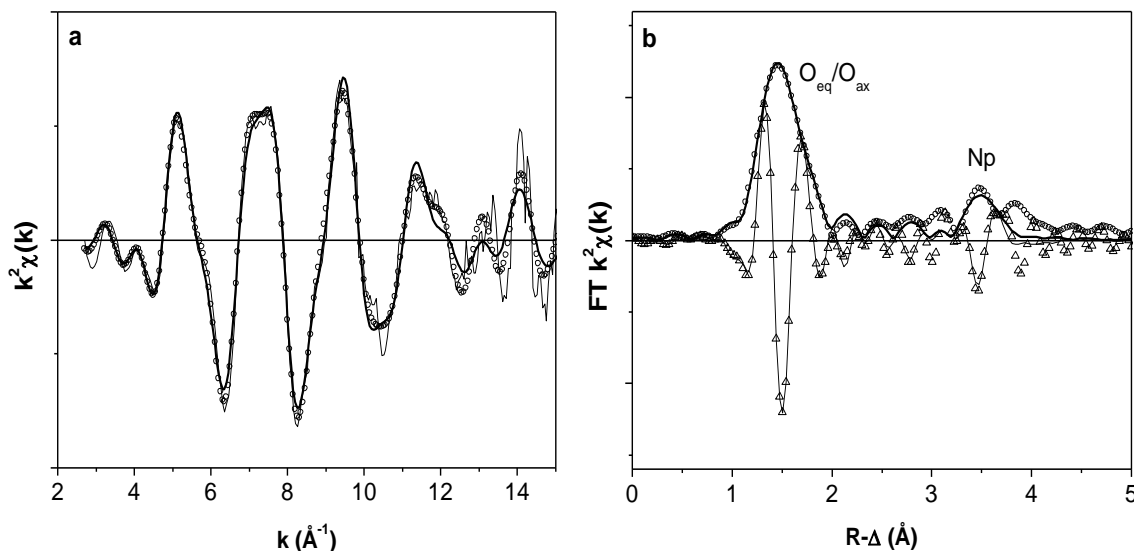


Figure 2: (a) Experimental and theoretical k^2 -weighted Np L_{III} -edge EXAFS spectra, and (b) Fourier transforms (modulus and imaginary parts) for the Np(VI) solid phase equilibrated in 2.5 M NaCl and $-\log[H^+] = 12.6$

Table 2: Structural parameters determined for the Np(VI) solid phase equilibrated in 2.5 M NaCl and $-\log[H^+] = 12.6$. Amplitude reduction factor (S_o^2) fixed to 1.0.

Shell	N	R [\AA]	σ^2 [\AA^2]	ΔE_0 [eV]	R-factor [%]
O_{ax}	0.5 ± 0.2	1.76 ± 0.02	0.0023	-7.54 ^a	2.3
O_{eq}	1.0 ± 0.3	2.12 ± 0.03	0.0002	-7.54 ^a	
Np	1.8 ± 0.5	3.71 ± 0.05	0.0078	-9.11	

a. general parameter for several shells

Significantly short Np– O_{ax} and Np– O_{eq} distances were determined from the fit of EXAFS data. These distances agree (within their uncertainties) with data recently reported for solid Np(VI) forming in alkaline TMA–OH solutions (1.80 ± 0.02 and 2.18 ± 0.04 , respectively; Gaona et al., 2011). The small coordination numbers fitted for both O_{ax} and O_{eq} can only be explained by the presence of destructive interferences between different O–backscatterers forming the Np coordination polyhedron; definitively higher N values are to be expected for Np(VI) under these experimental conditions.

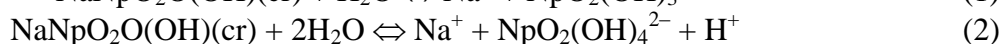
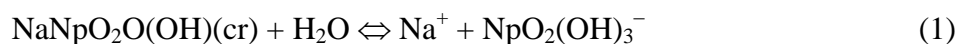
Solubility data and thermodynamic modelling

A summary of the Np(VI) solubility data determined for the five systems considered ($I = 0.1$ M, 0.5 M, 1.0 M, 2.5 M and 5.0 M NaCl) is shown in Figure 3. Samples for which solid phase characterization was performed are marked in the figure.

Three different regions/trends can be identified in the solubility data in Figure 3. These regions/trends may be derived in the different I series considered in the study:

- region a: $\sim 7 \leq -\log[H^+] \leq \sim 9.5$, showing a steep decrease in the solubility with a slope between -2 and -3 (not completely defined).
- region b: $\sim 9.5 \leq -\log[H^+] \leq \sim 11$, with a nearly pH-independent $[Np]$. Except for $I = 5.0$ M NaCl, solubility data for $t = 74 - 305$ days indicate that samples in this region are not yet in thermodynamic equilibrium. This region represents the solubility minimum of the curve ($10^{-7} - 10^{-8}$ M).
- region c: $\sim 11 \leq -\log[H^+] \leq \sim 13.5$, showing an increase in the solubility with a well-defined slope of $+1$.

Regions “b” and “c” agree very well with observations previously reported for U(VI) under similar experimental conditions (Altmaier et al., 2003b). According with these similarities and taking into account the results from solid phase characterization and slope analysis of the solubility curves, the equilibrium reactions (1) and (2) are proposed for regions “b” and “c”, respectively. Note that these reactions have been defined considering the same number of hydration H_2O as reported in Altmaier et al. (2003b) for U(VI) under analogous experimental conditions. This assumption is to be assessed by thermogravimetry experiments.



Two characteristic features were observed for those samples in region “a”: first, the Np concentration is unexpected high (with regard to previous U(VI) study under similar conditions); second: a continuous decrease of the redox potentials E_h with time was found from $+(800 \text{ to } 1000)$ mV to $+(500 \text{ to } 700)$ mV (data not shown). This is probably related to the degradation of NaClO and might be linked with a partial reduction of Np(VI) to Np(V). The solubility of $Np^V O_2 OH(am)$ under these $-\log[H^+]$ and I conditions is significantly higher (Neck et al., 1992; Petrov et al., 2011); we hypothesize that the equilibrium reaction $NaNpO_2O(OH)(cr) + 3H^+ + e^- \Leftrightarrow Na^+ + NpO_2^+ + 2H_2O$ is controlling both E_h and $[Np]$ in the system (slope of -3 to be expected), although other interpretations may also apply (*i.e.* partial formation of $Np^{VI} O_3(s)$ or $NaNp^V O_2(OH)_2(s)$). This hypothesis is to be experimentally assessed by solid phase characterization and VIS-NIR spectroscopy of the aqueous phase.

The specific ion interaction theory (SIT) was considered to derive $\log^{\circ} K_{s,1,4}^*$ and $\Delta \epsilon$ for the equilibrium reaction (2) (Figure 4). Reaction (1) was disregarded in this step because thermodynamic equilibrium had not been reached (even after 305 days, see discussion above). The combination of experimental $\Delta \epsilon$ with $\epsilon(H^+, Cl^-) = 0.12 \text{ kg} \cdot \text{mol}^{-1}$ and $\epsilon(Na^+, Cl^-) = 0.03 \text{ kg} \cdot \text{mol}^{-1}$ reported in Guillaumont et al. (2003) allowed the calculation of $\epsilon(Na^+, NpO_2(OH)_4^{2-})$. Conditional $\log^{\circ} K_{s,1,4}^*$ determined experimentally, as well as calculated $\log^{\circ} K_{s,1,4}^*$ and $\epsilon(Na^+, NpO_2(OH)_4^{2-})$ are summarized in Table 3. Note that these values might be subject of further modifications as a result of the thermogravimetry experiments (see above).

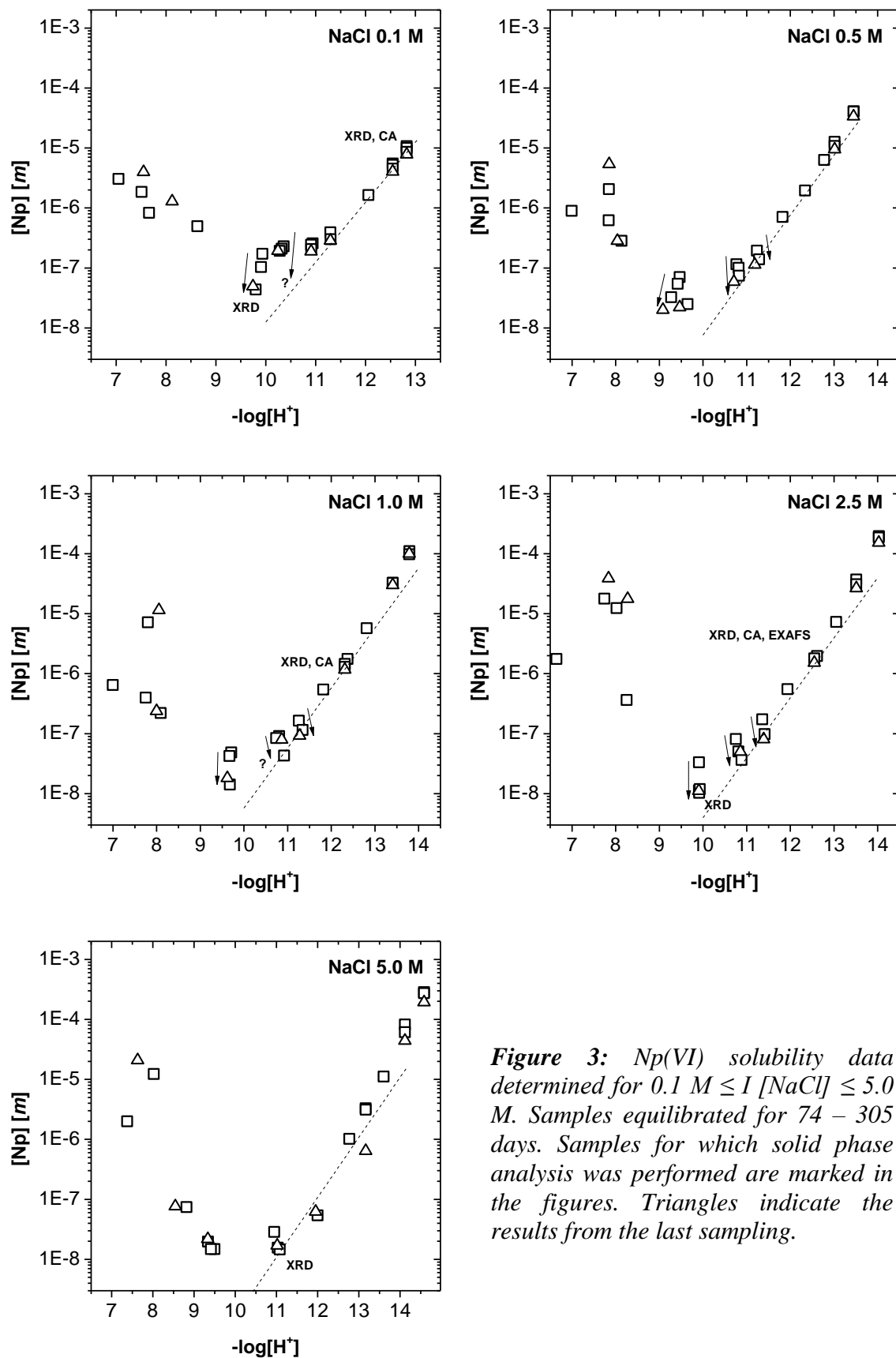


Figure 3: *Np(VI) solubility data determined for $0.1 \text{ M} \leq I [\text{NaCl}] \leq 5.0 \text{ M}$. Samples equilibrated for 74 – 305 days. Samples for which solid phase analysis was performed are marked in the figures. Triangles indicate the results from the last sampling.*

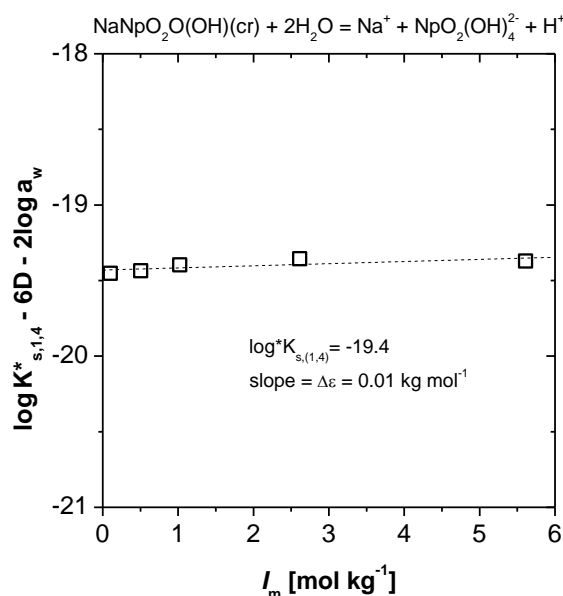


Figure 4: Determination of $\log^*K_{s,(1,4)}^o$ based on the extrapolation to $I = 0$ by linear SIT regression.

Table 3: Conditional equilibrium constants $\log^*K_{s,(1,4)}$ (molal scale) for the reaction $\text{NaNpO}_2\text{O}(\text{OH})(\text{cr}) + 2\text{H}_2\text{O} \rightleftharpoons \text{Na}^+ + \text{NpO}_2(\text{OH})_4^{2-} + \text{H}^+$ and preliminary data for $\log^*K_{s,(1,4)}^o$ and $\varepsilon(\text{Na}^+, \text{NpO}_2(\text{OH})_4^{2-})$ calculated according with SIT.

[NaCl]		$\log^*K_{s,(1,4)}$	$\log^*K_{s,(1,4)}^o$	$\varepsilon(\text{Na}^+, (1,4))$
$\text{mol}\cdot\text{L}^{-1}$	$\text{mol}\cdot\text{kg}^{-1}$			
0.1	0.10	-18.8		
0.5	0.51	-18.4		
1.0	1.02	-18.2		
2.5	2.61	-18.0		
5.0	5.61	-18.0		
$I = 0$			-19.4	-0.16

Summary and Conclusions

Solubility experiments and solid phase characterization of Np(VI) systems in alkaline NaCl solutions have shown the predominance of Na–neptunate phases with Np:Na ratio ~ 1 , likely $\text{NaNpO}_2\text{O}(\text{OH})(\text{cr})$ (or $\text{Na}_2\text{Np}_2\text{O}_7\cdot\text{H}_2\text{O}(\text{cr})$). Based on the slope analysis of the solubility data, the aqueous species $\text{NpO}_2(\text{OH})_3^-$ and $\text{NpO}_2(\text{OH})_4^{2-}$ were defined to be in equilibrium with this solid in the pH-range 9 to 14. Thermodynamic equilibrium after 305 days was only assumed for the reaction $\text{NaNpO}_2\text{O}(\text{OH})(\text{cr}) + 2\text{H}_2\text{O} \rightleftharpoons \text{Na}^+ + \text{NpO}_2(\text{OH})_4^{2-} + \text{H}^+$, for which $\log^*K_{s,(1,4)}^o$ and $\varepsilon(\text{Na}^+, (1,4))$ were determined according

with the SIT theory. None of these aqueous species and solid compounds of Np(VI) is currently selected in the NEA thermodynamic reviews (Guillaumont et al., 2003).

These results further indicate the potential relevance of Na–Np(VI) solid phases in controlling Np(VI) solubility in cementitious and NaCl–dominated saline environments.

Acknowledgement

V. Petrov (Moscow State University) is kindly acknowledged for the purification of the ²³⁷Np stock solution. The contribution of M. Böttle and E. Soballa (KIT–INE) to ICP–OES and SEM–EDS analysis is highly appreciated. Special thanks are due to J. Tits and E. Wieland (Paul Scherrer Institut) for stimulating discussions on Np chemistry under hyperalkaline conditions. The research leading to these results has received funding from the European Union's European Atomic Energy Community's (Euratom) Seventh Framework Programme FP7/2007–2011 under grant agreement n° 212287 (RECOSY project).

References

Altmaier, M., Metz, V., Neck, V., Muller, R., Fanghanel, T. (2003a). Solid-liquid equilibria of Mg(OH)₂(cr) and Mg₂(OH)₃Cl·4H₂O(cr) in the system Mg–Na–H–OH–O–Cl–H₂O at 25 degrees C. *Geochimica et Cosmochimica Acta*, 67, 3595–3601.

Altmaier, M., Neck, V., Metz, V., Müller, R., Schlieker, M., Fanghanel, Th. (2003b). Solubility of U(VI) in NaCl and MgCl₂ solution. *Proceedings of the Migration 2003 Conference*, Gyeongju (Korea).

Altmaier, M., Neck, V., Müller, R., Fanghanel, Th. (2005). Solubility of ThO₂·xH₂O(am) in carbonate solution and the formation of ternary Th(IV) hydroxide-carbonate complexes. *Radiochimica Acta*, 93, 83–92.

Dardenne, K., Brendebach, B., Denecke, M.A., Liu, X., Rothe, J., Vitova, T. (2009). New developments at the INE-Beamline for actinide research at ANKA, in 14th International Conference on X-ray Absorption Fine Structure (XAFS14), Camerino (Italy).

Denecke, M.A., Rothe, J., Dardenne, K., Blank, H., Hormes, J. (2005). The INE-beamline for actinide research at ANKA. *Physica Scripta*, T115, 1001–1003.

Gaona, X., Tits, J., Dardenne, K., Liu, X., Rothe, J., Denecke, M. A., Wieland, E., and Altmaier, M. (2011). Spectroscopic investigations of Np(V/VI) redox speciation in hyperalkaline TMA–OH solutions. *Radiochimica Acta* (submitted).

Gasperin, M. (1985). Synthèse en monocristaux et structure du monouranate de sodium β-Na₂UO₄. *Journal of Solid State Chemistry*, 60, 316–319.

Guillaumont, R., Fanghanel, J., Neck, V., Fuger, J., Palmer, D.A., Grenthe, I., Rand, M.H.: *Chemical Thermodynamics Vol. 5. Update on the Chemical Thermodynamics of Uranium, Neptunium, Plutonium, Americium and Technetium*. (OECD, NEA-TDB) Elsevier, North Holland, Amsterdam (2003).

- Keller, C., Koch, L., Walter, K.H. (1965). Die Reaktion der Oxide der Transurane mit Alkalioxiden – I: Ternäre Oxide der sechswertigen Transurane mit Lithium und Natrium. *Journal of Inorganic Nuclear Chemistry*, 27, 1205-1223.
- Lemire, R. J., Fuger, J., Nitsche, H., Potter, P. E., Rand, M. H., Rydberg, J., Spahiu, K., Sullivan, J. C., Ullman, W. J., and Vitorge, P., Wanner, H. (2001). *Chemical Thermodynamics 4. Neptunium and Plutonium*. NEA OECD, Elsevier.
- Neck, V., Kim, J.I., Kanellakopulos, B. (1992). Solubility and hydrolysis behaviour of Neptunium(V). *Radiochimica Acta*, 56, 25-30
- Petrov, V., Gaona, X., Fellhauer, D., Dardenne, K., Kalmykov, S., Altmaier, M. (2011). Np(V) solubility and solid phase transformation in dilute to concentrated NaCl solutions. *Proceedings of the Migration 2011 Conference*, Beijing (China).
- Ravel, B., Newville, M. (2005). ATHENA, ARTEMIS, HEPHAESTUS: data analysis for X-ray absorption spectroscopy using IFEFFIT. *Journal of Synchrotron Radiation*, 12, 537-541.
- Rehr, J.J., Albers, R.C. (2000). Theoretical approaches to x-ray absorption fine structure. *Reviews of Modern Physics*, 72, 621-654 (2000).
- Stern, E. A., Newville, M., Ravel, B., Yacoby, Y., Haskel, D. (1995). The UWXAFS analysis package: philosophy and details. *Physica B*, 208&209, 117-120.

DIELECTRIC MONITORING OF DRY PYRITE DURING ITS EXPOSURE TO AIR OR PURE OXYGEN

Michel Perdicakis*, Romuald Thomahowski, Cindy Malhomme

Laboratoire de Chimie Physique et Microbiologie pour l'Environnement (LCPME)
UMR 7564, Nancy-Université – CNRS, 54602 Villers-lès-Nancy Cedex (FR)

* Corresponding author: perdi@lcpme.cnrs-nancy.fr

Abstract

Dielectric measurements were performed during the stepwise exposure of dry pyrite microparticles (40-80 μm range) to ambient air or pure oxygen. Each oxidation step generally leads to an increase of the particles impedance, and the Nyquist diagrams shape progressively changes. When the samples are kept in anoxic conditions after an oxidation step, the impedance is apt to decrease to lower values; however, sometimes complex and still unexplained phenomena occur. In the framework of the nuclear spent fuel deep repository, these impedance changes could significantly modify the reactivity of pyrite contained in argillaceous rocks after construction of the underground installations and atmospheric oxygen penetration in the excavation zone.

Introduction

In many countries, it is planned that the long life highly radioactive nuclear spent fuel will be stored in deep argillaceous rocks. The sites selected for this purpose are anoxic and satisfy several recommendations as mechanical stability, low permeability and low redox potential. Pyrite (FeS_2), iron(II) carbonate, iron(II) bearing clays and organic matter that are present in very small amounts (about 1% w:w) in soils play a major role in their reactivity and are considered today as responsible for the low redox potential values of these sites (*Ignatiadis et al. 2010, Pearson et al. 2003*). That is why pyrite has been the subject of numerous studies investigating its reactivity toward various nuclides as uranium, selenium and iodide as well as against oxidation. Indeed, if pyrite is stable in deep geological environments under reducing conditions, it will be oxidized during mining works and after construction of the underground installations when atmospheric oxygen of open galleries will enter the clay formation in the excavation disturbed zone (*De Cannière et al. 2008*).

Dielectric measurements using high-frequency electromagnetic fields are extremely sensitive to small changes in material properties. Indeed, molecular relaxation of the order of only a few nanometers involves dipole changes that can be observed by

dielectric, or impedance, spectroscopy (Núñez *et al.* 2004). This technique has been already successfully applied to study interfacial phenomena in various areas, such as polymeric materials (Mijovic *et al.* 1998), semiconductors (Bueno *et al.* 2007) carbon (Basu *et al.* 2008), metallic (Tsangaris *et al.* 1996) and other materials. Moreover, it has been used to monitor the aggregation of clays (Roy *et al.* 2000) and the reactivity of natural minerals, conducting (Etahiri *et al.* 1997) or not conducting (Bessière *et al.* 1990), mainly for the better understanding of ores flotation mechanisms (Bessière *et al.* 1989).

This study was initiated by an attempt to use dielectric spectroscopy to in-situ monitor the interactions of pyrite with soluble selenium and iodide species. During preliminary experiments on the characterization of dry pristine pyrite, that were performed just after its anoxic grinding, we have remarked that once this mineral was exposed to air for a short time its impedance rose rapidly. However, along the stay of pyrite in the hermetically closed dielectric cell, its impedance progressively decreased and finally became almost the same as that before the exposure to air. It was as if pyrite had “repaired” the damage induced by its exposure to air. We considered that the observed phenomenon was worth being explored further: (i) because of the importance of the pyrite oxidation during the mining works in relation the underground installations construction and (ii) for avoiding the misinterpretation of other dielectric measurements on pyrite reactivity. In this way, we performed four series of dielectric measurements (of about a month each) where pyrite particles were stepwise exposed to air, or to pure oxygen, for increasing periods of time. After each oxidation step, we waited until the measured impedance was stabilized before progressing to the next step.

Experimental

Pyrite

Pyrite samples came from Logroño, Spain (pyrite SP) and Peru (pyrite P). The major impurity of the Spanish pyrite is arsenic; this impurity has probably some connection with the fact that the electrical resistance of pyrite P (measured with a multimeter) is about 1000 times higher than that of pyrite SP.

Instrumentation

Dielectric measurements were carried out at room temperature and in a frequency ranging from 0.1 to 100 MHz, by using the model 4194 A impedance/gain-phase analyser connected to its measurement unit (Hewlett Packard). The impedance meter was connected to a computer via a GPIB interface and monitored by an application that we created using the TestPointTM software. Experiments were made in previously standardised homemade capacitive cells (Fig. 1). Static measurements were performed with an axial cell (Fig. 1 A), that is equipped with a tight fitting stopper, and measurements with flowing air or oxygen were made using a cylindrical cell that was adapted to the gas circuit (Fig. 1 B).

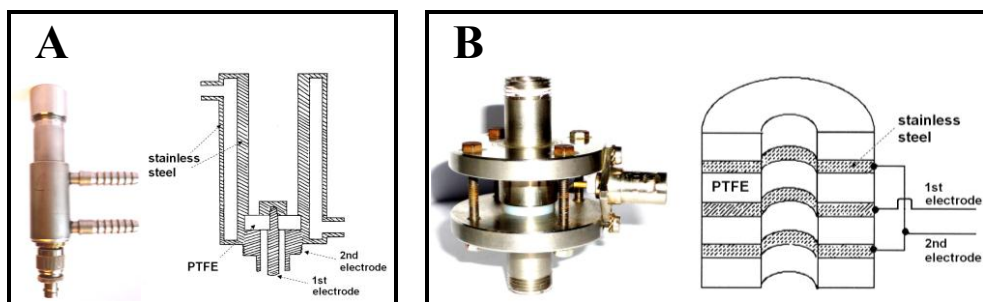


Figure 1: Photographs and schematic representations of the dielectric cells: (A) Axial cell, (B) cylindrical cell.

Procedures

Preliminary impedance measurements were performed with pyrite that was dry ground and sieved in the air in a porcelain mortar just before use in order to limit its oxidation by atmospheric oxygen. Actually, the pyrite oxidation being extremely slow in the absence of moisture, surface analyses by XPS of freshly ground pyrite indicated essentially pure mineral with no evidence of surface oxidation products.

For the main measurements, pyrite was ground and sieved as previously described, but in a glove bag purged with argon (5.0 from Messer) until the oxygen content had dropped below 0.5 percent. The dielectric cells were filled with the 40-80 μm granulometric fraction of pyrite and hermetically closed inside the glove bag. During the experiments undertaken with the cylindrical cell (Fig. 1 B), the latter was continuously flushed with argon (5.0) or the oxidizing gas (ambient air or oxygen – 5.0 from Messer).

Results and discussion

In this section, we will start with preliminary measurements concerning both pyrite samples (from Spain and Peru) that led us to choose pyrite from Spain in the 40-80 μm granulometric fraction for this work. Then, we will examine the experiments carried out with the axial cell without gas flow and using air as the oxidizing agent. Finally, the focus will be put on the experiments obtained with the cylindrical cell under gas flow and using air or oxygen as the oxidants.

In a practical point of view, a high-frequency alternative current is applied to the capacitive cell containing the pyrite sample and the corresponding complex impedance, Z^* ($Z^* = |Z|e^{j\theta}$), is measured as a function of the frequency. The impedance meter furnishes the magnitude ($|Z|$) and the phase difference (θ). These broad measurements are corrected afterwards to take into account the proper characteristics of the electrical circuit (empty cell and cables). Usually, the analysis of the dielectric properties of a given material is made using the following physical quantities: (i) the resistance, Z' , that is the real part of impedance, and the reactance, Z'' , that is the imaginary part, and (ii) the complex permittivity, ϵ^* , or complex dielectric constant, ($\epsilon^* = \epsilon' - j\epsilon''$) where ϵ' is the real permittivity and ϵ'' the dielectric loss factor. In the present work, the ϵ' and ϵ''

physical quantities will not be used. Actually, on the one hand, the standardization of the cells used can be made using only liquid standards and among common liquid compounds formamide has the higher relative permittivity (dielectric constant) value, i.e. 109. On the other hand, the relative permittivity value for sulphide minerals can reach several thousands. In our opinion, such an extrapolation is always speculative.

Preliminary measurements

These dielectric measurements were performed with pyrite from Spain and Peru using particles in the 400-800, 40-80 and <40 μm ranges as well as massive samples. The pyrite particles were dry ground and sieved in the air just before use. The impedance of massive samples was measured using sharp test points. Fig. 2 displays all the data acquired using two different log-log representations: (i) the evolution of the magnitude ($|Z|$) versus the frequency (A1 and B1), and (ii) the variation of the real part of the impedance Z' against the imaginary part of the impedance Z'' (Nyquist diagram) (A2 and B2).

By considering these diagrams one can point out the following remarks: (i) pyrite from Spain (A1) is more conducting than pyrite from Peru (B1) (the particles size below 40 μm excepted), (ii) for pyrite from Spain, the impedance increases when the particles size decreases whereas the impedance of pyrite from Peru seems to be unaffected by the particles size, (iii) the $Z''=f(Z')$ representation (A2 and B2) is most suitable for the analysis of the experimental data. This is particularly clear in the case of pyrite from Peru. If now we consider diagrams in figures A2 and B2, we can remark that both mineral show analogous behaviours. Therefore, the $Z''=f(Z')$ representation will be adopted for all the experimental data.

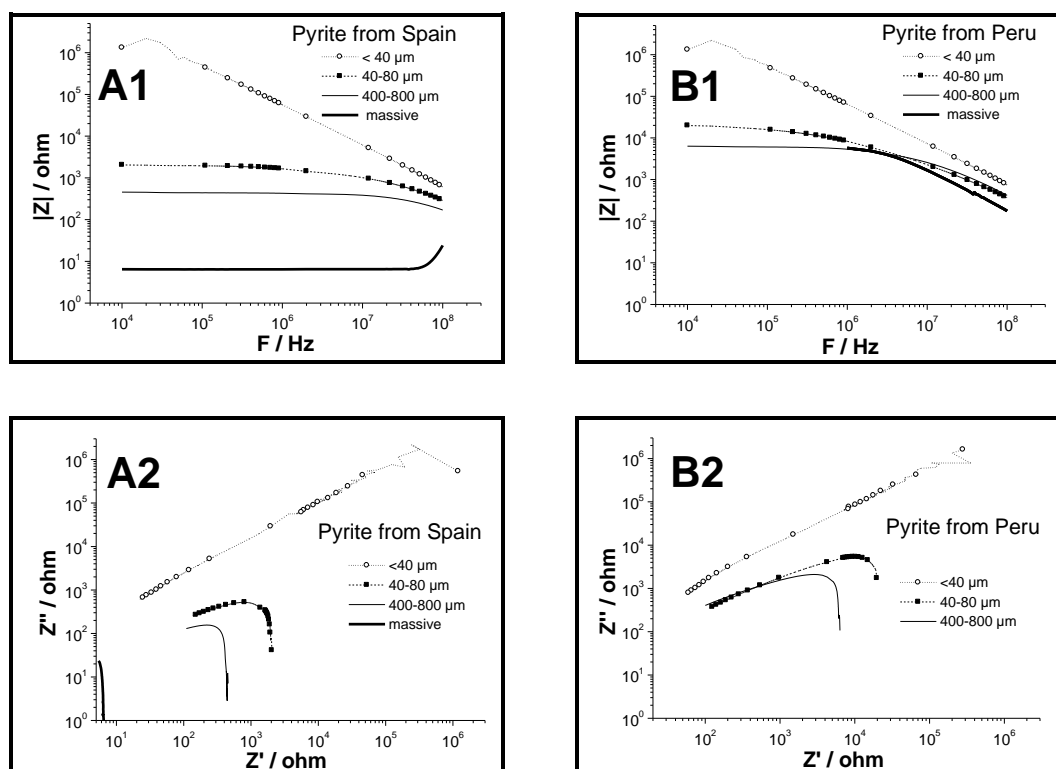


Figure 2: Comparison of dielectric characteristics of the two samples of pyrite. Impedance ($|Z|$) as a function of frequency (figures on the top) and $Z''=f(Z')$ (figures on the bottom) for different particles size: (A) pyrite from Spain, (B) pyrite from Peru.

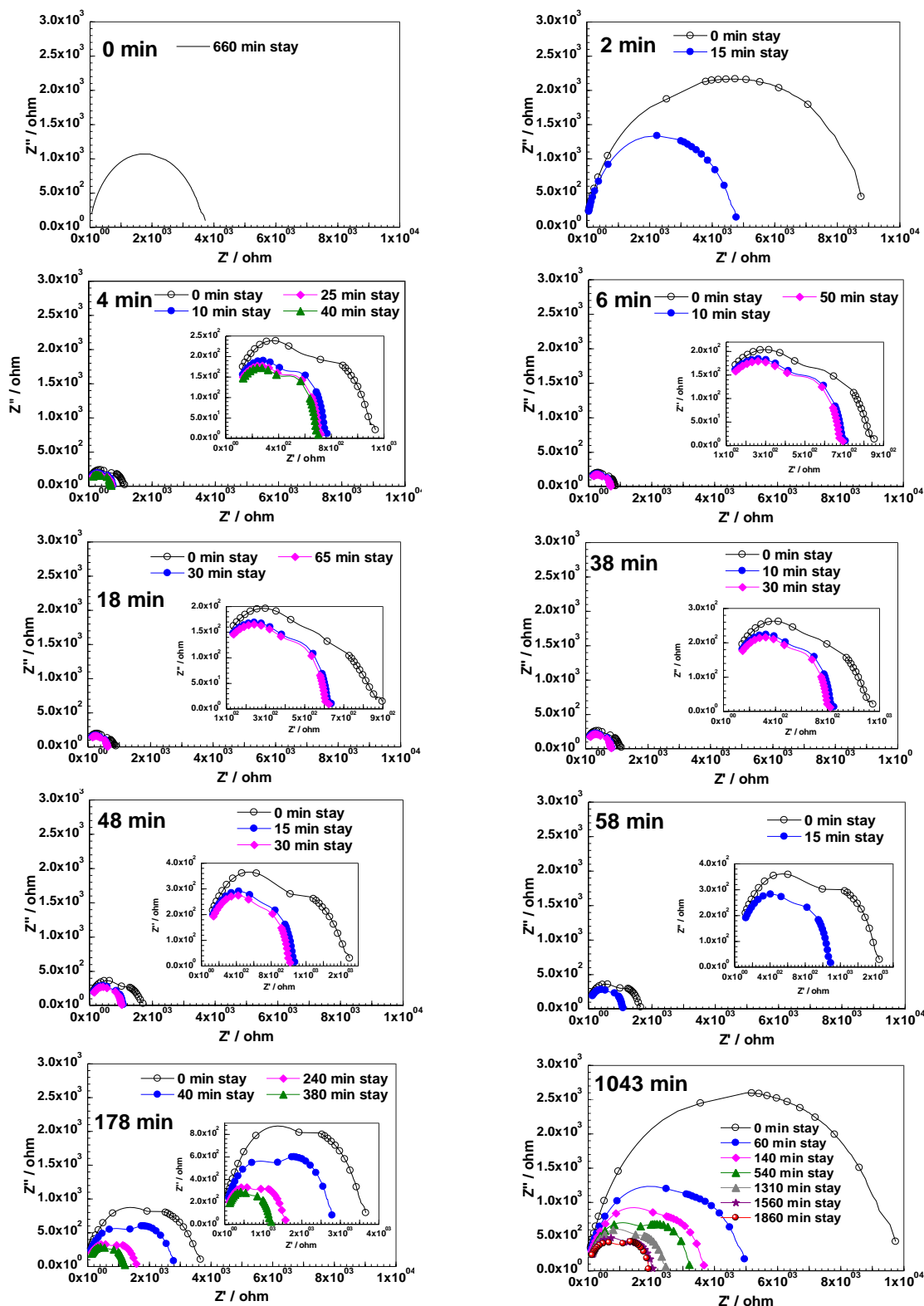


Figure 3: Dielectric monitoring of the FeS_2 oxidation by air and without gas flow using the axial cell. Each diagram represents the $Z''=f(Z')$ evolution after an oxidation step. The legends indicate cumulative oxidation times (high bold characters) and the times elapsed after the closing of the cell. Diagrams given in insets represent zooms of the main graphs.

Concerning the first remark, one may easily notice that the observed conductance increase when the particles size decreases is unusual and can only be explained by the presence of an insulating layer on the particles surface. It is most probably due to the formation of an oxidation layer on pyrite that is so thin that it cannot be detected by XPS spectroscopy. Actually, the global impedance of a particle is the sum of the impedances of the bulk particle and of the superficial oxidation layer. When the particles size diminishes, the contribution of the oxidation layer becomes more and more important and, in the case of the finest particle size ($< 40 \mu\text{m}$), the contribution of the bulk particle is negligible and so pyrite from Spain and pyrite from Peru have virtually the same impedance. That is the reason why in the following the grinding and handling operations were carried out in an argon atmosphere.

Considering the second remark, it is evident that the raw measurement of impedance ($|Z|$) is sufficient to instantaneously monitor the oxidation of pyrite from Spain whereas the calculation of Z' and Z'' is needed in the case of pyrite from Peru. This is why, pyrite from Spain was chosen for this study.

Experiments performed with the axial cell without gas flow

For these experiments, pyrite was ground under an argon atmosphere, and the dielectric cell was filled anoxically within the glove bag.

After the dielectric characterization of the unoxidized pyrite, the mineral was oxidized by steps of increasing durations by opening and closing the cell at the beginning and end of each step. After each oxidation step, the evolution of the pyrite impedance was monitored until an apparent equilibrium value is reached.

Figure 3 comprises a series of graphs that display Nyquist diagrams ($Z''=f(Z')$) that we recorded along an experiment. The legend of each graph comprises the cumulative oxidation time in high bold characters, and the times elapsed after the closing of the cell. The cumulative oxidation time will be used as the label of the corresponding graph in this text. One can remark that after the first oxidation step ("2 min"), the resistance, Z' , suddenly increases, and then decreases progressively once the aeration is stopped. After the "4 min" oxidation step Z' is about 10 times smaller whereas the shape of the Nyquist plot has completely changed. One will see at the end of the next section that this dramatic decrease of Z' is probably in relation with a humidification of the sample. Considering the rest of the diagrams in Fig. 3, one can notice that in a general manner, after each new oxidation the resistance of pyrite rises and then progressively falls after the closure of the dielectric cell. One thing that is impressive is the fact that, even after about 1.3 day of stay in the hermetically closed cell, Z' is still decreasing.

In view of these results, we checked the electronics and fixtures, and nothing was out of the ordinary, then we repeated the experiment. Both experiments led to similar results. At the end of the second experiment we got out the pyrite powder from the cell, and we spread it out on a sheet of paper for about a week. Linear and log-log Nyquist plots relative to the dielectric characterization of this powder are shown in figure 4. What is worthwhile is that even after a week of stay of the pyrite powder in air, once it is put in the cell Z' decreases again. The log-log representation shows that the curve shape is close to that for the $<40 \mu\text{m}$ granulometric fraction in fig. 2 (A2 and B2).

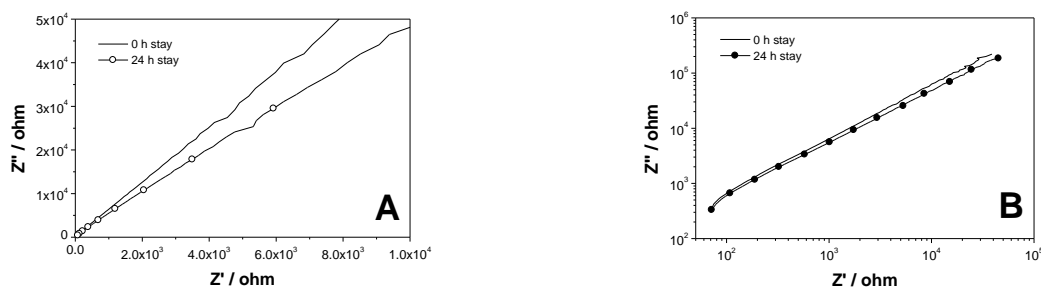


Figure 4: Dielectric characterization of FeS₂ after oxidation for about a week in air. Influence of the stay for one day in the closed the axial cell. Linear (A) and log-log (B) representations.

At this point of analysis, arise the following two questions: (i) For what duration the oxidation reaction is continued once the dielectric cell is closed ? (ii) What is the influence of the air moisture on the oxidation reaction?

To answer the questions we used the cylindrical dielectric cell that allows the user to continuously flow a gas through the pyrite microparticles. By switching between an oxygen flow and an argon flow the oxidation reaction can be stopped almost immediately.

Experiments performed with the cylindrical cell under gas flow

A first experiment was carried out using alternative flows of air and argon, which led to results that, after treatment, give Nyquist plots whose shape is close to that of $Z''=f(Z')$ curves in Fig. 4. These results will be not commented in this paper.

Figure 5 displays the results that were obtained by passing alternatively argon and pure dry oxygen through the dielectric cell (a reminder: if the shape of the Nyquist plots obtained with the two cells can be compared, this is not the case for the values of Z' and Z''). As in Fig. 4, the legends of the graphs of this figure display the cumulative oxidation times in high bold characters and the times elapsed after the re-establishment of the argon flow through the cell. As it is the case in the experiment described in the preceding section, a high increase of Z' is observed only in the beginning of the experiment ("0.5 min" and "1.0 min" of oxidation). On the other hand, the Nyquist plots vary less when the cylindrical cell is under an argon flow than when the coaxial the cell is only hermetically closed. Moreover, the shape of the $Z''=f(Z')$ curves is significantly different. However, that is perhaps the most noticeable difference is: (i) the presence of negative values for Z'' (see i.e. "3h", "4h", "6h") that, from an electrical point of view, indicates the presence of an inductive contribution and (ii) the fact that great changes are observed in the corresponding Nyquist plots. For the moment, any attempt for interpreting these differences would be unduly speculative.

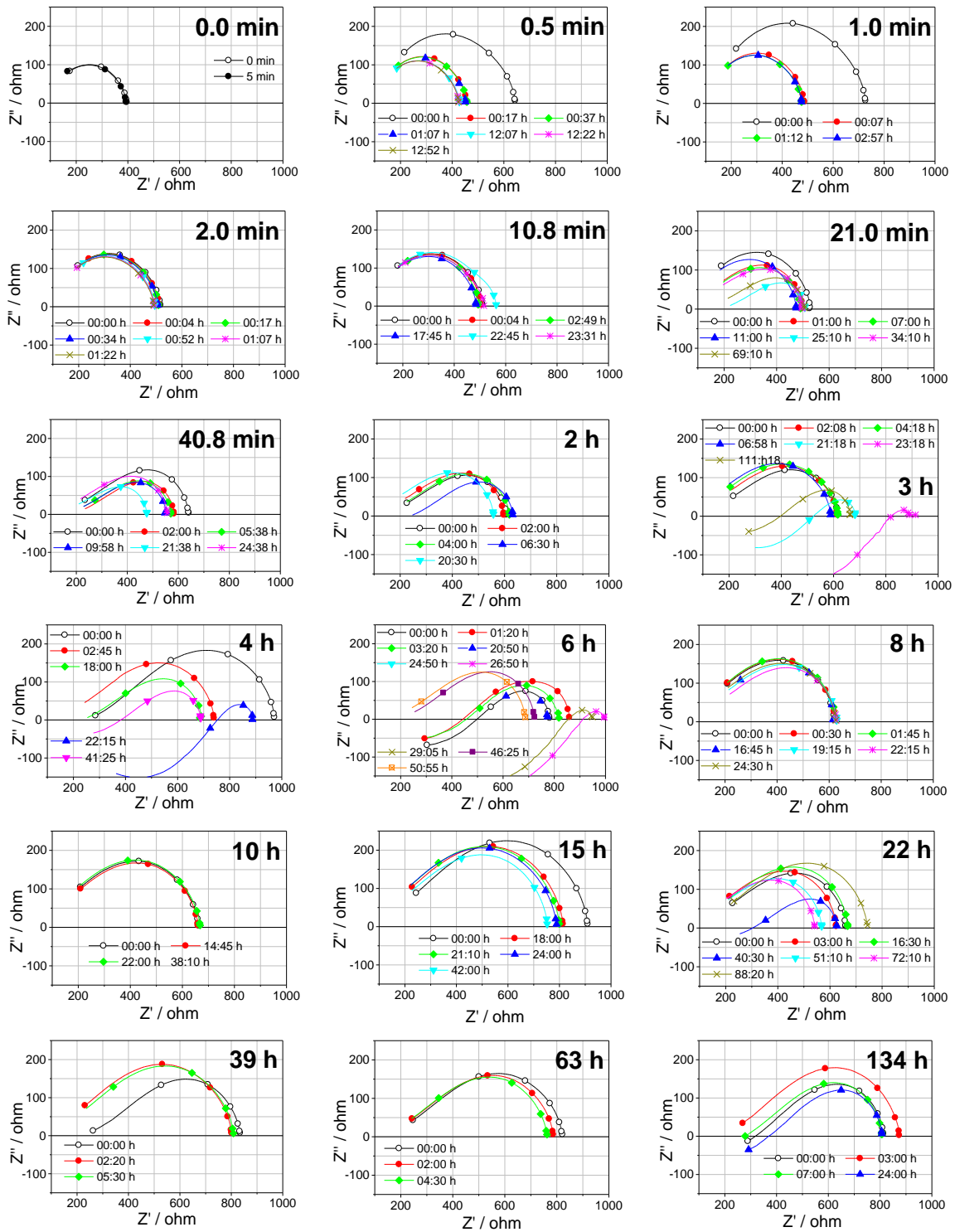


Figure 5: Dielectric monitoring of the FeS_2 oxidation by dry oxygen using the cylindrical cell under argon or oxygen flow. Each diagram represents the $Z''=f(Z')$ evolution after an oxidation step. The legends indicate cumulative oxidation times (high bold characters) and the times elapsed after the re-establishment of the argon flow through the cell.

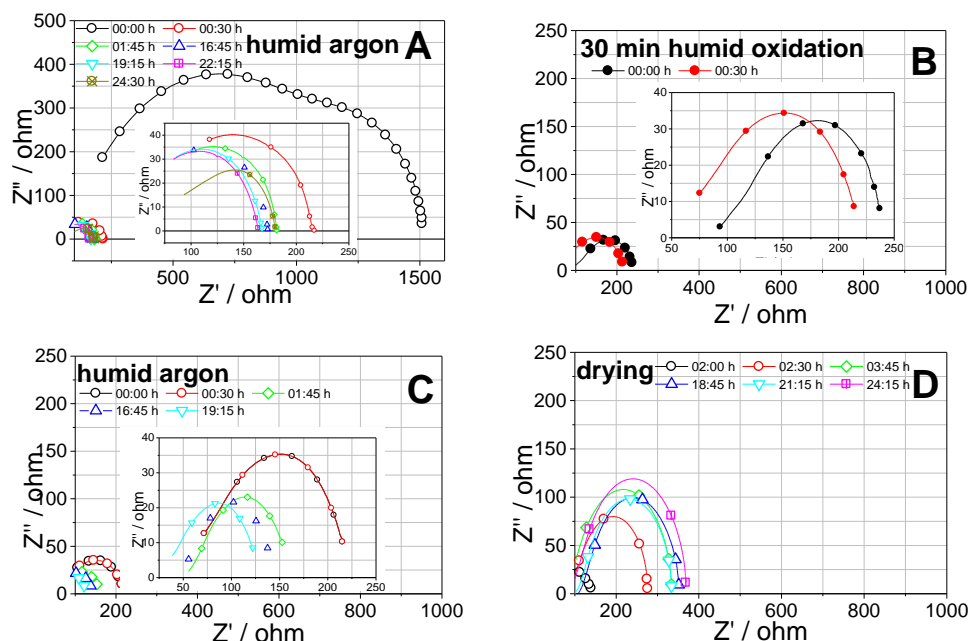


Figure 6: Dielectric measurements performed with the axial cell under water-saturated argon and oxygen flow. $Z''=f(Z')$ evolution during: (A) humidification, (B) oxidation, (C) humidification and (D) drying. Diagrams given in insets represent zooms of the main graphs.

Figure 6 shows the influence of moisture on the dielectric measurements that were performed with pyrite particles that were previously oxidized using dry oxygen for about 200 h. When the flow of humid air is established through the dielectric cell (Fig. 6A) the resistance Z' of the microparticles falls down rapidly that confirms the hypothesis that we emitted in preceding section about the transition "2 min"→"4 min" in Fig. 3. Fig. 6B demonstrates that the presence of humid oxygen radically changes the shape of the $Z''=f(Z')$ plots since the re-establishment of humid argon (Fig. 6C) does not modify this shape but only diminishes the Z' value. Finally, the drying of the sample with a dry argon flow (Fig 6D) has as the effect the increase of both parameters Z' and Z'' .

Short discussion

The oxidation experiments we performed showed that very slight modifications were made here. Indeed, Raman spectroscopy cannot detect any modification between the spectra of pristine pyrite and oxidized pyrite. The thing that is important here is a possible effect on the reactivity of such oxidized pyrite. Several papers in literature are dealing with the "dry oxidation" of sulphide minerals at ambient temperature (Steger *et al.* 1978, 1980, Boursiquot *et al.* 2001), but it is about oxidations performed with atmospheric air where the moisture plays a major role. Much remains to be done in the "true" pyrite oxidation area. It has been only very recently that theoreticians were interested in interactions of gaseous species (oxygen, nitrogen and nitrogen oxides) with pyrite (Sacchi 2012) in order to explain its catalytic properties in the adsorption and dissociation of nitrogen oxides. It is possible that the conductivity changes that we

observed after each exposure of the FeS₂ sample to oxygen are due to the adsorption of O₂ on its surface. Actually, dielectric measurements are extremely sensitive and very often they can detect adsorption phenomena that involve less than a monolayer of adsorbate. With regard to the impedance decrease observed when the sample is maintained in anoxic conditions (after its exposure to oxygen), it could be due to rearrangement of the oxygen molecules on the mineral surface and/or a very slow surface oxidation followed by a bulk oxidation that can slightly modify the pyrite non-stoichiometry. Indeed, during studies in aqueous media with non-stoichiometric Cu_xS, *Castel (1977)* observed a slow stoichiometric change of composition of the sulphide as a function of the solution redox potential.

Summary and Conclusions

During this work, we showed that when dry pyrite microparticles were exposed stepwise to ambient air, or pure oxygen, once the sample was put in anoxic conditions the initial impedance increase was followed by a tendency of decreasing towards the impedance value before the oxidation step. Sometimes, the Nyquist diagrams plots during the stay of the samples in anoxic conditions showed an unusual dielectric behaviour. If the ambient air is used as the oxidizing agent, the presence of moisture renders the phenomena more complex. The observed changes in the dielectric spectra are probably due to extremely fine transformations on the pyrite surface that cannot be detected with usual spectroscopic techniques.

In the case of the repository of the nuclear spent fuel in deep argillaceous rocks, such changes affecting the electrical conduction properties of pyrite could significantly modify the reactivity of this mineral – as a reducing compound towards oxidizing radionuclides or as a catalyst – after construction of the underground installations as a consequence of the atmospheric oxygen penetration in the excavation zone.

The main objective of this work its was to check the reproducibility of the measurements and if no artefacts occurred. The systematic study of other parameters as the particles size, the temperature, moisture degree... as well as the use of a well-suited and complementary technique would bring essential information in order to better understand the observed phenomena.

Acknowledgement

The research leading to these results has received funding from the European Union's European Atomic Energy Community's (Euratom) Seventh Framework Programme FP7/2007-2011 under grant agreement n° 212287 (RECOSY project).

References

- Bessière J., Thiébaud J. M., Chlihi K., El Housni M., (1989). Dielectric methods: a novel technique for the study of flotation mechanisms of sulfide ores. *Industrie Minerale, Mines et Carrieres: les Techniques*, 3, 57-61.
- Bessière J., Chlihi K., Thiébaud J. M., Roussy G., (1990). Dielectric study of the activation and deactivation of sphalerite by metallic ions. *Int. J. Miner. Process.*, 28, 1-13.
- Basu R., Iannacchione G. S., (2008). High-resolution dielectric spectroscopy and electric-field dependence of carbon allotropes including multiwall and single-wall nanotubes. *Appl. Phys. Lett.*, 92, 052906/1-052906/3.
- Boursiquot S., Mullet M., Abdelmoula M., Génin J. M., Ehrhardt J. J., (2001). The dry oxidation of tetragonal FeS_{1-x} mackinawite. *Phys. Chem. Miner.*, 28, 600-611.
- Bueno P. R., Varela J. A., Longo E., (2007). Admittance and dielectric spectroscopy of polycrystalline semiconductors. *J. Eur. Ceram. Soc.*, 4313-4320.
- Castel E. (1977). Etude électrochimique de quelques propriétés du sulfure cuivreux non stœchiométrique. Ph. D. Thesis, Université Pierre et Marie Curie (Paris VI).
- De Cannière P., Wang L., Aerts S., De Craen M., (2008). Geochemistry of Sulphur Species Harmful for Metallic Barriers in clay Environment in the Frame of Geological Disposal of Radioactive Waste. SACNUC Workshop (Sulphur-Assisted Corrosion in Nuclear Waste Disposal Systems), Book of Abstracts p.11. Brussels, 21-23 October 2008.
- Etahiri A., Humbert B., El Kacemi K., Marouf B., Bessière J., (1997). Dielectric study of sodium dodecyl sulfate (SDS) adsorption onto galena. Comparison with sodium amyl xanthate and dodecyl ammonium chloride. *Int. J. Miner. Process.*, 52, 49-63.
- Ignatiadis I., Chainet F., Betelu S., Gaucher E., Tournassat C., (2010). Abiotic pyrite reactivity versus nitrate, selenate and selenite using chemical and electrochemical methods. Clays in natural and engineered barriers for radioactive waste confinement, 4th International Meeting, Book of Abstracts p. 395-396. Nantes (France), 29 March - 1 April 2010.
- Mijovic J., Fitz B. D., (1998). Dielectric Spectroscopy of Reactive Polymers. In "Application Notes on Dielectric and Impedance Spectroscopy", application note 2, Novocontrol Technologies GmbH (http://www.novocontrol.de/html/info_app_notes.htm).
- Núñez L., Gómez-Barreiro S., Gracia-Fernández C.A., Núñez M.R., (2004). Use of the dielectric analysis to complement previous thermoanalytical studies on the system diglycidyl ether of bisphenol A/1,2 diamine cyclohexane. *Polymer*, 45, 1167-1175.
- Pearson F.J., Arcos D., Bath A., Boisson J.-Y., Fernández A.M., Gäbler H.-E., Gaucher E., Gautschi A., Griffault L., Hernán P., Waber H. N., (2003). Mont Terri Project - Geochemistry of Water in the Opalinus Clay Formation at the Mont Terri Rock Laboratory. Reports of the Federal Office for Water and Geology, Geology Series, N°5, Bern.

Roy G., Pelletier M., Thomas F., Despas C., Bessière J., (2000). Aggregation in Na-, K- and Ca-montmorillonite dispersions, characterized by impedance spectroscopy. *Clay Miner.*, 52, 49-63.

Sacchi M., Galbraith M. C. E., Jenkins S. J., (2012). The interaction of iron pyrite with oxygen, nitrogen and nitrogen oxides: a first-principles study. *Phys. Chem. Chem. Phys.*, 14, 3627–3633.

Steger H. F., Desjardins L. E., (1978). Oxidation of sulfide minerals. 4. Pyrite, chalcopyrite and pyrrhotite. *Chem. Geol.*, 23, 225-237.

Steger H. F., Desjardins L. E., (1980). Oxidation of sulfide minerals. 5. Galena, sphalerite and chalcocite. *Can. Mineral.*, 18, 365-372.

Tsangaris G. M., Kouloumbi N., Kyvelidis S., (1996). Interfacial relaxation phenomena in particulate composites of epoxy resin with copper or iron particles. *Mater. Chem. Phys.*, 44, 245-250.

AN ATTEMPT FOR FABRICATING ULTRAMICROELECTRODES COMPATIBLE WITH SODIUM CHLORIDE BRINES³

Michel Perdicakis*, Asma Chebil, Mathieu Etienne, Ajfane Cheikh-Ibrahim

Laboratoire de Chimie Physique et Microbiologie pour l'Environnement, UMR 7564,
Nancy-Université – CNRS, 405 rue de Vandœuvre, 54602 Villers-lès-Nancy Cedex
(FR)

* Corresponding author: perdi@lcpme.cnrs-nancy.fr

Abstract

In the framework of Recosy project we have had to determine redox solutions in concentrated brines by using ultramicroelectrodes (UMEs). At the beginning of the investigation, we noticed that the UMEs we used were inoperative in brines. We attempted to remedy this by testing eight platinum UMEs having diameters ranging between 10 and 50 μm in NaCl solutions whose concentration varied from 5.84 to 29.22% w:w. The UMEs used were either commercial or homemade, and their insulating body was formed of various glasses (Pyrex, soft glass, quartz, quartz-Suprasil) or polymeric resins (epoxy, polyester). For convenience reasons, dissolved oxygen was used as the main electroactive species but some experiments were carried out with ferrocene dimethanol. In the most of cases the electrodes are damaged when immersed in the concentrated solutions. Generally, the more concentrated the brine is, the more the electrodes are affected; however, the phenomena are not so simple. More specifically, the reduction oxygen seemed to be responsible for enhanced degradation of the electrodes. The UMEs whose the insulating part is made of “quartz-suprasil” seem to be the less affected by the brines.

Introduction

The preferred option for the long term management of long lived and/or high level radioactive wastes consists in their disposal in deep geological repositories. Salt deposits, clay/shale, granite and tuff formations are considered as potential host rocks for such repositories (*IAEA 2001*). Repositories hosted in salt rock sites are mainly located in Germany (Schacht Asse II in Lower-Saxony - closed in 1995, Morsleben in

³ This work has been presented as oral presentation under the title “Can we use ultramicroelectrodes to perform electrochemistry in brines?” at the “ABC-Salt II workshop: Actinide Brine Chemistry in a Salt-Based Repository”, 7 and 8 November, 2011, Karlsruhe, Germany.

Saxony-Anhalt - closed in 1998, and Gorleben, - on hold) and in the United States (Waste Isolation Pilot Plant in New Mexico, in operation since 1999). In principle, the selected deep salt beds are free of flowing water, impermeable and geologically stable. However, in order to anticipate the consequences of a possible introduction of water in the repositories, several investigations on the chemistry in concentrated brines (actinide chemistry, brine chemistry, microbial effects, experimental techniques, thermodynamic databases and modelling) are currently in progress (see for example, *Kienzler et al. 2010*, *Reed et al. 2010*, *Moog et al. 2010*). The need for performing such studies was corroborated by the inflow of NaCl brine (12 m³ per day) started in 1988 in Asse Salt Mine (*Bossy 2006*).

Among the very wide range of techniques currently available to scientists for investigations in concentrated brines, electrochemistry is particularly well-suited for corrosion studies, redox potential measurements or determination of complex formation constants. The capabilities of the electrochemical techniques were considerably increased by the use of electrodes in the micrometric range that are called “ultramicroelectrodes” (UMEs), or simply “microelec-trodes” according to the particular origin of electrochemists. UMEs present several advantages towards traditional electrodes because of their small size. In addition to the applications that exploit this microscopic size for detection or production of species in restricted volumes or for “scanning electrochemical microscopy” experiments (*Bard et al. 1994*), other specific applications of UMEs are based on their intrinsic characteristics: reduced ohmic drop, reduced time constants and steady state diffusional currents without the necessity of forced convection (*Amatore 1995*).

The application of voltammetric techniques at UMEs led to marked improvement of the signal noise ratio and the increase of the detection limits. In this way, after the fabrication of the iridium based UMEs (*Kounaves 1990*, *Kovacs 1995*), the Buffle group in Geneva has developed several electrochemical devices based on UMEs for trace metals detection by voltammetry in natural waters (*De Vitre 1991*, *Tercier 1995*, *Belmont 1996*, *Belmont-Hébert 1998*, *Tercier-Waeber 1999*). From a practical point of view, the Italian company *Idronaut* manufactured the only existing oceanographic submersible voltammetric probe for in-situ trace element monitoring and profiling. It consists of an array of 5 x 20 interconnected iridium microdiscs, having a diameter of 5 µm that allows simultaneous measurements of Cu(II), Pb(II), Cd(II) and Zn(II) with a sensitivity at the ppt level, as well as Mn(II) and Fe(II) at the ppb level. Moreover, the European research project *Shoal*, that aims to develop number of robotic fish that will work together in order to monitor and search for pollution in ports and other aquatic areas uses, develops novel chemical sensor subsystems based on 4 arrays of microdiscs for copper, lead, dissolved oxygen and phenols measurements.

In the framework of the RECOSY project, we tried to make use of the higher sensitivity of UMEs to measure very low concentrations of redox indicators in concentrated NaCl solutions (*Cortot et al. 2009*). The goal was to determine redox potentials in brines by monitoring voltammetrically the concentrations of the reduced and oxidized forms of a redox indicator added to the solution beforehand. These attempts completely failed. Actually, we showed that the voltammetric response of UMEs –that perfectly work in diluted media or pure water– becomes completely meaningless once immersed in NaCl brines.

The purpose of this work was to find the reasons why UMEs do not work properly in brines whereas traditional millimetric electrodes are working satisfactorily and, if possible, to build UMEs that are compatible with these highly concentrated media in order to take full advantage of their intrinsic characteristics.

Experimental

Chemicals

Sodium chloride (puriss. p.a. grade) used for preparing brines solutions and 1,10-ferrocenedimethanol (98%) were both from Sigma-Aldrich. All solutions were prepared in conical sample containers made of polypropylene (VWR International) with high purity water (18 MΩ-cm) from a Purelab Option water purification system (ELGA).

Ultramicroelectrodes

Commercial ultramicroelectrodes

We expected to use 10 µm Pt new (unused) UMEs from Autolab to avoid any contamination, but these electrodes after a short malfunction period ceased providing an electrochemical signal. Hence, we used only UMEs more than 10 years old, but perfectly functioning, that were available in our lab. It was about the G0225 10 µm diameter Pt “Micro-Electrode” from Princeton Applied Research and the MEPT10 10 µm diameter Pt “ultramicroelectrode” from Tacussel. Both were prepared by sealing a Pt fine wire in glass. The G0225 UME is still available whereas the Tacussel company has ceased its activities.

Quartz fibre ultramicroelectrodes

These electrodes were prepared by cutting with a scalpel a standard quartz-platinum/tungsten fibre raw material (quartz 80 µm OD, 25 µm ID and platinum/tungsten 25 µm D) EF3PtT80 from Thomas Recording GmbH and carefully polishing its cross section.

Homemade ultramicroelectrodes

UMEs were prepared by sealing platinum microwires (50 µm diameter 99.9% from ChemPur) in an insulating material. According to the nature of this material, two different procedures were used.

UMEs prepared using polymeric materials: a platinum microwire, which had been previously soldered to a copper wire, is mounted in a rod of polymeric resin. (epoxy: Araldit DBF from Huntsman Advanced Materials or polyester: SeriFix from Struers) using a plastic medical syringe as a mould as it is shown schematically in Fig. 1A. After the resin curing process is complete, the mould is destroyed and the rod of resin is truncated. Then, the UME that is constituted by the cross section of mounted platinum wire is polished as described afterwards.

UMEs prepared using glass materials: In all cases, the platinum microwire is sealed in a capillary by heating the glass under gentle vacuum to melt it around the microwire. According to the melting temperature of the glass material, the capillary is heated using

a simple electrical resistor or a CO₂ laser beam provided with a focusing mirror after adaptation of a P-2000 micropipette puller (Sutter Instrument Co). The electrical resistor was used with capillaries made of soft glass or Pyrex (Fig 1B), and the laser beam with capillaries made of quartz or quartz-Suprasil from Heraeus Quarzglas GmbH (Fig 1C).

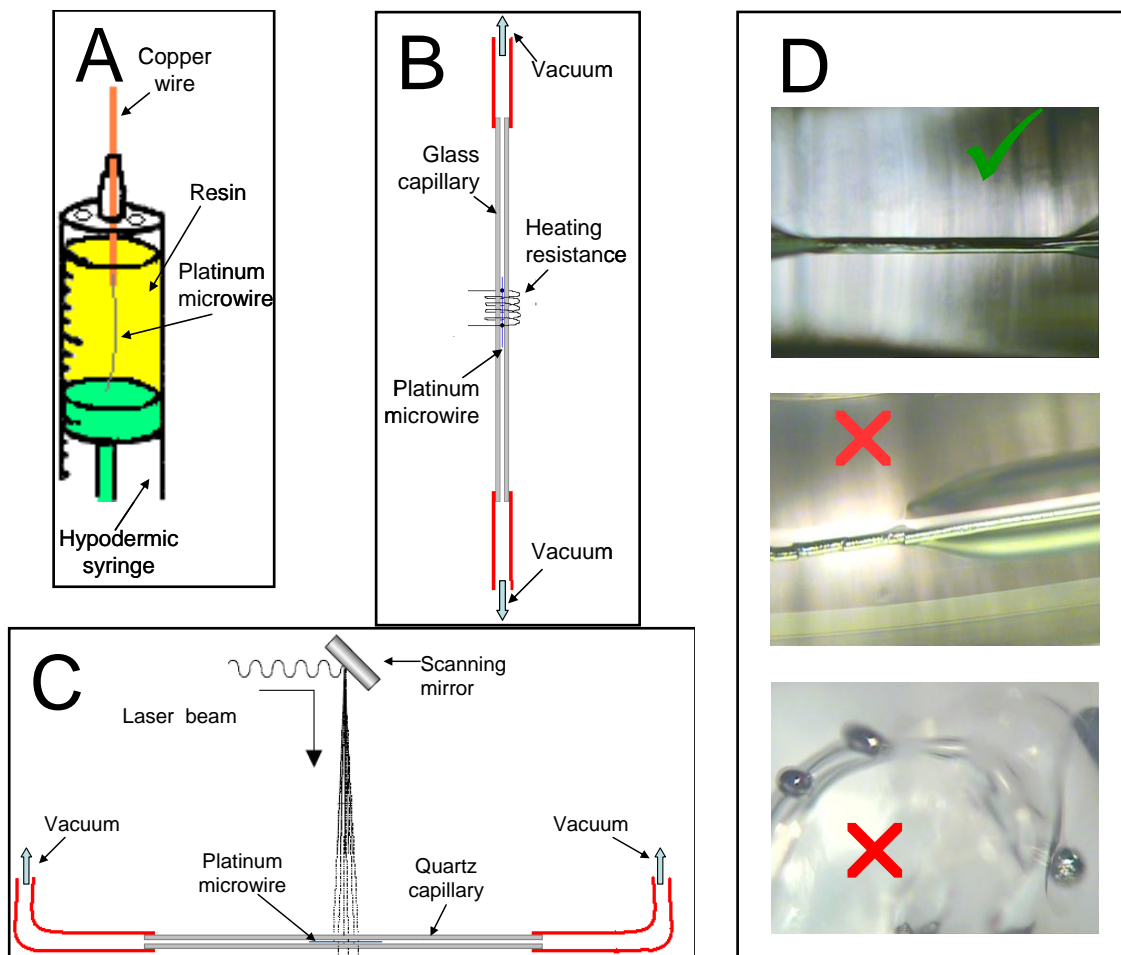


Figure 1: Fabrication of different kinds of ultramicroelectrodes: (A) Mounting of a platinum microwire in a rod of polymeric resin. (B) Sealing of platinum microwires in glass capillaries. (C) Sealing of platinum microwires in quartz capillaries. (D) Photographs under the optical microscope of the platinum/quartz-Suprasil sealing.

Drs. Schuster and Roy kindly provided us with quartz-Suprasil capillaries of their own making (see acknowledgements). However, the preparation of UMEs using quartz Suprasil is somewhat problematic. Because the melting point of platinum (1772°C) and the softening point of quartz-suprasil (~1600°C) are relatively close, an extremely precise focusing of the laser beam on the quartz surface is essential, unless, as it is shown in Fig. 1D, the platinum wire is broken or melted. Unfortunately, the micropipette puller used does not permit such a precise focusing to be made easily. In all cases, after sealing the platinum inside the capillaries the latter were cut at their middle and, in this way, in principle two UMEs can be obtained after polishing of the

cross section of the platinum microwire. The electric contact is established by soldering a fine copper wire to the platinum microwire inside the capillary with a silver loaded epoxy resin.

Polishing of the ultramicroelectrodes

All the UMEs used, commercial or home-made, were wet polished, manually or on a polishing wheel (Dap-V polishing machine from Struers), until 2400 grit silicon carbide abrasive paper (Struers).

Electrochemical measurements

Voltammetric experiments were performed with a model 174A polarographic analyzer (EG&G-PAR) interfaced via a computer AD card and monitored by an application created using the TestPointTM software. The polypropylene conical sample containers used for the preparation of brines were used as electrochemical cells. The experiments were done without deaeration of the solutions, and the containers were sealed with a thermoplastic self-sealing film (Parafilm M®) to avoid the water evaporation. Three holes practiced on the film surface holes have allowed us to introduce the voltammetric electrodes: a Pt UME or a 2 mm Pt rotating disk electrode (PtRDE) as the working electrode, a platinum wire as the counter electrode and a saturated calomel electrode (SCE) filled with NaCl as the reference one. All potentials were referred to the so modified SCE electrode. The RDE shroud was fabricated from PTFE, and the electrode was rotated at 600 rpm.

Results

Preliminary results

In this subsection, we describe some surprising preliminary results we obtained when we tried to use UMEs in brines, which lead us to undertake this study and to define the working hypotheses as well as the systematic approach that we adopted in the following. The experiments were performed using traditional glassware without any particular precautions. All the measurements recorded are displayed in Fig. 2.

The voltammograms recorded at the 2 mm Pt RDE (Fig. 2A) for non deaerated solutions of NaCl (1 M, 2 M, and saturated) do not require particular comments. As expected, on the anodic side, the electrochemical window is limited by the oxidation of chloride ions at about 1 V vs. SCE and on the cathodic one by the water reduction. One can notice that the more concentrated the solution is, the less intense the voltammetric signal for oxygen reduction becomes, due to the significant decrease of oxygen solubility, and, to a lesser extent, to that of its diffusion coefficient (cf. Table 1).

Figure 2B shows that the 50 μ m Pt UME prepared by sealing a Pt microwire in Pyrex (Pyrex Pt UME), which is working satisfactorily in pure deionised water, after immersion in the saturated brine, deaerated or not, gives a completely meaningless response. This is also the case for an UME prepared by sealing a 50 μ m Pt microwire in soft glass (soft glass Pt UME) as it is shown in figures 1C and 1D or for a commercial 10 μ m Pt UME (Fig. 1C). Only the Pt UME prepared by sealing a 50 μ m Pt microwire

in quartz glass delivers an almost acceptable response for the dissolved oxygen reduction (Fig. 1D). This same UME was used satisfactorily to examine the electrochemical oxidation of ferrocene dimethanol in the non deaerated saturated NaCl brine (Fig. 1E). However, after prolonged immersion (during 12 hours) of the electrode in the brine, the electrochemical signal is dramatically deteriorated, and a severe polishing is required in order to reach a strongly deformed anodic voltammetric wave.

Remark:

In the framework of the RECOSY project, we participated in a four-day intercomparison exercise (*Altmaier 2010*) where researchers from 15 different organizations determined Eh for six series of anoxic samples comprising artificial, natural or microbial solutions and suspensions. During this exercise, among other samples, we investigated by means of UMEs three equimolar solutions of ferrous and ferric ions ($[\text{Fe}^{2+}] = [\text{Fe}^{3+}] = 10^{-4} \text{ M}$) in 5 M NaCl at pH 2, 6-7 and 12. However the UMEs (Epoxy Pt-UME) were used to determine step by step zero current potentials (OCPs) and not to measure limiting currents by recording complete voltammograms as in the present work. Afterwards the determined OCPs were compared with the Eh values we measured potentiometrically.

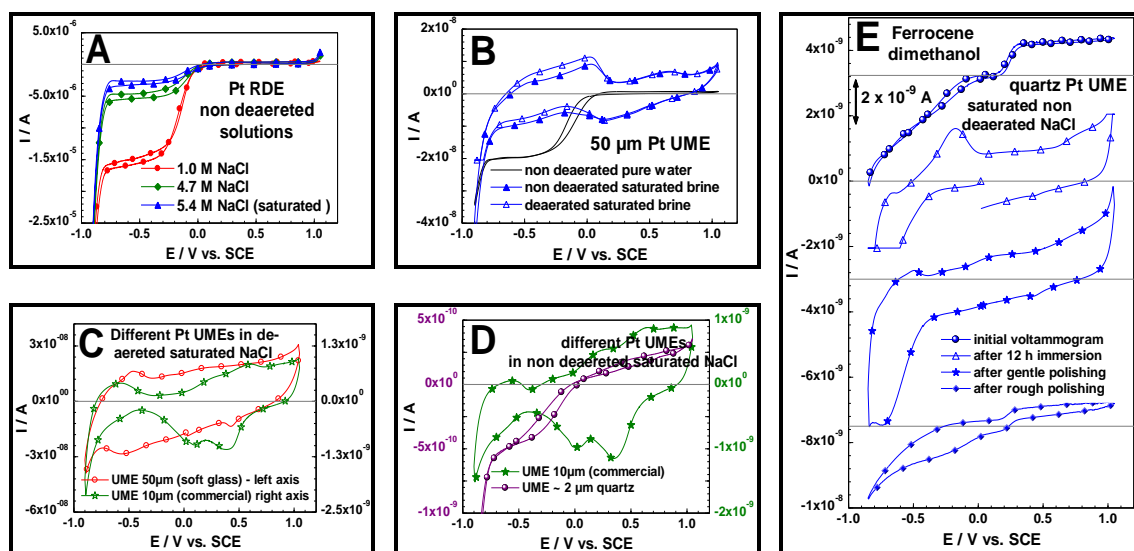


Figure 2: Voltammograms recorded in brines at different electrodes during the preliminary study: (A) at a 2 mm platinum rotating disk electrode in non deaerated solutions, (B) at a 50 μm Pt UME with a Pyrex body in pure water and in a saturated NaCl brine the both non deaerated and in deaerated saturated NaCl brine, (C) at a 50 μm Pt UME with a soft glass body and at a 10 μm commercial Pt UME (glass) in deaerated saturated NaCl brine, (D) at a 10 μm commercial Pt UME (glass) and at a $\sim 2 \mu\text{m}$ homemade Pt UME with a quartz body in non deaerated saturated NaCl brine and (E) at a $\sim 2 \mu\text{m}$ homemade Pt UME with a quartz body in a 0.4 mM ferrocene dimethanol solution in non deaerated saturated NaCl brine; effect of the long-term immersion in the brine.

This brief preliminary study had shown clearly that traditional UMEs that are perfectly functioning in diluted solutions are unsuitable for investigating concentrated brines. In the literature, several papers are dealing with the corrosion of glasses in sodium chloride media (*Wickert et al. 1999*) for purposes in relation with the understanding of

archaeological glasses alteration (*Doménech-Carbó et al. 2008, Dal Bianco et al. 2004*) or with the underground disposal of nuclear glasses (*Chave et al. 2007, Baillif et al. 2000, Godon et al. 1988, Cox et al. 1989, 1993, Ledieu et al. 2004, Devreux et al. 2004*). These studies showed that during the corrosion of glasses their surfaces were enriched in silica, while other constituents were removed or deposited at the surface. Among these constituents are iron, manganese, cerium or copper species that are electroactive. Therefore, a possible reason for the dysfunction of UMEs in brines is the release of electroactive species by the material that constitutes their insulating body. For that reason, in the systematic study presented in the following section we will also consider UMEs made of materials that do not contain electroactive species (quartz-Suprasil) or materials well-known for their resistance to brines (epoxy and polyester resins).

Table 1: Characteristics of the NaCl solutions used at ambient temperature.

NaCl concentration % w:w	NaCl concentration mol/L	Density g/cm ³	Viscosity cm ² s ⁻¹	O ₂ solubility in brines exposed to air mmol/L	O ₂ diffusion coefficient D (10 ⁵) cm ² /s
0.00	0.000	1.000	1.002 ^b	0.2556 ^c , 0.2775 ^d	1.98 ^e 2.20 ^f 3.40 ^g 2.11 ^h 1.97 ^e
5.84 ^b	0.846 1.041 ^b 2.00	1.041 ^b	1.057 ^b	0.1840 ^c , 0.1754 ^d	1.75 ^g 1.93 ^h 1.12 ^g 1.87 ^h
11.68 ^b	2.161 ^b 3.00	1.080 ^b	1.146 ^b	0.1298 ^c , 0.1111 ^d	1.69 ^h
17.53 ^b	3.394 ^b 4.00	1.098 ^b	1.282 ^b	0.0899 ^c , 0.0725 ^d	1.55 ^h
23.37 ^b	4.704 ^b	1.176 ^b	1.508 ^b	0.0608 ^c , 0.0501 ^d	
29.22	6.060			0.0404 ^c	

^a saturated solution, ^b values determined by interpolation from molar concentration, density and viscosity reported in literature at 20°C (*CRC Handbook, 1974*), ^c calculated according to the model established by *Tromans (2000)*, ^d determined by interpolation from data provided by *Cramer (1980)*, ^e *van Stroe and Janssen (1993)*, ^f *Ferrel et al. (1967)*, ^g *Hung et al. (1972)*, ^h *Ho et al. (1988)*.

Systematic study

For convenience, this study was done in non deaerated solutions and most of the experiments were conducted using dissolved oxygen as the electroactive species. However several voltammograms were also recorded with ferrocene dimethanol. Actually, the degassing of concentrated brines without taking adequate caution against water evaporation will uselessly complicate the experiments not only by the brine concentration increase but also sometimes by the formation of NaCl crystals on the UME surface as we have noticed during the preliminary study. All the voltammograms were started from the zero current potential (OCP) and the scans were limited around the electroactive species redox potential in order to avoid the occurring of multiple phenomena. Moreover, in certain cases, the UMEs were tested again after a three-day immersion in the 29.22% w:w brine.

Remark: because of A-D conversion problems encountered during certain voltammetric records some experimental points are missing in the corresponding i-E curves, however this defect does not affect their interpretation.

Dissolved oxygen used as the electroactive species

The voltammograms for the reduction of dissolved oxygen in pure water and NaCl solutions at 5.84%, 11.68%, 17.53%, 23.37% and 29.22% w:w recorded with a 50 μ m Pt UME fabricated by sealing a platinum microwire into Pyrex glass (Pyrex Pt-UME) are displayed in Fig. 3A. The shape of the i-E curves is very similar to those recorded at a 2 mm Pt RDE (Fig. 1A). However, the difference between forward and reverse scans in the voltammograms is quite higher and the current becomes significantly positive at the end of the reverse scan. As the oxygen limiting currents decrease with the increase of the NaCl concentration, the comparison between these voltammograms is easier if the intensities are normalized with respect to the plateau current. For that reason, the whole of the voltammetric curves were arbitrarily normalized to the current at -0.6 V (Fig. 3B). In this figure, one can notice that, from 11.68% w:w NaCl the curves start to be seriously affected by the brines, especially during the during the reverse scan.

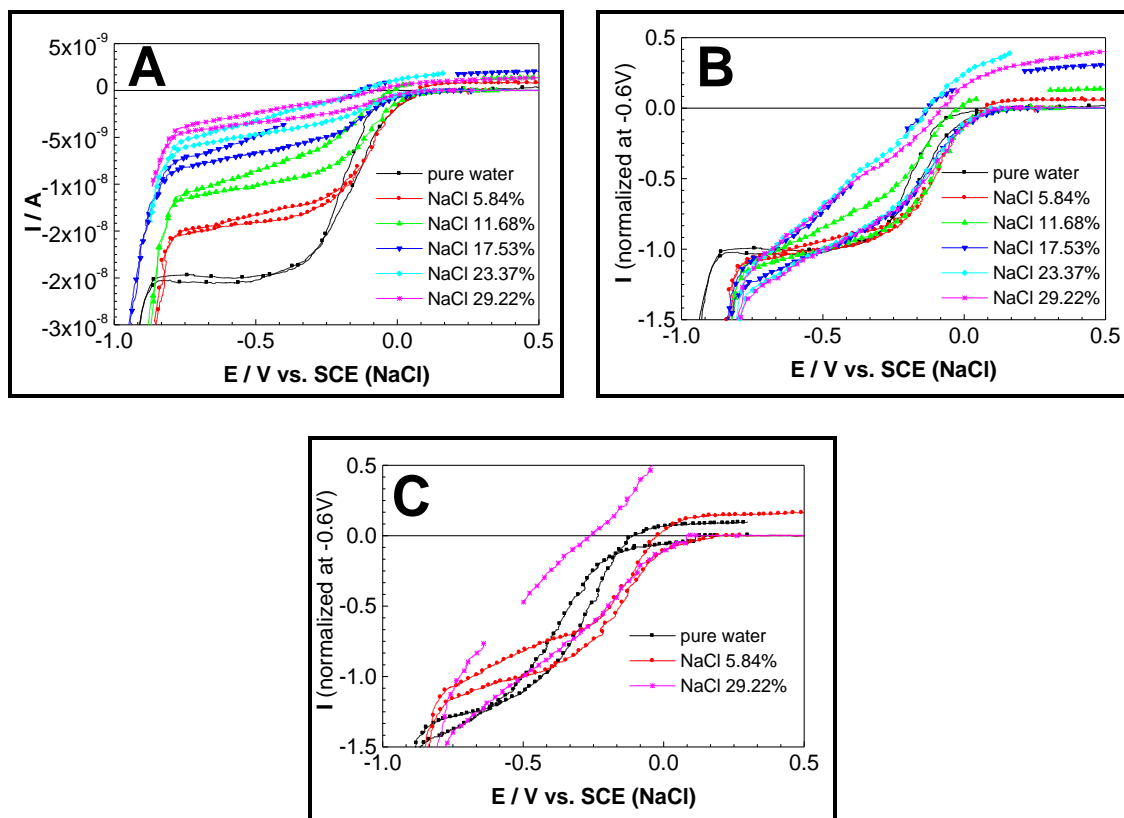


Figure 3: Voltammograms, raw and normalized at -0.6 V, recorded for the reduction of dissolved oxygen at the homemade 50 μ m Pyrex Pt-UME in pure water and NaCl solutions at various concentrations (5.84%, 11.68%, 17.53%, 23.37%, and 29.22% w:w). Influence of the electrodes storage in saturated NaCl (29.22% w:w) for 3 days.

In Figure 3C, we reported the voltammograms that we recorded in pure water and NaCl

solutions at 5.84% and 29.22% w:w with the Pyrex Pt-UME after its storage in saturated NaCl for 3 days. All the voltammograms, even this recorded in pure water, are affected by the storage in the concentrated brine.

The normalized voltammograms for the other UMEs that we tested are represented in Fig. 4. As with the Pyrex Pt-UME, the damage induced by the concentrated brines on the electrodes can be easily remarked during the reverse scans. The Quartz fibre Pt-UME, that is routinely used in the laboratory without particular problems for “scanning electrochemical microscopy” experiments, is the less resistant. It is the same for the Soft glass Pt-UME, that electrochemists are using very often because its construction is very easy by reason of its low melting point, which is scarcely better. The other UMEs tested are quite satisfactory until the 11.68% NaCl concentration included; with higher concentrations, the currents recorded are quite less negative and even positive during the reverse scans. The UME whose insulating part is made in very pure quartz (Suprasil-quartz) led to the best results.

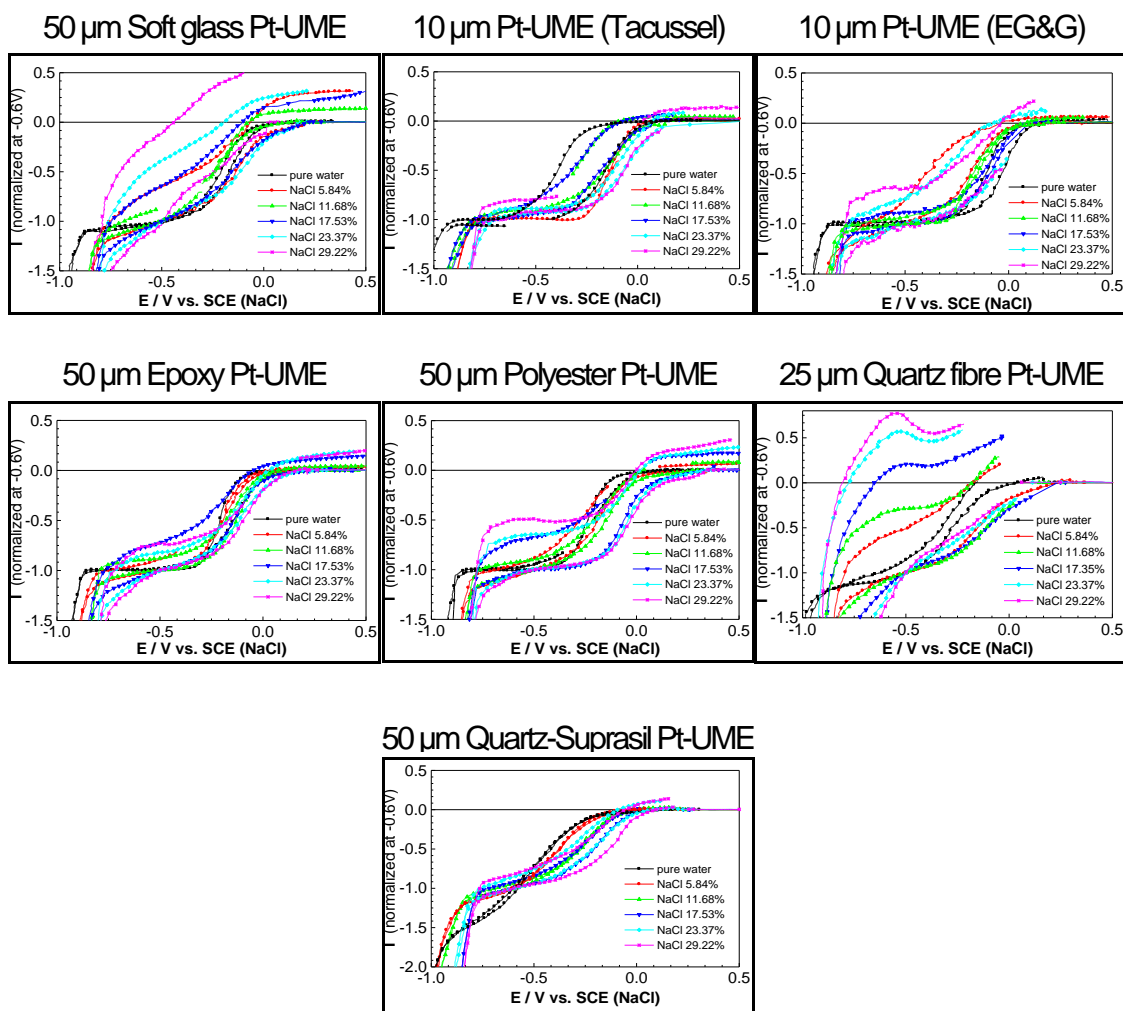


Figure 4: Normalized voltammograms recorded for the reduction of dissolved oxygen at different electrodes in pure water and in NaCl solutions at various concentrations (5.84%, 11.68%, 17.53%, 23.37%, and 29.22% w:w).

The voltammetric curves that are displayed in Fig. 5 were recorded using UMEs that were stored beforehand in saturated NaCl (29.22% w:w) for 3 days. One can remark that among the UMEs that do not function too badly before the stay in the concentrated brine, the commercial electrode Pt-UME (EG&G) and the homemade Epoxy Pt-UME ceased working whereas the functioning of the commercial Pt-UME (Tacussel) and the homemade Polyester Pt-UME was only just modified.

As regards the 50 μm Quartz-Suprasil Pt-UME the voltammograms recorded after this 3 days stay are almost identical to the preceding ones and now, this UME undergoes more extended tests.

We will now consider the results obtained with ferrocene dimethanol which is an almost ideal electrochemical system whose kinetics are “rapid”.

Ferrocene dimethanol used as the electroactive species

A limited number of experiments were done until now, however the results are interesting and this is why we displayed the corresponding voltammograms in Fig. 6. The results for the Soft glass Pt-UME excepted, all the other electrodes tested seem to almost correctly working once immersed in the brines. However, the commercial electrodes Pt-UME (EG&G) and Pt-UME (Tacussel) –and not Quartz-Suprasil Pt-UME– provide the most satisfactory voltammograms. Moreover, the Pt-UME (Tacussel) is working satisfactorily even after the three day immersion in the saturated brine. In this way, the relative resistance of an electrode seems to be dependant not only on the brines concentration, but also on the electroactive species that undergoes the electrochemical process.

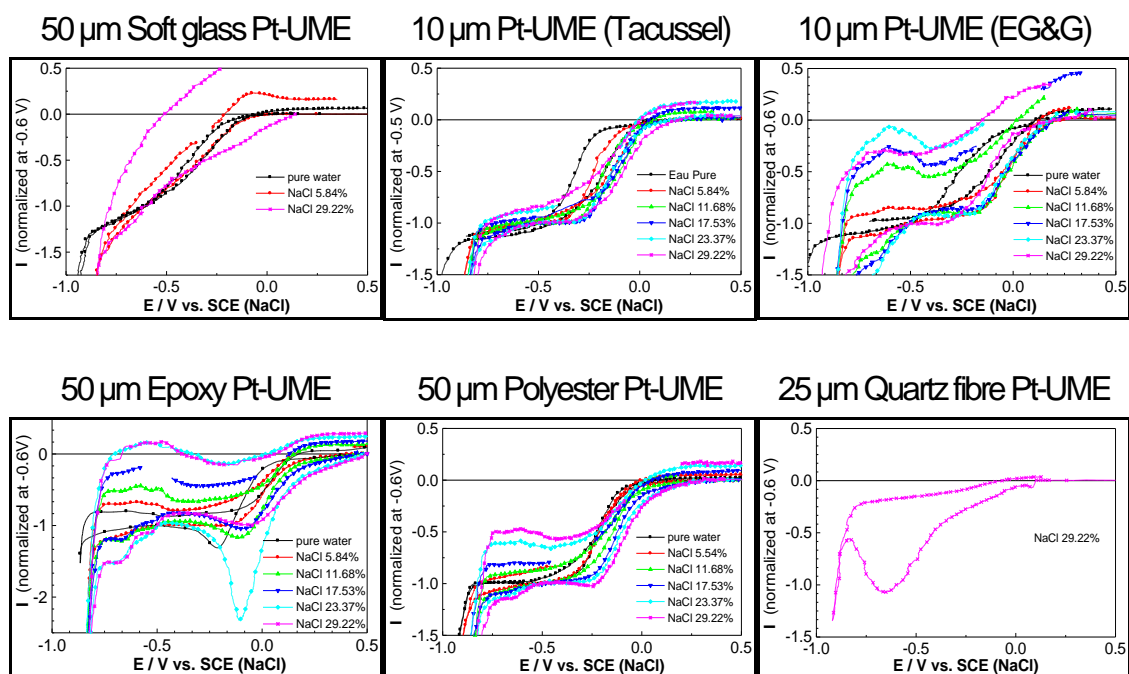


Figure 5: Normalized voltammograms recorded for the reduction of dissolved oxygen in pure water and in NaCl solutions at various concentrations (5.84%, 11.68%, 17.53%, 23.37%, and 29.22% w:w) using UMEs that were stored in saturated NaCl (29.22% w:w) for 3 days.

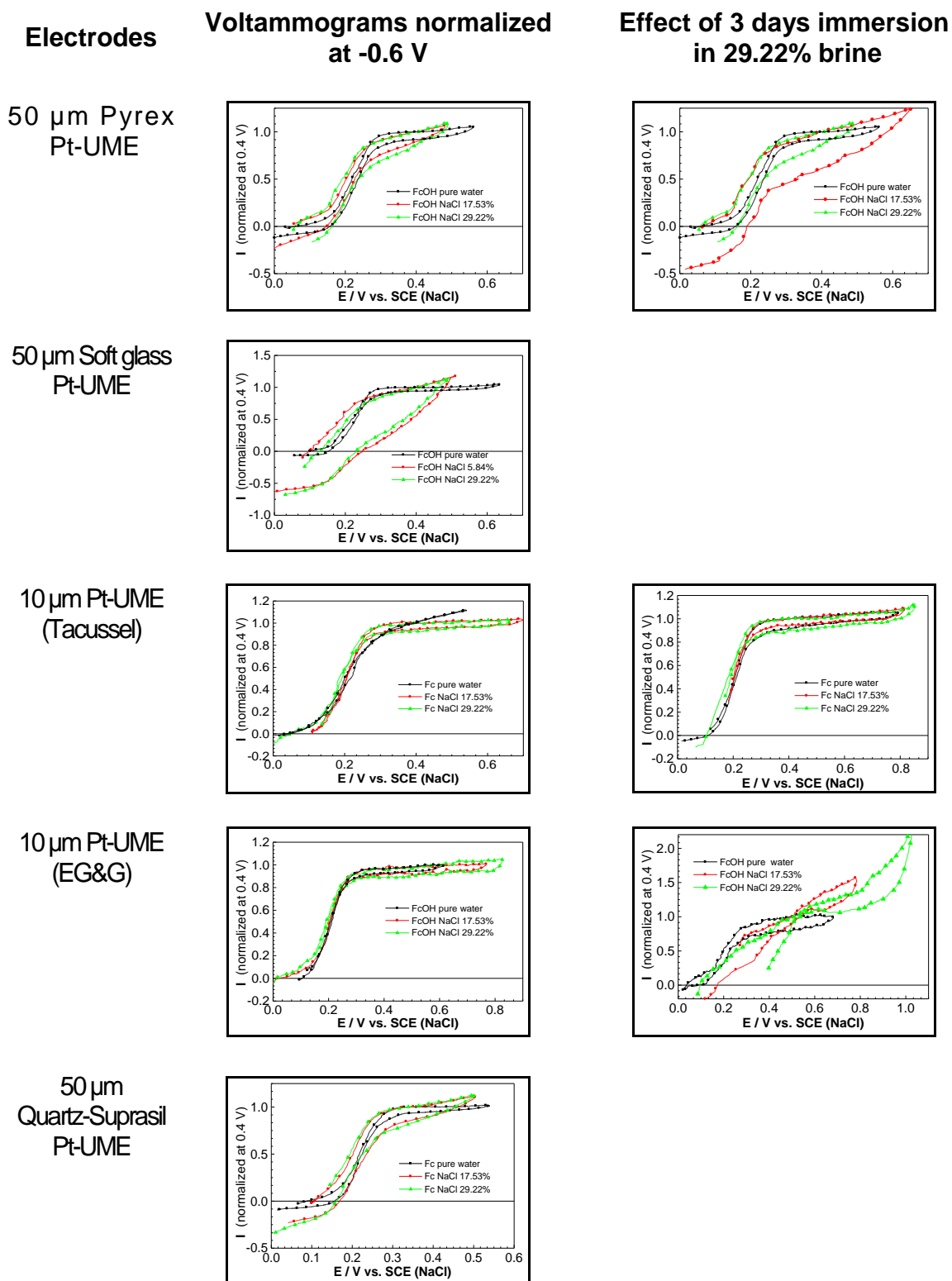


Figure 6: Normalized voltammograms recorded for the oxidation of 0.5 mM ferrocene dimethanol at different electrodes in non deaerated pure water and in non deaerated NaCl solutions at 17.53% and 29.22% w:w. Influence of the electrodes storage in saturated NaCl (29.22% w:w) for 3 days.

Summary and Conclusions

We tested in NaCl brines ranging from 5.84 to 29.22% w:w. eight platinum UMEs, commercial or homemade, using dissolved oxygen and ferrocene dimethanol as the electroactive species. The bodies of the UMEs were made of different glasses or polymeric resins. In the most of cases the electrodes are damaged when immersed in the concentrated solutions. This alteration can be easily monitored by the recording of voltammograms either immediately after the immersion of the UMEs in the brines or after a three-day immersion in the 29.22% w:w brine. When the UMEs are damaged, the corresponding voltammograms are more or less distorted. The tests performed have allowed us to eliminate definitively two electrodes that furnished deeply altered voltammetric curves.

Generally, the more concentrated the brine is, the more the electrodes are affected; however, the phenomena are not so simple and this work, that, to our knowledge, is the first attempt to evaluate the use of UMEs in concentrated NaCl solutions must be considered as a preliminary one.

We emitted the hypothesis that the release of electroactive species by the material that constitutes insulating body of the electrodes is behind the UMEs dysfunction. For that reason, we considered UMEs made of materials that do not contain electroactive species (quartz-Suprasil) or materials well-known for their resistance to brines (epoxy and polyester resins).

When dissolved oxygen is used as the electroactive species the degradation of the electrodes is easily noticeable by the deformation of the voltammetric curves particularly during the reverse scans. The UMEs whose the insulating part is made of “quartz-suprasil” are the less affected by the brines.

Summary and Conclusions

We tested in NaCl brines ranging from 5.84 to 29.22% w:w. eight platinum UMEs, commercial or homemade, using dissolved oxygen and ferrocene dimethanol as the electroactive species. The bodies of the UMEs were made of different glasses or polymeric resins. In the most of cases the electrodes are damaged when immersed in the concentrated solutions. This alteration can be easily monitored by the recording of voltammograms either immediately after the immersion of the UMEs in the brines or after a three-day immersion in the 29.22% w:w brine. When the UMEs are damaged, the corresponding voltammograms are more or less distorted. The tests performed have allowed us to eliminate definitively two electrodes that furnished deeply altered voltammetric curves.

Generally, the more concentrated the brine is, the more the electrodes are affected; however, the phenomena are not so simple and this work, that, to our knowledge, is the first attempt to evaluate the use of UMEs in concentrated NaCl solutions must be considered as a preliminary one.

We emitted the hypothesis that the release of electroactive species by the material that constitutes insulating body of the electrodes is behind the UMEs dysfunction. For that reason, we considered UMEs made of materials that do not contain electroactive species (quartz-Suprasil) or materials well-known for their resistance to brines (epoxy and polyester resins).

When dissolved oxygen is used as the electroactive species the degradation of the electrodes is easily noticeable by the deformation of the voltammetric curves particularly during the reverse scans. The UMEs whose the insulating part is made of “quartz-suprasil” are the less affected by the brines.

Summary and Conclusions

We tested in NaCl brines ranging from 5.84 to 29.22% w:w. eight platinum UMEs, commercial or homemade, using dissolved oxygen and ferrocene dimethanol as the electroactive species. The bodies of the UMEs were made of different glasses or polymeric resins. In the most of cases the electrodes are damaged when immersed in the concentrated solutions. This alteration can be easily monitored by the recording of voltammograms either immediately after the immersion of the UMEs in the brines or after a three-day immersion in the 29.22% w:w brine. When the UMEs are damaged, the corresponding voltammograms are more or less distorted. The tests performed have allowed us to eliminate definitively two electrodes that furnished deeply altered voltammetric curves.

Generally, the more concentrated the brine is, the more the electrodes are affected; however, the phenomena are not so simple and this work, that, to our knowledge, is the first attempt to evaluate the use of UMEs in concentrated NaCl solutions must be considered as a preliminary one.

We emitted the hypothesis that the release of electroactive species by the material that constitutes insulating body of the electrodes is behind the UMEs dysfunction. For that reason, we considered UMEs made of materials that do not contain electroactive species (quartz-Suprasil) or materials well-known for their resistance to brines (epoxy and polyester resins).

When dissolved oxygen is used as the electroactive species the degradation of the electrodes is easily noticeable by the deformation of the voltammetric curves particularly during the reverse scans. The UMEs whose the insulating part is made of “quartz-suprasil” are the less affected by the brines.

However, the fabrication of UMEs by sealing platinum microwires in capillaries made of highly pure quartz is quite difficult because the melting point of platinum and the softening point of quartz-Suprasil are relatively close.

When ferrocene dimethanol is used as the electroactive species, the voltammetric curves recorded showed that the quartz-Suprasil Pt-UME is probably slightly altered whereas other electrodes seem to function correctly.

Therefore, the chemical resistance of the UMEs that we tested strongly depends on the nature of the insulating material used to make their insulating body but it also depends, to a lesser extent, on the nature of the electroactive species used.

At this point of progress of this work several questions still arise:

- (i) what is the corrosion extent of the UMEs insulating material when the latter are simply immersed in concentrated brines? Can this corrosion be quantified from SEM micrographs?
- (ii) what is the exact influence of the electroactive species in the bulk solution, or electrochemically generated ones at the electrode surface, on the corrosion process? Actually, one can easily understand that a species that is produced during the reduction of molecular oxygen as OH^- ion, which is highly reactive in brines because it is desolvated, can participate to the corrosion pathway. In this case, a simple pH effect would allow us to answer this question. It is the same for the methanol ferrocenium ions that are released during the anodic oxidation of methanol ferrocene that can behind solubilisation or precipitation phenomena involving species that are released by the glass or the polymeric material.
- (iii) what is the influence of the Pt disk on the corrosion phenomenon? The distortions of voltammograms that are observed when the UMEs are immersed in brines are probably linked with phenomena occurring at the metal/insulating material interface. A possible explanation is that brines, or the species generated by the electroactive species transformation, preferentially attack the insulating material close to the platinum disk. Therefore, crevices are created at the insulating material/platinum interface. Inside these crevices, the mixing of the brine with the species released by the insulating material leads to the formation of a new and extremely concentrated medium or a gel where specific electrochemical reactions take place and produce signals that are superimposed to this of the electroactive species. The same phenomena probably occur when millimetric electrodes are used, but they are not detected because of the much higher distance between the platinum/insulating material interface and the large pristine surface area of the platinum disc.
- (iv) what is the contribution of the capacitive current on the voltammograms that we recorded?

Among these questions, there are certain that are relatively easy to answer, at least in part, especially with regard to the particular role that the electrochemical reduction of dissolved oxygen seems to play against the degradation of the UMEs. So it is important to check if similar phenomena do not occur with other electroactive species, in particular, with iron species. If this is the case, it would be possible to use UMEs in brines so long as the solutions are rigorously deaerated.

The fabrication process of UMEs whose body is made of quartz-Suprasil is worth to be improved because these electrodes seem to be promising not only for their utilization in concentrated brines but also to in-situ monitor radiolysis experiments where all the glassware materials used are required to not interact with the irradiation beam. This can be attained by using platinum alloys with higher melting point than pure platinum.

Acknowledgements

The authors wish to thank Dr. Kay Schuster from the Institute of Photonic Technology (Jena, Germany) and Dr. Philippe Roy from the XLIM Research Institute (University of

Limoges, France) who kindly provided us with quartz Suprasil capillaries for the UMEs construction.

The research leading to these results has received funding from the European Union's European Atomic Energy Community's (Euratom) Seventh Framework Programme FP7/2007-2011 under grant agreement n° 212287 (RECOSY project).

References

- Altmaier M., Gaona X., Fellhauer D., Buckau G., (2010). Intercomparison of Redox Determination Methods on Designed and Near-Natural Aqueous Systems - FP 7 EURATOM Collaborative Project "Redox Phenomena Controlling Systems". Report-Nr. KIT-SR 7572, Karlsruher Institut für Technologie (KIT), D-76131 Karlsruhe.
- Amatore C., (1995). Electrochemistry at Ultramicroelectrodes. in: "Physical Electrochemistry" pp 131-208, I. Rubinstein (editor), Marcel Dekker, Inc. New York.
- Baillif P., Chouikhi B., Touray J. C., (2000). Dissolution mechanisms of boro-silicate glass fibres in saline solution with added dissolved silica. J. Mater. Sci. 35, 967-973.
- Bard A. J., Fen F.R., Mirkin M., (1994). Scanning Electrochemical Microscopy, in: "Electroanalytical Chemistry: a Series of Advances" Vol. 18, pp 244-373, A. J. Bard (editor), Marcel Dekker, New York.
- Belmont C., Tercier M. L., Buffle J., Fiaccabrino J. C., Koudelka-Hep M., (1996). Mercury-plated iridium-based microelectrode arrays for trace metals detection by voltammetry: optimum conditions and reliability. Anal.Chim.Acta, 329, 203-214.
- Belmont-Hébert C., Tercier M. L., Buffle J., (1998). Fiaccabrino J. C., De Rooij, N. F., Koudelka-Hep M., (1998). Gel-Integrated Microelectrode Arrays for Direct Voltammetric Measurements of Heavy Metals in Natural Waters and Other Complex Media. Anal. Chem., 70, 2949-2956.
- Bossy H., (2006). The Closure of the Asse Research Mine. Joint Convention on the Safety of Spent Fuel Management and on the Safety of Radioactive Waste Management, second review meeting, 15-24 May 2006, Vienna.
- Chave T., Frugier P., Ayrat A., Gin S., (2007). Solid state diffusion during nuclear glass residual alteration in solution. J. Nucl. Mater. 362, 466-473.
- Cortot J., Lambert E., Cheikh-Ibrahim A., Etienne M., Perdicakis M., (2009). Investigations with a view to developing an amperometric device for the determination of the redox potential. Presentation at the 1st Annual RECOSY Project Workshop, 10-12 February 2009, Barcelona.
- Cox G. A., Ford B. A., (1993). The long-term corrosion of glass by ground- water. J. Mater. Sci. 28, 5637-5647.
- Cramer S. D., (1980). The Solubility of Oxygen in Brines from 0 to 300°C. Ind. Eng. Chem. Process Des. Dev. 19, 300-305.

CRC Handbook of Chemistry and Physics 1974-1975 55th Edition, pp. D225, F49 (1974)

Dal Bianco B., Bertinello R., Milanese L., Barison S., (2004). Glasses on the seabed: surface study of chemical corrosion in sunken Roman glasses. *J. Non-Cryst. Solids* 343, 91-100.

Devreux F., Ledieu A., Barboux P., Minet Y., (2004). Leaching of borosilicate glasses. II. Model and Monte-Carlo simulations. *J. Non-Cryst. Solids* 343, 13-25.

De Vitre R. R., Tercier M.-L., Buffle J., (1991). In situ voltammetric measurements in natural waters, the advantages of microelectrodes. *Anal. Proc.* 28, 74-75.

Doménech-Carbó A., Doménech-Carbó M. T. Osete-Cortina L., (2008). Electrochemical Study of Iron Oxide Deposits in Weathered Archaeological Glass. *Int. J. Electrochem. Sci.* 3, 609-630

Ferrel R. T., Himmelblau D. M., (1967). Diffusion Coefficients of Nitrogen and Oxygen in Water. *J. Chem. Eng. Data* 12, 449-451.

Godon N., Thomassin J. H., Touray J. C., Vernaz E., (1988). Experimental alteration of R7T7 nuclear model glass in solutions with different salinities (90 ° C, 1 bar): implications for the selection of geological repositories. *J. Mater. Sci.* 23, 126-134.

Ho C. S., Ju L. K., Baddour R. F., Wang D. I. C., (1988). Simultaneous measurement of oxygen diffusion coefficients and solubilities in electrolyte solutions with a polarographic oxygen electrode. *Chem. Engng. Sci.* 43, 3093-3107.

Hung G. W., Dinius R. H., (1972). Diffusivity of Oxygen in Electrolyte Solutions. *J. Chem. Eng. Data* 17, 111-115.

IAEA - International Atomic Energy Agency, (2001). The use of scientific and technical results from underground research laboratory investigations for the geological disposal of radioactive waste. TECDOC-1243, Vienna, September 2001.

Idronaut S.r.l - 20861 Brugherio (MB) Italy - <http://www.idronaut.it>.

Kienzler B., Metz V., Brendebach B., Finck N., Plaschke M., Rabung Th., Rothe J., Schild D., (2010). Chemical status of U(VI) in cemented waste forms under saline conditions. *Radiochim. Acta*, 98, 675-684.

Kounaves S. P., (1990). Iridium Based Ultramicroelectrodes, development and use in electrochemical analysis. *Platinum Metals Rev.*, 34, 131-134.

Kovacs G. T. A., (1995). Microfabricated heavy metal ion sensor. *Sensors and Actuators B: Chemical*, 23, 41-47.

Ledieu A., Devreux F., Barboux P., Sicard L., Spalla O., (2004). Leaching of borosilicate glasses. I. Experiments. *J. Non-Cryst. Solids* 343, 36-12.

Moog H. C., Herbert H. J., Brendler V., Richter A., Altmaier M., Marquardt C., Voigt W., Wilhelm S., (2010). THEREDA: The thermodynamic reference database for nuclear waste disposal in Germany. Abstracts of Papers, 240th ACS National Meeting, August 22-26, 2010, Boston, MA, United States.

Nemer M. B., Xiong Y. L., Ismail A. E., Jang J. H., (2011). Solubility of $\text{Fe}_2(\text{OH})_3\text{Cl}$ (pure-iron end-member of hibbingite) in NaCl and Na_2SO_4 brines. *Chem. Geol.* 280, 26-32.

Reed D. T., Borkowski M., Richmann M. K., Lucchini J. F., Swanson J., Ams D., Khaing H., (2010). High ionic-strength subsurface chemistry of actinides. Abstracts of Papers, 240th ACS National Meeting, August 22-26, 2010, Boston, MA, United States.

Shoal is a European Research Project Managed by BMT funded under the Seventh Framework Programme for ICT (<http://www.roboshoal.com/>).

Tercier M. L., Parthasarathy N., Buffle J., (1995). Reproducible, reliable and rugged mercury-plated Ir-based microelectrode for in-situ measurements in natural waters. *Electroanalysis*, 7, 55-63.

Tercier-Waeber M. L., Buffle J., Confalonieri F., Riccardi G., Sina A., Graziottin F., Fiaccabrino G. C., Koudelka-Hep M. (1999). Submersible voltammetric probes for in situ real-time trace element measurements in surface water, groundwater and sediment–water interface. *Meas. Sci. Technol.* 10, 1202-1213.

Tromans D., (2000). Modeling Oxygen Solubility in Water and Electrolyte Solutions. *Ind. Eng. Chem. Res.* 39, 805-812.

van Stroe A. J., Janssen L. J. J., (1993). Determination of the diffusion coefficient of oxygen in sodium chloride solutions with a transient pulse technique. *Anal. Chim. Acta* 279, 213-219.

Wickert C. L., Vieira A. E., Dehne J. A., Wang X., Wilder D. M., Barkatt A., (1999). Effects of salts on silicate glass dissolution in water: kinetics and mechanisms. *Phys. Chem. Glasses Part B*, 3, 157-170.

U REMOVAL KINETICS IN THE PRESENCE OF MAGNETITE AND MAGHEMITE NANOPARTICLES

Florian M. Huber^{1*}, Dieter Schild¹, Tonya Vitova¹, Jörg Rothe¹, Regina Kirsch²,
Thorsten Schäfer¹

¹ Karlsruhe Institute for Technology (KIT), Institute for Nuclear Waste Disposal (INE),
(GER)

² Institute of Radiochemistry, Forschungszentrum Dresden-Rossendorf, (GER)

* Corresponding author: florian.huber@kit.edu

Abstract

The interaction of hexavalent U with a freshly synthesized nanoparticulate magnetite ($\text{Fe}^{\text{II}}\text{Fe}^{\text{III}}\text{O}_4$) (stoichiometric ratio $x(\text{Fe}(\text{II})/\text{Fe}_{\text{TOT}}) = 0.25 - 0.33$), a partly oxidized synthetic nanoparticulate magnetite ($x = 0.11 - 0.27$) and maghemite nanoparticles ($x = 0$) under anoxic conditions and exclusion of CO_2 as function of pH, contact time and total U concentration (3×10^{-5} M) has been examined. Short term kinetic batch experiments (contact time of 90 d) for four different pH values have been conducted. Spectroscopic techniques (XPS) were applied to probe for the presence and amount of reduced U on the magnetite surface. Batch kinetic studies revealed a fast initial U removal from aqueous solution with $> 90\%$ magnetite associated U after 24 hours within the pH range 5-11. Redox speciation by XPS verifies the presence of tetravalent U on the magnetite surface. A clear correlation of the amount of available Fe(II) on the magnetite surface and the amount of tetravalent U is observed. Thermodynamic calculations based on the experimentally determined redox potentials corroborate the spectroscopic findings of U oxidation states. Overall, the results reflect the importance of magnetite bond structural bound Fe(II) as redox partner for uranyl reduction.

Introduction

The release of U into the environment through anthropogenic induced geochemical perturbations (e.g. migration out of a nuclear waste repository; use of depleted U for military devices; U exploration and acid mine drainage) is a potential threat to mankind and biosphere due to U chemo-toxicity. To develop sound risk assessment strategies and U remediation concepts, a mechanistic understanding of the behavior of U in natural environments and its interaction with geologic materials is of crucial necessity. The

mixed-valent iron oxide magnetite, $\text{Fe}^{(\text{III})}[\text{Fe}^{(\text{II})}\text{Fe}^{(\text{III})}]\text{O}_4$ possesses an inverse spinel crystal structure and a stoichiometric ratio $x(\text{Fe}(\text{II})/\text{Fe}_{\text{TOT}}) = 0.33$ (Cornell and Schwertmann, 1996). Magnetite occurs naturally in e.g. igneous and plutonic rocks as accessory mineral phase. Furthermore, it can be found as corrosion product of stainless steel, e.g. canisters in the framework of the multi-barrier concept of deep geological waste disposals (Grambow et al., 1996) representing an important Fe(II) source for redox reactions with radionuclides.

Experimental studies on sorption and/or reduction of U(VI) in presence of magnetite are still accumulating, mostly motivated by the importance of elucidating effective immobilization processes of ($\text{U}(\text{VI}) \Rightarrow \text{U}(\text{IV})$) and the role of aqueous, surface sorbed or structural bound Fe(II). U data of sorption and reduction studies with magnetite in presence of carbonate at pH values representative for granitic ground-waters (pH 8-9) for contact times up to 150 days were presented by (El Aamrani, 1999). These authors applied X-ray photoelectron spectroscopy (XPS) to identify the U surface species on magnetite and found evidences for a coupled reduction-oxidation process of U(VI) and Fe(II), respectively, in the presence of bicarbonate. Though, they found no U(IV) at slightly acidic pH (4.81) in the absence of carbonate. XPS results presented by Missana et al. (2003a,b) and Scott et al. (2003) indicate U reduction in the presence of structural bound Fe(II) on mineral phases. U(VI) reduction is also feasible by means of sorbed ferrous iron in presence of an Fe(III) containing solid phase (nanoparticulate hematite) as shown by (Liger et al., 1999). The influence of bicarbonate in the system uranyl-magnetite for pH 6, 8 and 10 with contact times of 42 days using XPS was investigated by (Regenspurg et al., 2009). A facilitated U(VI) reduction attributed to the formation of siderite representing an additional $\text{Fe}^{(\text{II})}$ pool was found. Most recently, Ilton and co-workers presented spectroscopic indications (XPS) of the formation of U(V) in the presence of magnetite and explained the stability of U(V) by sorption/incorporation/precipitation in either secondary iron phases or mixed valent U phases (Ilton et al., 2010). No evidences of U(IV) on basis of XPS and X-ray absorption spectroscopy (XAS) measurements were found by these authors. However, no Eh measurements of the XPS samples were given to link the experimental findings to thermodynamic calculations and other data published.

Materials and Methods

Solid phase characterization

Three nanoparticulate solid phases have been applied in the experiments, namely a freshly prepared magnetite suspension (hereafter called, fmag), a maghemite suspension prepared using the fmag suspension (hereafter called mgh) and an older magnetite suspension which was stored over more than 2 years in a Ar glove box showing partially oxidization due to repeated exposure to low oxygen contents in the glove box (hereafter called, partly-oxidized magnetite (po-mag)). The three solid phases were synthesized using a procedure proposed by (Schwertmann and Cornell, 1991). Characterization of the solid phases were done by means of X-ray diffraction (XRD), scanning electron microscopy (SEM) and energy dispersive X-ray spectroscopy (EDX) and specific surface area (BET). The XRD patterns for all mineral phases used

throughout the study verify that no additional mineral phases than the ones synthesized are present. BET N₂-adsorption yielded a specific surface area of 19.7 m²/g, 14.78 m²/g and 11.14 m²/g for the po-mag, fmag and mgh, respectively. All mineral phases exhibit particle sizes around 100-300 nm as determined from the SEM pictures in accordance with TEM investigations by Missana et al. (2003b). Derivation of the particle sizes by means of the Scherrer equation (Patterson, 1939) on basis of the XRD spectra yielded values around 30-60 nm. EDX spectra for the po-mag revealed only Fe and O with mean atomic concentrations of 31.2 % and 68.2 %, the fmag yields mean concentrations of 42.8 % to 56.8 % for Fe and O, respectively. Regarding mgh, the amount of Fe increased to a mean value of approximately 45 % while the amount of O decreases to 55% atomic percent. In a few samples, impurities of S and Si (< 0.5 at.-%) were detected most likely as artifacts from the solid phase synthesis. Determination of the isoelectrical point (pH_{iep}) yielded values for fmag and po-mag of pH 5.5 and pH 6, respectively. Literature values for commercial, synthesized and natural magnetite range between pH ~ 4 and ~ 8 (Illes and Tombacz, 2006; Kosmulski, 2001; Mansour et al., 2009).

Batch Experiments

The batch type experiments were conducted at room temperature (~ 21 °C) in a glove box under Ar atmosphere (< 1 ppm O₂). All chemicals used ultra pure grade. Batch samples have been prepared in polyethylene vials (Zinsser, 20 mL) in all experiments. Both the magnetite and maghemite suspensions were applied for the experiments by dilution of the stock solutions with Milli-Q water (18.2 MΩ), purged with Ar before use, to strip out dissolved carbonate and oxygen. An ionic strength of 0.01 M was set by using NaCl as background electrolyte. The pH was adjusted by addition of HCl and NaOH (Backer, CO₂ free). Finally, U was spiked to the samples from a 1 g/L stock solution of UO₂(NO₃)₂ (ICP-MS reference standard) to achieve the desired concentrations. If necessary, pH was readjusted slowly by addition of NaOH or HCl immediately after the addition of U. Determination of pH was done applying a semi-micro Ross electrode (81-03, Orion Co.) in combination with a digital pH meter (720A, Orion Co.). The set-up was calibrated using at least 4 commercial buffer solutions (Merck). Besides pH, the redox potential of the samples was measured using a Pt combined electrode (Metrohm) coupled to the Orion pH meter. We measured the redox potential of our samples in contact with the suspension without stirring the samples. We consistently monitored (read out every 60 s) the evolution of the redox potential and stopped the measurement when a plateau value was reached. That is, the measurement sometimes took several hours up to one day, for details see (Huber et al., 2011). In course of the experiments, pH was frequently measured and readjusted several times if necessary. After the desired contact time, samples were ultra-centrifuged at 694000 g (Beckman XL-90, rotor type 90Ti) in sealed vials for one hour to separate the solid phase and possible colloidal Fe phases. After centrifugation, the samples were immediately transferred back into the glove box and an aliquot of the supernatant was taken using a syringe. This intricate procedure was necessary since preliminary tests using filtration (10 kD; Microsep, Pall Life Science) of the suspension to remove the solid phase indicated a possible U sorption and/or a sorption of U associated colloidal phases on the filter material. Moreover, this ultra-centrifugation procedure has been proven to be suitable to effectively remove Th(IV) “eigencolloids” from solution (Altmaier et al., 2004). Aliquots of the ultra-centrifuged supernatant have been analyzed

by inductively coupled plasma mass-spectrometry (ICP-MS) for determination of U and Fe_(TOT) concentrations.

Po-mag sample series (Series #1). The po-mag suspension was stored over a period of approximately 2 years in a Ar glove box before using in the experiments exhibiting partial oxidization (Fe(II)/Fe_{TOT} = 0.2 in average as verified by XPS) due to the repeated exposure to the glove box atmosphere which always contains trace amounts of oxygen. Short term (1 d up to 90 d) kinetic experiments (hereafter called Series #1) have been conducted. 4 sample series at 4 different pH values (~ 2.5, 5, 8 and 11) with a U concentration of 3×10^{-5} M have been prepared. Samples have been taken after 1, 2, 3, 6, 14, 48, 57 and 90 d, respectively (Table 2). XPS measurements have been undertaken subsequently after the desired contact times of 1d.

Fmag sample series (Series #2). The fmag suspension was prepared immediately before the start of the experiments assuring that no or minor oxidization had occurred. Batch experiments with the freshly prepared magnetite using the same conditions as in Series #1 have been conducted (hereafter called Series #2) but with a different contact time (13 days). Here, three different pH values have been adjusted (pH ~ 5, 8, 11) (Table 3). Again, XPS measurements have been carried out after the end of the experiments to probe for the valence state of U. The results are compared to the results obtained in Series #1 to evaluate the influence of a slightly oxidized magnetite in relation to a freshly prepared magnetite in terms of U reduction, respectively.

Maghemite Samples (Series #3).

Experiments using maghemite (hereafter called Series #3) have been conducted using the same conditions as for the two magnetite series ($[U]_{TOT} = 3 \times 10^{-5}$ M and ionic strength I = 0.01 M NaCl). As it was the case for Series #2 three pH values have been adjusted (pH ~5, ~8 and ~11) and a contact time of 13 d has been applied (Table 3).

X-ray Photoelectron Spectroscopy (XPS).

XPS provides an effective surface sensitive method for determination of the valence state of Fe and U at the magnetite surface. After ultra-centrifugation of the samples, the supernatant was separated from the solid magnetite phase. Subsequently, preparation of the samples for XPS measurements was done in the glove box under Ar atmosphere. The separated solid phase was dried at room temperature, pressed on In foil and mounted on the sample holder. Transfer of the prepared samples under Ar atmosphere to the XP spectrometer was achieved by means of an O-ring sealed vacuum transfer vessel (PHI model 04-110). XPS measurements at room temperature were carried out by using a Physical Electronics Inc. (PHI) model 5600ci instrument equipped with a standard dual anode X-ray source, Mg K_α (1253.6 eV) and Al K_α (1486.6 eV), and with a monochromatized Al K_α source operating at 100 W source power.

Results and Discussion

U Speciation

In Figure 1a and 1b predominance diagrams for the experiments are depicted. Generally speaking, polynuclear U species dominate the speciation. At acidic pH (2 to 5) above $E_{h(SHE)} = 0.1$ V the free uranyl ion predominates followed by the polynuclear species $(UO_2)_3(OH)_5^+$ from pH 5 to ~ 8 . Between pH ~ 8 and ~ 9.5 $(UO_2)_3(OH)_7^-$ prevails. The pentavalent U species, UO_2^+ , dominates in a small area between pH 2 and 5.5 for $E_{h(SHE)}$ values within $+0.1$ V and $\sim +0.08$ V. Above pH ~ 9.5 the negatively charged third mononuclear hydrolysis species, $UO_2(OH)_3^-$, becomes dominant. Between pH 2 to ~ 5 the borderline of U reduction is located at $E_{h(SHE)} = \sim 0.09$ V and afterwards decreases to an $E_{h(SHE)}$ of approximately -0.38 V at pH 12. Beneath the borderline, the amorphous U species, $UO_{2(am)}$, dominates the speciation.

Redox Potential (E_h) Measurements

The aquatic chemistry of redox-sensible radionuclides like U is governed by the solution redox potential. Determination of the samples redox potential allows a more precise interpretation and analysis of the results. A literature review on the U-magnetite system revealed a substantial lack of experimentally determined redox potential data. This prevents not only a comparison between results presented by different authors for the same system studied but also hinders the interpretation of the results presented without thermodynamic calculations. It is therefore of utmost importance to conduct redox potential measurements, although it should be clearly stated that a systematical procedure for redox measurements is still not established in the literature (e.g. (Schüring, 2000)). Several authors dealt with the issue of redox potential determination both in synthetic and natural systems (see e.g. (Grenthe et al., 1992; Lindberg and Runnells, 1984) and references therein) concluding that severe uncertainties can sometimes be accompanied with redox potential measurements.

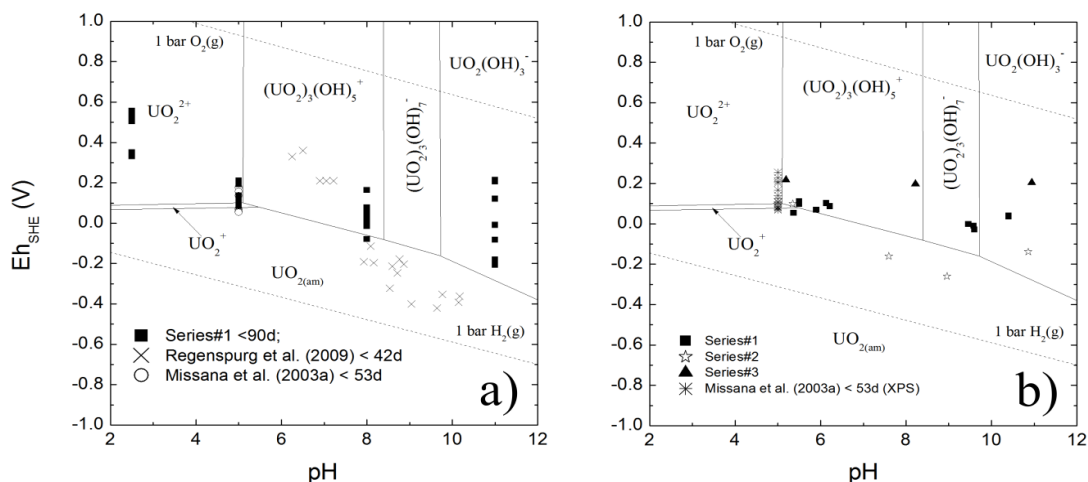


Figure 1: Predominance plots for the U speciation calculated with the Hydra/Medusa code using NEA constants. a) $[U]_{TOT} = 3 \times 10^{-5}$ M. Additionally inserted are redox potentials obtained in this study in comparison to literature data by Regensburg et al. (2009) and Missana et al. (2003a). b) $[U]_{TOT} = 3 \times 10^{-5}$ M. Only samples measured are shown.

Nonetheless, if the measurements are carried out in a consistent way they can at least be used in a qualitative way. The pH and Eh of the batch samples have been measured and compared to literature data using comparable synthesis protocols and U concentrations (Missana et al., 2003; Regenspurg et al., 2009) (Figure 1). For Series #1, between pH 2 to 4, the $E_{h(SHE)}$ represent strongly oxidizing conditions with hexavalent U dominating the U speciation. Around pH 5 $E_{h(SHE)}$ in this study and the data published by (Missana et al., 2003) are comparable showing a range of +0.3 V down to +0.05 V. The values by Missana et al. (2003b) become lower with increasing contact time to a final value after 53 d of ~ 30 mV which is slightly lower than the values measured in this study. At this pH, $E_{h(SHE)}$ continuously approach the calculated U(VI)/U(IV) borderline making U reduction thermodynamically feasible. At pH ~ 6 $E_{h(SHE)}$ in this work are in the range of ~ 0.1 V which is ~ 0.2 V lower (more negative) than the data measured by Regenspurg et al. (2009), whereas in the neutral to slightly alkaline pH range both data sets show similar values in the range of $\sim +0.1$ V to ~ -0.1 V. The $E_{h(SHE)}$ values for maghemite (Series #3 in Figure 2b) are independent of pH located in the range of $\sim +0.2$ V. Overall, the values obtained in this work and available literature data using comparable experimental conditions and similar magnetite phases fit satisfactorily well to each other regarding the uncertainties coupled to redox potential measurements as stated above.

Batch Experiment Results

In Figure 2 results of the kinetic batch experiments for U are depicted. Table 1 lists additional details about the results.

Regarding the samples at pH 2.5, U concentrations decrease slightly to $\sim 2.5 \times 10^{-5}$ M until 48 d and afterwards increase to a concentration of $\sim 3.17 \times 10^{-5}$ M after 90 d. The scatter in the data is referred to analytical uncertainties of the ICP-MS measurements. Moreover, precipitation of a U solid phase should not occur since the concentrations are below the solubility of e.g. schoepite for the pH conditions prevailing (Langmuir, 1978). A reduction to a tetravalent colloidal U phase cannot be excluded a priori (Neck and Kim, 2001) but is unlikely regarding the thermodynamic modeling results on basis of the measured redox potentials (+ 0.56 V).

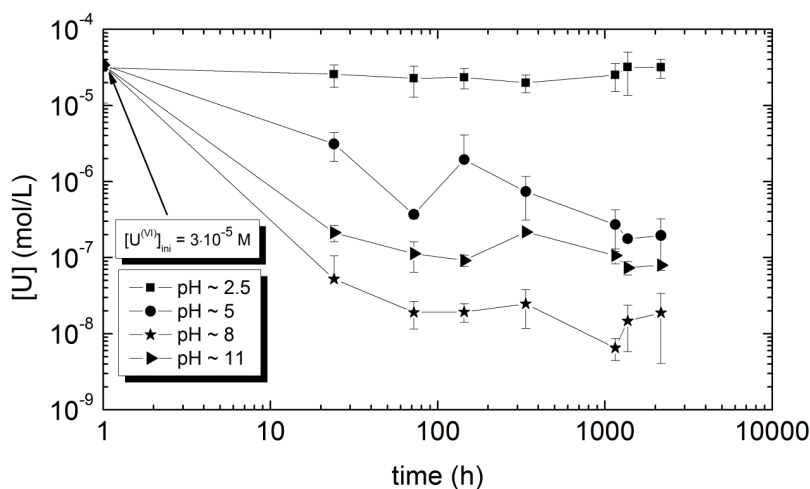


Figure 2: Results of the kinetic batch experiments using po-mag as solid phase.

Concerning the sample series at pH 5 a fast decrease in concentration of about one order of magnitude (3.1×10^{-6} M) is visible after 24h. An ongoing decrease in U concentration is detectable until the end of the experiments with a final concentration after 90 d of $\sim 1.9 \times 10^{-7}$ M which is more than two orders of magnitude lower than the initial concentration. The scattering of the data at 6 d and 14 d is most probably related to slight fluctuations in pH and Eh. Regarding Eh/pH conditions given in Figure 1b the positively charged $(\text{UO}_2)_3(\text{OH})_5^+$ species and the amorphous tetravalent $\text{UO}_{2(\text{am})}$ species dominate at this pH, thus both sorption and/or reduction can be responsible for the U removal from solution. Moreover, regarding the solubility of hexavalent U, precipitation of a U containing mineral phase (U-oxide/hydroxide; Fe-U phase) like e.g. schoepite cannot be excluded which could as well explain the decrease in U concentration. On the other hand, the sample preparation procedure was chosen in a way to minimize precipitation. That is, after spiking of U to the suspension, the pH of the samples was around pH ~ 2.4 where no precipitation and only slight sorption should occur. Subsequently, pH was slowly adjusted by addition of small amounts of HCl and NaOH favoring sorption to the magnetite surface before a precipitation should occur.

The fastest and most pronounced decrease in U concentration is observed for the pH 8 sample series. Here, after one day U concentration is almost 3 orders of magnitude lower ($\sim 5.2 \times 10^{-8}$ M) than the initial U concentration at the beginning of the experiments. In the course of the experiment a less pronounced decrease in U concentration is observed possibly indicating near equilibrium conditions after 90 d ($\sim 1.9 \times 10^{-8}$ M). Here, sorption of the hexavalent $(\text{UO}_2)_3(\text{OH})_5^+$ species to the negatively charged magnetite surface seems a reasonable explanation for the U removal. Moreover, besides a precipitation of a hexavalent U phase a reduction to the tetravalent $\text{UO}_{2(\text{am})}$ is thermodynamically feasible.

In case of the sample series at pH 11, an initial concentration decrease after 1 d of about 2 orders of magnitude ($\sim 2.1 \times 10^{-7}$ M) is measured which again is less pronounced in the further course of the experiment ($\sim 7.9 \times 10^{-8}$ M after 90 d) as it is the case for the series at pH 8. The calculated speciation for pH 11 yields the negatively charged $\text{UO}_2(\text{OH})_3^-$ species which may lead to a lesser pronounced sorption behavior to the likewise negatively charged magnetite due to electrostatic effects. This circumstance may also explain the lower sorption compared to pH 8 where a positively charged U species prevails. In general, it can be stated that the processes responsible for the removal of the U from the solution (sorption, precipitation and/or reduction) show initially fast kinetics reaching near equilibrium conditions after 24 h. These results tally well to results presented by (Scott et al., 2005) for U interaction with natural magnetite single crystals at pH ~ 4.8 (U concentration = $\sim 4 \times 10^{-5}$ M and $\sim 4.4 \times 10^{-4}$ M) showing fast initial U removal (sorption) kinetics. Furthermore, the macroscopic batch kinetic results presented by Missana et al. (2003a) also show a U removal in the presence of magnetite of about 90 % after 1 d contact time for pH ~ 7 (U concentration = 4.4×10^{-7} M).

Table 1: Results of the batch experiments (samples in bold style are measured by XPS).

Series #	Sample name	Contact Time (d)	pH	U [initial] (M)	U [final] (M)	U removed (%)	U (M/m ²)
#1	po-mag#1	1	2.5	3×10 ⁻⁵	2.56×10 ⁻⁵	14.50	1.11×10 ⁻⁰⁷
#1	po-mag#2	1	5	3×10⁻⁵	3.11×10⁻⁶	89.63	6.81×10⁻⁰⁷
#1	po-mag#3	1	8	3×10⁻⁵	5.25×10⁻⁸	99.83	7.58×10⁻⁰⁷
#1	po-mag#4	1	11	3×10 ⁻⁵	2.13×10 ⁻⁷	99.29	7.54×10 ⁻⁰⁷
#1	po-mag#5	3	2.5	3×10 ⁻⁵	2.27×10 ⁻⁵	24.06	1.84×10 ⁻⁰⁷
#1	po-mag#6	3	5	3×10 ⁻⁵	3.70×10 ⁻⁷	98.77	7.50×10 ⁻⁰⁷
#1	po-mag#7	3	8	3×10 ⁻⁵	1.91×10 ⁻⁸	99.94	7.59×10 ⁻⁰⁷
#1	po-mag#8	3	11	3×10 ⁻⁵	1.13×10 ⁻⁷	99.62	7.57×10 ⁻⁰⁷
#1	po-mag#9	6	2.5	3×10 ⁻⁵	2.33×10 ⁻⁵	22.09	1.69×10 ⁻⁰⁷
#1	po-mag#10	6	5	3×10 ⁻⁵	1.94×10 ⁻⁶	93.52	7.10×10 ⁻⁰⁷
#1	po-mag#11	6	8	3×10 ⁻⁵	1.93×10 ⁻⁸	99.94	7.59×10 ⁻⁰⁷
#1	po-mag#12	6	11	3×10 ⁻⁵	9.20×10 ⁻⁸	99.69	7.57×10 ⁻⁰⁷
#1	po-mag#13	14	2.5	3×10 ⁻⁵	1.98×10 ⁻⁵	33.88	2.58×10 ⁻⁰⁷
#1	po-mag#14	14	5	3×10 ⁻⁵	7.39×10 ⁻⁷	97.54	7.41×10 ⁻⁰⁷
#1	po-mag#15	14	8	3×10 ⁻⁵	2.48×10 ⁻⁸	99.92	7.59×10 ⁻⁰⁷
#1	po-mag#16	14	11	3×10 ⁻⁵	1.09×10 ⁻⁷	99.64	7.57×10 ⁻⁰⁷
#1	po-mag#17	48	2.5	3×10 ⁻⁵	2.52×10 ⁻⁵	16.09	1.21×10 ⁻⁰⁷
#1	po-mag#18	48	5	3×10 ⁻⁵	2.72×10 ⁻⁷	99.09	7.52×10 ⁻⁰⁷
#1	po-mag#19	48	8	3×10 ⁻⁵	6.50×10 ⁻⁹	99.98	7.59×10 ⁻⁰⁷
#1	po-mag#20	48	11	3×10 ⁻⁵	1.06×10 ⁻⁷	99.65	7.57×10 ⁻⁰⁷
#1	po-mag#21	57	2.5	3×10 ⁻⁵	3.18×10 ⁻⁵	0.00	2.53×10 ⁻⁰⁹
#1	po-mag#22	57	5	3×10 ⁻⁵	1.77×10 ⁻⁷	99.41	7.55×10 ⁻⁰⁷
#1	po-mag#23	57	8	3×10 ⁻⁵	1.47×10 ⁻⁸	99.95	7.59×10 ⁻⁰⁷
#1	po-mag#24	57	11	3×10 ⁻⁵	7.35×10 ⁻⁸	99.76	7.58×10 ⁻⁰⁷
#1	po-mag#25	90	2.5	3×10 ⁻⁵	3.17×10 ⁻⁵	0.00	5.06×10 ⁻⁰⁹
#1	po-mag#26	90	5	3×10 ⁻⁵	1.95×10 ⁻⁷	99.35	7.54×10 ⁻⁰⁷
#1	po-mag#27	90	8	3×10 ⁻⁵	1.89×10 ⁻⁸	99.94	7.59×10 ⁻⁰⁷
#1	po-mag#28	90	11	3×10 ⁻⁵	7.98×10 ⁻⁸	99.73	7.57×10 ⁻⁰⁷
#1	po-mag#29	1	5.5	3×10⁻⁵	2.27×10⁻⁶	92.43	7.02×10⁻⁰⁷
#1	po-mag#30	1	9.58	3×10⁻⁵	3.76×10⁻⁶	87.45	6.64×10⁻⁰⁷
#1	po-mag#31	1	5.37	3×10⁻⁵	n.m.	-	
#1	po-mag#32	1	9.46	3×10⁻⁵	n.m.	-	
#1	po-mag#33	1	6.13	3×10⁻⁵	n.m.	-	
#1	po-mag#34	1	6.22	3×10⁻⁵	n.m.	-	
#1	po-mag#35	1	10.4	3×10⁻⁵	n.m.	-	
#1	po-mag#36	1	5.5	3×10⁻⁵	n.m.	-	
#1	po-mag#37	1	10.4	3×10⁻⁵	n.m.	-	
#2	fmag#1	13	7.6	3×10 ⁻⁵	3.63×10 ⁻⁹	99.9	1.01×10 ⁻⁰⁶
#2	fmag#2	13	10.86	3×10 ⁻⁵	2.04×10 ⁻⁸	99.9	1.01×10 ⁻⁰⁷
#2	fmag#3	13	5.35	3×10 ⁻⁵	9.50×10 ⁻⁶	96.8	6.93×10 ⁻⁰⁷
#3	mgh#1	13	10.94	3×10 ⁻⁵	6.83×10 ⁻⁸	99.9	1.34×10 ⁻⁰⁶
#3	mgh#2	13	8.22	3×10 ⁻⁵	2.01×10 ⁻⁹	99.9	1.34×10 ⁻⁰⁶
#3	mgh#3	13	5.19	3×10 ⁻⁵	2.52×10 ⁻⁶	91.6	1.23×10 ⁻⁰⁶

Spectroscopic Results

Since no conclusion about the U removal mechanism can be drawn solely on basis of the macroscopic batch results, spectroscopic measurements (XPS) are applied to reveal if sorption, reduction and/or precipitation are the mechanisms responsible for the decrease in aqueous U concentration.

Fe(II) speciation. Selected samples were analyzed to determine the Fe(II)/Fe_{TOT} ratios. Since Fe(II) is the only potential redox agent for U reduction present in the experiments, this information is crucial concerning their redox capacity. In this work, the Fe 2p spectra are measured to estimate Fe(II)/Fe_{TOT} ratios on the mineral surfaces. More precisely, the intensity of the shoulder on lower binding energy side at the Fe 2p_{3/2} elemental line is representative for the amount of Fe(II) present. The intensity of the shoulder is determined within a band of 708.5 eV to 708.7 eV binding energy and set into relation to spectra of a freshly prepared magnetite and a hematite powder (Fe₂O₃ puratronic, Alfa Aesar) by use of normalized spectra (Figure 3a). Error in Fe(II) portion determination in this way is estimated to be about $\pm 5\%$.

Table 4 lists the corresponding Fe(II)/Fe_{TOT} ratios after reaction with U for the samples measured. The Fe(II)/Fe_{TOT} ratio of the po-mag samples range between 10.9 % to 27.3 % with a mean value of 22 %, while the fmag samples range between 24.8 % to 33.2 % with a mean value of 30.1 %. The mgh samples show values of only 0-2 % Fe(II)/Fe_{TOT} on the surface which is in the range of the analytical uncertainty. These results confirm a partly oxidization of the po-mag with roughly 30 % lower Fe(II) content than the fmag samples. In addition, the amount of Fe(II)/Fe_{TOT} is clearly a function of pH reflecting the preferential dissolution of Fe(II) out of the magnetite structure at low pH, since the amount of Fe(II)/Fe_{TOT} increases with increasing pH (Jolivet and Tronc. 1988; White et al.. 1994). This trend follows the general curve of magnetite dissolution which is more pronounced in the acidic pH range. If U reduction occurs, an increase in Fe(III) (corresponding to a decrease in the Fe(II)/Fe_{TOT} ratio) should occur due to Fe(II) oxidization and the shoulder in the Fe 2p_{3/2} spectra should become less pronounced. However, the changes on the surface of the solid phases expected based on the U concentrations used before and after reaction are too small to be resolved by the analytical technique.

U speciation. The U 4f_{7/2} elemental line was used to determine the redox state of U in the selected batch samples of all three different series. Concerning different U valence states, a chemical shift is observed. A separation between the bands for U(VI) to U(V) and U(V) to U(IV) is reported in the literature with values of 0.9 eV (Bera et al.. 1998) and 0.6 eV (Schindler et al.. 2009), respectively. Schindler et al. (2009) conducted XPS measurements using various U containing mineral phases and reported binding ranges for the different valence states as follows: U(VI) within 381.1 – 382.6 eV. U(V) within 380.5 – 381.2 eV and U(IV) within 380.2 – 380.7 eV, respectively. The range of values reflect the fact, that the binding energies vary (chemical shift) as a function of compound chemical composition, crystal structure and type and number of nearest-neighbour ions. The binding energy ranges determined in the present study are for U(VI) and U(IV) 381.1 – 381.7 eV and 380.1 - 380.6 eV, respectively. In addition to the

U 4f main peaks, small satellite peaks at higher binding energies are sometimes used for spectral interpretation (Keller and Jorgensen, 1975). (Ilton et al., 2010). These satellites are positioned (towards higher binding energies of the U 4f peaks) at 6-7 eV for U(IV), 7.8-8.5 eV for U(V) and 4 and 10 eV for U(VI), respectively. The shape of the U 4f_{7/2} peak and satellites are used for determination of the different valence states (Schindler et al., 2009). However, in the present work these satellite peaks are of low intensity due to low surface concentrations of U. That is, if the signal to noise ratio is low the intensities of the satellite peaks are within noise level and not resolved.

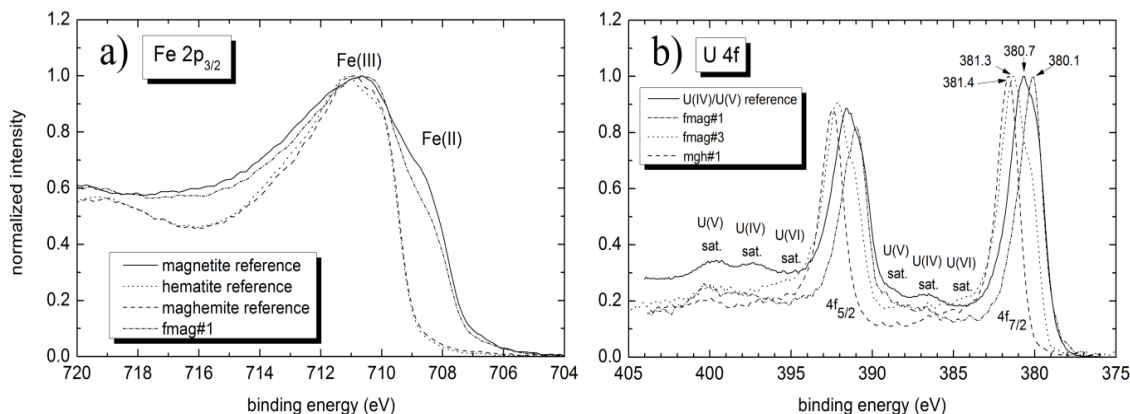


Figure 3: a) XPS Fe 2p_{3/2} spectra for the magnetite reference, sample fmag#3, hematite reference and maghemite reference showing the amount of Fe(II) and Fe(III). B) XPS U 4f spectra of the UO_x-Pd film with U(IV,V), fmag#1 and fmag#3 samples. Additionally, the peak position of U(VI), U(V) and U(IV) are indicated in conjunction with their corresponding satellites of the U 4f peaks.

As a “reference” for U(IV) and U(V), we measured U 4f spectra of an oxidized UO₂-Pd thin film vapour-deposited onto a semiconducting silicon wafer and stored in air (received from Institute of Transuranium Elements, JRC-ITU, Karlsruhe). The 4f_{7/2} spectrum consists of two main components with binding energies at 379.9 eV, assigned to U(IV) and 380.9 eV assigned to U(V). Two satellites of the 4f spectrum are observed, one satellite with spacing of 6.5 eV to the 4f main lines assigned to U(IV) and a second satellite with spacing of 8.1 eV to the 4f main lines of U(V). Binding energies of 4f_{7/2} elemental lines and satellites spacings coincide with reported values (Ilton et al., 2010 in case of U(V); (Ilton et al., 2007) reports U(IV) satellites spacing between 6.3 to 6.8 eV) and thus confirm the appropriate assignments to the 4f main components concerning U valence in our study (Figure 3b). Satellites characteristic for U(VI) oxides are not detected in the UO₂-Pd sample although U(VI) cannot be excluded to be present at low concentration on the outermost surface, since a curve fit to the U 4f_{7/2} spectrum indicates less than 8 % of U is U(VI). In case of U(VI), a binding energy of 381.4 eV was determined on basis of the sample magh#1 (maghemite; pH 10.94;) which showed only U(VI) on the mineral surface (Figure 6).

To estimate the amounts of the U valence states of U reacted magnetite, U 4f_{7/2} spectra are curve fitted by Gaussian-Lorentzian sum functions with same Gaussian fractions and FWHM.

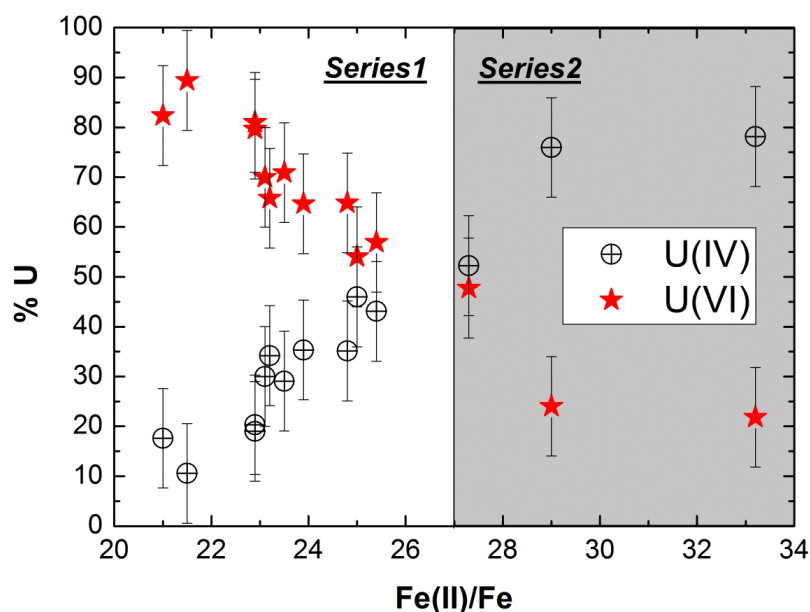


Figure 4: U speciation as function of $\text{Fe(II)/Fe}_{\text{TOT}}$ content for all samples measured by XPS in the experiments. Note the trend in increasing U(IV) with increasing $\text{Fe(II)/Fe}_{\text{TOT}}$ content and vice versa. the trend of decreasing U(V) and U(VI) with increasing $\text{Fe(II)/Fe}_{\text{TOT}}$ content. respectively in case of Series#1 and Series#2.

Series#1 (po-mag; $\leq 90d$ contact time). In total 11 different batch samples have been measured after a contact time of 1 d (Figure 4 and Table 2). The $\text{Fe(II)/Fe}_{\text{TOT}}$ ratios of all samples are located in the range between 21 % up to 25.3 %. For low Fe(II) amounts (21 % to ~ 23 %). the U speciation determined by XPS is dominated by U(VI) with ~ 65 % - 90 % and only about 10 % - 35% for U(IV). With increasing Fe(II) (up to 25 %). the amount of U(VI) decreases to ~ 50 % to 60 % and the amount of U(IV) increases to ~ 40 % – 45 %. Consequently, the sample with the highest $\text{Fe(II)/Fe}_{\text{TOT}}$ ratio (27.3 %) shows the highest amount of U(IV) (~ 52 %) and 48 % of U(VI). To sum up, Series#1 indicates that the reduction of U can be correlated to the available $\text{Fe(II)/Fe}_{\text{TOT}}$ ratio on the magnetite surface leading to an increase in U(IV) with rising $\text{Fe(II)/Fe}_{\text{TOT}}$ ratio.

Series#2 (fmag; 13 d contact time). Three samples at pH ~ 5.3 . ~ 7.6 and ~ 10.9 have been analyzed after a contact time of 13 days (Figure 3 and 4). The fmag#3 sample has a considerable lower $\text{Fe(II)/Fe}_{\text{TOT}}$ ratio (24.8 %) as the fmag#1 and fmag#2 sample with ratios of 29 % and 33.2 %. respectively. In consequence, the fmag#3 sample has the lowest U(IV) content (37%) compared to the fmag#1 and fmag#2 samples with ~ 76 % and ~ 78 %. respectively. Again, these findings further corroborate the trend that with increasing

Table 2: Overview of all samples measured by XPS.

Series	sample name	contact time (d)	pH (-)	Eh (V)	Fe(II)/Fe _{TOT} (-)	U(IV) (%)	U(VI) (%)
#1	po-mag#2	1	5.9	0.07	25.4	43	57
#1	po-mag#3	1	9.6	-0.028	23.9	35	65
#1	po-mag#29	1	5.5	0.112	23.5	29	71
#1	po-mag#30	1	9.58	-0.01	22.9	19	81
#1	po-mag#31	1	5.37	0.054	23.1	30	70
#1	po-mag#32	1	9.46	-0.001	22.9	20	80
#1	po-mag#33	1	6.13	0.102	27.3	52	48
#1	po-mag#34	1	6.22	0.088	25	46	54
#1	po-mag#35	1	10.4	0.041	23.2	34	66
#1	po-mag#36	1	5.5	0.099	21	18	82
#1	Po-mag#37	1	10.4	0.035	21.5	11	89
#2	fmag#1	13	7.6	32.6	29	76	24
#2	fmag#2	13	10.86	48.1	33.2	78	22
#2	fmag#3	13	5.35	152.4	24.8	37	63
#3	magh#1	13	10.94	204.7	0	100	0
#3	magh#2	13	8.22	197.7	0	96	4
#3	magh#3	13	5.19	218.7	2	92	8

Fe(II)/Fe_{TOT} ratio the amount of U(IV) increases and in turn, the amount of U(VI) decreases as it has been observed in Series#1 and Series#2a.

Series#3 (magh). Identically to Series#2, three maghemite reacted uranium samples have been probed by XPS after a contact time of 13 d to determine both the Fe(II) content and the U speciation. The ratio of Fe(II)/Fe_{TOT} for all three samples is below ~ 2 % within the analytical uncertainty. It was observed that the magh#1 sample shows only U(VI) whereas for magh#2 and magh#3 about 4 and 8% U(IV) are measureable, respectively. A correlation of the amount of U(IV) on the maghemite surface with pH is obvious with decreasing U(IV) for increasing pH. This may indicate that a pronounced dissolution of maghemite at more acidic pH (magh#3 at pH 5.3) releases bulk Fe(II) which has not been fully oxidized in the synthesis step. This Fe(II) may become available for the sorbed U(VI) leading to a reduction of U(VI) to U(IV). Following this line of explanation, maghemite is more stable at higher pH (Cornell and Schwertmann, 1996) explaining the absence of Fe(II) at pH 10.94 (magh#3) where no U(IV) has been observed.

Summary and Conclusions

The prevailing study confirmed the reduction of hexavalent U by nanoparticulate magnetite by means of XPS measurements at concentrations of $\sim 3 \times 10^{-5}$ M. As reduced species, tetravalent U was observed on the magnetite surface. A correlation between the Fe(II) content on the surface of magnetite and the amount of tetravalent U was found. Consequently, the highest tetravalent U content was observed in case of the interaction

with a freshly prepared magnetite which possesses the highest amount of Fe(II) on the surface underpinning the above mentioned correlation.

Removal processes show fast kinetics within 24 h with more than 90 % U associated to the magnetite surface. Specifically, a fast reduction was observed after 1 d contact time with up to 80 % reduced U on the magnetite surface. Overall, the results show that magnetite, both partly oxidized or “non-oxidized”, can effectively reduce hexavalent U, thus representing an effective retention pathway. The presence of pentavalent U, as previously reported in the literature cannot be confirmed or ruled out by XPS investigations under the experimental conditions.

Acknowledgement

The research leading to these results has received funding from the European Union's European Atomic Energy Community's (Euratom) Seventh Framework Programme FP7/2007-2011 under grant agreement n° 212287 (RECOSY project).

References

- Altmaier, M., Neck, V. and Fanghanel, T., 2004. Solubility and colloid formation of Th(IV) in concentrated NaCl and MgCl₂ solution. *Radiochimica Acta*, 92(9-11): 537-543.
- Bera, S., Sali, S.K., Sampath, S., Narasimhan, S.V. and Venugopal, V., 1998. Oxidation state of uranium: an XPS study of alkali and alkaline earth uranates. *Journal of Nuclear Materials*, 255(1): 26-33.
- Cornell, R.M. and Schwertmann, U., 1996. *The Iron Oxides -structure, properties, reactions, occurrence and uses-*. VCH-Verlag, Weinheim, 573 pp.
- El Aamrani, F.C., T.; de Pablo, J., 1999. Experimental and modeling study of the interaction between uranium(VI) and magnetite - TR-99-21. SKB.
- Grambow, B., Smailos, E., Geckeis, H., Müller, R. and Hentschel, H., 1996. Sorption and reduction of uranium(VI) on iron corrosion products under reducing saline conditions. *Radiochimica Acta*, 74: 149-154.
- Grenthe, I., Stumm, W., Laaksuharju, M., Nilsson, A.C. and Wikberg, P., 1992. Redox potentials and redox reactions in deep groundwater systems. *Chemical Geology*, 98(1-2): 131-150.
- Huber, F., Kunze, P., Geckeis, H. and Schäfer, T., 2011. Sorption reversibility kinetics in the ternary system radionuclide–bentonite colloids/nanoparticles–granite fracture filling material. *Applied Geochemistry*, 26(12): 2226-2237.
- Illes, E. and Tombacz, E., 2006. The effect of humic acid adsorption on pH-dependent surface charging and aggregation of magnetite nanoparticles. *Journal of Colloid and Interface Science*, 295(1): 115-123.

- Ilton, E.S. et al.. 2010. Influence of dynamical conditions on the reduction of U(VI) at the magnetite solution interface. *Environmental Science & Technology*. 44(1): 170-176.
- Ilton, E.S., Boily, J.F. and Bagus, P.S.. 2007. Beam induced reduction of U(VI) during X-ray photoelectron spectroscopy: The utility of the U4f satellite structure for identifying uranium oxidation states in mixed valence uranium oxides. *Surface Science*. 601(4): 908-916.
- Jolivet, J.P. and Tronc, E.. 1988. Interfacial Electron-transfer in colloidal spinel iron-oxide - Conversion of Fe₃O₄-gamma-Fe₂O₃ in aqueous medium. *Journal of Colloid and Interface Science*. 125(2): 688-701.
- Keller, C. and Jorgensen, C.K.. 1975. Photoelectron-spectra of uranium(V) in mixed oxides showing characteristic satellite signals. *Chemical Physics Letters*. 32(3): 397-400.
- Kosmulski, M.. 2001. Chemical properties of material surfaces. *Surfactant Science series*. Dekker, New York. 753 pp.
- Langmuir, D.. 1978. Uranium solution-mineral equilibria at low temperatures with applications to sedimentary ore deposits. *Geochim Cosmochim Acta*. 42: 547 - 569.
- Liger, E., Charlet, L. and Van, C.P.. 1999. Surface catalysis of uranium(VI) reduction by iron(II). *Geochim. Cosmochim. Acta*. 63: 2939.
- Lindberg, R.D. and Runnells, D.D.. 1984. Groundwater redox reactions: An analysis of equilibrium state applied to Eh measurements and geochemical modeling. *Science*. 225: 925 - 927.
- Mansour, C. et al.. 2009. Sorption of sulfate ions onto magnetite. *Journal of Colloid and Interface Science*. 331(1): 77-82.
- Missana, T., Maffiotte, U. and Garcia-Gutierrez, M.. 2003. Surface reactions kinetics between nanocrystalline magnetite and uranyl. *Journal of Colloid and Interface Science*. 261(1): 154-160.
- Neck, V. and Kim, J.I.. 2001. Solubility and hydrolysis of tetravalent actinides. *Radiochim. Acta*. 89: 1-16.
- Patterson, A.L.. 1939. The Scherrer Formula for X-Ray Particle Size Determination. *Physical Review*. 56(10): 978.
- Regenspurg, S., Schild, D., Schäfer, T., Huber, F. and Malmström, M.E.. 2009. Removal of uranium(VI) from the aqueous phase by iron(II) minerals in presence of bicarbonate. *Applied Geochemistry*. 24: 1617–1625.
- Schindler, M., Hawthorne, F.C., Freund, M.S. and Burns, P.C.. 2009. XPS spectra of uranyl minerals and synthetic uranyl compounds. I: The U 4f spectrum. *Geochimica et Cosmochimica Acta*. 73(9): 2471-2487.
- Schüring, J.S., H.D.; Fischer, W.R.; Böttcher, J.; Duijnsveld, W.H.M. (Eds.) (Editor). 2000. *Redox - Fundamentals, Processes and Applications*. Springer, Berlin. 273 pp.
- Schwertmann, U. and Cornell, R.M.. 1991. *Iron Oxides in the Laboratory (Preparation and Characterization)*. VCH Verlagsgesellschaft mbH, Weinheim. 137 pp.

Scott. T.B.. Allen. G.C.. Heard. P.J. and Randell. M.G.. 2005. Reduction of U(VI) to U(IV) on the surface of magnetite. *Geochimica et Cosmochimica Acta*. 69(24): 5639-5646.

White. A.F.. Peterson. M.L. and Hochella. M.F.. 1994. Electrochemistry and dissolution kinetics of magnetite and ilmenite. *Geochimica Et Cosmochimica Acta*. 58(8): 1859-1875.



ISSN 1869-9669
ISBN 978-3-86644-921-3

